Anomalous Structural and Spin Transition Behaviours in Stimuli-Responsive Metal-Organic Frameworks

Zixi Xie

A thesis submitted in fulfilment of the requirements for the degree of

Doctor of Philosophy

School of Chemistry

Faculty of Science

The University of Sydney

December 2022

Statement of Student Contribution

I declare that this thesis contains work carried out by myself except where otherwise acknowledged. This work has not been submitted in any form for another dissertation or diploma at any other institution. Information derived from the published or unpublished work of others has been acknowledged in the text and a list of references is provided.

DFT calculations were performed by Dr Ramzi Kutteh. The powder diffraction data collected at the Australian Synchrotron was measured by Dr Anita D'Angelo. The single crystal X-ray diffraction data collected at the Australian Synchrotron was measured by Dr William Lewis, Dr Hunter Windsor and technician staff.

Zixi Xie

December 2022

Abstract

Inspired by nature, the design of artificial stimuli-responsive metal–organic frameworks (SR-MOFs) that are able to dynamically respond to their environment has attracted considerable interest. This is primarily due to their promising applications found within various domains of research including sensing, molecular machines, information storage devices, and biomedicine. MOF materials that exhibit spin crossover (SCO) are one subset of SR-MOFs. The metal nodes of such materials can undergo reversible electronic reconfigurations between the high spin (HS) and low spin (LS) states in response to different stimuli such as temperature, light, and pressure. Not only are these electronic transitions in nature, but they also are able to trigger structural phase transitions and lattice flexing. One key challenge in the design of SR-MOF materials is to achieve targeted and controllable properties under different stimuli. Thus, uncovering the interplay between external stimuli, intrinsic structure, and spin state properties is relevant for creating desirable materials.

This thesis discusses the syntheses and characterisations of a family of new SR-MOFs and their electronic and structural responsivity to temperature, pressure, and guest molecule encapsulation as stimuli. Mixed pillaring ligands and cyanidometallate linkers were used to produce tunable structural properties and SCO behaviours. Anomalous lattice motions associated with negative thermal expansion (NTE) and negative linear compressibility (NLC) induced by temperature and pressure, respectively, were demonstrated.

The SCO performance and structural properties of SR-MOFs can be modulated by guest molecule encapsulation within their porous network structures. A detailed study was performed on how xylene isomers possessing similar physical properties could be discriminated on the basis of how they influence SCO. The single-component xylene isomers were adsorbed into the pores of the prototypical 3D Hofmann-like framework $[Fe(Tz)Au(CN)_2)_2]\cdot EtOH$ (Tz = 3,6-bis(4-pyridyl)-1,2,4,5-tetrazine) to form $[Fe(Tz)(Au(CN)_2)_2]\cdot$*p*-xylene (**TzAu·PX**), $[Fe(Tz)(Au(CN)_2)_2]\cdot$*o*-xylene (**TzAu·OX**), and $[Fe(Tz)(Au(CN)_2)_2]\cdot$*m*-xylene (**TzAu·MX**). Rare asymmetric multi-step SCO behaviours were observed in these three materials upon guest encapsulation. NTE within the Hofmann layers was observed in **TzAu·PX** and **TzAu·OX** owing to their wine-rack structures. SCO site distortion, lattice flexing, C–H···N interactions, and aurophilic and π···π interactions were examined to illustrate the relationship between structure and SCO in these materials. The uptake and SCO behaviours for binary mixtures of xylene isomers were also studied.

The analogous 3D Hofmann-like MOF containing the Dz ligand (Dz = 3,6-bis(4-pyridyl)-1,2-diazine) was also prepared, as were the equivalent single-component xylene isomer clathrates $[Fe(Dz)(Au(CN)_2)_2]\cdot$*p*-xylene (**DzAu·PX**), $[Fe(Dz)(Au(CN)_2)_2]\cdot$*o*-xylene (**DzAu·OX**), and $[Fe(Dz)(Au(CN)_2)_2]\cdot$*m*-xylene (**DzAu·MX**). Similarly, these systems were examined to gain a deeper

understanding of the relationships between host–guest, structural, and SCO properties. Gradual incomplete two-step SCO, incomplete one-step SCO, and no SCO were observed in **DzAu·PX**, **DzAu·MX**, and **DzAu·OX**, respectively. The interplay between the structural properties of these materials and their weakly cooperative SCO was explored. Comparing the Tz- and Dz-based frameworks reveals the influences of ligand field strength, host–host, and host–guest interactions in modulating their SCO behaviours. The uptake of binary-component xylene mixtures within the pores shows an overwhelming preference for MX over PX and OX over PX in the equimolar mixtures of two xylenes.

Not only can SCO be tuned by altering the guest molecules, but also by the building units, i.e., the cyanidometallate spacers themselves. The influence of cyanidometallate linkers on the structural and magnetic properties of these systems was explored. The 3D Hofmann-like frameworks consisting of single-component bridging dicyanidoaurate(I) or dicyanidoargenate(I) linkers or binary-component mixtures of both linkers were synthesised: $[Fe(Dz)(Ag(CN)_2)_2]\cdot EtOH$ (**DzAg·EtOH**), $[Fe(Tz)(Ag(CN)_2)_2]\cdot EtOH$ (**TzAg·EtOH**), $[Fe(Dz)(Au(CN)_2)_2]\cdot EtOH$ (**DzAu·EtOH**), $[Fe(Tz)(Au(CN)_2)_2]\cdot EtOH$ (**TzAu·EtOH**), $[Fe(Tz)((Au(CN)_2)_{0.5}(Ag(CN)_2)_{0.5})_2]\cdot EtOH$, (**$TzAu_{0.5}Ag_{0.5}$·EtOH**), $[Fe(Dz)((Au(CN)_2)_{0.5}(Ag(CN)_2)_{0.5})_2]\cdot EtOH$ (**$DzAu_{0.5}Ag_{0.5}$·EtOH**), and $[Fe(Tz)((Au(CN)_2)_{0.7}(Ag(CN)_2)_{0.3})_2]\cdot EtOH$ (**$DzAu_{0.7}Ag_{0.3}$·EtOH**). Anomalous lattice motions (NTE) were observed in the Tz-based materials. The higher proportion of dicyanidoaurate(I) linkers in the frameworks promoted a greater degree of scissor motion and subsequent lattice flexing. The Tz-based frameworks all display one-step SCO. In the Dz-based frameworks, **DzAu·EtOH** exhibits four-step SCO, while the rest exhibit three-step SCO. The spin transition temperatures can be controlled by altering the ratio of the two cyanidometallate linkers. It was observed that increasing the relative amount of dicyanidoargentate(I) led to an increase in the spin transition temperatures for both the Tz- and Dz-based frameworks. The host–host C–H···N and metallophilic interactions were examined and provided insight into the mechanism of lattice motions, distortions, and SCO in these materials. $[Fe(Dz)(H_2O)_2(Pt(CN)_2)_2]\cdot 2(H_2O)$ (**DzPt**) and $[Fe(Dz)(H_2O)_2(Pd(CN)_2)_2]\cdot 2(H_2O)$ (**DzPd**) were also synthesised, with both adopting accordion-like topologies. However, no SCO was observed in either of these materials.

Tuning the spin transition temperatures and extent of scissor motions were achieved by altering the ratio of Tz and Dz pillaring ligands. The series of mixed ligand frameworks of the form $[Fe(Tz)_x(Dz)_{1-x}(Au(CN)_2)_2]\cdot n$EtOH ($x$ =1.0–0.2) were synthesised. All the series members that adopt an orthorhombic phase exhibit one-step SCO and scissor motions. Notably, with a decrease of the relative amount of Tz ligand, a greater thermal expansion coefficient and lower spin transition temperature were observed. $[Fe(Tz)_{0.2}(Dz)_{0.8}(Au(CN)_2)_2]\cdot n$EtOH exhibits the largest extent of NTE ($\alpha_a = -3277 \times 10^{-6}\ K^{-1}$) and PTE ($\alpha_b = +7187 \times 10^{-6}\ K^{-1}$). When continuously reducing the amount of Tz to x = 0.15, 0.1, and 0, structural interconversion between an orthorhombic and monoclinic phase was

demonstrated in these materials *via* controlling temperature. The shape memory behaviour was observed in bulk powder **DzAu·EtOH**, which has the capability to memorise both phases. The materials with $x = 0.15$ and 0.1 show a unique thermal cycling dependence on their four-step SCO behaviours, which is attributed to the gradual process of the phase transition. Investigating this family of doped materials elucidates the role that C–H···N host–host interactions have on their resulting structural properties and SCO behaviours.

Investigations into pressure-induced SCO are rare in the literature. **TzAu·EtOH**, **DzAu·EtOH**, and $[Fe(Tz)_{0.5}(Dz)_{0.5}Au(CN)_2)_2]\cdot x(EtOH)$ (**[$Tz_{0.5}Dz_{0.5}$]**) were synthesised and their pressure-induced SCO behaviours were examined. Both **TzAu·EtOH** and **[$Tz_{0.5}Dz_{0.5}$]** exhibit NLC along one lattice direction and PLC along another (i.e., scissor motions induced by pressure). A greater magnitude of scissor motion was observed in **TzAu·EtOH** this is associated with the number of the C–H···N hydrogen bonding interactions, distortion of the SCO sites, and flexing of the lattices. Interestingly, all the materials display a counterintuitive behaviour that includes stabilisation of the HS state upon pressurisation.

Overall, controlling the structural and SCO properties in SR-MOFs can be achieved by tuning external stimuli such as temperature, pressure, and guest molecules. Alternatively, a similar level of control can be achieved by altering the inner building blocks of SR-MOFs. The systems discussed in this thesis include both the pillaring ligands and cyanidometallates. The insights gained into these SR-MOFs reveal the complex interplay between the various stimuli, reversible SCO behaviours, and structural distortions. This work should pave the way towards the rational design of controllable 'smart' materials.

Acknowledgements

First and foremost, I would like to express my sincerest gratitude to my supervisor, Professor Cameron Kepert, for his continued support, and for his advice and expertise which guided me to deeper investigate the research project. Thank you for giving me the freedom to take my research project. Thank you for always supporting me to attend conferences to present my research work and for helping with scholarships and funding applications. I would like to extend thank you to my ANSTO co-supervisor Professor Vanessa Peterson for her guidance and enthusiasm toward my project. She has enlightened me with her vast knowledge of powder diffraction and structural analysis. Also, a big thank you to my auxiliary supervisor Professor Deanna D'Alessandro for her useful discussions and encouragement.

A big thank you to the past and present members of the Molecular Materials group. Special thank you to Dr Hunter Windsor, Dr Marcello Solomon, Dr David Dharma and Andrew Braz for editing my thesis chapters, useful advice and discussions. Great thank you to Senior Lecture Lauren Macreadie for your enthusiasm and support, and especially thank you for all the help to the International School of Crystallography in Italy. Thank you to Qinyi Gu, Andrew Braz and Harrison Moore for the interesting conversations since Honours.

Outside the Molecular Materials group, I would like to thank Associate Professor Suzanne Neville from UNSW for her support and discussions. I enjoyed the time collaborating with you and publishing our research outcomes. Thank you to Dr Samuel Duyker for your help and advice in powder X-ray diffraction measurements at Sydney Analytical, neutron powder diffraction measurements at ANSTO, data analysis and my manuscripts. Thank you to Dr William Lewis for collecting single crystal X-ray diffraction data and answering my crystallography questions. Thank you to Dr Ramzi Kutteh for the DFT calculations. Thank you to Dr Anita D'Angelo for collecting the powder diffraction data collected at the Australian Synchrotron. Thank you to the technician staff at ANSTO for the support of measurements. Thank you to the technician staff who support and take care of the instruments within the School of Chemistry, Sydney Analytical and Australian Centre for Microscopy and Microanalysis (ACMM), Dr Rene Macquart, Dr Natasha Sciortino, Dr Paul Fitzgerald, Dr Michelle Wood, Dr Joonsup Lee, Dr Sarah Kelloway, Dr Ahmed Owais, Dr Ashalatha Indiradevi Kamalasanan Pillai and Dr Hongwei Liu. Thank you to the National Deuteration Facility staff and technicians who help with the neutron diffraction measurements set up at ANSTO.

I would like to thank the love and care of my friends. A special thank you to my housemate Nian Kee Tan and my lovely friend Yen Theng Cheng. Most importantly, the biggest thank you must go to my parents for all your unconditional love. Thank you for your endless support and encouragement. Thank you for all the messages and video calls during these years so I wouldn't get too homesick.

Without you all backing me, I wouldn't have made it this far.

I would also like to acknowledge several funding sources: Postgraduate Research Scholarship on Responsive Metal Organic Frameworks, Australian Institute for Nuclear Science and Engineering (AINSE) Postgraduate Research Award (PGRA), Postgraduate Research Support Scheme (PRSS), International School of Crystallography funding and RACI Women in Materials Chemistry promotion Program funding.

Table of Contents

Statement of Student Contribution i

Abstract ii

Acknowledgements v

Table of Contents vii

List of Figures xiii

List of Tables xxvii

General Abbreviations and Symbols xxix

Ligand and Compound Abbreviations xxxi

List of Publications and Conference Presentations xxxiii

Chapter 1 1

1.1 Background and Motivation 2

1.2 Stimuli-Responsive Metal-Organic Frameworks (SR-MOFs) and Spin Crossover (SCO) Phenomenon 2

1.2.1 Overview of SR-MOFs 2

1.2.2 Overview of SCO 3

1.2.3 Thermally-Induced SCO 6

1.2.4 Pressure-Induced SCO 8

1.2.5 Light-Induced SCO 10

1.2.6 Guest Influence on SCO 10

1.2.7 Hofmann Frameworks 12

1.3 Flexible Metal-Organic Frameworks (FMOFs) 14

1.3.1 Elasticity and Memory Effect 14

1.3.2 Anomalous Structural Distortion 16

1.4 Strategies for Designing Controllable MOFs 18

1.4.1 Postsynthetic Modification (PSM) Approach 18

1.4.2 Core-shell Approach 18

1.4.3 Mixed-ligands and Mixed-metals Approach 19

1.5 Research Aims 20
1.6 References 22
Chapter 2 32
2.1 General Materials 33
2.2 Synthesis 33
2.2.1 Synthesis of 3,6-bis(4-pyridyl)-1,2,4,5-tetrazine (Tz) 33
2.2.2 Synthesis of 3,6-bis(4-pyridyl)-1,2-diazine (Dz) 33
2.2.3 Synthesis of Bulk Powder $[Fe(Tz)(Au(CN)_2)_2]\cdot n(EtOH)$ (**TzAu·EtOH**) 34
2.2.4 Synthesis of Single Crystals $[Fe(Tz)(Au(CN)_2)_2]\cdot n(EtOH)$ 34
2.2.5 Synthesis of Bulk Powder $[Fe(Dz)(Au(CN)_2)_2]\cdot n(EtOH)$ (**DzAu·EtOH**) 34
2.2.6 Synthesis of Single Crystals $[Fe(Dz)(Au(CN)_2)_2]\cdot n(EtOH)$ 35
2.2.7 Guest Exchange Method 35
2.2.8 Synthesis of Single Crystals $[Fe(Tz)(Ag(CN)_2)_2]\cdot n(EtOH)$ (**TzAg·EtOH**) 36
2.2.9 Synthesis of Bulk Powder $[Fe(Tz)(Ag(CN)_2)_2]\cdot n(EtOH)$ 36
2.2.10 Synthesis of Single Crystals $[Fe(Tz)((Au(CN)_2)_{0.5}(Ag(CN)_2)_{0.5})_2]\cdot n(EtOH)$ (**$TzAu_{0.5}Ag_{0.5}$·EtOH**) 36
2.2.11 Synthesis of Bulk Powder $[Fe(Tz)((Au(CN)_2)_{0.5}(Ag(CN)_2)_{0.5})_2]\cdot n(EtOH)$ 36
2.2.12 Synthesis of Single Crystals $[Fe(Dz)(Ag(CN)_2)_2]\cdot n(EtOH)$ (**DzAg·EtOH**) 37
2.2.13 Synthesis of Bulk Powder $[Fe(Dz)(Ag(CN)_2)_2]\cdot n(EtOH)$ 37
2.2.14 Synthesis of Single Crystals $[Fe(Dz)((Au(CN)_2)_{0.5}(Ag(CN)_2)_{0.5})_2]\cdot n(EtOH)$ (**$DzAu_{0.5}Ag_{0.5}$·EtOH**) 37
2.2.15 Synthesis of Bulk Powder $[Fe(Dz)((Au(CN)_2)_{0.5}(Ag(CN)_2)_{0.5})_2]\cdot n(EtOH)$ 38
2.2.16 Synthesis of Bulk Powder $[Fe(Dz)((Au(CN)_2)_{0.7}(Ag(CN)_2)_{0.3})_2]\cdot n(EtOH)$ (**$DzAu_{0.7}Ag_{0.3}$·EtOH**) 38
2.2.17 Synthesis of Single Crystals $[Fe(Dz)(H_2O)_2Pt(CN)_4]\cdot 2(H_2O)$ (**DzPt**) 38
2.2.18 Synthesis of Bulk Powder $[Fe(Dz)(H_2O)_2Pt(CN)_4]\cdot 2(H_2O)$ 38
2.2.19 Synthesis of Single Crystals $[Fe(Dz)(H_2O)_2Pd(CN)_4]\cdot 2(H_2O)$ (**DzPd**) 39
2.2.20 Synthesis of Bulk Powder $[Fe(Dz)(H_2O)_2Pd(CN)_4]\cdot 2(H_2O)$ 39
2.2.21 Synthesis of Bulk Powder $[Fe(Tz)_x(Dz)_{1-x}Au(CN)_2)_2]\cdot n(EtOH)$ 39
2.3 Experimental Techniques 39

2.3.1 Nuclear Magnetic Resonance (NMR) Spectroscopy 39
2.3.2 Powder X-ray Diffraction (PXRD) and Variable Temperature Powder X-ray Diffraction (VT-PXRD) 40
2.3.3 Single Crystal X-ray Diffraction (SCXRD) 41
2.3.4 Variable Temperature (VT) Magnetic Susceptibility 41
2.3.5 Variable Pressure (VP) Magnetic Susceptibility 42
2.3.6 Infrared (IR) Spectroscopy 43
2.3.7 Variable Temperature Raman Spectroscopy (VT-Raman) 44
2.3.8 Variable Temperature UV-Vis-Near Infrared (VT-UV) 44
2.3.9 Differential Scanning Calorimetry (DSC) 44
2.3.10 Thermogravimetric Analysis (TGA) 44
2.3.11 X-ray Photoelectron Spectroscopy (XPS) 45
2.3.12 Scanning Electron Microscopy (SEM) and Energy-dispersive X-ray Spectroscopy (EDS) 45
2.3.13 Density Functional Theory Calculations (DFT) 45
2.3.14 High-pressure Neutron Powder Diffraction (NPD) 46
2.4 References 46
Chapter 3 48
3.1 Overview 49
3.2 Structural Characterisation of TzAu·Guest (Guest = OX, PX, MX) 50
3.2.1 Single Crystal Structure of **TzAu·OX** 50
3.2.2 Powder X-Ray Diffraction of **TzAu·OX** 54
3.2.3 Single Crystal Structure of **TzAu·PX** 55
3.2.4 Powder X-Ray Diffraction of **TzAu·PX** 57
3.2.5 Powder X-Ray Diffraction Structure of **TzAu·MX** 60
3.3 Spin Crossover Behaviours of TzAu·Guest (Guest = OX, PX, MX) 61
3.3.1 Variable Temperature Magnetic Susceptibility of **TzAu·MX** 61
3.3.2 Variable Temperature Magnetic Susceptibility of **TzAu·OX** 62
3.3.3 Variable Temperature Magnetic Susceptibility of **TzAu·PX** 66
3.3.4 Raman Spectroscopy 69

3.4 Binary Xylene Mixtures on TzAu 70
3.4.1 Powder X-ray Diffraction of TzAu Framework with Xylene Guest Mixtures 70
3.4.2 Variable Temperature Magnetic Susceptibility of TzAu with a binary mixture solvent of PX, OX, and MX 75
3.4.3 NMR of guest components within the frameworks 78
3.5 Conclusions and Future Work 79
3.6 References 82
Chapter 4 85
4.1 Overview 86
4.2 Structure Characterisation of DzAu·Guest (Guest = OX, PX, MX) 87
4.2.1 Single Crystal Structure of **DzAu·OX** 87
4.2.2 Powder X-Ray Diffraction of **DzAu·OX** 93
4.2.3 Single Crystal X-ray Structure of **DzAu·MX** 94
4.2.4 Powder X-Ray Diffraction of **DzAu·MX** 98
4.2.5 Single Crystal X-ray Structure of **DzAu·PX** 98
4.2.6 Powder X-Ray Diffraction of **DzAu·PX** 103
4.3 Spin Crossover Behaviours of DzAu·Guest (Guest = OX, PX, MX) 103
4.3.1 Variable Temperature Magnetic Susceptibility of **DzAu·OX** 103
4.3.2 Variable Temperature Magnetic Susceptibility of **DzAu·MX** 104
4.3.3 Variable Temperature Magnetic Susceptibility of **DzAu·PX** 105
4.4 Binary Xylene Mixtures on DzAu Framework 106
4.4.1 Powder X-ray Diffraction of DzAu Framework with Xylene Mixtures as Guests 106
4.4.2 Variable Temperature Magnetic Susceptibility of DzAu with a Binary Mixture Solvent of PX, OX, and MX 108
4.4.3 NMR of Various Guest Components within the Frameworks 108
4.5 Discussion 109
4.6 Conclusions and Future work 112
4.7 References 113
Chapter 5 116
5.1 Overview 117

5.2 Structure Characterisation of [Fe(Tz)(Ag(CN)$_2$)$_2$] (**TzAg·EtOH**) 118
5.3 Spin Crossover Behaviour of **TzAg·EtOH** 122
5.4 Structure Characterisation of [Fe(Dz)(Ag(CN)$_2$)$_2$] (**DzAg·EtOH**) 123
5.5 Spin Crossover Behaviour of **DzAg·EtOH** 129
5.6 Structure Characterisation of [Fe(Dz)(H$_2$O)$_2$Pt(CN)$_4$]·2(H$_2$O) 130
5.7 Structure Characterisation of [Fe(Dz)(H$_2$O)$_2$(Pd(CN)$_4$]·2(H$_2$O) (**DzPd**) 132
5.8 Structure Characterisation of Mixed Cyanidometallate Frameworks 134
5.8.1 [Fe(Tz)((Au(CN)$_2$)$_{0.5}$(Ag(CN)$_2$)$_{0.5}$)$_2$] (**TzAu$_{0.5}$Ag$_{0.5}$·EtOH**) 134
5.8.2 [Fe(Dz)((Au(CN)$_2$)$_{0.5}$(Ag(CN)$_2$)$_{0.5}$)$_2$] (**DzAu$_{0.5}$Ag$_{0.5}$·EtOH**) 138
5.9 Spin Crossover Behaviour of Mixed Cyanidometallate Frameworks 142
5.9.1 **TzAu$_{0.5}$Ag$_{0.5}$·EtOH** 142
5.9.2 **DzAu$_{0.5}$Ag$_{0.5}$·EtOH** 143
5.9.3 **DzAu$_{0.7}$Ag$_{0.3}$·EtOH** 143
5.10 Raman Spectroscopy on Single and Mixed Cyanidometallate Frameworks 145
5.11 XPS on Single and Mixed Cyanidometallate Frameworks 147
5.12 SEM and EDS Mapping on Mixed Cyanidometallate Frameworks 150
5.13 Discussion 151
5.14 Conclusions and Future Work 152
5.15 References 154
Chapter 6 157
6.1 Overview 158
6.2 SCO Behaviours Under Pressure 159
6.2.1 Variable Temperature Magnetic Susceptibility of **TzAu·EtOH** Under Pressure 159
6.2.2 Variable Temperature Magnetic Susceptibility of **[Tz$_{0.5}$Dz$_{0.5}$]** Under Pressure 161
6.2.3 Variable Temperature Magnetic Susceptibility of **DzAu·EtOH** Under Pressure 162
6.3 Lattice Motion Under Pressure 164
6.3.1 Variable Pressure Neutron Powder Diffraction (VP-NPD) of **TzAu·EtOH** 164
6.3.2 Variable Pressure Neutron Powder Diffraction of **[Tz$_{0.5}$Dz$_{0.5}$]** 166
6.4 Conclusion and Future Work 169

6.5 References 170
Chapter 7 172
7.1 Overview 173
7.2 Investigation of $[Fe(Tz)_x(Dz)_{1-x}(Au(CN)_2)_2]\cdot n$EtOH ($x$ = 0.2–1.0) 174
7.2.1 Structural Characterisation of Single Crystals 174
7.2.2 Spin Crossover Manipulation *via* Tuning Ligand Composition 178
7.2.3 SCO-Induced Colossal Thermal Expansion 179
7.2.4 Solid-Solution Manipulated Thermal Expansion 180
7.3 Investigation of $[Fe(Tz)_x(Dz)_{1-x}(Au(CN)_2)_2]\cdot n$EtOH ($x$ = 0) (**DzAu·EtOH**) 185
7.3.1 Structural Characterisation and Phase Transitions 185
7.3.2 Variable Temperature Solid-State Diffuse Reflectance 190
7.3.3 Structural Characterisation in Desolvation Phase 190
7.3.4 Magnetic Properties Associated with Structural Properties 192
7.4 Investigation of $[Fe(Tz)_x(Dz)_{1-x}(Au(CN)_2)_2]\cdot n$EtOH ($x$ = 0.1 and 0.15) 194
7.4.1 Structural Characterisation of Gradual Phase Transition 194
7.4.2 Thermal Induced History-Dependent SCO Behaviours 199
7.5 Conclusions and Future Work 202
7.6 References 204
Chapter 8 207
8.1 Final Conclusions 208
8.2 Future Directions 210
Appendix A 212
Appendix B 222
Appendix C 228
Appendix D 238
Appendix E 242

List of Figures

Figure 1.1: Schematic of strategies employed in the of synthesis SR-MOFs. Adapted from Nagarkar *et al.*.[46] 3

Figure 1.2: Ligand field splitting diagram and adiabatic potential wells for LS and HS states in an octahedral Fe(II) system with metal–donor atomic distance, r(Fe–N)..... 5

Figure 1.3: The different types of SCO behaviours: (a) gradual, (b) abrupt, (c) hysteretic, (d) multi-step, (e) incomplete (adapted from Gütlich *et al.*).[62] 6

Figure 1.4: (a) The change of hysteresis and spin transition temperature at different scan rates. (b) zero scan rate was estimated by extrapolating the $T_{1/2}$ value as a function of the scan rate..... 7

Figure 1.5: (a) Schematic representation of the effect of pressure on the HS and LS state potential wells, where P2 > P1. (b) $\chi_M T$ versus T of $[FePd(CN)_4(thiome)_2]\cdot 2H_2O$ under pressures up to 0.68 Gpa (adapted from Sciortino *et al.*).[106] (c) Temperature-dependent magnetic susceptibility behaviour of $[Fe(4,4\text{-bipy})_2(Ag(CN)_2)_2]$ (adapted from Niel *et al.*).[108] (d) Magnetic susceptibility versus temperature plots for $[Fe(btr)_2(NCS)_2]\cdot H_2O$ under the pressure at 0.8, 1.0, 6.7, 9.6, and 10.5 kbar in the temperature range 20–300 K (adapted from Garcia *et al.*). [109] 9

Figure 1.6: (a) Structure of $[Fe_2(azpy)_4(NCS)_4]\cdot$EtOH (top) and desolvated framework (bottom). (b) effective magnetic moment versus temperature plots for different guest molecules in $[Fe_2(azpy)_4(NCS)_4]$ (1). Adapted from Halder *et al.*[128] 11

Figure 1.7: Schematic diagrams of the (a) coordination sphere of a Hofmann framework, (b) 3D Hofmann-type framework and (c) 3D Hofmann-like framework. Adapted from Ni *et al.*[129] 13

Figure 1.8: Crystal structure of **DzAu·EtOH** in monoclinic phase by the *de novo* synthesis (top) and PSM process from **TzAu·EtOH** to form orthorhombic phase **DzAu·EtOH** framework (bottom). Adapted from Clements *et al.*[144-145] 14

Figure 1.9: (Left) Breathing-like behaviour in MIL-53 framework with adsorption (solid line) and desorption (dashes) of CO_2. (Right) Phase transition between large pore (LP) phase and narrow pore (NP) phases in the framework. Adapted from Chanut *et al.*[156] 15

Figure 1.10: Schematic illustration of a shape memory effect. Adapted from Sakata *et al.*[171] 16

Figure 1.11: Hofmann grids of $[Fe(bpac)(Au(CN)_2)_2]\cdot 2$EtOH framework showing lattice changes between HS and LS state (top). Schematic Hofmann girds undergoing a scissoring motion due to temperature (bottom). Adapted from Mullaney *et al.*[185] 17

Figure 1.12: Schematic illustration of *de novo* and PSM methods for MOF synthesis. Adapted from Wang *et al.*[191] 18

Figure 1.13: Schematic illustration of the formation of a MIXMOF with two ligands (top). An example of a synthetic process for generating a series of carboxylate MIXMOFs. Adapted from Kleist *et al.*[205] 20

Figure 2.1: Structural drawing of Tz ligand..... 33

Figure 2.2: Structural drawing of Dz ligand. 34
Figure 2.3: Schematic of the sample holder used for measuring variable temperature magnetic susceptibility at ambient pressure. 42
Figure 2.4: (a) Photograph of Quantum Design High Pressure Cell (top) used for measuring variable temperature magnetic susceptibility at applied pressure. Schematic of Quantum Design High Pressure Cell connects with VSM adaptor and large bore rod. (b) Schematic of the inside of Quantum Design High Pressure Cell. 43
Figure 3.1: Single crystal structure of **TzAu·OX** at 100 K: (a) asymmetric unit with thermal ellipsoids set at 50% probability. (b) The calculated pore structure as shown projected along the *c*-axis showing the A and B pores, with yellow and brown representing the outside and inside regions, respectively. (c) View down the *b*-axis. Atom colours: Fe (red), Au (yellow), N (blue), C (grey), H (white). 50
Figure 3.2: Single crystal X-ray structure of **TzAu·OX** at 100 K: (a) Perspective view down the *c*-axis showing the solvent-accessible channel, and (b) as viewed down the *a*-axis. The OX guest molecules have been omitted for clarity. Atom colours: Fe (red), Au (yellow), N (blue), C (grey), H (white). ... 52
Figure 3.3: Schematic of the scissor motion for **TzAu·OX** with changing temperature. Hofmann layers adopt a rhombic shape as seen down the a-axis. θ decreases upon heating with the expansion of the *b*-axis and subsequent compression of the *c*-axis. 54
Figure 3.4: (a) VT-PXRD peak evolution of **TzAu·OX** in the 8.0–9.0° 2θ range over the temperature range 300–100–300 K. (b) Pawley refinement of the synchrotron PXRD data measured at room temperature. Experimental pattern (blue), calculated fit (green), background (red), the difference (cyan), and *hkl* positions (vertical bars). 55
Figure 3.5: Single crystal X-ray structure of **TzAu·PX** shows the (a) asymmetric unit at 100 K, (b) the extended crystal structure as viewed along the *c*-axis, and (c) the overlay of asymmetric units at 100 K (blue) and 310 K (red). Thermal ellipsoids are shown at 50% probability. Atom colours: Fe (red), Au (yellow), N (blue), C (grey), H (white). 56
Figure 3.6: PXRD peak evolution of **TzAu·PX** as a function of temperature showing (a) the first thermal cycle and (b) the second thermal cycle. 58
Figure 3.7: (a) PXRD pattern of **TzAu·PX** at 310 K showing the first thermal cycle (black) and the second thermal cycle (red). (b) Pawley refinement of the synchrotron PXRD data of **TzAu·PX** measured at room temperature. Experimental pattern (blue), calculated fit (green), background (red), the difference (cyan), and *hkl* (vertical bars). (c) PXRD pattern of **TzAu·PX** at 100 K. Experimental pattern (red), simulated pattern (black), and *hkl* indices (blue tick marks). (d) Experimental PXRD pattern of **TzAu·PX** at 100 K showing the first thermal cycle (black), second thermal cycle (red), and third thermal cycle (blue). 59
Figure 3.8: (a) Pawley refinement of a synchrotron PXRD pattern obtained for **TzAu·MX** at room temperature. Experimental pattern (blue), calculated fit (green), background (red), the difference (cyan), and *hkl* (vertical bars). (b) PXRD peak evolution of **TzAu·MX** as a function of temperature (300–100–

300 K). 60
Figure 3.9: PXRD peak evolution of **TzAu·MX** as a function of temperature (300–100–300 K) of (a) batch one and (b) batch two. The peaks are likely from amorphous components in red. 61
Figure 3.10: Variable temperature magnetic susceptibility plot of **TzAu·PX** measured at a scan rate of 2 K min^{-1}. 62
Figure 3.11: Variable temperature magnetic susceptibility plot of **TzAu·OX** measured at a scan rate of 2 K min^{-1}. 63
Figure 3.12: Variable temperature magnetic susceptibility plot of **TzAu·OX** mixed with paratone oil. Data were collected at 2 K min^{-1}. 64
Figure 3.13: Variable temperature magnetic susceptibility plot of **TzAu·OX** between a temperature range of 300–200 K (black), 200–230–200–230 K (blue), and 230–120–300 K (red). 65
Figure 3.14: Variable temperature magnetic susceptibility plots of **TzAu·OX** recorded at scan rates of 0.5 (black), 1 (red) and 2 K min^{-1} (blue). 66
Figure 3.15: Variable temperature magnetic susceptibility plots of **TzAu·PX** recorded at 2 K min^{-1} and showing the first thermal cycle (black) and second thermal cycle (blue). 67
Figure 3.16: Variable temperature magnetic susceptibility plots of **TzAu·PX** with temperature scanning between 300–200 K (black), 200–230–200–230 K (blue), and 230–120–300 K (red). 68
Figure 3.17: Variable temperature magnetic susceptibility plots of **TzAu·PX** recorded at scan rates of 1 (black), 2 (blue) and 4 K min^{-1} (red). 69
Figure 3.18: Raman spectra of **TzAu·PX**, **TzAu·OX**, and **TzAu·MX**. Inset: close up of the cyanide stretching region. 70
Figure 3.19: Synchrotron PXRD patterns of **TzAu·PX** (black), **TzAu·MX** (red), and TzAu·PM (blue) were collected at room temperature. The two examples of exclusive peaks belonging to **TzAu·MX** (2θ = 4.9° and 6.4°) are labelled with black asterisks. 2θ = 4.1° and 9.1° labelled with red asterisks show peaks from **TzAu·PX** and **TzAu·PM50** with the same position. 71
Figure 3.20: Synchrotron PXRD patterns of **TzAu·PO50** (black), **TzAu·PX** (red), and **TzAu·OX** (blue) were collected at room temperature with 2θ in the range of 2°–18°. (b) A close-up of the PXRD patterns (2θ = 7.3°–9.3°). The black asterisks show the peaks belonging to **TzAu·PO50** and **TzAu·PX**. 72
Figure 3.21: Synchrotron PXRD patterns of **TzAu·MO50** (black), **TzAu·MX** (red), and **TzAu·OX** (blue) were collected at room temperature: (a) with a 2θ range of 2°–16°. 2θ = 3.9° is labelled with an asterisk. (b) A close-up of the PXRD patterns (2θ = 3.9°–4.7°) with *hkl* values shown in square brackets. 72
Figure 3.22: PXRD patterns of **TzAu·PO73** (blue), **TzAu·PO50** (red), and **TzAu·PO37** (black), were collected at room temperature. Insert: close-up of the patterns in the region 2θ = 14.2–15.0°. 73
Figure 3.23: PXRD patterns of **TzAu·PM73** (red), **TzAu·PM50** (black), and **TzAu·PM37** (blue) were collected at room temperature. Insert: close-up of the patterns in the region 2θ = 15.3–16.2°. 74

Figure 3.24: PXRD patterns of **TzAu·MO37** (red), **TzAu·MO50** (black), and **TzAu·MO73** (blue) were collected at room temperature. Inset: zoomed in view of the region between 2θ = 11.2–11.7°. . 75
Figure 3.25: Variable temperature magnetic susceptibility plots of **TzAu·PM37** (black), **TzAu·PM50** (dark yellow), and **TzAu·PM73** (blue) collected at a scan rate of 2 K min^{-1} 76
Figure 3.26: Variable temperature magnetic susceptibility plots of **TzAu·MO37** (green), **TzAu·MO50** (blue), and **TzAu·MO73** (red) collected at a scan rate of 2 K min^{-1} 77
Figure 3.27: Variable temperature magnetic susceptibility plots of **TzAu·PO37** (red), **TzAu·PO50** (blue), and **TzAu·PO73** (yellow) recorded at a scan rate of 2 K min^{-1} 78
Figure 4.1: Single crystal X-ray structure of **DzAu·OX** at 100 K: (a) asymmetric unit with thermal ellipsoids set at 50% probability, (b) the extended framework structure as viewed down the *a*-axis with solvent molecules omitted for clarity, (c) the extended framework structure with solvent molecules viewed down the *c*-axis and (d) *b*-axis. Atom colours: Fe (red), Au (yellow), N (blue), C (grey), and H (white). 88
Figure 4.2: Single crystal X-ray structure of **DzAu·OX** at 100 K showing π···π interactions: (a) between a pyridyl ring (blue) and OX molecule (yellow), (b) between another pyridyl ring (red) and the disordered OX molecule (pink). Right: disordered OX fragment with the two orientations modelled at 59% (pink) and the other at 41%. The dashed line in green represents the π···π interactions. Atom colours: Fe (red), Au (yellow), N (blue), C (grey), and H (white)..... 89
Figure 4.3: (a) Structural overlay of **DzAu·OX** (light blue) at 100 K and **DzAu·EtOH** (red) at 90 K. (b) Structural overlay of **DzAu·OX** (light blue) at 100 K (LS state) and **DzAu·OX** (light orange) at 230 K (HS state)..... 91
Figure 4.4: The calculated pore environments of **DzAu·OX** displayed in either yellow (outside of the pores) or brown (inside of the pores): (a) view down the *c*-axis and (b) view down the *a*-axis. Guest molecules have been omitted for clarity. Atom colours: Fe (red), Au (yellow), N (blue), C (grey), and H (white). 92
Figure 4.5: (a) Simulated PXRD pattern (red) and experimental PXRD pattern (black) of **DzAu·OX** at 100 K. (b) VT-PXRD patterns of **DzAu·OX** (100 K, 120 K, 150 K, 250 K, and 280 K). 93
Figure 4.6: Single crystal X-ray structure of **DzAu·MX** at 100 K: (a) asymmetric unit with thermal ellipsoids set at 50% probability. (b) The framework structure is viewed down the *c*-axis. (c) MX guest molecules: one MX guest (C31·····C38) with occupancy of 1; another MX shows disorder and was refined with two positions of $-CH_3$ labelled as C48A and C48B. (d) The framework structure is viewed down the *b*-axis with solvent molecules omitted for clarity. The inter-ligand C–H···N interactions are shown in green dashes. Atom colours: Fe (red), Au (yellow), N (blue), C (grey), and H (white)..... 94
Figure 4.7: (a) Single structure of **DzAu·MX** at 100 K viewed down the *b*-axis and (b) viewed down the *a*-axis. Two neighbouring Hofmann layers with the upper layer shown in purple and the lower layer in green. The two layers are connected with Au···Au interactions in yellow. (c) The calculated pore

structure is shown projected along the *a*-axis and (d) viewed down the *c*-axis. Pore features are displayed in either yellow or brown and represent the outside or inside of the pores, respectively. Solvent molecules omitted for clarity. Atom colours: Fe (red), Au (yellow), N (blue), C (grey), and H (white). 96

Figure 4.8: The overlay of single crystal X-ray structures of **DzAu·MX** at 100 K (blue) and 230 K (red) showing the different degrees of distortion of the ligand and undulation of the Hofmann layers: (a) asymmetric units and (b) view down the c-axis. Hydrogen atoms and guest molecules have been omitted for clarity..... 97

Figure 4.9: Simulated PXRD pattern (red) from crystal structure collected at 230 K and experimental PXRD pattern (black) of **DzAu·MX** at room temperature. 98

Figure 4.10: Single crystal X-ray structure of **DzAu·PX** at 100 K: (a) asymmetric unit with thermal ellipsoids set at 50% probability. (b) The calculated pore environment of the framework as viewed down the *c*-axis. Pore features coloured in yellow and brown represent the outside and inside regions, respectively. (c) View down the *a*-axis. (d) Two Fe(II) sites are represented as polyhedra, with LS and HS states coloured in blue and red, respectively. Solvent molecules are omitted for clarity. Atom colours: Fe (red), Au (yellow), N (blue), C (grey), and H (white). 100

Figure 4.11: The overlay of single crystal X-ray structures of **DzAu·PX** at 100 K (orange), 155 K (grey), and 230 K (violet) of (a) the asymmetric units with hydrogen atoms omitted for clarity, (b) view down the *c*-axis, (c) view down the *a*-axis, and (d) view down the *b*-axis. The guest molecules have been omitted in (a), (c), and (d) for clarity..... 102

Figure 4.12: (a) VT-PXRD peak evolution of **DzAu·PX** showing the peak shifts due to the spin transition (2θ = 15.5–16.4°) over the temperature range 300–100–300 K. (b) Simulated pattern (red) obtained from the single crystal X-ray structure of **DzAu·PX**, and experimental PXRD pattern (black) of **DzAu·PX** at 100 K. 103

Figure 4.13: Variable temperature magnetic susceptibility plot of **DzAu·OX**. Inset: close-up of the 175–292 K region. 104

Figure 4.14: Variable temperature magnetic susceptibility plot of **DzAu·MX**. Inset: close-up of the 128–165 K region. 105

Figure 4.15: Variable temperature magnetic susceptibility plot of **DzAu·PX**. 106

Figure 4.16: Comparison of PXRD patterns of (a) **DzAu·OX** (blue), **DzAu·MX** (red), and **DzAu·PX** (black). (b) The PXRD patterns of **DzAu·PM50** (black), **DzAu·MO50** (red), and **DzAu·PO50** (blue) were collected at room temperature between the range 2θ = 2–20°. 107

Figure 4.17: (a) PXRD patterns of **DzAu·PX** (black), **DzAu·MX** (red), and **DzAu·PM50** (blue). Inset: close-up of the region 2θ = 4.25–5.63°. (b) PXRD patterns of **DzAu·PX** (black), **DzAu·OX** (red), and **DzAu·PO50** (blue). Inset: close-up of the region 2θ = 5.26–6.43°. (c) PXRD patterns of **DzAu·MX** (black), **DzAu·OX** (red), and **DzAu·MO50** (blue). Inset: close-up of the region 2θ = 5.26–6.43°. All data were collected at room temperature. 107

Figure 4.18: Variable temperature magnetic susceptibility plots of (a) **DzAu·PM50**, (b) **DzAu·PO50**, and (c) **DzAu·MO50**. 108
Figure 5.1: Single crystal structure of **TzAg·EtOH** at 100 K: (a) asymmetric unit; (b) framework structural shows with solvent molecules omitted for clarity down the *b*-axis; (c) the void profile of the framework is shown in green; (d) framework structural shows with solvent molecules omitted for clarity down the *c*-axis. Atom colours: Fe (red), Ag (yellow), N (blue), C (grey), H (white). 119
Figure 5.2: VT-PXRD peak evolution of **TzAg·EtOH** (2θ = 9.0–11.0°, *hkl* = [040] and [004], temperature range: 320–100–320 K). 121
Figure 5.3: (a) Comparison of experimental PXRD pattern of **TzAg·EtOH** (black) and simulated pattern (red) from single crystal X-ray data at 100 K. (b) Pawley refinement of **TzAg·EtOH** at 100 K; experimental pattern (black crosses), calculated fit (red), background (green), the difference (light blue). 122
Figure 5.4: Variable temperature magnetic susceptibility measurement of **TzAg·EtOH**. 122
Figure 5.5: Single crystal structure of **DzAg·EtOH** at 100 K: (a) asymmetric unit and atoms are shown as thermal ellipsoids at the 50% probability; (b) the framework structure is viewed down the *a*-axis; (c) perspective view of the framework structure down the *b*-axis. Atom colours: Fe (red), Ag (yellow), N (blue), C (grey), H (white). Solvent molecules omitted for clarity. 123
Figure 5.6: Unit cell parameters of **DzAg·EtOH** at 100, 180, 195 and 260 K: (a) *a*-axis, (b) *b*-axis, (c) *c*-axis and (d) volume. 124
Figure 5.7: Single crystal structure of **DzAg·EtOH** at 100 K as viewed down the *c*-axis (a) with the packing of Hofmann grids, (b) and showing two layers with Fe(II) in polyhedron (violet for the upper layer and red for the lower layer). Solvent omitted for clarity. 126
Figure 5.8: (a) Structural overlay of **DzAg·EtOH** framework as viewed down the *b*-axis; (b) Hofmann layer overlay at 100 (blue), 180 (red), 195 (dark grey) and 260 K (magenta). Solvent omitted for clarity. The disordered and hydrogen atoms are omitted for clarity. 127
Figure 5.9: DzAg·EtOH shows inter-ligand C–H···N interactions (green dashes) viewed down the *b*-axis. Two disordered diazine rings are shown. Solvent omitted for clarity. 128
Figure 5.10: Pawley refinement of the PXRD data of the **DzAg·EtOH** framework measured at room temperature in the 2θ range of 8.5–9.5°. Experimental pattern (blue), calculated fit (green), background (red), the difference (cyan) and *hkl* (vertical bar). 128
Figure 5.11: VT-PXRD peak evolution of **DzAg·EtOH** (2θ = 8.5–9.5°, temperature range: 300–100–300 K). 129
Figure 5.12: Variable temperature magnetic susceptibility measurement of **DzAg·EtOH**. 130
Figure 5.13: Single crystal structure of **DzPt** at 100 K: (a) asymmetric unit and atoms are shown as thermal ellipsoids at 50% probability; (b) framework structure viewed down the *a*-axis with hydrogen bonds N–H···O in blue dashes and O–H···O in green dashes; (c) down the *a*-axis with showing two layers connected by hydrogen bondings, (d) and down the *c*-axis. Atom colours: Fe (red), Pt (purple),

N (blue), C (grey), O (light green), H (white).....132
Figure 5.14: Single crystal structure of **DzPd** at 100 K: (a) asymmetric unit and atoms are shown as thermal ellipsoids at 50% probability; (b) framework structure viewed down the *a*-axis; (c) hydrogen bonds N–H···O shown in blue dashes and O–H···O in green dashes; (d) down the *b*-axis, (e) and down the *c*-axis. Atom colours: Fe (red), Pd (orange), N (blue), C (grey), O (light green), H (white).....133
Figure 5.15: Single crystal structure of **TzAu$_{0.5}$Ag$_{0.5}$·EtOH** at 100 K: (a) asymmetric unit; (b) framework structure viewed down the *b*-axis; (c) viewed down the *c*-axis; (d) perspective view of the framework structure down the *a*-axis. Solvent molecules omitted for clarity. Au···Au and Ag···Ag interactions shown in green dashes. Au and Ag atoms are located in disorder. Atom colours: Fe (red), Ag (yellow), Au(orange), N (blue), C (black), H (pink).....136
Figure 5.16: Single crystal structure of **DzAu$_{0.5}$Ag$_{0.5}$·EtOH** at 100 K: (a) asymmetric unit and atoms are shown; (b) framework structure viewed down the *a*-axis; (c) viewed down the *b*-axis; (d) and down the *c*-axis. Solvent molecules are omitted for clarity. Atom colours: Fe (red), Ag (yellow), Au(orange), N (blue), C (black), H (pink). 140
Figure 5.17: VT-PXRD peak evolution of **DzAu$_{0.5}$Ag$_{0.5}$·EtOH** (2θ = 6.9–7.5°, temperature range: 300–100–300 K). 141
Figure 5.18: Variable temperature magnetic susceptibility measurement of (a) **TzAu$_{0.5}$Ag$_{0.5}$·EtOH** and (b) comparison of **TzAg·EtOH** (black), **TzAu$_{0.5}$Ag$_{0.5}$·EtOH** (red) and **TzAu·EtOH** (blue). 142
Figure 5.19: Variable temperature magnetic susceptibility measurement of **DzAu$_{0.5}$Ag$_{0.5}$·EtOH**. ..143
Figure 5.20: Variable temperature magnetic susceptibility measurement of **DzAu$_{0.7}$Ag$_{0.3}$·EtOH**. ..144
Figure 5.21: Variable temperature magnetic susceptibility measurements of **DzAg·EtOH** (black), **DzAu$_{0.5}$Ag$_{0.5}$·EtOH** (red), **DzAu$_{0.7}$Ag$_{0.3}$·EtOH** (magenta) and **DzAu·EtOH** (blue). 145
Figure 5.22: Raman spectra of **TzAu·EtOH** (black), **TzAu$_{0.5}$Ag$_{0.5}$·EtOH** (blue) and **TzAg·EtOH** (orange) in the range of 200 – 2300 cm^{-1}. Inset: close-up of the Raman spectra in the range of 2130–2250 cm^{-1}, showing the cyanide (C≡N) stretching band. 146
Figure 5.23: Raman spectra of **DzAu·EtOH** (blue), **DzAu$_{0.5}$Ag$_{0.5}$·EtOH** (red) and **DzAg·EtOH** (black) with the range of 200–2300 cm^{-1}. Inset: close-up of the Raman spectra in the range of 2100–2250 cm^{-1}, which shows cyanide (C≡N) stretching band.....147
Figure 5.24: X-ray photoemission spectra for (a) a survey scan of **TzAg**, (b) a high-resolution scan of Ag 3*d* shows two peaks with a red curve representing experimentally measured data of **TzAg**, (c) a survey scan of **TzAu** and (d) a high-resolution scan of Au 4*f* shows two peaks with a red curve representing experimentally measured data of **TzAu**. The peaks were fitted showing a blue curve with the completed peak features in yellow, and the background in green. The deviation from experimental data and simulated fit in the light blue shown on the top of the peak with a black horizontal line as a baseline. 148
Figure 5.25: X-ray photoemission spectra for (a) a survey scan of **DzAu**, (b) a high-resolution scan of

Au 4*f* shows two peaks with a red curve representing experimentally measured data of **DzAu**, (c) a survey scan of **DzAg** and (d) a high-resolution scan of Ag 3*d* shows two peaks with a red curve representing experimentally measured data of **DzAg**. The peaks were fitted showing a blue curve with the completed peak features in yellow, and the background in green. The deviation from experimental data and simulated fit in the light blue shown on the top of the peak with a black horizontal line as a baseline. 149

Figure 5.26: (a) SEM image of **TzAu$_{0.5}$Ag$_{0.5}$** (b) EDS mapping and elemental analysis of Fe (cyan), (c) Au (green) and (d) Ag (purple). 151

Figure 6.1: (a) Variable temperature magnetic susceptibility data of **TzAu·EtOH** at a scan rate of 1 (blue), 2 (red) and 5 K min^{-1} (purple). (b) The $T_{1/2}$ value as a function of scan rate (1, 2 and 5 K min^{-1}). 160

Figure 6.2: Variable temperature magnetic susceptibility data of **TzAu·EtOH** at a scan rate of 1 K min^{-1} (a) at 0.33, 0.35, 0.36, 0.37, 0.39, 0.45 GPa and (b) 0.54, 0.62, 0.76 and 0.99 GPa. (c) Spin transition temperature against pressures of **TzAu·EtOH**. (d) Hysteresis width against pressure of **TzAu·EtOH**. 161

Figure 6.3: Variable temperature magnetic susceptibility data of **[Tz$_{0.5}$Dz$_{0.5}$]** at 0.32 (red), 0.35 (orange), 0.45 (yellow), 0.60 (green) and 0.78 GPa (blue) at scan rate of 1 K min^{-1}. 162

Figure 6.4: Variable temperature magnetic susceptibility data of **DzAu·EtOH** at 0.32 (black), 0.34 (blue) and 0.36 GPa (green) at a scan rate of 0.5 K min^{-1} 163

Figure 6.5: NPD data of **TzAu·EtOD** at ambient pressure (black), 0.40 GPa (red), 0.68 GPa (blue), 0.98 GPa (green) and 1.23 GPa (purple). Data are presented as lines and offset in the y-axis for clarity. 164

Figure 6.6: The change of lattice parameters on (a) *a*-axis, (b) *b*-axis, (c) *c*-axis and (d) volume versus pressure for **TzAu·EtOD**. 166

Figure 6.7: NPD data of **[Tz$_{0.5}$Dz$_{0.5}$]** for (a) the first batch at ambient pressure (black) and 0.55 GPa (red), (b) the second batch at ambient pressure (red), 0.25 GPa (orange), 0.82 GPa (yellow), 1.02 GPa (green) and 1.18 GPa (blue). Data are presented as lines and offset in the y-axis for clarity. 167

Figure 6.8: The change of lattice parameters on (a) *a*-axis, (b) *b*-axis, (c) *c*-axis and (d) volume versus pressure for **[Tz$_{0.5}$Dz$_{0.5}$]**. 168

Figure 7.1: Single crystal structure of **[Tz$_{0.5}$Dz$_{0.5}$]** at 100 K: (a) showing the structure fragment, which consists of one Tz and one Dz ligand; (b) viewed along the *c*-axis, showing the pyridyl ring disorder and the 50:50 disorder of the tetrazine and diazine rings; (c) viewed along the *b*-axis, showing one possible ordering of Tz and Dz ligands (C: black, N: blue, Fe: red, Au: orange, H: pink, Au···Au interactions: orange dotted lines and C–H···N interactions: red dotted lines). 176

Figure 7.2: (a) Variable temperature magnetic susceptibility data for bulk powder MIXMOF samples from **[Tz$_{0.2}$Dz$_{0.8}$]** to **[Tz$_{1.0}$Dz$_{0.0}$]**. (b) SCO transition temperatures in the cooling and heating process versus percentage of Tz ligand containing (determined by IR spectroscopy) in the series of frameworks

from **[$Tz_{0.2}Dz_{0.8}$]** to **[$Tz_{1.0}Dz_{0.0}$]**. 178
Figure 7.3: PXRD patterns for bulk powder samples of **[$Tz_{0.2}Dz_{0.8}$]** to **[$Tz_{1.0}Dz_{0.0}$]** measured at room temperature. Inset: close-up of the diffraction patterns showing changes in the peak intensity and peak shifts with different ligand compositions (2θ = 22.5–23.2°). 180
Figure 7.4: Unit cell information of **[$Tz_{0.5}Dz_{0.5}$]** extracted from VT-PXRD data: (a) *a*-axis versus temperature (300–200 K), (b) thermal expansion coefficients α on the *a*-axis versus temperature, (c) the *b*-axis versus temperature, (d) thermal expansion coefficients α on the *b*-axis versus temperature (300–200 K). Markers represent data and curves represent the fitted model.. 182
Figure 7.5: Thermal expansion coefficient for **[Tz_xDz_x]** (x = 0.2, 0.4, 0.5, 0.6, 0.8, 1.0) (a) *a*-axis (top) and *b*-axis (bottom). Dimension change versus temperature (b) *a*-axis (top) and *b*-axis (bottom). Curves are included as a visual guide. 183
Figure 7.6: (a) Schematic diagram of scissor motion. Au atom in yellow and Fe in red. (b) θ angle calculated by fitted *a* and *b* unit cell parameters versus temperature. (c) $\Delta\theta$ versus different Tz compositions in the frameworks. 184
Figure 7.7: (a) VT-PXRD peak evolution (2θ = 9.8–14.0°) of **DzAu·EtOH** with cooling and heating in the temperature range 300–100–335 K; (b) VT-PXRD data for identifying the phase interconversion between orthorhombic phase and monoclinic phase. Data are presented as lines and offset in the y-axis for clarity. 186
Figure 7.8: Schematic illustration of the shape memory effect. As-made bulk powder material **O-RT** presents in the orthorhombic phase at room temperature and upon cooling converts to monoclinic phase **M-LT** at 250 K (process Ⅰ). The material locks in the monoclinic phase **M-RT** with heating back to room temperature (process Ⅱ). With continuous heating (process Ⅲ), phase conversion from monoclinic to orthorhombic phase happened **O-RT** at 335 K. **O-RT** retains orthodromic phase at 300 K (process Ⅳ). 188
Figure 7.9: Schematic illustration of the mechanism of phase transition from the orthorhombic phase (top) to the monoclinic phase (bottom) upon cooling. While cooling, the rotation of the diazine rings occurs, which changes the hydrogen bonding and alters the C–H···N host–host interactions within the framework. Ethanol solvent within the pores was omitted for clarity. C: black, N: blue, Fe: red, Au: orange, H: pink, C–H···N interactions: green dotted lines. 189
Figure 7.10: Variable temperature solid-state diffuse reflectance (a) for the cooling process from 280 K to 200 K, insert: comparison of cooling the warming process at 280 K; (b) for the heating process from 200 K to 280 K, insert: comparison of cooling the warming process at 240 K. 190
Figure 7.11: (a) Schematic illustration of the desolvation and resolvation process of both **1-O** and **1-M**. **1-ΦM** phase generated *via* two pathways: 1. cooling to **1-M** (process ⅰ) and desolvation (process ⅱ) and for absorption of mother liquor ethanol, the material returns to the original **1-O** (process ⅲ). This pathway represents in yellow arrows; 2. direct desolvation from **1-O** (process ⅳ) and returned to

the original phase by resolvation (process v) This pathways represent in green arrows. (b) The structure of desolvated phase at 0 K was calculated using DFT. C: black, N: blue, Fe: red, Au: orange, H: pink, C–H···N interactions: green dotted lines. (c) PXRD pattern of desolvation process started from **1-O** material *via* process i forming monoclinic phase (**1-M-i**) and **1-ΦM-ii** formed by desolvation. By resolvation, the material was transferred to the original orthorhombic phase **1-O-iii** (d) Direct desolvation procedure was applied on the original **1-O** material to form desolvation phase (**1-ΦM-iv**), The material changed back to original phase by resolvation (**1-O-v**). Data are presented as lines and offset in the y-axis for clarity. 192

Figure 7.12: Schematic demonstration of PSM method from **DzAu·EtOH** (top left) to 1 (bottom left) in orthorhombic phase presenting single-step SCO (two states). As-synthesised powder sample can interconvert between the orthorhombic (bottom right) and monoclinic phase (up right). Both bulk powder samples **1-M** and **1-O** display four-step SCO behaviours. 193

Figure 7.13: Variable temperature magnetic susceptibility measurement of **1-ΦM**. 194

Figure 7.14: (a) PXRD patterns of **[$Tz_{0.1}Dz_{0.9}$]** measured at 300 K in its original orthorhombic phase (yellow), after a thermal cycle measured at 300 K in a mixed phase (blue), heated to 330 K returning to orthorhombic phase (red). (b) PXRD patterns of **[$Tz_{0.15}Dz_{0.85}$]** were measured at 300 K in its original orthorhombic phase (black), after a thermal cycle measured at 300 K in a mixed phase (red), heated to 330 K returning to orthorhombic phase (blue). 195

Figure 7.15: VT-PXRD peak evolution (2θ = 9–14°) with cooling and heating in the temperature range 300–100–330 K. (a) **[$Tz_{0.1}Dz_{0.9}$]**; (b) **[$Tz_{0.15}Dz_{0.85}$]**. 196

Figure 7.16: PXRD patterns of (a) and (b) starting from the first collection in the original orthorhombic phase at 300 K. The following patterns were collected after sequential thermal cycles measured at 300 K until 10 data collections to show the gradual process of phase transition. 197

Figure 7.17: Lattice parameters of **[$Tz_{0.1}Dz_{0.9}$]** (red) and **[$Tz_{0.15}Dz_{0.85}$]** (black) extracted from PXRD patterns with the data refined in the orthorhombic phase. The patterns were collected from original phases and followed by each thermal cycle at 300 K. The change of each lattice parameter versus each collection of the (a) *a*-axis, (b) *b*-axis and (c) *c*-axis. (d) Percentage of conversion from orthorhombic phase to monoclinic phase versus each collection times of **[$Tz_{0.1}Dz_{0.9}$]** (red) and **[$Tz_{0.15}Dz_{0.85}$]** (black). 198

Figure 7.18: Magnetic susceptibility measurements over ten thermal cycles of (a) **[$Tz_{0.1}Dz_{0.9}$]** and (b) **[$Tz_{0.15}Dz_{0.85}$]**. 199

Figure 7.19: Magnetic susceptibility measurements of **[$Tz_{0.1}Dz_{0.9}$]** with the first five thermal cycles in the temperature range of 300–200–300 K and the rest three cycles in 300–55–300 K. 200

Figure 7.20: Magnetic susceptibility measurements of **[$Tz_{0.1}Dz_{0.9}$]** (a) the first cycle with the temperature range of 300–55–200 K, second cycles and the third with the same temperature range in 200–55–200 K. (b) The fourth cycle in 200–55–300 K, the fifth in 300–55–200 K and the sixth in 200–

55–200 K.....201
Figure 7.21: Comparison of **[$Tz_{0.1}Dz_{0.9}$]** (red) and **[$Tz_{0.15}Dz_{0.85}$]** (black) for the ratio of the monoclinic phase versus thermal cycle number. 202
Figure 7.22: Structure of HTz ligand (HTz= 3,6-bis(4-pyridyl)-1,4-dihydro-1,2,4,5-tetrazine). 204
Figure 8.1: Structure drawing of (a) 1,4-di(pyridine-4-yl) benzene and (b) 2,5-bis(pyrid-4-yl) pyridine. 211
Figure A.1: TGA of the **TzAu·OX** framework over a temperature range of 75–400 °C. The OX solvent loss within the pore is about 1.5 molecules per formula unit……..……..214
Figure A.2: Room temperature PXRD pattern (Mo-Kα radiation source, λ = 0.71073 Å) of **TzAu·OX** (red) and OX solvent (black)……214
Figure A.3: TGA of the **TzAu·PX** framework over a temperature range of 27–360 °C. The PX solvent loss within the pore is about 1.2 molecules per formula unit……..216
Figure A.4: PXRD peak evolution of **TzAu·PX** as a function of temperature showing the third thermal cycle……..……..216
Figure A.5: Pawley refinement of the synchrotron PXRD data of the **TzAu·PX** measured at 310 K after one thermal cycle. The refined space group is in *C*2/*c* with unit cell information in a = 30.44 Å, b = 18.23 Å, c = 12.46 Å and β = 98.35. Experimental pattern (blue), calculated fit (green), background (red), the difference (cyan) and hkl (vertical bar)……..217
Figure A.6: TGA of the **TzAu·MX** framework over a temperature range of 27–360 °C. The MX solvent loss within the pore is about 1.1 molecules per formula unit……217
Figure A.7: Variable temperature magnetic susceptibility measurement of **TzAu·PX** at 2 K min^{-1} with the second thermal cycle in red and third thermal cycle in blue……218
Figure A.8: DSC measurement of **TzAu·PX** at 10 K min^{-1} with cooling process (black) and heating process (red) of a thermal cycle……218
Figure A.9: DSC measurement of **TzAu·MX** at 10 K min^{-1} with cooling process (black) and heating process (red) of a thermal cycle……219
Figure A.10: DSC measurement of **TzAu·OX** at 10 K min^{-1} with cooling process (black) and heating process (red) of a thermal cycle……219
Figure B.1: VT-PXRD of **DzAu·PX** over the temperature range of 300–100–300 K for (a) cooling process and (b) heating process……..……..224
Figure B.2: VT-PXRD of **DzAu·PO50** over the temperature range of 300–100–300 K for (a) cooling process and (b) heating process……..……..224
Figure B.3: VT-PXRD of **DzAu·PM50** over the temperature range of 300–100–300 K for (a) cooling process and (b) heating process……225
Figure C.1: X-ray photoemission spectra for (a) a high-resolution scan of Au 4*f* in **$TzAu_{0.5}Ag_{0.5}$**, (b) a high-resolution scan of Ag 3*d*, (c) a high-resolution scan of Au 4*f* in **$DzAu_{0.5}Ag_{0.5}$** (d) and a high-resolution scan of Ag 3*d*. (e) a high-resolution scan of Au 4*f* in $DzAu_{0.7}Ag_{0.3}$ (f) and a high-resolution

scan of Ag 3*d*. The peaks in each spectrum were fitted with a red curve representing experimentally measured data. The peaks were fitted showing in blue curve with the completed peak features in yellow, background in green. The deviation from experimental data and simulated fit in the light blue shows on the top of the peak with a black horizontal line as a baseline……..……..233
Figure C.2: (a) SEM EDS image of **DzAu$_{0.5}$Ag$_{0.5}$** (b) EDS mapping and elemental analysis of Fe (purple), (c) Au (cyan) and (d) Ag (red)……..234
Figure C.3: (a) SEM EDS image of **DzAu$_{0.7}$Ag$_{0.3}$** (b) EDS mapping and elemental analysis of Fe (light yellow), (c) Au (greem) and (d) Ag (purple)…….……..235
Figure D.1: Variable temperature magnetic susceptibility data of **TzAu·EtOH** at a scan rate of 1 (blue), 2 (red) and 5 K min^{-1} (black) at (a) 0.33, (b) 0.35, (c) 0.36, (d) 0.37, (e) 0.39, (f) 0.45, (g) 0.54, (h) 0.62 and (h) 0.76 GPa……..……238
Figure E.1: IR spectra of the series of frameworks **[Tz$_x$Dz$_{1-x}$]** (x = 0.2–1, Δx = 0.1) from 800–860 cm^{-1}. The relative percentage of Tz doping is provided in the figure legend. The peak at *ca.* 837 cm^{-1} is assigned to the Tz ligand, and the peak at *ca.* 816 cm^{-1} is assigned to the Dz ligand. The plot of the percentage of Tz ligand for each framework in the MIXMOF series calculated from the integration of the Tz peak in the IR spectra (y-axis), against the stoichiometric ratio of Tz used during bulk powder synthesis (x-axis), showing excellent linear correlation (y = -0.34 + 0.99x), with R^2 = 0.999. The single crystal sample of **[Tz$_{0.5}$Dz$_{0.5}$]** is represented by a red asterisk……..241
Figure E.2: (a) The asymmetric unit of **[Tz$_{0.5}$Dz$_{0.5}$]** at 100 K with thermal ellipsoids at 50% probability. (b) Overlay of the single crystal structures: **[Tz$_{1.0}$Dz$_{0.0}$]** at 100 K (in blue), **[Tz$_{0.5}$Dz$_{0.5}$]** at 100 K (in yellow) and PSM **[Tz$_{0.0}$Dz$_{1.0}$]** at 90 K (in red)…….……243
Figure E.3: The plot of the first derivative of $\chi_M T$ against temperature for the MIXMOF series **[Tz$_{1.0}$Dz$_{0.0}$]** to **[Tz$_{0.2}$Dz$_{0.8}$]**……243
Figure E.4: Evolution of the unit cell (a) *a*-, (b) *b*-, (c) *c*-axes and (d) volume of **[Tz$_{1.0}$Dz$_{0.0}$]** powder framework (300–220–300 K) determined from Le Bail refinements of the VT-PXRD data. (e) Variable temperature magnetic susceptibility data (black) overlaid with PXRD data, cooling branch (blue)..244
Figure E.5: Evolution of the unit cell (a) *a*-, (b) *b*-, (c) *c*-axes and (d) volume of **[Tz$_{0.8}$Dz$_{0.2}$]** powder framework (300–200–300 K) determined from Le Bail refinements of the VT-PXRD data. (e) Variable temperature magnetic susceptibility data (black) overlaid with PXRD data, cooling branch (blue), heating branch (red). ……245
Figure E.6: Evolution of the unit cell (a) *a*-, (b) *b*-, (c) *c*-axes and (d) volume of **[Tz$_{0.6}$Dz$_{0.4}$]** powder framework (300–200–300 K) determined from Le Bail refinement of the VT-PXRD data. (e) Variable temperature magnetic susceptibility data (black) overlaid with PXRD data, cooling branch (blue), heating branch (red)……..……246
Figure E.7: Evolution of the unit cell (a) *a*-, (b) *b*-, (c) *c*-axes and (d) volume of **[Tz$_{0.5}$Dz$_{0.5}$]** powder framework (300–200–300 K) determined from Le Bail refinements of the VT-PXRD data. (e) Variable temperature magnetic susceptibility data (black) overlaid with PXRD data, cooling branch (blue),

heating branch (red)…….247
Figure E.8: Evolution of the unit cell (a) *a*-, (b) *b*-, (c) *c*-axes and (d) volume of **[Tz$_{0.4}$Dz$_{0.6}$]** powder framework (300–200–300 K) determined from Le Bail refinements of the VT-PXRD data. (e) Variable temperature magnetic susceptibility data (black) overlaid with PXRD data, cooling branch (blue), heating branch (red).……..……..248
Figure E.9: Evolution of the unit cell (a) *a*-, (b) *b*-, (c) *c*-axes and (d) volume of **[Tz$_{0.2}$Dz$_{0.8}$]** powder framework (300–200–300 K) determined from Le Bail refinements of the VT-PXRD data. (e) Variable temperature magnetic susceptibility data (black) overlaid with PXRD data, cooling branch (blue), heating branch (red).……..……..……..……249
Figure E.10: Comparison of the change in acute compression angle θ, of the MIXMOF series **[Tz$_x$Dz$_{1-x}$]** (x = 1.0, 0.8, 0.6, 0.5, 0.4, 0.2) at different temperatures (300–220 K)……..……..…250
Figure E.11: Comparison of the change in unit cell volume of the MIXMOF series**[Tz$_x$Dz$_{1-x}$]** (x = 1.0, 0.8, 0.6, 0.5, 0.4, 0.2) at different temperatures (300–220 K)……..……..……..…251
Figure E.12: Comparison of the change in the unit cell (a) *a*-, (b) *b*-, (c) *c*-axes, (d) volume and (e) θ value versus the percentage Tz composition in the MIXMOF series **[Tz$_x$Dz$_{1-x}$]** (x = 1.0, 0.8, 0.6, 0.5, 0.4, 0.2) at different temperatures: 300 K, 270 K, 260 K, 250 K and 220 K.……..……...……251
Figure E.13: *a*-axis changes versus temperature with model fit (line) in MIXMOFs (a) **[Tz$_{1.0}$Dz$_{0.0}$]**, (b) **[Tz$_{0.8}$Dz$_{0.2}$],** (c) **[Tz$_{0.6}$Dz$_{0.4}$]**, (d) **[Tz$_{0.5}$Dz$_{0.5}$]**, (e) **[Tz$_{0.4}$Dz$_{0.6}$]**, (f) **[Tz$_{0.2}$Dz$_{0.8}$]**.....252
Figure E.14: *b*-axis changes versus temperature with model fit (line) in MIXMOFs (a) **[Tz$_{1.0}$Dz$_{0.0}$]**, (b) **[Tz$_{0.8}$Dz$_{0.2}$],** (c) **[Tz$_{0.6}$Dz$_{0.4}$]**, (d) **[Tz$_{0.5}$Dz$_{0.5}$]**, (e) **[Tz$_{0.4}$Dz$_{0.6}$]**, (f) **[Tz$_{0.2}$Dz$_{0.8}$]**.....253
Figure E.15: Magnetism changes versus temperature with model fit (line) in MIXMOFs (a) **[Tz$_{1.0}$Dz$_{0.0}$]**, (b) **[Tz$_{0.8}$Dz$_{0.2}$],** (c) **[Tz$_{0.6}$Dz$_{0.4}$]**, (d) **[Tz$_{0.5}$Dz$_{0.5}$]**, (e) **[Tz$_{0.4}$Dz$_{0.6}$]**, (f) **[Tz$_{0.2}$Dz$_{0.8}$]**.....254
Figure E.16: Coefficients of thermal expansion in the *a*-axis versus temperature in MIXMOFs (a) **[Tz$_{1.0}$Dz$_{0.0}$]**, (b) **[Tz$_{0.8}$Dz$_{0.2}$],** (c) **[Tz$_{0.6}$Dz$_{0.4}$]**, (d) **[Tz$_{0.5}$Dz$_{0.5}$]**, (e) **[Tz$_{0.4}$Dz$_{0.6}$]**, (f) **[Tz$_{0.2}$Dz$_{0.8}$]**.....255
Figure E.17: Coefficients of thermal expansion in the *b*-axis versus temperature in MIXMOFs (a) **[Tz$_{1.0}$Dz$_{0.0}$]**, (b) **[Tz$_{0.8}$Dz$_{0.2}$],** (c) **[Tz$_{0.6}$Dz$_{0.4}$]**, (d) **[Tz$_{0.5}$Dz$_{0.5}$]**, (e) **[Tz$_{0.4}$Dz$_{0.6}$]**, (f) **[Tz$_{0.2}$Dz$_{0.8}$]**.....256
Figure E.18: VT-PXRD data from 300 K–200 K–300 K for (a) **[Tz$_{1.0}$Dz$_{0.0}$]** in the 10.1º - 11.2º 2θ range, (b) **[Tz$_{0.5}$Dz$_{0.5}$]** in the 21.5–24.0º 2θ range……..……..258
Figure E.19: (a) Evolution of modelled hydrogen bond changes versus temperature based on fitted lattice parameter *a*-axis and *b*-axis by using Equation 1. (b) Comparison of modelled hydrogen bond changes and measured hydrogen bond based on single crystal data **[Tz$_{1.0}$Dz$_{0.0}$]** versus temperature…258
Figure E.20: VT-PXRD patterns of **DzAu·EtOH** for the cooling process (2θ = 4–33°). (c) VT-PXRD patterns of **1-[Tz$_0$Dz$_1$]** for the heating process (2θ = 4–33°).……..……..……..……..……259
Figure E.21: PXRD pattern of in situ desolvation of **1-M**, **1-M** (black), in 10 minutes collection (red), in 15 minutes collection (blue).……..……..……..……..……..……..……..……259
Figure E.22: VT-PXRD peak evolution of **1-ΦM** generated from **1-M** (left) and **1-O** (right) over the temperature range: 300 K–100K–340 K.……..……..……..……..……..……..……260

Figure E.23: VT-PXRD peak evolution of **1-ΦM** generated from **1-O** (a) upon cooling 300 K to 100 K; (b) upon heating from 100 K to 330 K.....260
Figure E.24: VT-PXRD peak evolution of **1-Φ** generated from **1-M** (a) upon cooling 300 K to 100 K; (b) upon heating from 100 K to 330 K.....261
Figure E.25: Evolution of unit cell (a) *a*-, (b) *b*-, (c) *c*-axes and (d) volume of **DzAu·EtOH** powder framework (300–100– 325 K) of the VT-PXRD data, cooling branch (blue); heating branch (red); mixed orthorhombic phase (green).....262
Figure E.26: Pawley refinement of the PXRD pattern of (a) **1-O-RT** and (b) **1-M-RT** at 300 K; experimental pattern (blue), calculated fit (green), background (red), difference (cyan) and hkl (vertial bar).....264
Figure E.27: (a) Overlay structures of **1** with solvent at 90 K (blue) and calculated desolvated structure (red). (b) Comparison of PXRD pattern of experimental desolvated structure (black) and simulated PXRD pattern from DFT calculation (red). *hkl* indices (blue vertical bar) are from DFT calculated structure.....264
Figure E.28: VT-PXRD peak evolution of **[$Tz_{0.1}Dz_{0.9}$]** with two thermal cycles (280 – 100 – 280 – 100 – 340 K).....265
Figure E.29: Lattice parameters of **[$Tz_{0.1}Dz_{0.9}$]** (red) and **[$Tz_{0.15}Dz_{0.85}$]** (black) extracted from PXRD patterns with the data refined in the orthorhombic phase. The patterns were collected from original phases and followed by each thermal cycle at 300 K. The change of each lattice parameters versus each collections of (a) *a*-axis, (b) *b*-axis, (c) *c*-axis and (d) volume…….266
Figure E.30: (a) Variable temperature magnetic susceptibility measurement of **HTzAu·EtOH** and (b) PXRD patterns of **HTzAu·EtOH** (black) and **TzAu·EtOH** (red)……..……266

List of Tables

Table 3.1: Physical properties of xylene isomers. 49
Table 3.2: Comparison of selected structural parameters for **TzAu·OX** in the HS and LS states. 53
Table 3.3: Selected structural parameters for **TzAu·PX** in the HS and LS states. 56
Table 3.4: The ratio of the pure binary solvent mixture and binary solvent mixture within each TzAu frameworks. 79
Table 4.1: Comparison of the unit cell parameters of **DzAu·OX** and **DzAu·EtOH** (the unit cell information obtained from literature[13]) at 100 and 90 K, respectively. 90
Table 4.2: Comparison of the selected structural parameters for **DzAu·OX** (100 K and 230 K) and **DzAu·EtOH** (90 K). 91
Table 4.3: The unit cell parameters of **DzAu·MX** at 100 K and 230 K. 95
Table 4.4: Comparison of selected structural parameters for **DzAu·MX** at 100 K and 230 K. 95
Table 4.5: The unit cell parameters of **DzAu·PX** at 100, 155 and 230 K. 99
Table 4.6: Comparison of selected structural parameters for **DzAu·PX** at 100 K, 155 K, and 230 K. 101
Table 4.7: The ratio of the pure binary solvent mixture and binary solvent mixture within the DzAu framework. 109
Table 4.8: Comparison of the unit cell parameters of **DzAu·OX**, **DzAu·MX**, **DzAu·PX** and **DzAu·EtOH**. 109
Table 5.1: Comparison of selected structural parameters for **TzAg·EtOH** at 100 K. 120
Table 5.2: Comparison of the unit cell parameters of **DzAg·EtOH** at 100, 180, 195 and 260 K. 124
Table 5.3: Comparison of selected structural parameters for the **DzAg·EtOH** framework at 100, 180, 195 and 260 K. 125
Table 5.4: Comparison of selected structural parameters for the **DzPd** and **DzPt** at 100 K. 134
Table 5.5: Comparison of the unit cell parameters for the **TzAg·EtOH**, **$TzAu_{0.5}Ag_{0.5}$·EtOH** and **TzAu·EtOH** at 100 K and the difference in θ between HS and LS state. 135
Table 5.6: Comparison of selected structural parameters for **$TzAu_{0.5}Ag_{0.5}$·EtOH** at 100 K and 320 K. 137
Table 5.7: Comparison of the unit cell parameters for **DzAg·EtOH**, **$DzAu_{0.5}Ag_{0.5}$·EtOH** at 100 K and **DzAu·EtOH** at 90 K.[38] 138
Table 5.8: Comparison of selected structural parameters for **$DzAu_{0.5}Ag_{0.5}$·EtOH** at 100, 160, 179 and 230 K. 139
Table 5.9: XPS results of Au 4*f* and Ag 3*d* binding energy. 150
Table 7.1: Comparison of unit cell parameters, selected bond lengths, and selected angles for **$[Tz_{1.0}Dz_{0.0}]$**, **$[Tz_{0.5}Dz_{0.5}]$** and PSM **$[Tz_{0.0}Dz_{1.0}]$** frameworks. 177
Table A.1: Crystallographic data for **TzAu·OX** at 100 and 300 K. 213

Table A.2: Crystallographic data for **TzAu·PX** at 100 and 310 K…….215

Table B.1: Crystallographic data for **DzAu·OX** at 100 and 230 K……..221

Table B.2: Crystallographic data for **DzAu·MX** at 100 and 230 K…….222

Table B.3: Crystallographic data for **DzAu·PX** at 100, 155 and 230 K……..223

Table C.1: Crystallographic data for **TzAg·EtOH** at 100 K……227

Table C.2: Crystallographic data for **DzAg·EtOH** at 100, 180, 195 and 260 K…….228

Table C.3: Crystallographic data for **DzPt** at 100 K……229

Table C.4: Crystallographic data for **DzPd** at 100 K……..230

Table C.5: Crystallographic data for **$TzAu_{0.5}Ag_{0.5}$·EtOH** at 100 and 320 K…….……...231

Table C.6: Crystallographic data for **$DzAu_{0.5}Ag_{0.5}$·EtOH** at 100, 160, 179 and 230 K……..232

Table D.1: Spin transition temperatures for **TzAu·EtOH** at 0.33, 0.35, 0.36, 0.37, 0.39, 0.45, 0.54, 0.62, 0.76 and 0.99 GPa with the scan rate of 1, 2 and 5 K min^{-1}. The 'zero scan rate' spin transition temperatures were extrapolated based on the measured scan rates……..…238

Table D.2: Lattice information of **TzAu·EtOD** (with ethanol as a pressure medium) extracted from NPD data at different pressures.……...……239

Table D.3: Lattice information of the second batch **[$Tz_{0.5}Dz_{0.5}$]** (with fluorinert FC-70 as a pressure medium) extracted from NPD data at different pressures…….……239

Table E.1: Crystallographic data for **[$Tz_{0.5}Dz_{0.5}$]** in the LS state……..……242

Table E.2: Parameters for the Equation 1 to model the unit cell changes versus temperature based on VT-PXRD data for MIXMOFs: **[$Tz_{1.0}Dz_{0.0}$]**, **[$Tz_{0.8}Dz_{0.2}$]**, **[$Tz_{0.6}Dz_{0.4}$]**, **[$Tz_{0.5}Dz_{0.5}$]**, **[$Tz_{0.4}Dz_{0.6}$]** and **[$Tz_{0.2}Dz_{0.8}$]**.....257

Table E.3: Maximum thermal expansion α_a and α_b induced by spin transition……..……..257

Table E.4: Latter parameters of bulk powder **DzAu·EtOH** using Pawley refinement…….263

General Abbreviations and Symbols

°	degrees
θ	diffraction angle
θ	scissor motion angle
χ_M	molar magnetic susceptibility
δ	chemical shift (NMR)
Δ_o	ligand field splitting parameter
ΔT	temperature difference
γ_{HS}	high spin molar fraction
λ	wavelength
μ	absorption coefficient (SCXRD)
ρ	density (SCXRD)
Σ	octahedral distortion parameter (SCXRD)
1D	one-dimensional
2D	two-dimensional
3D	three-dimensional
Å	angstrom
a, b, c	unit cell parameters (lengths)
α, β, γ	unit cell parameters (angles)
a.u.	arbitrary units
ca.	*circa*, about/approximately
cf.	*confer*, compare
et al.	Et alii
e.g.	Exempli gratia
i.e.	Id est
C	celsius
CIF	crystallographic information file
cm	centimetre
cm^{-1}	wavenumber
d	doublet (NMR)
d	atomic distance (SCXRD)
d	deuterated (NMR solvents)
EtOH	ethanol
$CHCl_3$	chloroform
CO_2	carbon dioxide
H_2O	water
N_2	nitrogen
DMSO	dimethylsulfoxide
MeOH	methanol
OX	*o*-xylene
PX	*p*-xylene
MX	*m*-xylene
IR	infrared Spectroscopy
g	gram
GoF	goodness of fit (SCXRD)
h	hour
HS	high spin
J	coupling constant (NMR)
K	kelvin
k_B	Boltzmann constant
LS	low spin
m	medium peak intensity (IR)
m	multiplet (NMR)

mg	milligram
MHz	megahertz
min	Minute
MIXMOF	mixed-ligands metal-organic framework
MMMOF	mixed-metals metal-organic framework
mL	millilitre
mm	millimetre
mmol	millimole
MOF	Metal-organic framework
mol	mole
nm	nanometre
NMR	Nuclear Magnetic Resonance
V	Unit cell volume
VT	variable temperature
VP	variable pressure
IR	Infrared Spectroscopy
UV	UV-vis-Near Infrared
NPD	neutron powder diffraction
DSC	differential scanning calorimetry
XPS	X-ray photoelectron spectroscopy
SEM	scanning electron microscopy
EDS	energy-dispersive X-ray spectroscopy
P	electron pairing energy
PFA	perfluoroalkoxy
PP	polypropylene
ppm	parts per million
PPMS	Physical Property Measurement System
PSM	Postsynthetic modification
SBU	Secondary building units
SR-MOF	Stimuli-Responsive Metal-Organic Framework
PXRD	Powder X-ray Diffraction
DFT	Density Functional Theory
TGA	Thermogravimetric Analysis
MD	Molecular Dynamics
LIESST	Light-Induced Excited Spin-State Trapping
NTE	negative thermal expansion
PTE	positive thermal expansion
NLC	negative linear compressibility
PLC	positive linear compressibility
ANSTO	Australian Nuclear Science and Technology Organisation
r	bond length
R	residual (SCXRD)
RT	Room temperature
s	second
s	singlet (NMR)
s	strong peak intensity (IR)
S	total spin quantum number
SCO	spin crossover
SCXRD	Single Crystal X-ray Diffraction
T	tesla
T	temperature
$T_{½}$	transition temperature
$T_{½}\uparrow$	transition temperature upon heating
$T_{½}\downarrow$	transition temperature upon cooling

V	volume (SCXRD)
VSM	Vibrating Sample Magnetometer
w	weak peak intensity (IR)
Z	formula units per unit cell (SCXRD)
K_l	compressibility
α	thermal expansion coefficient

Ligand and Compound Abbreviations

Dz	3,6-bis(4-pyridyl)-1,2-diazine
Tz	3,6-bis(4-pyridyl)-1,2,4,5-tetrazine
HTz	3,6-bis(4-pyridyl)-1,4-dihydro-1,2,4,5-tetrazine
TzAu·EtOH or **[$Tz_{1.0}Dz_{0.0}$]**	$[Fe(Tz)(Au(CN)_2)_2]\cdot x(EtOH)$
DzAu·EtOH or **[$Tz_{0.0}Dz_{1.0}$]**	$[Fe(Dz)(Au(CN)_2)_2]\cdot x(EtOH)$
1-O	$[Fe(Dz)(Au(CN)_2)_2]\cdot x(EtOH)$ in orthorhombic phase
1-O-RT	$[Fe(Dz)(Au(CN)_2)_2]\cdot x(EtOH)$ in orthorhombic phase at room temperature
1-M	$[Fe(Dz)(Au(CN)_2)_2]\cdot x(EtOH)$ in monoclinic phase
1-M-RT	$[Fe(Dz)(Au(CN)_2)_2]\cdot x(EtOH)$ in monoclinic phase at room temperature
1-ΦM	$[Fe(Dz)(Au(CN)_2)_2]$
TzAu·OX	$[Fe(Tz)(Au(CN)_2)_2]\cdot(OX)$
TzAu·PX	$[Fe(Tz)(Au(CN)_2)_2]\cdot(PX)$
TzAu·MX	$[Fe(Tz)(Au(CN)_2)_2]\cdot(MX)$
DzAu·OX	$[Fe(Dz)(Au(CN)_2)_2]\cdot(OX)$
DzAu·PX	$[Fe(Dz)(Au(CN)_2)_2]\cdot(PX)$
DzAu·MX	$[Fe(Dz)(Au(CN)_2)_2]\cdot(MX)$
TzAg·EtOH	$[Fe(Tz)(Ag(CN)_2)_2]\cdot x(EtOH)$
DzAg·EtOH	$[Fe(Dz)(Ag(CN)_2)_2]\cdot x(EtOH)$
$TzAu_{0.5}Ag_{0.5}$·EtOH	$[Fe(Tz)((Au(CN)_2)_{0.5}(Ag(CN)_2)_{0.5})_2]\cdot x(EtOH)$
$DzAu_{0.5}Ag_{0.5}$	$[Fe(Dz)((Au(CN)_2)_{0.5}(Ag(CN)_2)_{0.5})_2]\cdot x(EtOH)$
$DzAu_{0.7}Ag_{0.3}$	$[Fe(Dz)(Au(CN)_2)_{0.7}(Ag(CN)_2)_{0.3}]_2]\cdot x(EtOH)$
DzPt	$[Fe(Dz)(H_2O)_2Pt(CN)_4]\cdot 2(H_2O)$
DzPd	$[Fe(Dz)(H_2O)_2Pd(CN)_4]\cdot 2(H_2O)$
[$Tz_{0.1}Dz_{0.9}$]	$[Fe(Tz)_{0.1}(Dz)_{0.9}Au(CN)_2)_2]\cdot x(EtOH)$
[$Tz_{0.15}Dz_{0.85}$]	$[Fe(Tz)_{0.15}(Dz)_{0.85}Au(CN)_2)_2]\cdot x(EtOH)$
[$Tz_{0.2}Dz_{0.8}$]	$[Fe(Tz)_{0.2}(Dz)_{0.8}Au(CN)_2)_2]\cdot x(EtOH)$
[$Tz_{0.3}Dz_{0.7}$]	$[Fe(Tz)_{0.3}(Dz)_{0.7}Au(CN)_2)_2]\cdot x(EtOH)$
[$Tz_{0.4}Dz_{0.6}$]	$[Fe(Tz)_{0.4}(Dz)_{0.6}Au(CN)_2)_2]\cdot x(EtOH)$
[$Tz_{0.5}Dz_{0.5}$]	$[Fe(Tz)_{0.5}(Dz)_{0.5}Au(CN)_2)_2]\cdot x(EtOH)$
[$Tz_{0.6}Dz_{0.4}$]	$[Fe(Tz)_{0.6}(Dz)_{0.4}Au(CN)_2)_2]\cdot x(EtOH)$
[$Tz_{0.7}Dz_{0.3}$]	$[Fe(Tz)_{0.7}(Dz)_{0.3}Au(CN)_2)_2]\cdot x(EtOH)$
[$Tz_{0.8}Dz_{0.2}$]	$[Fe(Tz)_{0.8}(Dz)_{0.2}Au(CN)_2)_2]\cdot x(EtOH)$
[$Tz_{0.9}Dz_{0.1}$]	$[Fe(Tz)_{0.9}(Dz)_{0.1}Au(CN)_2)_2]\cdot x(EtOH)$
HTzAu·EtOH	$[Fe(HTz)(Au(CN)_2)_2]\cdot x(EtOH)$
TzAu·PM37	$[Fe(Tz)(Au(CN)_2)_2]$ soaked in PX and MX mixture with PX:MX = 3:7
TzAu·PM50	$[Fe(Tz)(Au(CN)_2)_2]$ soaked in PX and MX mixture with PX:MX = 5:5

TzAu·PM73	$[Fe(Tz)(Au(CN)_2)_2]$ soaked in PX and MX mixture with PX:MX = 7:3
TzAu·PO37	$[Fe(Tz)(Au(CN)_2)_2]$ soaked in PX and OX mixture with PX:OX = 3:7
TzAu·PO50	$[Fe(Tz)(Au(CN)_2)_2]$ soaked in PX and OX mixture with PX:OX = 5:5
TzAu·PO73	$[Fe(Tz)(Au(CN)_2)_2]$ soaked in PX and OX mixture with PX:OX = 7:3
TzAu·MO37	$[Fe(Tz)(Au(CN)_2)_2]$ soaked in MX and OX mixture with MX:OX = 3:7
TzAu·MO50	$[Fe(Tz)(Au(CN)_2)_2]$ soaked in MX and OX mixture with MX:OX = 5:5
TzAu·MO73	$[Fe(Tz)(Au(CN)_2)_2]$ soaked in MX and OX mixture with MX:OX = 7:3
DzAu·PM50	$[Fe(Dz)(Au(CN)_2)_2]$ soaked in PX and MX mixture with PX:MX = 5:5
DzAu·PO50	$[Fe(Dz)(Au(CN)_2)_2]$ soaked in PX and OX mixture with PX:OX = 5:5
DzAu·MO50	$[Fe(Dz)(Au(CN)_2)_2]$ soaked in MX and OX mixture with MX:OX = 5:5
DzAu·PM91	$[Fe(Dz)(Au(CN)_2)_2]$ soaked in PX and MX mixture with PX:MX = 9:1
DzAu·PO91	$[Fe(Dz)(Au(CN)_2)_2]$ soaked in PX and OX mixture with PX:OX = 9:1

List of Publications and Conference Presentations

Publications contain work performed during the candidate's PhD that were not presented in this thesis

1. Xu, L.; **Xie, Z.**; Zenere, K. A.; Clegg, J. K.; Kenny, E.; Rijs, N. J.; Jameson, G. N. L.; Kepert, C. J.; Powell, B. J.; Neville, S. M., *Dalton Trans*. **2022**.
2. Ahmed, M.; Arachchige, K. S. A.; **Xie, Z.**; Price, J. R.; Cruddas, J.; Clegg, J. K.; Powell, B. J.; Kepert, C. J.; Neville, S. M., *Inorg. Chem.* **2022**
3. Wang, T.; Sabatini, R. P.; Chan, B.; Hou, J.; Huynh, V. T.; Proschogo, N.; **Xie, Z.**; Wang, T.; Gao, L.; Zhang, J.; Hawkett, B. S.; Clarke, R. J.; Kepert, C. J.; Chen, V.; Lakhwani, G.; D'Alessandro, D. M., *ACS Mater. Lett.* **2021,** *3* (11), 1599-1604.
4. Ong, X.; Ahmed, M.; Xu, L.; Brennan, A. T.; Hua, C.; Zenere, K. A.; **Xie, Z.**; Kepert, C. J.; Powell, B. J.; Neville, S. M., *Chemistry* **2021**, *3* (1), 360-372.
5. Ezzedinloo, L.; Zenere, K. A.; **Xie, Z.**; Ahmed, M.; Scottwell, S.; Bhadbhade, M.; Brand, H. E. A.; Clegg, J. K.; Hua, C.; Sciortino, N. F.; Parker, L. C.; Powell, B. J.; Kepert, C. J.; Neville, S. M., *Eur. J. Chem*. **2021**, *27* (16), 5136-5141.
6. Ahmed, M.; **Xie, Z.**; Thoonen, S.; Hua, C.; Kepert, C. J.; Price, J. R.; Neville, S. M., *Chem. Commun.* **2021,** *57* (1), 85-88.

Conference presentations from parts of this thesis

1. ANBUG-AINSE Neutron Scattering Symposium, oral presentation: *Investigation of anomalous thermal and pressure-induced distortion in spin crossover materials.*, Sydney, Novermber 9-11th, 2022
2. RACI National Congress, oral presentation: *Reversible Structural Transition in a Responsive Metal Organic Framework Material.* Brisbane, Australia, 3-8th July, 2022.
3. International School of Crystallography, Diffuse Scattering: The Crystallography of Dynamics, Defects, and Disorder, poster presentation: *The interplay between spin crossover phenomenon and structural properties in responsive metal-organic frameworks*. Erice, Italy, June 3-11th, 2022
4. Virtual Conference of the ANSTO clip day 2022, oral presentation: *Anomalous Thermal and Pressure-Induced Distortion in a Spin Crossover Framework*., February 23-24th, 2022.
5. Virtual Conference of the Inorganic Chemistry Division of the RACI (IC 21), oral presentation: *Spin Crossover Induced Negative Thermal Expansion in Stimuli-Responsive Metal-Organic Frameworks*. July 6-8th, 2021.
6. Crystal 33 Virtual Conference of the Society of Crystallographers in Australia and New Zealand, poster presentation: *Investigating the magnetic and structural properties of spin crossover metal-organic frameworks*., May 25-27th, 2021.
7. RACI Inorganic Division Conference (IC 19), poster presentation: *Tuneable Spin Crossover Behaviours in Metal-Organic Frameworks*. Wollongong, Australia, December 15-19th, 2019.
8. The 6th International conference on metal-organic frameworks and open framework compounds, poster presentation: *Interchangeable Spin Crossover Behaviour in Mixed-Ligand Metal-Organic Frameworks via Reversible Solid-State Phase Transitions.* Auckland, New Zealand, December 9-13th, 2018.

9. NSW Inorganic One-Day Symposium, oral presentation: *The 'Breathing-like' Effect and Spin Crossover Behaviour in Mixed-Ligand Metal-Organic Frameworks.* Sydney, Australia, November 19th, 2018.

Chapter 1

Introduction

1.1 Background and Motivation

The development of 'smart materials' possessing emergent properties is a thriving and intriguing research topic owing to their potential applications in a broad range of fields, such as artificial machines, digital technology and medical treatment. Control over their functionalities is paramount in designing such materials, with metal-organic frameworks (MOFs) proving a promising class of materials due to the diverse choices of metal centres and coordinated organic linkers available.[1-4] The highly porous nature of MOFs makes them very desirable candidates for investigations into their framework architecture and functional tunability.[5-7] Understanding the correlation between their underlying structural properties at the atomic level and variable performances is also a key challenge.

1.2 Stimuli-Responsive Metal-Organic Frameworks (SR-MOFs) and Spin Crossover (SCO) Phenomenon

1.2.1 Overview of SR-MOFs

MOFs are generally constructed *via* the 'building block' approach whereby metal clusters, also known as secondary building units (SBUs), self-assemble and coordinate with organic ligands (or linkers) forming one-, two- or three-dimensional topologies depending on the geometry of the metal ion and denticity of the linkers.[5-9] The various choice of metal centres and bridging ligands for MOF designs creates infinite possibilities for changing sizes, shapes, and functional properties of the materials.[10-12] Thus, developing strategies for the rational design of MOFs is paramount to employing their advanced functions for applications in guest absorption and/or separation,[13-15] information storage,[16-17] sensing,[18-20] magnetism,[21-22] drug delivery,[23-25] and catalysis.[26-27]

Inspired by nature, stimuli-responsive materials (SRMs) are functional artificial materials designed to respond to external stimuli.[28-29] Such materials have been applied in many fields including physical chemistry, biochemistry, and material science[30-31] and support various applications in drug delivery,[32-34] biosensors,[35] catalyses,[36-38] and storage devices.[10, 39] One significant subset of SRMs are stimuli-responsive metal-organic frameworks (SR-MOFs)[37, 40-41], which have attracted great interest due to the advantages MOFs provide with their large pore sizes, transformability, crystallinity, and their tunable stimuli responses.[42-44] Whilst most MOFs are considered rigid, SR-MOFs constructed from carefully chosen building blocks present dynamic behaviours in both local and long range structures.[40, 45]

SR-MOFs can be generated by different strategies (Figure 1.1): a) responsive building units in a direct synthesis using stimuli-responsive metals or ligands; b) guest exchange to responsive guest molecules; c) ligand exchange to a stimuli sensitive species by post-synthetic modification (PSM); d) metal exchange, which uses a similar method as ligand exchange; e) activation of 'dormant' functional

groups through covalent modification; f) core-shell approach which is the encapsulation of a responsive core.[28, 46]

The stimuli applied to SR-MOFs can be classified into either chemical and/or physical stimuli. Chemical stimuli involve neutral molecules (eg., gas and solvent), ionic molecules, redox and pH changes, while physical stimuli include temperature, light, pressure, and ultrasound.[47-48] Developing materials responsive to multi stimuli is a significant interest, with those that exhibit spin crossover behaviour attracting increased attention in recent years.

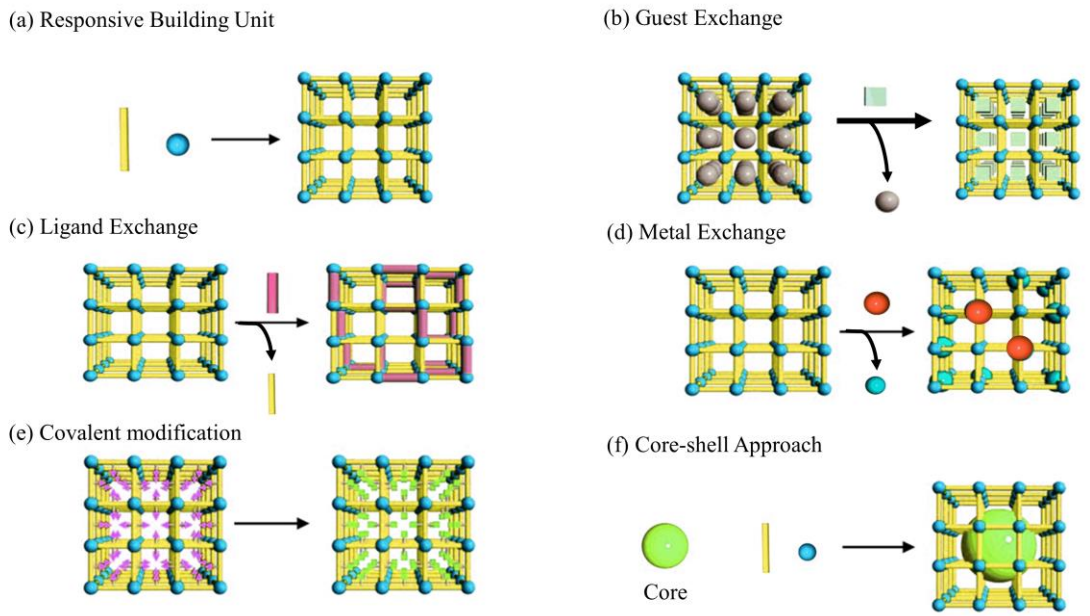

Figure 1.1: Schematic of strategies employed in the of synthesis SR-MOFs. Adapted from Nagarkar *et al.*.[46]

1.2.2 Overview of SCO

Spin crossover (SCO) is the reversible switching of a metal ion's electronic state between high spin (HS) and low spin (LS) states that occurs in materials containing certain transition metal ions (d^4-d^7).[49-55] This bistability of spin states in SCO materials can be triggered by external stimuli such as temperature, pressure, and light.[55-58] SCO behaviour can also be manipulated by replacing and/or removing guest molecules within the pores of the framework. MOFs possessing SCO behaviour are a type of SR-MOF owing to their high sensitivity in responding to physical or chemical stimuli.[10, 59] Such sensitive materials possess potential applications most notably in molecular sensing, information storage devices, and optical devices.[49, 51] Yet, designing SCO materials with both desired and controllable switching behaviour through the manipulation of their stimuli response is a formidable challenge where a deep understanding of structure-property relationships is crucial.

The first reported display of SCO behaviour was by Cambi *et al*. in a Fe(III) dithiocarbamate

system in 1931.[60] Although still most commonly observed in Fe(II) system, the SCO phenomenon has been since been observed in many more transition metal ions such as Mn(II), Cr(II), Co(II), Co(III), Mn(III) and Ni(III).[57, 61-63] This work will focus primarily on Fe(II) systems due to the pronounced differences in properties displayed in these materials.

In an octahedral ligand field, splitting of the ground state *d*-orbital occurs, forming higher energy e_g orbitals (d_{z^2}, $d_{x^2-y^2}$) and lower energy t_{2g} orbitals (d_{xy}, d_{xz}, d_{yz}) separated by the ligand field splitting parameter (Δ_o). In the HS state electrons are distributed across both the lower and higher orbitals, whilst in the LS state electrons favour occupying the lower energy t_{2g} orbital. In the paramagnetic HS state of an Fe(II) ion with the electronic configuration ($3d^6$), four electrons occupy the t_{2g} orbitals and two electrons occupy the e_g orbitals, with a maximum total spin of $S = 2$, $^5T_{2g}$ ground term. In the diamagnetic LS state, all six electrons are paired in the e_g orbitals, with $S = 0$, $^1A_{1g}$ ground term.[64-65] The switching between the HS and LS state depends on the magnitude of the ligand field splitting parameter (Δ_o) and mean electron pairing energy (P). When $\Delta_o < P$ the *d*-electrons of the metal ion are favoured to be unpaired and thus adopt the HS configuration. The HS state is entropically favoured due to electrons partially occupying antibonding orbitals. Conversely, if $\Delta_o > P$ the LS state is favoured, with electrons all populating in the t_{2g} orbitals (Figure 1.2). Here, the LS state is enthalpically favoured and stabilised by low temperatures. SCO occurs when $\Delta_o \approx P$, with the zero point energy differences of each spin state (ΔE_{HL}), considered to be on the order of k_BT (k_B = Boltzmann constant, T = temperature). SCO is emergent when the entropic and enthalpic effects are balanced with $\Delta G = \Delta H - T\Delta S = 0$. The temperature at this point is known as the spin transition temperature, $T_{1/2}$, defined by equal fractions of HS and LS states i.e., $\gamma_{HS} = 0.5$ (γ is the relative stoichiometric fraction, γ_{HS} is the molar HS fraction). For SCO materials displaying hysteretic behaviour, the transition temperature on cooling is denoted by $T_{1/2}\downarrow$, whilst for the heating process it is denoted by $T_{1/2}\uparrow$. The molar magnetic susceptibility ($\chi_M T$) is commonly used in the evaluation of the spin states as this directly measures changes in magnetic behaviour. A plot of molar magnetic susceptibility or molar HS fraction as a function of temperature derives a SCO profile. In Fe(II) system, the $\chi_M T$ value is *ca.* 3.4 cm^3 K mol^{-1} ($\gamma_{HS} = 1$) in the HS state with paramagnetic Fe(II) sites while the $\chi_M T$ value is 0 cm^3 K mol^{-1} ($\gamma_{HS} = 0$) in the LS state with diamagnetic Fe(II) sites.

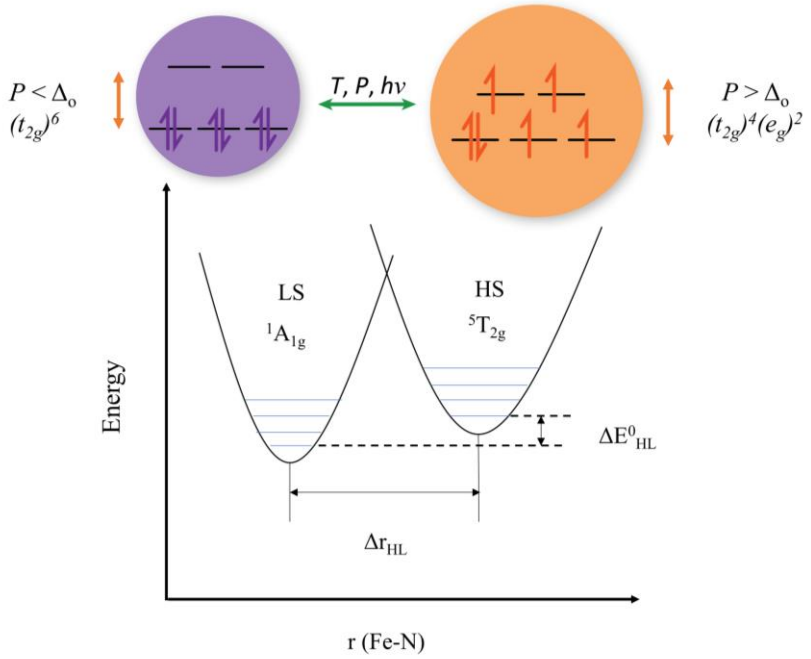

Figure 1.2: Ligand field splitting diagram and adiabatic potential wells for LS and HS states in an octahedral Fe(II) system with metal–donor atomic distance, r(Fe–N).

Cooperativity describes the propagation of changes in SCO sites across a lattice when a spin transition occurs.[66] Communication between SCO sites in a crystal structure can be influenced by inter- and intra-molecular interactions such as hydrogen bonding, aromatic stacking interactions, and coordination bonding.[66-69] Five distinct spin transition types are seen in SCO materials, namely gradual, abrupt, hysteretic, multi-step, and incomplete (Figure 1.3).[49] For materials with weak cooperativity such as in the solution state, a gradual SCO profile over a wide temperature range is noticed, although this can occur in solid state systems as well. For stronger cooperativity in the solid state, different features can emerge depending on the magnitude of electron-phonon coupling between SCO sites and lattice vibrations. Materials with strong cooperativity display an abrupt SCO curve. Designing a material with a combination of these SCO features has attracted great interest, owing to the multiple practical applications possible. For example, combining abrupt and hysteretic SCO behaviour in one material may be used in memory devices as such material possesses the ability to memory pathway attributed to hysteresis.[51, 70] Multi-step transitions are also very interesting phenomena as the mechanism responsible for such behaviours is dependent on the material. Two main conditions by which a multi-step SCO transition may arise: 1. crystallographically inequivalent SCO sites in a system can independently undergo a spin transition, attributed to distinct ligand field splitting energies, thus presenting as multi-spin states; 2. SCO sites are also influenced by the spin state of neighbouring centres, generally found in the elastically frustrated systems.[71-72] Elastic interactions between SCO centres of identical spin states

(ie., HS–HS or LS–LS), are defined as ferroelastic interactions.[73-74] Conversely, the interactions of neighbouring SCO sites with opposite electronic configurations (i.e., HS–LS) are dominated by antiferroelastic interactions.[75-78] As the energy barrier between each SCO undergoing a transition is distinctive, communication between adjacent SCO sites is disrupted leading to stepwise conversion to the LS state. Incomplete SCO is generally attributed to various sources such as a remnant paramagnetic component, structural defects, or large guest molecules preventing a volume change due to an 'internal pressure'.[57, 79-80]

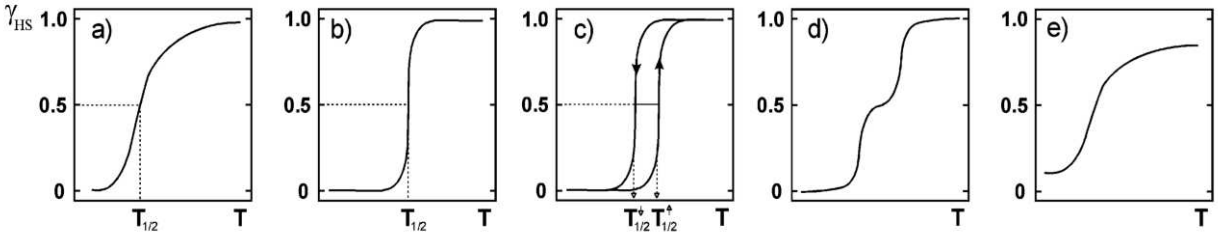

Figure 1.3: The different types of SCO behaviours: (a) gradual, (b) abrupt, (c) hysteretic, (d) multi-step, (e) incomplete (adapted from Gütlich *et al.*).[62]

The structural and physical changes associated with SCO behaviours can be characterised by various techniques. Analysis of variable temperature magnetic susceptibility data provides information on the entire process of spin transition, for example, whether the materials undergo complete SCO and if they are in a multi-step system, and what are the HS fractions in each intermediate plateau between individual stepwise transitions. In the HS state, some electrons occupy antibonding orbitals, leading to weaker and longer Fe–N bonds than those observed in the LS state, with Fe–N *ca*. 2.1 Å in the HS state and *ca*. 1.9 Å in the LS state.[62] Unit cell parameters, lattice flexing, and atom positions are different due to the volume change and bonding strength arising from SCO transitions. Structural change induced by SCO can be characterised using single crystal X-ray diffraction (SCXRD) and powder X-ray diffraction (PXRD) measurements.[53, 57] A colour change is also usually observed when a spin transition occurs, which can be monitored by ultraviolet-visible (UV-Vis) spectroscopy. Other techniques such as infrared spectroscopy (IR), Raman spectroscopy, Mössbauer spectroscopy, and differential scanning calorimetry (DSC) are also used to characterise spin transition, although to a lesser extent.[62, 81]

1.2.3 Thermally-Induced SCO

There have been intensive studies focusing on thermally-induced SCO materials.[51, 82-83] One of the many challenges with creating a practical SCO material is incorporating several desirable and controllable SCO behaviours such as wide hysteresis, close to room temperature spin transition, and multiple transitions.[84-88]

One of the strategies employed to overcome this hurdle is *via* changes in ligand ratios, an approach previously reported in the Fe(II) triazole-based one-dimensional chain, $[Fe(R_1trz)_{3-3x}(R_2trz)_{3x}](A)_n$ (Rtrz = 1,2,4-triazole functionalised ligand, A = counter anion). Here systematic adjustment of the R_1trz and R_2trz ligand compositions allows for fine-tuning of the SCO temperature.[89-91] Similarly, gradual ligand substitution in the mixed-ligand coordination polymer $[Fe(btzx)_{3-3x}(btix)_{3x}](ClO_4)_2$ (btzx = 1,4-bis(tetrazol-1-ylmethyl)benzene, btix = 1,4-bis(triazol-1-ylmethyl)benzene) leads to the appearance of a spin transition at lower temperatures when compared to the pure-ligand materials as a result of different chemical environments.[92] In a distinct approach, oxidative addition of iodine to the open metal sites of Pt(II) in the porous framework $[Fe(pz)(Pt^{II/IV}(CN)_4(I)_n)]$ (pz = pyrazine) results in gradual modulation of the SCO temperature in the range 300–400 K.[93]

SCO materials can be scan rate dependent. Hysteresis widths and spin transition temperatures in a material can be artificially controlled by changing the scan rate when conducting magnetic susceptibility measurements.[94] A sample measured in a faster scan rate usually results in wider hysteresis with lower $T_{1/2}\downarrow$ and higher $T_{1/2}\uparrow$, generally attributed to kinetic effects and slow communication throughout the lattice.[95] . By extrapolating the $T_{1/2}$ value as a function of scan rate, the 'true' hysteresis width or so called 'zero scan rate' hysteresis width can be estimated (Figure 1.4).[82, 96]

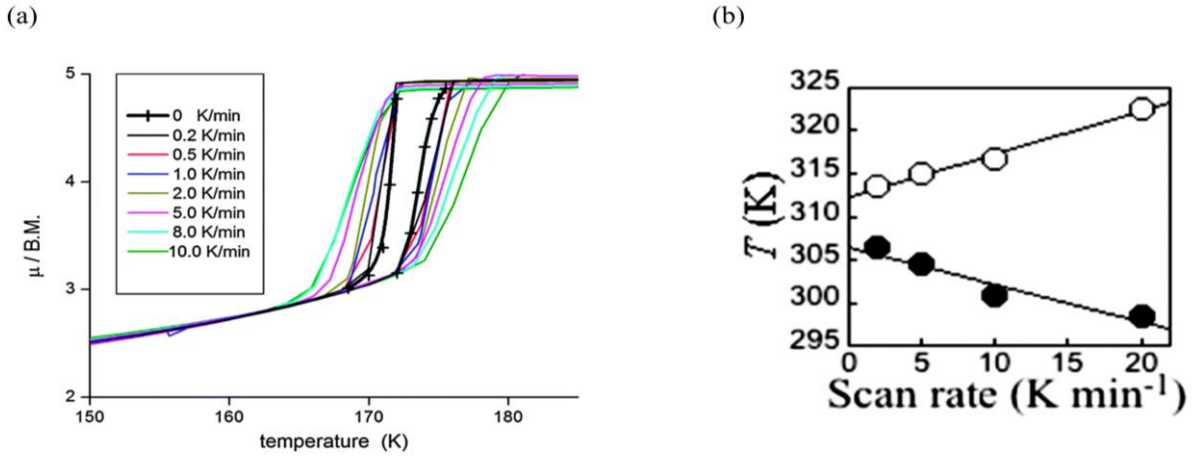

Figure 1.4: (a) The change of hysteresis and spin transition temperature at different scan rates. (b) zero scan rate was estimated by extrapolating the $T_{1/2}$ value as a function of the scan rate. Adapted from Brooker *et al*.[82,96]

In developing strategies for rationally designed SCO materials, insight into the correlation between SCO profiles and structural properties is paramount, with detailed investigations into the structural changes caused by SCO such as metal-ligand bond length, octahedral distortion, octahedral volume and lattice distortion needing to be considered.[81, 83, 97-98]

1.2.4 Pressure-Induced SCO

When compared with temperature-induced SCO, reported studies of pressure-induced SCO remain scarce due to difficult experimental constraints associated with measurements.[99] Ewald *et al*. first published pressure-dependent magnetic conversion of Fe(III) dithiocarbamate complexes in solution in 1964.[100-101] Since then, several examples of pressure-induced SCO have been observed in both discrete complexes and extended framework materials.[102-106] These studies on such materials revealed that pressure-induced SCO is related to the volume of the metal centre environment.[107] The metal-ligand bond distances and volume of SCO coordination sites are smaller in the LS state than in the HS state, which causes the LS state to be favoured with increasing pressure. The potential wells increase vertically with applying higher pressure (Figure 1.5a). The spin transition temperature increases are attributed to the enhancement of the zero-point energy difference ΔE^0_{HL} and reduction of the activation energy ΔW^0_{HL}, thus favouring the LS state (Figure 1.5).[107]

As the LS state is thermodynamically favoured with higher pressure, it is common to observe materials undergo complete SCO behaviour at elevated pressure. For example, $[FePd(CN)_4(thiome)_2]\cdot 2H_2O$ remains in the HS state at ambient pressure, but undergoes complete SCO when the applied pressure reaches 0.68 GPa. Transition temperatures are also known to increase as a result of elevated pressures.[106] Another example, $[Fe(4,4'\text{-bipy})_2(Ag(CN)_2)_2]$, shows the SCO behaviour change from a complete HS state and undergoes a partial conversion to the LS state and finally fully LS at 0.7 GPa.[108] However, there have been a few studies showing anomalous behaviours where the materials are seemingly stabilised in the HS state under pressure. The polymeric compound $[Fe(btr)_2(NCS)_2]\cdot H_2O$ (btr = 4,4′-bis-1,2,4-triazole) exhibits a HS state under pressure, likely due to pressure-induced phase transition, which blocks the formation of a spin transition.[109] $[Fe(dpp)_2(NCS)_2]\cdot py$ also displays a similar behaviour of stabilisation in the HS state under pressure. The antagonistic structural effect of SCO in this material is attributed to scissor-like motion with the application of pressure.[110]

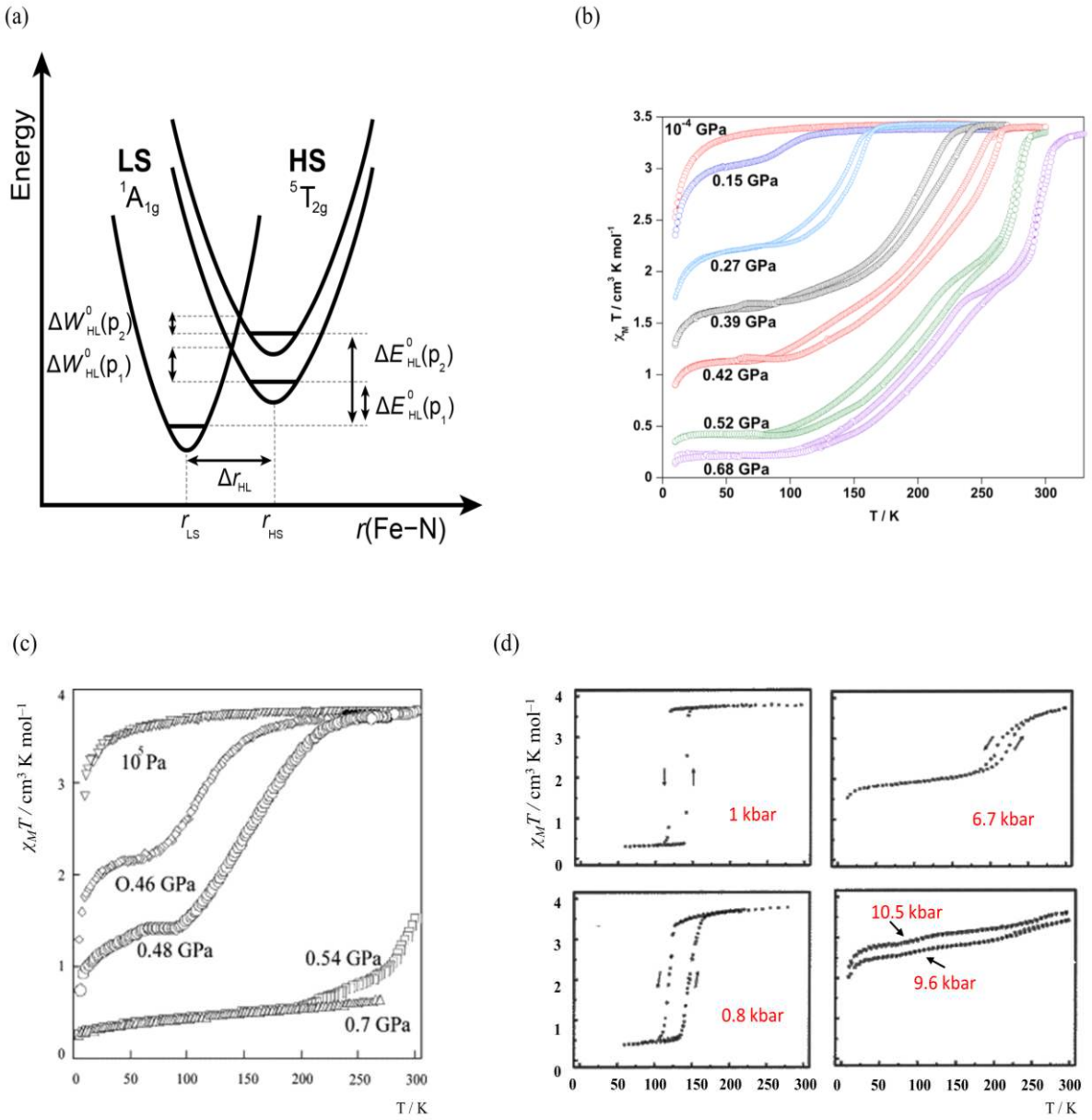

Figure 1.5: (a) Schematic representation of the effect of pressure on the HS and LS state potential wells, where P2 > P1. (b) $\chi_M T$ versus T of $[FePd(CN)_4(thiome)_2]\cdot 2H_2O$ under pressures up to 0.68 Gpa (adapted from Sciortino *et al.*).[106] (c) Magnetic susceptibility versus temperature plots for $[Fe(4,4\text{-bipy})_2(Ag(CN)_2)_2]$ under pressures up to 0.7 Gpa (adapted from Niel *et al.*).[108] (d) Magnetic susceptibility versus temperature plots for $[Fe(btr)_2(NCS)_2]\cdot H_2O$ under the pressure at 0.8, 1.0, 6.7, 9.6, and 10.5 kbar in the temperature range 20–300 K (adapted from Garcia *et al.*).[109]

As well as the abruptness and temperature of transitions, the width of thermal hysteresis is also commonly observed to be changed at higher pressures. Some materials have displayed wider hysteresis with increasing pressure, attributed to enhanced cooperative interactions across the lattice.[111-113] However, the 3D coordination polymer $[Fe(pmd)(H_2O)(Ag(CN)_2)_2]\cdot H_2O$ exhibits a decrease in

hysteresis followed by a dramatically increased width to 31 K in the pressure range 0.25–0.30 GPa, likely due to a structural phase transition and change in the bulk modulus of the material.[114] The polymeric chain compound $[Fe(hyptrz)_3]A_2 \cdot H_2O$ (hyptrz = 4-(3′-hydroxypropyl)-1,2,4-triazole and A = 4-chlorobenzenesulfonate) presents a diminished hysteresis, followed by no hysteresis and finally the re-emergence of hysteresis with continuously increasing pressure.[115] The hysteresis width remained unchanged at different pressure values in the polymeric compound $[Fe(hyetrz)_3](3\text{-nitrophenylsulfonate})_2 \cdot 3H_2O$ (where hyetrz = 4-(2′-hydroxyethyl)-1,2,4-triazole).[116] It is thus worth considering the pressure effect on the completeness, temperature, and hysteresis width of a SCO transition when designing tuneable stimuli-responsive materials for specific applications under pressure.

1.2.5 Light-Induced SCO

SCO behaviour can also be induced by light as was first discovered by McGarvey *et al.* in 1982 when they used pulsed laser radiation to induce a spin transition in several Fe(II) complexes.[117] The conversion of LS to a metastable HS state is typically facilitated by excitations using green light, with such materials capable of remaining in the HS state even at very low temperatures as long as radiation is continuously applied. Such a phenomenon is named light-induced excited-spin-state trapping (LIESST).[118-121] The opposite phenomenon of a switch from a metastable HS state to a LS state can be induced by irradiating with red light (typically) in a process called reverse-LIESST that was first reported in 1986.[122] Another reversion process is by heating at a very slow rate, which can enable the material to return to the LS state.[123] T(LIESST) is defined as the temperature of the transition from the metastable HS state to the LS state, usually determined from the first derivative. Understanding the underlying principles of the LIESST effect is crucial to providing a guideline for the sensible design of materials with controllable LIESST temperatures.[124-127]

1.2.6 Guest Influence on SCO

Aside from physical stimuli, guest molecules as chemical stimuli have also been shown to influence the SCO effect. Guest dependent SCO behaviour was first observed in the nanoporous MOF $Fe_2(azpy)_4(NCS)_4 \cdot (guest)$ (azpy = trans-4,4′-azopyridine).[131] The material displays complete SCO when containing ethanol whilst remaining fully HS in the desolvated framework. This distinctive SCO behaviour in the framework with the removal of ethanol can be explained by structural modifications including the formation of a more regular rhombic grid and the removal of the hydrogen bonding interactions (Figure 1.6). With other adsorbed guest molecules, different SCO behaviours are noticed that are associated with subtle changes in structural symmetry and host–guest interactions.[128] These guest-induced SCO materials were extensively investigated as they have tunable features and variable

SCO behaviours. Such materials have a number of potential applications such as memory devices and molecular sensors.[129]

SCO behaviour can be influenced by the physical properties of guests and their interactions with the host materials. The guest size effect in a nanoporous MOF was reported by Southon *et al*. with a comparison of methanol, ethanol, acetone, acetonitrile, and toluene.[79] It was shown a size-dependent trend with a larger molecular size resulting in lower spin transition temperatures. The larger the guest size increased the internal pressure so the HS state was favoured. The dielectric constant of guest molecules can also influence the SCO behaviour in solvated systems. A study on $[Fe(NCS)_2(bpbd)_2]$ (bpbd 2,3-bis(4′-pyridyl)-2,3-butanediol) with the absorption of guests with different dielectric constants showed smaller dielectric constant stabilised the LS state.[130]

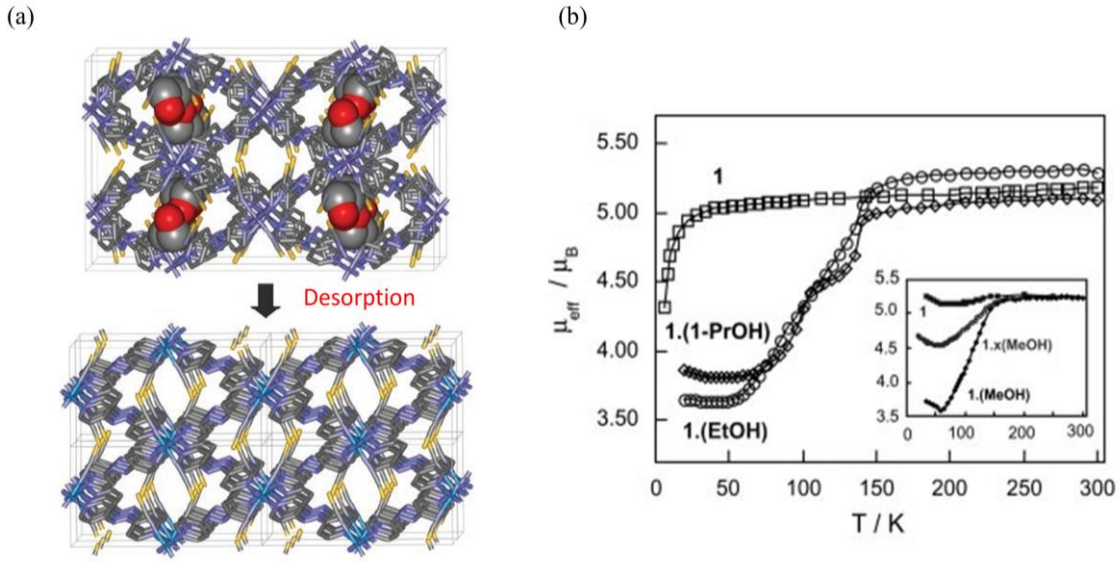

Figure 1.6: (a) Structure of $[Fe_2(azpy)_4(NCS)_4]\cdot EtOH$ (top) and desolvated framework (bottom). (b) Effective magnetic moment versus temperature plots for different guest molecules in $[Fe_2(azpy)_4(NCS)_4]$ (1). Adapted from Halder *et al*.[128]

The π···π interactions from introducing aromatic guests is one of the significant factors, which determine SCO behaviours. The location of the guests is usually in between the bridging ligands, which facilitate strong aromatic interactions, such as in the case of $[Fe(pz)(Pt(CN)_4)]$ where three five-membered aromatic rings (furan, pyrrole, and thiophene) as guests were studied.[131] The competition between the steric effect and the π···π interactions are most noticed in porous materials containing aromatic rings as a guest.[131-133] In order to reduce steric effects whilst also maintaining strong cooperativity through aromatic interactions, a large pore size framework was generated. This framework can incorporate benzene, naphthalene, anthracene, and ferrocene as guests, which perform stepwise and hysteretic SCO behaviours.[68] Although there are several studies detailing the interactions of different aromatic guest effects on SCO, the effect of isomer aromatic guests, which have subtle

discrepancies in physical properties on SCO performances has not been investigated. The detailed study on xylene isomer guests in two MOF analogues is discussed in Chapters 3 and 4.

Hydrogen bonding interactions are known to play a vital role in enhancing cooperativity in SCO materials. The SCO behaviour in $[Fe(2,5\text{-bpp})(Au(CN)_2)_2]\cdot x$Solv (2,5-bpp = 2,5-bis(pyrid-4-yl) pyridine; Solv = ethanol, *n*-propanol, isopropyl alcohol, *2*-butanol and isobutanol) was reported, with each showing different degrees of hydrogen bonding. Variations in SCO frameworks involving different aprotic guests are attributed to the interplay between hydrogen bonding, internal pressure, and electrostatic effects.[134] There are examples whereby varying the number of guest molecules to change the host–guest interactions lead to distinct SCO behaviours.[135-138] Generalising the effect of hydrogen bonding on SCO behaviour is still quite difficult in solid state systems.[139] Studies into the systematic control of the degree of hydrogen bonding in host frameworks have not been examined in great detail. It is worth further studying the hydrogen bonding interactions between the host–host and host–guest to reveal the interplay between framework topology and switchable electronic configurations. In order to gain insight into the effects of hydrogen bonding interactions on SCO behaviour and structural properties of extended systems, a series of MOFs with varying degrees of hydrogen bonding has been generated and is examined in Chapter 7 of this work.

1.2.7 Hofmann Frameworks

The first Hofmann clathrate, $[Ni(NH_3)Ni(CN)_4]\cdot 2C_6H_6$ was synthesised by Karl Hofmann in 1897. The prototypical topology of this material consists of a 2D structure with octahedral Ni(II) centres coordinated axially to NH_3 and equatorially to square planar $[Ni(CN)_4]^{2-}$ units with benzene molecules in the pores.[140] In 1996, a 2D Hofmann-type structure $[Fe(C_5H_5N)_2Ni(CN)_4]$ was first observed to undergo a single-step SCO transition.[67] It is worth noting that $[Ni(NH_3)Ni(CN)_4]\cdot 2C_6H_6$ lacks any SCO behaviour. The comparison of these two Hofmann-type materials indicates that π-electrons of aromatic N-donor atoms play a significant role in the spin transition. Thus, to generate Hofmann-type materials potentially exhibiting SCO behaviours, the SCO metal sites need to be equatorially coordinated with square planar $[M'(CN)_4]^{2-}$ (M′ = Ni(II), Pd(II), Pt(II)), and axially with N-donor aromatic ligands.[129] A similar type of framework materials coordinated with linear $[M'(CN)_2]^-$ (M′ = Au(I), Ag(I), Cu(I)) instead of square planar linkers are defined as Hofmann-like frameworks (Figure 1.7). The first 3D Hofmann-type frameworks were reported $[Fe(pz)M(CN)_4]\cdot nH_2O$ (pz = pyrazine, M = Ni(II), Pd(II), Pt) in 2001 by Niel *et al*.[136] This work demonstrated a strategy to create 3D frameworks by changing the denticity of the axially coordinated ligand from unitopic (forming 2D framework) to ditopic. Since then, more work on SCO behaviours in Hofmann framework materials has been reported and various SCO behaviours observed by careful consideration of pillar ligands, cyanidometallate linkers, and guest molecules.[71, 141-143]

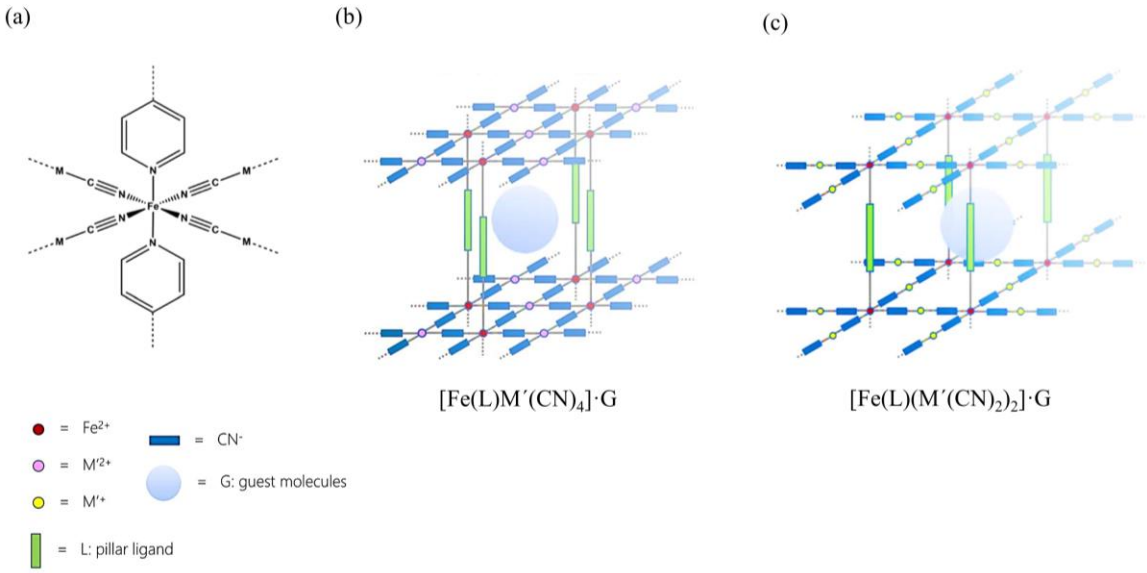

Figure 1.7: Schematic diagrams of the (a) coordination sphere of a Hofmann framework, (b) 3D Hofmann-type framework and (c) 3D Hofmann-like framework. Adapted from Ni *et al.*[129]

Clements *et al.* first reported a four-step hysteretic SCO framework $[Fe(Dz)Au(CN)_2)_2]\cdot 4(EtOH)$ (**DzAu·EtOH**, Dz = 3,6-bis(4-pyridyl)-1,2-diazine) by *de novo* synthesis.[144] This framework adopts a monoclinic phase. This material can also be generated by PSM from a single-crystal-to-single-crystal transformation of $[Fe(Tz)Au(CN)_2)_2]\cdot 2(EtOH)$ (**TzAu·EtOH**, Tz = 3,6-bis(4-pyridyl)-1,2,4,5-tetrazine). Interestingly, **DzAu·EtOH** formed by PSM displays a single-step SCO and forms an orthorhombic phase Figure 1.8).[145] Whilst significant in its outcome, this work poses new questions about the manipulation of the structural interconversion of $[Fe(Dz)Au(CN)_2)_2]$ and the subsequent effect of new host-host interactions on its SCO behaviour. The Tz ligand contains two more nitrogen atoms than the Dz ligand, thus a framework consisting of Tz ligand contains many more hydrogen bonds. Tz- and Dz-based frameworks consisting of different cyanidometallate linkers are ideal platforms to investigate ligand field effect, host–host and host–guest interactions, and therefore to reveal the relationship between their structural and magnetic properties.

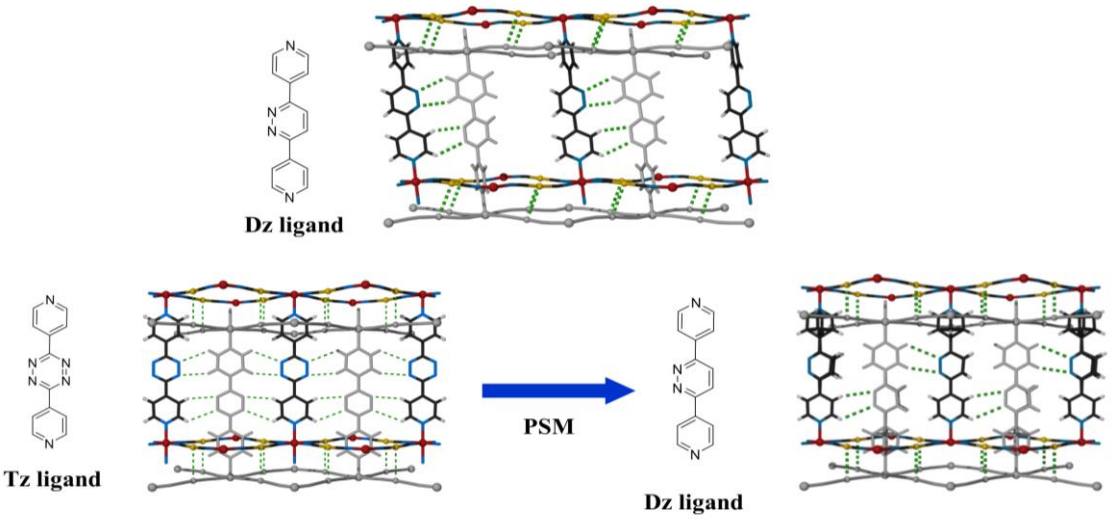

Figure 1.8: Crystal structure of **DzAu·EtOH** in monoclinic phase by the *de novo* synthesis (top) and PSM process from **TzAu·EtOH** to form orthorhombic phase **DzAu·EtOH** framework (bottom). Adapted from Clements *et al*.[144-145]

The aforementioned pressure studies on SCO materials are limited in scope, with investigations of 3D Hofmann frameworks still quite rare. Several published 3D Hofmann frameworks present either incomplete or no SCO at ambient pressure but display a favourable LS state under pressure.[108, 146-147] Little attention has been paid to 3D Hofmann frameworks, which display complete SCO behaviours at ambient pressure. Single crystal structure studies at high pressure still remain very rare, thus[148] further work to examine the correlations between the lattice motion and electronic configurations is needed.

1.3 Flexible Metal-Organic Frameworks (FMOFs)

1.3.1 Elasticity and Memory Effect

It is an emerging challenge to develop and control functional scalable devices in the nanoscale field. One major challenge in this area is to generate FMOFs, which display transformation from the original structural phase to the deformed phase *via* stimuli as the majority of the MOFs are rigid and robust while only less than 10% of these display flexibility.[45, 149] One dynamic mode in FMOFs is a breathing-like motion owing to their 'wine-rack' topology where the pore size and volume of frameworks can reversibly expand or contact by applied stimuli or guest exchange.[150-152] The MIL-53 series is an example of a breathing-like framework that exhibits a reversible structural transition in response to temperature.[153-154] Guest absorption also causes a transition between narrow and large pores demonstrating the breathing-like behaviour in the MIL-53 family (Figure 1.9).[155-157] SCO MOFs are another type of FMOF, which undergo a breathing-like behaviour due to the differences in the volume

of the coordination sphere between HS and LS states. SCO MOFs are worthy of further exploration as such materials combine changes in electronic configuration and lattice deformation in response to stimuli. Herein, this thesis involves research on uncovering the underlying coupling between structural motion and SCO behaviours in response to multiple stimuli.

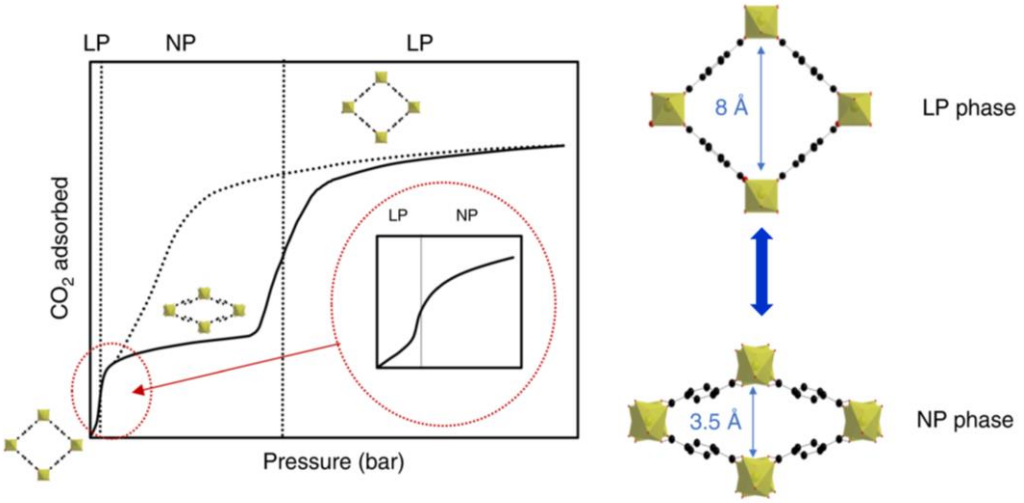

Figure 1.9: (Left) Breathing-like behaviour in MIL-53 framework with adsorption (solid line) and desorption (dashes) of CO_2. (Right) Phase transition between large pore (LP) phase and narrow pore (NP) phases in the framework. Adapted from Chanut *et al.*[156]

Another type of structural flexibility is called 'shape memory'. Such materials are able to have their morphologies altered by external stimuli, such as temperature, pressure, and the adsorption or desorption of guest molecules with the deformed materials able to be recovered to the original state in response to further stimulus.[158-160] The difference between breathing-like behaviour and 'shape memory' behaviour is the former is elastic; once the stimulus is removed the material returns from the deformed structural phase to the original one; while the latter can retain the deformed shape when the stimulus is removed, but can return to the original phase once another stimulus is applied. Materials possessing a 'shape memory' effect and which have the ability to memorise their original and deformed phases have broad applications in the field of information storage.[158, 161] 'Shape memory' effects are well-documented in polymers[159, 162-163] and metal alloys,[164-166] but remain rare in MOFs.[45, 167-172] Sakata *et al.* first discovered a shape memory behaviour induced by crystal downsizing in a porous framework in 2013 (Figure 1.10).[171] The original phase is 'closed' without solvent in the pores. The deformed phase was generated by the adsorption of guest molecules forming the open phase. A temporary phase was formed by the removal of solvents, followed by a heating treatment to convert it back to the original 'closed' phase. The $[Fe(Dz)Au(CN)_2)_2]$ framework has previously been shown to form two phases *via* different synthetic methods. This material is an ideal candidate in which to explore the combination of two phases in one material and also the manipulation of these phases to achieve 'shape memory'

behaviour. As discussed in Chapter 7, this study investigates a synthetic approach to probe the structural mechanism associated with 'shape memory' behaviour.

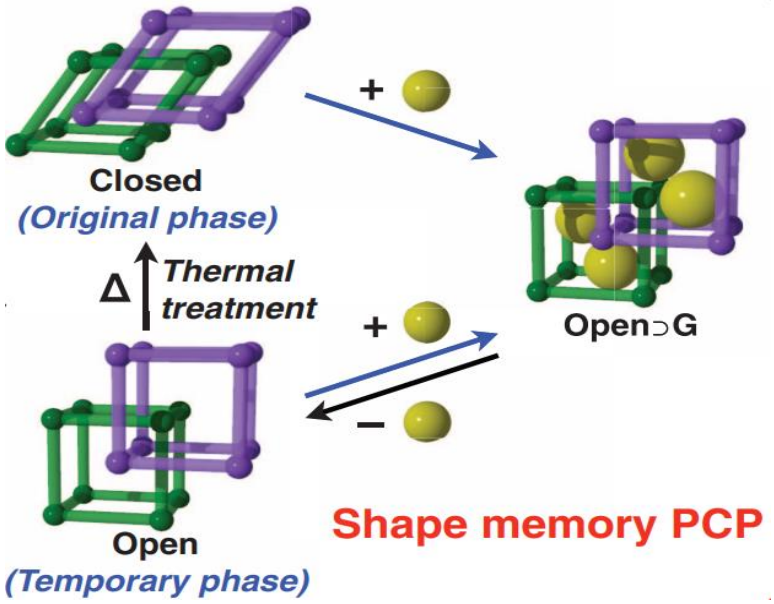

Figure 1.10: Schematic illustration of a 'shape memory' effect. Adapted from Sakata *et al*.[171]

1.3.2 Anomalous Structural Distortion

Most materials have flexible mechanical actions and expand with the application of heat, a process known as positive thermal expansion (PTE). Very few materials undergo negative thermal expansion (NTE), a counterintuitive phenomenon whereby materials contract with increasing temperature. Such anomalous structural behaviour has been found in several different types of materials, such as ferroelectric materials,[173,174] fulleride materials,[175] valence transitions in perovskite oxides,[176-179] and cyanide-bridged frameworks.[180-181]

In recent years the NTE phenomenon has been found in select MOFs which display rotation, transverse vibration, and lattice flexing motions.[182-185] Mullaney *et al*. reported the first SCO-induced colossal thermal expansion (coefficient of thermal expansion is greater than 100×10^{-6} K^{-1}) in $[Fe(bpac)(Au(CN)_2)_2]\cdot 2EtOH$ (bpac = 1,2-bis(4′-pyridyl)acetylene). Here, the Hofmann grid $[Fe(Au(CN)_2)_2]$ is in a rhombic 'wine-rack' shape (Figure 1.11). When the material converts from the HS state to the LS state, octahedral SCO sites are more regular and Au–CN–Fe linkages are more linear. These changes result in a scissor-like motion in the Hofmann grids, which results in the expansion along one axis and contraction in another axis in the rhombic grids. The materials exhibiting such anomalous NTE behaviour have the ability to moderate and compensate for PTE. Designing materials with controllable SCO-induced NTE and PTE is still quite a challenge, which requires further investigation to better understand the correlation between electronic transitions and lattice movement.

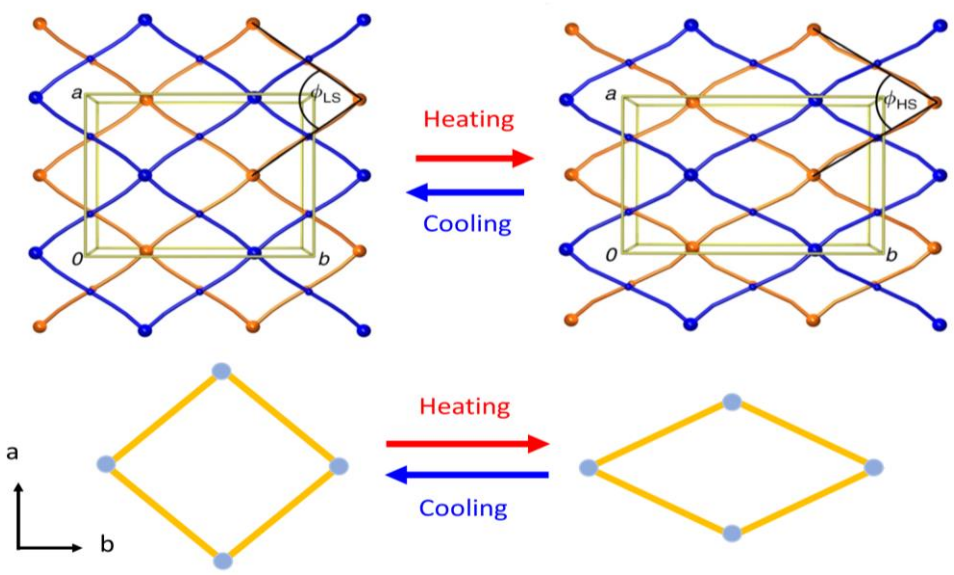

Figure 1.11: Hofmann grids of $[Fe(bpac)(Au(CN)_2)_2]\cdot 2EtOH$ framework showing lattice changes between HS and LS state (top). Schematic Hofmann girds undergoing a scissoring motion due to temperature (bottom). Adapted from Mullaney *et al*.[185]

Similar to NTE, negative linear compression (NLC) is another anomalous structural motion in response to compression. The materials exhibiting NLC undergo uniaxial expansion under uniform compression.[186] Research on NLC in MOFs is extremely rare due to mechanistic differences of NLC when compared to other solid state materials. For example in a hybrid zinc formate framework, NLC occurs due to the contraction of Zn−O bonds and tilting of the ligands.[187] Another example in $Mn(pba)_2$ (pba^- = 3-(pyridine-4-yl)benzoic), NLC is seen in one direction while positive linear compression (PLC) is observed in another direction due to flexing of the 'wine-rack' units.[188] The first SCO induced NLC was observed by Fang in the framework $[Fe(bpac)(Au(CN)_2)_2]\cdot 2EtOH$ and was attributed to a scissor motion of the cyanidometallate linkers under pressure.[189] Further understanding of the effects of lattice movement caused by SCO in other NLC materials is required in order to rationally design controllable materials with attractive properties. Such materials are desirable applied in many scenarios such as sensitive pressure sensors, deep-sea optical fibres, and 'smart' body armour.[188]

1.4 Strategies for Designing Controllable MOFs

1.4.1 Postsynthetic Modification (PSM) Approach

One approach to accessing and tuning the unique structural and functional properties of MOFs for a multitude of applications is to integrate desirable building units. However, the limitation in the conventional *de novo* method is largely caused by the incompatibility of some functional groups to form desired MOFs. Hoskins and Robson hypothesised a novel strategy to construct frameworks through PSM.[190] This technique was later utilised by Wang and Cohen who used the PSM method to generate a post-synthetically modified MOF using a chemical process (Figure 1.12).[191] This method opens the possibility to introduce even more functionalities into MOFs than using the simple building block approach. PSM can also simplify the synthesis process such that a MOF can be synthesised directly from the parent MOF instead of from starting reagents. However, one limitation of the PSM method is that some of the modified MOFs are not chemically stable and also form in low yield.[192-194]

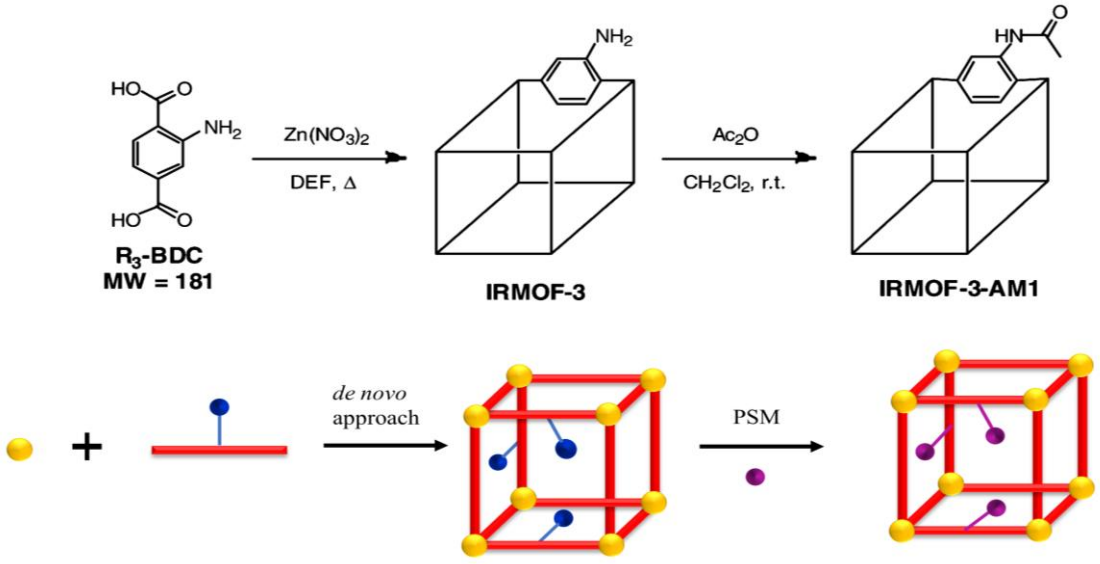

Figure 1.12: Schematic illustration of *de novo* and PSM methods for MOF synthesis. Adapted from Wang *et al.*[191]

1.4.2 Core-shell Approach

Another method to create MOFs with tunable properties is *via* the core-shell approach. By using this approach, materials with different properties can be combined into one, displaying a synergistic effect with functionalities better than the individual core and shell components by themselves.[195] A variety of derived materials can be created by controlling the composition of the core and shell. The core-shell MOFs possess enhanced performance in catalysis, gas sorption and sensing.[195]

A core-shell material commonly has a chemically stable shell to protect the core such as in metal

nanoparticle@MOF and MOF@MOF composites.[196] A conventional method to synthesise a core-shell material *via* a stepwise strategy. However, to overcome the inconvenient synthetic process and limitation of the lattice-matching requirement, Yang *et al*. developed a one-step synthesis by controlling nucleation kinetics to generate core-shell MOFs.[197] There are also other synthetic methods such as *in situ* synthesis, self-assembly synthesis and self-template synthesis, with each method having its advantages and limitations. Although the core-shell MOFs exhibit controllable high performance, choosing a compatible synthetic environment for the core and shell is still a key challenge.

1.4.3 Mixed-ligands and Mixed-metals Approach

Using a solid-solution methodology to generate unique MOF materials such as mixed-ligand (MIXMOFs) or mixed-metal MOFs (MMMOFs) is also a feasible approach towards tuning their functionality. In this approach, two or more ligands/metals of similar structural geometry and solubility are incorporated into a single framework.[198-201] The mixed components are generally homogenously distributed in MOFs. The resulting materials are all isoreticular with two or more ligands that are randomly distributed in predefined coordination positions (Figure 1.13). The pronounced advantage of this approach over the aforementioned is the easy quantitative control of the ligands/metal ratios *via* direct synthesis from reagents.

Since the proportions of these ligands/metals can be freely tuned, such materials provide an ideal platform for investigating structural properties and performance through continuous subtle changes in composition. Baxter *et al*. have reported a series of MIXMOFs by adjusting the ratio of two ligands to achieve continuous tuning of lattice parameters showing thermal expansion from negative to positive thermal expansion.[202] Kitagawa and co-workers demonstrated tunable pore flexibility in a series of MOFs containing varying ratios of two ligands. The optimal performance of gas separation was found by varying the ligand components in the series of MIXMOFs.[203] MIXMOFs are also applied as catalysts, light-harvesting devices and sensors.[204-205]

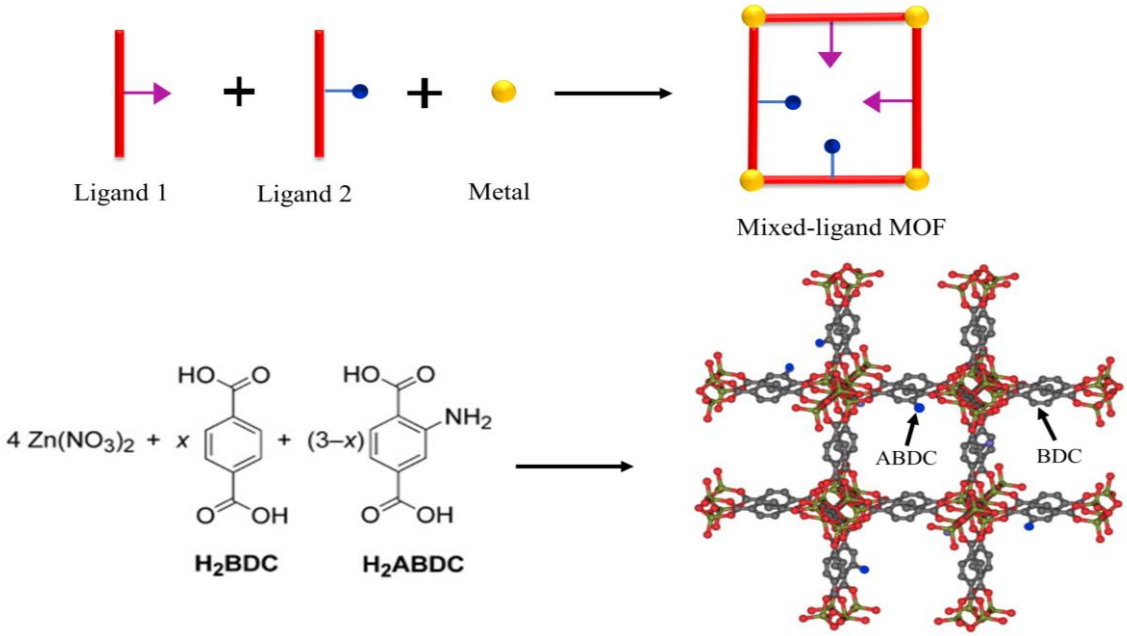

Figure 1.13: Schematic illustration of the formation of a MIXMOF with two ligands (top). An example of a synthetic process for generating a series of carboxylate MIXMOFs. Adapted from Kleist *et al*.[205]

The study of MIXMOF and the correlation between structural properties and performances are still poorly understood and requires further study. Herein, this project focuses on elucidating the structural and magnetic behaviours in response to different stimuli (temperature and pressure) *via* this solid-state approach to gradually alter the composition of SCO MOFs (detailed in Chapters 5, 6 and 7).

1.5 Research Aims

As aforementioned, further understanding of SCO behaviours in SR-MOFs is significant because of the versatile potential applications of these materials. Investigations of structural and electronic mechanisms at the atomic level under multi-stimuli are crucial in creating smart materials. However, the study on underlying principles remains lacking. This PhD aims to further probe these processes by generating SR-MOFs to demonstrate the intrinsic mechanism in response to multi-stimuli.

Although there are several guest-influenced SCO studies, SCO behaviours on guests with very similar physical properties have not been well investigated. Therefore, this PhD projects includes analysing the differences in structural and SCO properties of each xylene isomer in a 3D Hofmann-like framework $[Fe(Tz)(Au(CN)_2)_2]$. The structural comparisons are between the parent framework $[Fe(Tz)(Au(CN)_2)_2]$ containing ethanol molecules in the pores and each xylene encapsulated framework. The parent framework has ethanol in the pores and shows hydrogen bonding interactions between the host and guests. However, there is a lack of understanding of aromatic effects in this framework. Thus,

by the guest exchange to individual xylene isomers, the π···π interactions on structural and electronic configuration properties are studied and compared. Thorough research on the structural expansion and contraction induced by SCO is required to understand the coupling between switchable electronic configurations and lattice motion. Detailed studies on the effects of binary isomer solvent mixtures open up applications in sensitive molecular detective devices.

Another 3D Hofmann-like framework $[Fe(Dz)(Au(CN)_2)_2]$ was synthesised using a similar Dz ligand. This project aims to understand how the subtle differences in guest molecules can influence one material and how the differences in ligands can affect the framework properties. This Dz-based framework is an ideal material to compare with its Tz-based analogue as they have different ligand field strengths and the number of hydrogen bondings between the pillared ligands. This illustrates the interplay between framework structure and SCO behaviours. Comparisons of the effect of each xylene isomer on the two frameworks are examined. An investigation of the uptake of binary xylene mixtures in the $[Fe(Dz)(Au(CN)_2)_2]$ framework will be performed to determine which xylene isomer is predominantly adsorbed and to elucidate its separation strength.

The structural properties of frameworks are varied by the choice of different cyanidometallate linkers. The study of different cyanidometallate linkers in SCO MOFs provides a deeper understanding of collective influences on metallophilic interactions between the Hofmann layers and lattice motions induced by spin transition and SCO performances. The mixed cyanidometallate linker effect on SCO MOFs also requires more work to illustrate the distribution of linkers; the subtle difference in structural and magnetic properties between the materials with different components; and the differences between the single-component linker analogues. The knowledge of these materials can open up new avenues to finely tune to promising properties.

The SCO property of a MOF is not only influenced by the choice of cyanidometallate linkers but is also greatly affected by the pillaring ligands as well. Cooperativity between the SCO sites can be affected by hydrogen bonding interactions. The quantitative study on how the amount of hydrogen bonding can influence SCO behaviours remains unclear. Designing a series of MIXMOFs $[Fe(Tz)_x(Dz)_{1-x}(Au(CN)_2)_2]$ with a varied number of mixed Tz and Dz ligands, which present different amounts of hydrogen bonding will explore the gradual effect of spin transition. Hydrogen bonding interactions between the pillared ligands influence the flexibility of the frameworks, thus quantitative analysis of the extent of lattice flexing motion (i.e., NTE and PTE) controlled by the number of hydrogen bonding will be performed. With the lowest amount of hydrogen bonding occurring in the $[Fe(Dz)(Au(CN)_2)_2]$ framework, investigation of structural properties crystal phase interconversion will be analysed.

Apart from temperature as a physical stimulus for SCO, this research will focus on pressure-induced SCO to further elucidate the underlying mechanisms of the transitions. The aim of this study

on a single component Tz- and Dz-based framework and a MIXMOF (using a combination of Tz and Dz ligands) is to investigate their structural distortion and unique SCO behaviours under applied pressure. Understanding the extent of flexibility and whether these frameworks display NLC in one direction (i.e., scissor motion) under pressure will reveal the role of intra- and inter- molecular interactions on framework structure and dynamics.

In summary, we aim to systematically demonstrate the various factors that can influence the properties of SCO MOFs. This will be achieved through internal structure modification by varying pillaring ligands as well as cyanidometallate linkers. Combined with this approach, altering the encapsulated guest molecule and other external stimuli such as temperature and pressure will be investigated. Finally, control of framework properties will be detailed based on a comprehensive understanding of our material system, paving the way towards the creation of further 'smart' materials with tunable functionalities.

1.6 References

1. Freund, R.; Canossa, S.; Cohen, S. M.; Yan, W.; Deng, H.; Guillerm, V.; Eddaoudi, M.; Madden, D. G.; Fairen-Jimenez, D.; Lyu, H.; Macreadie, L. K.; Ji, Z.; Zhang, Y.; Wang, B.; Haase, F.; Wöll, C.; Zaremba, O.; Andreo, J.; Wuttke, S.; Diercks, C. S., *Angew. Chem. Int. Ed.* **2021,** *60* (45), 23946-23974.

2. James, S. L., *Chem. Soc. Rev.* **2003,** *32* (5), 276-88.

3. Furukawa, H.; Cordova, K. E.; O'Keeffe, M.; Yaghi, O. M., *Science* **2013,** *341* (6149), 1230444.

4. Kreno, L. E.; Leong, K.; Farha, O. K.; Allendorf, M.; Van Duyne, R. P.; Hupp, J. T., *Chem. Rev.* **2012,** *112* (2), 1105-25.

5. Schoedel, A.; Li, M.; Li, D.; O'Keeffe, M.; Yaghi, O. M., *Chem. Rev.* **2016,** *116* (19), 12466-12535.

6. Yaghi, O. M.; O'Keeffe, M.; Ockwig, N. W.; Chae, H. K.; Eddaoudi, M.; Kim, J., *Nature* **2003,** *423* (6941), 705-714.

7. Kinoshita, Y.; Matsubara, I.; Higuchi, T.; Saito, Y., *Bull. Chem. Soc. Jpn.* **1959,** *32* (11), 1221-1226.

8. Tranchemontagne, D. J.; Mendoza-Cortés, J. L.; O'Keeffe, M.; Yaghi, O. M., *Chem. Soc. Rev.* **2009,** *38* (5), 1257.

9. Ha, J.; Lee, J. H.; Moon, H. R., *Inorg. Chem. Front.* **2020,** *7* (1), 12-27.

10. Nagarkar, S. S.; Desai, A. V.; Ghosh, S. K., *Chem. Asian J.* **2014,** *9* (9), 2358-76.

11. Zhou, H.-C.; Long, J. R.; Yaghi, O. M., *Chem. Rev.* **2012,** *112* (2), 673-674.

12. Zhou, H.-C. J.; Kitagawa, S., *Chem. Soc. Rev.* **2014,** *43* (16), 5415-5418.

13. Mueller, U.; Schubert, M.; Teich, F.; Puetter, H.; Schierle-Arndt, K.; Pastré, J., *J. Mater. Chem.* **2006,** *16* (7), 626-636.

14. He, Y.; Zhou, W.; Qian, G.; Chen, B., *Chem. Soc. Rev.* **2014,** *43* (16), 5657-5678.

15. Van De Voorde, B.; Bueken, B.; Denayer, J.; De Vos, D., *Chem. Soc. Rev.* **2014,** *43* (16), 5766-5788.

16. Ding, G.; Wang, Y.; Zhang, G.; Zhou, K.; Zeng, K.; Li, Z.; Zhou, Y.; Zhang, C.; Chen, X.; Han, S.-T., *Adv. Funct. Mater.* **2019,** *29* (3).

17. Park, M.-J.; Lee, J.-S., *RSC Adv.* **2017,** *7* (34), 21045-21049.

18. Chen, B.; Xiang, S.; Qian, G., *Acc. Chem. Res.* **2010,** *43* (8), 1115-1124.

19. Cui, Y.; Yue, Y.; Qian, G.; Chen, B., *Chem. Rev.* **2012,** *112* (2), 1126-1162.

20. Hu, Z.; Deibert, B. J.; Li, J., *Chem. Soc. Rev.* **2014,** *43* (16), 5815-5840.

21. Ricco, R.; Malfatti, L.; Takahashi, M.; Hill, A. J.; Falcaro, P., *J. Mater. Chem. A.* **2013,** *1* (42), 13033.

22. Coronado, E.; Mínguez Espallargas, G., *Chem. Soc. Rev.* **2013,** *42* (4), 1525-1539.

23. Horcajada, P.; Gref, R.; Baati, T.; Allan, P. K.; Maurin, G.; Couvreur, P.; Férey, G.; Morris, R. E.; Serre, C., *Chem. Rev.* **2012,** *112* (2), 1232-1268.

24. Della Rocca, J.; Liu, D.; Lin, W., *Acc. Chem. Res.* **2011,** *44* (10), 957-968.

25. Horcajada, P.; Chalati, T.; Serre, C.; Gillet, B.; Sebrie, C.; Baati, T.; Eubank, J. F.; Heurtaux, D.; Clayette, P.; Kreuz, C.; Chang, J.-S.; Hwang, Y. K.; Marsaud, V.; Bories, P.-N.; Cynober, L.; Gil, S.; Férey, G.; Couvreur, P.; Gref, R., *Nat. Mater.* **2010,** *9* (2), 172-178.

26. Liu, J.; Chen, L.; Cui, H.; Zhang, J.; Zhang, L.; Su, C.-Y., *Chem. Soc. Rev.* **2014,** *43* (16), 6011-6061.

27. Zhang, T.; Lin, W., *Chem. Soc. Rev.* **2014,** *43* (16), 5982-5993.

28. Tan, F.; Lopez-Periago, A.; Light, M. E.; Cirera, J.; Ruiz, E.; Borras, A.; Teixidor, F.; Vinas, C.; Domingo, C.; Planas, J. G., *Adv. Mater.* **2018**, e1800726.

29. Moulin, E.; Faour, L.; Carmona-Vargas, C. C.; Giuseppone, N., *Adv. Mater.* **2020,** *32* (20), 1906036.

30. Theato, P.; Sumerlin, B. S.; O'Reilly, R. K.; Epps, T. H., 3rd, *Chem. Soc. Rev.* **2013,** *42* (17), 7055-6.

31. Wei, M.; Gao, Y.; Li, X.; Serpe, M. J., *Polymer Chemistry* **2017,** *8* (1), 127-143.

32. Cai, W.; Wang, J.; Chu, C.; Chen, W.; Wu, C.; Liu, G., *Adv. Sci (Weinh).* **2019,** *6* (1), 1801526.

33. Municoy, S.; Alvarez Echazu, M. I.; Antezana, P. E.; Galdoporpora, J. M.; Olivetti, C.; Mebert, A. M.; Foglia, M. L.; Tuttolomondo, M. V.; Alvarez, G. S.; Hardy, J. G.; Desimone, M. F., *Int. J. Mol. Sci.* **2020,** *21* (13).

34. Zhou, Z.; Vazquez-Gonzalez, M.; Willner, I., *Chem. Soc. Rev.* **2021**.

35. Lu, Y.; Aimetti, A. A.; Langer, R.; Gu, Z., *Nat. Rev. Mater.* **2016,** *2* (1).

36. Blanco, V.; Leigh, D. A.; Marcos, V., *Chem. Soc. Rev.* **2015,** *44* (15), 5341-70.

37. Li, C.; Wang, K.; Li, J.; Zhang, Q., *ACS Mater. Lett.* **2020,** *2* (7), 779-797.

38. Vassalini, I.; Alessandri, I., *Catalysts* **2018,** *8* (12).

39. Roy, B.; Reddy, M. C.; Hazra, P., *Chem. Sci.* **2018,** *9* (14), 3592-3606.

40. Liu, Z.; Zhang, L.; Sun, D., *Chem. Commun.* **2020,** *56* (66), 9416-9432.

41. Kanoo, P.; Haldar, R.; Reddy, S. K.; Hazra, A.; Bonakala, S.; Matsuda, R.; Kitagawa, S.;

Balasubramanian, S.; Maji, T. K., *Chemistry* **2016,** *22* (44), 15864-15873.

42. Rowsell, J. L. C.; Yaghi, O. M., *Microporous Mesoporous Mater.* **2004,** *73* (1-2), 3-14.

43. Horike, S.; Shimomura, S.; Kitagawa, S., *Nat. Chem.* **2009,** *1* (9), 695-704.

44. Dong, J.; Wee, V.; Zhao, D., *Nat. Mater.* **2022**.

45. Shivanna, M.; Yang, Q.-Y.; Bajpai, A.; Sen, S.; Hosono, N.; Kusaka, S.; Pham, T.; Forrest, K. A.; Space, B.; Kitagawa, S.; Zaworotko, M. J., *Sci. Adv.* **2018,** *4* (4), eaaq1636.

46. Nagarkar, S. S.; Desai, A. V.; Ghosh, S. K., *Chem. Asian J.* **2014,** *9* (9), 2358-2376.

47. Karimzadeh, S.; Javanbakht, S.; Baradaran, B.; Shahbazi, M.-A.; Hashemzaei, M.; Mokhtarzadeh, A.; Santos, H. A., *Chem. Eng. J.* **2021,** *408*.

48. Karmakar, A.; Mileo, P. G. M.; Bok, I.; Peh, S. B.; Zhang, J.; Yuan, H.; Maurin, G.; Zhao, D., *Angew. Chem. Int. Ed.* **2020,** *59* (27), 11003-11009.

49. Gütlich, P.; Goodwin, H. A., Spin Crossover—An Overall Perspective. In *Spin Crossover in Transition Metal Compounds I*, Gütlich, P.; Goodwin, H. A., Eds. Springer Berlin Heidelberg: Berlin, Heidelberg, 2004; pp 1-47.

50. Guionneau, P., *Dalton Trans.* **2014,** *43* (2), 382-393.

51. Harding, D. J., An Overview of Spin Crossover Nanoparticles. In *Novel Magnetic Nanostructures*, 2018; pp 401-426.

52. Bousseksou, A.; Molnar, G.; Salmon, L.; Nicolazzi, W., *Chem. Soc. Rev.* **2011,** *40* (6), 3313-35.

53. Gütlich, P., *Eur. J. Inorg. Chem* **2013,** *2013* (5-6), 581-591.

54. Molnár, G.; Salmon, L.; Nicolazzi, W.; Terki, F.; Bousseksou, A., *J. Mater. Chem. C* **2014,** *2* (8), 1360-1366.

55. Létard, J.-F.; Guionneau, P.; Goux-Capes, L., Towards Spin Crossover Applications. In *Spin Crossover in Transition Metal Compounds III*, Gütlich, P.; Goodwin, H. A., Eds. Springer Berlin Heidelberg: Berlin, Heidelberg, 2004; pp 221-249.

56. Gütlich, P.; Garcia, Y.; Goodwin, H. A., *Chem. Soc. Rev.* **2000,** *29* (6), 419-427.

57. Gütlich, P.; Gaspar, A. B.; Garcia, Y., *Beilstein J. Org. Chem.* **2013,** *9*, 342-391.

58. Gütlich, P.; Hauser, A.; Spiering, H., *Angew. Chem., Int. Ed. Engl.* **1994,** *33* (20), 2024-2054.

59. Urban, M. W., *Stimuli-Responsive Materials: From Molecules to Nature Mimicking Materials Design*. Royal Society of Chemistry: 2019.

60. Cambi, L.; Szegö, L., *Ber. Dtsch. Chem. Ges (A and B Series)* **1931,** *64* (10), 2591-2598.

61. Cui, H.-H.; Wang, J.; Chen, X.-T.; Xue, Z.-L., *Chem. Commun.* **2017,** *53* (67), 9304-9307.

62. Gütlich, P.; Goodwin, H. A., Spin Crossover—An Overall Perspective. In *Top. Curr. Chem.*, Springer Berlin Heidelberg: 2004; pp 1-47.

63. Reinen, D.; Friebel, C.; Propach, V., *Zeitschrift fr anorganische und allgemeine Chemie* **1974,** *408* (2), 187-204.

64. König, E.; Ritter, G., *Solid State Commun.* **1976,** *18* (3), 279-282.

65. Lemercier, G.; Bousseksou, A.; Seigneuric, S.; Varret, F.; Tuchagues, J. P., *Chem. Phys. Lett.* **1994,** *226* (3-4), 289-294.

66. Murray, K. S.; Kepert, C. J., Cooperativity in Spin Crossover Systems: Memory, Magnetism and Microporosity. In *Top. Curr. Chem.*, Springer Berlin Heidelberg: 2004; pp 195-228.

67. Kitazawa, T.; Gomi, Y.; Takahashi, M.; Takeda, M.; Enomoto, M.; Miyazaki, A.; Enoki, T., *J. Mater. Chem.* **1996,** *6* (1), 119.

68. Li, J.-Y.; He, C.-T.; Chen, Y.-C.; Zhang, Z.-M.; Liu, W.; Ni, Z.-P.; Tong, M.-L., *J. Mater. Chem. C.* **2015,** *3* (30), 7830-7835.

69. Zhang, C.-J.; Lian, K.-T.; Huang, G.-Z.; Bala, S.; Ni, Z.-P.; Tong, M.-L., *Chem. Commun.* **2019,** *55* (74), 11033-11036.

70. Murray, K. S., *Spin-Crossover Materials* **2013**, 1-54.

71. Milin, E.; Patinec, V.; Triki, S.; Bendeif, E.-E.; Pillet, S.; Marchivie, M.; Chastanet, G.; Boukheddaden, K., *Inorg. Chem.* **2016,** *55* (22), 11652-11661.

72. Cruddas, J.; Powell, B. J., *J. Am. Chem. Soc.* **2019,** *141* (50), 19790-19799.

73. Liu, F.-L.; Li, D.; Su, L.-J.; Tao, J., *Dalton Trans.* **2018,** *47* (5), 1407-1411.

74. Cruddas, J.; Powell, B. J., *Inorg. Chem. Front.* **2020,** *7* (22), 4424-4437.

75. Klein, Y. M.; Sciortino, N. F.; Ragon, F.; Housecroft, C. E.; Kepert, C. J.; Neville, S. M., *Chem. Commun.* **2014,** *50* (29), 3838-3840.

76. Paez-Espejo, M.; Sy, M.; Boukheddaden, K., *J. Am. Chem. Soc.* **2016,** *138* (9), 3202-3210.

77. Traiche, R.; Sy, M.; Boukheddaden, K., *J. Phys. Chem. C* . **2018,** *122* (7), 4083-4096.

78. Liu, J.; Gao, Y.; Wang, T.; Xue, Q.; Hua, M.; Wang, Y.; Huang, L.; Lin, N., *ACS Nano* **2020,** *14* (9), 11283-11293.

79. Southon, P. D.; Liu, L.; Fellows, E. A.; Price, D. J.; Halder, G. J.; Chapman, K. W.; Moubaraki, B.; Murray, K. S.; Létard, J.-F.; Kepert, C. J., *J. Am. Chem. Soc.* **2009,** *131* (31), 10998-11009.

80. Valverde-Muñoz, F. J.; Gaspar, A. B.; Shylin, S. I.; Ksenofontov, V.; Real, J. A., *Inorg. Chem.* **2015,** *54* (16), 7906-7914.

81. Garcia, Y.; Niel, V.; Muñoz, M. C.; Real, J. A., Spin Crossover in 1D, 2D and 3D Polymeric Fe(II) Networks. In *Top. Curr. Chem.*, Springer Berlin Heidelberg: 2004; pp 229-257.

82. Brooker, S., *Chem. Soc. Rev.* **2015,** *44* (10), 2880-2892.

83. Konig, E.; Ritter, G.; Kulshreshtha, S. K., *Chem. Rev.* **1985,** *85* (3), 219-234.

84. Krober, J.; Codjovi, E.; Kahn, O.; Groliere, F.; Jay, C., *J. Am. Chem. Soc.* **1993,** *115* (21), 9810-9811.

85. Li, Z.-Y.; Dai, J.-W.; Shiota, Y.; Yoshizawa, K.; Kanegawa, S.; Sato, O., *Eur. J. Chem.* **2013,** *19* (39), 12948-12952.

86. Hayami, S.; Kawahara, T.; Juhász, G.; Kawamura, K.; Uehashi, K.; Sato, O.; Maeda, Y., *J. Radioanal. Nucl. Chem.* **2003,** *255* (3), 443-447.

87. Hayami, S.; Gu, Z.-Z.; Yoshiki, H.; Fujishima, A.; Sato, O., *J. Am. Chem. Soc.* **2001,** *123* (47), 11644-11650.

88. Létard, J.-F.; Guionneau, P.; Codjovi, E.; Lavastre, O.; Bravic, G.; Chasseau, D.; Kahn, O., *J. Am. Chem. Soc.* **1997,** *119* (44), 10861-10862.

89. Roubeau, O., *Chemistry* **2012,** *18* (48), 15230-44.

90. Kahn, O.; Martinez, C. J., *Science* **1998,** *279*, 44-48.

91. Lavrenova, L. G.; Shakirova, O. G., *Eur.J. Inorg.Chem.* **2013,** *2013* (5-6), 670-682.

92. Calvo Galve, N.; Coronado, E.; Gimenez-Marques, M.; Minguez Espallargas, G., *Inorg. Chem.* **2014,** *53* (9), 4482-90.

93. Ohtani, R.; Yoneda, K.; Furukawa, S.; Horike, N.; Kitagawa, S.; Gaspar, A. B.; Munoz, M. C.; Real, J. A.; Ohba, M., *J. Am. Chem. Soc.* **2011,** *133* (22), 8600-5.

94. Fujinami, T.; Nishi, K.; Hamada, D.; Murakami, K.; Matsumoto, N.; Iijima, S.; Kojima, M.; Sunatsuki, Y., *Inorg. Chem.* **2015,** *54* (15), 7291-7300.

95. Kulmaczewski, R.; Olguín, J.; Kitchen, J. A.; Feltham, H. L. C.; Jameson, G. N. L.; Tallon, J. L.; Brooker, S., *J. Am. Chem. Soc.* **2014,** *136* (3), 878-881.

96. Miller, R. G.; Narayanaswamy, S.; Tallon, J. L.; Brooker, S., *New J. Chem.* **2014,** *38* (5), 1932.

97. Kahn, O., Kröber, J. and Jay, C., *Adv. Mater.* **1992,** (4), 718-728.

98. Guionneau, P.; Marchivie, M.; Bravic, G.; Létard, J.-F.; Chasseau, D., Structural Aspects of Spin Crossover. Example of the $[Fe^{II}Ln(NCS)_2]$ Complexes. In *Spin Crossover in Transition Metal Compounds II*, Springer Berlin Heidelberg: 2004; Vol. 234, pp 97-128.

99. Gaspar, A. B.; Molnár, G.; Rotaru, A.; Shepherd, H. J., *C. R. Chim.* **2018,** *21* (12), 1095-1120.

100. Ewald, A. H.; Martin, R. L.; Ross, I. G.; White, A. H., *Proceedings of the Royal Society of London. Series A. Mathematical and Physical Sciences* **1964,** *280* (1381), 235-257.

101. Ewald, A. H.; Martin, R. L.; Sinn, E.; White, A. H., *Inorg. Chem.* **1969,** *8* (9), 1837-1846.

102. Granier, T.; Gallois, B.; Gaultier, J.; Real, J. A.; Zarembowitch, J., *Inorg. Chem.* **1993,** *32* (23), 5305-5312.

103. Shepherd, H. J.; Bartual-Murgui, C.; Molnár, G.; Real, J. A.; Muñoz, M. C.; Salmon, L.; Bousseksou, A., *New J. Chem.* **2011,** *35* (6), 1205.

104. Gaspar, A. B.; Levchenko, G.; Terekhov, S.; Bukin, G.; Valverde-Muñoz, J.; Muñoz-Lara, F. J.; Seredyuk, M.; Real, J. A., *Eur. J. Inorg. Chem* **2013,** *2014* (3), 429-433.

105. Molnár, G.; Niel, V.; Real, J.-A.; Dubrovinsky, L.; Bousseksou, A.; Mcgarvey, J. J., *J. Phys. Chem. B* **2003,** *107* (14), 3149-3155.

106. Sciortino, N. F.; Ragon, F.; Zenere, K. A.; Southon, P. D.; Halder, G. J.; Chapman, K. W.; Piñeiro-López, L.; Real, J. A.; Kepert, C. J.; Neville, S. M., *Inorg. Chem.* **2016,** *55* (20), 10490-10498.

107. Ksenofontov, V.; Gaspar, A. B.; Levchenko, G.; Fitzsimmons, B.; Gütlich, P., *J. Phys. Chem. B* **2004,** *108* (23), 7723-7727.

108. Niel, V.; Muñoz, M. C.; Gaspar, A. B.; Galet, A.; Levchenko, G.; Real, J. A., *Eur. J. Chem.* **2002,** *8* (11).

109. Garcia, Y.; Ksenofontov, V.; Levchenko, G.; Schmitt, G.; Gütlich, P., *J. Phys. Chem. B* **2000,** *104* (21), 5045-5048.

110. Shepherd, H. J.; Palamarciuc, T.; Rosa, P.; Guionneau, P.; Molnar, G.; Letard, J. F.; Bousseksou, A., *Angew. Chem. Int. Ed.* **2012,** *51* (16), 3910-4.

111. Martinez, V.; Gaspar, A. B.; Munoz, M. C.; Bukin, G. V.; Levchenko, G.; Real, J. A., *Chemistry* **2009,** *15* (41), 10960-71.

112. Ksenofontov, V.; Spiering, H.; Schreiner, A.; Levchenko, G.; Goodwin, H. A.; Gütlich, P., *J. Phys. Chem. Solids* **1999,** *60* (3), 393-399.

113. Ksenofontov, V.; Levchenko, G.; Spiering, H.; Gütlich, P.; Létard, J. F.; Bouhedja, Y.; Kahn, O., *Chem. Phys. Lett.* **1998,** *294* (6), 545-553.

114. Galet, A.; Gaspar, A. B.; Muñoz, M. C.; Bukin, G. V.; Levchenko, G.; Real, J. A., *Adv. Mater.* **2005,** *17* (24), 2949-2953.

115. Garcia, Y.; Ksenofontov, V.; Levchenko, G.; Gütlich, P., *J. Mater. Chem.* **2000,** *10* (10), 2274-2276.

116. Garcia, Y.; van Koningsbruggen, P. J.; Lapouyade, R.; Fournès, L.; Rabardel, L.; Kahn, O.; Ksenofontov, V.; Levchenko, G.; Gütlich, P., *Chem. Mater.* **1998,** *10* (9), 2426-2433.

117. Mcgravey, J. J.; Lawthers, I., *J. Chem. Soc., Chem. Commun.* **1982,** (16), 906-907.

118. Decurtins, S.; Gutlich, P.; Hasselbach, K. M.; Hauser, A.; Spiering, H., *Inorg. Chem.* **1985,** *24* (14), 2174-2178.

119. Decurtins, S.; Gütlich, P.; Köhler, C. P.; Spiering, H., *J. Chem. Soc., Chem. Commun.* **1985,** (7), 430-432.

120. Nakaya, M.; Ohtani, R.; Lindoy, L. F.; Hayami, S., *Inorg. Chem. Front.* **2021,** *8* (2), 484-498.

121. Hayami, S.; Gu, Z.-Z.; Shiro, M.; Einaga, Y.; Fujishima, A.; Sato, O., *J. Am. Chem. Soc.* **2000,** *122* (29), 7126-7127.

122. Hauser, A., *Chem. Phys. Lett.* **1986,** *124* (6), 543-548.

123. Létard, J.-F.; Guionneau, P.; Nguyen, O.; Costa, J. S.; Marcén, S.; Chastanet, G.; Marchivie, M.; Goux-Capes, L., *Eur. J. Chem.* **2005,** *11* (16), 4582-4589.

124. Létard, J.-F.; Costa, J. S.; Marcen, S.; Carbonera, C.; Desplanches, C.; Kobayashi, A.; Daro, N.; Guionneau, P.; Ader, J.-P., *J. Phys. Conf. Ser.* **2005,** *21*, 23-29.

125. Boilleau, C.; Suaud, N.; Guihéry, N., *Chem. Phys.* **2012,** *137* (22), 224304.

126. Létard, J.-F., *J. Mater. Chem.* **2006,** *16* (26), 2550-2559.

127. Kahn, O., *Curr. Opin. Solid State Mater. Sci.* **1996,** *1* (4), 547-554.

128. Halder, G. J.; Kepert, C. J.; Moubaraki, B.; Murray, K. S.; Cashion, J. D., *Science* **2002,** *298* (5599), 1762.

129. Ni, Z.-P.; Liu, J.-L.; Hoque, M. N.; Liu, W.; Li, J.-Y.; Chen, Y.-C.; Tong, M.-L., *Coord. Chem. Rev.* **2017,** *335*, 28-43.

130. Neville, S. M.; Halder, G. J.; Chapman, K. W.; Duriska, M. B.; Moubaraki, B.; Murray, K. S.; Kepert, C. J., *J. Am. Chem. Soc.* **2009,** *131* (34), 12106-12108.

131. Aravena, D.; Castillo, Z. A.; Muñoz, M. C.; Gaspar, A. B.; Yoneda, K.; Ohtani, R.; Mishima, A.; Kitagawa, S.; Ohba, M.; Real, J. A.; Ruiz, E., *Eur. J. Chem.* **2014,** *20* (40), 12864-12873.

132. Pham, C. H.; Paesani, F., *J. Phys. Chem. Lett.* **2016,** *7* (19), 4022-4026.

133. Ohba, M.; Yoneda, K.; Agustí, G.; Muñoz, M. C.; Gaspar, A. B.; Real, J. A.; Yamasaki, M.; Ando, H.; Nakao, Y.; Sakaki, S.; Kitagawa, S., *Angew. Chem. Int. Ed.* **2009,** *48* (26), 4767-4771.

134. Li, J.-Y.; Chen, Y.-C.; Zhang, Z.-M.; Liu, W.; Ni, Z.-P.; Tong, M.-L., *Eur. J. Chem.* **2015,** *21* (4), 1645-1651.

135. Bonhommeau, S.; Molnár, G.; Galet, A.; Zwick, A.; Real, J.-A.; Mcgarvey, J. J.; Bousseksou, A., *Angew. Chem. Int. Ed.* **2005,** *44* (26), 4069-4073.

136. Niel, V.; Martinez-Agudo, J. M.; Muñoz, M. C.; Gaspar, A. B.; Real, J. A., *Inorg. Chem.* **2001,** *40* (16), 3838-3839.

137. Zenere, K. A.; Duyker, S. G.; Trzop, E.; Collet, E.; Chan, B.; Doheny, P. W.; Kepert, C. J.; Neville, S. M., *Chem. Sci.* **2018,** *9* (25), 5623-5629.

138. Ezzedinloo, L.; Zenere, K. A.; Xie, Z.; Ahmed, M.; Scottwell, S.; Bhadbhade, M.; Brand, H. E. A.; Clegg, J. K.; Hua, C.; Sciortino, N. F.; Parker, L. C.; Powell, B. J.; Kepert, C. J.; Neville, S. M., *Eur. J. Chem.* **2021,** *27* (16), 5136-5141.

139. Halcrow, M. A., *Chem. Soc. Rev.* **2011,** *40* (7), 4119-42.

140. Hofmann, K. A.; Küspert, F., *Z. Anorg. Allg. Chem.* **1897,** *15* (1), 204-207.

141. Murphy, M. J.; Zenere, K. A.; Ragon, F.; Southon, P. D.; Kepert, C. J.; Neville, S. M., *J. Am. Chem. Soc.* **2017,** *139* (3), 1330-1335.

142. Brennan, A. T.; Zenere, K. A.; Brand, H. E. A.; Price, J. R.; Bhadbhade, M. M.; Turner, G. F.; Moggach, S. A.; Valverde-Muñoz, F. J.; Real, J. A.; Clegg, J. K.; Kepert, C. J.; Neville, S. M., *Inorg. Chem.* **2020,** *59* (19), 14296-14305.

143. Piñeiro-López, L.; Valverde-Muñoz, F. J.; Seredyuk, M.; Bartual-Murgui, C.; Muñoz, M. C.; Real, J. A., *Eur. J. Inorg. Chem* **2018,** *2018* (3-4), 289-296.

144. Clements, J. E.; Price, J. R.; Neville, S. M.; Kepert, C. J., *Angew. Chem. Int. Ed.* **2016,** *55* (48), 15105-15109.

145. Clements, J. E.; Price, J. R.; Neville, S. M.; Kepert, C. J., *Angew. Chem. Int. Ed.* **2014,** *53* (38), 10164-10168.

146. Li, Y.; Kong, Q.-R.; Guo, Y.; Tang, Z., *Dalton Trans.* **2021,** *50* (4), 1384-1389.

147. Agustí, G.; Gaspar, A. B.; Muñoz, M. C.; Real, J. A., *Inorg. Chem.* **2007,** *46* (23), 9646-9654.

148. Turner, G. F.; Campbell, F.; Moggach, S. A.; Parsons, S.; Goeta, A. E.; Munoz, M. C.; Real, J. A., *Angew. Chem. Int. Ed.* **2020,** *59* (8), 3106-3111.

149. Schneemann, A.; Bon, V.; Schwedler, I.; Senkovska, I.; Kaskel, S.; Fischer, R. A., *Chem. Soc. Rev.* **2014,** *43* (16), 6062-6096.

150. Alhamami, M.; Doan, H.; Cheng, C.-H., *Materials* **2014,** *7* (4), 3198-3250.

151. Dybtsev, D. N.; Chun, H.; Kim, K., *Angew. Chem. Int. Ed.* **2004,** *43* (38), 5033-5036.

152. Allendorf, M. D.; Stavila, V., *CrystEngComm* **2015,** *17* (2), 229-246.

153. Liu, Y.; Her, J.-H.; Dailly, A.; Ramirez-Cuesta, A. J.; Neumann, D. A.; Brown, C. M., *J. Am. Chem. Soc.* **2008,** *130* (35), 11813-11818.

154. Chen, L.; Mowat, J. P. S.; Fairen-Jimenez, D.; Morrison, C. A.; Thompson, S. P.; Wright, P. A.; Düren, T., *J. Am. Chem. Soc.* **2013,** *135* (42), 15763-15773.

155. Formalik, F.; Neimark, A. V.; Rogacka, J.; Firlej, L.; Kuchta, B., *J. Colloid. Interface. Sci.* **2020,** *578*, 77-88.

156. Chanut, N.; Ghoufi, A.; Coulet, M. V.; Bourrelly, S.; Kuchta, B.; Maurin, G.; Llewellyn, P. L., *Nat. Commun.* **2020,** *11* (1), 1216.

157. Schneemann, A.; Bon, V.; Schwedler, I.; Senkovska, I.; Kaskel, S.; Fischer, R. A., *Chem. Soc. Rev.* **2014,** *43* (16), 6062-96.

158. Otsuka, K.; Wayman, C. M., *Shape Memory Materials*. Cambridge University Press: 1999.

159. Behl, M.; Lendlein, A., *Mater. Today* **2007,** *10* (4), 20-28.

160. Schmidt, A. M., *Macromol. Rapid Commun.* **2006,** *27* (14), 1168-1172.

161. Xia, Y.; He, Y.; Zhang, F.; Liu, Y.; Leng, J., *Adv. Mater.* **2021,** *33* (6), e2000713.

162. Mather, P. T.; Luo, X.; Rousseau, I. A., *Annu. Rev. Mater. Res.* **2009,** *39* (1), 445-471.

163. Govindarajan, T.; Shandas, R., *Polymers* **2014,** *6* (9), 2309-2331.

164. Lagoudas, D. C., *Shape memory alloys: modeling and engineering applications*. Springer: 2008.

165. Otsuka, K.; Ren, X., *Intermetallics* **1999,** *7* (5), 511-528.

166. Duerig, T. W.; Melton, K.; Stöckel, D., *Engineering aspects of shape memory alloys*. Butterworth-heinemann: 2013.

167. Sakata, Y.; Furukawa, S.; Kondo, M.; Hirai, K.; Horike, N.; Takashima, Y.; Uehara, H.; Louvain, N.; Meilikhov, M.; Tsuruoka, T.; Isoda, S.; Kosaka, W.; Sakata, O.; Kitagawa, S., *Science* **2013,** *339* (6116), 193-196.

168. Tiba, A. A.; Conway, M. T.; Hill, C. S.; Swenson, D. C.; Macgillivray, L. R.; Tivanski, A. V., *Chem. Commun.* **2021,** *57* (1), 89-92.

169. Yang, H.; Trieu, T. X.; Zhao, X.; Wang, Y.; Wang, Y.; Feng, P.; Bu, X., *Angew. Chem. Int. Ed.* **2019,** *58* (34), 11757-11762.

170. Wieme, J.; Lejaeghere, K.; Kresse, G.; Van Speybroeck, V., *Nat. Commun.* **2018,** *9* (1).

171. Sakata, Y.; Furukawa, S.; Kondo, M.; Hirai, K.; Horike, N.; Takashima, Y.; Uehara, H.; Louvain, N.; Meilikhov, M.; Tsuruoka, T.; Isoda, S.; Kosaka, W.; Sakata, O.; Kitagawa, S., *Science* **2013,** *339* (6116), 193-6.

172. Shivanna, M.; Yang, Q.-Y.; Bajpai, A.; Patyk-Kazmierczak, E.; Zaworotko, M. J., *Nat. Commun.* **2018,** *9* (1).

173. Rong, Y.; Li, M.; Chen, J.; Zhou, M.; Lin, K.; Hu, L.; Yuan, W.; Duan, W.; Deng, J.; Xing, X., *Phys. Chem .Chem. Phys.* **2016,** *18* (8), 6247-51.

174. Hao, Y.; Gao, Y.; Wang, B.; Qu, J.; Li, Y.; Hu, J.; Deng, J., *Appl. Phys. Lett.* **2001,** *78* (21), 3277-3279.

175. Arvanitidis, J.; Papagelis, K.; Margadonna, S.; Prassides, K.; Fitch, A. N., *Nature* **2003,** *425* (6958), 599-602.

176. Kulmaczewski, R.; Trzop, E.; Collet, E.; Vela, S.; Halcrow, M. A., *J. Mater. Chem. C* **2020,** *8* (25), 8420-8429.

177. Liu, Z.; Gao, Q.; Chen, J.; Deng, J.; Lin, K.; Xing, X., *Chem. Commun.* **2018,** *54* (41), 5164-5176.

178. Pan, Z.; Chen, J.; Yu, R.; Patra, L.; Ravindran, P.; Sanson, A.; Milazzo, R.; Carnera, A.; Hu, L.; Wang, L.; Yamamoto, H.; Ren, Y.; Huang, Q.; Sakai, Y.; Nishikubo, T.; Ogata, T.; Fan, X. a.; Li, Y.; Li, G.; Hojo, H.; Azuma, M.; Xing, X., *Chem. Mater.* **2019,** *31* (4), 1296-1303.

179. Azuma, M.; Chen, W. T.; Seki, H.; Czapski, M.; Olga, S.; Oka, K.; Mizumaki, M.; Watanuki, T.; Ishimatsu, N.; Kawamura, N.; Ishiwata, S.; Tucker, M. G.; Shimakawa, Y.; Attfield, J. P., *Nat. Commun.* **2011,** *2*, 347.

180. Goodwin, A. L.; Kepert, C. J., *Phys. Rev. B: Condens. Mater. Phys.* **2005,** *71* (14).

181. Phillips, A. E.; Goodwin, A. L.; Halder, G. J.; Southon, P. D.; Kepert, C. J., *Angew. Chem. Int. Ed.* **2008,** *47* (8), 1396-9.

182. Miller, W.; Smith, C. W.; Mackenzie, D. S.; Evans, K. E., *J. Mater. Sci.* **2009,** *44* (20), 5441-5451.

183. Liu, Z.; Gao, Q.; Chen, J.; Deng, J.; Lin, K.; Xing, X., *Chem. Commun.* **2018,** *54* (41), 5164-5176.

184. Cliffe, M. J.; Hill, J. A.; Murray, C. A.; Coudert, F.-X.; Goodwin, A. L., *Physical Chemistry Chemical Physics* **2015,** *17* (17), 11586-11592.

185. Mullaney, B. R.; Goux-Capes, L.; Price, D. J.; Chastanet, G.; Letard, J. F.; Kepert, C. J., *Nat. Commun.* **2017,** *8* (1), 1053.

186. Cairns, A. B.; Goodwin, A. L., *Phys. Chem. Chem. Phys.* **2015,** *17* (32), 20449-20465.

187. Li, W.; Probert, M. R.; Kosa, M.; Bennett, T. D.; Thirumurugan, A.; Burwood, R. P.; Parinello, M.; Howard, J. A. K.; Cheetham, A. K., *J. Am. Chem. Soc.* **2012,** *134* (29), 11940-11943.

188. Zeng, Q.; Wang, K.; Zou, B., *ACS Mater. Lett.* **2020,** *2* (4), 291-295.

189. Fang, A. The University of Sydney, **2021**.

190. Hoskins, B. F.; Robson, R., *J. Am. Chem. Soc.* **1990,** *112* (4), 1546-1554.

191. Wang, Z.; Cohen, S. M., *J. Am. Chem. Soc.* **2007,** *129* (41), 12368-12369.

192. Wang, Z.; Cohen, S. M., *Angew. Chem. Int. Ed.* **2008,** *47* (25), 4699-702.

193. Wang, Z.; Cohen, S. M., *Chem. Soc. Rev.* **2009,** *38* (5), 1315.

194. Tanabe, K. K.; Cohen, S. M., *Chem. Soc. Rev.* **2011,** *40* (2), 498-519.

195. Zhao, Z.; Ding, J.; Zhu, R.; Pang, H., *J. Mater. Chem. A.* **2019,** *7* (26), 15519-15540.

196. Gu, Y.; Wu, Y. N.; Li, L.; Chen, W.; Li, F.; Kitagawa, S., *Angew. Chem. Int. Ed.* **2017,** *56* (49), 15658-15662.

197. Yang, X.; Yuan, S.; Zou, L.; Drake, H.; Zhang, Y.; Qin, J.; Alsalme, A.; Zhou, H.-C., *Angew. Chem. Int. Ed.* **2018,** *57* (15), 3927-3932.

198. Fukushima, T.; Horike, S.; Inubushi, Y.; Nakagawa, K.; Kubota, Y.; Takata, M.; Kitagawa, S., *Angew. Chem. Int. Ed.* **2010,** *49* (28), 4820-4.

199. Kleist, W.; Maciejewski, M.; Baiker, A., *Thermochim. Acta* **2010,** *499* (1-2), 71-78.

200. Marx, S.; Kleist, W.; Huang, J.; Maciejewski, M.; Baiker, A., *Dalton. Trans.* **2010,** *39* (16), 3795-8.

201. Burrows, A. D., *CrystEngComm* **2011,** *13* (11).

202. Baxter, S. J.; Schneemann, A.; Ready, A. D.; Wijeratne, P.; Wilkinson, A. P.; Burtch, N. C., *J. Am. Chem. Soc.* **2019,** *141* (32), 12849-12854.

203. Fukushima, T.; Horike, S.; Inubushi, Y.; Nakagawa, K.; Kubota, Y.; Takata, M.; Kitagawa, S., *Angew. Chem. Int. Ed.* **2010,** *49* (28), 4820-4824.

204. Cedeno, R. M.; Cedeno, R.; Gapol, M. A.; Lerdwiriyanupap, T.; Impeng, S.; Flood, A.; Bureekaew, S., *Inorg. Chem.* **2021,** *60* (12), 8908-8916.

205. Kleist, W.; Jutz, F.; Maciejewski, M.; Baiker, A., *Eur. J. Inorg. Chem* **2009,** *2009* (24), 3552-3561.

Chapter 2

Experimental Methods and Techniques

2.1 General Materials

All solvents and reagents were purchased from commercially available sources and were used without further purification unless otherwise stated.

2.2 Synthesis

2.2.1 Synthesis of 3,6-bis(4-pyridyl)-1,2,4,5-tetrazine (Tz)

3,6-bis(4-pyridyl)-1,2,4,5-tetrazine (Tz) (Figure 2.1) was synthesised by adaption of literature method.[1] Hydrazine monohydrate (25 mL, 79.6 mmol), and deionised water (5 mL) were added to 4-cyanopyridine (5.5 g, 52.8 mmol). HCl (36%, 5 mL) was added dropwise to the mixture. The solution was stirred and heated to reflux for 3 h. After the mixture was cooled, the orange dihydro intermediate was filtered and collected. The dry intermediate was added to 150 ml of glacial acetic acid. A 10 ml of 70% HNO_3 was added dropwise with stirring for 2h. The mixture turned from brown to pink solution. The pink precipitate was collected after filtration. Recrystallisation from hot pyridine gave purple Tz ligand (1.4 g, yield 23%). ^{1}H NMR (300 MHz, dimethyl sulfoxide-d_6, 300 K): δ = 8.97 ppm (dd, J(H,H) =1.7 Hz, 4.7 Hz, 4H; H_1), 8.46 ppm (dd, J(H,H)=1.5 Hz, 4.5 Hz, 4H; H_2). IR: $\tilde{\upsilon}$ =3052 cm^{-1}(m), 3033 cm^{-1}(m), 1960 cm^{-1}(m), 1734 cm^{-1}(w), 1710 cm^{-1}(m), 1674 cm^{-1}(w), 1590 cm^{-1}(m), 1560 cm^{-1}(m), 1557 cm^{-1}(m), 1496 cm^{-1}(m), 1407 cm^{-1}(s), 1346 cm^{-1}(m), 1263 cm^{-1}(m), 1218 cm^{-1}(m), 1203 cm^{-1}(m), 1190 cm^{-1}(m), 1133 cm^{-1}(w), 1113 cm^{-1}(m), 1083 cm^{-1}(w), 1064 cm^{-1}(m), 1057 cm^{-1}(m), 992 cm^{-1}(m), 922 cm^{-1}(s), 879 cm^{-1}(m), 830 cm^{-1}(s), 736 cm^{-1}(m), 715 cm^{-1}(m), 660 cm^{-1}(w).

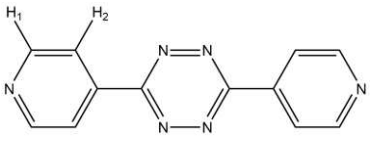

Figure 2.1: Structural drawing of Tz ligand.

2.2.2 Synthesis of 3,6-bis(4-pyridyl)-1,2-diazine (Dz)

3,6-bis(4-pyridyl)-1,2-diazine (Dz) ligand (Figure 2.2) was synthesised by adaption of literature methods.[2] Chloroform (51 mL, 0.6 mol) and 2,5-norbornadiene (2 mL, 0.02 mmol) were added to Tz (0.5 g, 0.002 mmol). The mixture solution was refluxed with stirring for 24 h. The resulting solution was evaporated, and orange powder was collected. The white Dz ligand formed after washing with ethanol. ^{1}H NMR (300 MHz, dimethyl sulfoxide-d_6, 300 K): δ = 8.82 ppm (d, J(H,H)=5.7 Hz, 4H; H_1), 8.57 ppm (s, 2H; H_3), 8.23 (d, J = 5.7 Hz, 4H; H_2). IR: $\tilde{\upsilon}$ =3050 cm^{-1}(m), 1597 cm^{-1}(m), 1593 cm^{-1}(m), 1577 cm^{-1}(m), 1561 cm^{-1}(m), 1551 cm^{-1}(m), 1538 cm^{-1}(m), 1531 cm^{-1}(m), 1489 cm^{-1}(m), 1404 cm^{-1}(s), 1322 cm^{-1}(m), 1310 cm^{-1}(m), 1269 cm^{-1}(m), 1223 cm^{-1}(m), 1162 cm^{-1}(m), 1141 cm^{-1}(m), 1121 cm^{-1}(m),

1119 cm^{-1}(m), 1083 cm^{-1}(m), 1011 cm^{-1}(m), 993 cm^{-1}(m), 958 cm^{-1}(w), 879 cm^{-1}(m), 870 cm^{-1}(w), 832 cm^{-1}(m), 810 cm^{-1}(s), 769 cm^{-1}(m), 736 cm^{-1}(w), 714 cm^{-1}(w), 661 cm^{-1}(w), 640 cm^{-1}(w), 626 cm^{-1}(w).

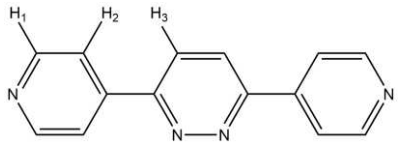

Figure 2.2: Structural drawing of Dz ligand.

2.2.3 Synthesis of Bulk Powder $[Fe(Tz)(Au(CN)_2)_2]\cdot n(EtOH)$ (**TzAu·EtOH**)

The bulk powder product **TzAu·EtOH** was synthesised by using a fast mixing procedure at room temperature. The bulk powder material has the same properties as the single crystal sample. The Tz ligand (27.8 mg, 0.12 mmol) and potassium dicyanidoaurate (67.8 mg, 0.24 mmol) were dissolved in ethanol (150 mL). Separately, ethanol (100 mL) was added to iron(II) perchlorate (30 mg, 0.12 mmol). The iron(II) perchlorate solution was added dropwise to the solution of ligand and potassium dicyanidoaurate. The mixture was stirred slowly for *ca*. 17 h. The product was collected by centrifugation and washed with ethanol several times.

2.2.4 Synthesis of Single Crystals $[Fe(Tz)(Au(CN)_2)_2]\cdot n(EtOH)$

Single crystals of **TzAu·EtOH** were synthesised by the vial-in-vial slow diffusion method. Tz ligand (10 mg, 0.039 mmol), and potassium dicyanidoaurate (22.6 mg, 0.079 mmol) were added to a large vial. Iron(II) perchlorate hydrate (10 mg, 0.039 mmol) was added in a small vial. The small vial was placed inside the large vial. Ethanol was added very slowly to avoid disturbing the reactants until the level of the solution was slightly above the top of the small vial. The large vial was sealed, and the reagents were left to grow dark purple crystals over several weeks.

2.2.5 Synthesis of Bulk Powder $[Fe(Dz)(Au(CN)_2)_2]\cdot n(EtOH)$ (**DzAu·EtOH**)

The bulk powder form of **DzAu·EtOH** was synthesised using a fast mixing procedure. The Dz ligand (27.6 mg, 0.12 mmol) and potassium dicyanidoaurate (67.8 mg, 0.24 mmol) were dissolved in ethanol (150 mL). A solution of iron(II) perchlorate (30 mg, 0.12 mmol) in ethanol (100 mL) was added dropwise to the solution mixed with ligand and potassium dicyanidoaurate. The mixture was stirred slowly for *ca*. 17 h at 50 ºC. The product was collected by centrifugation and washed with ethanol several times.

2.2.6 Synthesis of Single Crystals of $[Fe(Dz)(Au(CN)_2)_2]\cdot n(EtOH)$

Single crystals of **DzAu·EtOH** were synthesised by the vial-in-vial slow diffusion method. Dz ligand (10 mg, 0.039 mmol), and potassium dicyanidoaurate (22.6 mg, 0.079 mmol) were added to a large vial. Iron(II) perchlorate hydrate (10 mg, 0.039 mmol) was added to a small vial. The small vial was placed inside the large vial. Ethanol was added very slowly to avoid disturbing the reactants until the level of the solution was slightly above the top of the small vial. The large vial was sealed, and the reagents were left to grow light orange crystals over several weeks.

2.2.7 Guest Exchange Method

Single crystals of $[Fe(Tz)(Au(CN)_2)_2]\cdot(OX)$ (**TzAu·OX**), $[Fe(Tz)(Au(CN)_2)_2]\cdot(PX)$ (**TzAu·PX**), $[Fe(Dz)(Au(CN)_2)_2]\cdot(OX)$ (**DzAu·OX**), $[Fe(Dz)(Au(CN)_2)_2]\cdot(PX)$ (**DzAu·PX**) and $[Fe(Dz)(Au(CN)_2)_2]\cdot(MX)$ (**DzAu·MX**) were generated using a guest exchange method. **TzAu·EtOH** or **DzAu·EtOH** crystals were transferred in small vials. The mother liquor EtOH supernatant was decanted. The crystals were added to the corresponding guest solvents and soaked for 10 min. The solvents were decanted, and fresh solvents were added again. Crystals were left to stand and the guest exchange process was repeated 5 times.

The bulk powder forms of $[Fe(Tz)(Au(CN)_2)_2]\cdot(OX)$ (**TzAu·OX**), $[Fe(Tz)(Au(CN)_2)_2]\cdot(PX)$ (**TzAu·PX**), $[Fe(Tz)(Au(CN)_2)_2]\cdot(MX)$ (**TzAu·MX**), $[Fe(Dz)(Au(CN)_2)_2]\cdot(OX)$ (**DzAu·OX**), $[Fe(Dz)(Au(CN)_2)_2]\cdot(PX)$ (**DzAu·PX**) and $[Fe(Dz)(Au(CN)_2)_2]\cdot(MX)$ (**DzAu·MX**) were generated using the same guest exchange method with a slightly different procedure. The bulk powders were transferred to centrifuge tubes and the mother liquor EtOH was decanted. The corresponding guest solvents were added to the powders respectively and soaked for 20 min. Following sedimentation of the powder, the supernatant was decanted. The guest exchange process was repeated five times.

Binary xylene solvents in the different molar ratios were prepared (PX:MX = 3:7, 5:5, 7:3, 9:1; MX:OX = 3:7, 5:5, 7:3 and PX:OX = 3:7, 5:5, 7:3, 9:1). The powdered parent frameworks **TzAu·EtOH** and **DzAu·EtOH** were soaked in different ratio of binary solvents by using the aforementioned guest exchange method, which generated 14 bulk powder materials: **TzAu·PM37** (PX:MX = 3:7), **TzAu·PM50** (PX:MX = 5:5), **TzAu·PM73** (PX:MX = 7:3), **TzAu·PO37** (PX:OX = 3:7), **TzAu·PO50** (PX:OX = 5:5), **TzAu·PO73** (PX:OX = 7:3), **TzAu·MO37** (MX:OX = 3:7), **TzAu·MO50** (MX:OX = 5:5), **TzAu·MO73** (MX:OX = 7:3), **DzAu·PM50** (PX:MX = 5:5), **DzAu·PO50** (PX:OX = 5:5), **DzAu·MO50** (MX:OX = 5:5), **DzAu·PM91** (PX:MX = 9:1) and **DzAu·PO91** (PX:OX = 9:1). The actual binary xylene ratios absorbed within the pores of the materials were charaterised by NMR mentioned in Section 2.3.1.

2.2.8 Synthesis of Single Crystals $[Fe(Tz)(Ag(CN)_2)_2]\cdot n(EtOH)$ (**TzAg·EtOH**)

Single crystals of **TzAg·EtOH** were synthesised by the vial-in-vial slow diffusion method. Tz ligand (9.3 mg, 0.039 mmol), and potassium dicyanidoargentate (15.6 mg, 0.079 mmol) were added to a large vial. Iron(II) perchlorate hydrate (10 mg, 0.039 mmol) was added to a small vial. The small vial was placed inside the large vial. A solvent mixture of EtOH:DCM (1:1) was added very slowly to avoid disturbing the reactants until the level of the solution was slightly above the top of the small vial. The large vial was sealed, and the reagents were left to grow dark purple crystals over several weeks. The solvent exchange method to fresh ethanol was applied to the material and crystals were soaked in ethanol.

2.2.9 Synthesis of Bulk Powder $[Fe(Tz)(Ag(CN)_2)_2]\cdot n(EtOH)$

The bulk powder form of **TzAg·EtOH** was synthesised using a fast mixing procedure. The Tz ligand (27.8 mg, 0.12 mmol) and potassium dicyanidoargentate (46.9 mg, 0.24 mmol) were dissolved in ethanol (150 mL). A solution of iron(II) perchlorate (30 mg, 0.12 mmol) was generated by dissolving in ethanol (100 mL) and was added dropwise to the solution mixed with ligand and potassium dicyanidoaurate. The mixture was stirred slowly for *ca*. 17 h at room temperature. The product was collected by centrifugation and washed with ethanol several times.

2.2.10 Synthesis of Single Crystals $[Fe(Tz)((Au(CN)_2)_{0.5}(Ag(CN)_2)_{0.5})_2]\cdot n(EtOH)$ (**$TzAu_{0.5}Ag_{0.5}$·EtOH**)

Single crystals of **$TzAu_{0.5}Ag_{0.5}$·EtOH** material were synthesised by the vial-in-vial slow diffusion method. Tz ligand (9.3 mg, 0.039 mmol), potassium dicyanidoaurate (11.3 mg, 0.039 mmol) and potassium dicyanidoargentate (7.8 mg, 0.039 mmol) were added to a large vial. Iron(II) perchlorate hydrate (10 mg, 0.039 mmol) was added to a small vial. The small vial was placed inside the large vial. Ethanol was added very slowly to avoid disturbing the reactants until the level of the solution was slightly above the top of the small vial. The large vial was sealed, and the reagents were left to grow dark purple crystals over several weeks.

2.2.11 Synthesis of Bulk Powder $[Fe(Tz)((Au(CN)_2)_{0.5}(Ag(CN)_2)_{0.5})_2]\cdot n(EtOH)$

The bulk powder form of **$TzAu_{0.5}Ag_{0.5}$·EtOH** was synthesised using a fast mixing procedure. The Tz ligand (27.8 mg, 0.12 mmol), potassium dicyanidoargentate (23.4 mg, 0.12 mmol) and potassium dicyanidoaurate (33.9 mg, 0.12 mmol) were dissolved in ethanol (150 mL). A solution of iron(II)

perchlorate (30 mg, 0.12 mmol) was generated by dissolving in ethanol (100 mL) and was added dropwise to the solution mixed with ligand and potassium dicyanidoaurate. The mixture was stirred slowly for *ca*. 17 h at room temperature. The product was collected by centrifugation and washed with ethanol several times.

2.2.12 Synthesis of Single Crystals $[Fe(Dz)(Ag(CN)_2)_2]\cdot n(EtOH)$ (**DzAg·EtOH**)

Single crystals of **DzAg·EtOH** material were synthesised by the vial-in-vial slow diffusion method. Dz ligand (9.2 mg, 0.039 mmol), and potassium dicyanidoargentate (15.6 mg, 0.079 mmol) were added to a large vial. Iron(II) perchlorate hydrate (10 mg, 0.039 mmol) was added to a small vial. The small vial was placed inside the large vial. Ethanol was added very slowly to avoid disturbing the reactants until the level of the solution was slightly above the top of the small vial. The large vial was sealed, and the reagents were left to grow dark orange crystals over several weeks.

2.2.13 Synthesis of Bulk Powder $[Fe(Dz)(Ag(CN)_2)_2]\cdot n(EtOH)$

The bulk powder form of **DzAg·EtOH** was synthesised using a fast mixing procedure. The Dz ligand (27.6 mg, 0.12 mmol) and potassium dicyanidoargentate (46.9 mg, 0.24 mmol) were dissolved in ethanol (150 mL). A solution of iron(II) perchlorate (30 mg, 0.12 mmol) was generated by dissolving in ethanol (100 ml) and was added dropwise to the solution mixed with ligand and potassium dicyanidoaurate. The mixture was stirred slowly for *ca*. 17 h at room temperature. The product was collected by centrifugation and washed with ethanol several times.

2.2.14 Synthesis of Single Crystals $[Fe(Dz)((Au(CN)_2)_{0.5}(Ag(CN)_2)_{0.5})_2]\cdot n(EtOH)$ (**$DzAu_{0.5}Ag_{0.5}$·EtOH**)

Single crystals of **$DzAu_{0.5}Ag_{0.5}$·EtOH** were synthesised by the vial-in-vial slow diffusion method. Dz ligand (9.2 mg, 0.039 mmol), potassium dicyanidoaurate (11.3 mg, 0.039 mmol) and potassium dicyanidoargentate (7.8 mg, 0.039 mmol) were added to a large vial. Iron(II) perchlorate hydrate (10 mg, 0.039 mmol) was added to a small vial. The small vial was placed inside the large vial. Ethanol was added very slowly to avoid disturbing the reactants until the level of the solution was slightly above the top of the small vial. The large vial was sealed, and the reagents were left to grow dark purple crystals over several weeks.

2.2.15 Synthesis of Bulk Powder $[Fe(Dz)((Au(CN)_2)_{0.5}(Ag(CN)_2)_{0.5})_2]\cdot n(EtOH)$

The bulk powder form of **$DzAu_{0.5}Ag_{0.5}\cdot EtOH$** was synthesised using a fast mixing procedure. The Dz ligand (27.6 mg, 0.12 mmol), potassium dicyanidoargentate (23.4 mg, 0.12 mmol) and potassium dicyanidoaurate (33.9 mg, 0.12 mmol) were dissolved in ethanol (150 mL). A solution of iron(II) perchlorate (30 mg, 0.12 mmol) was generated by dissolving in ethanol (100 ml) and was added dropwise to the solution mixed with ligand, potassium dicyanidoargentate and potassium dicyanidoaurate. The mixture was stirred slowly for *ca*. 17 h at room temperature. The product was collected by centrifugation and washed with ethanol several times.

2.2.16 Synthesis of Bulk Powder $[Fe(Dz)((Au(CN)_2)_{0.7}(Ag(CN)_2)_{0.3})_2]\cdot n(EtOH)$ (**$DzAu_{0.7}Ag_{0.3}\cdot EtOH$**)

The bulk powder form of **$DzAu_{0.7}Ag_{0.3}\cdot EtOH$** was synthesised using a fast mixing procedure. The Dz ligand (27.6 mg, 0.12 mmol), potassium dicyanidoargentate (14.1 mg, 0.071 mmol) and potassium dicyanidoaurate (47.5 mg, 0.16 mmol) were dissolved in ethanol (150 mL). A solution of iron(II) perchlorate (30 mg, 0.12 mmol) was generated by dissolving in ethanol (100 ml) and was added dropwise to the solution mixed with ligand, potassium dicyanidoargentate and potassium dicyanidoaurate. The mixture was stirred slowly for *ca*. 17 h at room temperature. The product was collected by centrifugation and washed with ethanol several times.

2.2.17 Synthesis of Single Crystals $[Fe(Dz)(H_2O)_2Pt(CN)_4]\cdot 2(H_2O)$ (**DzPt**)

Single crystals of **DzPt** were synthesised by the vial-in-vial slow diffusion method. Dz ligand (9.2 mg, 0.039 mmol), and potassium tetracyanidoplatinate (14.8 mg, 0.039 mmol) were added to a large vial. Iron(II) perchlorate hydrate (10 mg, 0.039 mmol) was added in a small vial. The small vial was placed inside the large vial. A solvent mixture of 1:1 EtOH:H_2O was added very slowly to avoid disturbing the reactants until the level of the solution was slightly above the top of the small vial. The large vial was sealed, and the reagents were left to grow yellow crystals over several weeks.

2.2.18 Synthesis of Bulk Powder $[Fe(Dz)(H_2O)_2Pt(CN)_4]\cdot 2(H_2O)$

The bulk powder form of **DzPt** was synthesised using a fast mixing procedure. The Dz ligand (27.6 mg, 0.12 mmol) and potassium tetracyanidoplatinate (44.4 mg, 0.12 mmol) were dissolved in a solvent mixture of 1:1 EtOH:H_2O (150 mL). A solution of iron(II) perchlorate (30 mg, 0.12 mmol) was generated by dissolving in a solvent mixture of 1:1 EtOH:H_2O (100 mL) and was added dropwise to

the solution mixed with ligand and potassium tetracyanidoplatinate. The mixture was stirred slowly for *ca*. 17 h at room temperature. The product was collected by centrifugation and washed with ethanol several times.

2.2.19 Synthesis of Single Crystals $[Fe(Dz)(H_2O)_2Pd(CN)_4]\cdot 2(H_2O)$ (**DzPd**)

Single crystals of **DzPd** were synthesised by the vial-in-vial slow diffusion method. Dz ligand (9.2 mg, 0.039 mmol), and potassium tetracyanidopalladate (11.3 mg, 0.039 mmol) were added to a large vial. Iron(II) perchlorate hydrate (10 mg, 0.039 mmol) was added in a small vial. The small vial was placed inside the large vial. A solvent mixture of 1:1 EtOH:H_2O was added very slowly to avoid disturbing the reactants until the level of the solution was slightly above the top of the small vial. The large vial was sealed, and the reagents were left to grow yellow crystals over several weeks.

2.2.20 Synthesis of Bulk Powder $[Fe(Dz)(H_2O)_2Pd(CN)_4]\cdot 2(H_2O)$

The bulk powder form of **DzPd** was synthesised using a fast mixing procedure. The Dz ligand (27.6 mg, 0.12 mmol) and potassium tetracyanidopalladate (33.9 mg, 0.12 mmol) were dissolved in a solvent mixture of 1:1 EtOH:H_2O (150 mL). A solution of iron(II) perchlorate (30 mg, 0.12 mmol) was generated by dissolving in a solvent mixture of 1:1 EtOH:H_2O (100 ml) and was added dropwise to the solution mixed with ligand and potassium tetracyanidopalladate. The mixture was stirred slowly for *ca*. 17 h at room temperature. The product was collected by centrifugation and washed with ethanol several times.

2.2.21 Synthesis of Bulk Powder $[Fe(Tz)_x(Dz)_{1-x}Au(CN)_2)_2]\cdot n(EtOH)$

Bulk powder mixed-ligand samples of $[Fe(Tz)_x(Dz)_{1-x}Au(CN)_2)_2]\cdot n(EtOH)$ (x = 0.1, **$[Tz_{0.1}Dz_{0.9}]$**; 0.15, **$[Tz_{0.15}Dz_{0.85}]$**; 0.2, **$[Tz_{0.2}Dz_{0.8}]$**; 0.3, **$[Tz_{0.3}Dz_{0.7}]$**; 0.4, **$[Tz_{0.4}Dz_{0.6}]$**; 0.5, **$[Tz_{0.5}Dz_{0.5}]$**; 0.6, **$[Tz_{0.6}Dz_{0.4}]$**; 0.7, **$[Tz_{0.7}Dz_{0.3}]$**; 0.8, **$[Tz_{0.8}Dz_{0.2}]$**; 0.9, **$[Tz_{0.9}Dz_{0.1}]$**) were synthesised following the same procedure as **TzAu·EtOH** with appropriate stoichiometric amounts of Tz and Dz ligand. The percentage of Tz ligand included in each framework was characterised by infrared spectroscopy.

2.3 Experimental Techniques

2.3.1 Nuclear Magnetic Resonance (NMR) Spectroscopy

^{1}H NMR spectra of ligands were collected at 300 K on a Bruker AVANCE300 NMR spectrometer operating at 300 MHz. Ligands were measured in dimethyl sulfoxide-d_6 with a chemical shift of δ =

2.50 ppm. Chemical shifts (δ) is quoted in ppm with uncertainties of ±0.01 ppm and coupling constants (*J*) are quoted in Hz with uncertainties of ± 0.05 Hz. Deuterated solvents were purchased from Cambridge Isotope Laboratories Inc. and used as received.

The components of binary xylene solvent within the MOF materials described in Chapters 3 and 4 were characterised using NMR. The mixed xylene solvents for soaking the MOF samples (*ca.* 10 mg) were decanted. A sample of MOF was dried in nitrogen gas. The $CDCl_3$ solution (*ca.* 2mL) was added to each MOF sample and the solution was left to stand over night. ^1H NMR spectra were collected on the solution, to determine the ratio of xylenes adsorbed in each MOF.

2.3.2 Powder X-ray Diffraction (PXRD) and Variable Temperature Powder X-ray Diffraction (VT-PXRD)

PXRD patterns were collected on two in-house instruments and at the Australian Synchrotron. The facilities used for data collection were specified in each chapter. In order to prevent solvent loss of the MOF materials, samples were loaded into 0.5 or 0.3 mm glass capillaries, followed by flame sealing the open end. PXRD patterns were refined using both Le Bail and Rietveld methods within GSAS-II software suite.[3]

Where specified, patterns were obtained on a PANalytical X'Pert MPD using Cu-K_α radiation (λ = 1.54187 Å), within the 2θ range 4–33°, with a step size of 0.013°. Debye-Scherrer geometry patterns were collected over 30 min.

Where specified, PXRD data were also acquired on a STOE STADI P diffractometer equipped with a MULTI-MYTHEN detector and utilising Mo-K_α (λ = 0.71073 Å) radiation. Samples in the flame sealed glass capillaries were aligned on a spinning goniometer head with data acquired over a range of 2θ = 0–50°.

VT-PXRD measurements using in-house instruments were undertaken in the same manner as described above with the addition of using an Oxford Cryostream system to control the temperature. Different samples were measured under different temperature ranges and increments, as detailed in the following chapters.

Powder diffraction measurements were also conducted on the Powder Diffraction beamline (λ = 0.5907 Å) at the Australian Synchrotron part of ANSTO by Dr Anita D'Angelo to obtain high resolution of powder diffraction data. The X-ray energy used for the powder diffraction experiments was 21 keV. The samples were loaded in sealed 0.3 mm glass capillaries. Measurements were conducted at ambient temperature and pressure. The data were collected in two positions with starting positions at 2° and 2.5° due to a gap in the detector by 0.5°. Each position was measured at the same acquisition time (180 s).

The two positions were merged using PDViPeR software. LaB_6 was used as the standard to refine the wavelength. Variable temperature PXRD patterns were acquired over a range of temperatures detailed in the following chapters. The samples were prepared as above.

2.3.3 Single Crystal X-ray Diffraction (SCXRD)

Single crystals data were collected using the in-house sources or at the Australian Synchrotron, which was specified in the following chapters.

SCXRD data were obtained by using in-house Agilent Technologies SuperNova Single Source diffractometer with a micro-source. A Cu-K_α (λ = 1.54184 Å) or Mo-K_α radiation (λ=0.71073 Å) and radiation source were used and fitted with an EosS2 detector. The crystal samples were mounted in the solvent in a thin film of paratone oil. The data were collected in nitrogen cryostream from Oxford Cryosystem and various temperature collection details were in the chapters. CrysAlisPro[4] was used for data collection, integration and reduction. Empirical absorption correction was applied using spherical harmonics, implemented in SCALE3 ABSPACK scaling algorithm.

SCXRD data were obtained from the MX1 beamline radiation source and ADSC Quantum 210r detector using Blu-Ice software at the Australian Synchrotron facility in Melbourne, Australia and were collected by Dr William Lewis. The crystal samples were cold-mounted at 100 K to avoid desolvation.

All structures were solved using SHELXT[5] intrinsic phasing and were refined by using SHELXL-2014/7[6] within the OLEX2[7] user interface. Some of the crystal structures contain the disorder of the solvent molecules, which were refined without taking solvent into consideration. The disordered solvent in the framework was treated by using the SQUEEZE procedure in the program PLATON.[8-9] Pore volumes of materials were calculated using Mercury software.[10] Molecular graphics were generated by using OLEX2[7], CrystalMaker® X v 10.7.3[11] and Mercury software.[10]

2.3.4 Variable Temperature (VT) Magnetic Susceptibility

Variable temperature magnetic susceptibility measurement was conducted at ambient pressure on a Quantum Design Physical Property Measurement System (PPMS) Dynacool or Quantum Design VersaLab magnetometer. Both instruments are using a vibrating sample magnetometer (VSM) attachment. The information on the instrument, scan rate and temperature range used for each sample is detailed in the following chapters. Powder samples were loaded into hollow perfluoroalkoxy (PFA, a fluoropolymer) sample holders. The samples were firmly packed by centrifuge and by inserting a small amount of cotton wool inside the tubes. To prevent the solvent loss, both sides of a PFA tube were flame sealed (Figure 2.3). Data were obtained by continuous measurement under a magnetic field

of 3000 Oe (0.3 T) over various thermal cycles.

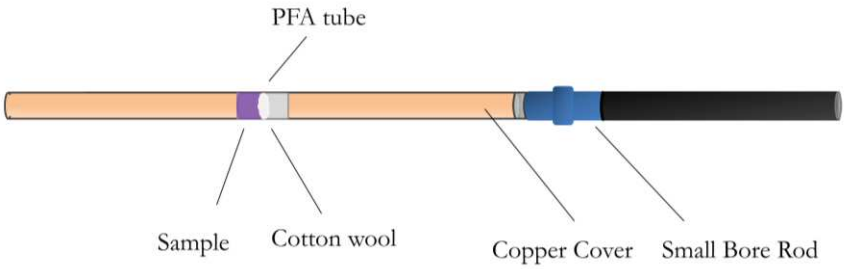

Figure 2.3: Schematic of the sample holder used for measuring variable temperature magnetic susceptibility at ambient pressure.

2.3.5 Variable Pressure (VP) Magnetic Susceptibility

Non-ambient pressure variable pressure magnetic susceptibility measurements of powder samples were all conducted using a PPMS Dynacool with VSM attachment. A sample of powder framework material in ethanol and a small amount of lead as pressure calibrant was loaded into a Teflon tube sealed with Teflon caps on both ends inside a Quantum Design High Pressure Cell (Figure 2.4). The pressure cell consists of two screwed cylinder pressurisation nuts, which attach to two side cylinders and can push the piston *via* contact with piston backups on both sides. The first data point of each sample was collected with the sample loaded into the cell where the cylinder pressurisation nuts were tightened finger tight. The pressure was then increased by tightening two screwed cylinder pressurisation nuts using pressurisation spanners on both sides until there were no gaps between pressurisation nuts and the side cylinders on both sides. The measurements at each pressure point were acquired under a magnetic field of 3000 Oe. The details of temperature ranges and scan rates for each sample are discussed in Chapter 6.

The applied pressure was determined by measuring the critical temperature in a superconducting state on a lead wire in the sample tube. Each pressure calibration data was measured at 40 Oe over a temperature range of 6–7.5–6 K at a 0.1 K min^{-1} scan rate. The applied pressure was calculated by using equation 2.1, where $T_{c,0}$ is the critical temperature in the superconducting state at ambient and T_c is the applied pressure critical temperature.

$$P = \ (T_{c,0} - T_c)/0.379 \quad (2.1)$$

(a)

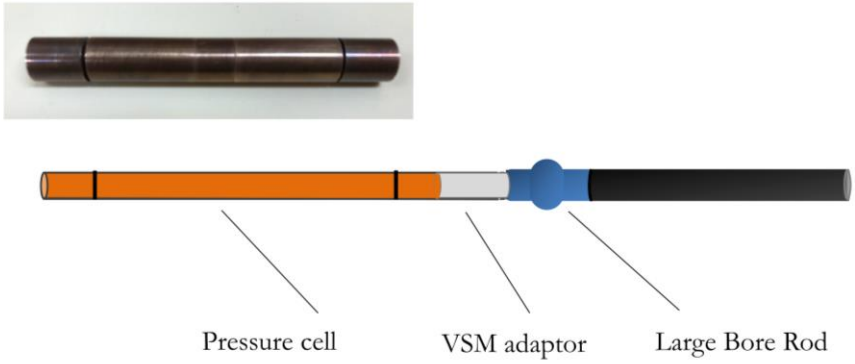

(b)

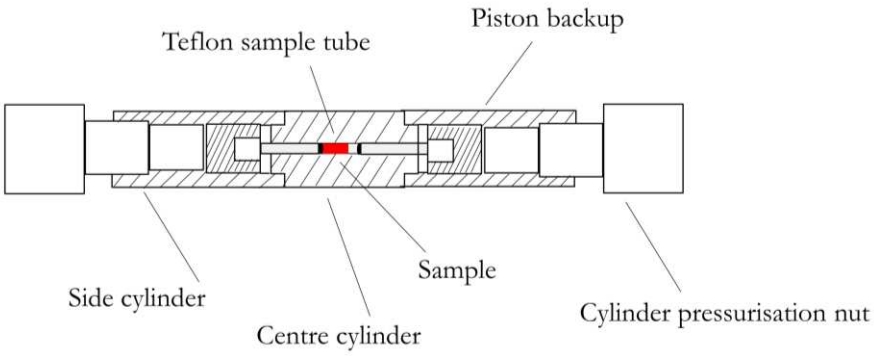

Figure 2.4: (a) Photograph of a Quantum Design High Pressure Cell (top) used for measuring variable temperature magnetic susceptibility at applied pressure. Schematic of a Quantum Design High Pressure Cell connects with VSM adaptor and large bore rod. (b) Schematic of the inside of a Quantum Design High Pressure Cell.

2.3.6 Infrared (IR) Spectroscopy

IR spectroscopic measurements were carried out on a Bruker Tensor 27 FTIR instrument with Hyperion 3000 microscope (15×objective) and a Mercury Cadmium Telluride and Focal Plane Array detector. Data were collected in transmission mode over the range 600–4000 cm^{-1} at 40 ºC with 128 scans for both background and samples. Samples were mounted on the Linkam-FTIR 600 variable temperature stage. Nitrogen gas was continuously flowed onto the Linkam stage with the temperature programmer connected.

2.3.7 Variable Temperature Raman Spectroscopy (VT-Raman)

Raman spectra were collected on a Renishaw inVia-Qontor Upright microscope. Data were collected using an excitation wavelength of 785 nm (10% laser power and L×50 objective) and with a 10 s exposure time (one or three accumulations depending on the data quality). The same Linkam stage as for IR was used, with the same attachment of a liquid nitrogen dewar, temperature programmer and cooling pump. Prior to measurement, the sample was loaded into a 0.5 mm glass capillary and flame-sealed to avoid desolvation.

2.3.8 Variable Temperature UV-Vis-Near Infrared (VT-UV)

Solid-state diffuse reflectance UV-Vis-Near Infrared measurements were carried out using a Cary 5000 spectrophotometer. The temperature was controlled by using a Harrick Praying Mantis attachment. Variable temperature measurements were controlled by an ATC-024 Harrick Temperature Controller, which cooled the Harrick dome with liquid nitrogen. A background measurement was obtained on a dry $BaSO_4$ powder. The bulk powder samples with solvent were mixed with a $BaSO_4$ matrix and mounted into a Harrick ambient pressure dome accessory equipped with SiO_2 windows to prevent solvent loss. The solid-state spectra were collected at a rate of 6000 cm^{-1} min^{-1} over a range of 3000-20000 cm^{-1}. The spectra were recorded at 10 ºC intervals. All spectra are reported as the Kubelka-Munk transform, where $F(R) = (1-R)^2 /2R$ (where R is the diffuse reflectance, which is relative to the $BaSO_4$ baseline).

2.3.9 Differential Scanning Calorimetry (DSC)

DSC experiments were performed on a Mettler Toledo DSC 823e instrument. The sample with solvent (*ca*. 10 mg) was added to a hermetic aluminium pan and both the sample pan and reference pan were press-sealed. Measurements were conducted at a scan rate of 10 K min^{-1} with a constant nitrogen flow of 50 mL min^{-1}. The temperature range for each sample is detailed in the following chapters.

2.3.10 Thermogravimetric Analysis (TGA)

Experiments were performed on a TA Instruments Discovery TGA. Each sample (*ca.* 10 mg) with solvent was loaded onto a platinum pan. The sample was held at room temperature for 10 min prior to heating to the temperature that the MOF samples degraded. The details of temperature ranges were mentioned in the following chapters. The measurements were conducted at a ramp rate of 1 °C min^{-1} under a nitrogen flow of 20 mL min^{-1}.

2.3.11 X-ray Photoelectron Spectroscopy (XPS)

XPS experiments were performed on a Thermo Fisher Scientific K-Alpha XPS system. The X-ray source of the instrument is Al-$K_{\alpha 1}$ micro-focused monochromator with 1486.7 eV equipped with a 180° double focusing hemispherical analyser with a 128 channel detector. The samples were dropped on the sample holder with conductive carbon tape. The samples were dried in the air before measurements. The samples were conducted on ion beam etching (30 s) before scans to prevent any contamination on the surface of the samples and ensure the measurements were conducted on the samples. Survey scans were acquired with a pass energy of 200 eV and high-resolution scans of Fe *2p*, Au *4f*, Ag *3d*, C *1s* and N *1s* levels with a pass energy of 50 eV. C 1*s* value of 284.8 eV binding energy was used for calibration. A flood gun was on with the analyser chamber under approximately 10^{-7} Pa to avoid sample charging during the measurement.

2.3.12 Scanning Electron Microscopy (SEM) and Energy-dispersive X-ray Spectroscopy (EDS)

SEM images were obtained using a Zeiss Sigma variable pressure (VP) High Definition (HD) Field Emission SEM microscope. High-resolution images were performed by the Schottky field emission gun (FEG). Powder samples were dispersed in the mother solvent to produce a suspension and were deposited on stubs on which silicon was stuck on carbon tape. After the samples were dried in the air, they were carbon coated to increase conductivity for obtaining high resolution of images. The measurements were conducted on 5 kV electron high tension (EHT).

The EDS spectra were performed with Zeiss Sigma VP HD equipped with Oxford instrument AZtec EDS and EBSD system with X-Max 20 mm^2 SDD EDS detector and high speed Nordlys-F+ EBSD. The measurements were performed using a high accelerating voltage (EHT = 20 kV). The samples were measured with a working distance of 8.5 mm. The spectral data were analysed using the AZtec software.

2.3.13 Density Functional Theory Calculations (DFT)

DFT-based geometry optimisations of the MOF were carried out with the VASP code[12-13] within the generalised gradient approximation (GGA), using the Perdew-Burke-Ernzerhof (PBE) exchange-correlation functional[13-14] and the projector augmented wave (PAW) method by Dr Ramzi Kutteh.[15-16] Two groups of geometry optimisations were performed on the monoclinic unit cell of the MOF (312 atoms) measured at 250 K, one without any correction for van der Waals interactions and the other with such a correction included using the DFT-D3 method of Grimme *et al*.[17] Each group comprised two

geometry optimisations, one carried out with symmetry constraints imposed throughout and the other without such constraints. Using the conjugate gradient algorithm with a convergence tolerance on the maximum force magnitude of 10^{-4} eV/Å (the same numerical criterion is also applied to the stress tensor components), each geometry optimisation started with a relaxation of the ionic positions, followed by one of the cell volumes, then one of the cell shape, with this sequence repeated as necessary, and concluded with a final relaxation of all quantities simultaneously. This strategy was adopted to avoid potential convergence problems. The electronic relaxation was performed using the Blocked-Davidson algorithm with a convergence tolerance on the energy change of 10^{-6} eV, a 2 × 2 × 1 Gamma-centered Monkhorst-Pack k-point mesh[18], and a plane wave energy cut-off of 520 eV.

2.3.14 High-pressure Neutron Powder Diffraction (NPD)

NPD measurements were carried out using WOMBAT,[19] the high-intensity neutron powder diffractometer at the OPAL reactor facility, Australian Nuclear Science and Technology Organisation (ANSTO). The powdered sample TzAu was mixed with some pieces of the lead block as an internal pressure standard.[20] The resulting slurry was loaded into a TiZr null matrix alloy sample holder, which was placed in a VX-5 Paris-Edinburgh hydraulic press equipped with boron nitride anvils.[21] The diffraction data were collected using 2.95 Å neutrons as determined using a LaB_6 reference (NIST SRM 660b). The radial collimator was set to take 60 s to scan 2° oscillation each way. The collection for each pressure point was started at 14° with 0.125° step size and each run in 8 min. The measurement at each pressure was collected for 2–8 h depending on the data quality.

2.4 References

1. Dinolfo, P. H.; Williams, M. E.; Stern, C. L.; Hupp, J. T., *J. Am. Chem. Soc.* **2004,** *126* (40), 12989-13001.

2. Clements, J. E.; Price, J. R.; Neville, S. M.; Kepert, C. J., *Angew. Chem. Int. Ed.* **2016,** *55* (48), 15105-15109.

3. Toby, B. H.; Von Dreele, R. B., *J. Appl. Crystallogr.* **2013,** *46* (2), 544-549.

4. CrysAlisPRO. Oxford Diffraction/Agilent Technologies UK Ltd: Yarnton, England.

5. Sheldrick, G. M., *Acta Crystallogr. A: Found. Adv.* **2015,** *71* (1), 3-8.

6. Sheldrick, G. M., *Acta Crystallogr. C Struct. Chem.* **2015,** *71* (1), 3-8.

7. Dolomanov, O. V.; Bourhis, L. J.; Gildea, R. J.; Howard, J. A. K.; Puschmann, H., *J. Appl. Crystallogr.* **2009,** *42* (2), 339-341.

8. Spek, A. L., *Acta. Crystallogr. C Struct. Chem.* **2015,** *71* (Pt 1), 9-18.

9. Spek, A. L., *J. Appl. Crystallogr.* **2003,** *36* (1), 7.

10. Macrae, C. F.; Sovago, I.; Cottrell, S. J.; Galek, P. T. A.; Mccabe, P.; Pidcock, E.; Platings, M.; Shields, G. P.; Stevens, J. S.; Towler, M.; Wood, P. A., *J. Appl. Crystallogr.* **2020,** *53* (1), 226-235.

11. *CrystalMaker®: a crystal and molecular structures program for Mac and Windows.*, CrystalMaker Software Ltd, Oxford, England.

12. Kresse, G.; Furthmüller, J., *Comput. Mater. Sci.* **1996,** *6* (1), 15-50.

13. Perdew, J. P.; Burke, K.; Ernzerhof, M., *Phys. Rev. Lett.* **1996,** *77* (18), 3865-3868.

14. Perdew, J. P.; Burke, K.; Ernzerhof, M., *Phys. Rev. Lett.* **1997,** *78* (7), 1396-1396.

15. Kresse, G.; Joubert, D., *Phys. Rev. B* **1999,** *59* (3), 1758-1775.

16. Blöchl, P. E., *Phys. Rev. B* **1994,** *50* (24), 17953-17979.

17. Grimme, S.; Antony, J.; Ehrlich, S.; Krieg, H., *Chem. Phys.* **2010,** *132* (15), 154104.

18. Monkhorst, H. J.; Pack, J. D., *Phys. Rev. B* **1976,** *13* (12), 5188--5192.

19. Studer, A. J.; Hagen, M. E.; Noakes, T. J., *Physica B: Condens. Matter* **2006,** *385-386*, 1013-1015.

20. Strässle, T.; Klotz, S.; Kunc, K.; Pomjakushin, V.; White, J. S., *Phys. Rev. B* **2014,** *90* (1).

21. Besson, J. M.; Nelmes, R. J.; Hamel, G.; Loveday, J. S.; Weill, G.; Hull, S., *Physica B: Condens. Matter* **1992,** *180-181*, 907-910.

Chapter 3

Investigation of SCO Behaviours Influenced by Adsorption of Guest Xylene Isomers in $[Fe(Tz)(Au(CN)_2)_2]$

3.1 Overview

The three isomers of xylene, called *o*-xylene (OX), *p*-xylene (PX), and *m*-xylene (MX), are produced from reformates or pyrolysis gasoline, and are all important as industrial feedstock chemicals.[1] PX is used as a precursor to synthesise terephthalic acid; OX is used as a precursor to synthesise plasticisers; and MX is a fuel additive.[2-3] A challenging issue in the chemical purifications and separations industry is to detect and separate these isomers as xylenes have only minor differences in their physical properties such as boiling points, kinetic diameters, densities, and polarisabilities (Table 3.1).[4-6] It is essential to design materials that have adequately sized and functionalised pore apertures such that they may accommodate and display a distinguished response to the xylene isomers.

Table 3.1: Physical properties of xylene isomers.

Property	PX	OX	MX
Density at 298 K / g mL^{-1}	0.86	0.88	0.86
Boiling point / K	411.5	417.5	412
Kinetic diameter / Å	5.8	6.8	6.8
Polarisability ($\times 10^{-25}$ cm^3)	137−149	141−149	142
Molecular length / Å[a]	9.2	8.0	8.6
Molecular width / Å[a]	6.7	7.5	7.4
Molecular thickness / Å[a]	4.2	4.2	4.2

[a] Calculated from the QSAR model of Materials Studio, after geometry optimisation with the universal forcefield.

Over the recent decades, MOFs have been extensively investigated because of their multifunctional properties. Such multifunctional materials support various applications, including within drug delivery,[7-9] biosensing,[10] catalysis,[11-12] and molecular storage.[13-14] The choice of the metal centre and bridging ligand for MOF design provides a large diversity in both the ultimate structure and functionality. The rational design of MOF topology by crystal engineering, and precise control of their applications, strongly relied on the ligand functionalities.[15] Adsorption capability in MOFs has attracted greater interest, especially in the chemical industrial field.[16-19] Most research has focused on designing MOFs that incorporate ligands of various lengths and chemical functionality; thus, these features influence the size and shape of pores and their capability to selectively adsorb guest molecules.[15, 20]

SCO MOFs that are sensitive to adsorbed guest molecules could be potential candidates for differentiating xylene isomers. A Hofmann-like framework material of the form, $[Fe(Tz)Au(CN)_2)_2]\cdot x(EtOH)$ (**TzAu·EtOH**), has an octahedral Fe(II) metal centre coordinated with four $[Au(CN)_2]^-$ linkers in the equatorial positions, and a pyridyl *N*-donor Tz (3,6-bis(4-pyridyl)-1,2,4,5-tetrazine) ligand on the two axial positions.[21] The framework possesses solvent-accessible channels of 8.9 × 5.2 Å (van der Waals radius considered), which indicates that it can accommodate

xylenes.

Herein, this chapter discusses the syntheses of the bulk polycrystalline powders and single crystals with encapsulation of xylenes, namely: $[Fe(Tz)Au(CN)_2)_2]\cdot(OX)$ (**TzAu·OX**), $[Fe(Tz)Au(CN)_2)_2]\cdot(PX)$ (**TzAu·PX**), and $[Fe(Tz)Au(CN)_2)_2]\cdot(MX)$ (**TzAu·MX**), which were generated using a solvent exchange method from as-synthesised **TzAu·EtOH**. The structural properties of each framework were studied in detail to understand their host–guest interactions, and SCO behaviours were examined to demonstrate their sensitivity towards xylene isomers.

The bulk polycrystalline powders were synthesised from a binary mixture of xylenes in various ratios to investigate the mixed solvent adsorption effect. The structural and magnetic properties of the frameworks were examined to determine the sensitivity of the materials to different xylene ratios. The adsorption behaviours in binary mixtures of isomers were also analysed.

3.2 Structural Characterisation of TzAu·Guest (Guest = OX, PX, MX)

3.2.1 Single Crystal Structure of **TzAu·OX**

The synthesis of the Tz ligand is described in Chapter 2 Section 2.2.1. X-ray quality single crystals of **TzAu·EtOH** were synthesised using a vial-in-vial slow diffusion technique, as outlined in Chapter 2 Section 2.2.4, and guest exchange (Chapter 2 Section 2.2.7) was performed to synthesise **TzAu·OX** from the as-made **TzAu·EtOH**. A single-crystal-to-single-crystal transformation proceeded *via* removal of the crystallisation mother liquor followed by soaking the framework in neat OX solvent to yield **TzAu·OX**. Variable temperature single crystal X-ray diffraction data were then collected on **TzAu·OX** using in-house diffractometer with a Cu-K_α (λ = 1.54184 Å) radiation.

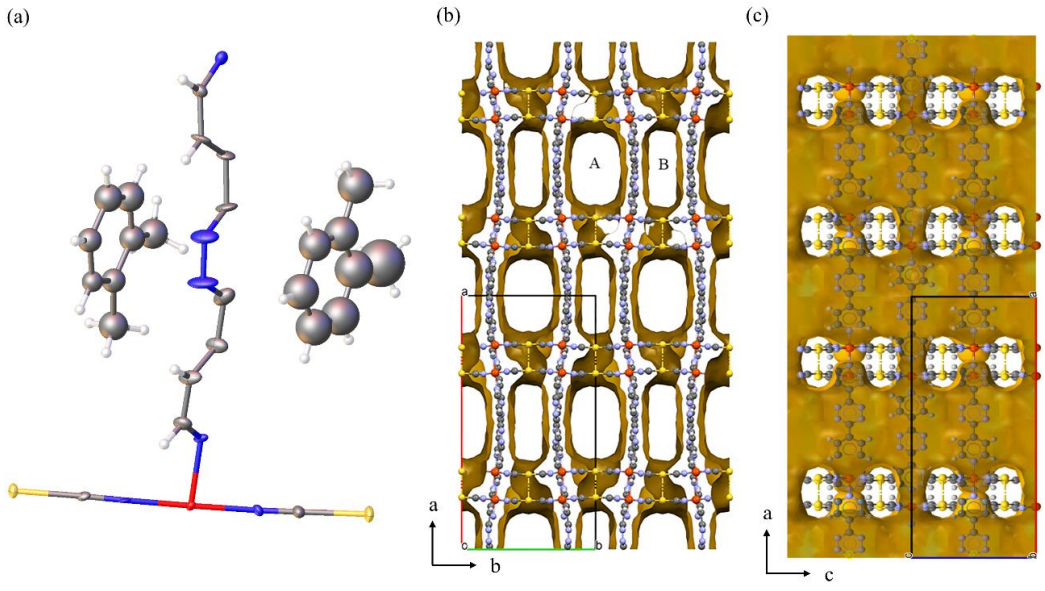

Figure 3.1: Single crystal structure of **TzAu·OX** at 100 K: (a) asymmetric unit with thermal ellipsoids set

at 50% probability. (b) The calculated pore structure as shown projected along the *c*-axis showing the A and B pores, with yellow and brown representing the outside and inside regions, respectively. (c) View down the *b*-axis. Atom colours: Fe (red), Au (yellow), N (blue), C (grey), H (white).

The network structure of **TzAu·OX** is isotopological of the as-synthesised **TzAu·EtOH** parent framework.[21] The Fe(II) nodes adopt an octahedral coordination geometry with the equatorial positions occupied by four $[Au(CN)_2]^-$ linkers on the *bc* plane forming as Hofmann layers and two *N*-donor Tz ligands in the axial positions (Figure 3.1). Aurophilic interactions link two independent single networks within the *bc* plane such that the overall structure is two-fold interpenetrated. The two nets are approximately orthogonally overlayed (with considerable 'wine-rack' shape) as viewed down the *a*-axis. The framework adopts an orthorhombic crystal system and was assigned to the centrosymmetric space group *Ibam*. At 100 K, the average Fe–N distance (<*d*(Fe–N)>) is 1.95 Å, indicating an LS Fe(II) configuration. The octahedral distortion parameter Σ(Fe) for **TzAu·OX**, which assigns the distortion of FeN_6 octahedra by summing the absolute deviation of the twelve *cis* N–Fe–N angles,[22-23] is 14.9° at 100 K.

Instead of there being a straight Tz ligand with two coplanar pyridyl rings in the parent **TzAu·EtOH** framework, the Tz ligands in **TzAu·OX** are bent (pyridyl nitrogen···diazine ring centroid··· pyridyl nitrogen) at an angle of 14.4° at 100 K due to larger guest molecules within the pores (Figure 3.2). Other Hofmann-type MOFs that have been reported have also noted such an effect after the inclusion of large guest molecules.[24] There is an undulation in the Hofmann plane (defined as the plane formed by four nitrogen atoms from the equatorially coordinated dicyanidoaurate ligands) that correspond to the bent ligand, leading to the gold atoms sitting out of the plane with Au1 to the plane at 0.30 Å and Au2 at 0.14 Å, respectively. The undulation of the Hofmann layers can also be depicted by a tilted angle (5.6°) between the Hofmann plane and the Fe(II) plane (the plane consists of four neighbouring Fe atoms, $[Fe_4(Au(CN)_2)_4]$). The tilted angles between the two planes are associated with the bent ligand.

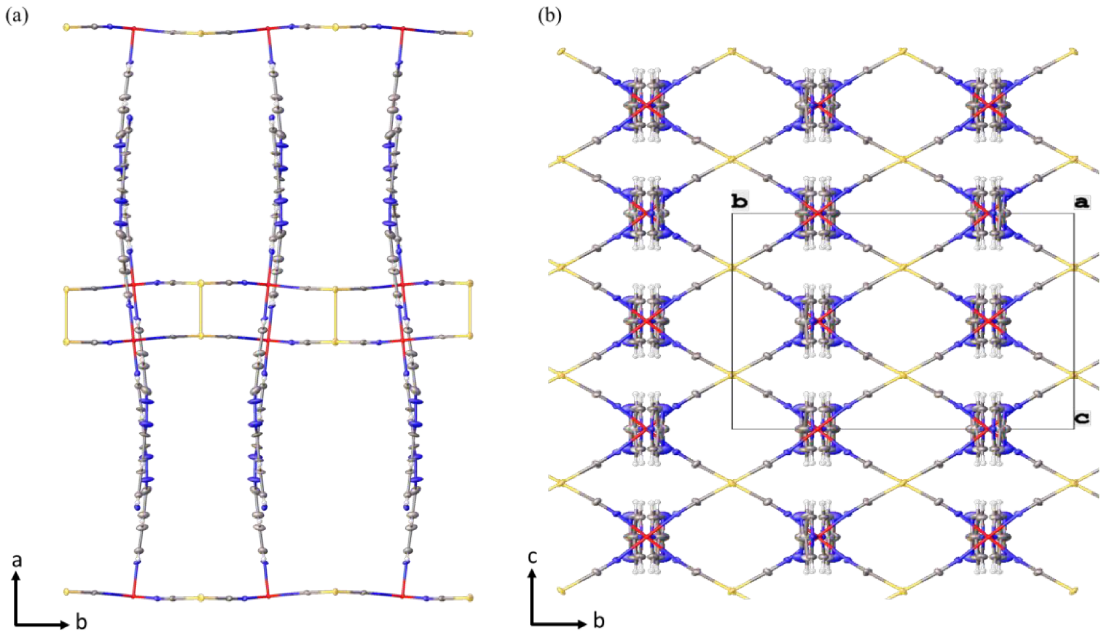

Figure 3.2: Single crystal X-ray structure of **TzAu·OX** at 100 K: (a) Perspective view down the *c*-axis showing the solvent-accessible channel, and (b) as viewed down the *a*-axis. The OX guest molecules have been omitted for clarity. Atom colours: Fe (red), Au (yellow), N (blue), C (grey), H (white).

When the larger sized OX guest molecules replace ethanol within the pores, the configuration of the pores changes such that two new pore environments form. The pores within the frameworks are two-dimensional and connect vertically and horizontally. The size of the large pore (A) is 8.3 × 5.9 Å, while the narrow pore (B) is 9.0 × 3.3 Å. There are 1.5 guest molecules in each formula unit. The material presents two-dimensional channels. A small channel was observed between the two closer Hofmann layers with aurophilic interactions, but no solvent was observed as the diameter is considerably smaller. The distance between guest molecules and the tetrazine rings in both pores are 3.36 Å (narrow pore) and 3.16 Å (large pore) at 100 K respectively, which indicates host–guest π···π stacking interactions.[25] The SQUEEZE function in PLATON was used[26] to estimate the total number of guest molecules within the pores, the end result being 1.5 OX molecules per formula unit. A solvent mask was calculated, and 670 electrons were found in a volume of 2662 $Å^3$ in one void per unit cell. This is consistent with the presence of 1.5[C_8H_{10}] per formula unit. The cell volume of the **TzAu·OX** is 5923 $Å^3$ with a void volume of 2671 $Å^3$, which corresponds to a 45% solvent accessible void. TGA data showing guest desorption was in good agreement with the SCXRD data (Figure A.1).

Crystallographic data for **TzAu·OX** were collected at 300 K. The average Fe–N distance is 2.16 Å at that temperature, which indicates HS states. This increase is also manifested in a volume expansion of the large pores and small pores by 8% and 26%, respectively. The Fe(II) octahedral distortion

parameter of 13.5° at this temperature is lower than in the LS state. This is unexpected given that opposite changes are generally observed where there is a more rigid octahedral geometry in the LS state. However, this converse behaviour has been noticed in **TzAu·EtOH** and other SCO materials.[21, 27] This is possibly attributed to the interplay between SCO and mechanical motion and/or distortion of the local Fe(II) sites. The volume of **TzAu·OX** increases in the HS state that facilitates octahedral tilting and lessening the torsions to an optimised geometry. For example, the Au···Au interaction distance lengthens in the HS state and the torsion angle for C1–Au1–Au2–C2 increases. The higher temperature promotes thermal motion of guest molecules in the expanded pores, which lengthens the available number of aromatic stacking interactions. These are 3.49 and 3.36 Å in the narrow and large pore environments, respectively. The increased total cell volume, especially due to the *a*-axis lengthening, releases the compression on the Tz ligands results in a reduced ligand bend of 13.8°. Moreover, the distances between the gold atoms and a Hofmann layer are increased to 0.39 Å (Au1) and 0.15 Å (Au2). The Hofmann layer is more distorted with the tilted angle between the Hofmann plane and Fe(II) plane being 6.1°.

Table 3.2: Comparison of selected structural parameters for **TzAu·OX** in the HS and LS states.

Parameter	**TzAu·OX** (100 K)	**TzAu·OX** (300 K)
<*d*(Fe–N)> / Å	1.95	2.16
Σ(Fe) / °	14.9	13.5
Au···Au / Å	3.0710(4)	3.1802(6)
Average Fe–N1(2)–C1(2) / °	172	165
Torsion angle C1–Au1–Au2–C2 / °	112.70	119.41
θ / °	76.09	71.81

A Hofmann layer formed with $[Fe(Au(CN)_2)_2]$ units in **TzAu·OX** present a rhombic 'wine-rack' shape by viewed down the *a*-axis (Figure 3.3). Each layers are superimposed, which is attributed to the perpendicular Au···Au interactions linking the layers. The acute compression angle (*θ*) is defined as the Au···Fe···Au angle within the *ab*-plane, which is used to describe the extent of Hofmann layer distortion. The layer is in the low energy mode when the angle approaches 90°. A scissor motion was observed in the **TzAu·OX** Hofmann layer similar to **TzAu·EtOH**. In the lattice motion behaviour for **TzAu·OX**, *θ* changes from 71.8° to 76.1° concurrently with the compression of the *b*-axis by 6% (16.8767(7) to 15.8630(6) Å). There is also an expansion of the *c*-axis by 2% (12.2366(6) to 12.4305(5) Å) upon cooling from 300 to 100 K. Despite the decreasing Fe−N bond lengths in the *bc* plane in the LS state, NTE was noticed in the *c* parameter. This was attributed to more linear coordination between the Fe(II) centre and the cyanide linkers that results in the change of *θ* displaying the scissor motion.

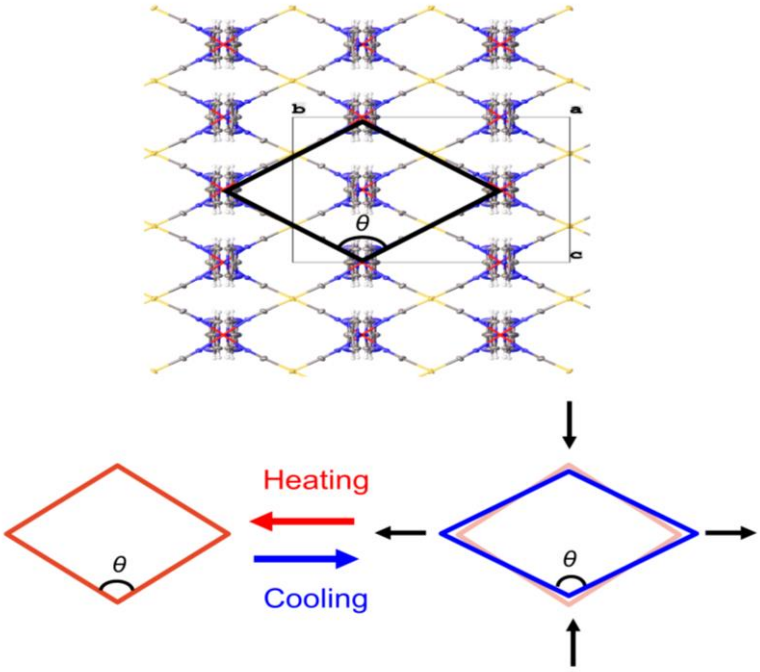

Figure 3.3: Schematic of the scissor motion for **TzAu·OX** with changing temperature. Hofmann layers adopt a rhombic shape as seen down the *a*-axis. θ decreases upon heating with the expansion of the *b*-axis and subsequent compression of the *c*-axis.

3.2.2 Powder X-Ray Diffraction of **TzAu·OX**

The bulk powder material **TzAu·OX** was made using a fast-mixing method to synthesise the **TzAu·EtOH** framework followed by a guest-exchange process (*cf.* Chapter 2 Section 2.2.4 and Chapter 2 Section 2.2.7). PXRD experiments were performed to examine whether the bulk polycrystalline powder pattern was consistent with the simulated pattern from the single crystal X-ray structure. A bulk powder sample was loaded as a suspension in a glass capillary, which was flame-sealed to avoid solvent loss. Data were collected at the Australian Synchrotron on the PD beamline (λ = 0.5907 Å) at ambient temperature. A powder pattern was fit using a Pawley refinement in GSAS-II[28] to extract lattice parameters of *a* = 30.81 Å, *b* = 16.82 Å, and *c* = 12.34 Å, which are in good agreement with the SCXRD data (Figure 3.4(b)). VT-PXRD experiments were also performed using a STOE STADI P diffractometer operating with Mo-K_α radiation (λ = 0.71073 Å) between the temperature range 300–100–300 K. A contour plot of the powder patterns as a function of temperature was made with two peaks as an example (Figure 3.4(a)). The two peaks, which correspond to the *hkl* = 002 and *hkl* = 222 reflections, shift remarkably to higher 2θ angles upon cooling to 220 K due to a single step SCO event. These two peaks shift back to lower 2θ angles at 240 K, which also matches the SCO transition.

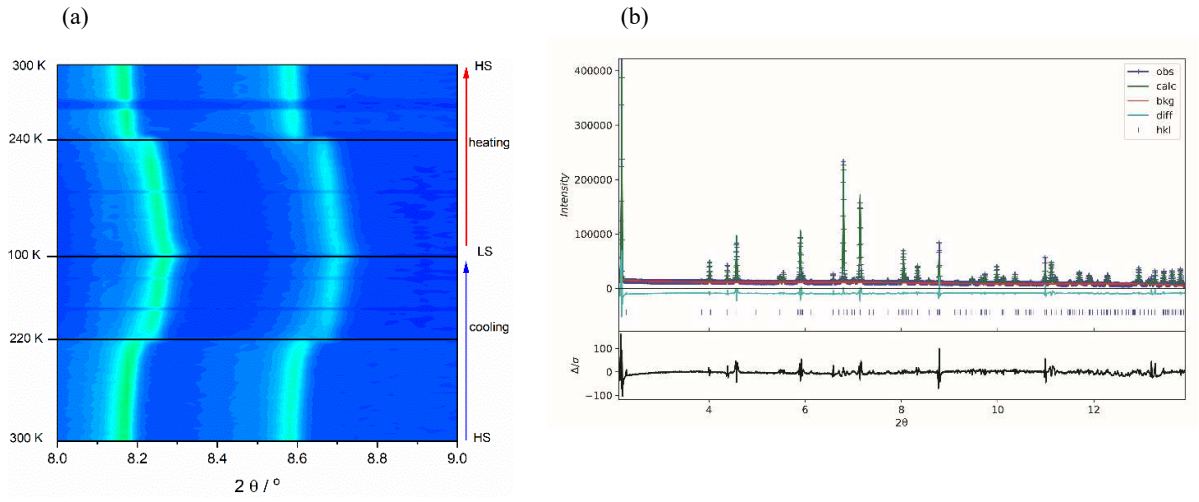

Figure 3.4: (a) VT-PXRD peak evolution of **TzAu·OX** in the 8.0–9.0° 2θ range over the temperature range 300–100–300 K. (b) Pawley refinement of the synchrotron PXRD data measured at room temperature. Experimental pattern (blue), calculated fit (green), background (red), the difference (cyan), and *hkl* positions (vertical bars).

3.2.3 Single Crystal Structure of **TzAu·PX**

Single crystals of **TzAu·PX** were generated using the same solvent exchange method as reported for **TzAu·OX**. X-ray data were collected at 100 K (in the LS state) and 310 K (in the HS state). The average Fe–N bond lengths are 1.93 Å (at 100 K) and 2.15 Å (at 300 K), indicating the material is in its LS and HS states, respectively, at these temperatures. The framework structure also possesses a Hofmann-like topology similar to **TzAu·OX** and was similarly solved in the centrosymmetric orthorhombic space group *Ibam* (Figure 3.5) but with a marginally smaller cell volume at the same temperature. Two different-sized pore environments were observed in **TzAu·PX**, which form large (8.2 × 5.9 Å) and narrow pores (8.9 × 3.4 Å) at 100 K. At 310 K, there is a slight expansion in both the large (9.1 × 4.3 Å) and narrow pore (8.6 × 6.0 Å) environments due to thermal expansion. The asymmetric unit has two partially occupied solvent molecules with both quarter-occupied. One PX molecule per formula unit was found in the refinement model. A solvent mask in OLEX2[29] was applied and 386 electrons were calculated in a volume of 2710 Å^3 in one void per unit cell, giving 0.8 PX molecules per formula unit. The small difference in the number of guest molecules is acceptable, especially since the guest molecules could only be modelled with fractional site occupancy factors.[30] Elevated thermal motion of the guest molecules is enhanced at higher temperatures (310 K) such that the guest positions could not be modelled. Nevertheless, to eliminate the solvent molecule contribution to the material, a solvent mask was applied to the structure, which showed a total solvent-accessible void space of 3016 Å^3 and 1.375 PX molecules per unit cell. More guests could be found with larger total void space. A TGA measurement was conducted, which showed one PX per formula unit was desorbed, supporting

the refinement result (Figure A.3).

The Tz ligand is less bent (12.3°) than what was observed for **TzAu·OX** at 100 K (14.4°), which is likely due to fewer solvent molecules within the pores in addition to the smaller pore size. The ligand tilting and undulations of the Hofmann layers increase with decreasing temperature in **TzAu·PX**. The tilted angle between the Hofmann plane and the Fe(II) sites plane is smaller than **TzAu·OX**, which also prompts shorter distances between the gold atoms to the Hofmann plane. Thus, there is an interplay between the size and amount of pore-included solvent and the undulation of the Hofmann layer.

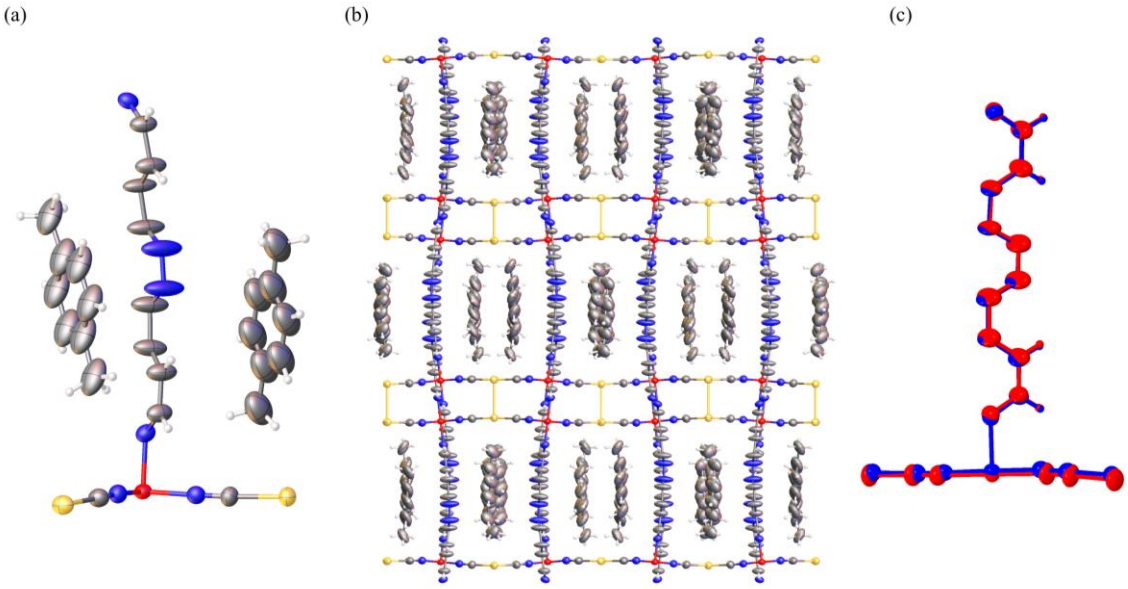

Figure 3.5: Single crystal X-ray structure of **TzAu·PX** shows the (a) asymmetric unit at 100 K, (b) the extended crystal structure as viewed along the *c*-axis, and (c) the overlay of asymmetric units at 100 K (blue) and 310 K (red). Thermal ellipsoids are shown at 50% probability. Atom colours: Fe (red), Au (yellow), N (blue), C (grey), H (white).

Table 3.3: Selected structural parameters for **TzAu·PX** in the HS and LS states.

Parameter	**TzAu·PX** (100 K)	**TzAu·PX** (310 K)
<d(Fe–N)> / Å	1.93	2.15
Σ(Fe) / °	17.00	13.40
Au···Au / Å	3.1602(11)	3.2629(8)
Average Fe–N1(2)–C1(2) / °	171	166
Tosion angle C1–Au1–Au2–C2 / °	114.74	122.12
θ / °	74.39	70.54

Octahedral distortion in the HS state is larger than in the LS state for **TzAu·PX**, which is similar to **TzAu·OX**. This is contrary to the expected values and is attributed to the interplay between the host–guest interactions, the extent of Hofmann layer distortions, and SCO behaviour that lead to additional lattice distortions. The angle of Fe–N–C in the Hofmann layers increases while the torsion angle of C1–Au1–Au2–C2 decreases in the LS state (Table 3.3). The change caused by SCO and distortion of the layers results in a scissor motion with the θ value increasing in the LS state, which shows NTE. Upon heating the distance between the gold atoms to the Hofmann planes increases and is associated with an increased angle between the Hofmann planes and Fe(II) planes in **TzAu·OX**. However, interestingly, in **TzAu·PX** the opposite behaviour is observed. That is, the distance between gold atoms and the Hofmann planes decreases, associated with a smaller angle between the Hofmann planes and Fe(II) planes. The different parameters of lattices, ligand distortion, octahedral geometry and extent of Hofmann layers undulation are noticed in **TzAu·OX** and **TzAu·PX** owing to different isomers uptake. Therefore, the investigation of structural properties of the frameworks with the absorption of isomers guests provides insight into the guest effect on framework materials.

3.2.4 Powder X-Ray Diffraction of **TzAu·PX**

The bulk powder sample of **TzAu·PX** was synthesised and characterised using the same method as for **TzAu·OX**. To obtain a set of unit cell dimensions and possible space group, synchrotron PXRD data were collected at the Australian Synchrotron (λ = 0.59074 Å). Powder patterns were fit using a Pawley refinement in GSAS-II[28] to extract lattice parameters and potential space group (*Ibam*), which were in good agreement with SCXRD data (Figure 3.7(b)). VT-PXRD was also conducted using a STOE STADI P diffractometer (Mo-K_α radiation, λ = 0.7107 Å) over the temperature range 310–100–310 K for three thermal cycles. A contour plot including multiple patterns of the first thermal cycle shows a different peak evolution compared to the second thermal cycle (Figure 3.6), while the third thermal cycle is the same as the second one (in Appendix A.4).

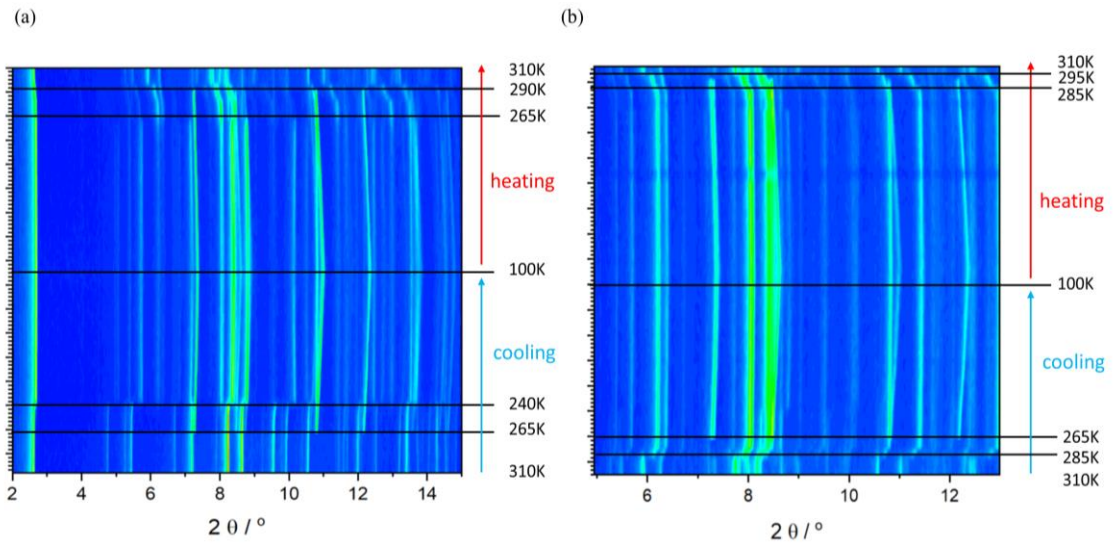

Figure 3.6: PXRD peak evolution of **TzAu·PX** as a function of temperature showing (a) the first thermal cycle and (b) the second thermal cycle.

In the cooling process of the first thermal cycle, there is some peak splitting behaviour at 265 K, and at this point the magnetic susceptibility measurement shows a sudden dip in the HS state (Section 3.3.3). When continually cooling to 240 K, several peaks (e.g., 2θ range in 5.4°–5.8° and 9.0°–10.5°) shift to a higher 2θ angle indicating a spin transition. Upon heating from 100 to 310 K, some peaks show a low angle shift between 265 and 290 K, indicating a three-step SCO behaviour. A detailed analysis of these SCO behaviours is referred to in Section 3.3.3. The first thermal cycle shows an asymmetric cooling and heating process with different step-wise and transition temperatures. The PXRD measurement at 310 K after the first thermal cycle shows the structural transition as the appearance of several new peaks after cycling compared with the original pattern at 310 K. The simulated PXRD pattern from the single crystal data measured at 100 K agrees with the PXRD pattern at the same temperature. This indicates that the Pawley refinement data performed on the 100 K dataset is likely correct for the orthorhombic phase (space group *Ibam*). Thus, the structural transition is predicted to occur upon heating. To examine the phase after the first thermal cycle measured at 310 K, the PXRD pattern of **TzAu·PX** at 310 K was indexed by Conograph,[31] which suggested that the framework is likely to adopt a monoclinic *C*-centred lattice. The pattern was fitted using GSAS-II[28] to confirm and extract unit cell information (in Appendix A.5), which provided the potential centrosymmetric space group *C*2/*c*.

In the second thermal cycle, peak shifting was evident in the cooling process at 285 K, which is the first spin transition over the entire two-step SCO curve. Some peak intensities increase at 265 K where a spike was observed in the magnetic susceptibility data. This is likely due to the presence of

defects. There is no obvious peak shifting at *ca*. 238 K where the SCO transition occurs, which may be due to the small spin transition temperature range. In the heating process, some peaks (e.g., 2θ = 5.8°–6.5°) shift to a lower angle at 285 K and back to their original 2θ values at 295 K indicating reversibility of the spin transition. There is no structural transition in the second thermal cycle as the patterns collected at 310 K before and after the cycle are identical.

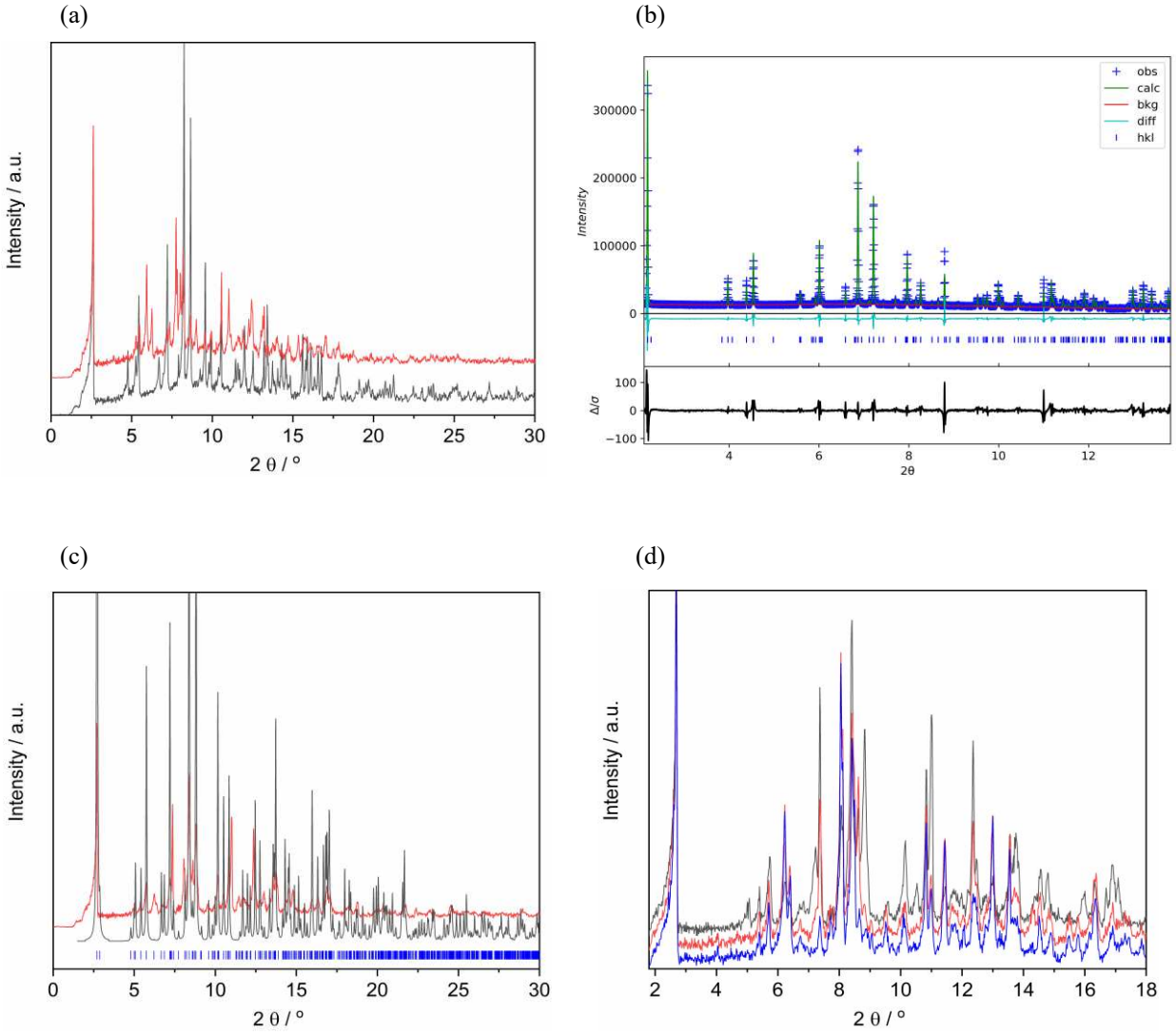

Figure 3.7: (a) PXRD pattern of **TzAu·PX** at 310 K showing the first thermal cycle (black) and the second thermal cycle (red). (b) Pawley refinement of the synchrotron PXRD data of **TzAu·PX** measured at room temperature. Experimental pattern (blue), calculated fit (green), background (red), the difference (cyan), and *hkl* (vertical bars). (c) PXRD pattern of **TzAu·PX** at 100 K. Experimental pattern (red), simulated pattern (black), and *hkl* indices (blue tick marks). (d) Experimental PXRD pattern of **TzAu·PX** at 100 K showing the first thermal cycle (black), second thermal cycle (red), and third thermal cycle (blue).

3.2.5 Powder X-Ray Diffraction Structure of **TzAu·MX**

Single crystals of **TzAu·MX** rapidly degraded after attempting a single-crystal-to-single-crystal transformation by guest exchange from ethanol to MX. Thus, the loss of crystallinity precluded characterisation of this framework by SCXRD. A powder sample of the same framework was synthesised using the same method as the previous guest exchanged samples. VT-PXRD experiments were conducted using a STOE STADI P diffractometer (Mo-K_α radiation) over a temperature range of 300–100–300 K. The bulk powder structure of **TzAu·MX** was determined from GSAS-II[28] and indicated a potential structure adopting the centrosymmetric orthorhombic space group *Cmmm*. A pattern was indexed and fitted using the Pawley refinement method (Figure 3.8(a)). The calculated and experimental patterns are well matched with the following determined unit cell information: a = 30.75 Å, b = 12.24 Å, and c = 8.44 Å. A contour plot of the PXRD patterns as a function of temperature is provided in Figure 3.8(b). The peak positions shift to larger 2θ values with a decrease of temperature in the 2θ range of 5.2°–5.8°, indicative of a HS to LS transition. The horizontal lines shown in Figure 3.8(b) indicate the spin transition temperatures. The first step of the SCO curve occurs at 245 K as the peaks shift to higher angles. The following spin transitions occur at 229, 215, 183 and 166 K. The framework adopts a LS configuration below 150 K and the relevant peaks shift back to their original 2θ values indicating the reversibility of each spin transition. Similar to the cooling process, the five-step SCO behaviour is recovered upon heating. However, the transition temperatures for each step of the heating process are different from the cooling process, thus indicating thermal hysteresis. The transition temperatures in the heating process are 184, 219, 231, 241 and 250 K. The SCO behaviour as observed from the PXRD measurements agrees well with the magnetic susceptibility data.

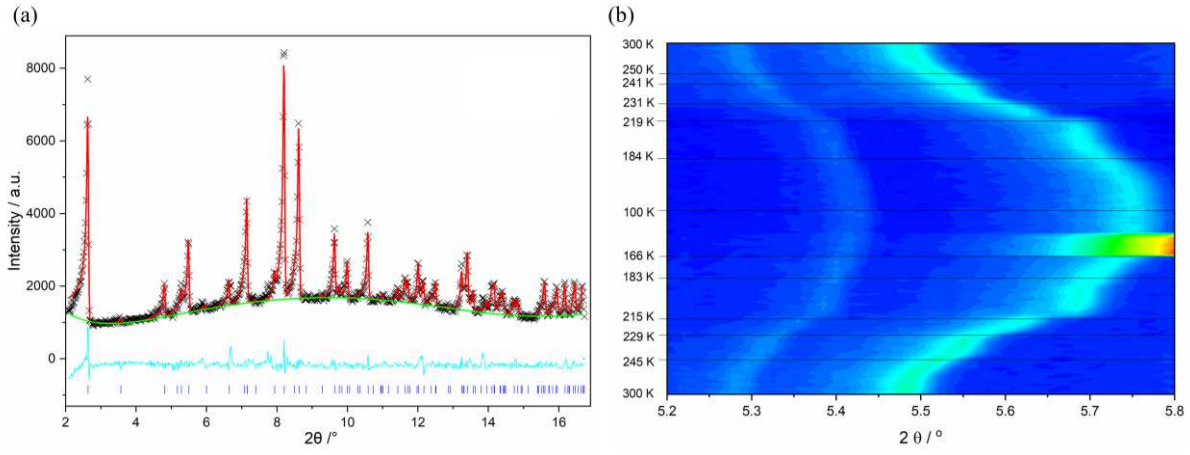

Figure 3.8: (a) Pawley refinement of a synchrotron PXRD pattern obtained for **TzAu·MX** at room temperature. Experimental pattern (blue), calculated fit (green), background (red), the difference (cyan), and *hkl* (vertical bars). (b) PXRD peak evolution of **TzAu·MX** as a function of temperature (300–100–300 K).

There are several relatively high-intensity peaks that suddenly appear and disappear with thermal cycling (Figure 3.9). Comparing them between two different batches of the **TzAu·MX**, they represent peaks at the same 2θ values. The peaks manifest at relatively low temperature ranges (166–148 K at 2θ = 5.8° and 148–231 K at 2θ = 6.2°) but appear and disappear at different temperatures. These peaks could arise from either frozen MX solvent, ice, or an amorphous component in the framework. In order to examine, which presumptions are more likely to result in these unusual peaks, PXRD data of pure MX solvent were collected at 100, 140, 180 and 200 K, but do not show any of the peaks to match with those circled in red in the **TzAu·MX** pattern of Figure 3.9. The simulated ice pattern was also compared with the **TzAu·MX** pattern. However, once again the peaks do not matched.[32] Therefore, these high-intensity peaks can be more justifiably linked to the freezing of amorphous components. Also, the amorphous components in the material maybe form two phases at different temperature ranges.

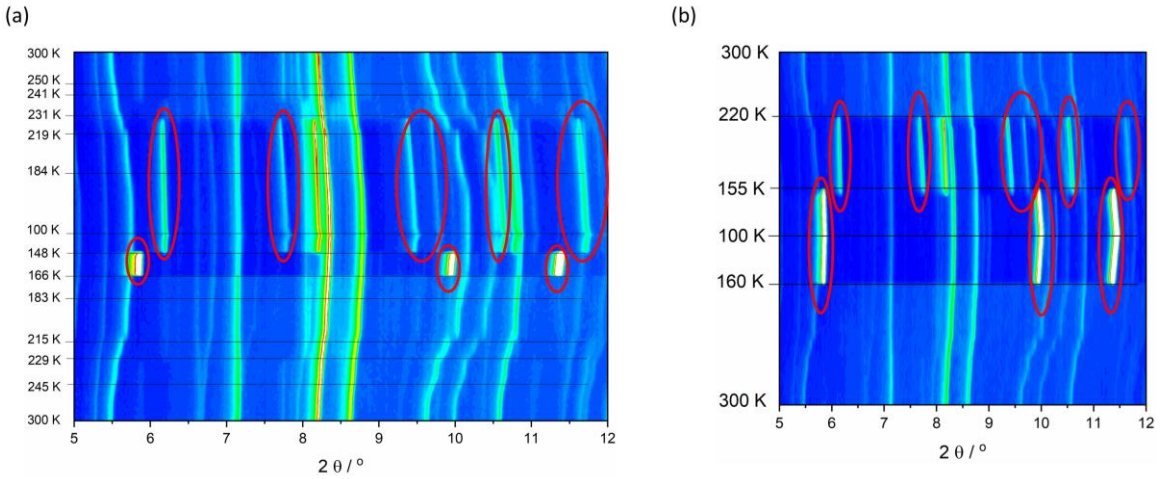

Figure 3.9: PXRD peak evolution of **TzAu·MX** as a function of temperature (300–100–300 K) of (a) batch one and (b) batch two. The peaks are likely from amorphous components in red.

3.3 Spin Crossover Behaviours of TzAu·Guest (Guest = OX, PX, MX)

3.3.1 Variable Temperature Magnetic Susceptibility of **TzAu·MX**

Variable temperature magnetic susceptibility measurements were performed on a bulk polycrystalline powder sample of **TzAu·MX** over a temperature range of 300–55–300 K. The measurement was carried out at a 2 K min^{-1} scan rate unless otherwise stated. The framework exhibits a rare case of asymmetric four/five-step SCO (Figure 3.10). There are only two examples of compounds that have been reported to show more than four-step SCO. One is in a discrete Fe(III) complex showing an asymmetric six/five-step SCO,[33] and another in an Fe(II) based Hofmann-like framework displaying seven/eight-step SCO.[34] **TzAu·MX** displays four hysteretic SCO loops excluding the first step.

TzAu·MX adopts its HS state at temperatures above 278 K. Upon cooling, the material undergoes the first spin transition at 245 K to reach a small plateau with a $\chi_M T$ value of 2.57 cm^3 K mol^{-1}. The second step occurs at 231 K, which is then followed by the third, fourth, and fifth steps at 215, 205 and 183 K, respectively. The framework reaches the complete LS state at 161 K where the $\chi_M T$ value then gradually decreases from 0.15 to 0.07 cm^3 K mol^{-1} by 55 K. At this temperature, the material adopts its completely LS state. An unusual spike feature in the $\chi_M T$ plot is observed at 184 K, which was also seen in the **TzAu·OX** and **TzAu·PX** frameworks. This phenomenon will be discussed in detail in the following section. The heating process reveals five-step SCO. Upon heating, the transition temperatures are 187, 219, 232, 241 and 255 K. That could possibly be due to the MX solvent motion within the pores causing the change of host–guest and guest-guest interactions.

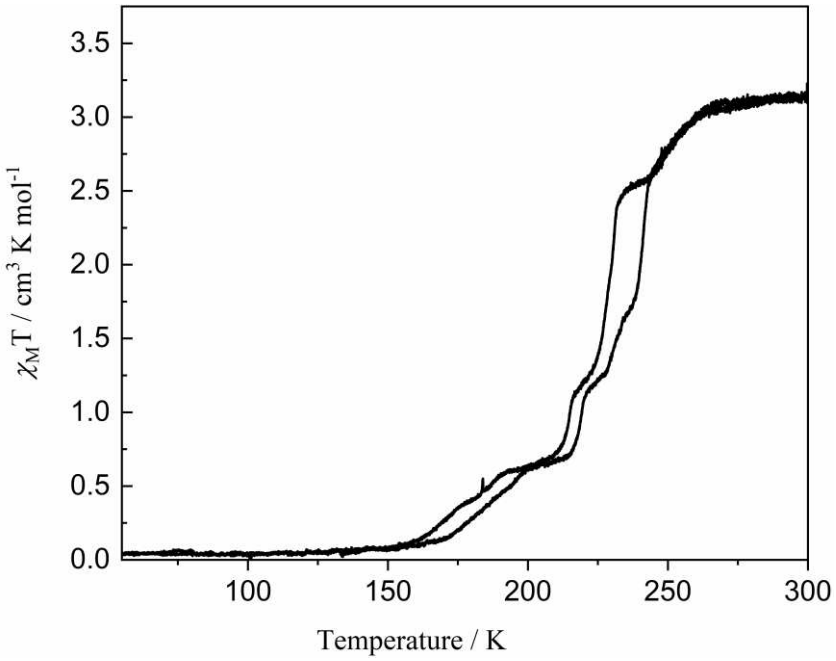

Figure 3.10: Variable temperature magnetic susceptibility plot of **TzAu·MX** measured at a scan rate of 2 K min^{-1}.

3.3.2 Variable Temperature Magnetic Susceptibility of **TzAu·OX**

The same method of sample synthesis and characterisation was carried out on **TzAu·OX** over the temperature range 300–110–300 K. The measurement reveals that the material undergoes complete SCO with thermal hysteresis (Figure 3.11). The $\chi_M T$ value of **TzAu·OX** is *ca.* 3.3 cm^3 K mol^{-1} at 300 K corresponding to a HS Fe(II) material. The $\chi_M T$ value decreases to *ca.* 0.09 cm^3 K mol^{-1} at 110 K and is indicative of an entirely LS material. The framework exhibits asymmetric SCO, with a spin transition centred at 217 K in the cooling process, and two-step SCO ($T_{½}\uparrow$ = 243 and 206 K) in the heating process.

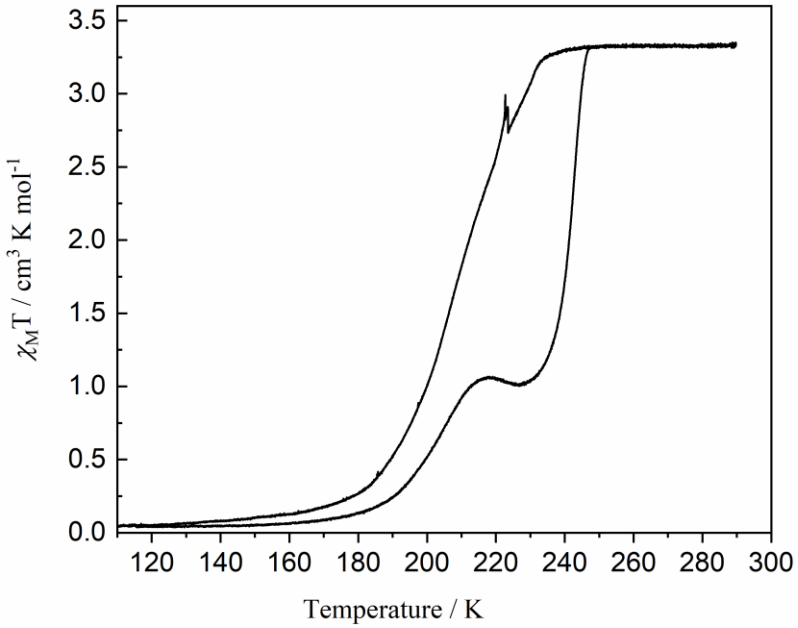

Figure 3.11: Variable temperature magnetic susceptibility plot of **TzAu·OX** measured at a scan rate of 2 K min^{-1}.

A sharp peak at 223 K with a $\chi_M T$ value rapidly increasing to 3.0 cm^3 K mol^{-1} is observed in the cooling process. The sudden increase of the $\chi_M T$ value suggests that the heat was generated within the framework causing the Fe(II) sites to almost transition back to the HS state. This effect is hypothesised to be caused by one of three different phenomena: (1) a structural phase transition occurring for **TzAu·OX** at that temperature; (2) thermal motion of OX guest molecules upon compression of the pores when cooling; (3) a liquid-to-solid phase transition OX guest molecule. VT-PXRD measurements were conducted but provided no evidence for a structural phase transition upon cooling, thus ruling out the first hypothesis (refer to Section 3.2.2).

To lend evidence to the second hypothesis, the SCO behaviour with suppressed OX motion was examined. The powdered sample was dispersed into a mixture of paratone oil and OX solvent, which acts to suppress solvent movement within the pores. The matrix effect is caused by glassy materials such as glycerol, nujol, and eicosane.[35] The viscoelasticity of such compounds affects the external pressure and interfacial interactions that can change the cooperativity and SCO behaviours.[36-37] Variable temperature magnetic susceptibility was performed on the sample mixed with paratone oil. The material displays more gradual and hysteretic SCO than without oil added (Figure 3.12). Moreover, the noticeably abrupt spike in the $\chi_M T$ value disappeared. The overall feature of the SCO behaviour is very similar to the material without oil added, which is one-step SCO ($T_{½}\downarrow$ = 205 K) in the cooling process and two-step SCO ($T_{½}\uparrow$ = 243 and 202 K) in the heating process. These different phenomena could be explained by the change in elastic interactions occurring between the framework, OX solvent molecules,

and oil. Thus, the results demonstrate the matrix effect from oil influencing the cooperativity and therefore affecting the SCO behaviours. They also prove that the spike feature is likely due to the movement of OX solvent.

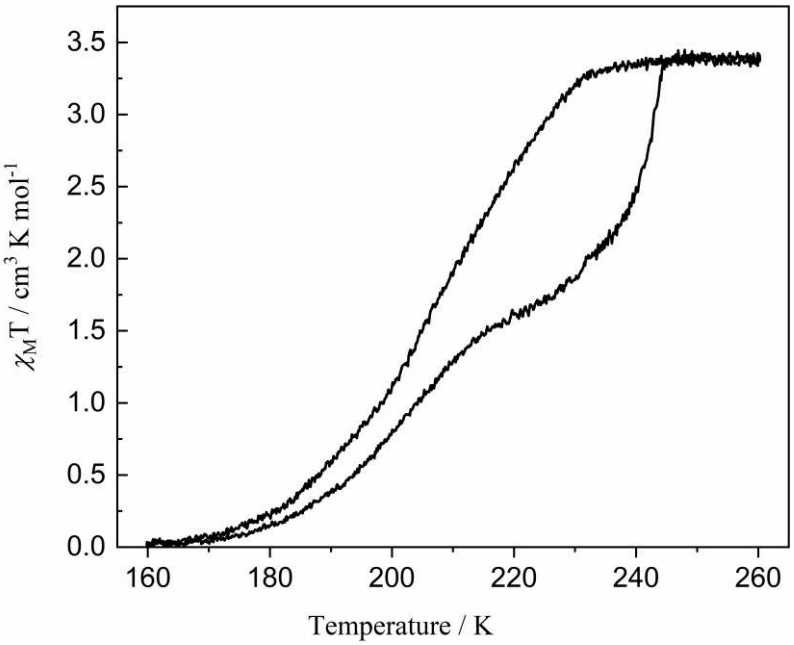

Figure 3.12: Variable temperature magnetic susceptibility plot of **TzAu·OX** mixed with paratone oil. Data were collected at 2 K min^{-1}.

In order to investigate the relationship between the OX phase (liquid or solid) within the pores, and the spike feature for the third hypothesis, magnetic susceptibility measurements were performed with a temperature sweep between 230 and 200 K where the spike should appear in the aforementioned data (Figure 3.13). The spike was seen upon cooling from 300 to 200 K as expected. However, the spike disappeared during the reverse temperature sweep back to 230 K; with continued cycling between 230 and 200 K, no spike was observed. This is likely because the solvent molecules were frozen and became settled in an optimised position in the pores such that no OX movement could occur within this short temperature range.

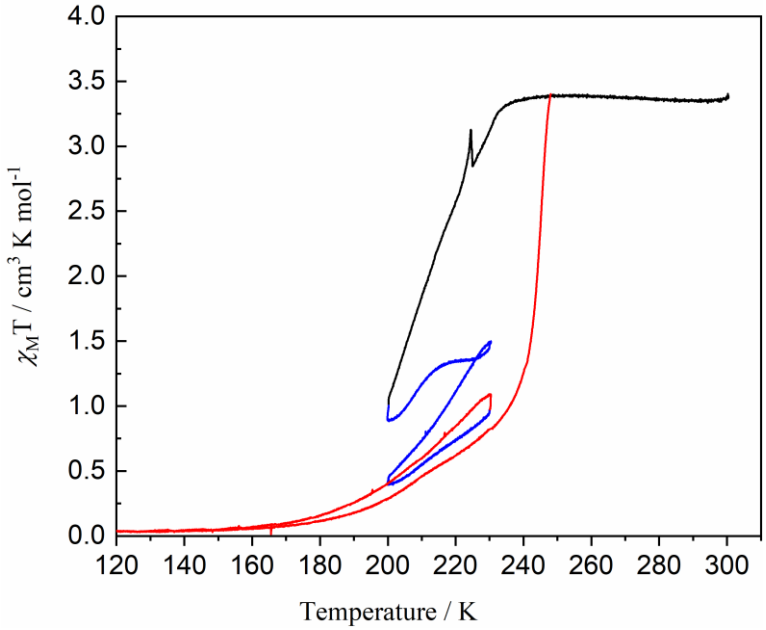

Figure 3.13: Variable temperature magnetic susceptibility plot of **TzAu·OX** between a temperature range of 300–200 K (black), 200–230–200–230 K (blue), and 230–120–300 K (red).

The magnetic susceptibility measurements performed on **TzAu·OX** were carried out at various scan rates (0.5, 1 and 4 K min^{-1}) to explore the kinetic effects (Figure 3.14). The SCO transition temperature decreases with an increasing scan rate in the cooling process, which is attributed to temperature lag. The SCO curves in the heating process display slightly lower transition temperatures with higher scan rates. The scan rate effect on transition temperatures has been noticed[38-39] and SCO behaviour of **TzAu·OX** displays a similar trend of transition temperatures due to varying scan rates. The framework reaches its LS state at a scan rate of 0.5 K min^{-1}. With increased scan rate, the $\chi_M T$ values increase in the low temperature region, resulting in an incomplete LS state due to kinetic trapping of some Fe(II) sites in the HS state. However, unusual loops are noticed at a slower scan rate (0.5 and 1 K min^{-1}) with decreasing $\chi_M T$ values at *ca.* 230 K, which are related to relaxation of the HS sites to the corresponding LS state. This effect of relaxation upon heating has been observed in other SCO materials.[40-42] The $\chi_M T$ spikes observed previously are also seen in each scan rate dataset and even in the slowest scan rate (0.5 K min^{-1}).

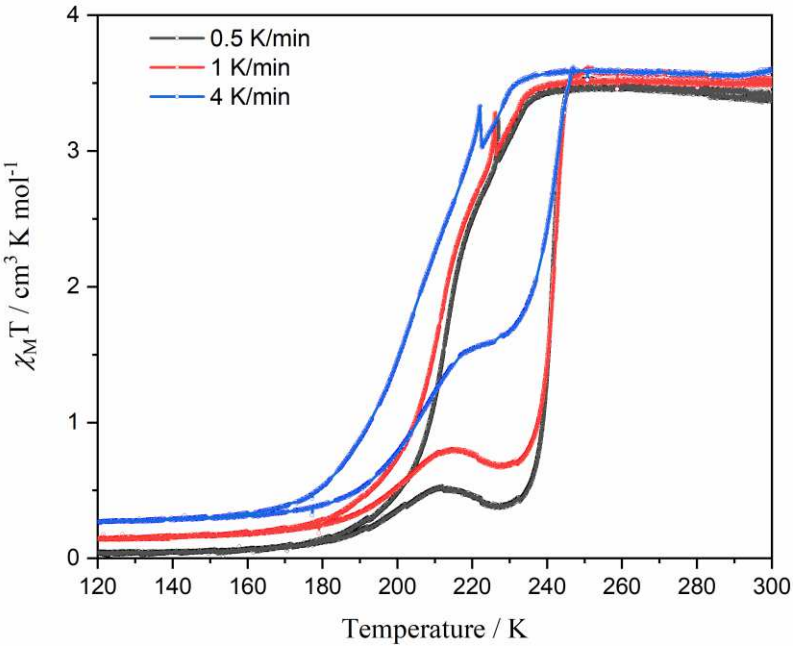

Figure 3.14: Variable temperature magnetic susceptibility plots of **TzAu·OX** recorded at scan rates of 0.5 (black), 1 (red) and 2 K min^{-1} (blue).

3.3.3 Variable Temperature Magnetic Susceptibility of **TzAu·PX**

Variable temperature magnetic susceptibility measurements were carried out on a bulk powder sample of **TzAu·PX** (Figure 3.15). The material adopts an entirely HS configuration above 250 K with a $\chi_M T$ value of 3.3 cm^3 K mol^{-1}. The $\chi_M T$ value gradually decreases in the cooling process, signalling a reduction of the HS component. There is a small decrease of the $\chi_M T$ value at 275 K during the cooling process of the first thermal cycle, which is likely due to a phase transition similar to that observed from the VT-PXRD data. In the first thermal cycle, the framework undergoes an abrupt and one-step spin transition centred at 235 K, which is a lower temperature than observed from the VT-PXRD measurements. The difference in transition temperatures between the magnetic susceptibility and VT-PXRD data is likely due to different temperature ramp rates as the former was recorded continuously at 2 K min^{-1}, while the latter is slower due to longer collection times being required to achieve satisfactory quality patterns for each temperature point. When cooling to 220 K, a $\chi_M T$ value of 0.5 cm^3 K mol^{-1} indicates that **TzAu·PX** adopts the LS state. The $\chi_M T$ value does not reach zero suggesting a small amount of residual paramagnetic components in the LS state at low temperatures. This phenomenon is commonly observed in some SCO systems and is attributed to potential surface and lattice defects as well as residual paramagnetic impurities in the sample.[43] It should be noted that the framework displays asymmetric SCO behaviour with three step-wise spin transitions in the heating process. The SCO transition temperatures upon heating are 258, 284 and 297 K. The asymmetric SCO

behaviour is possibly due to the PX solvent influencing the extent of host–guest interactions and a subsequent distortion of the framework.

A continuous second thermal cycle was conducted on **TzAu·PX**. **TzAu·PX** remains in its HS state above 285 K. Two steps of SCO were observed upon cooling, one of which was an abrupt spin transition centred at 280 K, and the second being a gradual spin transition centred at 237 K. There is a wide plateau region (265–239 K) in between the first and second steps where the framework contains approximately 11% HS Fe(II) sites. The sample reaches the LS state at *ca*. 230 K. The heating process shows three-step SCO with the transition temperatures 262, 284 and 297 K. The third thermal cycle shows the same behaviour as the second one (Appendix A.7). Upon heating to 298 K, the framework converts back to the HS state. In the HS state, the $\chi_M T$ value of the heating process is slightly higher than the cooling process, which is likely due to sample holder movement occurring within the instrument.

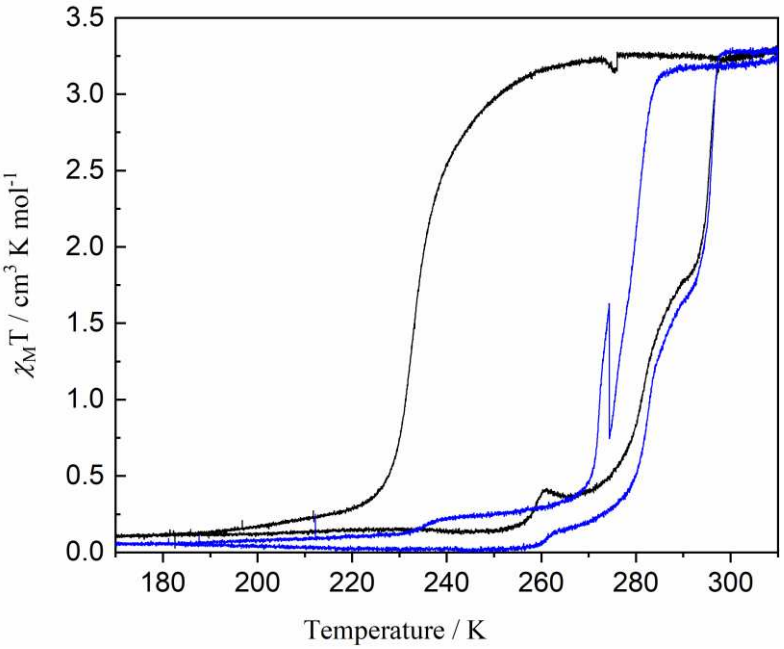

Figure 3.15: Variable temperature magnetic susceptibility plots of **TzAu·PX** recorded at 2 K min^{-1} and showing the first thermal cycle (black) and second thermal cycle (blue).

The spike in the $\chi_M T$ value is observed in **TzAu·PX** similar to **TzAu·OX**. Variable temperature magnetic susceptibility measurements were conducted with a temperature sweep between 275 and 265 K to examine whether the spike is related to the PX solvent (Figure 3.16). The spike was seen upon cooling from 310 to 265 K as expected. However, during the reverse temperature scan to 275 K, no spike in the $\chi_M T$ value was observed. To confirm the reproducibility of this behaviour, continued cycling measurements were collected in the short range 275–265 K. The phenomenon is similar to that observed

for **TzAu·OX**, which is likely due to solvent molecule immobilisation in an optimised position in the pores at 265 K. With a small range of the temperature change, there is no change of OX guest molecules within the pores that could affect the magnetic susceptibility response of the material. Therefore, the sudden increase of the $\chi_M T$ value could be related to the solvent motion and subsequent phase change.

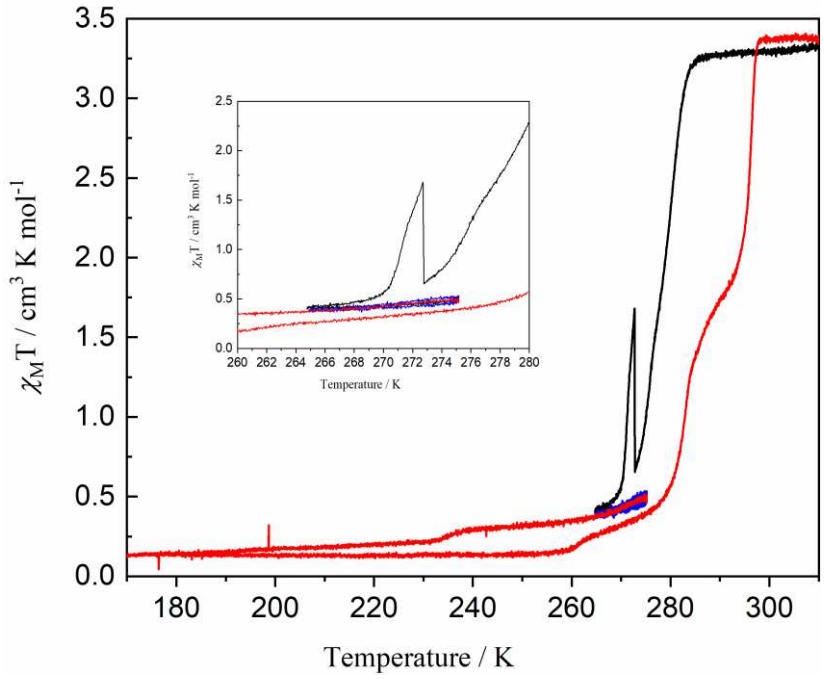

Figure 3.16: Variable temperature magnetic susceptibility plots of **TzAu·PX** with temperature scanning between 300–200 K (black), 200–230–200–230 K (blue), and 230–120–300 K (red).

To study the effect of scan rate, variable temperature magnetic susceptibility measurements of **TzAu·PX** were conducted at different scan rates at 1, 2 and, 4 K min^{-1} (Figure 3.17). An increased hysteresis width is predictably observed at faster scan rates. The data collected for the fastest scan rate (4 K min^{-1}) produces the smallest $T_{½}$↓ (278 and 235 K) and largest $T_{½}$↑ (264, 286 and 300 K) values. The clearest difference in the transition temperature depending on scan rate is observed in the first step of the cooling process and the first and second steps in the heating process. The slightly lower $\chi_M T$ value for the 2 K min^{-1} dataset is likely caused by sample holder movement occurring during the experiment.

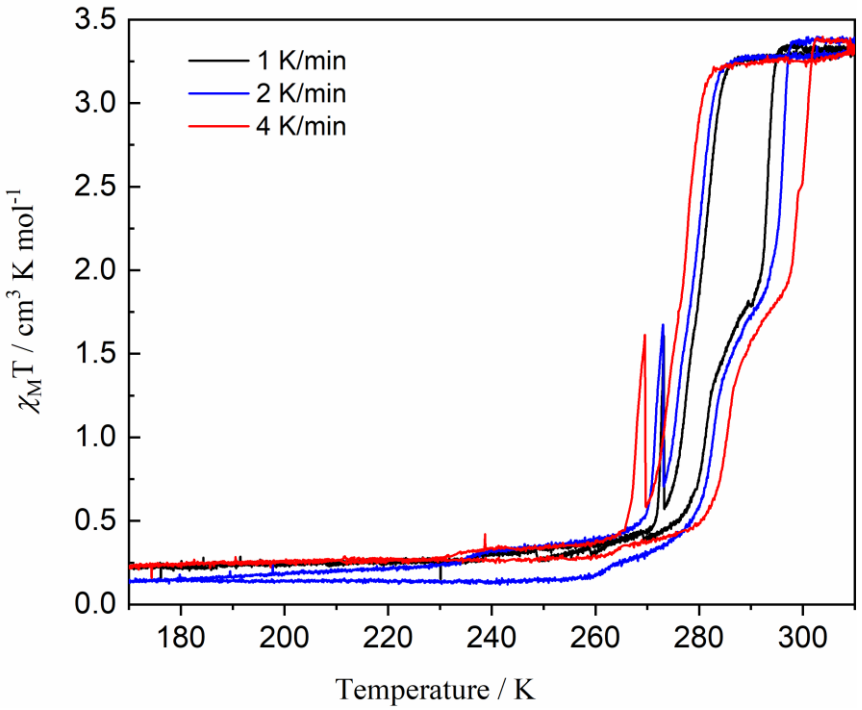

Figure 3.17: Variable temperature magnetic susceptibility plots of **TzAu·PX** recorded at scan rates of 1 (black), 2 (blue) and 4 K min^{-1} (red).

3.3.4 Raman Spectroscopy

Raman spectroscopy measurements were conducted at room temperature on **TzAu·PX**, **TzAu·OX**, and **TzAu·MX** to provide additional insight into the nature of host–guest interactions (Figure 3.18). The assignment of the cyanide (C≡N) stretching band was carried out, which appears at *ca.* 2200 cm^{-1}.[44-47] **TzAu·MX** displays the smallest Raman shift in its C≡N stretch ($\nu_{C\equiv N}$ = 2189 cm^{-1}), while the **TzAu·OX** and **TzAu·PX** frameworks have C≡N stretches at 2191 cm^{-1} and 2196 cm^{-1}, respectively. Spectral features in the region between 900 and 1600 cm^{-1} are attributed to pyridyl and aromatic ring stretching and bending vibrational modes.[44, 46] Multiple additional peaks are observed in **TzAu·MX** compared to the PX and OX analogues (e.g., peaks at 1000, 1249 and 1266 cm^{-1}). The bands below 600 cm^{-1} can be assigned as Fe–N vibrational modes.[46]

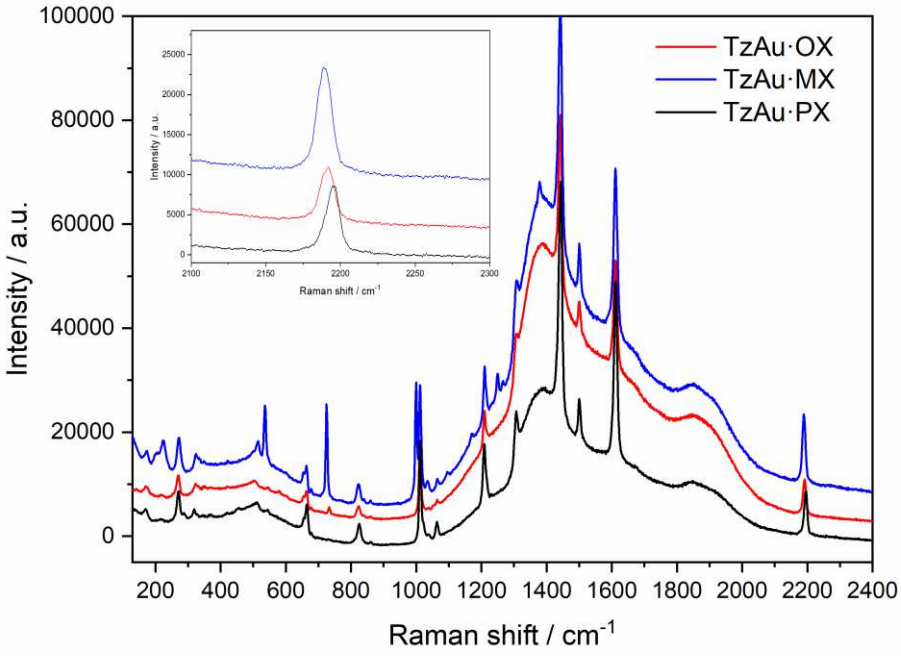

Figure 3.18: Raman spectra of **TzAu·PX**, **TzAu·OX**, and **TzAu·MX**. Inset: close up of the cyanide stretching region.

3.4 Binary Xylene Mixtures on TzAu

3.4.1 Powder X-ray Diffraction of TzAu Framework with Xylene Guest Mixtures

The bulk powder samples with binary xylene mixtures were generated as mentioned in Chapter 2 Section 2.2.7. The TzAu framework was exposed to equimolar binary mixtures of xylene isomers of PX/MX, PX/OX, and MX/OX to generate **TzAu·PM50**, **TzAu·PO50**, and **TzAu·MO50**), respectively. PXRD measurements were carried out at the Australian Synchrotron at room temperature on the PD beamline (λ = 0.59074 Å).

A comparison of TzAu with a single component of MX, PX, and binary PX/MX is shown in Figure 3.19. There are peaks at 2θ = 4.9° and 6.4° in **TzAu·MX**, but no peak in **TzAu·PM50**. This suggests that the peaks of **TzAu·PM50** are not the sum of both **TzAu·PX** and **TzAu·MX**, further indicating that **TzAu·PM50** formed a homogenous single phase material. There are additional peaks in **TzAu·PM50** that have the same peak positions as **TzAu·PX** (e.g., 2θ = 4.1° and 9.1°) rather than in **TzAu·MX**. This suggests that the structure of **TzAu·PM50** more closely resembles that of **TzAu·PX**, indicating that uptake of the PX solvent is likely predominant in the **TzAu·PM50** framework. Quantitative analysis of the binary solvent uptake results will be discussed in Section 3.4.3.

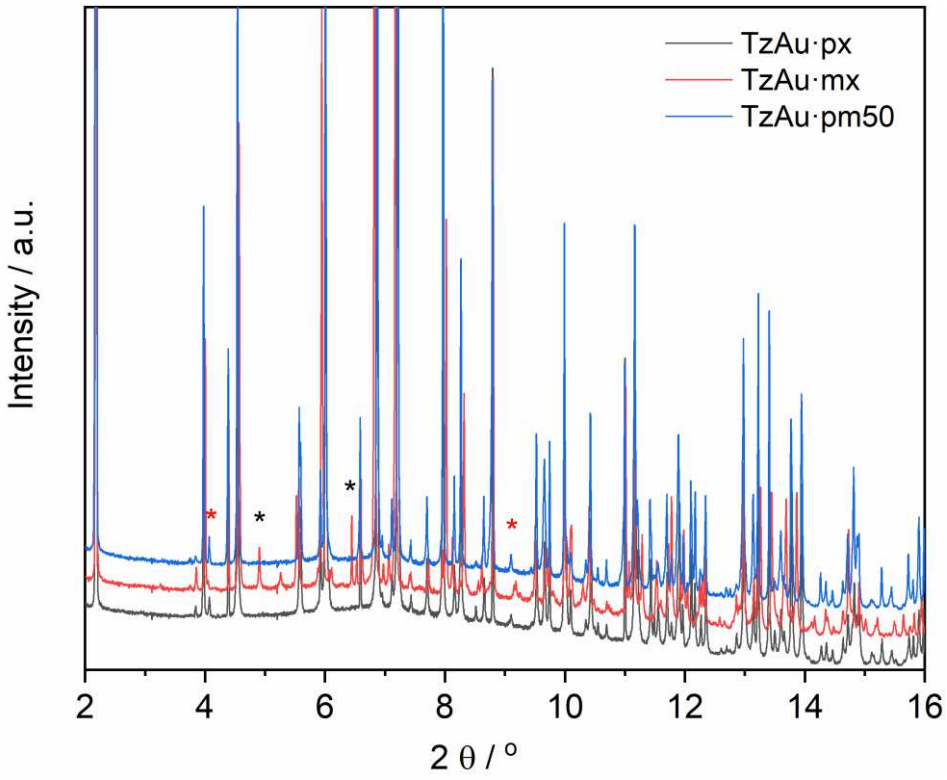

Figure 3.19: Synchrotron PXRD patterns of **TzAu·PX** (black), **TzAu·MX** (red), and TzAu·PM (blue) were collected at room temperature. The two examples of exclusive peaks belonging to **TzAu·MX** (2θ = 4.9° and 6.4°) are labelled with black asterisks. 2θ = 4.1° and 9.1° labelled with red asterisks show peaks from **TzAu·PX** and **TzAu·PM50** with the same position.

When comparing **TzAu·PX**, **TzAu·OX**, and **TzAu·PO50** in Figure 3.20, the PXRD patterns of **TzAu·PX** and **TzAu·OX** are distinctly similar because they adopt the same space group and similar lattice parameters. The PXRD pattern of **TzAu·PO50** is nearly identical to **TzAu·PX** given its similar peak positions (e.g., 2θ = 8.1, 8.3, 8.5 and 8.6°), while peaks belonging to **TzAu·OX** appear in different 2θ positions. This suggests that the unit cell information of **TzAu·PO50** is more akin to **TzAu·PX** than **TzAu·OX**. Thus, it is likely that the PX solvent is more predominant in the pores than OX.

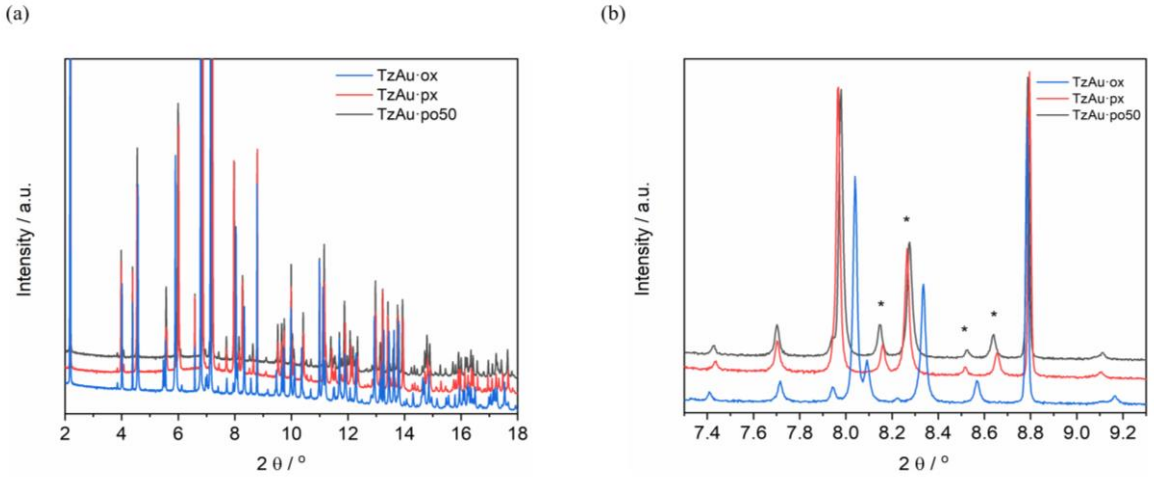

Figure 3.20: Synchrotron PXRD patterns of **TzAu·PO50** (black), **TzAu·PX** (red), and **TzAu·OX** (blue) were collected at room temperature with 2θ in the range of 2°–18°. (b) A close-up of the PXRD patterns (2θ = 7.3°–9.3°). The black asterisks show the peaks belonging to **TzAu·PO50** and **TzAu·PX**.

The PXRD patterns of **TzAu·MO50**, **TzAu·MX**, and **TzAu·OX** are compared in Figure 3.21. The peak centred at 2θ = 3.9° is present in both **TzAu·MX** and **TzAu·OX** but not in **TzAu·MO50**. There are also other peaks in either **TzAu·MX** or **TzAu·OX** that do not appear in **TzAu·MO50**. This suggests that a phase pure sample of **TzAu·MO50** has been formed. Two diffraction peaks (*hkl* = [020] and [400]) are shown in Figure 3.21(b). The three powdered frameworks all show a peak at *ca*. 4.0°, which corresponds to the *hkl* = [020] reflection. The peak positions from the three frameworks are marginally different with the smallest 2θ angle occurring in **TzAu·MO50** and the largest in in **TzAu·OX**. This indicates that **TzAu·MO50** has the largest *b*-axis. Another reflection (*hkl* = [400]) also has the smallest 2θ angle in **TzAu·MO50**, which suggests that **TzAu·MO50** has the largest *a*-axis.

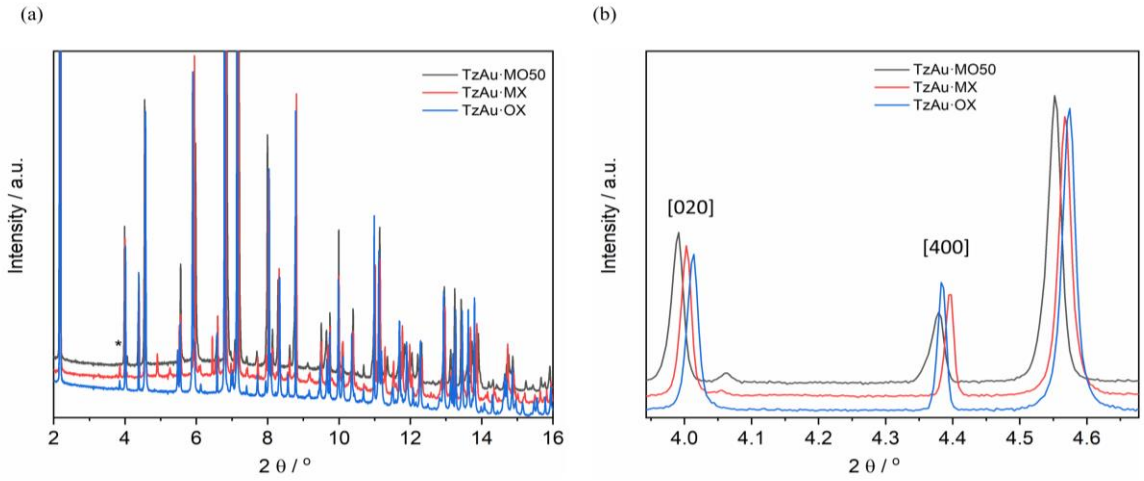

Figure 3.21: Synchrotron PXRD patterns of **TzAu·MO50** (black), **TzAu·MX** (red), and **TzAu·OX** (blue)

were collected at room temperature: (a) 2θ = 3.9° is labelled with an asterisk with a 2θ range of 2°–16°. (b) A close-up of the PXRD patterns (2θ = 3.9°–4.7°) with *hkl* values shown in square brackets.

The frameworks with a mass ratio of PX/OX = 7:3 (**TzAu·PO73**), PX/OX = 5:5 (**TzAu·PO50**), and PX/OX = 3:7 (**TzAu·PO37**) were generated to examine any potential structural changes with a different component of the PX and OX mixtures in the TzAu framework. The PXRD data of the TzAu framework were collected on a PANalytical X'Pert PRO MPD diffractometer outputting Cu-K_α radiation. The PXRD data of the following solvent mixtures were acquired on the same instrument and using the same settings. The PXRD patterns of the samples with different ratios of xylene mixtures contain the same peak distributions but with slight 2θ shifts in each of the peaks (Figure 3.22). Upon closer examination of the pattern differences in the 2θ range 14.2–15.0°, the peak of interest shifts to a smaller angle with increasing the ratio of the OX component, which indicates a small structural change in the lattices.

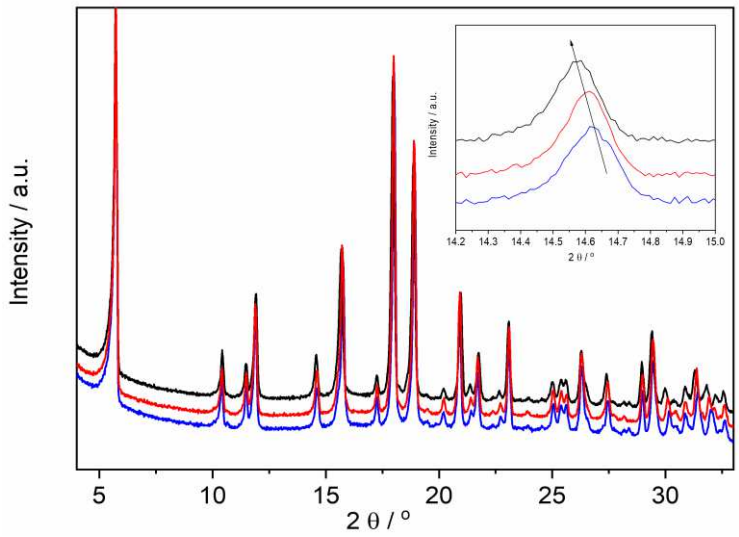

Figure 3.22: PXRD patterns of **TzAu·PO73** (blue), **TzAu·PO50** (red), and **TzAu·PO37** (black), were collected at room temperature. Insert: close-up of the patterns in the region 2θ = 14.2–15.0°.

To examine the unit cell differences between the frameworks with different components of the PX and MX mixtures in the TzAu framework, the frameworks were exchanged with a mass ratio of PX/MX = 7:3 (**TzAu·PM73**), PX/MX = 5:5 (**TzAu·PM50**), and PX/MX = 3:7 (**TzAu·PM37**) and were then characterised by PXRD (Figure 3.23). The three resulting frameworks all exhibit nearly identical powder patterns. Upon closer examination of the pattern differences in the 2θ range 15.3–16.2°, a peak shift to a smaller 2θ angle is observed with an increased ratio of the MX component.

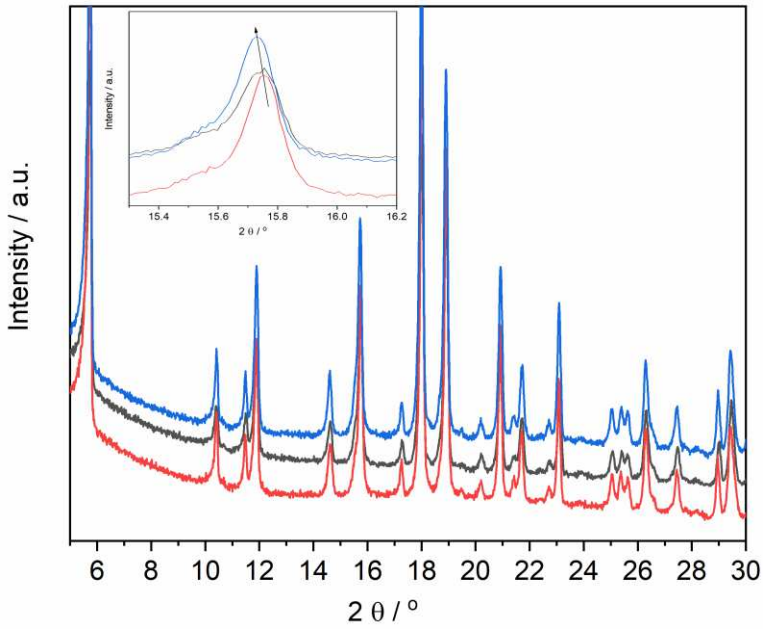

Figure 3.23: PXRD patterns of **TzAu·PM73** (red), **TzAu·PM50** (black), and **TzAu·PM37** (blue) were collected at room temperature. Insert: close-up of the patterns in the region 2θ = 15.3–16.2°.

The frameworks with a mass ratio of MX/OX = 7:3 (**TzAu·PO73**), MX/OX = 5:5 (**TzAu·PO50**), and MX/OX = 3:7 (**TzAu·PO37**) were generated and characterised by PXRD. The PXRD patterns of samples with different ratios of xylene mixtures show similar pattern features (Figure 3.24). Most of the peaks shift to smaller 2θ angles when increasing the ratio of the OX component. The inset (2θ = 11.2–11.7°) shows an example of peak shifting due to the change of solvent component. This suggests that the **TzAu·MO37** framework may have the largest unit cell as most of the peaks are positioned at relatively lower 2θ angles while **TzAu·MO73** possesses the smallest unit cell.

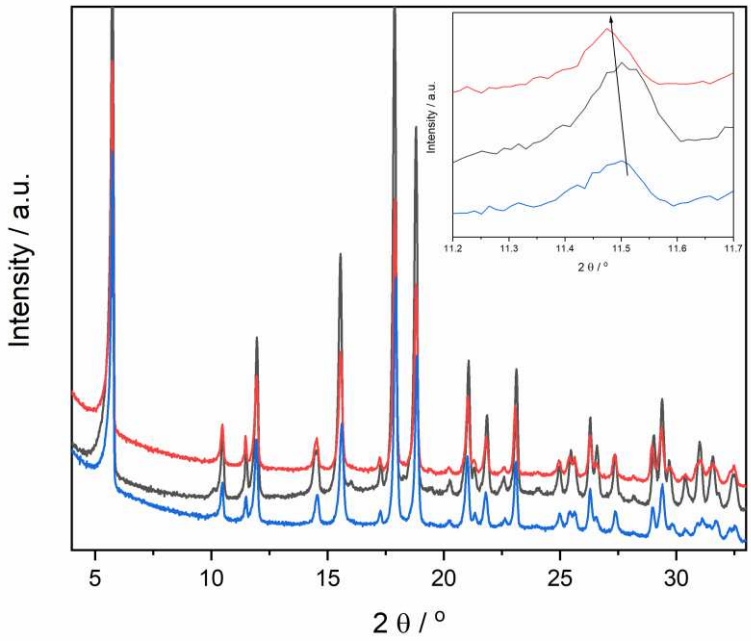

Figure 3.24: PXRD patterns of **TzAu·MO37** (red), **TzAu·MO50** (black), and **TzAu·MO73** (blue) were collected at room temperature. Inset: zoomed in view of the region between 2θ = 11.2–11.7°.

3.4.2 Variable Temperature Magnetic Susceptibility of TzAu with a binary mixture solvent of PX, OX, and MX

To obtain the SCO behaviours of the binary xylene mixtures, variable temperature magnetic susceptibility measurements were performed on **TzAu·PM37**, **TzAu·PM50**, and **TzAu·PM73** (Figure 3.25). The frameworks were prepared as in Chapter 2 Section 2.2.7. The SCO behaviours of **TzAu·PM37** and **TzAu·PM73** are similar and display relatively gradual and hysteretic single-step SCO. It is noted that in both of the frameworks, the SCO behaviour above 217 K in the cooling process and 224 K in the heating process is more abrupt than below the two temperatures. The transition temperatures of **TzAu·PM37** are $T_{½}\downarrow$ = 233 K and $T_{½}\uparrow$ = 238 K, while for **TzAu·PM73** they are $T_{½}\downarrow$ = 236 K and $T_{½}\uparrow$ = 244 K. The hysteresis width observed for **TzAu·PM73** is larger than **TzAu·PM37**. **TzAu·PM50** exhibits asymmetric SCO with a two-step spin transition upon cooling (the first step: $T_{½}\downarrow$ = 244 K and the second step: $T_{½}\downarrow$ = 198 K), and three-step behaviour during the heating process (the first step: $T_{½}\uparrow$ = 271 K, the second step: $T_{½}\uparrow$ = 236 K, the third step: $T_{½}\uparrow$ = 204 K). The $\chi_M T$ value is reduced slightly at 254 K, which could be due to an instrumental temperature lag.

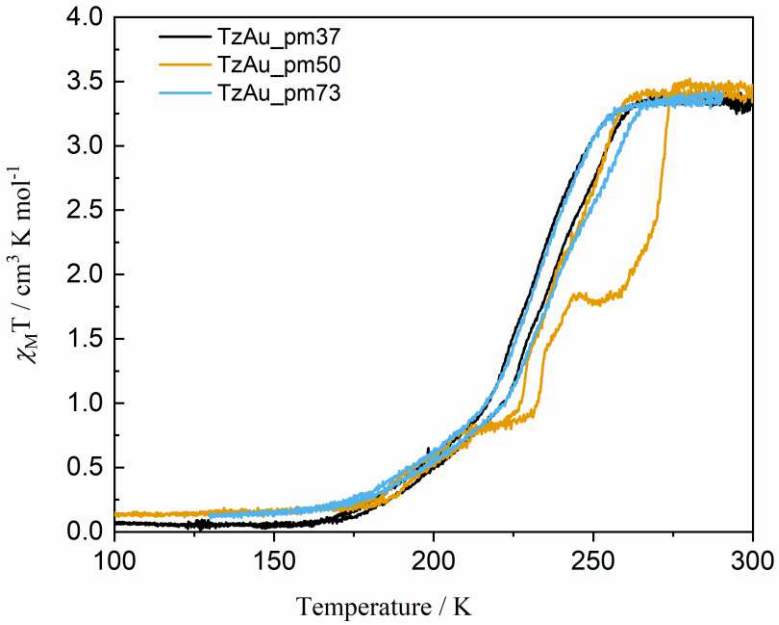

Figure 3.25: Variable temperature magnetic susceptibility plots of **TzAu·PM37** (black), **TzAu·PM50** (dark yellow), and **TzAu·PM73** (blue) collected at a scan rate of 2 K min^{-1}.

Variable temperature magnetic susceptibility measurements were conducted on **TzAu·MO37**, **TzAu·MO50**, and **TzAu·MO73**. **TzAu·MO37** and **TzAu·MO50** exhibit hysteretic four-step SCO while **TzAu·MO73** exhibits hysteretic single-step SCO (Figure 3.26). The transition temperatures of **TzAu·MO37** in the cooling process are $T_{½}\downarrow$ = 243, 221, 206 and 168 K, while the corresponding heating processes are $T_{½}\uparrow$ = 246, 224, 211 and 180 K. The first three spin transitions proceed with an open hysteresis loop, followed by a closed loop. **TzAu·MO50** exhibits similar SCO behaviour as **TzAu·MO37** with $T_{½}\downarrow$ = 245, 223, 209 and 175 K, and $T_{½}\uparrow$ = 248, 226, 215 and 184 K upon cooling and heating, respectively. **TzAu·MO73** exhibits single-step SCO with the transition temperatures 215 and 217 K for the cooling and heating processes, respectively.

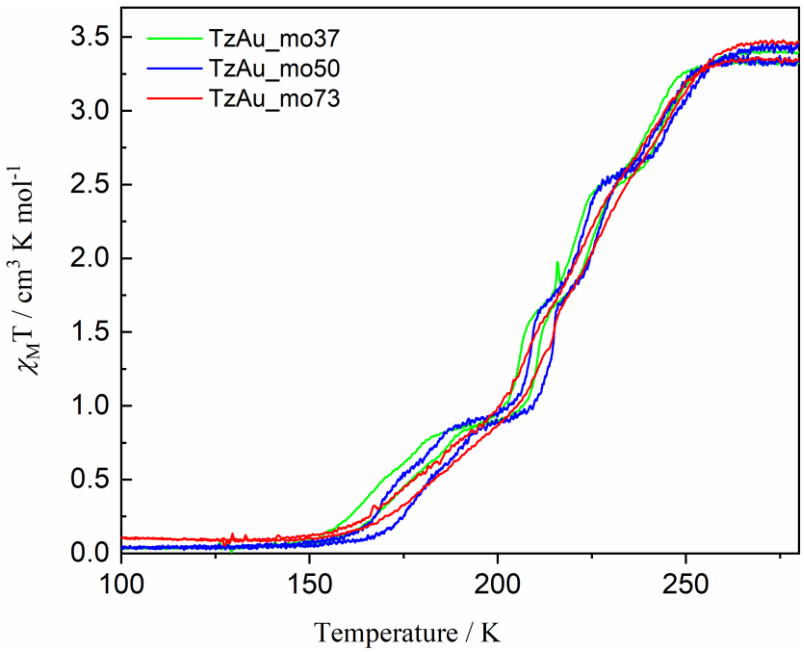

Figure 3.26: Variable temperature magnetic susceptibility plots of **TzAu·MO37** (green), **TzAu·MO50** (blue), and **TzAu·MO73** (red) collected at a scan rate of 2 K min^{-1}.

Variable temperature magnetic susceptibility measurements were conducted on **TzAu·PO37**, **TzAu·PO50**, and **TzAu·PO73** (Figure 3.27) All of these frameworks show asymmetric SCO behaviours. **TzAu·PO37** exhibits the narrowest hysteresis with abrupt and single-step SCO upon cooling ($T½↓$ = 231 K), while the heating process unusually exhibits four-step SCO ($T½↑$ = 278, 251, 270 and 279 K). **TzAu·PO50** and **TzAu·PO73** exhibit single-step SCO with transition temperatures upon cooling of $T½↓$ = 227 and 228 K, respectively. The heating process for both frameworks contains four stepwise spin transitions with $T½↑$ = 228, 251, 268 and 285 K for **TzAu·PO50**, and $T½↑$ = 227, 250, 273 and 289 K for **TzAu·PO73**. **TzAu·PO50** has the widest hysteresis width. At 261 K, the $\chi_M T$ value drops slightly, which may be due to a kinetic effect.

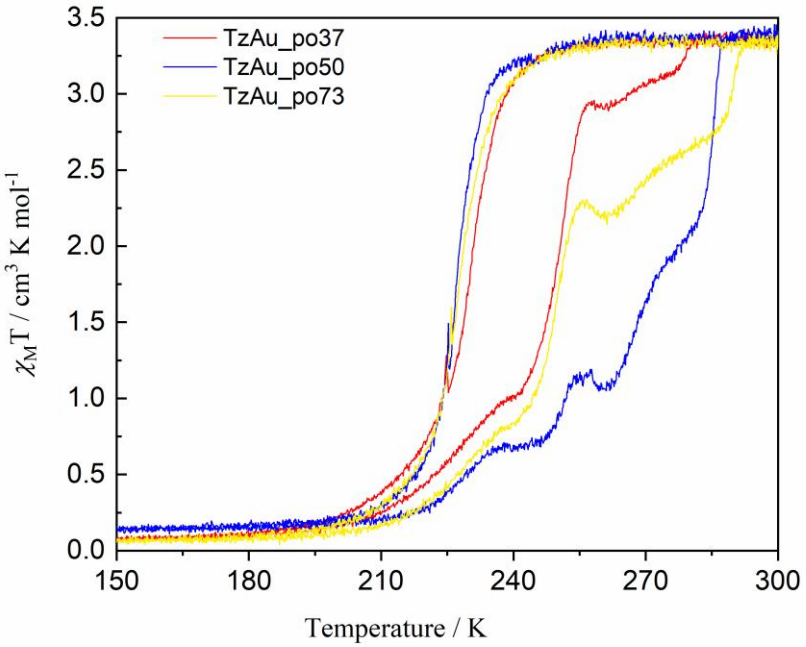

Figure 3.27: Variable temperature magnetic susceptibility plots of **TzAu·PO37** (red), **TzAu·PO50** (blue), and **TzAu·PO73** (yellow) recorded at a scan rate of 2 K min^{-1}.

It is interesting to note that the **TzAu·PO50** has the widest hysteresis width than the other ratios of PX and OX mixtures. The behaviour is similar in the TzAu framework when PX and MX are included within the pores. Both **TzAu·PO50** and **TzAu·PM50** exhibit asymmetric SCO and relatively wide hysteresis width.

3.4.3 NMR of guest components within the frameworks

To analyse the actual number of xylenes adsorbed in the frameworks, NMR exchange measurements were performed on these MOFs. NMR spectra of the pure binary solvents with various component ratios were first measured to verify the feasibility of the solvent exchange. The framework materials were soaked in different ratios of these pure binary xylenes and characterised by NMR. To examine the solvent molecules included within the pores, any surface adhered solvent on each of the frameworks was first removed by passing over with nitrogen. Subsequently, $CDCl_3$ (*ca.* 2 mL) was then added to each framework to extract the xylenes from within the pores into the supernatant. NMR spectra were collected on the supernatants to examine the ratio of binary xylenes adsorbed into the framework pores. The TzAu materials with MX/OX in the pores show approximately the same ratio of mixtures as the pure solvent except for **TzAu·MO50**, which has a slightly higher ratio of MX than OX (Table 3.4). The TzAu frameworks with PX/OX mixtures show a preference for PX to be adsorbed into the pores. The same preference was observed in the materials with containing PX/MX mixtures.

Table 3.4: The ratio of the pure binary solvent mixture and binary solvent mixture within each TzAu frameworks.

Solvent	The ratio of binary solvent	TzAu framework	The ratio of binary solvent within MOFs
MO37	0.27	**TzAu·MO37**	0.26
MO50	0.49	**TzAu·MO50**	0.56
MO73	0.70	**TzAu·MO73**	0.72
PO37	0.29	**TzAu·PO37**	0.42
PO50	0.49	**TzAu·PO50**	0.59
PO73	0.69	**TzAu·PO73**	0.73
PM37	0.30	**TzAu·PM37**	0.40
PM50	0.48	**TzAu·PM50**	0.63
PM73	0.71	**TzAu·PM73**	0.79

3.5 Conclusions and Future Work

In this chapter, a series of TzAu framework materials incorporating each xylene isomer as included guest molecules (**TzAu·MX**, **TzAu·PX**, **TzAu·OX**) were synthesised. These frameworks all possess a 3D Hofmann-like topology with an Fe(II) node coordinated on its four equatorial positions by $[Au(CN)_2]^-$ linkers and two axial positions by the Tz ligand. The crystal structures of **TzAu·PX** and **TzAu·OX** were solved in the same centrosymmetric orthorhombic space group *Ibam*, as opposed to the as-made **TzAu·EtOH** in the centrosymmetric orthorhombic space group *Cmma*. The change of the space group to lower symmetry is attributed to the PX or OX adsorption forming two different pore environments as two PX or OX molecules are coplanar in one environment, while there is only one molecule in the second and narrower pore environment. Host–guest and guest–guest aromatic stacking interactions are present in each of the three Hofmann-like frameworks. The pores are compressed in their LS states and accordingly exhibit a closer set of aromatic stacking interactions. Both **TzAu·PX** and **TzAu·OX** undergo scissor motions in which one cell direction displays NTE while the others display PTE. The lattice flexing mechanism is attributed to the change in Fe(II) coordination behaviour coupled with an electronic configuration transition induced by temperature. Interestingly, **TzAu·PX** undergoes a structural transition after the first thermal cycle, while no changes occur during the second and third thermal cycles. However, single crystal materials are not stable enough to be collected after one thermal cycle and the PXRD data of bulk powder samples of relatively low quality did not provide accurate and detailed information about the materials. Thus, density functional theory (DFT) and molecular dynamics (MD) simulations could be applied to further understand the complex structural transformations present in **TzAu·PX** and study its host–guest chemistry. The single crystal X-ray structure of **TzAu·MX** was not collected as all attempted samples degraded during the solvent exchange method. Computational simulations could be performed on these materials to obtain further structural

data.

The SCO behaviours of **TzAu·MX**, **TzAu·PX** and **TzAu·OX** were examined by variable temperature magnetic susceptibility. A rare asymmetric four/five-step SCO is shown in **TzAu·MX**. In the first step, SCO presents a closed loop while the rest are open loops. Its hysteresis is the narrowest among the three materials. **TzAu·MX** remains in the HS state even in the relatively low temperature compared with its counterparts. This is the spin transition temperatures in **TzAu·MX** are all very low.

Although the structural topologies are closely similar between **TzAu·OX** and **TzAu·PX**, their SCO behaviours are profoundly different. **TzAu·PX** shows a distinguished SCO behaviour in the first (one/three-step) and second thermal cycle (two/three-step). The first thermal cycle presents a notable wide hysteresis (62 K). The widest thermal hysteresis loop is at 70 K noticed in two different SCO components.[48-49] To the best of our knowledge, **TzAu·PX** exhibit the widest hysteresis among 3D Hofmann-like frameworks. Interestingly, in the second thermal cycle, one more step is shown in the cooling process and hysteresis is narrower. The difference between the thermal cycles is attributed to the structural transition of the material. The scan rate effect of **TzAu·PX** was also investigated showing larger hysteresis in the faster scan rate because of the temperature lagging. That examines SCO behaviour is scan rate dependent.

TzAu·OX exhibits asymmetric one/two-step hysteretic SCO. The OX solvent movement and freezing caused a sudden increase in magnetic susceptibility, which is a spike noticed in the cooling process. The reverse temperature sweep was conducted on the material showing no spike in that temperature range. Additionally, the matrix effect for **TzAu·OX** was examined by mixing with the oil. The oil mixture with the material can quench the solvent and lessen the thermal motion of the solvent. The oil as media was added into the framework, which changes the propagation of spin transition in Fe(II) sites. Therefore, a gradual SCO is shown due to the matrix effect. Moreover, the influence of varying scan rates of magnetic susceptibility was performed on **TzAu·OX**. The lower spin transition temperature is observed with increasing scan rate upon cooling. The above-mentioned magnetic susceptibility measurements indicate the spike is likely related to the OX reorientated in the pores and frozen.

The distinguished SCO behaviours with OX, PX and MX as a guest respectively in the pores indicate the TzAu framework is sensitive material in response to isomers. The adsorption of a binary mixture of xylene isomers was studied in the TzAu framework showing the SCO transition temperature, stepwise and hysteresis are depending on the component of the isomers. The actual adsorption of each isomer in the TzAu framework was investigated showing a preference for PX solvent in the binary mixture of PX/OX and PX/MX. That could possibly be due to the PX molecule is easier to be fitted in the pores.

However, there remains many interesting questions that warrant further investigation. The

structure of **TzAu·PX** after the first thermal cycle could be simulated using DFT. The energy change associated with the phase transition could be calculated, which could assist in the explanation of the structural change. Simulations could help understand the motion of PX solvent within the pores and the change of host–guest interactions caused by the structural transition. Although the single crystal X-ray structure of **TzAu·MX** could not be collected experimentally, based on the structural information obtained for **TzAu·OX** and **TzAu·PX**, and PXRD data for **TzAu·MX**, the structure of **TzAu·MX** could be simulated using DFT, which could provide more detailed information on the structural topology, pore sizes, and MX solvent position(s) in the pores. Therefore, a deeper understanding of the relationship between the guest and host framework properties could guide the rational design of more MOF materials for guest encapsulation studies.

SCO behaviours are varied when different xylene isomers are included within the pores of the TzAu framework, indicating a strong host–guest dependent SCO effect. The number of guest molecules adsorbed into the framework could also affect the SCO behaviour. Thus, it would be interesting to further study the performance of SCO with decreased uptake of a xylene isomer. *In-situ* desolvation of each xylene guest included framework could be conducted and compared with their magnetic properties at different stages of desolvation (i.e., containing different amounts of guest molecules) and the completely desolvated frameworks. Furthermore, the structures with different amounts of single component xylene molecules could be analysed. The structural characterisation due to a gradual desolvation process could be demonstrated, which could provide detailed insight into and any associated changes in the unit cell parameters, pore shape dimensions, degree of Hofmann layer distortion, and bent angle of the pillaring ligands. The sensitivity of the materials with varied ratios of binary xylene mixtures was also demonstrated. Even with small differences in the isomer components, the SCO behaviours are distinct. Further investigation could be carried out to determine the limits of sensitivity and whether different SCO behaviours can be observed with trace amounts of xylene mixtures.

The preference for PX solvent adsorption was observed in the binary xylene mixture in the TzAu framework. To understand the TzAu framework structures with various xylene components and reveal any solvent selectivity, grand canonical Monte Carlo (GCMC) simulations could be performed to model the TzAu frameworks. This could provide insight into stacking modes of solvent mixtures and energy differences of materials when the xylene ratios are varied. The adsorption capacity of binary isomers and maximum uptake of one xylene isomer over another could be calculated from these results. The adsorption behaviours of gas phase xylene isomer mixtures could be interesting to investigate in breakthrough experiments, which would demonstrate the differences in adsorption capacities and preferences between the solvent and gas phases.

Overall, this chapter has detailed distinguished SCO behaviours in the host TzAu framework due to the adsorption of a single component or binary mixtures of xylene isomers. The structural properties

of the frameworks were characterised and revealed the distortion of the frameworks being due to guest molecules and host–guest interactions. These results indicate the TzAu framework presents varied adsorption capabilities and sensitive guest-responsive SCO behaviours.

3.6 References

1. Gonzalez, M. I.; Kapelewski, M. T.; Bloch, E. D.; Milner, P. J.; Reed, D. A.; Hudson, M. R.; Mason, J. A.; Barin, G.; Brown, C. M.; Long, J. R., *J. Am. Chem. Soc.* **2018,** *140* (9), 3412-3422.

2. Kim, S.-I.; Lee, S.; Chung, Y. G.; Bae, Y.-S., *ACS Appl. Mater. Interfaces.* **2019,** *11* (34), 31227-31236.

3. Cui, X.; Niu, Z.; Shan, C.; Yang, L.; Hu, J.; Wang, Q.; Lan, P. C.; Li, Y.; Wojtas, L.; Ma, S.; Xing, H., *Nat. Commun.* **2020,** *11* (1).

4. Bej, S.; Das, R.; Murmu, N. C.; Banerjee, P., *Inorg. Chem.* **2020,** *59* (7), 4366-4376.

5. Sholl, D. S.; Lively, R. P., *Nature* **2016,** *532* (7600), 435-437.

6. Li, J.-R.; Kuppler, R. J.; Zhou, H.-C., *Chem. Soc. Rev.* **2009,** *38* (5), 1477.

7. Cai, W.; Wang, J.; Chu, C.; Chen, W.; Wu, C.; Liu, G., *Adv. Sci (Weinh).* **2019,** *6* (1), 1801526.

8. Municoy, S.; Alvarez Echazu, M. I.; Antezana, P. E.; Galdoporpora, J. M.; Olivetti, C.; Mebert, A. M.; Foglia, M. L.; Tuttolomondo, M. V.; Alvarez, G. S.; Hardy, J. G.; Desimone, M. F., *Int. J. Mol. Sci.* **2020,** *21* (13).

9. Zhou, Z.; Vazquez-Gonzalez, M.; Willner, I., *Chem. Soc. Rev.* **2021**.

10. Lu, Y.; Aimetti, A. A.; Langer, R.; Gu, Z., *Nat. Rev. Mater.* **2016,** *2* (1).

11. Blanco, V.; Leigh, D. A.; Marcos, V., *Chem. Soc. Rev.* **2015,** *44* (15), 5341-70.

12. Li, C.; Wang, K.; Li, J.; Zhang, Q., *ACS Mater. Lett.* **2020,** *2* (7), 779-797.

13. Nagarkar, S. S.; Desai, A. V.; Ghosh, S. K., *Chem. Asian J.* **2014,** *9* (9), 2358-76.

14. Roy, B.; Reddy, M. C.; Hazra, P., *Chem. Sci.* **2018,** *9* (14), 3592-3606.

15. Wang, H.; Peng, J.; Li, J., *Chem. Rec.* **2016,** *16* (3), 1298-1310.

16. Bonneau, M.; Lavenn, C.; Zheng, J.-J.; Legrand, A.; Ogawa, T.; Sugimoto, K.; Coudert, F.-X.; Reau, R.; Sakaki, S.; Otake, K.-I.; Kitagawa, S., *Nat. Chem.* **2022**.

17. Mukherjee, S.; Sensharma, D.; Qazvini, O. T.; Dutta, S.; Macreadie, L. K.; Ghosh, S. K.; Babarao, R., *Coord. Chem. Rev.* **2021,** *437*, 213852.

18. Rowsell, J. L. C.; Yaghi, O. M., *J. Am. Chem. Soc.* **2006,** *128* (4), 1304-1315.

19. Kong, X.-J.; Li, J.-R., *Engineering* **2021,** *7* (8), 1115-1139.

20. Eddaoudi, M.; Kim, J.; Rosi, N.; Vodak, D.; Wachter, J.; O'Keeffe, M.; Yaghi Omar, M., *Science* **2002,** *295* (5554), 469-472.

21. Clements, J. E.; Price, J. R.; Neville, S. M.; Kepert, C. J., *Angew. Chem. Int. Ed.* **2014,** *53* (38), 10164-10168.

22. Ketkaew, R.; Tantirungrotechai, Y.; Harding, P.; Chastanet, G.; Guionneau, P.; Marchivie, M.; Harding, D. J., *Dalton Trans.* **2021,** *50* (3), 1086-1096.

23. Guionneau, P.; Marchivie, M.; Bravic, G.; Létard, J.-F.; Chasseau, D., Structural Aspects of Spin Crossover. Example of the $[Fe^{II}Ln(NCS)_2]$ Complexes. In *Spin Crossover in Transition Metal Compounds II*, Springer Berlin Heidelberg: 2004; Vol. 234, pp 97-128.

24. Piñeiro-López, L. A.; Valverde-Muñoz, F. J.; Seredyuk, M.; Muñoz, M. C.; Haukka, M.; Real, J. A., *Inorg. Chem.* **2017,** *56* (12), 7038-7047.

25. Li, J.-Y.; He, C.-T.; Chen, Y.-C.; Zhang, Z.-M.; Liu, W.; Ni, Z.-P.; Tong, M.-L., *J. Mater. Chem. C.* **2015,** *3* (30), 7830-7835.

26. Spek, A. L., *Acta Crystallogr. Sect. C Struct. Chem.* **2015,** *71* (Pt 1), 9-18.

27. Pittala, N.; Thétiot, F.; Triki, S.; Boukheddaden, K.; Chastanet, G.; Marchivie, M., *Chem. Mater.* **2017,** *29* (2), 490-494.

28. Toby, B. H.; Von Dreele, R. B., *J. Appl. Crystallogr.* **2013,** *46* (2), 544-549.

29. Dolomanov, O. V.; Bourhis, L. J.; Gildea, R. J.; Howard, J. A. K.; Puschmann, H., *J. Appl. Crystallogr.* **2009,** *42* (2), 339-341.

30. Spek, A. L., *Acta Crystallogr. C Struct. Chem.* **2015,** *71* (1), 9-18.

31. Oishi-Tomiyasu, R., *J. Appl. Crystallogr.* **2014,** *47* (2), 593-598.

32. Bernal, J. D.; Fowler, R. H., *Chem. Phys.* **1933,** *1* (8), 515-548.

33. Li, Z.-Y.; Dai, J.-W.; Shiota, Y.; Yoshizawa, K.; Kanegawa, S.; Sato, O., *Eur. J. Chem.* **2013,** *19* (39), 12948-12952.

34. Peng, Y.-Y.; Wu, S.-G.; Chen, Y.-C.; Liu, W.; Huang, G.-Z.; Ni, Z.-P.; Tong, M.-L., *Inorg. Chem. Front.* **2020,** *7* (8), 1685-1690.

35. Raza, Y.; Volatron, F.; Moldovan, S.; Ersen, O.; Huc, V.; Martini, C.; Brisset, F.; Gloter, A.; Stéphan, O.; Bousseksou, A.; Catala, L.; Mallah, T., *Chem. Commun.* **2011,** *47* (41), 11501.

36. Tanasa, R.; Laisney, J.; Stancu, A.; Boillot, M.-L.; Enachescu, C., *Appl. Phys. Lett.* **2014,** *104* (3), 031909.

37. Plesca, D.; Railean, A.; Tanasa, R.; Stancu, A.; Laisney, J.; Boillot, M.-L.; Enachescu, C., *Magnetochemistry* **2021,** *7* (5), 59.

38. Brooker, S., *Chem. Soc. Rev.* **2015,** *44* (10), 2880-2892.

39. Kulmaczewski, R.; Olguín, J.; Kitchen, J. A.; Feltham, H. L. C.; Jameson, G. N. L.; Tallon, J. L.; Brooker, S., *J. Am. Chem. Soc.* **2014,** *136* (3), 878-881.

40. Milin, E.; Patinec, V.; Triki, S.; Bendeif, E.-E.; Pillet, S.; Marchivie, M.; Chastanet, G.; Boukheddaden, K., *Inorg. Chem.* **2016,** *55* (22), 11652-11661.

41. Garcia, Y.; Guionneau, P.; Bravic, G.; Chasseau, D.; Howard, Judith A. K.; Kahn, O.; Ksenofontov, V.; Reiman, S.; Gütlich, P., *Eur. J. Inorg. Chem* **2000,** *2000* (7), 1531-1538.

42. Fujinami, T.; Nishi, K.; Hamada, D.; Murakami, K.; Matsumoto, N.; Iijima, S.; Kojima, M.; Sunatsuki, Y., *Inorg. Chem.* **2015,** *54* (15), 7291-7300.

43. Neville, S. M.; Moubaraki, B.; Murray, K. S.; Kepert, C. J., *Angew. Chem. Int. Ed.* **2007,** *46* (12), 2059-2062.

44. Agustí, G.; Cobo, S.; Gaspar, A. B.; Molnár, G.; Moussa, N. O.; Szilágyi, P. Á.; Pálfi, V.; Vieu, C.; Carmen Muñoz, M.; Real, J. A.; Bousseksou, A., *Chem. Mater.* **2008,** *20* (21), 6721-6732.

45. Cobo, S.; Molnár, G.; Real, J. A.; Bousseksou, A., *Angew. Chem. Int. Ed.* **2006,** *45* (35), 5786-5789.

46. Molnár, G.; Niel, V.; Gaspar, A. B.; Real, J.-A.; Zwick, A.; Bousseksou, A.; McGarvey, J. J., *J. Phys. Chem. B* **2002,** *106* (38), 9701-9707.

47. Rubio-Giménez, V.; Bartual-Murgui, C.; Galbiati, M.; Núñez-López, A.; Castells-Gil, J.; Quinard, B.; Seneor, P.; Otero, E.; Ohresser, P.; Cantarero, A.; Coronado, E.; Real, J. A.; Mattana, R.; Tatay, S.; Martí-Gastaldo, C., *Chem. Sci.* **2019,** *10* (14), 4038-4047.

48. Hayami, S.; Gu, Z.-Z.; Yoshiki, H.; Fujishima, A.; Sato, O., *J. Am. Chem. Soc.* **2001,** *123* (47), 11644-11650.

49. Weber, B.; Bauer, W.; Obel, J., *Angew. Chem. Int. Ed.* **2008,** *47* (52), 10098-101.

Chapter 4

Investigation of SCO Behaviours Influenced by Adsorption of Guest Xylene Isomers in $[Fe(Dz)(Au(CN)_2)_2]$

4.1 Overview

MOF materials are widely used for guest sorption and separations, which can be attributed to the shape and size of their cavities.[1-2] A framework that is built up from different ligands can generate distinct pore environments that may affect guest uptake. It is of interest to compare the influence that different ligands have towards producing new framework architectures and to understand the underlying chemical and/or physical structure-function relationships that relationship between the resulting sorption and SCO behaviours.

In this chapter, which follows from the use of the Tz ligand in Chapter 3, the more electron-rich and lower symmetry ligand 3,6-bis(4-pyridyl)-1,2-diazine (Dz) was used to generate the 3D Hofmann-like framework [Fe(Dz)(Au(CN)$_2$)$_2$]·*x*EtOH (**DzAu·EtOH**). Herein, **DzAu·EtOH** was adsorbed with different unitary xylene isomers to generate the guest-exchanged phases **DzAu·OX**, **DzAu·PX,** and **DzAu·MX**. In building on the results of Chapter 3, this chapter provides further insight into the influence of the ligand on the resulting framework properties, which will lead to a deeper understanding of the interplay between the host topology and guest uptake effects. Distinct structures were formed upon the adsorption of different xylene isomers in the prototypical DzAu framework. Also, the same xylene isomer, when adsorbed in either TzAu or DzAu framework, was compared and distinct properties were observed. Binary xylene mixture uptake in DzAu frameworks was investigated to analyse for selectivity performance. Different selectivity in xylene uptake was observed in the TzAu and DzAu framework.

It is important to understand the relationship between structural and magnetic properties as even subtle differences between structures may lead to distinct SCO behaviours. Great efforts have been made to manipulate SCO behaviours by choosing different ligand field strengths of ligands.[3-5] In general, a lower spin transition temperature is caused by a weaker ligand field energy, while the opposite is often true for stronger ligand fields. However, besides the ligand field strength, other factors may also affect SCO behaviour such as distorted lattices, host–host, and host–guest interactions.[6-8] SCO framework materials often possess a strong guest-dependent sensitivity to their magnetic properties. It has been widely studied that the profile and number of spin transitions can be influenced by the size, dielectric constant, and type of guest molecule.[8-12] The guest-dependent SCO behaviour in 3D Hofmann-like MOFs affected by unitary and binary xylene isomers currently remains unknown. Thus, this chapter discusses the SCO behaviours of the DzAu framework with encapsulation of xylenes and provides a comparison with the TzAu framework in response to unitary and binary xylene isomers. The DzAu framework consists of the Dz ligand (which has a reduced symmetry and ligand field energy than the Tz ligand) and forms different space groups and pore configurations. The framework also shows a different response to the adsorption of xylene isomers. Thus, understanding how the host frameworks and guest molecules influence their respective SCO behaviours may help in the design of new and

desirable SCO materials.

4.2 Structure Characterisation of DzAu·Guest (Guest = OX, PX, MX)

4.2.1 Single Crystal Structure of **DzAu·OX**

The synthesis of the Dz ligand is described in the experimental chapter (Chapter 2 Section 2.2.2). A single crystal of **DzAu·EtOH** was synthesised by the vial-in-vial slow diffusion technique, as outlined in Chapter 2 Section 2.2.5. The guest exchange method (Chapter 2 Section 2.2.7) was then performed to prepare **DzAu·OX** from as-made **DzAu·EtOH**. A single-crystal-to-single-crystal transformation proceeded *via* the removal of the ethanol crystallisation mother liquor and by soaking of the framework in OX solvent overnight to produce **DzAu·OX**. Variable temperature SCXRD data were then collected for a crystal of **DzAu·OX** to obtain structural information (Figure 4.1).

The framework possesses the expected Hofmann-like topology in the monoclinic phase with the space group being *I*2/*a* (alternative setting of *C*2/*c* as seen in **DzAu·EtOH**). The framework contains a six-fold coordinated Fe(II) site comprised of two pillaring Dz ligands on the axial positions, and four $[Au(CN)_2]^-$ linkers on the equatorial positions. This motif is repeated such that a Hofmann grid is formed. The OX guest molecules could be located within the pores and refined accordingly. The Hofmann layers are separated by aurophilic interactions and form an acute angle of Au···Au–C (83.52°) observed as opposed to the more perpendicular geometry found within the Tz-based framework. Therefore, the neighbouring Hofmann layers are not overlayed and instead a shift between the interpenetrated Hofmann layers was observed down the *c*-axis. Unlike the rhombic Hofmann grids in the TzAu framework, the Hofmann grids in the DzAu frameworks (**DzAu·EtOH** and **DzAu·OX**) are more rectangular. This parameter was calculated using the same equation as for the TzAu framework ($\theta = 2 \times \arctan(a/b)$) and represents the Au···Fe···Au angle when viewing down the *c*-axis. The θ angle of **DzAu·OX** is 86.8°.

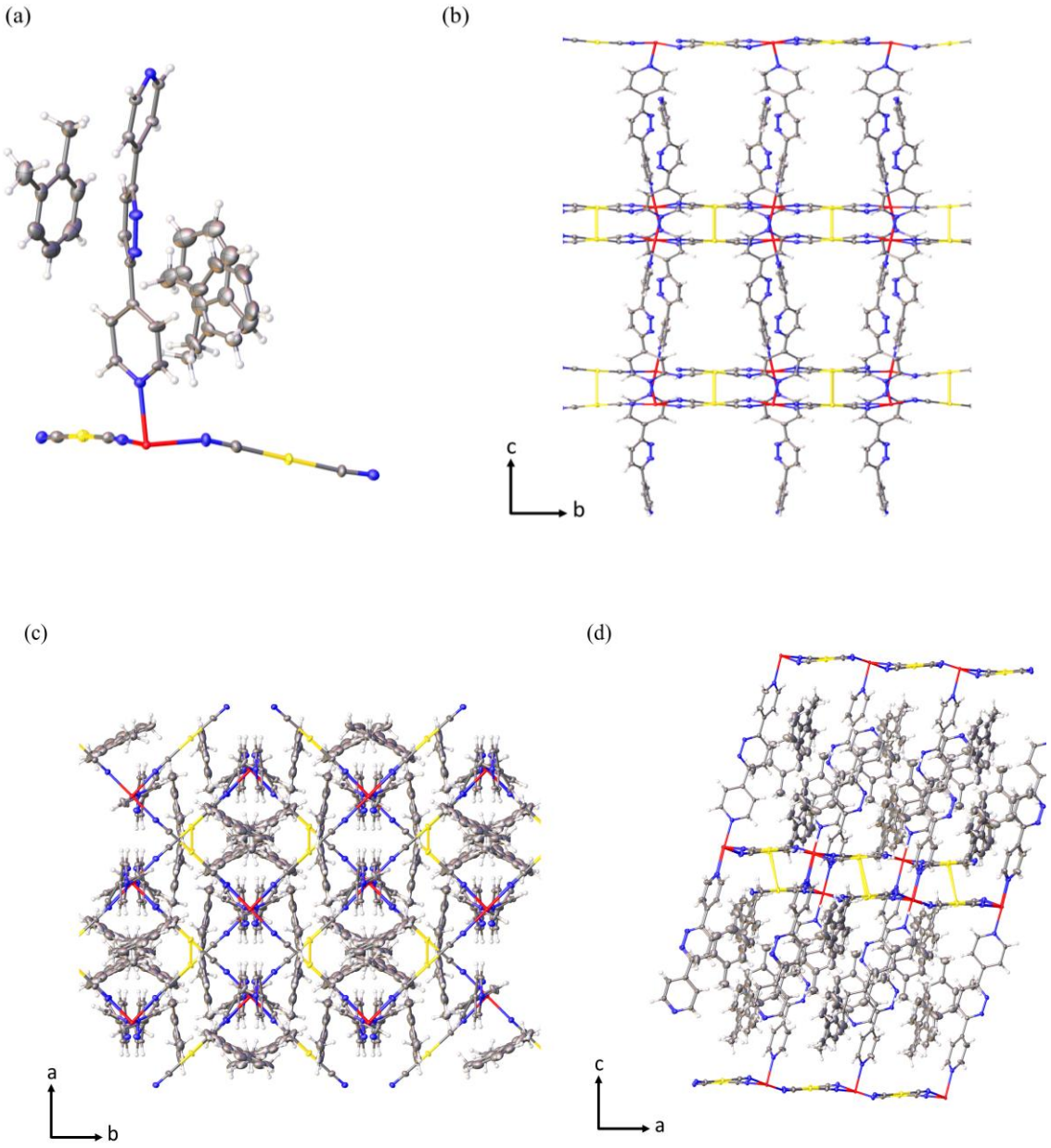

Figure 4.1: Single crystal X-ray structure of **DzAu·OX** at 100 K: (a) asymmetric unit with thermal ellipsoids set at 50% probability, (b) the extended framework structure as viewed down the *a*-axis with solvent molecules omitted for clarity, (c) the extended framework structure with solvent molecules viewed down the *c*-axis and (d) *b*-axis. Atom colours: Fe (red), Au (yellow), N (blue), C (grey), and H (white).

Similar to the prototypic framework **DzAu·EtOH**, C–H···N host–host interactions are present between the adjacent pillar ligands in **DzAu·OX**. The C–H···N interactions in **DzAu·OX** are almost identical at 3.426(5) Å (C22···N12) and 3.441(5) Å (C21···N13). The interactions distances are shorter than in **DzAu·EtOH** (3.522(10) and 3.541(10) Å), which is possibly due to a compressive effect in the neighbouring pores due to the OX molecules. Upon encapsulation of OX molecules, host–guest

interactions are also observed similar to the prototypic framework. There are two OX molecules per formula unit. One of the OX molecules (the ring C51–C52–C53–C54–C55–C57 filled in yellow shown in Figure 4.2 (a)) was refined at full occupancy. The molecule participates in host–guest interactions with the top pyridyl ring (C20–C21–C22–N14–C23–C24 with the ring filled in blue) in 3.252(5) Å. That indicates host–guest π···π interactions. Another OX molecule is disordered with the two orientations: one orientation was modelled at 59% occupancy (the ring filled in pink is shown in Figure 4.2 (b)) while the other at 41% occupancy (the ring without filled in colour). Another π···π interaction is between the OX (C41–C42–C43–C44–C45–C46 with the ring filled in pink) and the bottom pyridyl rings N11–C11–C12–C13–C14–C15 (with the ring filled in red) at a distance of 3.598(6) Å.

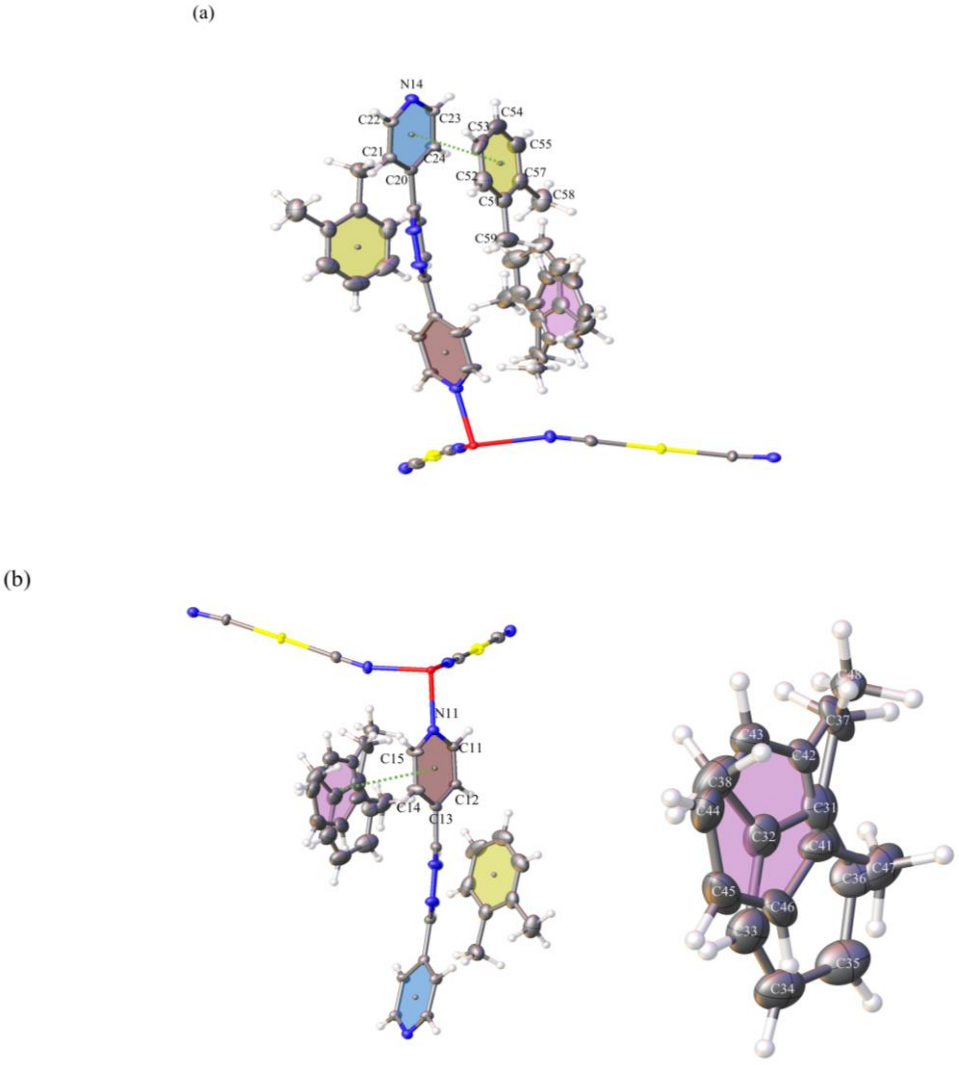

Figure 4.2: Single crystal X-ray structure of **DzAu·OX** at 100 K showing π···π interactions: (a) between a pyridyl ring (blue) and OX molecule (yellow), (b) between another pyridyl ring (red) and the disordered OX molecule (pink). Right: disordered OX fragment with the two orientations modelled at 59% (pink) and the other at 41%. The dashed line in green represents the π···π interactions. Atom colours: Fe (red), Au (yellow), N (blue),

C (grey), and H (white).

Upon encapsulation of the larger OX molecules in the pores, the unit cell parameters and degree of framework distortion shift considerably compared to the prototypic materials. The unit cell parameters of **DzAu·OX** at 100 K (Table 4.1) are all larger than **DzAu·EtOH**. Structural information of **DzAu·EtOH** was extracted according to the literature.[13] Note that a single crystal of **DzAu·EtOH** was collected at 90 K instead of 100 K. The change in lattice parameters due to thermal expansion for a 10 K difference is considerably small so the lattice information of **DzAu·OX** and **DzAu·EtOH** is comparable. The total unit cell volume of the **DzAu·OX** is 6676.0 Å^3, which is a 7% increase relative to **DzAu·EtOH**. Notably, the β angle is 103.1° in **DzAu·OX**, which is much larger than the equivalent angle in **DzAu·EtOH** (96.1°). These increases in unit cell parameters are presumably due to the inclusion of bulky OX molecules within the pores.

Table 4.1: Comparison of the unit cell parameters of **DzAu·OX** and **DzAu·EtOH** (the unit cell information obtained from literature[13]) at 100 and 90 K, respectively.

Sample	Temperature / K	*a* / Å	*b* / Å	*c* / Å	β / º	Volume /Å^3
DzAu·OX	100	14.4500(5)	15.2703(5)	31.0588(8)	103.062(3)	6676.0(4)
DzAu·EtOH	90	14.2256(2)	14.4645(3)	30.4429(5)	96.104(2)	6228.60(19)

To more clearly understand how the different solvents (EtOH and OX) affect the structure, the asymmetric units of **DzAu·EtOH** and **DzAu·OX** were overlayed as shown in Figure 4.3(a). The Dz ligand in both frameworks exhibits distinctly different torsional angles between the central core diazine component and the pyridyl rings, while the coordinated $[Au(CN)_2]^-$ linkers possess a similar degree of distortion. The average Fe–N distance in **DzAu·OX** is 2.17 Å, indicating it is in the HS state at 100 K. The Dz ligand length in **DzAu·OX** (11.174(4) Å) is shorter and more bent than for **DzAu·EtOH** (11.224(8) Å). The pyridyl rings and diazine rings are facing in different directions. The dihedral angle between the two pyridyl rings in **DzAu·OX** is 61.3°. The angle between the diazine ring and the bottom pyridyl ring (N11–C11–C12–C13–C14–C15) is 33.1°, which is larger than the equivalent angle between the diazine ring and the top pyridyl ring (28.7°). The Fe(II) site is coordinated to four $[Au(CN)_2]^-$ linkers that possess angles for Fe1–N1–C1, Fe1–N2–C2, Fe3–N3–C3, and Fe1–N4–C4 of 163.1, 177.2, 173.9 and 165.2° respectively. However, the Fe–N–C angles in **DzAu·EtOH** are close to linear, with an average Fe–N–C angle of 175.1°. The octahedral distortion parameter Σ(Fe) for **DzAu·OX** is 29.9°, which is more than double that for **DzAu·EtOH** (12.7°). The greater distortion in **DzAu·OX** is expected due to the accommodation of the large OX guest molecules.

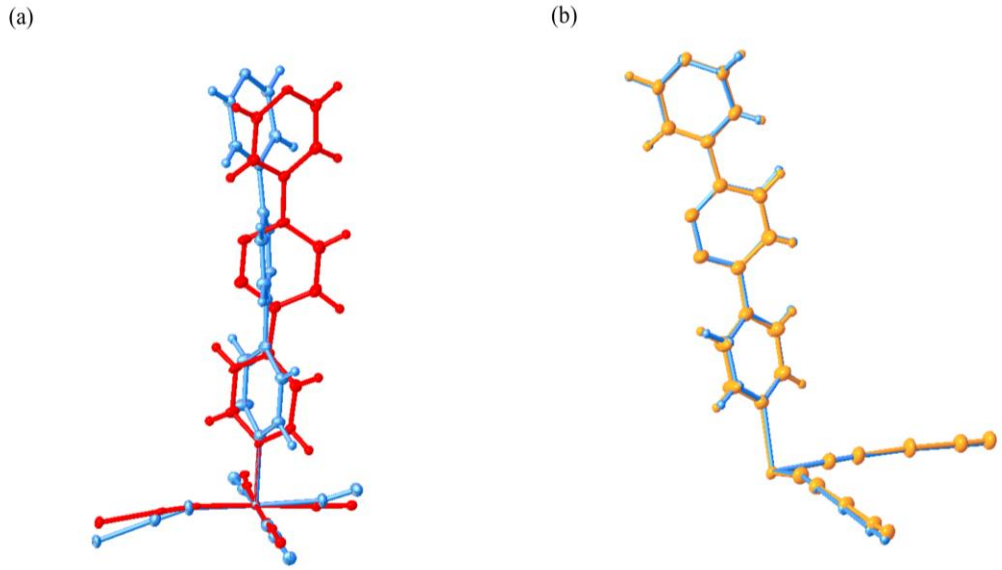

Figure 4.3: (a) Structural overlay of **DzAu·OX** (light blue) at 100 K and **DzAu·EtOH** (red) at 90 K. (b) Structural overlay of **DzAu·OX** (light blue) at 100 K (LS state) and **DzAu·OX** (light orange) at 230 K (HS state).

The Hofmann layer in **DzAu·OX** is more undulated than in **DzAu·EtOH**. The tilted angle between the Hofmann layer and Fe(II) plane is 10.6°, which is approximately as twice large as in **DzAu·EtOH**. The two Au(I) atom-to-Hofmann layer distances in **DzAu·OX** are also longer than in **DzAu·EtOH**, with the former being 0.29 Å (Au1) and 0.27 Å (Au2), and the latter being 0.24 Å (Au1) and 0.14 Å (Au2). However, the aurophilic contact distance (Au···Au) between the Hofmann layers is shorter in **DzAu·OX** at 3.076 Å.

Table 4.2: Comparison of the selected structural parameters for **DzAu·OX** (100 K and 230 K) and **DzAu·EtOH** (90 K).

Parameter	**DzAu·OX** (100 K)	**DzAu·OX** (230 K)	**DzAu·EtOH** (90 K)
$\langle d(\text{Fe–N})\rangle$ / Å	2.17	2.18	1.97
Σ(Fe) / °	29.9	25.8	12.7
Average Au···Au / Å	3.076	3.110	3.130
Average Fe–N–C / °	169.85	171.13	175.1
θ / °	86.8	88.2	89.0
Pore volume / Å^3	3074.36	3184.08	2728.47

In the **DzAu·OX** framework, two OX molecules per formula unit are present within the pores. The void volume is 3074 Å^3, which results in a solvent accessible volume of 46.1%, while the pore volume in **DzAu·EtOH** is smaller in 2728 Å^3 and results in a solvent accessible volume of 43.8%. The larger pore size in **DzAu·OX** is attributed to the larger molecular size of OX relative to EtOH. Unlike the relatively even pore size and shape in **DzAu·EtOH**, which can be attributed to a more even distribution of EtOH in the pores, the structure of **DzAu·OX** is such that there are two unique pore environments A

and B (Figure 4.4). This is possibly caused by OX guest molecules that are distributed unevenly in the pores. The pore shape of A is narrower at the top and broader at the bottom, while the opposite is the case for the B pore shape. The length of the A and B pores are 9.6 Å and 9.2 Å, respectively. The narrowest and broadest width of the pores was calculated using the distance of C atoms in the diazine rings and N atoms in the pyridyl rings. The pore widths of A and B are the same with the narrowest and broadest distances being 5.14 and 6.6 Å, respectively. A pore channel in between the Hofmann layers is also present, but no OX molecules were located in this region due to the channel size not being sufficiently large.

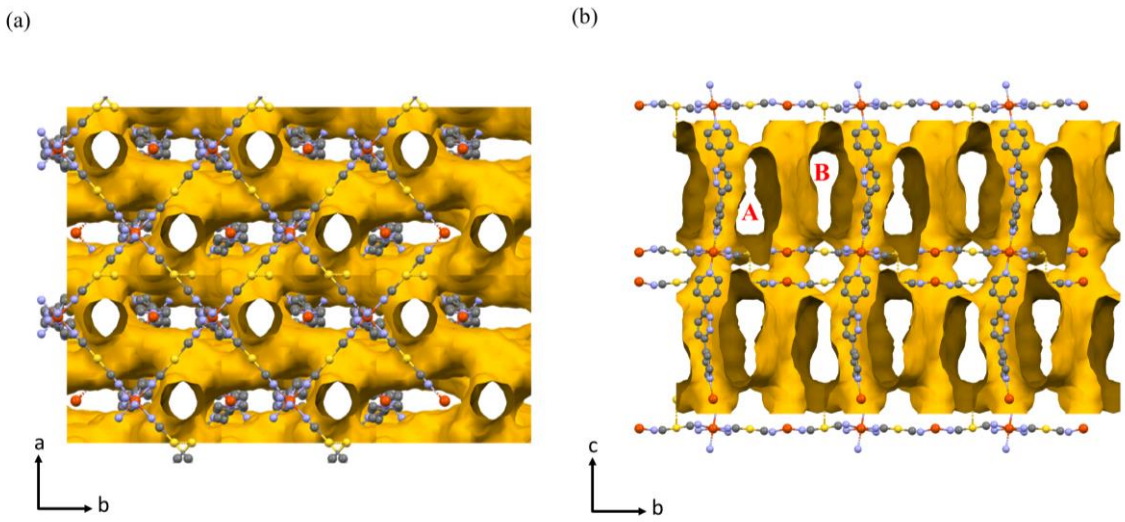

Figure 4.4: The calculated pore environments of **DzAu·OX** displayed in either yellow (outside of the pores) or brown (inside of the pores): (a) view down the *c*-axis and (b) view down the *a*-axis. Guest molecules have been omitted for clarity. Atom colours: Fe (red), Au (yellow), N (blue), C (grey), and H (white).

The single crystal X-ray structure of **DzAu·OX** at 230 K possesses the same space group as at 100 K. The average Fe–N distances at 230 K and 100 K are almost identical indicating both at the HS states. The extent of ligand distortion and ligand bending observed in **DzAu·OX** at these two temperatures is also very similar (Figure 4.3(b)). The lattice parameters *a* and *c* of **DzAu·OX** at 230 K increase by 1.46% and 0.23%, respectively (Appendix Table B.1). Unlike its prototypic framework in which all the unit cell parameters increase due to thermal expansion, the *b* lattice and *β* angle parameters counterintuitively decrease in **DzAu·OX** at higher temperature. The framework displays NTE in the *b* lattice parameter with a reduction of 0.97%. The change of lattice parameters at higher temperatures is potentially correlated to a more linear Fe–N–C angle and less distortion of the local FeN_6 coordination octahedra. The changes in the lattice cause an increase of θ to 88.2° at a higher temperature. The Hofmann grid approaches a more regular rectangular shape with θ being close to 90°. However, **DzAu·OX** does not possess any scissor motion. This is attributed to a shift of the Hofmann layers with

inclined Au···Au interactions. Therefore, neighbouring layers are not overlayed but are instead mismatched.

The Dz ligand is less distorted at 230 K than at 100 K. The angle between the two pyridyl rings in **DzAu·OX** is 55.4°. The angle between the diazine ring and the bottom pyridyl ring is 32.3°, while the angle between the diazine ring and the top pyridyl ring is 23.4°. These changes are related to the expansion of the framework and pore volumes at 230 K, which provide more space for OX guest molecules. The tilted angle between the Hofmann layer and the Fe(II) plane is smaller. The two Au(I) atoms in the Hofmann layer are also reduced to 0.25 Å (Au1) and 0.23 Å (Au2), which indicates that the Hofmann layer is less undulated at a higher temperature.

4.2.2 Powder X-Ray Diffraction of **DzAu·OX**

Bulk polycrystalline powder of **DzAu·OX** was generated from **DzAu·EtOH** by using a fast-mixing method followed by a guest-exchange method. PXRD data were collected using a PANalytical X'Pert MPD outputting Cu-K_α radiation (λ = 1.54184 Å). VT-PXRD data were also collected to examine the temperature dependent lattice parameter changes. The experimental PXRD pattern at 100 K is well-matched with the simulated PXRD pattern from the SCXRD data (Figure 4.5(a)). Peak shifting was observed in the VT-PXRD data, which indicates a change in unit cell parameters due to thermal expansion (Figure 4.5(b)). These changes also agree with the SCXRD data. However, no SCO transition was observed in the VT-PXRD data, as no peak shifts to higher angles upon cooling and returning to lower angles upon heating occurred. That result matches both single crystal information and magnetism result.

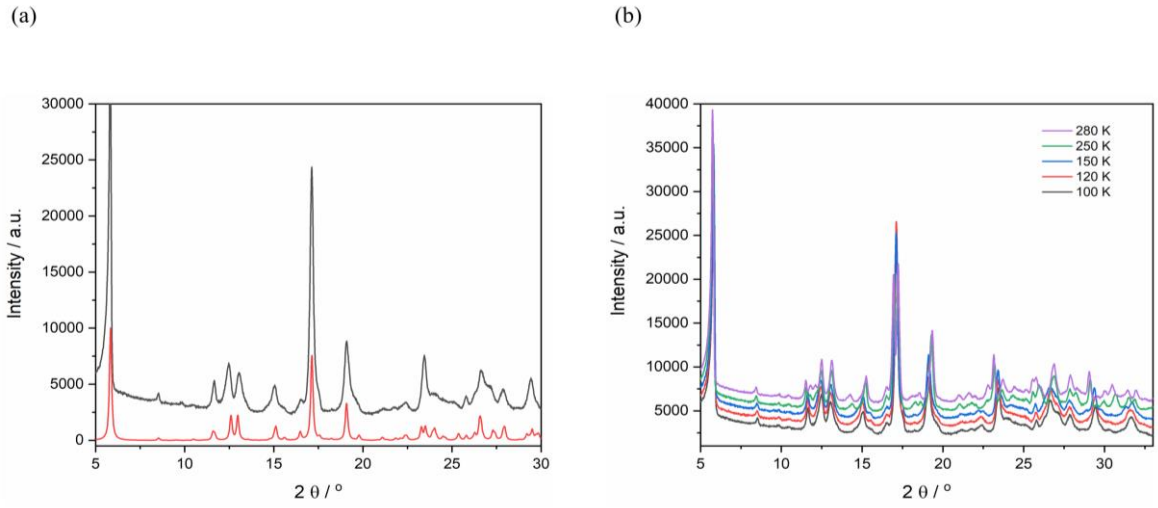

Figure 4.5: (a) Simulated PXRD pattern (red) and experimental PXRD pattern (black) of **DzAu·OX** at 100 K. (b) VT-PXRD patterns of **DzAu·OX** (100 K, 120 K, 150 K, 250 K, and 280 K).

4.2.3 Single Crystal X-ray Structure of **DzAu·MX**

A single crystal of **DzAu·MX** was generated from **DzAu·EtOH** using the same method as mentioned above. SCXRD data were collected at 100 K and 230 K. The single crystal structure of **DzAu·MX** adopts the monoclinic space group *I*2/*a* same as **DzAu·OX**. Similar to the prototypic framework, **DzAu·MX** is a 3D Hofmann-like framework but also contains MX guest molecules within the pores (Figure 4.6).

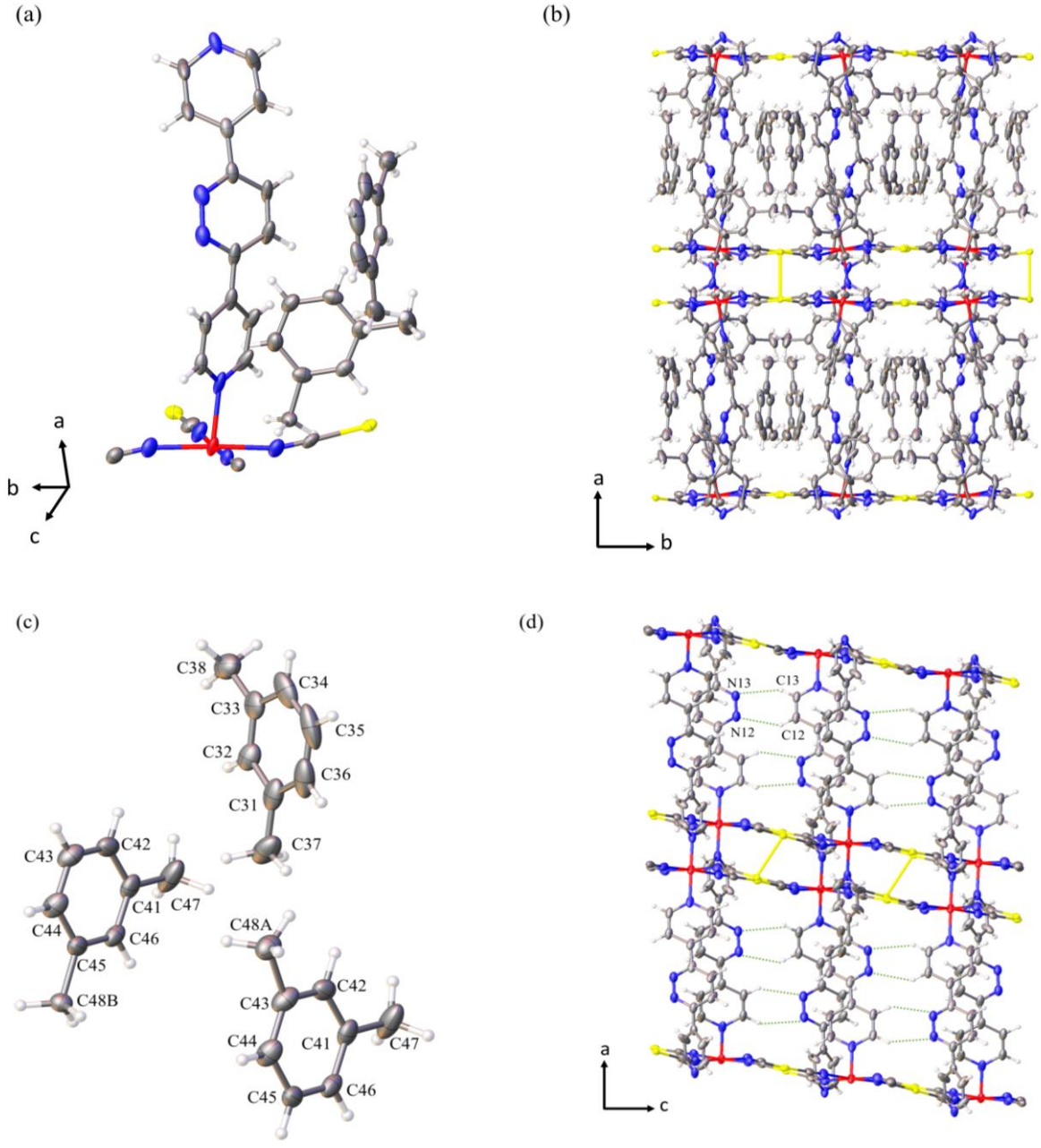

Figure 4.6: Single crystal X-ray structure of **DzAu·MX** at 100 K: (a) asymmetric unit with thermal ellipsoids set at 50% probability. (b) The framework structure is viewed down the *c*-axis. (c) MX guest molecules: one MX

guest (C31⋯C38) with occupancy of one; another MX shows disorder and was refined with two positions of $-CH_3$ labelled as C48A and C48B. (d) The framework structure is viewed down the *b*-axis with solvent molecules omitted for clarity. The inter-ligand C–H⋯N interactions are shown in green dashes. Atom colours: Fe (red), Au (yellow), N (blue), C (grey), and H (white).

The unit cell parameters *a*, *b*, and *c* in **DzAu·MX** at 100 and 230 K are shown in Table 4.3. The *a* and *c* parameters increase by 3% and 1%, respectively. Notably, NTE behaviour is observed in **DzAu·MX** along the *b* lattice with a slight decrease of 0.041 Å from 100 to 230 K. With increasing the temperature, β angle parameter decreases in 0.391º. The total volume of the **DzAu·MX** framework increases from 6511.5(3) to 6774.25(17) $Å^3$.

Table 4.3: The unit cell parameters of **DzAu·MX** at 100 K and 230 K.

Sample	Temperature / K	*a* / Å	*b* / Å	*c* / Å	β / º	Volume / $Å^3$
DzAu·MX	100	30.7776(8)	15.0014(4)	14.3529(3)	100.703(3)	6511.5(3)
	230	31.1211(4)	14.9604(2)	14.7889(2)	100.3124(14)	6774.25(17)

Structural analyses of **DzAu·MX** reveal the average bond distance of Fe–N is 2.178 Å at 230 K, indicating the Fe(II) sites are all in HS state. The average Fe−N bond length is 2.099 Å at 100 K indicating that the framework remains a *ca*. 60% HS configuration. The incomplete SCO behaviour observed from the crystal structure agrees with the magnetic susceptibility measurements. The octahedral geometry of Fe(II) sites (Σ(Fe) = 23.1°) is relatively high due to the high composition of the HS sites at 100 K. The Fe(II) sites is slightly less distorted with Σ(Fe) decreasing by 0.7° at 230 K. The average of four Fe−N−C angles on the equatorial position is almost identical with 171.2° at 100 K and 171.3° at 230 K.

Table 4.4: Comparison of selected structural parameters for **DzAu·MX** at 100 K and 230 K.

Parameter	DzAu·MX (100 K)	DzAu·MX (230 K)
<*d*(Fe−N)> / Å	2.099	2.178
Σ(Fe) / °	23.1	22.4
Au1⋯Au1 / Å	3.4207(6)	3.5182(6)
Au2⋯Au2 / Å	3.0745(6)	3.11519(10)
Average Fe–N–C / °	171.2	171.3
θ / °	87.5	89.3
Pore volume / $Å^3$	3005.3	3213.6
Percentage of the pore of unit cell volume / %	46.2	47.4
Torsion angle C1–Au1⋯Au1–C1/ °	85.6(3)	92.21(17)

The pillaring Dz ligand in **DzAu·MX** is bent due to encapsulation of the MX solvent, which forms

unique pore environments with pore features similar to **DzAu·OX** (Figure 4.7). The pore volume of **DzAu·MX** expands by 6.9% from 100 K to 230 K. The pore percentage of the unit cell volume of **DzAu·MX** also slightly increases from 46.2% to 47.4%. Two MX molecules were found per formula unit (Figure 4.6). One of the MX guests was refined in disorder showing two positions of the $–CH_3$ labelled as C48A and C48B. The possibility of two positions is approximately 50%. The ligand is twisted attributed to accommodate large guest molecules. The aromatic rings in the ligand are not coplanar. The distortion of the two pyridyl rings connected to the Fe(II) sites was shown. A higher degree of distortion was observed at higher temperatures (Figure 4.8). At 100 K, the dihedral angle between the two pyridyl rings connected to the Fe(II) site is 59.54°. At a higher temperature (230 K), the dihedral angle decreases to 50.58°. This is likely attributed to the expansion of the framework providing more space to accommodate an optimised ligand orientation.

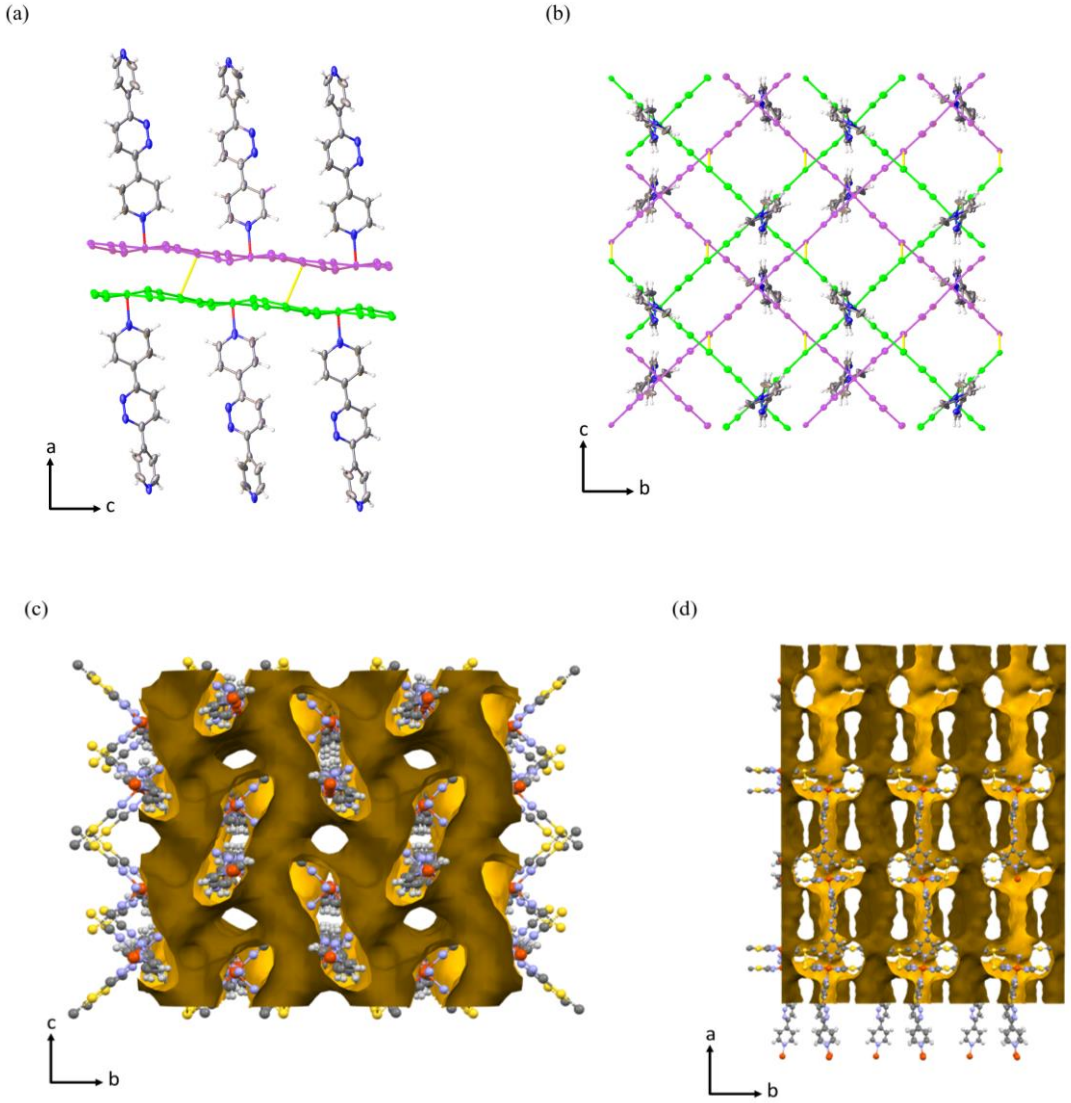

Figure 4.7: (a) Single structure of **DzAu·MX** at 100 K viewed down the *b*-axis and (b) viewed down the *a*-axis. Two neighbouring Hofmann layers with the upper layer shown in purple and the lower layer in green. The

two layers are connected with Au···Au interactions in yellow. (c) The calculated pore structure is shown projected along the *a*-axis and (d) viewed down the *c*-axis. Pore features are displayed in either yellow or brown and represent the outside or inside of the pores, respectively. Solvent molecules omitted for clarity. Atom colours: Fe (red), Au (yellow), N (blue), C (grey), and H (white).

The host–host C–H···N interactions are present between adjacent Dz pillaring ligands with distances of 3.400(6) Å (C11···N13) and 3.406(6) Å (C12···N12) at 100 K. The distances increase to 3.471(5) Å and 3.487(5) Å in C11···N13 and C12···N12, respectively at higher temperatures (230 K). The increase of host–host interactions is likely attributed to the thermal expansion of the structure. The inclined Au···Au interactions were shown in between the adjacent Hofmann layers. That causes a shift between the interpenetrated Hofmann layers observed down the *c*-axis. Thus, the layers are staggered (Figure 4.7(b)). The torsion angle of C1–Au1···Au1–C1 increases from 85.6(3)° at 100 K to 92.2(17)° at 230 K. The Hofmann layers are undulated. The distances of Au1 and Au2 to the Hofmann plane are 0.158 Å and 0.795 Å respectively at 100 K while increasing to 0.213 Å and 0.800 Å at 230 K. The Hofmann grids display close to the rectangular shape. The grids are more orthogonal at 230 K with θ = 89.3° compared with 87.5° at 100 K.

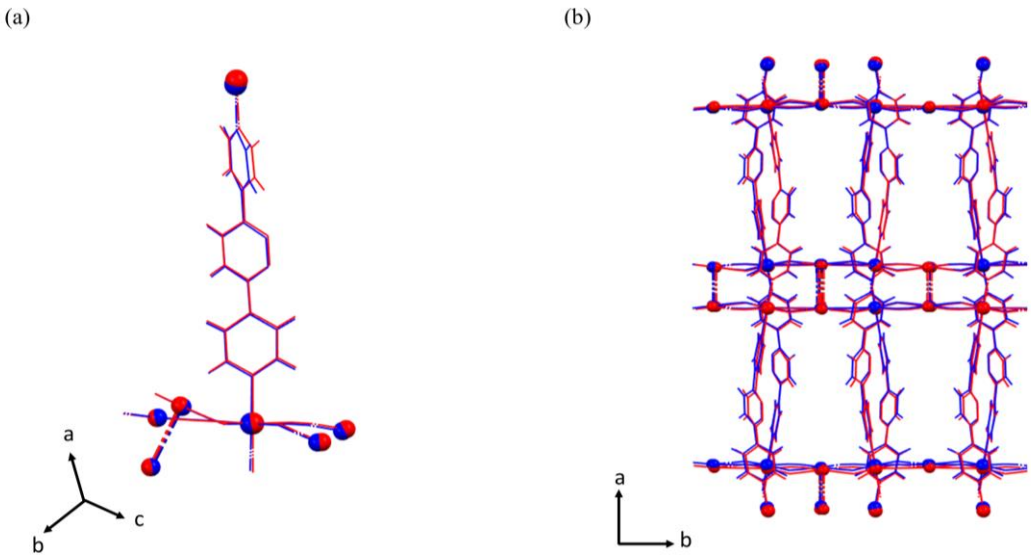

Figure 4.8: The overlay of single crystal X-ray structures of **DzAu·MX** at 100 K (blue) and 230 K (red) showing the different degrees of distortion of the ligand and undulation of the Hofmann layers: (a) asymmetric units and (b) view down the c-axis. Guest molecules have been omitted for clarity.

4.2.4 Powder X-Ray Diffraction of **DzAu·MX**

The bulk powder material of **DzAu·MX** was generated from **DzAu·EtOH** using a fast-mixing method followed by a guest-exchange method. PXRD measurements were conducted at the Australian Synchrotron on the PD beamline. The experimental PXRD pattern measured at room temperature was compared with the simulated PXRD pattern generated from the SCXRD data at 230 K. Most of the peaks are in agreement with each other with only a few peaks that are different. This is possibly caused by temperature discrepancies between the experimental and simulated patterns (Figure 4.9).

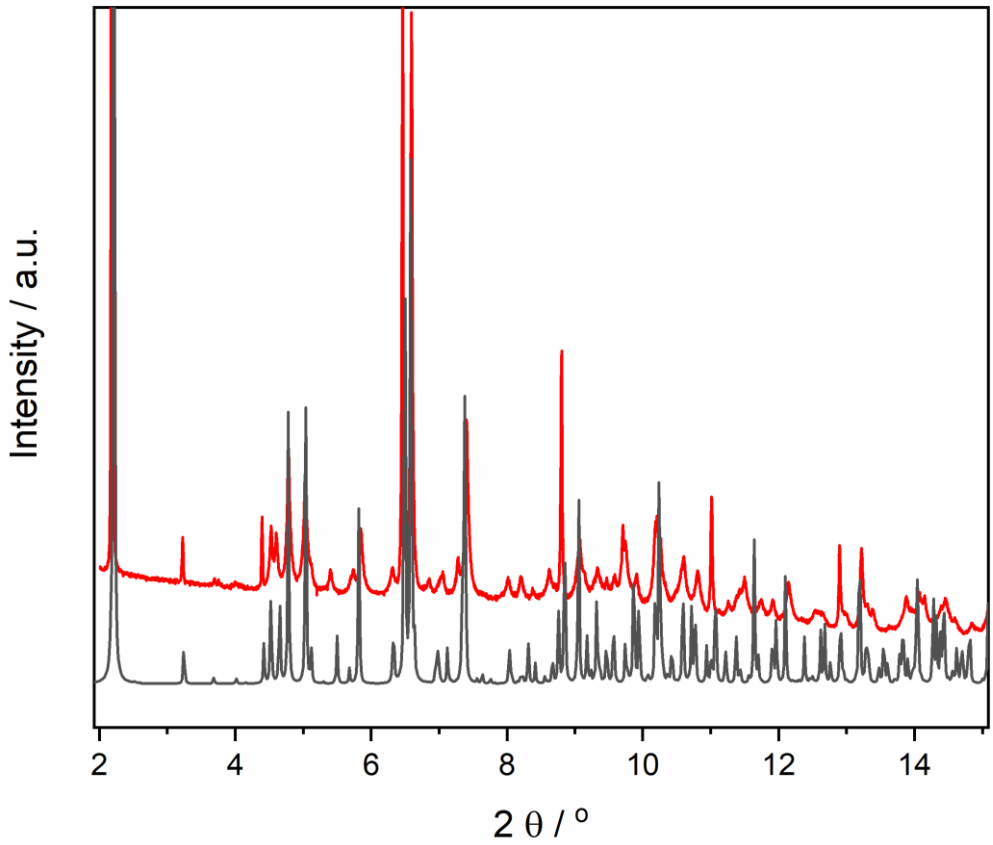

Figure 4.9: Simulated PXRD pattern (black) from crystal structure collected at 230 K and experimental PXRD pattern (red) of **DzAu·MX** at room temperature.

4.2.5 Single Crystal X-ray Structure of **DzAu·PX**

A single crystal of **DzAu·PX** was generated using the same method as mentioned above and SCXRD data were collected at 100, 155 and 230 K. The single crystal X-ray structure of **DzAu·PX** adopts the different space group (centrosymmetric monoclinic $P2_1/c$) as observed in the aforementioned materials. Compared to **DzAu·MX**, which shows NTE along the *b*-axis, all the unit cell parameters increase in **DzAu·PX** with increasing temperatures (Table 4.5). Therefore, with all the cell dimensions increasing at higher temperatures, the framework volume increases to 6850.07 $Å^3$ (+4.7%) at 230 K.

Table 4.5: The unit cell parameters of **DzAu·PX** at 100, 155 and 230 K.

Sample	Temperature / K	*a* / Å	*b* / Å	*c* / Å	*β* / º	Volume / Å^3
DzAu·PX	100	14.1378(9)	15.1132(10)	30.8906(16)	97.599(6)	6542.3(7)
	155	14.2684(3)	15.2505(3)	31.0517(5)	97.9344(16)	6692.1(2)
	230	14.4248(1)	15.3568(1)	31.2390(3)	98.107(1)	6850.07(9)

Two unique Fe(II) sites are present in the framework. At 100 K, the Fe1 and Fe2 sites adopt a LS and HS configuration with average Fe–N distances of 1.98 and 2.19 Å, respectively, with each unique site manifesting as alternating HS and LS strips in each Hofmann layer (Figure 4.10(d)). This phenomenon of two Fe(II) sites of varying spin states has been observed in other materials demonstrating incomplete SCO at low temperature.[11, 14-16] Thus, SCXRD data obtained for **DzAu·PX** is in agreement with the magnetic susceptibility results. The octahedral distortion parameters for Fe1 and Fe2 are appreciably different, with Fe2 (Σ(Fe2) = 24.40°) more than doubling that of the Fe1 site (Σ(Fe1) = 12.00°). In other words, Fe2 deviates further from an ideal octahedral geometry due to it adopting a HS state. The average angle of Fe(II) coordinated with the dicyanidoaurate linker in the Fe1 site (Fe1–N–C = 176.28°) is more linear than the Fe2 site (Fe2–N–C = 169.35°). This is attributed to the Fe1 site possessing a more rigidly octahedral coordination sphere in the LS state.

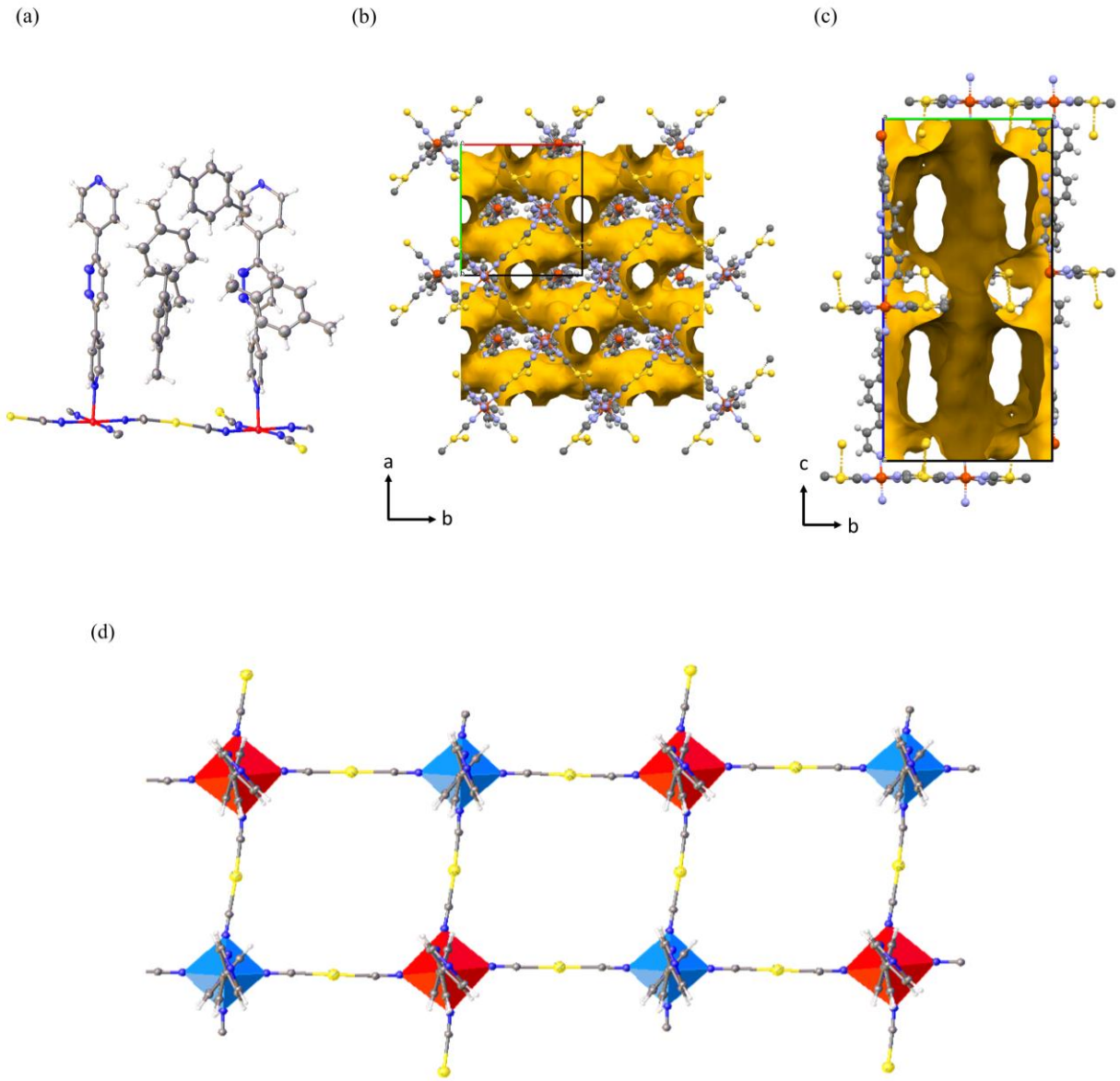

Figure 4.10: Single crystal X-ray structure of **DzAu·PX** at 100 K: (a) asymmetric unit with thermal ellipsoids set at 50% probability. (b) The calculated pore environment of the framework as viewed down the *c*-axis. Pore features coloured in yellow and brown represent the outside and inside regions, respectively. (c) View down the *a*-axis. (d) Two Fe(II) sites are represented as polyhedra, with LS and HS states coloured in blue and red, respectively. Solvent molecules are omitted for clarity. Atom colours: Fe (red), Au (yellow), N (blue), C (grey), and H (white).

The non-coplanar aromatic ring and undulated Hofmann layers were observed in this material, but the extents of twisting of the rings and undulation are slightly different at different temperatures. At 100 K, the aromatic rings in the ligand are distorted and the degree of ring distortion is slightly distinct in the two Fe sites. The angle between two pyridyl rings in Fe1 and Fe2 is 57.85° and 54.63° respectively. That angles are different for both Fe1 (57.98° at 155 K and 53.97° at 230 K) and Fe2 sites (54.42° at 155 K and 56.30° at 230 K). The tilted angle between the Hofmann plane and the Fe plane is 7.03° at

100 K. That tilted angle decreases to 5.67° at 155 K followed by an increase to 6.49° at 230 K. The average distance of gold atoms to the Hofmann plane remains unchanged at 0.11 Å when changing temperature. The host–host aurophilic interactions connect in between Hofmann layers with an average distance of 3.1539 Å at 100 K and gradually increase to 3.1919 Å at 230 K. The Au···Au interactions are inclined between the layers with a tilted angle of 76.0(6)° for the acute angle of Au3–Au2–C5 and 80.0(6)° for Au4–Au1–C4 at 100 K. Therefore, a shift of Hofmann grids also is observed. Another host–host C–H···N interactions are present between the adjacent pillar ligands with an average distance between C and N atom of 3.35 Å at 100 K and 3.41 Å at 230 K. The host–guest π···π interactions displayed between PX molecules and aromatic rings from the ligand are approximately identical at different temperatures with a distance of *ca*. 3.66 Å.

Table 4.6: Comparison of selected structural parameters for **DzAu·PX** at 100, 155 and 230 K.

Parameter	**DzAu·PX** (100 K)	**DzAu·PX** (155 K)	**DzAu·PX** (230 K)
<*d*(Fe1−N)> / Å	1.98	2.06	2.18
<*d*(Fe2−N)> / Å	2.19	2.19	2.18
Σ(Fe1) / °	12.00	14.40	16.44
Σ(Fe2) / °	24.40	21.40	21.62
Average Au···Au / Å	3.1539	3.1654	3.1919
Average Fe1–N–C / °	176.28	174.30	172.49
Average Fe2–N–C / °	169.35	169.00	169.47
θ / °	86.18	86.19	86.42
Pore volume / Å^3	2956	3063	3192

The pore size and features were calculated for **DzAu·PX** at 100 K (Figure 4.10). Two PX guest molecules per formula unit were found in the pores. The total pore volume at 100 K is 2955.54 Å^3, which corresponds to approximately 45.2% of the total unit cell volume. Two distinct pore environments are present in the framework; one has the dimensions of 9.6 × 6.7 Å and is more asymmetric, while the other has the dimensions 9.2 × 6.8 Å. The guest molecules in both pores participate in host–guest aromatic stacking interactions with the Dz ligand.

The pore size of **DzAu·PX** increases when heating from 155 to 230 K; the solvent accessible pore space increases from 45.8% to 46.6% due to thermal expansion. The crystal structures at each of the three temperatures (100, 155 and 230 K) were overlayed to achieve qualitative insight into the degree of any changes in bond lengths and distortions (Figure 4.11). The same two unique Fe(II) sites are present at higher temperatures. The average Fe1−N bond length increases to 2.06 Å at 155 K, indicating that Fe1 sites within the framework adopt a mixed 50% HS and LS state, while the Fe2 site remains in the HS state (<*d*(Fe2−N)> = 2.18 Å). The same alternating spin state patterning from the two Fe(II) sites is present at 155 K. At 230 K, both Fe(II) sites are in their HS states with both <*d*(Fe1−N)> and

<*d*(Fe2−N)> being 2.18 Å. The octahedral distortion parameter for Fe2 (Σ(Fe2) = 21.62°) remains higher than the same parameter for Fe1 (Σ(Fe1) = 16.44°) at this temperature. The Fe2 site has a larger octahedral distortion, which is attributed to its locking into the HS state. At 100 K, the two Fe(II) sites display opposite spin states with long-range ordered −HS−LS−HS−LS− patterning due to antiferroelastic interactions.[14, 17-19] Thus, only the Fe1 site undergoes a spin transition when cooling to 100 K resulting in incomplete two-step SCO.

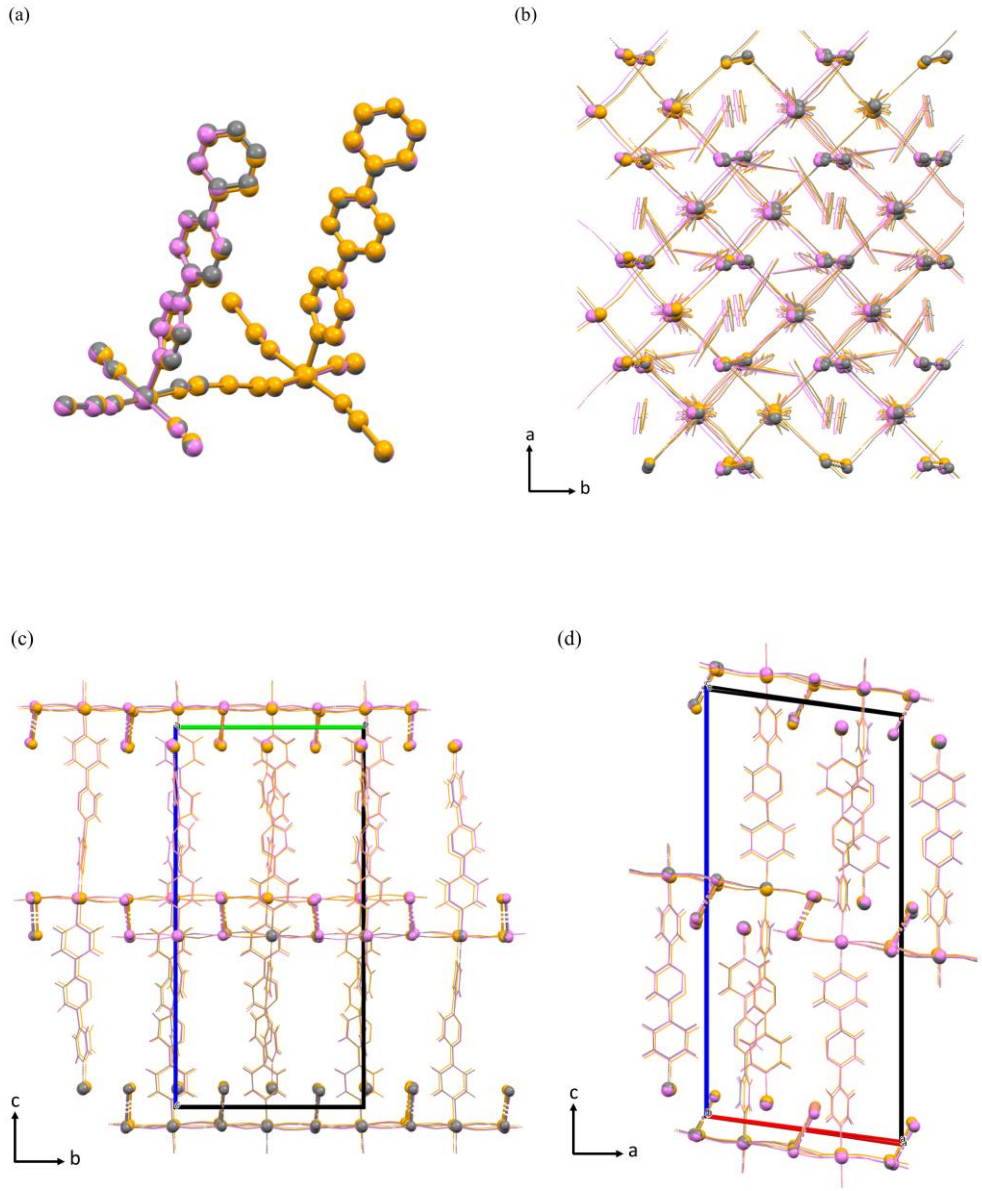

Figure 4.11: The overlay of single crystal X-ray structures of **DzAu·PX** at 100 K (orange), 155 K (grey), and 230 K (violet) of (a) the asymmetric units with hydrogen atoms omitted for clarity, (b) view down the *c*-axis, (c) view down the *a*-axis, and (d) view down the *b*-axis. The guest molecules have been omitted in (a), (c), and (d) for clarity.

4.2.6 Powder X-Ray Diffraction of **DzAu·PX**

PXRD data were collected from a PANalytical X'Pert MPD diffractometer out-putting Cu-K_α radiation. VT-PXRD data were also collected at several different temperatures (300–100–300 K) to examine changes in the unit cell parameters. These patterns are provided in Appendix Figure B.1. The experimental PXRD pattern of **DzAu·PX** at 100 K matches well with the simulated PXRD pattern obtained from SCXRD data. A contour plot of the diffraction peak positions as a function of temperature, showing two representative peaks, is provided as an example (Figure 4.12). Both peaks shift to higher 2θ angles upon cooling to 160 K in-line with the first expected spin transition. There is a second shift at 134 K indicating the second spin transition. The peaks shift back to lower angles in the heating process at 142 K and 166 K. Both peak positions return to their original values at 300 K. The peak evolution reveals two-step SCO behaviour, which is in agreement with the magnetic susceptibility data.

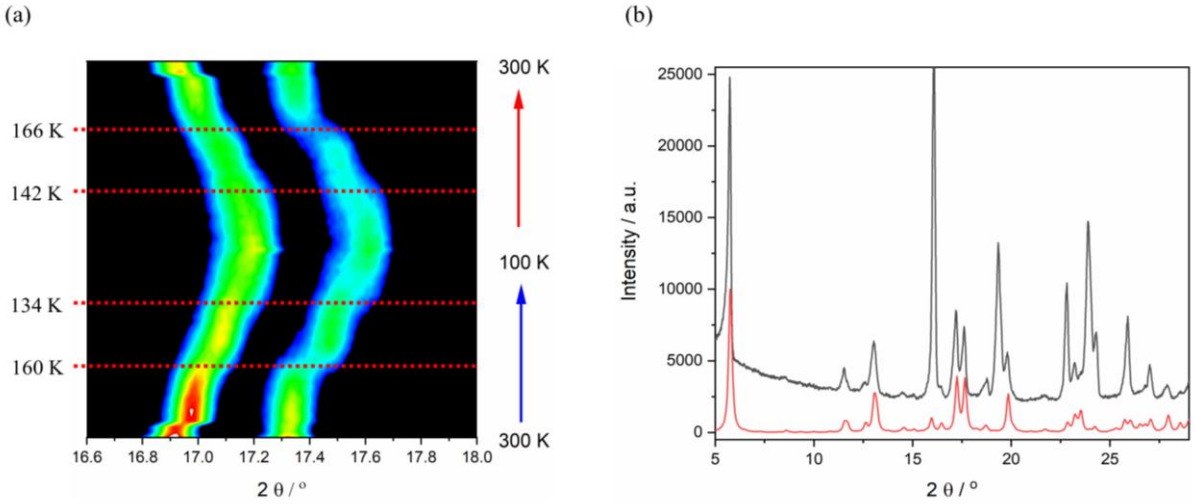

Figure 4.12: (a) VT-PXRD peak evolution of **DzAu·PX** showing the peak shifts due to the spin transition (2θ = 15.5–16.4°) over the temperature range 300–100–300 K. (b) Simulated pattern (red) obtained from the single crystal X-ray structure of **DzAu·PX**, and experimental PXRD pattern (black) of **DzAu·PX** at 100 K.

4.3 Spin Crossover Behaviours of DzAu·Guest (Guest = OX, PX, MX)

4.3.1 Variable Temperature Magnetic Susceptibility of **DzAu·OX**

DzAu·OX was characterised by magnetic susceptibility measurements, which revealed that the framework exhibits one-step and incomplete SCO. The magnetic susceptibility measurements for the materials in this chapter were collected at a scan rate of 2 K min^{-1} unless otherwise stated. The framework adopts a HS state until cooled to 113 K, which is then followed by a gradual decrease of the $\chi_M T$ value down to approximately 2.5 cm^3 K mol^{-1} at 60 K. The minimal decrease of the $\chi_M T$ value is predicted to be caused by zero-field splitting rather than SCO. Such behaviour has been observed in other SCO materials.[9, 20-21] There is a spike (red circle in Figure 4.13) present in the heating process at

249 K. This feature could be associated with a melting transition of OX solvent, which occurs at a similar temperature.

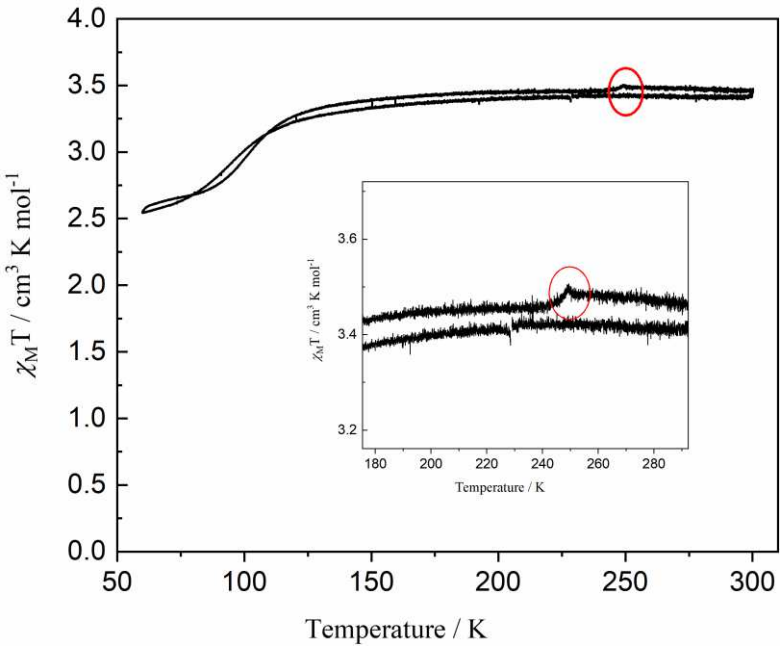

Figure 4.13: Variable temperature magnetic susceptibility plot of **DzAu·OX**. Inset: close-up of the 175–292 K region.

4.3.2 Variable Temperature Magnetic Susceptibility of **DzAu·MX**

Magnetic susceptibility data were collected for **DzAu·MX**. The framework exhibits one-step and hysteretic SCO (Figure 4.14). **DzAu·MX** remains in its HS state until approximately 135 K. The $\chi_M T$ value drops to 2.1 cm^3 K mol^{-1} at 60 K indicating about 40% of the Fe(II) sites transition to the LS state. The spin transition temperatures for the cooling and heating processes occur at 115 K and 122 K, respectively. There is a spike (in the red circle) present in the heating process at 228 K, which could be associated with the melting of MX (melting point of MX is *ca*. 225 K).

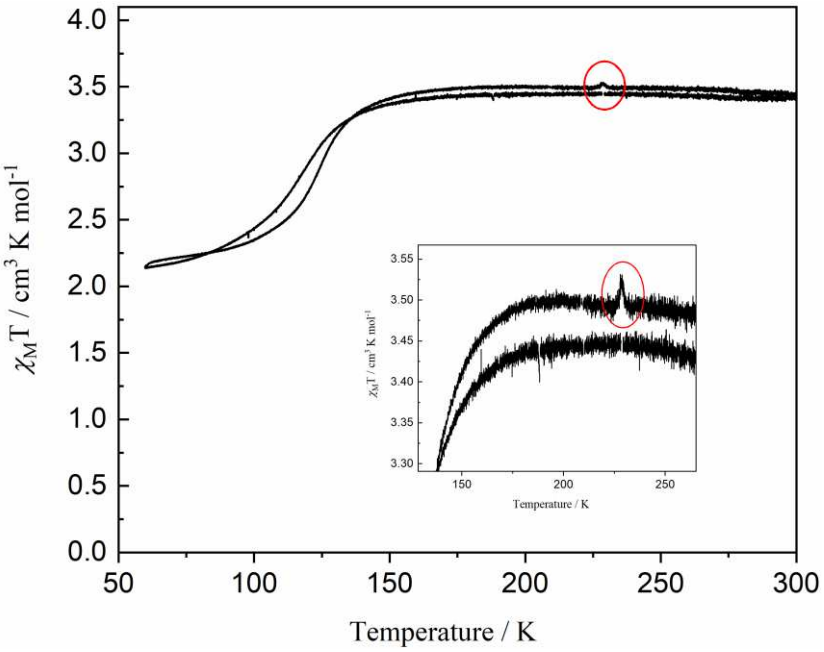

Figure 4.14: Variable temperature magnetic susceptibility plot of **DzAu·MX**. Inset: close-up of the 128–165 K region.

4.3.3 Variable Temperature Magnetic Susceptibility of **DzAu·PX**

DzAu·PX was characterised by variable temperature magnetic susceptibility and was revealed to undergo two-step, hysteretic, and incomplete SCO (Figure 4.15). The framework adopts its HS state until the temperature is reduced to approximately 184 K. The first spin transition of the cooling process has a critical temperature of 166 K, which is then followed by a second spin transition at 145 K. In the heating process, the first and second transition temperatures occur at 173 and 152 K, respectively. The $\chi_M T$ value reduces to 1.8 cm^3 K mol^{-1} at 60 K, indicating an approximately 50% HS lattice. The result matches the structural information obtained from SCXRD. Similarly, a spike feature in the heating process at 286 K may be associated with the melting of PX solvent (melting point of PX is 286 K).

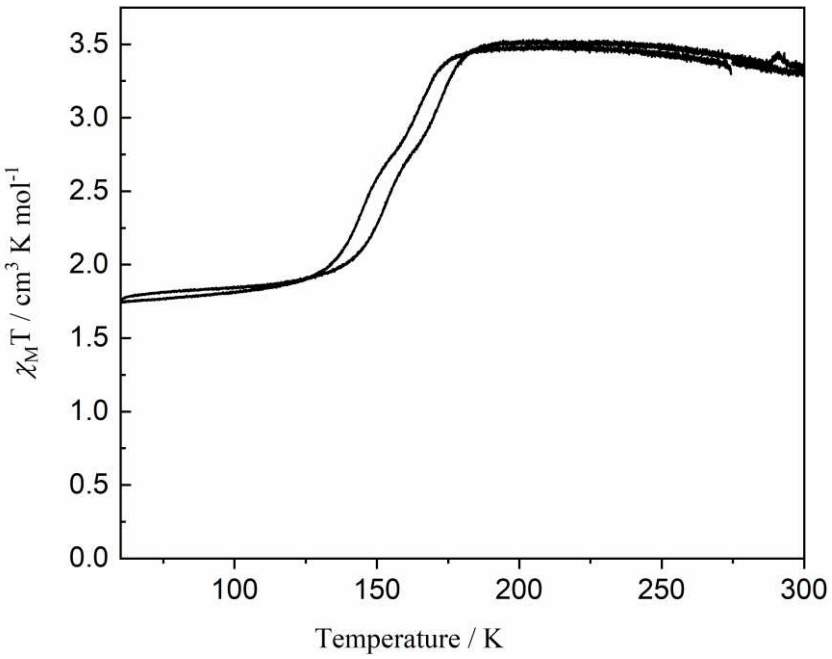

Figure 4.15: Variable temperature magnetic susceptibility plot of **DzAu·PX**.

4.4 Binary Xylene Mixtures on DzAu Framework

4.4.1 Powder X-ray Diffraction of DzAu Framework with Xylene Mixtures as Guests

To investigate the structures and absorption capability of the binary xylene guest molecules in DzAu frameworks, the bulk powder DzAu frameworks were washed with equimolar binary mixtures of the following xylenes: PX and MX (PM·50), PX and OX (PO·50), and MX and OX (MO·50). PXRD patterns of the single component xylene phases (**DzAu·PX**, **DzAu·MX**, and **DzAu·OX**) and phases with equimolar binary mixtures of xylenes (**DzAu·PM50**, **DzAu·PO50** and **DzAu·MO50**) were collected at the Australian Synchrotron at ambient temperature (Figure 4.16). The PXRD patterns of **DzAu·PX**, **DzAu·MX**, and **DzAu·OX** are similar with only a few small differences in peak positions and intensities due to their different lattice parameters and atomic positions. The PXRD patterns of three binary xylene mixed phases are also similar with only a few different peak features that are attributed to the frameworks showing combination features from mixed solvents. The patterns of **DzAu·PM50** and **DzAu·MO50** are almost identical in this respect, indicating that they possess similar structures.

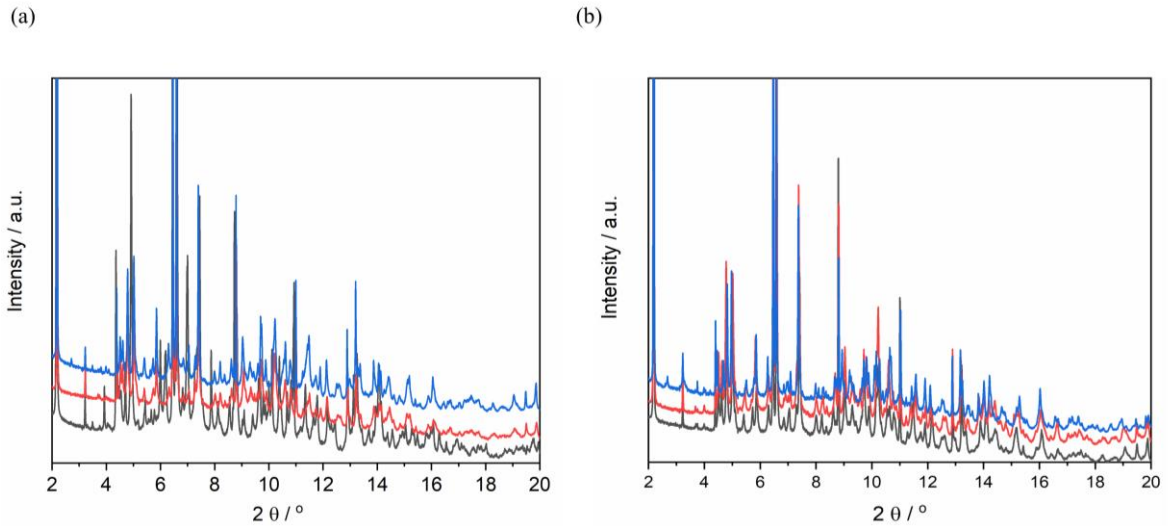

Figure 4.16: Comparison of PXRD patterns of (a) **DzAu·OX** (blue), **DzAu·MX** (red), and **DzAu·PX** (black). (b) The PXRD patterns of **DzAu·PM50** (black), **DzAu·MO50** (red), and **DzAu·PO50** (blue) were collected at room temperature between the range 2θ = 2–20°.

The equimolar binary xylene mixture frameworks were compared with the single-component xylene frameworks to provide insight into their structural differences. The peaks from **DzAu·PM50** are more similar to **DzAu·MX** than **DzAu·PX** (Figure 4.17(a)). This suggests that **DzAu·PM50** absorbed more MX than PX in the pores instead of a pure 1:1 mixture that it was soaked in. **DzAu·PM50**, therefore, appears to display some selectivity for MX over PX. The pattern of **DzAu·PO50** is more similar to **DzAu·OX**, which indicates that the material has a preference to absorb OX solvent in the pores (Figure 4.17(b)). The pattern of **DzAu·MO50** is similar to the patterns of **DzAu·MX** and **DzAu·OX** but with some minor peak shifts (Figure 4.17(c)).

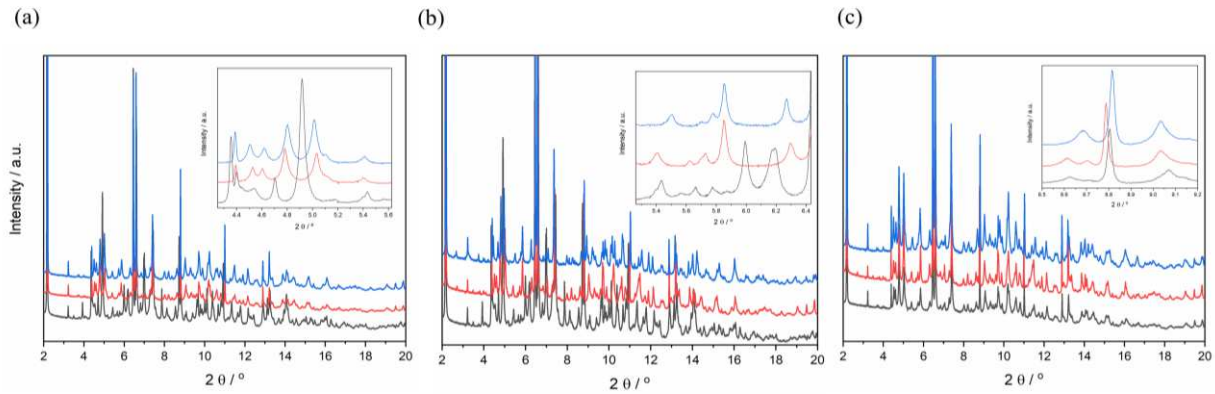

Figure 4.17: (a) PXRD patterns of **DzAu·PX** (black), **DzAu·MX** (red), and **DzAu·PM50** (blue). Inset: close-up of the region 2θ = 4.25–5.63°. (b) PXRD patterns of **DzAu·PX** (black), **DzAu·OX** (red), and

DzAu·PO50 (blue). Inset: close-up of the region 2θ = 5.26–6.43°. (c) PXRD patterns of **DzAu·MX** (black), **DzAu·OX** (red), and **DzAu·MO50** (blue). Inset: close-up of the region 2θ = 5.26–6.43°. All data were collected at room temperature.

4.4.2 Variable Temperature Magnetic Susceptibility of DzAu with a Binary Mixture Solvent of PX, OX, and MX

Magnetic susceptibility measurements were performed on **DzAu·PM50**, **DzAu·PO50**, and **DzAu·MO50** to study their potential SCO behaviours (Figure 4.18). **DzAu·PM50** displays one-step, hysteretic, and incomplete SCO with approximately 64% of the Fe(II) sites remaining in their HS state at 60 K. The spin transition temperature in the cooling process is $T_{½}\downarrow$ = 112 K while $T_{½}\uparrow$ is at 117 K. The SCO behaviour of **DzAu·PM50** is similar to **DzAu·MX** suggesting that MX solvent is predominantly within the pores rather than PX solvent. However, both **DzAu·PO50** and **DzAu·MO50** display no SCO behaviour, which are different from the materials with single-component of xylene.

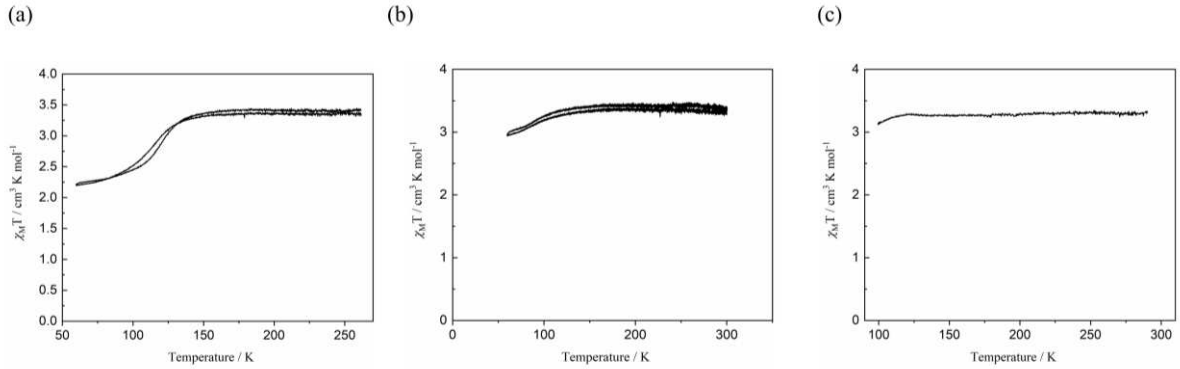

Figure 4.18: Variable temperature magnetic susceptibility plots of (a) **DzAu·PM50**, (b) **DzAu·PO50**, and (c) **DzAu·MO50**.

4.4.3 NMR of Various Guest Components within the Frameworks

NMR was performed on these MOFs to analyse the number of xylenes adsorbed in the pores. The sample preparation and measurements followed the same procedures as outlined in Chapter 3 Section 3.4.3. **DzAu·MO50** with MX/OX in the pores shows roughly the same ratio of mixtures as the pure solvent (Table 4.7). Noticeably, **DzAu·PO50** has predominantly OX solvent over PX within the pores. This shows that the DzAu framework is selective for OX over PX solvent. Similar behaviour was also observed in **DzAu·PM50**, which has an overwhelming preference for MX over PX. This indicates that the DzAu material can also be used to select between PX and MX. In order to further investigate the selectivity with a very high proportion of PX solvent, the two frameworks **DzAu·PM91** and

DzAu·PO91 with PX/MX = 9:1 and PX/OX = 9:1, respectively, were prepared by using the above mentioned guest exchange method. NMR results show that when the DzAu framework was exchanged with a very high concentration of PX solvent, there was no observed selectivity of two solvent PX/MX = 9:1 and PX/OX = 9:1. The ratio of different xylenes in the pores is approximately the same as the ratio of pure solvent mixtures.

Table 4.7: The ratio of the pure binary solvent mixture and binary solvent mixture within the DzAu framework.

Pure solvent	Ratio	MOFs	Ratio
MO·50	0.492	**DzAu·MO50**	0.484
PO·50	0.492	**DzAu·PO50**	0.184
PM·50	0.476	**DzAu·PM50**	0.089
PM·91	0.898	**DzAu·PM91**	0.891
PO·91	0.901	**DzAu·PO91**	0.966

4.5 Discussion

DzAu frameworks with absorbed xylene isomers possess different unit cell parameters compared to the prototypical framework (Table 4.8). The frameworks with xylenes in the pores all have a larger cell volume than **DzAu·EtOH** due to the absorption of the larger guest molecule. None of the xylene-absorbed frameworks displays complete SCO. This is attributed to the larger guest sizes and different host–guest interactions which affect cooperativity.

Table 4.8: Comparison of the unit cell parameters of **DzAu·OX**, **DzAu·MX**, **DzAu·PX** and **DzAu·EtOH**.

Sample	Temperature / K	*a* /Å	*b* / Å	*c* /Å	*β* / º	Volume / Å^3
DzAu·OX	100	14.4500(5)	15.2703(5)	31.0588(8)	103.062(3)	6676.0(4)
	230	14.6606(4)	15.1224(3)	31.1302(6)	101.090(2)	6772.8(3)
DzAu·MX	100	30.7776(8)	15.0014(4)	14.3529(3)	100.703(3)	6511.5(3)
	230	31.1211(4)	14.9604(2)	14.7889(2)	100.3124(14)°	6774.25(17)
DzAu·PX	100	14.1378(9)	15.1132(10)	30.8906(16)	97.599(6)	6542.3(7)
	230	14.4248(1)	15.3568(1)	31.2390(3)	98.107(1)	6850.07(9)
DzAu·EtOH	90	14.2256(2)	14.4645(3)	30.4429(5)	96.104(2)	6228.60(19)
	250	15.0135(10)	14.9245(8)	31.4557(17)	98.206(6)	6976.1(7)

The **DzAu·OX** framework adopts the same space group as the prototypical framework and

contains one unique Fe(II) site. The **DzAu·OX** framework also has the largest lattice parameters among the prototypical framework and other xylene encapsulated frameworks. Different from the prototypical material, no spin transition is observed in **DzAu·OX** with all the Fe(II) sites in the framework remaining in the HS state at 100 K. Similar to **TzAu·OX** framework displaying PTE and NTE along two axes in Hofmann layers, **DzAu·OX** also shows PTE along the *a*-axis and a small extent of NTE along the *b*-axis. **TzAu·OX** shows anomalous lattice motion with increasing θ angle by decreasing temperatures. However, opposite as **TzAu·OX**, θ increases with increasing temperatures in **DzAu·OX**. The anomalous NTE behaviour in the framework is likely associated with the change of octahedral distortion around the local FeN_6 site and Fe–N–C angles in the equatorial coordination sites. The extent of NTE is small in **DzAu·OX** possibly attributed to the no spin transition occurring. Thus, the change of lattice flexing and Fe(II) sites distortion is mainly caused by thermal motion. Unlike **TzAu·OX** showing overlayed rhombic Hofmann grids, the Hofmann grids in **DzAu·OX** are staggered. θ in **DzAu·OX** is slightly lower than 90º. The trend of θ by increasing temperature is orthogonal. That causes a small increase of θ at higher temperatures.

With the encapsulation of MX from EtOH in the pores, the space group remains unchanged. The structural parameters of **DzAu·MX** are similar to **DzAu·OX**. The overall unit cell volume of **DzAu·MX** is smaller than **DzAu·OX** at 100 K but a slightly larger volume of **DzAu·MX** was observed at 230 K. That is, the volume of **DzAu·OX** increases by 1.4% while the volume expansion of **DzAu·MX** is by 4.0%, which is approximately three times that of **DzAu·OX**. **DzAu·MX** has smaller β angle parameters at both temperatures than **DzAu·OX**. Similar to the **DzAu·OX** framework, **DzAu·MX** also shows slight NTE along the *b*-axis and β angle. A slightly larger degree of θ change between 100 and 230 K is observed in **DzAu·MX** ($\Delta\theta$ = 1.8º) than in **DzAu·OX** ($\Delta\theta$ = 1.4º). The change of θ is associated with lattice flexing and Fe(II) sites distortion. As **DzAu·MX** undergoes an incomplete one-step SCO, a larger extent of lattice motion induced by spin transition is observed resulting in a more obvious change of θ. Fe(II) sites change to about 60% HS state at 100 K, which matches with the incomplete single-step SCO behaviour observed from the magnetic susceptibility data.

With the encapsulation of PX from EtOH in the pores, the space group changed. The overall volume of the **DzAu·PX** framework is larger than **DzAu·EtOH** at 100 K. However, the *a*-axis in **DzAu·PX** is slightly shorter than in **DzAu·EtOH** at that temperature. **DzAu·PX** has two Fe(II) sites with distinct behaviour. There is one Fe(II) site that remains unchanged while another displays SCO. The increase in unit cell parameters with increasing temperatures in the **DzAu·PX** framework is likely due to one of the Fe(II) sites (Fe2) remaining in the HS state. Thus, there is no spin transition at this Fe(II) site and PTE causes the lattice increase. There is likely to be some SCO-induced NTE in the Fe1 site. However, PTE from the Fe2 site possesses a greater influence and compensates the NTE, which causes an overall expansion of the lattice parameters. The average Fe1–N–C angle becomes close to linear in the LS state than in the HS state indicating that a spin transition occurred, while the Fe2–N–C

angle is almost unchanged with changing temperature indicating that Fe2 remains in its HS state. The two Fe(II) sites adopt the same spin state due to antiferroelastic interactions.[22-24] The spin transition pathway across [Fe1−Fe2] for **DzAu·PX** is [HS−HS] ↔ [HS−$HS_{0.5}$] ↔ [HS−LS], which is in agreement with the magnetic susceptibility data which shows two-step, hysteretic, and incomplete SCO.

The SCO behaviours of **DzAu·OX**, **DzAu·MX**, and **DzAu·PX** are distinguished by either displaying no spin transitions, gradual one-step SCO, and gradual two-step SCO, respectively. The latter two in this case still both display incomplete SCO. SCO behaviour is related to the properties of the guest and subsequent host–guest interactions within the framework, which can affect the resulting cooperativity.[12, 25-27] Although the physical properties of the three xylene isomers are similar, their influence on the SCO behaviour in each guest-exchanged framework is different. This is attributed to the slightly different xylene molecular size and supramolecular interactions between the host framework. Each framework discussed here shows weak cooperativity by either there being no SCO or no abrupt spin transition. This is analogous to what may be observed in solution-state SCO systems.[28-30] When the guest molecules are exchanged from EtOH to xylene isomers, the degree of cooperativity decreases, which is attributed to the larger size guest molecules weakening propagation between the SCO centres. Based on the results from Chapter 3, the SCO behaviours are different between the TzAu and DzAu frameworks even though the same guest molecules are in the group. This suggests that the communication between the SCO centres is influenced by the framework structure. The relatively higher degree of disorder in the framework and higher distortion of the local FeN_6 sites may lessen the communication.

In the study of binary xylene components absorbed in the pores, structural differences were observed due to changes in the individual xylene isomer components. With the comparison of the PXRD patterns, the **DzAu·PM50** pattern is more similar to the **DzAu·MX** pattern, which implies that uptake within the pores favours MX over PX. Similarly, the preference for OX solvent over PX is also suggested based on the pattern of **DzAu·PO50**. Although quantitative analysis of the guest molecules may not be feasible from the PXRD data, qualitative information on the relative amount of isomer components in the framework, even if the differences are subtle, can be obtained by high-resolution data.

The SCO behaviours of the guest-exchanged frameworks with mixtures of different xylenes provide evidence for the preferential uptake of certain xylene isomers. The selectivity information of the isomer uptake was gained from both PXRD, magnetic susceptibility, and NMR analysis. Unfavourable adsorption of PX in **DzAu·PM50** or **DzAu·PO50** could be due to the longer molecular length of PX, which hinders its adsorption into the pores.

4.6 Conclusions and Future work

DzAu 3D Hofmann-like frameworks incorporating a single xylene isomer as a guest molecule (**DzAu·MX**, **DzAu·PX**, **DzAu·OX**) were synthesised. Each framework possesses the same 3D Hofmann-like topology similar to the parent guest-free framework. Both **DzAu·OX** and **DzAu·MX** adopts the same space group with one unique Fe(II) site as the prototypical framework (monoclinic *C*2/*c*), while **DzAu·PX** adopt the monoclinic $P2_1/c$ space group with two unique Fe(II) sites in the asymmetric unit. The Dz ligand in the **DzAu·OX** framework is more twisted than in **DzAu·EtOH** due to the larger size of OX compared to EtOH. Because of the larger molecules within the framework, the octahedral geometry in **DzAu·OX** is more distorted and the Hofmann layers are more undulated to accommodate the OX guest. There are two distinct pores in **DzAu·OX** and the shape of the two pores is different but almost the same size. As the Au···Au interactions are inclined, a displacement is shown in between the neighbouring Hofmann layers that are unlike the Tz-based framework with overlayed rhombic Hofmann grids. The **DzAu·MX** framework also contains a disordered ligand, tilted Au···Au interactions, and undulated Hofmann layers. **DzAu·MX** undergoes SCO to a 40% LS state at 100 K. There is a small degree of NTE with a similar trend of θ angle change by temperature as in **DzAu·OX**. **DzAu·PX** contains two Fe(II) sites; one undergoes SCO while the other remains in its HS state. **DzAu·PX** exhibits PTE along each lattice direction. The overall θ angle is almost unchanged. The Fe1–N–C angle becomes more linear in the cooling process. However, the change of Fe2–N–C angle is not monotonic, which has the smallest angle at 155 K and the largest angle at 230 K. This indicates that the two Fe(II) sites exhibit different spin transition behaviours. Therefore, it is likely that the two distinct Fe(II) sites in **DzAu·PX** display either NTE or PTE but overall there is PTE. Therefore, this system provides a pathway for designing materials that can exhibit both NTE and PTE behaviours. Thus, if the NTE and PTE behaviours could be tuned to be equal, the overall thermal expansion behaviour of the material could be designed to exhibit no lattice parameter changes with changing temperature, i.e., zero thermal expansion (ZTE).[31-35]

The single crystal X-ray structures of varied binary xylene and trinary xylene frameworks have not been generated. Future work could involve an investigation into the mixed xylene framework structures as it would be interesting to achieve further insight into the detailed structural differences caused by varied guest components. For example, the extent of ligand disorder, degree of ligand bending, distortion of Fe(II) centres, and flexing of the Hofmann grid. This will help to better understand the relationship between structural properties and guest uptake capabilities. In order to understand the bond stretching and vibrational motion occurring during the spin transition, variable temperature vibrational spectroscopy could be performed. *In situ* vibrational spectroscopy with a gradually changing ratio of mixed guests could be beneficial to observe the dynamic flexing mechanism in the framework. Experimental structural measurements with a combination of DFT and molecular dynamics (MD) simulations could aid in providing insight into molecular mechanisms occurring in frameworks

involving solvent uptake and the position of mixed guests within the pores. Additionally, computational work could aid in simulating selectivity differences of mixed xylenes in the framework.

The uptake capability of the vapour phase of xylene isomers in the DzAu system is worth further investigation. Several studies already exist concerning vapour phase xylene uptake in other MOF systems,[36-39] yet none have been performed in SCO materials. The partial pressures are changed by varying the composition of vapour phase xylenes, which influences the SCO behaviour and uptake capability. The selectivity of the vapour phase could be different from the liquid phase.

The complete conversion to the LS state is unfavourable in the frameworks that absorb either single- or binary- components of xylenes. SCO behaviours with the combination of the results in Chapter 3 are influenced by the host–host and host–guest interactions. The sizes and positions of the guests in the pores, and the degree of distortion of the framework, all influence the SCO behaviours. The magnetic susceptibility results indicate that these materials are very sensitive to subtle differences in the guest molecules. It would be interesting to systematically study the SCO response of this framework system with other guests such as polycyclic aromatic hydrocarbons and chiral guests. This would ultimately provide a deeper understanding of the effect of guest-dependent SCO behaviour in this system, which could be extended towards more in-depth detection or sensing studies of guest molecules.

4.7 References

1. Furukawa, H.; Cordova, K. E.; O'Keeffe, M.; Yaghi, O. M., *Science* **2013,** *341* (6149), 1230444.

2. Rowsell, J. L. C.; Yaghi, O. M., *Microporous Mesoporous Mater.* **2004,** *73* (1-2), 3-14.

3. Xue, S.; Rotaru, A.; Garcia, Y., *Hyperfine Interact.* **2019,** *240* (1).

4. Matouzenko, G. S.; Bousseksou, A.; Lecocq, S.; Van Koningsbruggen, P. J.; Perrin, M.; Kahn, O.; Collet, A., *Inorg. Chem.* **1997,** *36* (25), 5869-5879.

5. Cirera, J.; Paesani, F., *Inorg. Chem.* **2012,** *51* (15), 8194-8201.

6. Clements, J. E.; Price, J. R.; Neville, S. M.; Kepert, C. J., *Angew. Chem. Int. Ed.* **2014,** *53* (38), 10164-10168.

7. Li, J.-Y.; He, C.-T.; Chen, Y.-C.; Zhang, Z.-M.; Liu, W.; Ni, Z.-P.; Tong, M.-L., *J. Mater. Chem. C.* **2015,** *3* (30), 7830-7835.

8. Southon, P. D.; Liu, L.; Fellows, E. A.; Price, D. J.; Halder, G. J.; Chapman, K. W.; Moubaraki, B.; Murray, K. S.; Létard, J.-F.; Kepert, C. J., *J. Am. Chem. Soc.* **2009,** *131* (31), 10998-11009.

9. Halder, G. J.; Kepert, C. J.; Moubaraki, B.; Murray, K. S.; Cashion, J. D., *Science* **2002,** *298* (5599), 1762.

10. Li, B.; Wei, R.-J.; Tao, J.; Huang, R.-B.; Zheng, L.-S.; Zheng, Z., *J. Am. Chem. Soc.* **2010,** *132* (5), 1558-1566.

11. Murphy, M. J.; Zenere, K. A.; Ragon, F.; Southon, P. D.; Kepert, C. J.; Neville, S. M., *J. Am. Chem. Soc.* **2017,** *139* (3), 1330-1335.

12. Neville, S. M.; Halder, G. J.; Chapman, K. W.; Duriska, M. B.; Moubaraki, B.; Murray, K. S.; Kepert, C. J., *J. Am. Chem. Soc.* **2009,** *131* (34), 12106-12108.

13. Clements, J. E.; Price, J. R.; Neville, S. M.; Kepert, C. J., *Angew. Chem. Int. Ed.* **2016,** *55* (48), 15105-15109.

14. Ahmed, M.; Zenere, K. A.; Sciortino, N. F.; Arachchige, K. S. A.; Turner, G. F.; Cruddas, J.; Hua, C.; Price, J. R.; Clegg, J. K.; Valverde-Muñoz, F. J.; Real, J. A.; Chastanet, G.; Moggach, S. A.; Kepert, C. J.; Powell, B. J.; Neville, S. M., *Inorg. Chem.* **2022,** *61* (17), 6641-6649.

15. Zenere, K. A.; Duyker, S. G.; Trzop, E.; Collet, E.; Chan, B.; Doheny, P. W.; Kepert, C. J.; Neville, S. M., *Chem. Sci.* **2018,** *9* (25), 5623-5629.

16. Milin, E.; Patinec, V.; Triki, S.; Bendeif, E.-E.; Pillet, S.; Marchivie, M.; Chastanet, G.; Boukheddaden, K., *Inorg. Chem.* **2016,** *55* (22), 11652-11661.

17. Cruddas, J.; Powell, B. J., *Inorg. Chem. Front.* **2020,** *7* (22), 4424-4437.

18. Cruddas, J.; Powell, B. J., *J. Am. Chem. Soc.* **2019,** *141* (50), 19790-19799.

19. Paez-Espejo, M.; Sy, M.; Boukheddaden, K., *J. Am. Chem. Soc.* **2016,** *138* (9), 3202-3210.

20. Benaicha, B.; Van Do, K.; Yangui, A.; Pittala, N.; Lusson, A.; Sy, M.; Bouchez, G.; Fourati, H.; Gómez-García, C. J.; Triki, S.; Boukheddaden, K., *Chem. Sci.* **2019,** *10* (28), 6791-6798.

21. Martínez, V.; Gaspar, A. B.; Muñoz, M. C.; Ballesteros, R.; Ortega-Villar, N.; Ugalde-Saldívar, V. M.; Moreno-Esparza, R.; Real, J. A., *Eur. J. Inorg. Chem* **2009,** *2009* (2), 303-310.

22. Liu, F.-L.; Li, D.; Su, L.-J.; Tao, J., *Dalton Trans.* **2018,** *47* (5), 1407-1411.

23. Liu, J.; Gao, Y.; Wang, T.; Xue, Q.; Hua, M.; Wang, Y.; Huang, L.; Lin, N., *ACS Nano* **2020,** *14* (9), 11283-11293.

24. Nishino, M.; Boukheddaden, K.; Miyashita, S.; Varret, F., *Phys. Rev. B* **2003,** *68* (22).

25. Andreeva, A. B.; Le, K. N.; Kadota, K.; Horike, S.; Hendon, C. H.; Brozek, C. K., *Chem. Mater.* **2021,** *33* (21), 8534-8545.

26. Zenere, K. A.; Duyker, S. G.; Trzop, E.; Collet, E.; Chan, B.; Doheny, P. W.; Kepert, C. J.; Neville, S. M., *Chem. Sci.* **2018,** *9* (25), 5623-5629.

27. Kambara, T., *Chem. Phys.* **1981,** *74* (8), 4557-4565.

28. Murray, K. S.; Kepert, C. J., Cooperativity in Spin Crossover Systems: Memory, Magnetism and Microporosity. In *Top. Curr. Chem.*, Springer Berlin Heidelberg: pp 195-228.

29. Gütlich, P.; Hauser, A.; Spiering, H., *Angew. Chem., Int. Ed. Engl.* **1994,** *33* (20), 2024-2054.

30. Gütlich, P.; Garcia, Y.; Goodwin, H. A., *Chem. Soc. Rev.* **2000,** *29* (6), 419-427.

31. Phillips, A. E.; Halder, G. J.; Chapman, K. W.; Goodwin, A. L.; Kepert, C. J., *J. Am. Chem. Soc.* **2010,** *132* (1), 10-11.

32. Margadonna, S.; Prassides, K.; Fitch, A. N., *J. Am. Chem. Soc.* **2004,** *126* (47), 15390-15391.

33. Sleight, A., *Nature* **2003,** *425* (6959), 674-676.

34. Mohn, P., *Nature* **1999,** *400* (6739), 18-19.

35. Ren, Z.; Zhao, R.; Chen, X.; Li, M.; Li, X.; Tian, H.; Zhang, Z.; Han, G., *Nat. Commun.* **2018,** *9* (1).

36. Kim, S.-I.; Lee, S.; Chung, Y. G.; Bae, Y.-S., *ACS Appl. Mater. Interfaces.* **2019,** *11* (34), 31227-31236.

37. Bej, S.; Das, R.; Murmu, N. C.; Banerjee, P., *Inorg. Chem.* **2020,** *59* (7), 4366-4376.

38. Finsy, V.; Verelst, H.; Alaerts, L.; De Vos, D.; Jacobs, P. A.; Baron, G. V.; Denayer, J. F. M., *J. Am. Chem. Soc.* **2008,** *130* (22), 7110-7118.

39. Peralta, D.; Barthelet, K.; Pérez-Pellitero, J.; Chizallet, C.; Chaplais, G.; Simon-Masseron, A.; Pirngruber, G. D., *J. Phys. Chem. C* . **2012,** *116* (41), 21844-21855.

Chapter 5

Controlling Spin Crossover Behaviours and Structural Properties of Tz- and Dz-based Frameworks *via* Tuning Cyanidometallates

5.1 Overview

A key challenge in SCO materials is to understand the ligand effects on SCO behaviour, which can guide the rational design of materials with controllable SCO behaviours. The tunable SCO phenomenon has been achieved by modifying the metal centres,[1-2] the ligands,[3-4] the counterions[5] and guest molecules[6-7]. One of the methods to tune the SCO behaviours is by using the molecular alloy strategy, which changes the composition of the ligands or metals.[8] The insight into the ligand field strength and framework structure can provide a deeper understanding of the occurrence of SCO and the role of cooperativity.

This chapter focuses on the effect of the cyanidometallate linkers on the structural and magnetic properties of the frameworks. The materials of interest consist of single or mixed components of cyanidometallate linkers, which were synthesised to explore the effect of the metal modulation and SCO behaviours. Therefore, wisely designing materials with controllable properties can be achieved.

Herein, we first synthesised a single component cyanidometallated linker framework $[Fe(Tz)(Ag(CN)_2)_2]$ to investigate the temperature-induced SCO behaviours, SCO sites distortion, intra- and inter-molecular interactions and lattice motions. The framework was also compared with its Au analogue **TzAu·EtOH** to analyse the influence of cyanidometallate linkers on both structure and SCO behaviours.

To compare ligand effects to the structures and properties, a systematic study of the effect of cyanidometallate linkers on SCO behaviours in Dz-based frameworks is discussed. The synthesis and characterisation of framework materials $[Fe(Dz)(Ag(CN)_2)_2]$, $[Fe(Dz)(H_2O)_2Pt(CN)_4]\cdot 2(H_2O)$ and $[Fe(Dz)(H_2O)_2Pd(CN)_4]\cdot 2(H_2O)$ were performed to analyse the structural and magnetic properties. $[Fe(Dz)(Ag(CN)_2)_2]$ displays a 3D Hofmann-like topology analogous to its Au analogue $[Fe(Dz)(Au(CN)_2)_2]$. However, the SCO behaviours of these two materials are distinct. This chapter details the single crystal structure of $[Fe(Dz)(Ag(CN)_2)_2]$ and compares the differences between the Au analogue to understand the relationship between SCO behaviours and structures. The structural details of $[Fe(Dz)(Ag(CN)_2)_2]$ under variable temperatures explain the changes in structure distortion, host–host C–H···N interactions and argentophilic interactions. Moreover, $[Fe(Dz)(Ag(CN)_2)_2]$ and $[Fe(Tz)(Ag(CN)_2)_2]$ were compared to study the effect on the structure by coordinating different ligands at the axial position.

There have been reported SCO materials generated using square-planar tetracyanidoplatinate or tetracyanidopalladate units to form Hofmann-like structures.[9-14] It is very rare for materials constructed with these cyanidometallate linkers to have a non-Hofmann-like topology.[15-17] We generated two materials with tetracyanidoplatinate and tetracyanidopalladate forming non-Hofmann-like $[Fe(Dz)(H_2O)_2Pt(CN)_4]\cdot 2(H_2O)$ and $[Fe(Dz)(H_2O)_2Pd(CN)_4]\cdot 2(H_2O)$ frameworks. The Fe(II) centres

are axially coordinated with water molecules and $[M(CN)_4]^{2-}$ linkers (M = Pt or Pd), forming FeN_4O_2 octahedral geometry rather than the usual FeN_6 geometry.

There is an example reported of mixing different ratios of $[Au(CN)_2]^-$ and $[Ag(CN)_2]^-$ units to form a Hofmann-like MOF. However, the mixed-linker MOFs form in microcrystals so no single crystal structure was reported.[18] Herein, we successfully generated single crystal mixed cyanidometallate Hofmann-like frameworks by using Tz and Dz ligands $[Fe(Tz)(Au(CN)_2)_{0.5}(Ag(CN)_2)_{0.5}]$ $[Fe(Dz)(Au(CN)_2)_{0.5}(Ag(CN)_2)_{0.5}]$ and $[Fe(Dz)(Au(CN)_2)_{0.7}(Ag(CN)_2)_{0.3}]$ based on a molecular alloy strategy. That reveals the structural properties of these MOFs and compared them with their analogue MOFs with single linkers. Moreover, this study demonstrates the fine-tuning of scissor motion with one axis showing NTE and another with PTE. The magnetic properties were studied on these MOFs, which reveals SCO behaviours influenced by ligand field and host–host interactions. Atom composition and distribution, and vibrational modes of the materials have been characterised *via* various techniques.

This chapter elucidates the structural differences between frameworks built up with varied linkers in the axial and equatorial positions and demonstrates modifying SCO behaviours *via* changing the linker compositions. This guide designing materials with desirable structures and spin features.

5.2 Structure Characterisation of $[Fe(Tz)(Ag(CN)_2)_2]$ (TzAg·EtOH)

Single crystals of $[Fe(Tz)(Ag(CN)_2)_2]$ (**TzAg·EtOH**) were prepared and measured at the Australian Synchrotron using the MX1 beamline radiation source at 100 K. Single crystal data analysis of **TzAg·EtOH** reveals a 3D, interpenetrated, Hofmann-like framework (Figure 5.1). The **TzAg·EtOH** crystal adopts the orthorhombic phase, *Cmma* space group. The crystal structure of **TzAg·EtOH** is isotopologically with **TzAu·EtOH** and consists of the Fe(II) centres with Tz ligands coordinated axially and four linear dicyanidoargentate linkers coordinated equatorially. The topology is the same as the **TzAu** analogue but coordinated with four dicyanidoaurate linkers. The total volume of **TzAg·EtOH** is slightly larger than **TzAu·EtOH** (**TzAu·EtOH** single crystal information was extracted from the literature[19]). The adjacent Hofmann layers is connected by Ag···Ag interactions of length 3.1887(19) Å compared to **TzAu·EtOH** with Au···Au interactions in 3.2400(7) Å. The argentophilic interactions are weaker and shorter than aurophilic interactions.[19-22] Ag···Ag interactions are perpendicular to the Hofmann layers making the layers interdigitate. The rhombic $[Fe(Ag(CN)_2)_2]$ grids are observed by viewing down the *c*-axis. The acute compression angle (θ) which is the Ag···Fe···Ag angle within the *ab*-plane is 73.23°. The pillaring ligands are straight and the aromatic rings within the Tz ligand are coplanar.

Structural analyses at 100 K reveal the average bond distance of Fe–N is 1.945 Å, which is characteristic of Fe(II) in the LS state (Table 5.1). That agrees with the magnetic susceptibility result

vide infra. The Fe(II) octahedral distortion at this temperature is 15.4°. The distance between the two Fe(II) sites (Fe···Fe) in the adjacent layers is 15.067(3) Å. These two parameters are closely comparable to those for the **TzAu·EtOH** framework (Σ(Fe) = 15.5°, Fe···Fe = 15.099(3) Å). The angle of Fe–N1–C1 is 171.9(7)°, which is slightly more linear than the Au analogue framework (170.6(3)°). The host–host C–H···N interactions are between the pyridyl rings and the tetrazine rings from neighbouring ligands with 3.83 Å (C18–N12) and 3.76 Å (C13–N17). Those distances are slightly longer than in the **TzAu·EtOH** framework.[19]

The shape and size of pores of **TzAg·EtOH** are closely similar as the ligands are linear and Hofmann layers have no undulation. The pores containing solvent molecules are rectangular at 4.8 × 8.6 Å. Smaller channels between the adjacent Hofmann layers exist but the size of the channels is too small to accommodate guests. As EtOH solvent is disordered in the pores, it could not be located and refined. In order to estimate the number of EtOH molecules within the solvent-accessible pores the solvent mask function in Olex 2 was used,[23] which gives three EtOH per formula unit. These 307 electrons were found in the void space. The unit cell volume of **TzAg·EtOH** is 2983 Å^3 with 1397 Å^3 of void volume, which corresponds to a 45% solvent-accessible void.

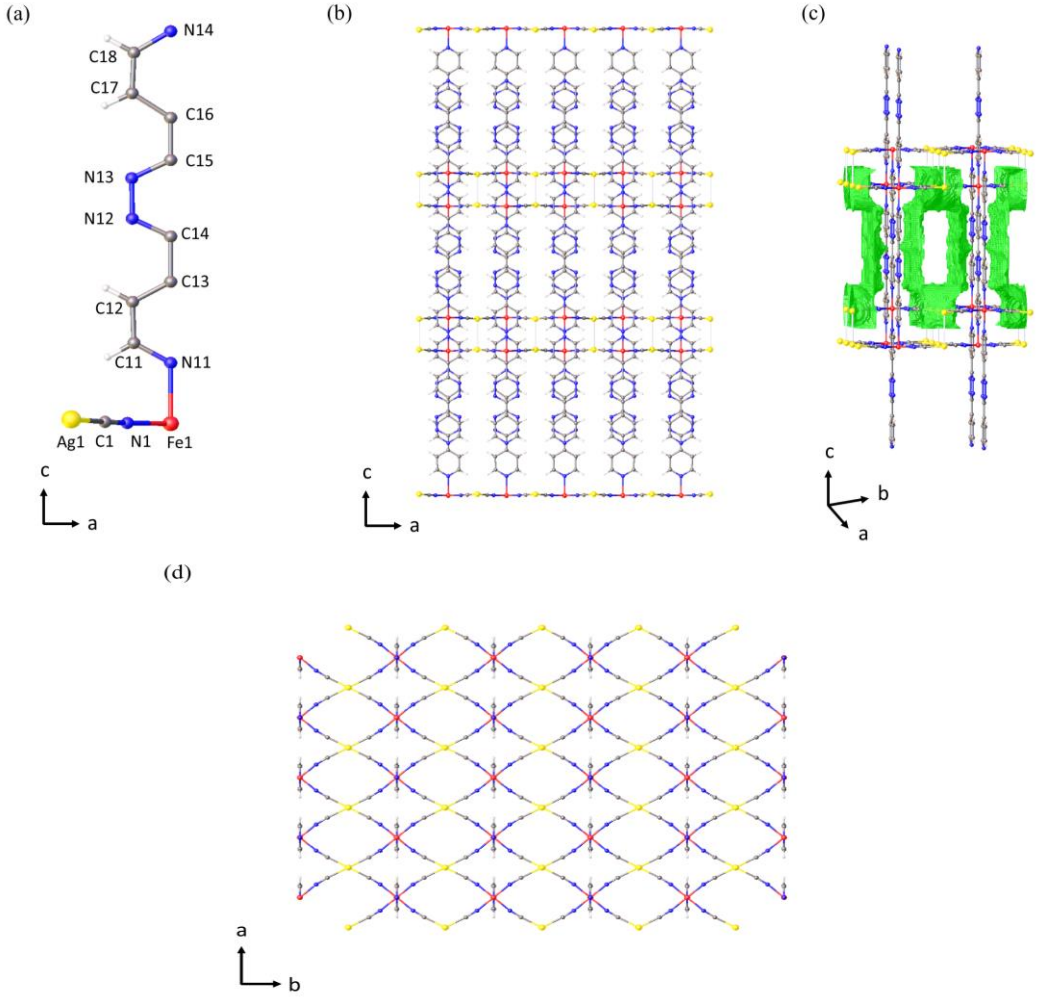

Figure 5.1: Single crystal structure of **TzAg·EtOH** at 100 K: (a) asymmetric unit; (b) framework structure

shows with solvent molecules omitted for clarity down the *b*-axis; (c) the void profile of the framework is shown in green; (d) framework structural shows with solvent molecules omitted for clarity down the *c*-axis. Atom colours: Fe (red), Ag (yellow), N (blue), C (grey), H (white).

Table 5.1: Comparison of selected structural parameters for **TzAg·EtOH** at 100 K.

Parameter	**TzAg·EtOH**
a / Å	12.129(2)
b / Å	16.324(3)
c / Å	15.067(3)
Volume / Å^3	2983.2(10)
<*d*(Fe–N)> / Å	1.945
Σ(Fe) / °	15.4
Ag···Ag / Å	3.1887(19)
Fe–N–C / °	171.8(7)
θ / °	73.23

VT-PXRD measurements were conducted on **TzAg·EtOH** by using the STOE STADI P diffractometer attached to an Oxford Cryostream system for controlling temperature. The sample was measured in the temperature range of 320–100–320 K to examine peak shifting attributed to SCO. A contour plot of the patterns as a function of temperature was made with two peaks as an example (Figure 5.2). A symmetric peak shifting behaviour is evident in the 2D contour plot where the peaks shift to higher angles upon cooling and reverse back to lower angles upon heating. The **TzAg·EtOH** powder sample is in the HS state at 320 K with 2θ values of both peaks at *ca*. 9.5° and 10.5°. Both peaks shift gradually to higher angles upon cooling with temperatures between 296 to 266 K, which corresponds to a single-step SCO transition. The material converts to the LS state below 260 K. The spin transition temperature of **TzAg·EtOH** in the heating process is between 276 K and 294 K, where the peaks display obvious shifting to lower angles. The peaks revert to the original positions at 320 K, where all the Fe(II) sites return to the HS state. The spin transition temperatures extracted from VT-PXRD are in good agreement with the magnetic susceptibility data vide infra.

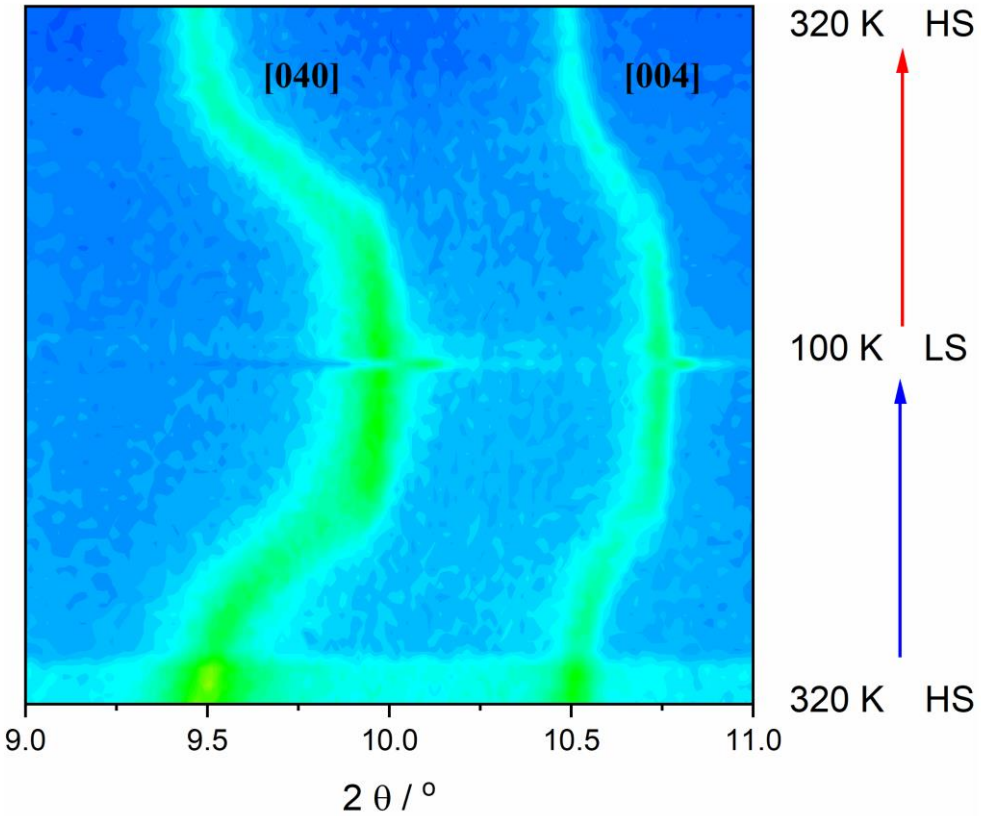

Figure 5.2: VT-PXRD peak evolution of **TzAg·EtOH** (2θ = 9.0–11.0°, *hkl* = [040] and [004], temperature range: 320–100–320 K).

The experimental PXRD data of **TzAg·EtOH** collected at 100 K matches well with the simulated pattern from single crystals (Figure 5.3). A Pawley refinement was performed on the PXRD pattern of **TzAg·EtOH** to extract the unit cell information and analyse the lattice changes of the powder sample at 100 K and 320 K. The powder sample was refined using the single crystal structure model of **TzAg·EtOH** in space group *Cmma* at 100 K. All of the peaks in the powder pattern at 100 K are fitted well with the unit cell parameters: a = 12.5051 Å, b = 16.0137 Å, c = 14.9928 Å. A fit of the powder pattern at 320 K gave the unit cell parameters a = 12.3351 Å, b = 16.6652 Å and c = 15.6970 Å. It is observed that the a-axis displays NTE while the b and c- axis display PTE. That is the **TzAg·EtOH** framework exhibits a scissor motion, with θ showing expansion upon cooling with θ = 75.97° at 100 K and θ = 73.02° at 320 K.

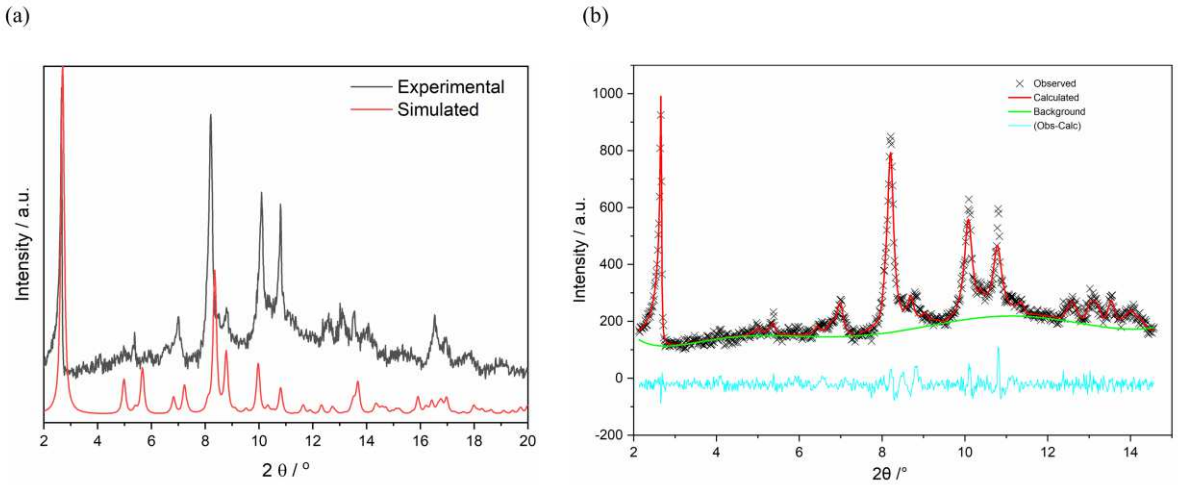

Figure 5.3: (a) Comparison of experimental PXRD pattern of **TzAg·EtOH** (black) and simulated pattern (red) from single crystal X-ray data at 100 K. (b) Pawley refinement of **TzAg·EtOH** at 100 K; experimental pattern (black crosses), calculated fit (red), background (green), the difference (light blue).

5.3 Spin Crossover Behaviour of TzAg·EtOH

Magnetic susceptibility measurements on **TzAg·EtOH** reveal a single-step, complete and hysteretic SCO (Figure 5.4). The $\chi_M T$ value is *ca.* 3.3 cm^3 K mol^{-1} above 319 K. The transition reaches the LS state at 230 K with the $\chi_M T$ value close to 0 cm^3 K mol^{-1}. SCO behaviour of **TzAg·EtOH** has a 6 K hysteresis ($T_{½}\uparrow$ = 279 K and $T_{½}\downarrow$ = 273 K), which is similar to **TzAu·EtOH**.[19] However, the transition between states is more gradual than the **TzAu·EtOH** framework; this is likely attributable to the weaker electron affinity in Ag than in Au,[24] with weaker argentophilic interactions reducing cooperativity between the Fe(II) centres.[25-26]

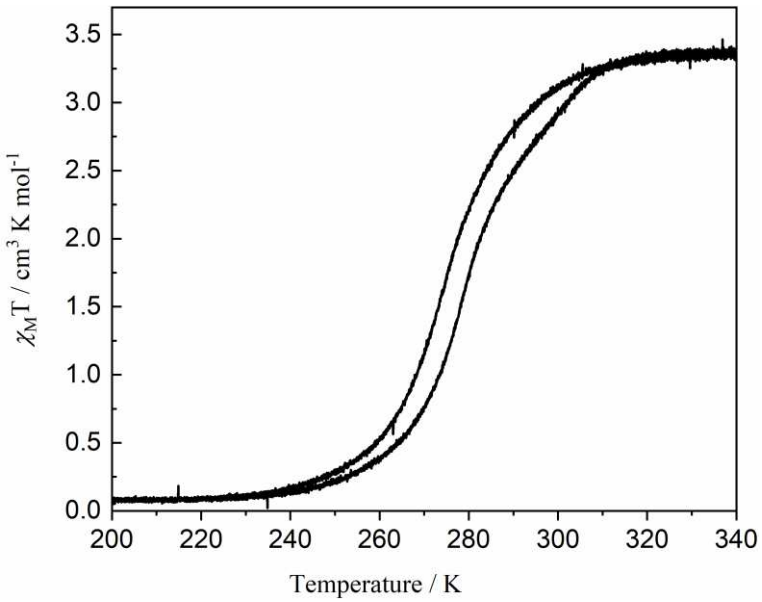

Figure 5.4: Variable temperature magnetic susceptibility measurement of **TzAg·EtOH**.

5.4 Structure Characterisation of [Fe(Dz)(Ag(CN)$_2$)$_2$] (DzAg·EtOH)

SCXRD analyses were conducted on **DzAg·EtOH** using the in-house instrument. The structural information of the material was collected at variable temperatures: 100, 180, 195 and 260 K. The topology of **DzAg·EtOH** is a 3D Hofmann-like framework with the same space group (*C*2/*c*) as the **DzAu·EtOH** framework (Figure 5.5). The pillaring Dz ligands on the axial position are slightly bent. The diazine rings are disordered and three aromatic rings within the ligands are not coplanar. The Hofmann layers are undulated, and a shift is observed between the adjacent layers. The staggered two layers are connected by the Ag···Ag interactions, which are tilted in between the *ab* plane. The four Fe(II) centres in the same Hofmann layer form a square grid.

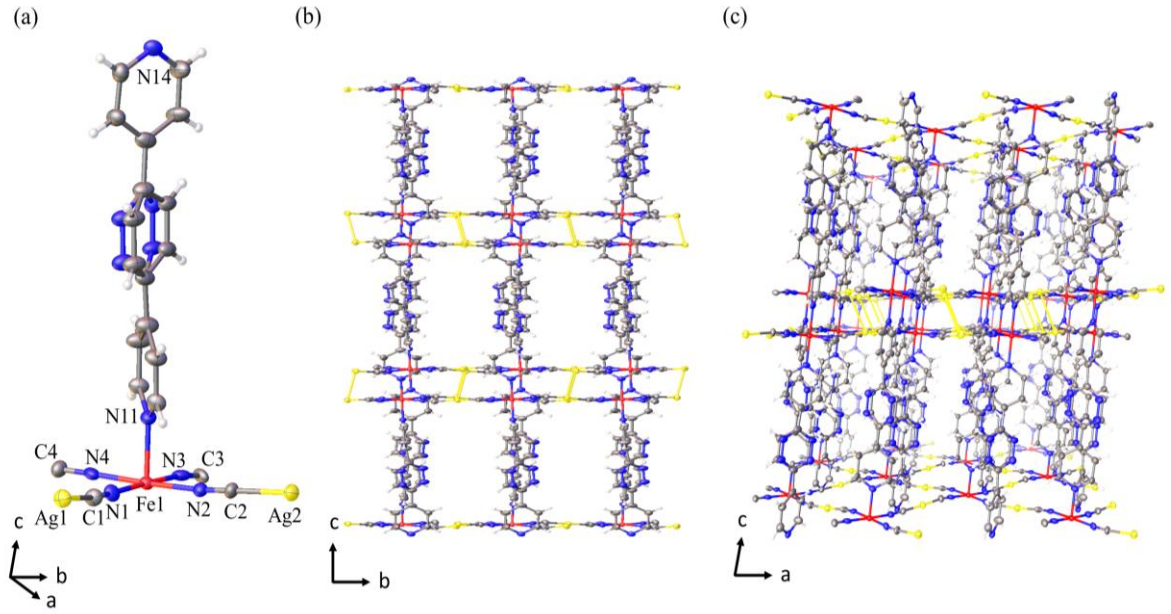

Figure 5.5: Single crystal structure of **DzAg·EtOH** at 100 K: (a) asymmetric unit and atoms are shown as thermal ellipsoids at the 50% probability; (b) the framework structure is viewed down the *a*-axis; (c) perspective view of the framework structure down the *b*-axis. Atom colours: Fe (red), Ag (yellow), N (blue), C (grey), H (white). Solvent molecules omitted for clarity.

VT studies were performed to examine of temperature on the SCXRD. The *a*, *b* and *c* lattice parameters of **DzAg·EtOH** at 100 K are the smallest among other temperatures (Table 5.2). The lattices expand with warming to 260 K. The relative expansion of the *a*-axis (4.4%) is approximately doubled compared with the *b*- (2.4%) and the *c*-axes (2.4%). The volume of the crystal increases by 9.1%. The trend of expansion in lattices is associated with the spin transition (Figure 5.6). However, it is noted that a slight decrease in the *b*-axis and β angle occurs when the temperature reaches 195 to 260 K. That may be caused by the structure relaxing to optimum lattices and intra- and inter-molecular interactions.

Table 5.2: Comparison of the unit cell parameters of **DzAg·EtOH** at 100, 180, 195 and 260 K.

Sample	Temperature / K	*a* / Å	*b* / Å	*c* / Å	*β* / °	Volume / Å^3
DzAg·EtOH	100	14.4174(9)	14.6635(9)	30.4923(17)	96.177(6)	6408.9(7)
	180	14.8198(15)	14.9258(17)	30.960(2)	97.410(8)	6791.0(11)
	195	14.970(2)	15.084(3)	31.105(3)	98.196(13)	6952.0(19)
	260	15.0542(18)	15.0092(14)	31.233(3)	97.802(12)	6991.9(12)

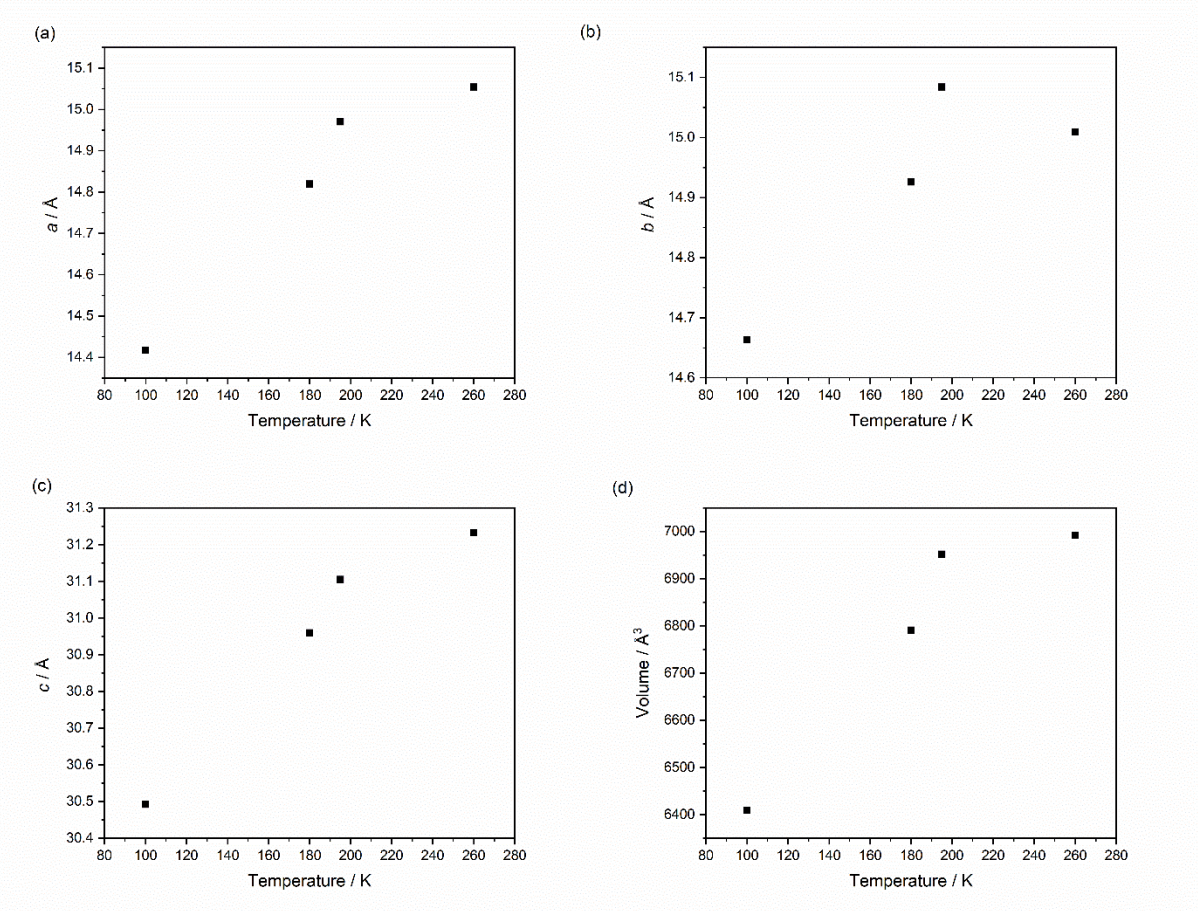

Figure 5.6: Unit cell parameters of **DzAg·EtOH** at 100, 180, 195 and 260 K: (a) *a*-axis, (b) *b*-axis, (c) *c*-axis and (d) volume.

The crystal of **DzAg·EtOH** collected at 100 K is indicative of the LS state as the average Fe−N distance is 1.976 Å. When the temperature rose to 180 K, the average Fe−N distance increased to 2.085 Å. This shows the crystal changed from a fully LS to 55% of the LS sites. The Fe−N bond length expands to 2.163 Å at 195 K followed by 2.173 Å at 260 K, which is indicative of the completed transition to the HS state. The structure data in Table 5.3 show the spin state transition, which is in agreement with the magnetic susceptibility. The octahedral distortion of **DzAg·EtOH** is lowest at 100 K, suggesting the octahedral geometry is the closest to orthogonal at that temperature. The octahedral geometry distorts more with increasing temperatures. The material has the largest distortion when

reaching 260 K with $\Delta\Sigma = 4.6$ ° ($\Delta\Sigma = \Sigma_{HS} - \Sigma_{LS}$). That change reflects the relationship between the spin transition and lattice distortion. The heightened octahedral distortion in the HS state is correlated with the expanding of the Fe−N bonds and enhancing the flexibility of the octahedral Fe sites.

Table 5.3: Comparison of selected structural parameters for the **DzAg·EtOH** framework at 100, 180, 195 and 260 K.

Parameter	100 K	180 K	195 K	260 K
<*d*(Fe−N)> / Å	1.976	2.085	2.163	2.173
Σ(Fe) / °	13.6	15.1	17.3	18.2
Ag···Ag / Å	3.1250(9)	3.1639(12)	3.1681(12)	3.216(4)
Average Fe–N–C / °	175.1	173.6	172.5	169.5
Torsion angle C2–Ag2–Ag1–C1 / °	88.0	90.9	89.8	92.0
θ / °	89.03	89.59	89.57	90.17

The SCO behaviours not only affect the local octahedral Fe(II) coordination, but also the flexing of Fe–N–C on the equatorial positions. The average angle of Fe–N–C is 169.5° at 260 K, which is the smallest. Upon reducing the temperatures, the angle tends to be more linear and reaches 175.1° at 100 K. The deviation of four Fe–N–C angles is larger at 260 K than at 100 K. The largest angle Fe1–N2–C2 is 175°, while the smallest one is 161° at 260 K, a difference of 14°. However, the difference between the largest and smallest angle is 5° at 100 K. That is the structure is more regular in the LS state. The Hofmann grids are close to a square shape and they adopt staggered packing with intermolecular argentophilic interactions in between (Figure 5.7). The distance of adjacent Fe(II) centres in the same Hofmann layer increases with increasing temperature from 10.28 Å (100 K) to 10.63 Å (260 K). The Ag···Ag interactions between the layers are shortened by 2.8% with decreasing temperatures from 3.216(4) Å (260 K) to 3.1250(9) Å (100 K). Accompanying the distance changes in the argentophilic interaction is a reduction in the C2–Ag2–Ag1–C1 torsion angle associated with the scissor motion of the layers.

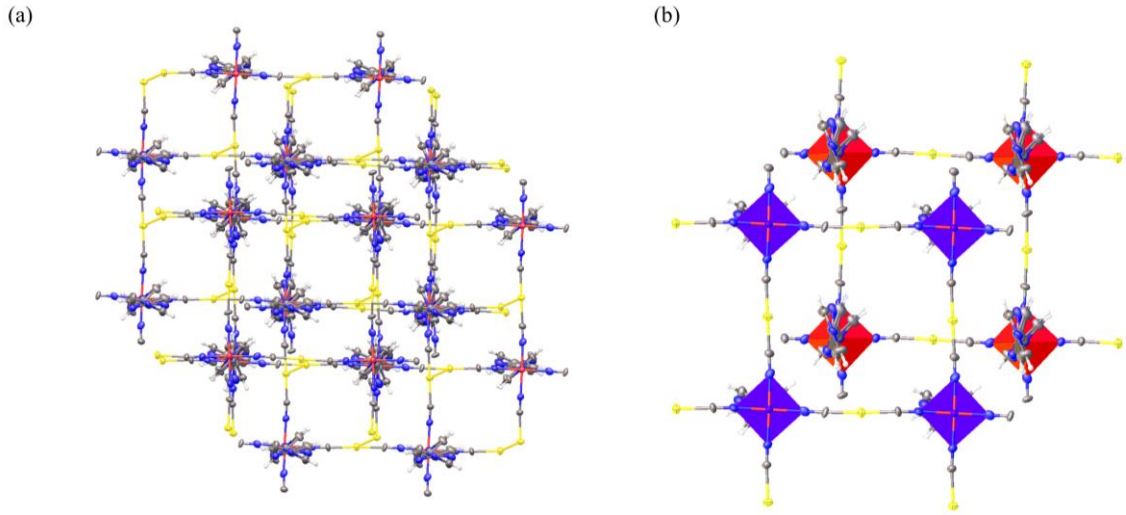

Figure 5.7: Single crystal structure of **DzAg·EtOH** at 100 K as viewed down the *c*-axis (a) with the packing of Hofmann grids, (b) and showing two layers with Fe(II) in polyhedron (violet for the upper layer and red for the lower layer). Solvent omitted for clarity.

The Dz ligands are more bent at higher temperatures with 172.7° (angle of N11···centroid of diazine ring···N14) at 260 K compared with 175.6° at 100 K (Figure 5.8). Although the ligands are more bent, the elongation in Fe–N bonds caused by SCO increases the Fe(II) distances between the Hofmann layers on the axial position by 0.37 Å from 100 K to 260 K. The dihedral angle of two pyridyl rings in a Dz ligand reduces by 8.3° when the temperature reaches 260 K. The diazine rings in the Dz ligand present a disorder with two nitrogen atoms (labelled as in pairs for two directions with N12A and N13A, N12B and N13B) facing on either side of the rings. However, the probability of the two facing directions is not equal to N12B and N13B at 78% at 100 K. That is, the diazine ring prefers to adopt one direction with the rings containing N12B, N13B, C17A and C18A. The occupancies of the nitrogen and carbon atoms in the diazine rings are almost identical at different temperatures. The undulation in the Hofmann layer was observed, and with higher temperatures the undulation is more defined. The angle between the Hofmann plane (the plane containing four nitrogen atoms in the equatorial position) and the plane with four Fe(II) centres is 5.7° at 100 K compared with 8.8° at 260 K. The distances between the Ag atoms and the Hofmann planes also reflect the distortion of the Hofmann layers. As the Ag atoms are either above or below the Hofmann planes, the layers are undulated. The largest distance between the Ag atoms and the Hofmann plane is 0.61 Å and the smallest is 0.18 Å at 100 K. The distortion increased at 260 K with the distance ranging between 0.19 Å and 0.97 Å, which is likely attributed to spin conversion to the HS state and thermal vibrational effects. As the Hofmann layers are not overlapping rhombic grids, there is no scissor motion observed. However, there is still a slight change in θ ($\theta = 2 \times (\arctan(a/b))$ due to SCO-induced lattices flexing and octahedral distortion. The θ is very close to orthogonal at 89.03° at 100 K and slightly open to 90.17° at 260 K.

The small change in θ suggests the stability of structure may be caused by hinged intra- and inter-molecular interactions.

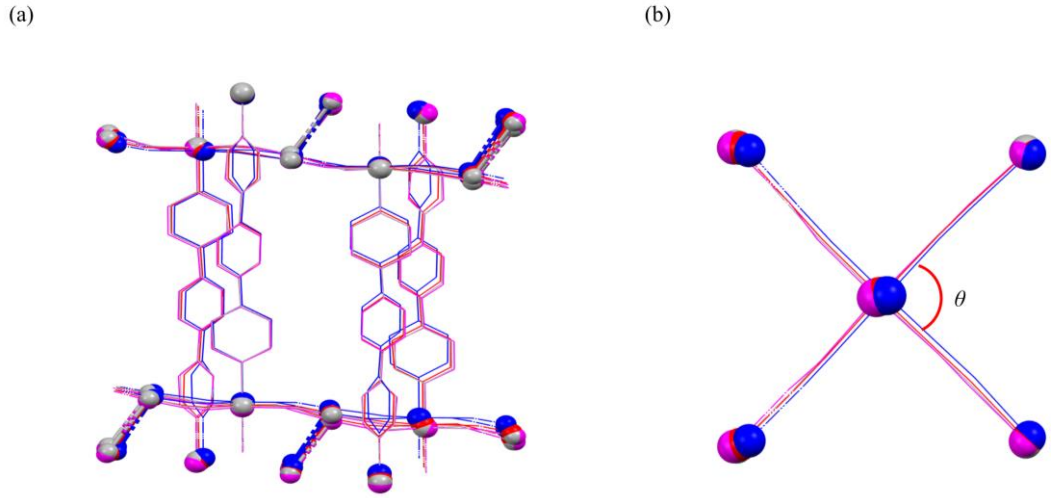

Figure 5.8: (a) Structural overlay of **DzAg·EtOH** framework as viewed down the *b*-axis; (b) Hofmann layer overlay at 100 (blue), 180 (red), 195 (dark grey) and 260 K (magenta). Solvent omitted for clarity. The disordered and hydrogen atoms are omitted for clarity.

The host–host C–H···N interactions between the pillaring Dz ligands are asymmetric due to the two possible locations of the diazine rings (Figure 5.9). The distances of N13B–C15 and N12B–C14 are 3.49 Å and 3.48 Å, respectively, at 100 K. It is interesting to note that the host–host C–H···N interactions of N13B–C15 and N12B–C14 reduced to 3.43 Å and 3.45 Å at 260 K. This could be attributed to the less twisted pyridyl rings and more bent ligands. EtOH solvent molecules are located in between the ligands which form host–guest interactions. As the solvents are light elements and highly disordered, these could not be located in the structural modelling. The solvent mask function was used to estimate the amount of solvent within the pores, which gives three EtOH per formula at 100 K. The pore volume is 2821.33 $Å^3$ at 100 K and expanded to 3260.28 $Å^3$ at 260 K. The cell volume of the **DzAg·EtOH** is 6408.9 $Å^3$ at 100 K which is a 44% solvent accessible void. That percentage of pore in the unit cell volume increased to 47% at 260 K.

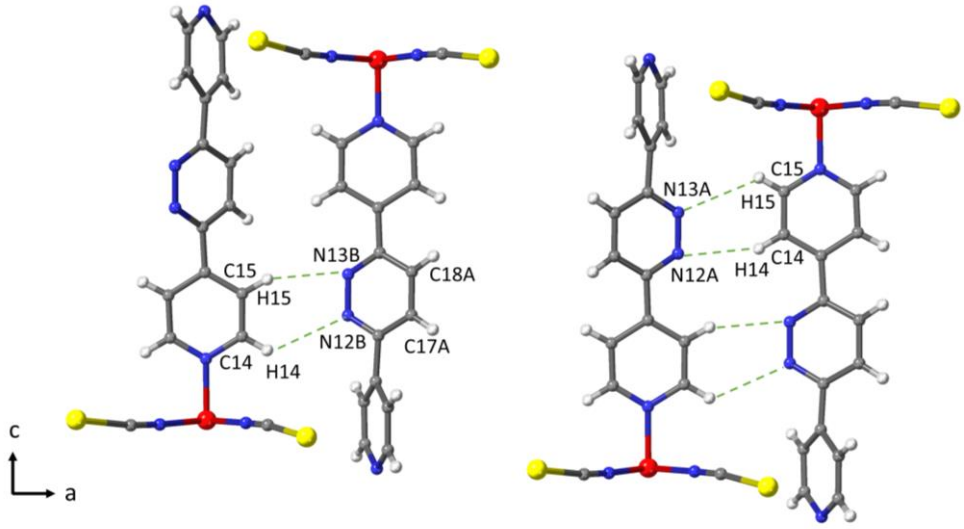

Figure 5.9: DzAg·EtOH shows inter-ligand C–H···N interactions (green dashes) viewed down the *b*-axis. Two disordered diazine rings are shown. Solvent omitted for clarity.

PXRD of the bulk powder **DzAg·EtOH** was performed at room temperature using the in-house PANalytical X'Pert PRO diffractometer to compare with the single crystal information and obtain the unit cell parameters. The powder sample was loaded in a sealed capillary. The pattern was fitted using a GSAS-II Pawley refinement to extract unit cell parameters at room temperature. The fitted pattern matches the experimental data (Figure 5.10).

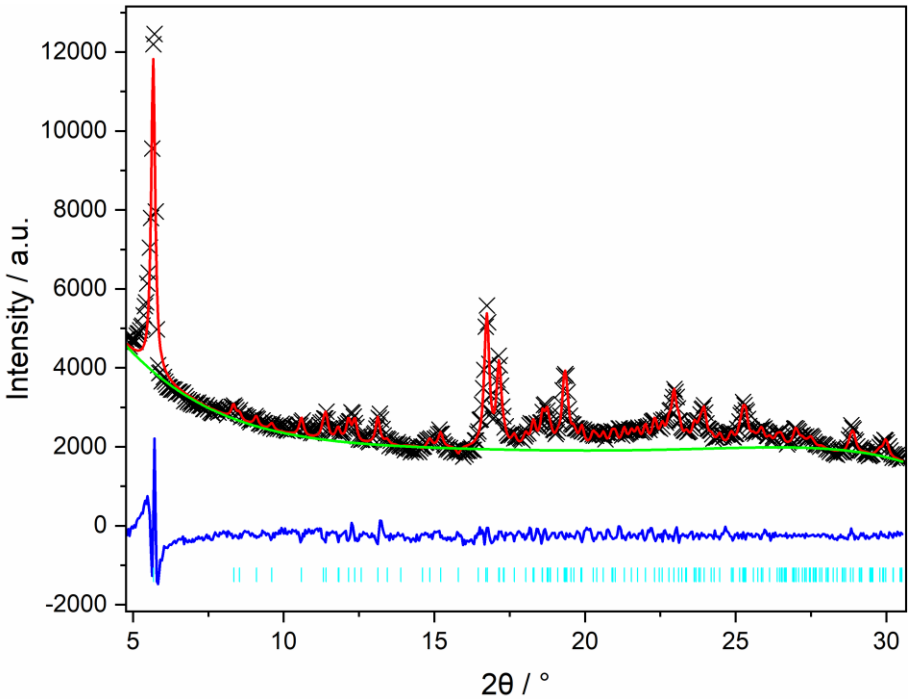

Figure 5.10: Pawley refinement of the PXRD data of the **DzAg·EtOH** framework measured at room temperature in the 2θ range of 8.5–9.5°. Experimental pattern (blue), calculated fit (green), background (red), the difference (cyan) and *hkl* (vertical bar).

To reveal the changes in lattice of **DzAg·EtOH** with temperature, VT-PXRD measurements were conducted using the in-house STOE STADI P diffractometer attached to an Oxford Cryostream system. The sample was measured in the temperature range of 300–100–300 K to examine peak shifting attributed to SCO. A contour plot of the patterns as a function of temperature was made with two peaks as an example (Figure 5.11). The peaks shift stepwise in the thermal cycle. The **DzAg·EtOH** powder sample is in the HS state at 300 K with 2θ values of both peaks at *ca*. 8.55° and 8.85°. Both peaks shift slightly to higher angles with temperatures between 300 to 202 K, which is due to thermal expansion. An obvious peak shift to higher angles occurs at *ca*. 202 K, which is attributed to the first step of the spin transition. Upon cooling, peak positions continue to shift to higher angles and display obvious shifting at 186 K and 174 K, where the second and third spin transition occurs. The sample gradually reaches the LS state at 100 K. The peaks revert to lower angles in the heating process. There is a pronounced peak shift to lower angles due to spin transition at 180 K, 192 K and 206 K where the three-step spin transition happens. The 2θ value of both peaks reverts to the original position when heating back to 300 K, which is the Fe(II) sites in **DzAg·EtOH** back to the HS state. The spin transition temperatures extracted from VT-PXRD are in good agreement with the magnetic susceptibility data in the following Section 5.5.

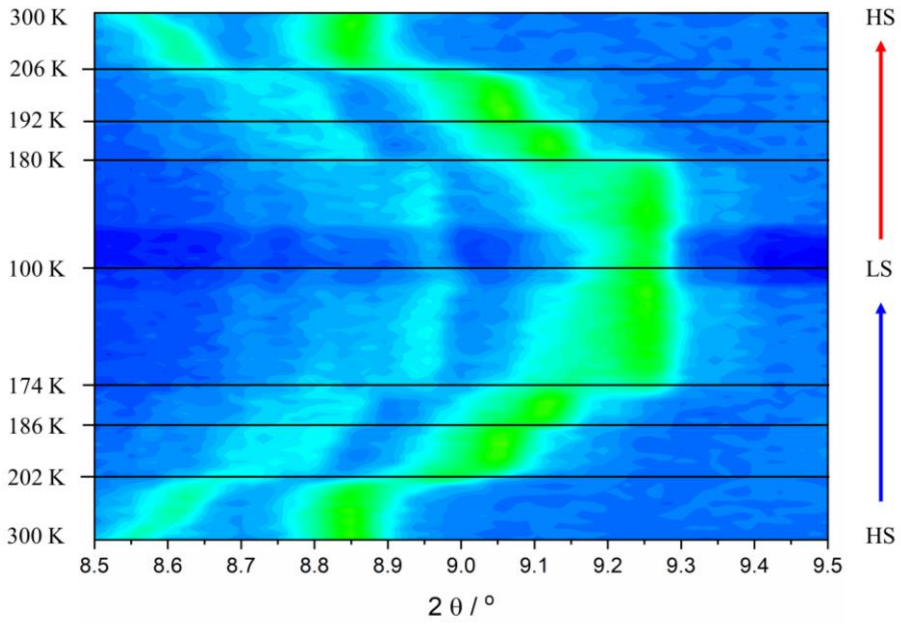

Figure 5.11: VT-PXRD peak evolution of **DzAg·EtOH** (2θ = 8.5–9.5°, temperature range: 300–100–300 K).

5.5 Spin Crossover Behaviour of DzAg·EtOH

Variable temperature magnetic susceptibility measurements were conducted on a bulk powder

sample of **DzAg·EtOH** over the temperature range of 280–120–280 K. The measurement of the material reveals a three-step and hysteretic SCO (Figure 5.12). The $\chi_M T$ value of **DzAg·EtOH** is 3.4 cm^3 K mol^{-1} at temperatures above 214 K, which is characteristic of Fe(II) sites in the HS state. The first spin transition temperature occurs at 201 K in the cooling process. After the transition, the material reaches the first intermediate state at 192 K, with the $\chi_M T$ value dropping to 2.4 cm^3 K mol^{-1}. This is about 30% Fe(II) sites converted to the LS state. The second spin transition is at 187 K, followed by the next inclined plateau at 180 K with $\chi_M T$ = 2.1 cm^3 K mol^{-1}, indicating approximately 40% of Fe sites in the LS state. The final spin transition to the LS state occurs at 174 K. The $\chi_M T$ value of 1.2 cm^3 K mol^{-1} at temperatures below 158 K suggests either an incomplete transition or the presence of paramagnetic impurity in the sample holder. There are also three spin transition temperatures in the heating process at 182, 193 and 206 K, respectively, and two intermediate states at 186 and 196 K; the three hysteresis loops in **DzAg·EtOH** are all open with hysteresis widths of 5, 6 and 8 K, respectively.

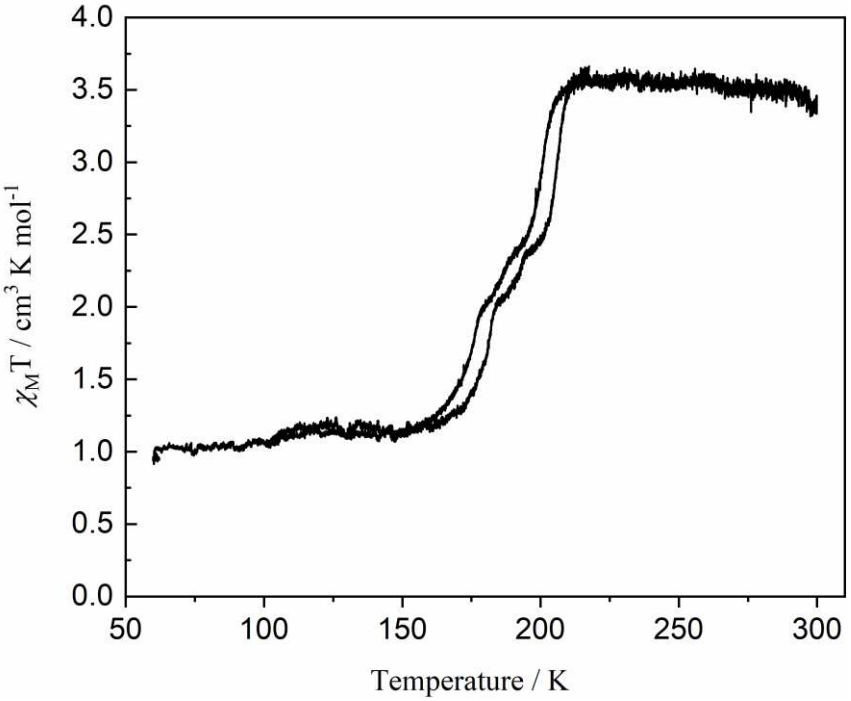

Figure 5.12: Variable temperature magnetic susceptibility measurement of **DzAg·EtOH**.

5.6 Structure Characterisation of $[Fe(Dz)(H_2O)_2Pt(CN)_4]\cdot 2(H_2O)$

Single crystals of $[Fe(Dz)(H_2O)_2Pt(CN)_4]\cdot 2(H_2O)$ (**DzPt**) were generated by the slow diffusion method in 1:1 EtOH : H_2O solution. Unlike other crystals with dicyanidoaurate or dicyanidoargenate anions generated with EtOH as the solvent, for **DzPt**, a mixture of ethanol and water was added, as $[Pt(CN)_4]^{2-}$ anions can be well dissolved with water. The crystals were measured at the Australian Synchrotron and the data were collected at 100 K. Most of the materials generated using

tetracyanidoplatinate anions form 3D Hofmann-like frameworks with square-planar tetracyanidoplatinate anions coordinated equatorially to Fe(II) centres.[27-31] However, the **DzPt** framework shows that Fe(II) centres coordinated one $[Pt(CN)_4]^{2-}$ anion and two water molecules in an equatorial position. Fe(II) centres are axially connected with Dz ligands (Figure 5.13). **DzPt** forms a very rare 3D accordion-like structure and only three other published materials forms with water binding with Fe(II) centres exist.[15-17] **DzPt** crystalises in the monoclinic $P2_1/c$ space group with unit cell parameters a = 6.9880(14), Å, b = 20.863(4) Å, c = 15.465(3) Å, β = 101.16(3)° and V = 2212.0(8) Å^3, which is very distinct from aforementioned Hofmann-like frameworks with coordination of dicyanidoaurate or dicyanidoargenate linkers.

Unlike other Hofmann-like structures that have FeN_6 octahedrons, **DzPt** forms FeN_4O_2 octahedral geometry. The octahedral distortion geometry of FeN_4O_2 is 16.21°. It is noted that four cyanide groups from $[Pt(CN)_4]^{2-}$ anion are not in the equatorial position, instead, only two are in the axial position and the other two are in the equatorial position forming 1D polymeric $[–Fe–NC–Pt(CN)_2–CN–]_\infty$ chains. The average distance of Fe−N is 2.17 Å indicative of the HS state. Two Fe−O bonds (Fe−O1 and Fe−O2) are 2.09 Å and 2.12 Å, respectively. Therefore, the material is in the HS state and there is no SCO transition. The average of four Pt−C bonds is 1.98 Å and four angles of C−Pt−C (C1−Pt1−C3, C1−Pt1−C4, C2−Pt1−C3 and C2−Pt1−C4) are close to orthogonal. There is a slight bending on C2−Pt1−C1 and C3−Pt1−C4 showing angles of 177.63(16)° and 177.33(16)° respectively. The bending on C1−N1−Fe1 and C2−N2−Fe1 is also observed with an average angle of 172.5° showing a slight undulation.

The twist of aromatic rings is observed with the dihedral angle between two pyridyl rings at 7.82° and the dihedral angles between diazine rings and pyridyl rings are 29.44° and 22.63°, respectively. The twisting of the rings is likely due to the optimum position of host–host and host–guest interactions. The host–host hydrogen bondings occur between the two water molecules coordinated Fe(II) and two nitrogen atoms in the diazine rings (N12···H2A−O2 and N13···H1B−O1, hydron bondings are in distances of 2.032(3) and 2.022(3) respectively). The host–host interactions connect between the lower (in green) and upper sheets (in blue) shown in Figure 5.12(c). That host–host interactions result in the restriction of movement of the diazine rings while the pyridyl rings are free to rotate to locate in the preferred positions. There are two water molecules per formula unit within the pores. One of the water molecules in the unit cell displays host–guest hydrogen bonding with the water coordinated to Fe(II) (O3···H1A−O1 with a distance of 2.120(4) Å). The other water molecule locates in a pore without showing host–guest interactions.

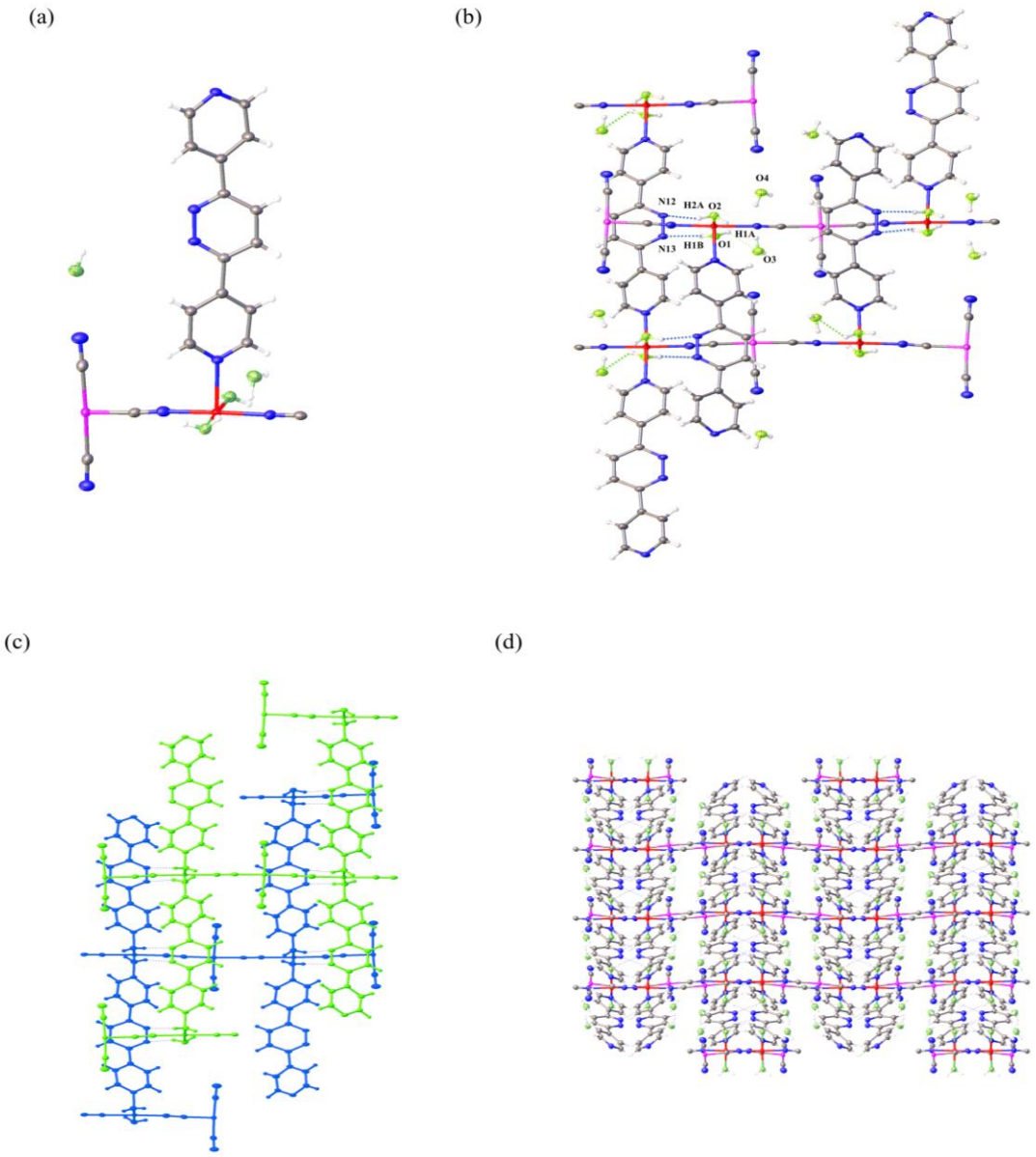

Figure 5.13: Single crystal structure of **DzPt** at 100 K: (a) asymmetric unit and atoms are shown as thermal ellipsoids at 50% probability; (b) framework structure viewed down the *a*-axis with hydrogen bonds N–H···O in blue dashes and O–H···O in green dashes; (c) down the *a*-axis with showing two layers connected by hydrogen bondings, (d) and down the *c*-axis. Atom colours: Fe (red), Pt (purple), N (blue), C (grey), O (light green), H (white).

5.7 Structure Characterisation of $[Fe(Dz)(H_2O)_2Pd(CN)_4]\cdot 2(H_2O)$ (DzPd)

DzPd was generated using the same method as **DzPt**. The crystal structure of **DzPd** was also characterised at the Australian Synchrotron and the data were collected at 100 K. **DzPd** crystals reveal the same topology as **DzPt** in the accordion-like framework in the monoclinic phase, $P2_1/c$ space group

with unit cell parameters a = 6.9340(14), Å, b = 20.883(4) Å, c = 15.555(3) Å, β = 101.65(3)° and V = 2206.0(8) Å^3. The structure of **DzPd** is very similar to **DzPt** material.

The asymmetric unit **DzPd** crystal has a Fe(II) centre coordinated by one $[Pd(CN)_4]^{2-}$ anion and two water molecules in an equatorial position. The Fe(II) centre axially connects with a Dz ligand (Figure 5.14). That is the 3D structure of **DzPd** has equatorial 1D polymeric $[–Fe–NC–Pt(CN)_2–CN–]_\infty$ chains and pillaring Dz ligands in the axial position. To the best of our knowledge, all the frameworks were synthesised by Fe(II) as centres of *N*-donor heterocyclic ligand and $[Pd(CN)_4]^{2-}$ linkers forming a Hofmann-like framework.[32-37] **DzPd** is the only example of a framework that forms in a non-Hofmann-like structure. The average distance of four Fe−N bonds is 2.167 Å, which is the same length as in **DzPt** (Table 5.4). That is indicative of high spin Fe(II) and, therefore, no spin transition occurs in this material. The FeN_4O_2 octahedral distortions in **DzPd** (17.34°) are slightly larger than those observed in **DzPt** (16.21°).

The two Fe−O bond lengths are 2.093(3) Å and 2.122(3) Å. There are two water molecules per formula unit within the pores. Both of the water molecules in the pores form host–guest interactions of hydrogen bonds (bond lengths in 1.96 Å and 2.05 Å) with each side of water coordinated with Fe(II) centres. Another type of hydrogen bond is from host–host interactions between coordinated water molecules and nitrogen atoms on diazine rings (N12–H1B···O1 and N13–H1A···O1).

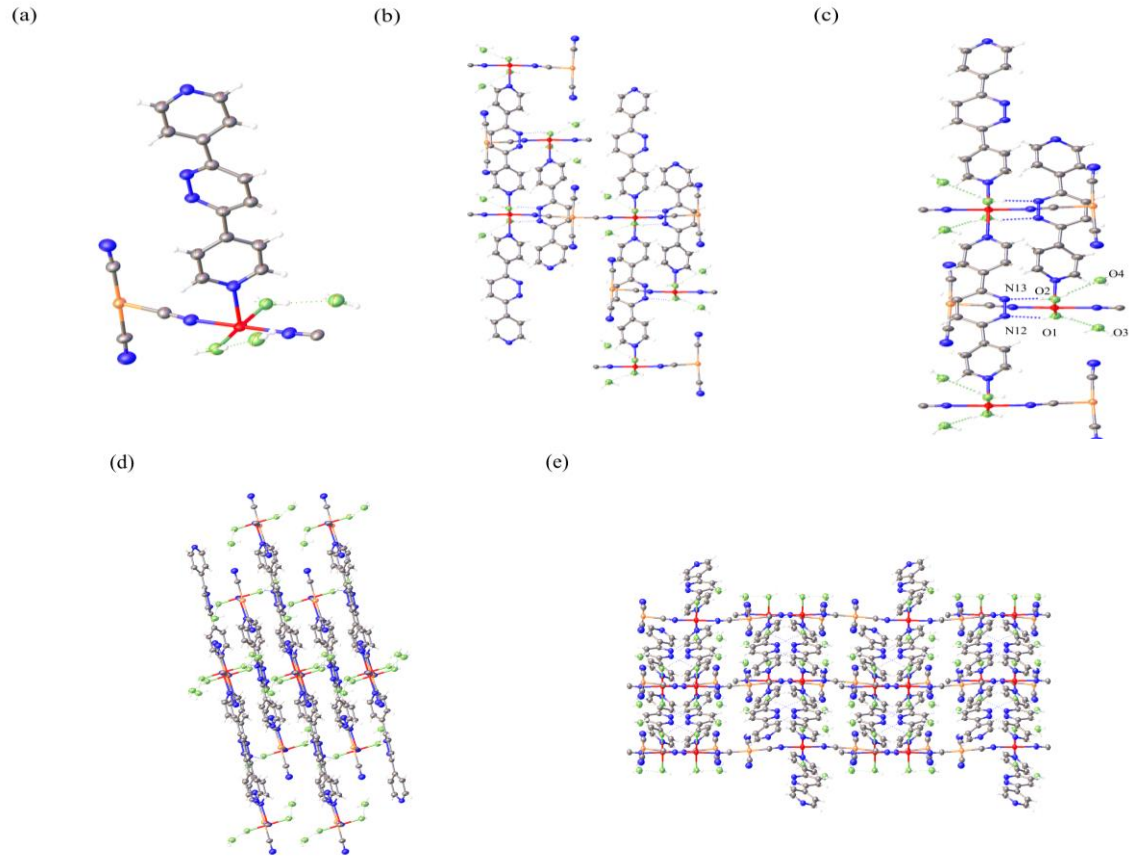

Figure 5.14: Single crystal structure of **DzPd** at 100 K: (a) asymmetric unit and atoms are shown as thermal

ellipsoids at 50% probability; (b) framework structure viewed down the *a*-axis; (c) hydrogen bonds N–H···O shown in blue dashes and O–H···O in green dashes; (d) down the *b*-axis, (e) and down the *c*-axis. Atom colours: Fe (red), Pd (orange), N (blue), C (grey), O (light green), H (white).

The average of four Pd−C bonds is 1.99 Å and four angles of C−Pd−C (C1−Pd1−C3, C1−Pd1−C4, C2−Pd1−C3 and C2−Pd1−C4) are also close to orthogonal as **DzPt**. The angles of C2−Pd1−C1 and C3−Pd1−C4 are in 177.23(16)° and 177.05(18)° respectively, which have slightly smaller angles than in the **DzPt**. The bending on C1−N1−Fe1 and C2−N2−Fe1 is also observed with an average angle of 172.7° showing slightly undulated chains.

The aromatic rings in the Dz ligands are twisted and the dihedral angle between two pyridyl rings in 8.79°. The dihedral angles between diazine rings and pyridyl rings are 30.10° and 22.28° respectively. The twisting of the rings is likely caused by the host–host interactions between water molecules coordinated with Fe(II) and nitrogen atoms on diazine rings, which hinged the further rotation of rings in the ligands. The Dz ligands in **DzPd** are also bent with angle in 173.5° and that is the same as in **DzPt**.

Table 5.4: Comparison of selected structural parameters for the **DzPd** and **DzPt** at 100 K.

Parameters	**DzPd**	**DzPt**
a / Å	6.9340(14)	6.9880(14)
b / Å	20.883(4)	20.863(4)
c / Å	15.555(3)	15.465(3)
β / º	101.65(3)	101.16(3)
Volume / Å^3	2206.0(8)	2212.0(8)
<*d*(Fe−N)> / Å	2.1665	2.1665
Σ(Fe) / °	17.34	16.21
Fe1–N1–C1 / °	171.7(4)	172.3(4)
Fe1–O1 / Å	2.089(4)	2.092(3)
Fe1–O2 / Å	2.113(4)	2.122(3)

5.8 Structure Characterisation of Mixed Cyanidometallate Frameworks

5.8.1 [Fe(Tz)((Au(CN)$_2$)$_{0.5}$(Ag(CN)$_2$)$_{0.5}$)$_2$] (**TzAu$_{0.5}$Ag$_{0.5}$·EtOH**)

The mixed linker single crystal structure of **TzAu$_{0.5}$Ag$_{0.5}$·EtOH** was generated by a slow diffusion method with iron(II) perchlorate hydrate, Tz ligand, potassium dicyanidoaurate and potassium dicyanidoargentate in equimolar amounts. The crystal structure of the material was characterised by in-

house diffractometer using Cu-K_α radiation. The structural data were collected at 100 and 320 K. The framework is a 3D Hofmann-like structure in the orthorhombic *Cmma* space group. The topology of the material is the same as its Au or Ag analogues. **TzAg·EtOH** has the largest parameter of *a*-, *b*-axis and volume, while the *c*-axis is the smallest compared with **$TzAu_{0.5}Ag_{0.5}$·EtOH** and **TzAu·EtOH** (Table 5.5). The lattice parameters of **$TzAu_{0.5}Ag_{0.5}$·EtOH** are in the middle of **TzAg·EtOH** and **TzAu·EtOH**.

Table 5.5: Comparison of the unit cell parameters for the **TzAg·EtOH**, **$TzAu_{0.5}Ag_{0.5}$·EtOH** and **TzAu·EtOH** at 100 K and the difference in θ between HS and LS state.

Parameter	**TzAg·EtOH**	**$TzAu_{0.5}Ag_{0.5}$·EtOH**	**TzAu·EtOH** [a]
a / Å	12.129(2)	12.0921(9)	12.066(2)
b / Å	16.324(3)	16.1918(14)	16.121(3)
c / Å	15.067(3)	15.0787(11)	15.099(3)
Volume / Å^3	2983.2(10)	2952.3(4)	2937.0(9)
Ag(Au)···Ag(Au) / Å	3.1887(19)	3.2210(11)	3.2400(7)
Fe–N–C / °	171.8(7)	171.7(6)	170.6(3)
θ / °	73.23	73.51	73.63(1)
$\Delta\theta$ / ° [b]	2.95	3.48	3.56

[a] Single crystal data of **TzAu·EtOH** were obtained from the literature.[19]

[b] $\Delta\theta$ ($\Delta\theta = \theta_{LS} - \theta_{HS}$) of **TzAg·EtOH** (difference of θ between 100 K and 320 K) was calculated from powder data while **$TzAu_{0.5}Ag_{0.5}$·EtOH** (difference of θ between 100 K and 320 K) and **TzAu·EtOH** (difference of θ between 200 K and 300 K) from single crystal data.

The asymmetric unit of **$TzAu_{0.5}Ag_{0.5}$·EtOH** consists of a single octahedral Fe(II) centre with the axial site occupied by half of the Tz ligand and one mixed cyanidometallate based linker in the equatorial position (Figure 5.15). The mixed cyanidometallate linker could be either $[Au(CN)_2]^-$ or $[Ag(CN)_2]^-$ anions. That is, Au and Ag atoms are located in the same position with estimated 39% occupancy of Au atoms and 61% of Ag. The ratio of Au and Ag in the crystal is not 1:1 as a synthesis that difference could be due to the small discrepancy between structure modelling and experimental crystal structure. Also, as SCXRD data were collected from one crystal, there could possibly have a difference between that certain crystal and the bulk material, which gives the average structure. To obtain the average atom composition of the material, XPS and EDS mapping was conducted (see sections 5.10 and 5.12). Bulk studies on the materials suggest a 1:1 ratio of Ag to Au. It is likely to have perpendicular Au···Au or Ag···Ag interactions connecting between the Hofmann layers, rather than Au···Ag interactions based on the results of XPS, which will be discussed. The $[Au(CN)_2]^-$ or $[Ag(CN)_2]^-$ metalloligands are homogenously mixed, which was analysed by SEM and EDS mapping

(see section 5.11). However, there may be short-range ordering present within the structure. The average distance between the layers is 3.2210(11) Å at 100 K and a slight expansion to 3.270(3) Å at 320 K. The host–host Au···Au interactions are stronger and with longer distances than Ag···Ag interactions. These host–host interactions have an influence on scissor motion. **TzAu·EtOH** has the largest $\Delta\theta$ induced by SCO. The longer Au···Au interactions improves the flexibility of the structure which allows for a greater θ.

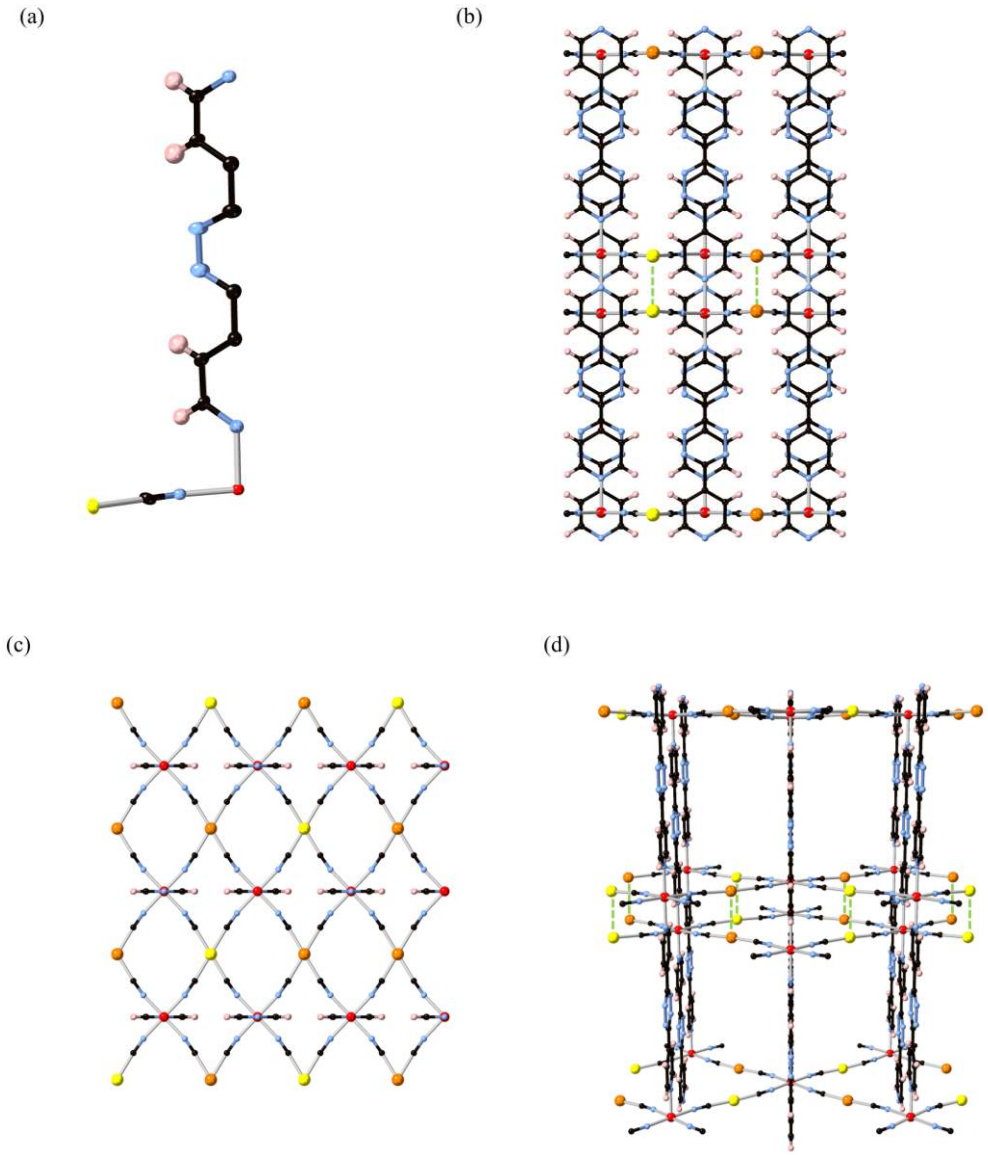

Figure 5.15: Single crystal structure of **TzAu$_{0.5}$Ag$_{0.5}$·EtOH** at 100 K: (a) asymmetric unit; (b) framework structure viewed down the *b*-axis; (c) viewed down the *c*-axis; (d) perspective view of the framework structure down the *a*-axis. Solvent molecules omitted for clarity. Au···Au and Ag···Ag interactions shown in green dashes. Au and Ag atoms are located in disorder. Atom colours: Fe (red), Ag (yellow), Au(orange), N (blue), C (black), H (pink).

The unit cell parameters on *b* and *c* lattices show thermal expansion from 100 to 320 K with an increase of 5.5% and 2.6%, respectively (Table 5.6). It is noted that the *a*-axis demonstrates a small extent of NTE behaviour, which has an expansion of 1.1% when cooling to 100 K. The framework is in the HS state as the average distance of Fe−N is 2.143 Å at 320 K. When the material was cooled down to 100 K, the bond distance shrinks to 1.955 Å indicating Fe(II) site in the LS state. The FeN_6 octahedral geometry is 18.2° at 320 K, which reduces to 16.9° at 100 K. That is the octahedral geometry is less distorted in the LS state.

Table 5.6: Comparison of selected structural parameters for **TzAu$_{0.5}$Ag$_{0.5}$·EtOH** at 100 K and 320 K.

Parameter	100 K	320 K
a / Å	12.0921(9)	11.964(2)
b / Å	16.1918(14)	17.076(3)
c / Å	15.0787(11)	15.468(3)
Volume / Å^3	2952.3(4)	3160.2
<*d*(Fe−N)> / Å	1.955	2.143
Σ(Fe) / °	16.9	18.2
Average Ag(Au)···Ag(Au) / Å	3.2210(11)	3.270(3)
Fe1–N1–C1 / °	171.7(6)	167.9(16)
θ / °	73.51	70.03

The aromatic rings in the Tz ligands are coplanar and the Tz ligands are straight. The angle of Fe1–N1–C1 is larger at 100 K at 171.7(6)° compared with a less linear one at 320 K 167.9(16)°, which is attributed to SCO-induced lattice flexing. The Hofmann layers are flat. As there is no tilted angle in the metalloligands, all the Hofmann grids are rhombic and overlapped as viewed down the *c*-axis. The NTE and straightening of the Fe1–N1–C1 affects the *θ* angle with the larger angle at 73.51° at a lower temperature. That is the framework displays a scissor motion. The change in *θ* angle in **TzAu$_{0.5}$Ag$_{0.5}$·EtOH** is slightly smaller than **TzAu·EtOH** (the change of *θ* angle in the **TzAu·EtOH** framework will be discussed in Chapter 6). The extent of lattice flexing can be tuned by the composition of metallocyanides.

The size and shape of pores are the same in **TzAu$_{0.5}$Ag$_{0.5}$·EtOH** as there is no distortion in ligands and Hofmann layers. The pores containing solvent molecules are rectangular in 5.2 × 8.9 Å at 320 K, which is slightly larger than at 100 K due to thermal expansion. Small channels are also located between the adjacent Hofmann layers but the size of the channels is too small to accommodate guests. As EtOH solvent is disordered in the pores, which cannot be located in the refinement. In order to estimate the number of EtOH molecules within the solvent-accessible pores solvent mask function in Olex 2 was used,[23] which gives three EtOH molecules per formula unit in **TzAu$_{0.5}$Ag$_{0.5}$·EtOH** at 320 K. A total of 292 electrons were found in a void per unit cell. The cell volume of the **TzAg·EtOH** is 3160 Å^3 with

the solvent accessible void space estimated to be 1403 Å^3. The host–host C–H···N interactions present in between the pyridyl rings and tetrazine rings from neighbouring ligands with 3.8 Å (C11– N13) and 3.7 (C12– N12) Å.

5.8.2 [Fe(Dz)((Au(CN)$_2$)$_{0.5}$(Ag(CN)$_2$)$_{0.5}$)$_2$] (**DzAu$_{0.5}$Ag$_{0.5}$·EtOH**)

Diffraction data on a single crystal of **DzAu$_{0.5}$Ag$_{0.5}$·EtOH** were collected at 100, 160, 179 and 230 K by using in-house diffractometer with Cu-K$_\alpha$ radiation source. The crystal of **DzAu$_{0.5}$Ag$_{0.5}$·EtOH** adopts the same 3D Hofmann-like topology as **DzAu·EtOH** and **DzAg·EtOH** in the monoclinic *C*2/*c* space group. The asymmetric unit of **DzAu$_{0.5}$Ag$_{0.5}$·EtOH** consists of a single octahedral Fe(II) centre with the axial site occupied by Dz ligand and two cyanidometallate linkers on the equatorial position, which could be either [Au(CN)$_2$]$^-$ or [Ag(CN)$_2$]$^-$ anions (Figure 5.15). That is Au and Ag atoms are located in the same position with estimated 35% occupancy of Au atoms and 65% of Ag.

The unit cell parameters of **DzAu·EtOH**, **DzAu$_{0.5}$Ag$_{0.5}$·EtOH** and **DzAg·EtOH** frameworks were compared to analyse the change of lattices caused by the composition of cyanidometallate linkers (Table 5.7). **DzAg·EtOH** framework has the largest lattice on the *a*-axis followed by **DzAu$_{0.5}$Ag$_{0.5}$·EtOH** and **DzAu·EtOH**. However, the **DzAu$_{0.5}$Ag$_{0.5}$·EtOH** framework has the largest parameters on the *b*-axis, *c*-axis and *β* angle among the three. Therefore, **DzAu$_{0.5}$Ag$_{0.5}$·EtOH** has the largest volume.

Table 5.7: Comparison of the unit cell parameters for **DzAg·EtOH**, **DzAu$_{0.5}$Ag$_{0.5}$·EtOH** at 100 K and **DzAu·EtOH** at 90 K.[38]

Parameter	**DzAg·EtOH**	**DzAu$_{0.5}$Ag$_{0.5}$·EtOH**	**DzAu·EtOH**
a / Å	14.4174(9)	14.3878(5)	14.2256(2)
b / Å	14.6635(9)	14.7123(5)	14.4645(3)
c / Å	30.4923(17)	30.5872(8)	30.4429(5)
β / º	96.177(6)	96.390(2)	96.104(2)
Volume / Å^3	6408.9(7)	6434.4(4)	6228.60(19)

The unit cell parameters *a*, *b* and *c* are decreasing from HS state to LS state and the changes are 4.2%, 1.8% and 2.1%, respectively (Table 5.8). Thus, the material has the largest volume at 230 K. The average Fe−N distance is 2.171 Å at 230 K indicating the framework is in the HS state. The bond length of Fe−N slightly decreases to 2.158 Å at 179 K in which some Fe(II) sites in the HS state convert to the LS state. The average Fe−N distance continues contracting to 2.104 Å at 160 K with approximately 39% spin transition. When the temperature reached 100 K, all the Fe(II) sites are in the LS state with an average Fe−N bond of 1.997 Å. The distorted FeN$_6$ octahedral coordination environment is more regular at lower temperatures and the difference in the octahedral geometry value between the HS and LS state

is 4.2°.

Table 5.8: Comparison of selected structural parameters for **DzAu$_{0.5}$Ag$_{0.5}$·EtOH** at 100, 160, 179 and 230 K.

Parameter	100 K	160 K	179 K	230 K
a / Å	14.3878(5)	14.7724(11)	14.9154(11)	14.9942(7)
b / Å	14.7123(5)	14.8766(12)	14.9695(12)	14.9759(7)
c / Å	30.5872(8)	30.9921(16)	31.1672(19)	31.2228(12)
β / º	96.390(2)	97.738(6)	98.279(6)	98.045(4)
Volume / Å^3	6434.4(4)	6748.9(8)	6886.4(9)	6942.1(5)
<*d*(Fe–N)> / Å	1.997	2.104	2.158	2.171
Σ(Fe) / °	13.2	18.7	16.3	17.4
Ag(Au)···Ag(Au) / Å	3.138	3.171	3.183	3.2158
Average Fe–N–C / °	175.0	172.6	173.1	172.8
θ / °	88.72	89.60	89.79	90.07

The pillaring Dz ligands on the axial position are bent. The bent angle of Dz ligand is 174.1° at 230 K while with a slight decrease to 173.3° at 179 K. The ligands are less bent with decreasing temperatures with the angle of 174.9° at 100 K. The two Fe(II) distance between the adjacent Hofmann layers reduces with decreasing temperature from 15.62 Å (230 K) to 15.30 Å (100 K) due to SCO and thermal expansion.

The diazine rings are disordered and three aromatic rings within the ligands are not coplanar. Unlike the diazine rings in **DzAg·EtOH** has two positions, the diazine rings in the **DzAu$_{0.5}$Ag$_{0.5}$·EtOH** framework has only one direction (Figure 5.16). The dihedral angle of two pyridyl rings is the largest at 100 K (66.3°) and the smallest at 230 K (56.7°). The Hofmann layers are undulated and a shift is observed between the adjacent layers. The staggered layers are connected by the Au···Au or Ag···Ag interactions, which are tilted in between the *ab* plane. The $[Au(CN)_2]^-$ or $[Ag(CN)_2]^-$ anions are mixed homogeneously in the framework with an average distance of Au···Au or Ag···Ag in 3.14 Å at 100 K, which increases to 3.216 Å at 230 K. The four Fe(II) centres in the same Hofmann layers form staggered square grids as viewed down the *c*-axis. As the Hofmann grid is not overlapped the rhombic shape, there is no scissor motion in this material. The *θ* value is also nearly orthogonal and shows a decreasing trend from the HS state to the LS state.

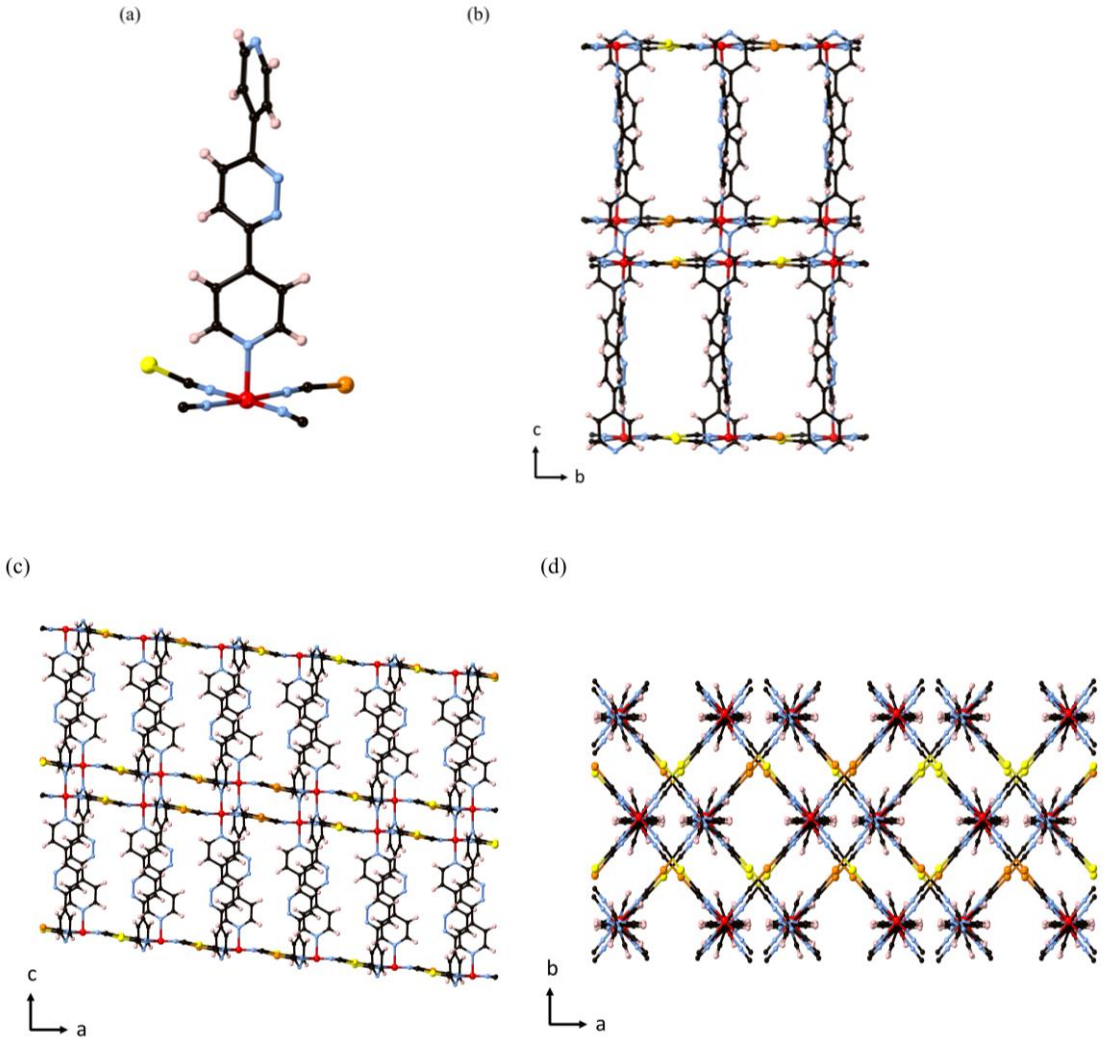

Figure 5.16: Single crystal structure of **DzAu$_{0.5}$Ag$_{0.5}$·EtOH** at 100 K: (a) asymmetric unit and atoms are shown; (b) framework structure viewed down the *a*-axis; (c) viewed down the *b*-axis; (d) and down the *c*-axis. Solvent molecules are omitted for clarity. Atom colours: Fe (red), Ag (yellow), Au(orange), N (blue), C (black), H (pink).

The degree of Hofmann layer undulation was investigated. The angle between the Hofmann plane contains four nitrogen atoms on the equatorial position and four Fe(II) sites from the same Hofmann layers was 5.8° in the LS state and less than 8.2° in the HS state, likely due to the increase of the regulation of the lattices in the LS state. The average angle of Fe–N–C in the equatorial position is more linear in the LS state at 175.0° than in the HS state at 172.8°.

The size and shape of pores are nearly identical in structure and the shape of pores is not regular rectangular as there is a distortion in ligands and Hofmann layers. Other small channels exhibit between

the adjacent Hofmann layers, but the size of the channels is too small to locate ethanol guests. As EtOH solvent is disordered in the pores it cannot be located in the refinement. In order to estimate the number of EtOH molecules within the solvent-accessible pores, solvent mask function in Olex 2 was used,[23] which gives about three EtOH molecules per formula unit in the **DzAu$_{0.5}$Ag$_{0.5}$·EtOH** framework. 619 electrons were found in a void per unit cell. The cell volume of the **DzAg·EtOH** is 6942 Å^3 with the solvent-accessible void space to be 3103 Å^3. Besides aurophilic and argentophilic interactions, host–host C–H···N interactions are present in between the pyridyl rings and diazine rings from neighbouring ligands with about 3.5 Å.

VT-PXRD measurements were conducted on **DzAu$_{0.5}$Ag$_{0.5}$·EtOH** by using the STOE STADI P diffractometer in the temperature range 300–100–300 K to examine peak shifting attributed to SCO. A contour plot of the patterns as a function of temperature was made with a peak (*hkl* = [20-4]) as an example (Figure 5.17). The peak shifts stepwise in the thermal cycle. The **DzAu$_{0.5}$Ag$_{0.5}$·EtOH** powder sample is in the HS state at 300 K with a 2θ value of the peak at *ca*. 7.0°. The peak shifts slightly to higher angles with temperatures between 300 to 198 K, which is due to thermal expansion. An obvious peak shift to higher angles is observed at *ca*. 198 K, which is attributed to the first step of the spin transition. The angle increases by about 0.2°. Upon cooling, peak positions continue to shift to higher angles and display obvious shifting at 170 K and 152 K, where the second and third spin transition occurs. The change of angles in the first step is more pronounced than in the second and third steps, which correspond to a larger change of the $\chi_M T$ value and a more abrupt spin transition in the first step than the rest. The sample gradually reached the LS state at 100 K. The peaks revert to lower angles in the heating process. The pronounced peak shifted to lower angles due to spin transition at 158 K, 172 K and 200 K where the three-step spin transition happens. The 2θ value of the peak reverts to the original position when heating back to 300 K, which is all the Fe(II) sites in **DzAu$_{0.5}$Ag$_{0.5}$·EtOH** back to the HS state. The spin transition temperatures extracted from VT-PXRD results are in good agreement with the magnetic susceptibility data.

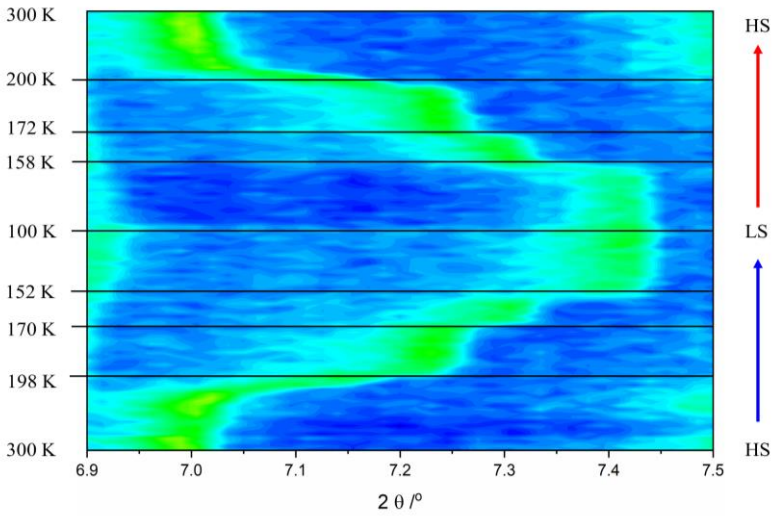

Figure 5.17: VT-PXRD peak evolution of **DzAu$_{0.5}$Ag$_{0.5}$·EtOH** (2θ = 6.9–7.5°, temperature range: 300–100–

300 K).

5.9 Spin Crossover Behaviour of Mixed Cyanidometallate Frameworks

5.9.1 **TzAu$_{0.5}$Ag$_{0.5}$·EtOH**

Variable temperature magnetic susceptibility measurements were carried out on bulk powder samples of **TzAu$_{0.5}$Ag$_{0.5}$·EtOH**, which revealed a gradual, hysteretic one-step SCO. The $\chi_M T$ value of **TzAu$_{0.5}$Ag$_{0.5}$·EtOH** is 3.4 cm^3 K mol^{-1} above 310 K, which is corresponding to the expected value for Fe(II) sites. The material undergoes a gradual drop of the $\chi_M T$ value until 278 K, followed by a relatively abrupt spin transition to the LS state. The $\chi_M T$ value gradually decreases to 0.7 cm^3 K mol^{-1} at 250 K upon cooling indicative of Fe(II) sites in the LS state. The $\chi_M T$ value is slightly higher than 0 cm^3 K mol^{-1}, which is likely due to the small amount of paramagnetic impurity in the sample holder. The heating mode is symmetric as the cooling mode, but spin transition occurs at higher temperatures. The hysteresis of the material is 4 K ($T_{½}\downarrow$ = 278 K, $T_{½}\uparrow$ = 274 K).

TzAu$_{0.5}$Ag$_{0.5}$·EtOH, **TzAg·EtOH** and **TzAu·EtOH** all display a hysteretic one-step SCO. **TzAu$_{0.5}$Ag$_{0.5}$·EtOH** and **TzAg·EtOH** have nearly identical spin transition temperatures, but **TzAg·EtOH** is more gradual than **TzAu$_{0.5}$Ag$_{0.5}$·EtOH**. and has slightly higher SCO temperatures (Figure 5.18). **TzAu·EtOH** is the most abrupt among these three. The abruptness and SCO temperature are due to cooperativity, which is associated with ligand field strength and host–host interactions.[26] The argentophilic interaction is weaker than aurophilic interaction, which likely affects the SCO behaviours. Thus, SCO behaviours can be tuned by rationally controlling the composition of cyanidometallate linker.

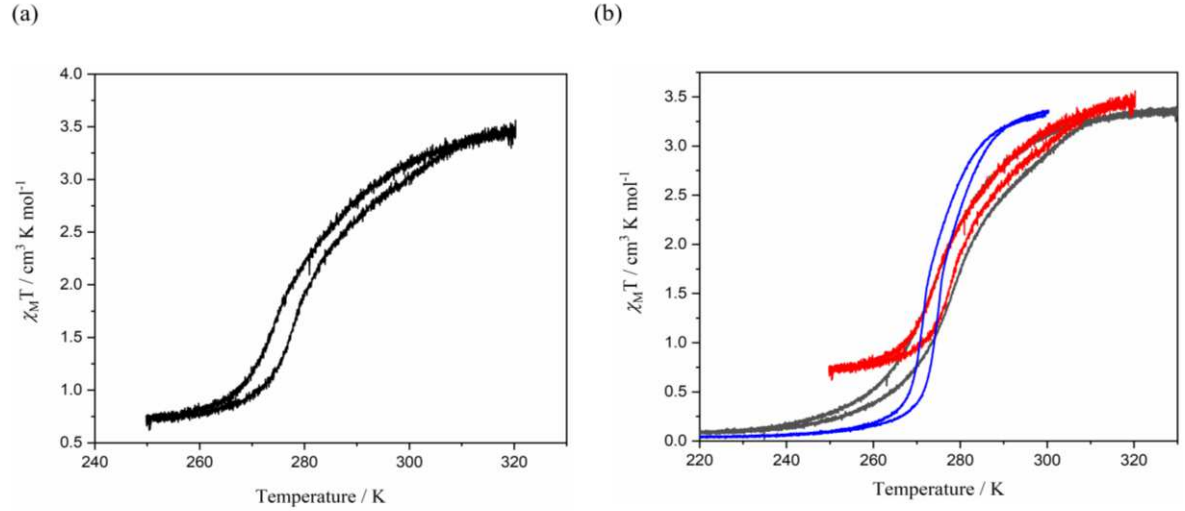

Figure 5.18: Variable temperature magnetic susceptibility measurement of (a) **TzAu$_{0.5}$Ag$_{0.5}$·EtOH** and (b) comparison of **TzAg·EtOH** (black), **TzAu$_{0.5}$Ag$_{0.5}$·EtOH** (red) and **TzAu·EtOH** (blue).

5.9.2 **DzAu$_{0.5}$Ag$_{0.5}$·EtOH**

Variable temperature magnetic susceptibility measurements of **DzAu$_{0.5}$Ag$_{0.5}$·EtOH** were carried out. The material presents a complete, three-step hysteresis SCO (Figure 5.19). The $\chi_M T$ value is nearly constant at *ca*. 3.50 cm^3 K mol^{-1} until 205 K, indicating the Fe(II) sites are in the HS state. The first transition temperature is centred at 196 K in the cooling process. A plateau occurs at 185 K after the first transition, with $\chi_M T$ value of 1.85 cm^3 K mol^{-1}, corresponding to a *ca*. 50% of conversion from the HS state to the LS state. The $\chi_M T$ value continues to decrease below 172 K. The second and third transition temperatures are centred at 167 K and 156 K with an inclined third plateau in between at 161 K, with a $\chi_M T$ value of 1.22 cm^3 K mol^{-1}. Thus, approximately 33% of Fe(II) sites are in the HS state. The material converts to a completely LS state at *ca*. 130 K. The spin transition behaviours in the heating process are similar to the cooling process with a symmetric three-step process. Transition temperatures in the heating process are 161, 174 and 201 K. The material is in the fully HS state when the temperature is higher than 208 K. The first hysteresis loop is open while the other two are open loops. The hystereses of the first and third loop are both *ca*. 5 K while the second one is 7 K.

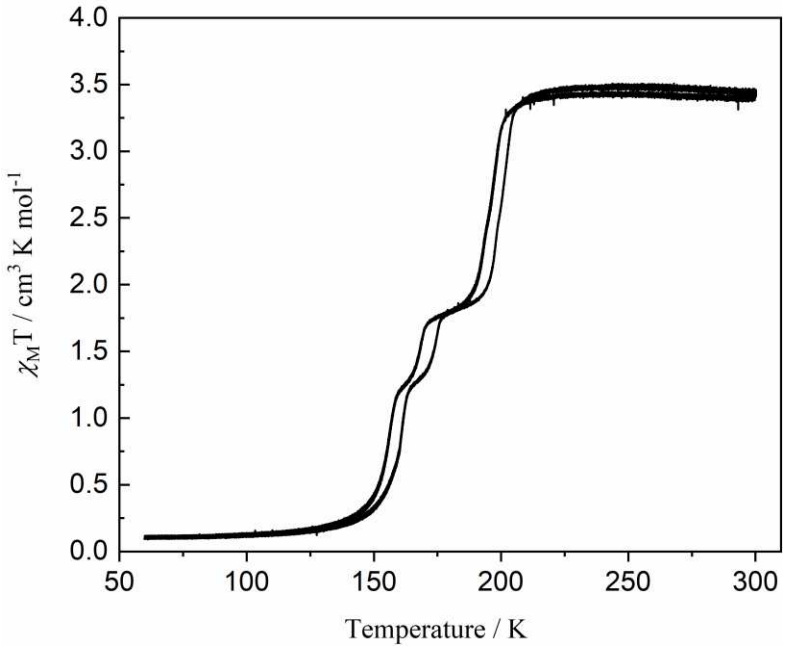

Figure 5.19: Variable temperature magnetic susceptibility measurement of **DzAu$_{0.5}$Ag$_{0.5}$·EtOH**.

5.9.3 **DzAu$_{0.7}$Ag$_{0.3}$·EtOH**

Variable temperature magnetic susceptibility measurements on powdered **DzAu$_{0.7}$Ag$_{0.3}$·EtOH** display a complete, hysteretic three-step SCO (Figure 5.20). At temperatures above 208 K, the material is in the HS state with $\chi_M T$ = 3.3 cm^3 K mol^{-1}. The material undergoes an abrupt drop of the $\chi_M T$ value until *ca*. 167 K, reaching an intermediate state with an inclined plateau (167–150 K). At this

intermediate step, 50% of the Fe(II) sites are converted to LS state. The hysteresis of the first spin transition is 5 K ($T_{½}\downarrow$ = 184 K, $T_{½}\uparrow$ = 189 K). The second and third spin transition temperatures in the cooling process are 144 K and 127 K respectively, while in the heating process is 135 K and 151 K. A short plateau is observed in between the second and third spin transition at 134 K with $\chi_M T$ = 1.3 cm^3 K mol^{-1}, which is *ca*. 35% of Fe(II) sites remaining in the HS state. The hysteretic loops in between the second and third are open. The hysteretic width is greater than in the first one. With continuing cooling, the Fe(II) sites in **DzAu$_{0.7}$Ag$_{0.3}$·EtOH** were all transferred to the LS state at *ca*. 88 K.

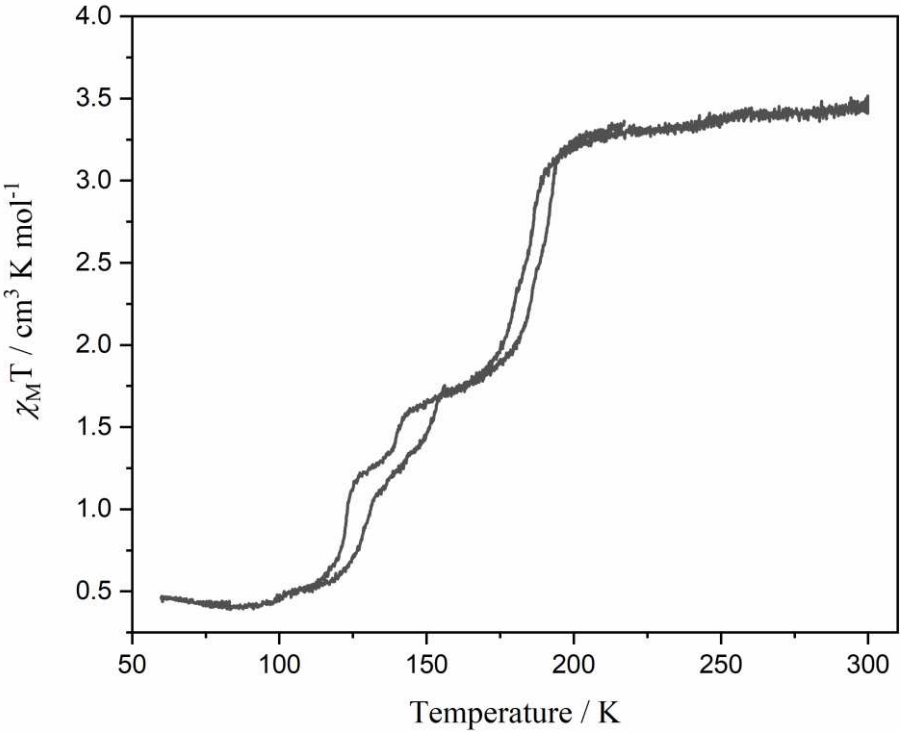

Figure 5.20: Variable temperature magnetic susceptibility measurement of **DzAu$_{0.7}$Ag$_{0.3}$·EtOH**.

The SCO behaviours of **DzAg·EtOH**, **DzAu$_{0.5}$Ag$_{0.5}$·EtOH**, **DzAu$_{0.7}$Ag$_{0.3}$·EtOH** and **DzAu·EtOH** were compared to understand the influence of different cyanidometallate linkers on spin transition (Figure 5.21). Generally, **DzAg·EtOH**, **DzAu$_{0.5}$Ag$_{0.5}$·EtOH** and **DzAu$_{0.7}$Ag$_{0.3}$·EtOH** display a three-step SCO while **DzAu·EtOH** displays a four-step SCO behaviour. **DzAg·EtOH** has the highest SCO temperatures, followed by **DzAu$_{0.5}$Ag$_{0.5}$·EtOH**, **DzAu$_{0.7}$Ag$_{0.3}$·EtOH** and **DzAu·EtOH**. Also, **DzAg·EtOH** has the highest temperature of conversion to the LS state. **DzAu$_{0.5}$Ag$_{0.5}$·EtOH** and **DzAu$_{0.7}$Ag$_{0.3}$·EtOH** are both three-step SCO but **DzAu$_{0.7}$Ag$_{0.3}$·EtOH** has lower temperatures in each intermediate state. The temperature and stepwise SCO behaviours can be manipulated by changing the ratio of $[Au(CN)_2]^-$ and $[Ag(CN)_2]^-$ linkers. The SCO temperature can be tuned to be higher with doping more $[Ag(CN)_2]^-$ linkers in the framework; this may be attributed to one, or a combination of two effects, namely the likely increased ligand field strength of $[Ag(CN)_2]^-$ and/or a systematic modification of local steric effects around the Fe(II) sites.

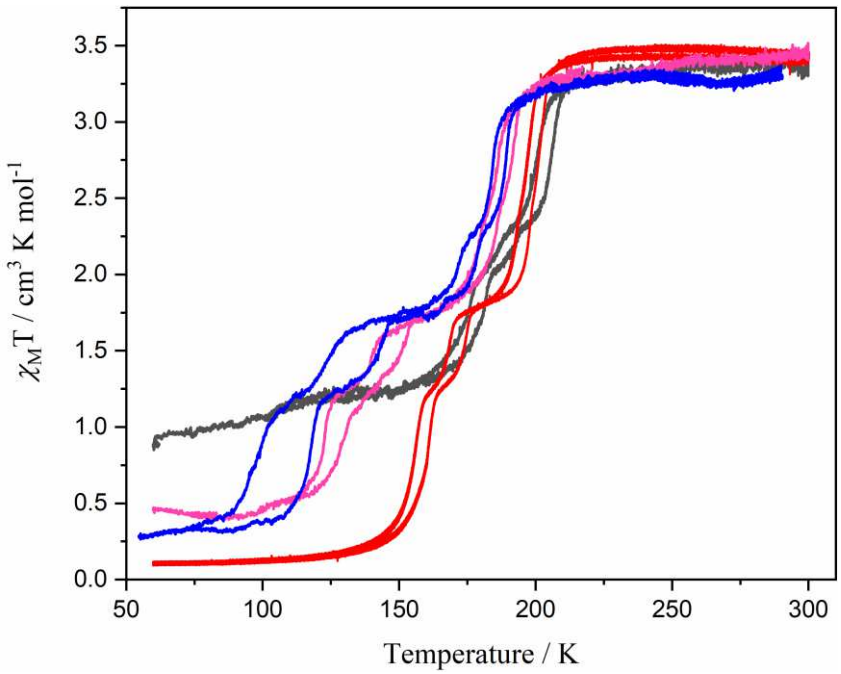

Figure 5.21: Variable temperature magnetic susceptibility measurements of **DzAg·EtOH** (black), **DzAu$_{0.5}$Ag$_{0.5}$·EtOH** (red), **DzAu$_{0.7}$Ag$_{0.3}$·EtOH** (magenta) and **DzAu·EtOH** (blue).

5.10 Raman Spectroscopy on Single and Mixed Cyanidometallate Frameworks

Raman spectroscopy measurements were conducted on **TzAg·EtOH**, **TzAu$_{0.5}$Ag$_{0.5}$·EtOH**, **TzAu·EtOH**, **DzAg·EtOH**, **DzAu$_{0.5}$Ag$_{0.5}$·EtOH** and **DzAu·EtOH** at room temperature, to provide insights into the differences of vibrational modes and analysis of the cyanide (C≡N) stretch among these framework materials. The C≡N stretch appears in Raman spectra around 2200 cm^{-1}.[27, 39-40] Spectral features appear in 600–1700 cm^{-1}, which are attributable mainly to vibrations from aromatic rings in the ligands, while those below 600 cm^{-1} correspond to metal-ligand vibrations (i.e. Fe–N and Ag–C stretching peaks).[39, 41]

The C≡N band in **TzAu·EtOH** appears at 2193 cm^{-1}, which corresponds to the cyanide stretching band from [Au(CN)$_2$]$^-$ linkers (Figure 5.22). **TzAg·EtOH** has a cyanide band from [Ag(CN)$_2$]$^-$ linkers at 2174 cm^{-1}. **TzAu$_{0.5}$Ag$_{0.5}$·EtOH** has two C≡N bands and each one has the same position as from [Au(CN)$_2$]$^-$ and [Ag(CN)$_2$]$^-$ linkers in the pure Au and Ag analogue frameworks. The matching of two peaks in **TzAu$_{0.5}$Ag$_{0.5}$·EtOH** confirms this material consists of both cyanidometallate linkers.

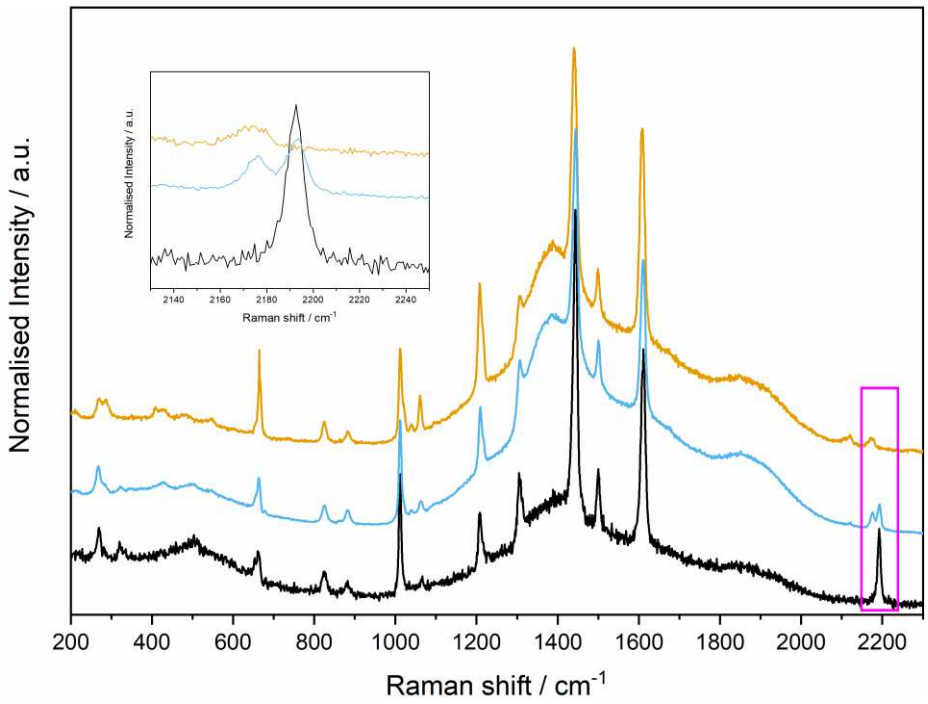

Figure 5.22: Raman spectra of **TzAu·EtOH** (black), **TzAu$_{0.5}$Ag$_{0.5}$·EtOH** (blue) and **TzAg·EtOH** (orange) in the range of 200 – 2300 cm^{-1}. Inset: close-up of the Raman spectra in the range of 2130–2250 cm^{-1}, showing the cyanide (C≡N) stretching band.

In **DzAu·EtOH** and **DzAg·EtOH**, cyanide bands from $[Au(CN)_2]^-$ and $[Ag(CN)_2]^-$ linkers are at 2194 and 2170 cm^{-1} (Figure 5.23). The peak position of each one is nearly identical as in **TzAu·EtOH** and **TzAg·EtOH**. The cyanide bands from $[Au(CN)_2]^-$ linkers have a higher energy than from $[Ag(CN)_2]^-$ linkers. **DzAu$_{0.5}$Ag$_{0.5}$·EtOH** presents two peaks, which have the same position as $[Au(CN)_2]^-$ and $[Ag(CN)_2]^-$ linkers. This suggests **DzAu$_{0.5}$Ag$_{0.5}$·EtOH** consists of both cyanidometallate linkers. The Raman results for these mixed cyanidometallate materials also indicate they only have Ag···Ag and Au···Au interactions rather than having Ag···Au interactions; otherwise, there could show more than two cyanide bands.

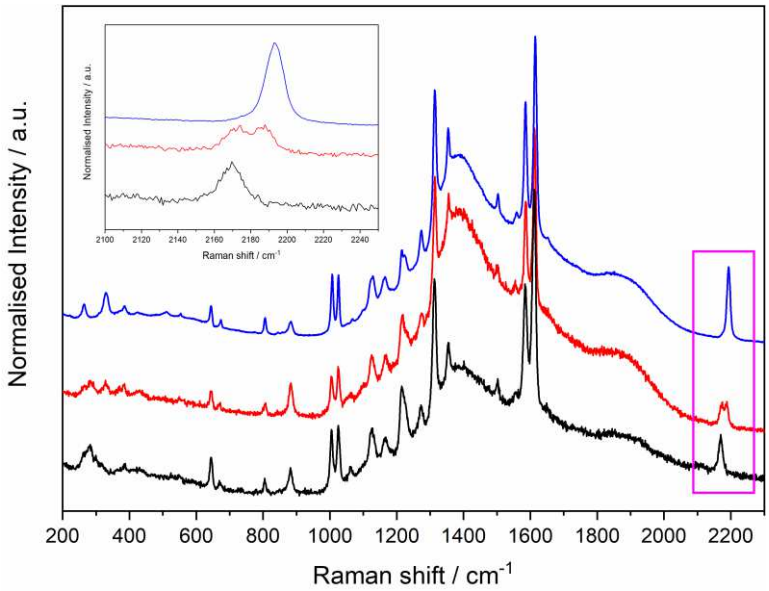

Figure 5.23: Raman spectra of **DzAu·EtOH** (blue), **DzAu$_{0.5}$Ag$_{0.5}$·EtOH** (red) and **DzAg·EtOH** (black) with the range of 200–2300 cm^{-1}. Inset: close-up of the Raman spectra in the range of 2100–2250 cm^{-1}, which shows cyanide (C≡N) stretching band.

5.11 XPS on Single and Mixed Cyanidometallate Frameworks

To identify the elements and obtain the ratio of elements, XPS measurements were conducted. Samples were dried in the air before measurements. XPS survey scans and high-resolution scans of gold or silver elements of **TzAu**, **TzAg**, **DzAu** and **DzAg** (Figure 5.24) were measured as reference samples, which were used to compare with binding energy changes in **TzAu$_{0.5}$Ag$_{0.5}$**, **DzAu$_{0.5}$Ag$_{0.5}$** and **DzAu$_{0.7}$Ag$_{0.3}$**. The ratios of gold and silver atoms from the mixed cyanidometalate frameworks were determinated by peak-area fitting.

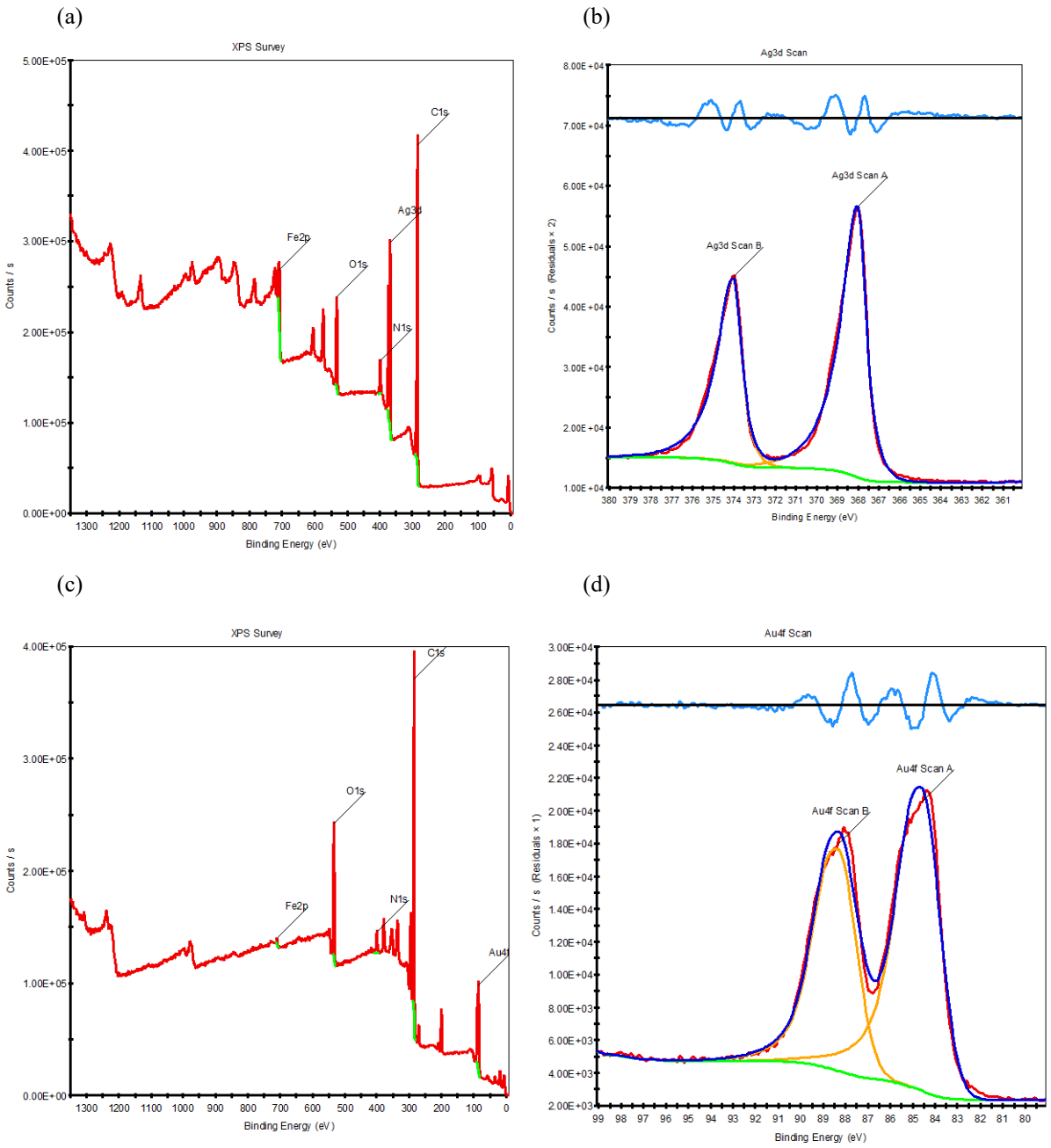

Figure 5.24: X-ray photoemission spectra for (a) a survey scan of **TzAg**, (b) a high-resolution scan of Ag 3*d* shows two peaks with a red curve representing experimentally measured data of **TzAg**, (c) a survey scan of **TzAu** and (d) a high-resolution scan of Au 4*f* shows two peaks with a red curve representing experimentally measured data of **TzAu**. The peaks were fitted showing a blue curve with the completed peak features in yellow, and the background in green. The deviation from experimental data and simulated fit in the light blue shown on the top of the peak with a black horizontal line as a baseline.

The XPS survey scan shows peaks of Fe 2*p*, Au 4*f*, N 1*s*, C 1*s* and O 1*s* in **TzAu** (Figure 5.25). That matches with all of the elements in the material and the peak position located in the right range of elements as the literature.[42-45] There are two asymmetric peaks of Au 4*f* with binding energies of 84.61

and 88.34 eV. The peak assigned to the O 1*s* is likely from remaining ethanol within the pores. In **DzAu**, Au 4*f* has higher binding energies of 85.06 and 88.74 eV. The **TzAg** survey scan displays peaks of Fe 2*p*, Ag 3*d*, N 1*s*, C 1*s* and O 1*s*. The Ag 3*d* peaks are 368.00 and 374.00 eV while in the **DzAg** the higher binding energy of 368.74 and 374.76 eV was observed.

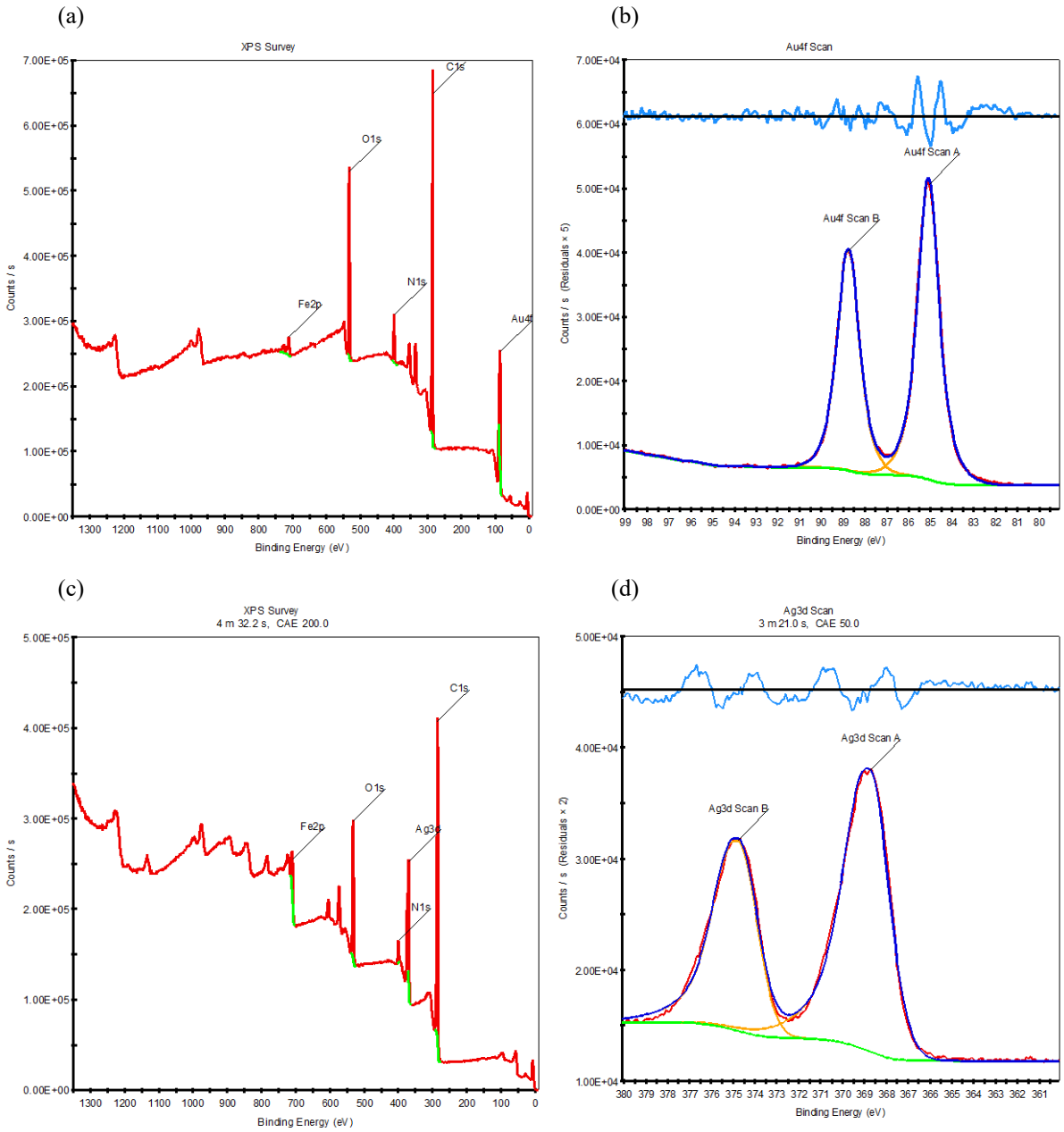

Figure 5.25: X-ray photoemission spectra for (a) a survey scan of **DzAu**, (b) a high-resolution scan of Au 4*f* shows two peaks with a red curve representing experimentally measured data of **DzAu**, (c) a survey scan of **DzAg** and (d) a high-resolution scan of Ag 3*d* shows two peaks with a red curve representing experimentally measured data of **DzAg**. The peaks were fitted showing a blue curve with the completed peak features in yellow, and the background in green. The deviation from experimental data and simulated fit in the light blue shown on the top of the peak with a black horizontal line as a baseline.

The Au and Ag peaks from **TzAu$_{0.5}$Ag$_{0.5}$**, **DzAu$_{0.5}$Ag$_{0.5}$** and **DzAu$_{0.7}$Ag$_{0.3}$** were fitted and peak areas were calculated. The XPS survey scan of **TzAu$_{0.5}$Ag$_{0.5}$** displays doublet peaks of Au 4*f* and Ag 3*d*. The ratio of Au and Ag elements was extracted from the XPS result with 52% of Au and 48% of Ag in the sample. **DzAu$_{0.5}$Ag$_{0.5}$** and **DzAu$_{0.7}$Ag$_{0.3}$** both show doublet peaks of Au 4*f* and Ag 3*d*. The doublet peak of Au 4*f* in **DzAu$_{0.5}$Ag$_{0.5}$** has larger binding energy than in **DzAu$_{0.7}$Ag$_{0.3}$**. The difference in the binding energy of Ag 3*d* in both materials is subtle with **DzAu$_{0.5}$Ag$_{0.5}$·EtOH** having a slightly larger value (Table 5.9). **DzAu$_{0.5}$Ag$_{0.5}$** contains 52% of Ag while **DzAu$_{0.7}$Ag$_{0.3}$** has 31% of Ag. The results closely match the synthetic ratio. **DzAg** shows the largest binding energy among **DzAu$_{0.5}$Ag$_{0.5}$** and **DzAu$_{0.7}$Ag$_{0.3}$**. The binding energy of Au and Ag in **TzAu$_{0.5}$Ag$_{0.5}$** is larger than in **DzAu$_{0.5}$Ag$_{0.5}$**. This may be associated with orthogonal Au···Au or Ag···Ag interactions rather than inclined interactions, which strengthen this host–host interaction.

Table 5.9: XPS results of Au 4*f* and Ag 3*d* binding energy.

	Binding energy (eV)			
MOFs	Au 4*f*		Ag 3*d*	
TzAu	84.61	88.34	N/A	N/A
TzAu$_{0.5}$Ag$_{0.5}$	85.14	88.81	368.77	374.79
TzAg	N/A	N/A	368.00	374.00
DzAu	85.06	88.74	N/A	N/A
DzAu$_{0.7}$Ag$_{0.3}$	85.16	88.84	368.39	374.40
DzAu$_{0.5}$Ag$_{0.5}$	84.94	88.57	368.37	374.37
DzAg	N/A	N/A	368.74	374.76

5.12 SEM and EDS Mapping on Mixed Cyanidometallate Frameworks

To analyse the shape of powder crystals, SEM images were conducted on powdered **TzAu$_{0.5}$Ag$_{0.5}$**, **DzAu$_{0.5}$Ag$_{0.5}$** and **DzAu$_{0.7}$Ag$_{0.3}$**. EDS mapping was carried out on these samples to provide insight into the distribution of cyanidoargentate and cyanidoaurate ligands in the mixed cyanidometallate frameworks (Figure 5.26). All of the samples were carbon-coated to increase conductivity to obtain high-resolution images.

TzAu$_{0.5}$Ag$_{0.5}$ sample shows clusters of cuboidal crystals in the SEM image. EDS mapping of **TzAu$_{0.5}$Ag$_{0.5}$** was conducted to identify the composition and distribution of elements. The mapping displays the homogenous distribution of Fe, Au and Ag in the powder sample. **DzAu$_{0.5}$Ag$_{0.5}$** and **DzAu$_{0.7}$Ag$_{0.3}$** samples also present crystal clusters with metals homogeneously distributed. The ratio of the elements in the samples could not be analysed accurately as many factors affect the accuracy, for example, the surface of the specimen needs to be flat.[46] As the samples are not satisfied these conditions, the EDS mapping is mainly for qualitative analysis.

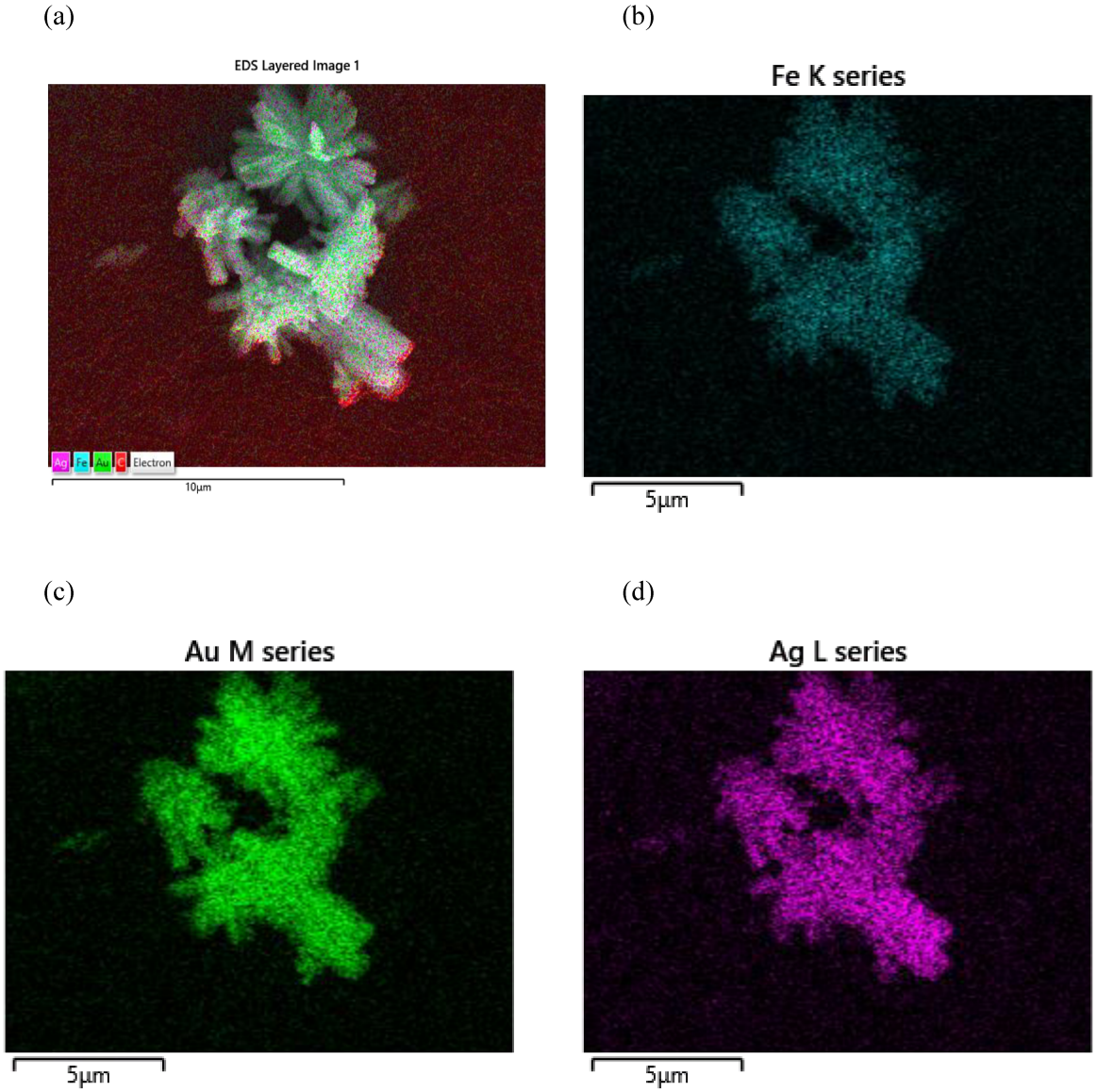

Figure 5.26: (a) SEM image of **TzAu$_{0.5}$Ag$_{0.5}$** (b) EDS mapping and elemental analysis of Fe (cyan), (c) Au (green) and (d) Ag (purple).

5.13 Discussion

Tz and Dz ligands are chemically very similar, the difference being in the middle ring between the two pyridyl rings, which is a tetrazine ring (with four nitrogen atoms) for the former and a diazine ring (with two nitrogen atoms) for the latter. Despite their similarity, distinctively different structures in space groups and unit cell parameters are observed, by comparison of the framework materials in pairs: **TzAg·EtOH** and **DzAg·EtOH**, **TzAu$_{0.5}$Ag$_{0.5}$** and **DzAu$_{0.5}$Ag$_{0.5}$**, **TzAu·EtOH** and **DzAu·EtOH**. SCO behaviours in the materials with these two ligands are also distinct, which is attributed to the difference in the framework topology.

The Tz ligand has higher symmetric than the Dz ligand and all the aromatic rings are coplanar. The Hofmann layers in the Tz ligand-based framework materials are in rhombic shape, flat and overlapped. This leads to these materials adopting a relatively higher symmetric space group. Because of the superimposed rhombic grids, the materials undergo thermally-induced scissor motions induced by SCO. However, there is no scissor motion in frameworks consisting of Dz ligands. The reason for that is related to the aromatic rings in the Dz ligand being tilted and disordered, and the metallophilic interactions between the Hofmann layers being inclined. Thus, the grids are staggered and θ is nearly orthogonal, which inhibits θ from increasing induced by SCO upon cooling. The key factor in building up frameworks with scissor motion is to have overlayed grids, which can undergo lattice flexing motion simultaneously.

The Tz-based frameworks present one-step SCO and convert it to the LS state at a relatively higher temperature than the Dz analogues. However, Dz-based frameworks display either three-step SCO in **DzAg·EtOH**, **$DzAu_{0.5}Ag_{0.5}$·EtOH** and **$DzAu_{0.7}Ag_{0.3}$·EtOH** or four-step SCO in **DzAu·EtOH**. The differences in SCO behaviour are influenced by the electronic properties of the ligands and structural properties of the frameworks. The Dz ligand is more electron rich than the Tz ligand and has a lower ligand field, which is associated with the lower spin transition temperature. Besides the intrinsic property of the ligands, SCO behaviours are likely attributed to the extent of symmetry and distortion of the frameworks. Therefore, based on the results of the structure-property relationships in these systems, materials with a lower ligand field and a higher degree of frameworks disorder can potentially lead to multi-step SCO and lower spin transition temperatures.

The comparison study on different cyanidometallate linkers reveals the relationship between structure and SCO behaviours. A comparison of **TzAg·EtOH**, **$TzAu_{0.5}Ag_{0.5}$·EtOH** and **TzAu·EtOH** show a decreasing trend in the spin transition temperature. It is the same trend as in **DzAg·EtOH**, **$DzAu_{0.5}Ag_{0.5}$·EtOH** and **$DzAu_{0.7}Ag_{0.3}$·EtOH** and **DzAu·EtOH** with each step of the transition temperatures decreasing by reducing the dicyanidoargentate linker component. Thus, generating materials involving weaker argentophilic interactions rather than aurophilic interactions could form these materials in higher spin transition temperatures.

5.14 Conclusions and Future Work

This chapter investigated the properties of materials with different ligands (Tz or Dz ligand) and cyanidometallate linkers. The structures, magnetic properties, vibrational spectroscopy, the binding energy of the elements and images of atom distribution were characterised for each framework. Mixed cyanidometallate frameworks were found to be homogeneously mixed. The synthetic ratio of cyanidometallate linkers is nearly identical to that formed frameworks.

The frameworks **TzAg·EtOH** and **TzAu$_{0.5}$Ag$_{0.5}$·EtOH** were generated and both adopt the orthorhombic phase in *Cmma* space group. The topology of each is nearly identical. The subtle differences in the structures were examined. The strength of the metallophilic interactions affects the distances between the Hofmann layers and the extent of lattice flexing. That is associated with SCO behaviours and scissor motion. By comparing with **TzAu·EtOH**, it reveals that a greater proportion of components of dicyanidoaurate linkers give higher spin transition temperature and a larger degree of scissor motion. Thus, the NTE on the *a*-axis and SCO can be tuned by changing the composition of dicyanidoaurate and dicyanidoargentate linkers. It is similar to the alloy, which can manipulate its properties *via* changing the compositions. Future work can focus on designing MOFs using various symmetric ligands, which display more regular topologies with rhombic grids. It is likely that NTE would be observed. The relationship between the ligand properties and the extent of NTE would be deeper understood. As these Tz ligand-based materials present NTE behaviours induced by SCO, it would be interesting to further investigate whether the extent of NTE and SCO behaviours can be changed by applying pressure.

The Dz ligand-based materials (**DzAg·EtOH**, **DzAu$_{0.5}$Ag$_{0.5}$·EtOH** and **DzAu$_{0.7}$Ag$_{0.3}$·EtOH**) with different cyanidometallate linkers were also synthesised and characterised. The frameworks **DzAg·EtOH** and **DzAu$_{0.5}$Ag$_{0.5}$·EtOH** both adopt the monoclinic *C*2/*c* space group. The increase of disorder in the ligands and distortion of the Hofmann layer are observed in the Dz ligand-based materials compared with the Tz ligand-based materials. The lattices in the Dz ligand-based materials (**DzAg·EtOH**, **DzAu$_{0.5}$Ag$_{0.5}$·EtOH** and **DzAu·EtOH**) present PTE. The largest volume among these three materials is DzAu$_{0.5}$Ag$_{0.5}$ as it has the largest *b*- and *c*-axial parameters. The multi-step SCO behaviours were demonstrated not only by magnetic susceptibility measurements but also SCXRD and VT-PXRD, showing good agreement. With increasing the composition of dicyanidoaurate linkers the spin transition temperatures decrease. Also, the increase of stepwise from three-step to four-step is observed. **DzAu$_{0.7}$Ag$_{0.3}$·EtOH** appears close to the critical Au:Ag ratio at which the four-step behaviour becomes evident.

DzPt and **DzPd** both present a distinct topology compared with the materials consisting of dicyanidoargentate and dicyanidoaurate linkers, which are all Hofmann-like frameworks. **DzPd** is the first reported accordion-like framework rather than other materials coordinated with $[Pd(CN)_4]$ anion in Hofmann-like topology. The unique structure in **DzPt** and **DzPd** is attributed to each Fe(II) centre coordinated with two water molecules and one $[Pt(CN)_4]^{2-}$ or $[Pd(CN)_4]^{2-}$ on the equatorial position. They form FeN_4O_2 octahedral distortion geometry instead of FeN_6. Therefore, no SCO behaviour is observed in both **DzPt** and **DzPd** materials. It would be interesting to generate materials with a mixture of $[Pt(CN)_4]^{2-}$ or $[Pd(CN)_4]^{2-}$ with $[Au(CN)_2]^-$ or $[Ag(CN)_2]^-$ to investigate whether a homogeneous Hofmann-like framework can be formed and SCO behaviour occur in this material. Further work can also involve synthesising frameworks consisting of $[Pt(CN)_4]^{2-}$ or $[Pd(CN)_4]^{2-}$ but with solvents other

than water to grow a Hofmann-like framework. **DzPt** and **DzPd** coordinated with water may be due to the steric effect of Dz ligand so smaller ligands could be tried to generate Hofmann-like materials with SCO behaviours. One of the post-synthetic modification methods: solvent-assisted linker exchange[47-48] can be used to create a Hofmann-like framework with Dz ligand and $[Pt(CN)_4]^{2-}$ or $[Pd(CN)_4]^{2-}$. That is first to generate **DzAg·EtOH** or **DzAu·EtOH** framework as parent framework and soaking into solvents with either $[Pt(CN)_4]^{2-}$ or $[Pd(CN)_4]^{2-}$ linkers. A daughter MOF after linker exchange could produce an isostructural analogue as the parent MOF.

The deeper understanding of the effect of host–host interactions and ligands provide guidance on the precise tuning of MOFs structural and magnetic properties. That will be used in designing devices with controllable functionalities.

5.15 References

1. Mullaney, B. R.; Goux-Capes, L.; Price, D. J.; Chastanet, G.; Letard, J. F.; Kepert, C. J., *Nat. Commun.* **2017,** *8* (1), 1053.

2. Baldé, C.; Desplanches, C.; Gütlich, P.; Freysz, E.; Létard, J. F., *Inorg. Chim. Acta* **2008,** *361* (12-13), 3529-3533.

3. Calvo Galve, N.; Coronado, E.; Giménez-Marqués, M.; Mínguez Espallargas, G., *Inorg. Chem.* **2014,** *53* (9), 4482-4490.

4. Krober, J.; Codjovi, E.; Kahn, O.; Groliere, F.; Jay, C., *J. Am. Chem. Soc.* **1993,** *115* (21), 9810-9811.

5. Quesada, M.; Prins, F.; Bill, E.; Kooijman, H.; Gamez, P.; Roubeau, O.; Spek, A. L.; Haasnoot, J. G.; Reedijk, J., *Eur. J. Chem.* **2008,** *14* (28), 8486-8499.

6. Aravena, D.; Castillo, Z. A.; Muñoz, M. C.; Gaspar, A. B.; Yoneda, K.; Ohtani, R.; Mishima, A.; Kitagawa, S.; Ohba, M.; Real, J. A.; Ruiz, E., *Eur. J. Chem.* **2014,** *20* (40), 12864-12873.

7. Murphy, M. J.; Zenere, K. A.; Ragon, F.; Southon, P. D.; Kepert, C. J.; Neville, S. M., *J. Am. Chem. Soc.* **2017,** *139* (3), 1330-1335.

8. Kahn, O.; Martinez, C. J., *Science* **1998,** *279* (5347), 44-48.

9. Piñeiro-López, L. A.; Valverde-Muñoz, F. J.; Seredyuk, M.; Muñoz, M. C.; Haukka, M.; Real, J. A., *Inorg. Chem.* **2017,** *56* (12), 7038-7047.

10. Sciortino, N. F.; Scherl-Gruenwald, K. R.; Chastanet, G.; Halder, G. J.; Chapman, K. W.; Létard, J.-F.; Kepert, C. J., *Angew. Chem. Int. Ed.* **2012,** *51* (40), 10154-10158.

11. Brennan, A. T.; Zenere, K. A.; Kepert, C. J.; Clegg, J. K.; Neville, S. M., *Inorg. Chem.* **2021,** *60* (6), 3871-3878.

12. Valverde-Munoz, F. J.; Kazan, R.; Boukheddaden, K.; Ohba, M.; Real, J. A.; Delgado, T., *Inorg. Chem.* **2021,** *60* (12), 8851-8860.

13. Sciortino, N. F.; Neville, S. M.; Letard, J. F.; Moubaraki, B.; Murray, K. S.; Kepert, C. J., *Inorg. Chem.* **2014,** *53* (15), 7886-93.

14. Zenere, K. A.; Duyker, S. G.; Trzop, E.; Collet, E.; Chan, B.; Doheny, P. W.; Kepert, C. J.; Neville, S. M., *Chem. Sci.* **2018,** *9* (25), 5623-5629.

15. Zhao, J.; Huang, H.; Liu, M.; Wang, J.-H.; Liu, K.; Li, Z.-Y., *RSC Adv.* **2019,** *9* (45), 26450-26455.

16. Piñeiro-López, L.; Valverde-Muñoz, F. J.; Seredyuk, M.; Znovjyak, K., *IUCrData* **2017,** *2* (10).

17. Haraguchi, T.; Otsubo, K.; Sakata, O.; Kawaguchi, S.; Fujiwara, A.; Kitagawa, H., *Chem. Commun.* **2016,** *52* (35), 6017-6020.

18. Peng, Y.-Y.; Wu, S.-G.; Chen, Y.-C.; Liu, W.; Huang, G.-Z.; Ni, Z.-P.; Tong, M.-L., *Inorg. Chem. Front.* **2020,** *7* (8), 1685-1690.

19. Clements, J. E.; Price, J. R.; Neville, S. M.; Kepert, C. J., *Angew. Chem. Int. Ed.* **2014,** *53* (38), 10164-10168.

20. Rawashdeh-Omary, M. A.; Omary, M. A.; Patterson, H. H., *J. Am. Chem. Soc.* **2000,** *122* (42), 10371-10380.

21. Niel, V.; Thompson, A. L.; Muñoz, M. C.; Galet, A.; Goeta, A. E.; Real, J. A., *Angew. Chem. Int. Ed.* **2003,** *42* (32), 3760-3763.

22. Galet, A.; Niel, V.; Muñoz, M. C.; Real, J. A., *J. Am. Chem. Soc.* **2003,** *125* (47), 14224-14225.

23. Dolomanov, O. V.; Bourhis, L. J.; Gildea, R. J.; Howard, J. A. K.; Puschmann, H., *J. Appl. Crystallogr.* **2009,** *42* (2), 339-341.

24. Jansen, M., *Angew. Chem., Int. Ed. Engl.* **1987,** *26* (11), 1098-1110.

25. Li, J.-Y.; Ni, Z.-P.; Yan, Z.; Zhang, Z.-M.; Chen, Y.-C.; Liu, W.; Tong, M.-L., *CrystEngComm* **2014,** *16* (28), 6444-6449.

26. Hiiuk, V. M.; Shylin, S. I.; Barakhtii, D. D.; Korytko, D. M.; Kotsyubynsky, V. O.; Rotaru, A.; Shova, S.; Gural'Skiy, I. Y. A., *Inorg. Chem.* **2022,** *61* (4), 2093-2104.

27. Agustí, G.; Cobo, S.; Gaspar, A. B.; Molnár, G.; Moussa, N. O.; Szilágyi, P. Á.; Pálfi, V.; Vieu, C.; Carmen Muñoz, M.; Real, J. A.; Bousseksou, A., *Chem. Mater.* **2008,** *20* (21), 6721-6732.

28. Li, Y.; Liu, M.; Yao, Z.-S.; Tao, J., *Dalton Trans.* **2020,** *49* (21), 7245-7251.

29. Meneses-Sánchez, M.; Turo-Cortés, R.; Bartual-Murgui, C.; Da Silva, I.; Muñoz, M. C.; Real, J. A., *Inorg. Chem.* **2021,** *60* (16), 11866-11877.

30. Valverde-Muñoz, F. J.; Seredyuk, M.; Muñoz, M. C.; Znovjyak, K.; Fritsky, I. O.; Real, J. A., *Inorg. Chem.* **2016,** *55* (20), 10654-10665.

31. Liu, F.-L.; Li, D.; Su, L.-J.; Tao, J., *Dalton Trans.* **2018,** *47* (5), 1407-1411.

32. Niel, V.; Martinez-Agudo, J. M.; Muñoz, M. C.; Gaspar, A. B.; Real, J. A., *Inorg. Chem.* **2001,** *40* (16), 3838-3839.

33. Ahmed, M.; Zenere, K. A.; Sciortino, N. F.; Arachchige, K. S. A.; Turner, G. F.; Cruddas, J.; Hua, C.; Price, J. R.; Clegg, J. K.; Valverde-Muñoz, F. J.; Real, J. A.; Chastanet, G.; Moggach, S. A.; Kepert, C. J.; Powell, B. J.; Neville, S. M., *Inorg. Chem.* **2022,** *61* (17), 6641-6649.

34. Brennan, A. T.; Zenere, K. A.; Brand, H. E. A.; Price, J. R.; Bhadbhade, M. M.; Turner, G. F.; Moggach, S. A.; Valverde-Muñoz, F. J.; Real, J. A.; Clegg, J. K.; Kepert, C. J.; Neville, S. M., *Inorg. Chem.* **2020,** *59* (19), 14296-14305.

35. Klein, Y. M.; Sciortino, N. F.; Ragon, F.; Housecroft, C. E.; Kepert, C. J.; Neville, S. M., *Chem. Commun.* **2014,** *50* (29), 3838-3840.

36. Martínez, V.; Gaspar, A. B.; Muñoz, M. C.; Ballesteros, R.; Ortega-Villar, N.; Ugalde-Saldívar, V. M.; Moreno-Esparza, R.; Real, J. A., *Eur. J. Inorg. Chem* **2009,** *2009* (2), 303-310.

37. Ahmed, M.; Arachchige, K. S. A.; Xie, Z.; Price, J. R.; Cruddas, J.; Clegg, J. K.; Powell, B. J.; Kepert, C. J.; Neville, S. M., *Inorg. Chem.* **2022**.

38. Clements, J. E.; Price, J. R.; Neville, S. M.; Kepert, C. J., *Angew. Chem. Int. Ed.* **2016,** *55* (48), 15105-15109.

39. Omary, M. A.; Webb, T. R.; Assefa, Z.; Shankle, G. E.; Patterson, H. H., *Inorg. Chem.* **1998,** *37* (6), 1380-1386.

40. Ong, X.; Ahmed, M.; Xu, L.; Brennan, A. T.; Hua, C.; Zenere, K. A.; Xie, Z.; Kepert, C. J.; Powell, B. J.; Neville, S. M., *Chemistry* **2021,** *3* (1), 360-372.

41. Molnár, G.; Niel, V.; Gaspar, A. B.; Real, J.-A.; Zwick, A.; Bousseksou, A.; McGarvey, J. J., *J. Phys. Chem. B* **2002,** *106* (38), 9701-9707.

42. Grosvenor, A. P.; Kobe, B. A.; Biesinger, M. C.; Mcintyre, N. S., *Surf. Interface Anal.* **2004,** *36* (12), 1564-1574.

43. Casaletto, M. P.; Longo, A.; Martorana, A.; Prestianni, A.; Venezia, A. M., *Surf. Interface Anal.* **2006,** *38* (4), 215-218.

44. Tang, H.; Cai, S.; Xie, S.; Wang, Z.; Tong, Y.; Pan, M.; Lu, X., *Adv. Sci.* **2016,** *3* (2), 1500265.

45. Rignanese, G.-M.; Pasquarello, A.; Charlier, J.-C.; Gonze, X.; Car, R., *Phys. Rev. Lett.* **1997,** *79* (25), 5174-5177.

46. Newbury, D. E.; Ritchie, N. W. M., *Scanning* **2013,** *35* (3), 141-168.

47. Burnett, B. J.; Barron, P. M.; Hu, C.; Choe, W., *J. Am. Chem. Soc.* **2011,** *133* (26), 9984-9987.

48. Karagiaridi, O.; Bury, W.; Mondloch, J. E.; Hupp, J. T.; Farha, O. K., *Angew. Chem. Int. Ed.* **2014,** *53* (18), 4530-4540.

Chapter 6

Spin Crossover Behaviours and Anomalous Structural Distortion Under Pressure in Hofmann-like Frameworks

6.1 Overview

The vast majority of materials contract under hydrostatic pressure. However, a small number of materials display a counterintuitive behaviour whereby expansion is observed under applied pressure. Such an unexpected phenomenon is known as negative linear compressibility (NLC). Materials that exhibit NLC have unique traits that have the capability to compensate for positive linear compressibility (PLC) and possess structural scalability. Therefore, such materials have potential applications in these pressure sensors, body armour and optical fibers.[1-2] NLC has been found to occur in some inorganic frameworks such as $Zn(CN)_2$, BiB_3O_6 and $Ag_3[Co(CN)]_6$.[2-3] However, examples of MOFs that display NLC are very rare.[3] Thus, developing materials that exhibit NLC and understanding the structural mechanisms involved on the atomic scale under pressure is of paramount importance.

NLC likely arises in the materials that adopt 'wine rack' or 'honeycomb' networks. The framework materials $[Ag(en)]NO_3$ (en, ethylenediamine),[4] $Zr_3(\mu_3\text{-}OH)_4(OH)_4(C_{46}H_{34}O_8)]\cdot 10DEF$ (DEF = N,N-diethylformamid)[5] and MIL systems contain 'wine rack' motifs and have attached greater attention for their NLC properties.[6] Materials possessing 'wine rack' topologies potentially display anisotropic expansion mechanisms with increasing pressure depending on the motifs, with one direction leading to a contraction and another to expansion. However, limited research has been directed towards SCO MOFs under pressure. Investigating the coupling of switchable electronic configurations in response to pressure is of interest in SCO materials. Given the complex interplay between structural and spin state energetics, a range of highly exotic behaviours are anticipated to be observed in such SCO MOF materials.

TzAu·EtOH has a 'wine rack' Hofmann grid that is anticipated to exhibit NLC and is therefore an ideal platform to study lattice motions and the collective SCO effect under pressure. The ligand effect on the magnitude of NLC and lattice flexing was investigated by comparing the structural properties of the MOF $[Fe(Tz)_{0.5}(Dz)_{0.5}Au(CN)_2)_2]\cdot x(EtOH)$ (**$[Tz_{0.5}Dz_{0.5}]$**) that consists of two pillared ligands in 50% ratio, namely the Tz and Dz ligand. The SCO behaviour of the MOF containing only the Dz ligand $[Fe(Dz)Au(CN)_2)_2]\cdot x(EtOH)$ (**DzAu·EtOH**) was also demonstrated. This work demonstrates the coupling of lattice motions of NLC and switchable spin transitions under pressure. Furthermore, pressure-induced SCO on these three SCO MOFs was examined to reveal the effect of ligand field strength and their structural and magnetic implications. Therefore, the work in this chapter develops guidelines for creating controllable materials that exhibit SCO and NLC behaviours in response to pressure.

6.2 SCO Behaviours Under Pressure

6.2.1 Variable Temperature Magnetic Susceptibility of **TzAu·EtOH** Under Pressure

Variable temperature magnetic susceptibility measurements of **TzAu·EtOH** were performed under variable pressures on a PPMS Dynacool magnetometer to examine the pressure-induced SCO. The powdered material as a suspension in ethanol and a small amount of lead as a pressure calibrant were loaded into a Teflon tube sealed with Teflon caps on both ends inside a Quantum Design High-Pressure Cell. The applied pressure was determined by measuring the critical temperature in a superconducting state on a lead wire in the sample tube. Data were collected in sweep mode at scan rates of 1, 2, and 5 K min^{-1} for each pressure point except at 0.99 GPa, which was only measured at 1 K min^{-1} as the temperature range is out of the instrument limit. The spin transition temperatures for each pressure point at different scan rates are tabulated in Appendix Table D.1.

The data at the first pressure point were collected at 0.33 GPa and show abrupt and complete one-step SCO with hysteresis (Figure 6.1). The $\chi_M T$ value of **TzAu·EtOH** is 3.4 cm^3 K mol^{-1} above 280 K at a scan rate of 1 K min^{-1}, indicating the HS state. An abrupt decrease of the $\chi_M T$ value is observed until reaching 262 K when the $\chi_M T$ value reaches approximately 0 cm^3 K mol^{-1}, indicating a conversion to the complete LS state. The spin transition temperatures are 266 K and 281 K in the cooling and heating processes, respectively, and therefore constitute a thermal hysteresis width of 15 K. The hysteresis width of **TzAu·EtOH** at 0.33 GPa is five times wider than at ambient pressure ($T_{½}\downarrow$ = 274 K and $T_{½}\uparrow$ = 277 K, ΔT = 3 K) at the same scan rate.[7] Note that the material measured at ambient pressure was loaded in a PFA sample holder while the variable pressure measurements were performed in a Quantum Design high pressure cell. Temperature lag is more significant in high pressure cells due to the necessarily thicker wall of the cell. Thus, a wider hysteresis width was observed with lower $T_{½}\downarrow$ and higher $T_{½}\uparrow$ values than the actual spin transition temperatures.

To understand the scan rate effect and estimate the 'zero scan rate' spin transition temperature of a material, variable temperature magnetic susceptibility measurements at 1, 2 and 5 K min^{-1} were carried out. With increasing scan rate, a wider hysteresis with lower $T_{½}\downarrow$ and higher $T_{½}\uparrow$ is observed. The same trend in spin transition temperatures and hysteresis due to different scan rates is commonly observed in other materials.[8-9] The 'true hysteresis' or 'true spin transition' was calculated by extrapolating the $T_{1/2}$ value as a function of scan rate (1, 2 and 5 K min^{-1}). Thus, the spin transition temperatures at zero scan rate are $T_{½}\downarrow$ = 271 K and $T_{½}\uparrow$ = 275 K with a narrower hysteresis at 4 K min^{-1} than the measured scan rate of 1 K min^{-1}.

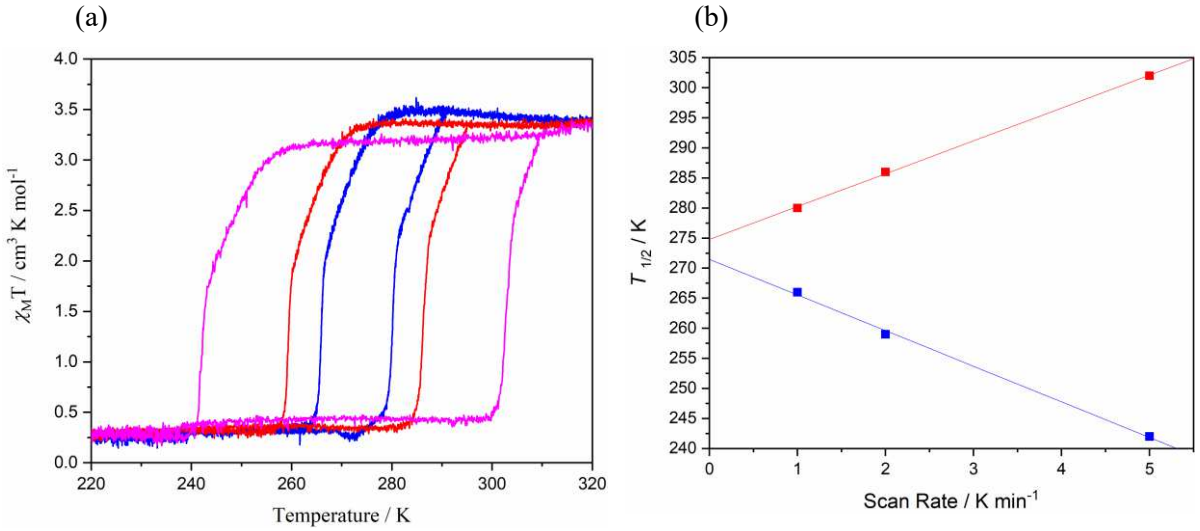

Figure 6.1: (a) Variable temperature magnetic susceptibility data of **TzAu·EtOH** at a scan rate of 1 (blue), 2 (red) and 5 K min^{-1} (purple). (b) The $T_{1/2}$ value as a function of scan rate (1, 2 and 5 K min^{-1}).

Measurements under applied pressure were performed at 0.33, 0.35, 0.36, 0.37, 0.39, 0.45, 0.54, 0.62, 0.76, and 0.99 GPa. All of the magnetic susceptibility data for **TzAu·EtOH** that were collected at a scan rate of 1 K min^{-1} under pressure show one-step and hysteretic SCO behaviours (Figure 6.2). The material is able to transition to a completely LS state at pressures below 0.45 GPa, while at higher pressures (> 0.54 GPa) the SCO behaviour becomes incomplete. At 0.45 GPa, **TzAu·EtOH** remains in the HS state above 337 K. Abrupt one-step SCO occurs with a hysteresis width of ΔT = 18 K ($T_{½}\downarrow$ = 322 K and $T_{½}\uparrow$ = 340 K). **TzAu·EtOH** transitions to the LS state at *ca.* 293 K. It is interesting to note that at the same temperature (293 K), **TzAu·EtOH** adopts a LS configuration at a pressure of 0.45 GPa, while it remains in the HS state at 0.33 GPa. This result demonstrates that the different spin state configurations can be alternated by varying the pressure.

The spin transition temperatures gradually increase with increasing pressure between 0.33 and 0.76 GPa. The hysteresis widths slightly increase below 0.62 GPa. The $T_{½}\downarrow$ values at 0.54 and 0.62 GPa are the same at 330 K, but at 0.62 GPa, there is a slightly higher $T_{½}\uparrow$ value of 354 K compared to at 0.54 GPa ($T_{½}\uparrow$ = 351 K). At pressures lower than 0.62 GPa, spin transition temperatures in both the cooling and heating process increase with pressurisation. However, at 0.76 GPa, a lower $T_{½}\downarrow$ = 325 K and higher $T_{½}\uparrow$ = 361 K than spin transition temperatures at 0.62 GPa is observed. The wider hysteresis and more incomplete SCO occur at 0.76 GPa. At 0.99 GPa, there is a pronounced enlargement of the hysteresis width; at this pressure, the spin transition temperatures decrease dramatically ($T_{½}\downarrow$ = 292 K and $T_{½}\uparrow$ = 346 K) compared to at 0.76 GPa. Approximately 50% of the SCO sites convert to the LS state. The material exhibits the widest hysteresis width of 54 K at 0.99 GPa. Stabilisation of the HS state with pressurisation is rare.[10] Generally, the spin transition temperature of a SCO compound should shift to higher temperatures with increasing pressure as it favours the more densely packed LS state and shorter

metal–ligand bond lengths.[11-12] Overall, the spin transition temperatures and hysteresis widths increase in **TzAu·EtOH** at elevated pressures (Figure 6.2 (c) and (d)).

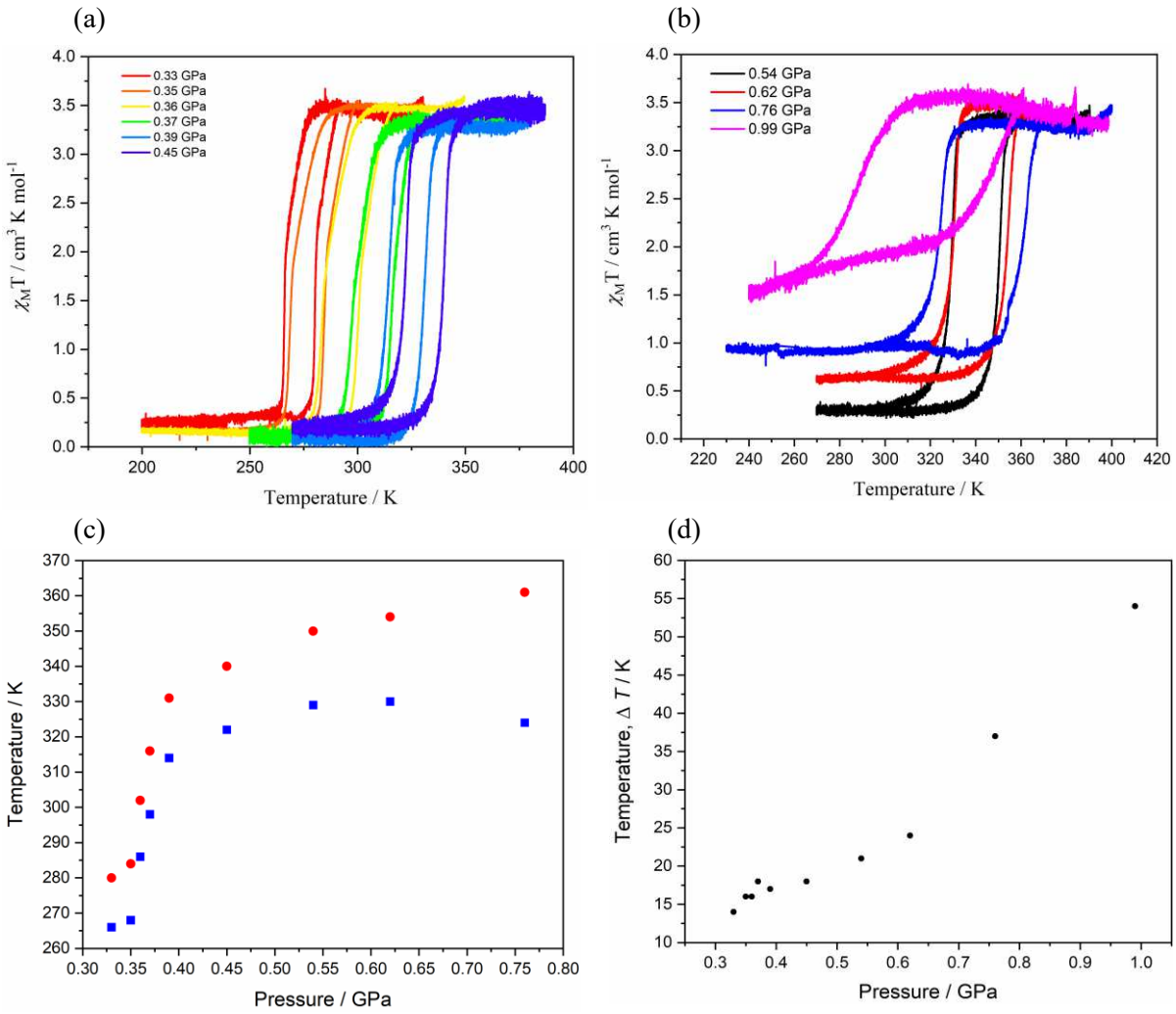

Figure 6.2: Variable temperature magnetic susceptibility data of **TzAu·EtOH** at a scan rate of 1 K min^{-1} (a) at 0.33, 0.35, 0.36, 0.37, 0.39, 0.45 GPa and (b) 0.54, 0.62, 0.76 and 0.99 GPa. (c) Spin transition temperature against pressures of **TzAu·EtOH**. (d) Hysteresis width against pressure of **TzAu·EtOH**.

6.2.2 Variable Temperature Magnetic Susceptibility of **[Tz$_{0.5}$Dz$_{0.5}$]** Under Pressure

Variable temperature magnetic susceptibility measurements of **[Tz$_{0.5}$Dz$_{0.5}$]** were performed under variable pressures at 0.32, 0.35, 0.45, 0.60, and 0.78 GPa (Figure 6.3). The data were collected in sweep mode at a scan rate of 1 K min^{-1}. The material exhibits complete and one-step SCO at the first pressure point (0.32 GPa) with an associated hysteresis width of ΔT = 14 K ($T_{½}\downarrow$ = 276 K and $T_{½}\uparrow$ = 290 K). At 0.35 GPa, the spin transition temperatures increase with $T_{½}\downarrow$ = 304 K and $T_{½}\uparrow$ = 318 K. The material measured at 0.32 GPa can undergo a complete LS state with the $\chi_M T$ value close to 0 cm^3 K mol^{-1}. However, at 0.35 GPa, the material presents an incomplete LS state transition with a slightly higher $\chi_M T$ at about 0.3 cm^3 K mol^{-1}. At 0.45 GPa, the SCO behaviour of **[Tz$_{0.5}$Dz$_{0.5}$]** is incomplete and one-step

with a hysteresis of $\Delta T = 18$ K ($T_{½}\downarrow = 328$ K and $T_{½}\uparrow = 346$ K). Above 335 K, the material remains in the HS state at this pressure point. The $\chi_M T$ value reaches 1.9 cm^3 K mol^{-1} at 290 K, indicating an approximate 50% conversion to the LS state. When the pressure is increased to 0.60 GPa, the highest spin transition temperatures ($T_{½}\downarrow = 333$ K and $T_{½}\uparrow = 356$ K) and widest hysteresis ($\Delta T = 23$ K) are observed among the selected pressure points. The $\chi_M T$ value at this pressure is 2.8 cm^3 K mol^{-1} at 310 K, indicating that approximately 80% of the SCO sites adopt their HS state. The material locks into the HS state when the pressure reaches 0.78 GPa.

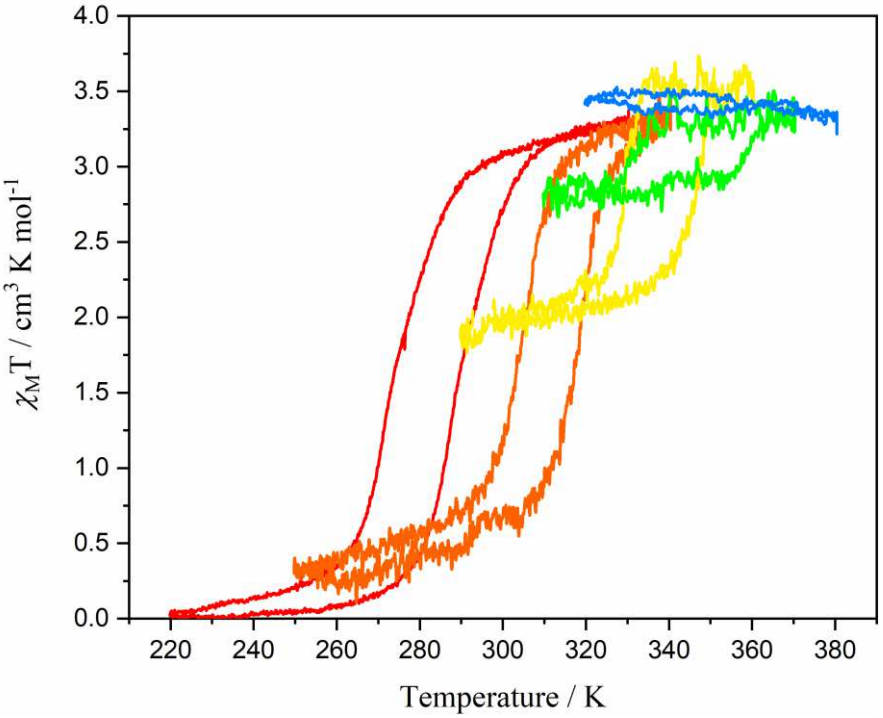

Figure 6.3: Variable temperature magnetic susceptibility data of **[Tz$_{0.5}$Dz$_{0.5}$]** at 0.32 (red), 0.35 (orange), 0.45 (yellow), 0.60 (green) and 0.78 GPa (blue) at scan rate of 1 K min^{-1}.

6.2.3 Variable Temperature Magnetic Susceptibility of **DzAu·EtOH** Under Pressure

Variable temperature magnetic susceptibility measurements of **DzAu·EtOH** under variable pressures (at 0.32, 0.34, and 0.36 GPa) were performed at a scan rate of 0.5 K min^{-1}. Unlike **DzAu·EtOH**, which exhibits four-step SCO at ambient pressure, incomplete three-step SCO with hysteresis is observed at 0.32 GPa (Figure 6.4). The $\chi_M T$ values remain relatively constant until approximately 175 K. The first step of the spin transition occurs at 169 K in the cooling process and 182 K in the heating process. When cooling to 155 K, an intermediate plateau is observed with a $\chi_M T$ value of 2.2 cm^3 K mol^{-1}. With continuous cooling, the second and third spin transitions occur at 120 and 94 K, respectively, with a small inclined plateau in between. The $\chi_M T$ value decreases to 1.1 cm^3 K

mol^{-1} at 60 K indicating that approximately 70% of the SCO sites adopt the LS state. In the heating process, the $\chi_M T$ values slightly decrease to 0.7 cm^3 K mol^{-1} at 87 K, but with a further increase of temperature the $\chi_M T$ values increase as predicted. The reduction in the $\chi_M T$ values is also observed between the temperature ranges of 126–140 K and 166–176 K, which is likely due to a temperature lag effect. The second and third spin transitions occur at 139 K and 109 K, respectively, upon heating. At 186 K, the SCO sites transition back to the HS state.

With an increase of pressure to 0.34 GPa, **DzAu·EtOH** also exhibits incomplete and hysteretic three-step SCO. The first step of the SCO profile occurs at 173 K in the cooling process, which is higher than that observed when at 0.32 GPa. The spin transition reaches a wide plateau region that spans the temperature range 153 K–125 K. Upon further cooling, the second spin transition occurs at 119 K and is followed by the third spin transition at 91 K. The $\chi_M T$ value decreases to 2.3 cm^3 K mol^{-1} at 60 K. The three-step SCO is recovered upon heating, with the three spin transition temperatures being centred at 192, 145, and 111 K from the first to third, respectively.

At 0.36 GPa, the SCO profile of the material is a loop with the $\chi_M T$ values fluctuating within the range of 3.3–3.9 cm^3 K mol^{-1} across the entire the measured temperature range, indicating that the material remains in the HS state and is SCO inactive. Note that the magnetic susceptibility data of **DzAu·EtOH** at different pressure points have a relatively poor signal-to-noise ratio, which is possibly due to a small sample mass.

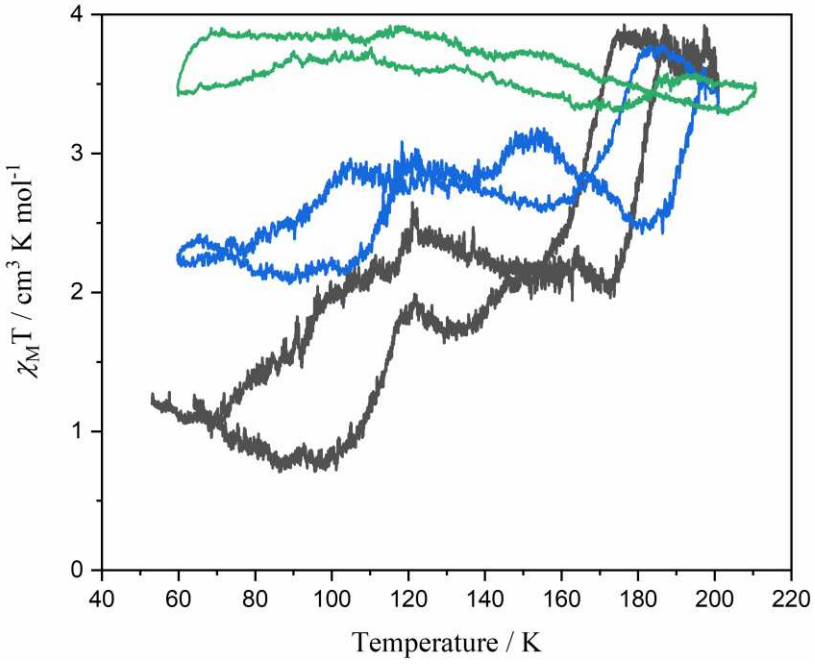

Figure 6.4: Variable temperature magnetic susceptibility data of **DzAu·EtOH** at 0.32 (black), 0.34 (blue) and 0.36 GPa (green) at a scan rate of 0.5 K min^{-1}.

6.3 Lattice Motion Under Pressure

6.3.1 Variable Pressure Neutron Powder Diffraction (VP-NPD) of **TzAu·EtOH**

To identify a specific pressure-induced distortion in the lattice of **TzAu·EtOH**, VP-NPD experiments were performed using the Wombat instrument (a high intensity powder neutron diffractometer) at the Australian Centre for Neutron Scattering. A Paris-Edinburgh press was used to obtain *in situ* pressure-dependent data. Deuterated Tz ligand was used to generate the corresponding deuterated **TzAu·EtOD** framework (the sample was soaked into deuterated ethanol), which was used for the NPD measurement. **TzAu·EtOD** with deuterated ethanol as a pressure medium was loaded into a titanium-zirconium matrix alloy. A few pieces of lead were also added into the sample holder to function as a pressure calibrant.

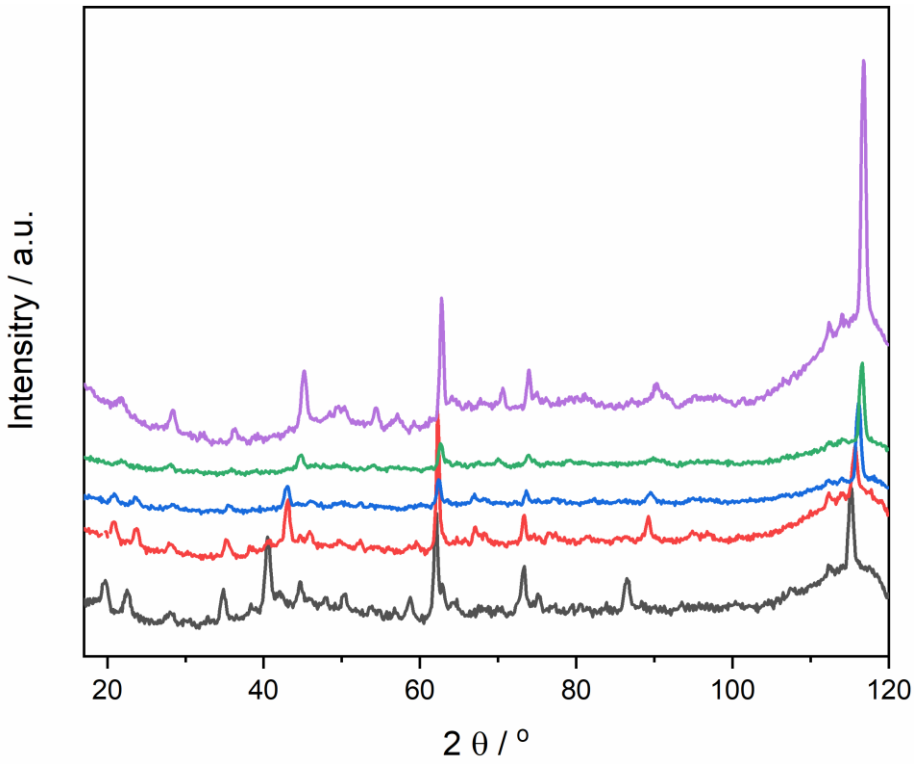

Figure 6.5: NPD data of **TzAu·EtOD** at ambient pressure (black), 0.40 GPa (red), 0.68 GPa (blue), 0.98 GPa (green) and 1.23 GPa (purple). Data are presented as lines and offset in the y-axis for clarity.

NPD data were collected at four pressure points above ambient pressure (Figure 6.5). The applied pressures occurring within the sample holder were extracted from NPD data of the Pb peaks. The peak positions shift dramatically under pressure indicating a change of lattice dimensions. Lattice information of the Pb and deuterated powdered **TzAu·EtOD** was obtained from the fitted patterns by performing Pawley refinements in GSAS-II.[13] The Rydberg–Vinet equations[14] (1) and (2) below were

used to calculate the pressure values for each pattern based on the extracted lattice information (V is the Pb volume at each pressure point). Therefore, the pressure values above ambient conditions are 0.40, 0.68, 0.98 and 1.23 GPa respectively.

$$P = 3B_0(1-\mathcal{X})\mathcal{X}^{-2}\, e^{(\frac{3}{2}(B_0'-1)(1-\mathcal{X}))}, \text{ where } B_0 = 41.2 \text{ and } B_0' = 5.72 \quad (1)$$

$$\mathcal{X} = (\frac{V}{V_0})^{\frac{1}{3}}, \text{ where } V_0 \text{ is the compression volume under ambient conditions} \quad (2)$$

$$K_l = -\frac{1}{l}\left(\frac{\partial l}{\partial P}\right)T \quad (3)$$

Each lattice parameter *a*, *b*, and *c* of **TzAu·EtOD** as a function of pressure were plotted in Figure 6.6. Linear fits versus pressures were used, which enabled a calculation of the compressibility (K_l) using equation (3) in each direction. Notably, the *b*-axis decreases with increasing pressure and thus shows a positive linear compressibility of 67.4 TPa^{-1}. The volume of **TzAu·EtOD** also decreases with increasing pressure. Interestingly, NLC phenomena appear in the *a*- and *c*-axes and increase in value with increasing pressure. Their compressibility values are -7.3 TPa^{-1} and -16.5 TPa^{-1}, respectively. Therefore, the framework grid when viewed down the *c*-axis shows that the material performs a scissor-type flexing behaviour, while the *a*-axis expands and the *b*-axis compresses with increasing pressure. The θ values (Au···Fe···Au angle, θ = 2 × arctan (a/b)) depict the extent of scissor motions in the material with an enlarged change of angle of 71.58° to 77.04° ($\Delta\theta$ = 5.47°) with increasing pressure. This counterintuitive behaviour is likely due to the greater extent of Fe(II) sites to experience lattice distortions and flexing on their equatorial positions after applying pressure.

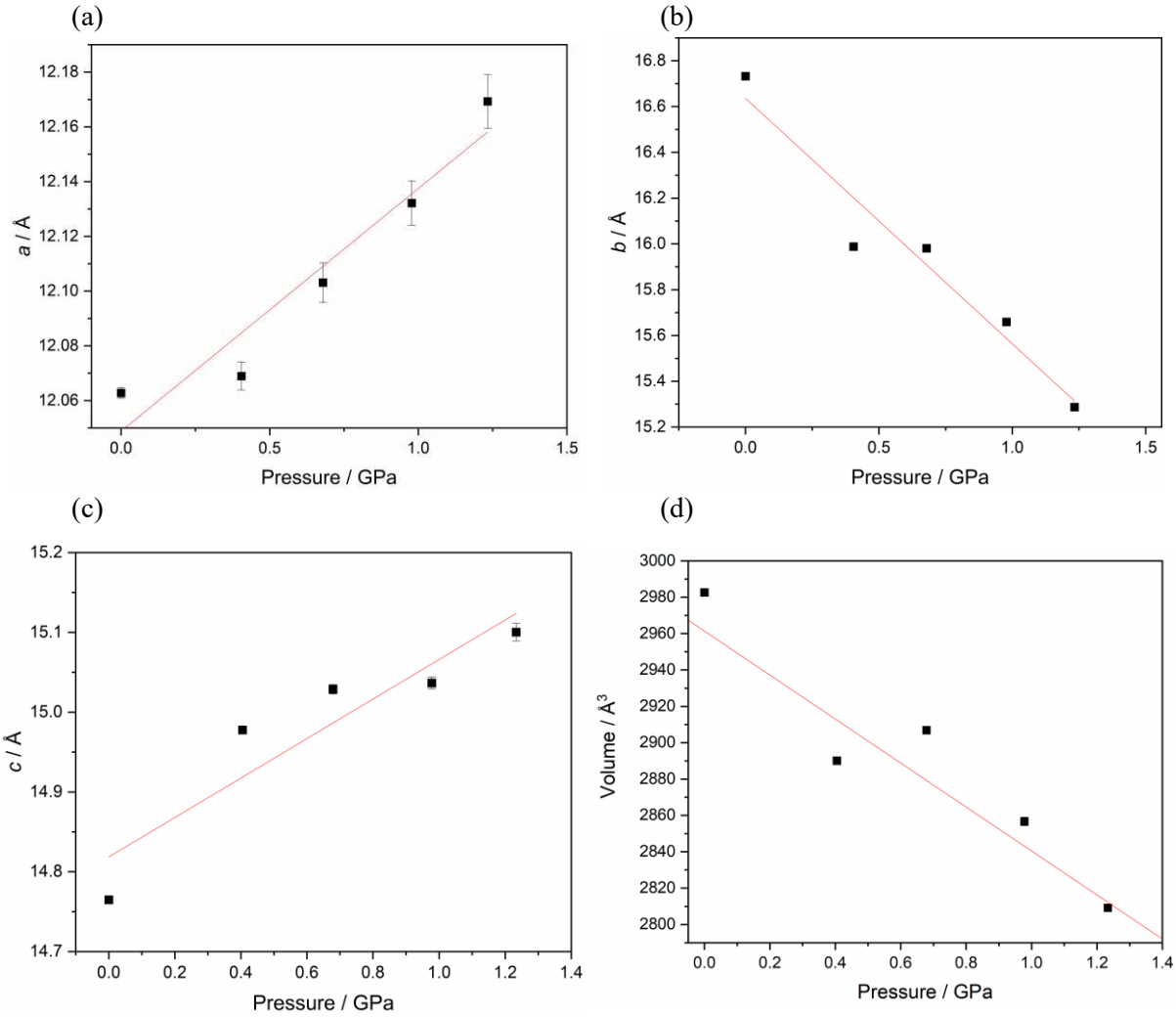

Figure 6.6: The change of lattice parameters on (a) *a*-axis, (b) *b*-axis, (c) *c*-axis and (d) volume versus pressure for **TzAu·EtOD**. All the parameters versus pressure were plotted with error bars.

6.3.2 Variable Pressure Neutron Powder Diffraction of **[$Tz_{0.5}Dz_{0.5}$]**

The differences in ligand field strength and the amount of host–host interactions within a framework can change the overall flexibility of a lattice and the extent of possible distortions that may take place. **[$Tz_{0.5}Dz_{0.5}$]**, which has fewer hydrogen bonding motifs than **TzAu·EtOH** occurring between the pillar ligands, is expected to have a more flexible structure and a larger degree of both NLC and PLC coefficients. Thus, NPD measurements under pressure were performed on **[$Tz_{0.5}Dz_{0.5}$]** to investigate the mixed ligand effect on the lattice motions. The deuterated **[$Tz_{0.5}Dz_{0.5}$]** material was synthesised from the deuterated Tz and Dz ligands and was then soaked in deuterated ethanol.

Two batches of **[$Tz_{0.5}Dz_{0.5}$]** were measured with the first and second batches using deuterated ethanol and fluorinert FC-70 as pressure media, respectively. Pb was added as a pressure calibrant for both batches. For the first batch, the neutron data of two pressure points were collected with one at

ambient pressure and another at 0.55 GPa (Figure 6.7). The pressure values were extracted from the Pb diffraction peaks to obtain the unit cell information. However, most of the diffraction peaks from the sample when using ethanol as a pressure medium were lost especially within the 2θ range lower than 40° at 0.55 GPa. Lattice information for the Pb calibrant and deuterated **[$Tz_{0.5}Dz_{0.5}$]** were obtained from the fitted patterns by conducting Pawley refinements in GSAS-II.[13] The unit cell parameters of the first batch of **[$Tz_{0.5}Dz_{0.5}$]** are a = 12.0131 Å, b = 16.9024 Å, and c = 15.1753 Å at ambient pressure. At 0.55 GPa, the a-axis increases (a = 12.0468 Å) showing NLC, while the b-axis decreases (b = 16.5018 Å). This indicates that a scissor motion is occurring in the ab Hofmann plane. The c-axis decreases slightly to 15.1717 Å, and the total volume decreases by 2% at this higher pressure.

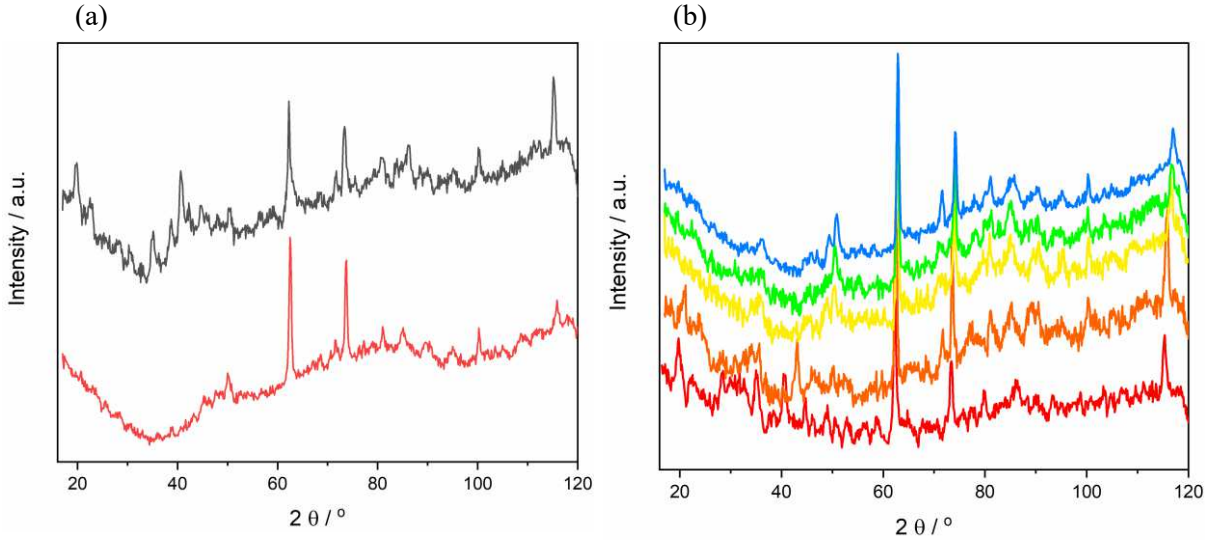

Figure 6.7: NPD data of **[$Tz_{0.5}Dz_{0.5}$]** for (a) the first batch at ambient pressure (black) and 0.55 GPa (red), (b) the second batch at ambient pressure (red), 0.25 GPa (orange), 0.82 GPa (yellow), 1.02 GPa (green) and 1.18 GPa (blue). Data are presented as lines and offset in the y-axis for clarity.

To demonstrate the effect of pressure medium on the diffraction pattern, NPD measurements were performed on the second batch of **[$Tz_{0.5}Dz_{0.5}$]** using fluorinert FC-70. Five pressure points were collected from ambient pressure (Figure 6.8). Comparing the two pressure media, fluorinert FC-70 provides better data with more diffraction peaks than deuterated ethanol. Thus, more accurate unit cell information can be extract from the second batch. Peak shifts belonging to the sample indicate that lattice changes are occurring under pressure. When increasing the pressure, fewer peaks are present in the NPD patterns, suggesting a loss of sample crystallinity. The NPD patterns were fitted by Pawley refinements, which allowed lattice information of the Pb and **[$Tz_{0.5}Dz_{0.5}$]** to be obtained (Appendix Table D.3). The obtained pressure values from ambient pressure are 0.25, 0.82, 1.02, and 1.18 GPa. At ambient pressure, the extracted unit cell information for **[$Tz_{0.5}Dz_{0.5}$]** are a = 11.9235 Å, b = 16.7126 Å, and c = 15.2422 Å. The differences in lattice parameters between the first and second batches of **[$Tz_{0.5}Dz_{0.5}$]** are likely due to the different pressure media used. The same trend is observed as in the first batch. With increasing pressure, the a-lattice increases (NLC) while the b- and c- lattices decrease. The

lattice parameters were plotted as a function of pressure, and linear equations were used to fit the trend of lattice changes to calculate the compressibility. The compressibilities are -13.1 TPa^{-1}, 27.5 TPa^{-1}, and 8.1 TPa^{-1} for the *a*-, *b*-, and *c*-axes, respectively. The θ value for each pressure point was calculated and shows a gradual increase from 71.01° to 73.64° ($\Delta\theta$ = 2.63°) with increasing pressure.

When comparing **TzAu·EtOH** and **[$Tz_{0.5}Dz_{0.5}$]**, the former exhibits approximately half the magnitude of NLC along the *a*-axis, while more than the double extent of PLC along the *b*-axis. It is interesting to note that the *c*-axis exhibits NLC in **TzAu·EtOH** but only PLC in **[$Tz_{0.5}Dz_{0.5}$]**. The extent of scissor motions in **TzAu·EtOH** is larger than in **[$Tz_{0.5}Dz_{0.5}$]** with a more than doubled θ value. The differences between the two materials are potentially associated with the number of hydrogen bonding interactions occurring between the individual pillaring ligands, and also the ligand field strength itself.

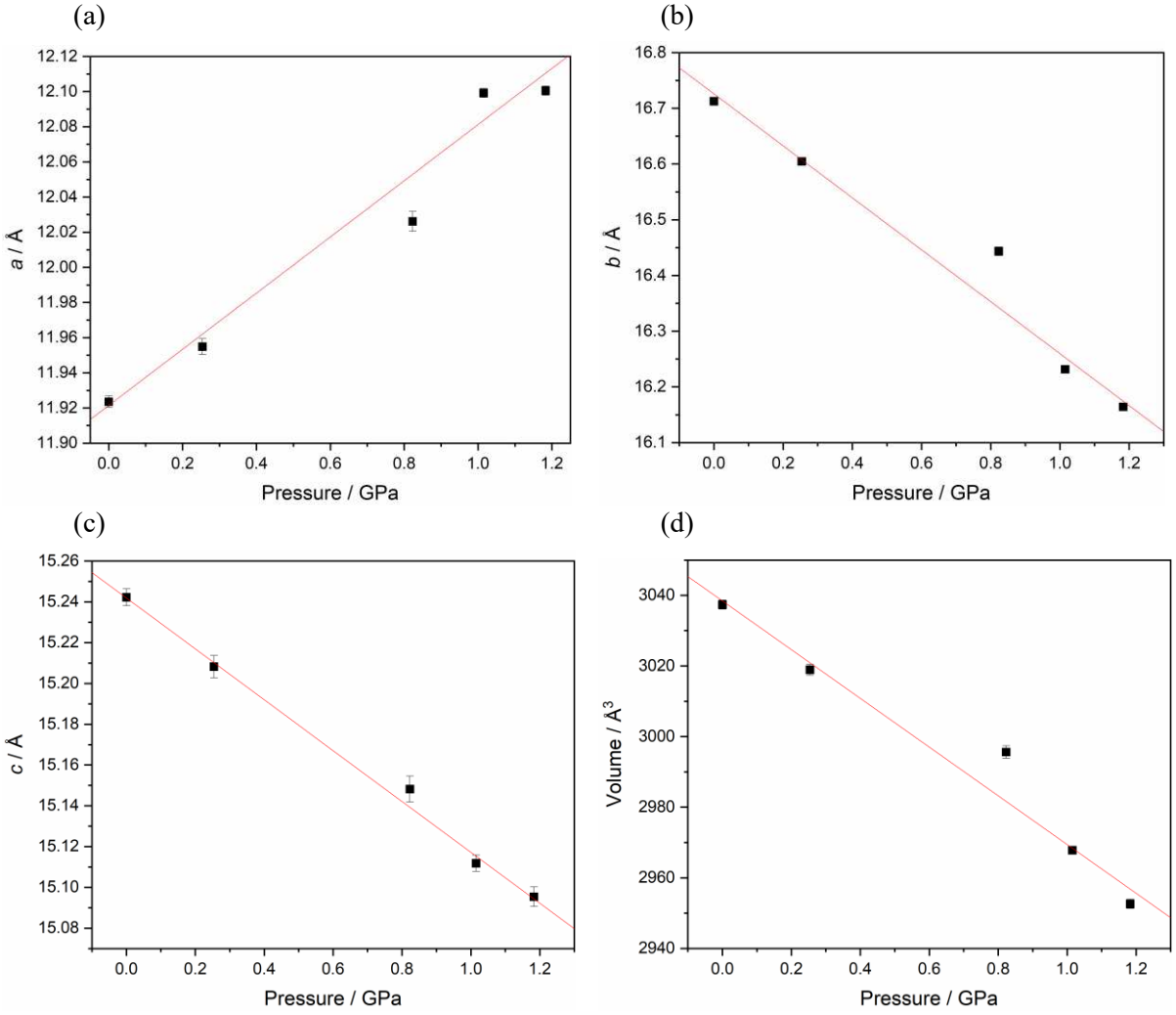

Figure 6.8: The change of lattice parameters on (a) *a*-axis, (b) *b*-axis, (c) *c*-axis and (d) volume versus pressure for **[$Tz_{0.5}Dz_{0.5}$]**.

6.4 Conclusion and Future Work

In this chapter, three Hofmann-like frameworks **TzAu·EtOH**, **[$Tz_{0.5}Dz_{0.5}$],** and **DzAu·EtOH** were prepared to study the pressure effect on their structures and SCO behaviours. Both **TzAu·EtOH** and **[$Tz_{0.5}Dz_{0.5}$]** displayed one-step and hysteretic SCO at variable pressures. Both frameworks exhibited an overall increasing trend of spin transition temperatures with increasing pressure. The thermal hysteresis widths of the spin transitions were enhanced by pressurisation. The SCO behaviour of **TzAu·EtOH** becomes incomplete above 0.62 GPa, and at 0.99 GPa approximately 50% of the SCO sites convert to the LS state. For **[$Tz_{0.5}Dz_{0.5}$]**, there is incomplete SCO at lower pressure values (0.35 GPa) and no SCO at 0.78 GPa, with all the SCO sites adopting the HS state. **DzAu·EtOH** exhibits four-step SCO at ambient pressure, incomplete three-step SCO with pressurisation, and no SCO at 0.36 GPa. All three materials follow the general trend of stabilisation of the HS state at higher pressures.

These three materials display distinct SCO behaviours measured at the same pressure points, which are associated with ligand field strength and host–host interactions. The ligand field strengths are also different among these three frameworks. The framework with more of the Tz ligand has the strongest ligand field strength and therefore the highest spin transition temperatures of the series. The hydrogen bonding C–H···N interactions occur between the pyridyl and diazine or tetrazine rings. The inter-ligand host–host interactions act as hinges between the pillaring ligands and also influence the SCO behaviour. Compared to **TzAu·EtOH**, **[$Tz_{0.5}Dz_{0.5}$]** possesses approximately 75% of the C–H···N interactions while **DzAu·EtOH** has approximately the half number of the interactions. The different numbers of the C–H···N interactions affect the degree of lattice flexing. The framework with fewer host–host interactions is more flexible. The lattice flexibility and SCO site distortion results in the distinct SCO behaviours in three frameworks. A more detailed investigation of controlling SCO behaviours and structural flexibility by ligand doping discusses in Chapter 7.

It is very rare in SCO materials to see a stabilisation of the HS state with pressurisation. Most materials show the opposite i.e., stabilisation of the LS state with higher pressure. This is due to a shortening of the metal-ligand bond distances at the SCO sites, promoting the thermodynamically favoured LS state.[10, 12] The unexpected behaviour observed in this chapter is possibly caused by the increased structural distortions, or even a partial loss of crystallinity that may lead to a reduction in communication or cooperativity between the SCO sites.

TzAu·EtOH and **[$Tz_{0.5}Dz_{0.5}$]** were characterised by VP-NPD to reveal the interplay between structural and spin state energetics under pressure. Both materials exhibit antagonism between their SCO and lattice flexing with an expansion of the *a*-axis and compression of the *b*-axis with pressurisation. These distortions correspond to the scissor-type lattice flexing within the Hofmann grids under pressure. The lattice motion leads to a local distortion of the metal centres and therefore a stabilisation of the HS state due to decreased ligand field splitting at the Fe(II) centres. **TzAu·EtOH**

shows more pronounced PLC along the *b*-axis while less noticeable NLC along the *a*-axis than compared to **[$Tz_{0.5}Dz_{0.5}$]**. Overall, **TzAu·EtOH** displays a larger magnitude of lattice flexing than **[$Tz_{0.5}Dz_{0.5}$]** with a larger θ value under pressure. This is likely due to the hydrogen bonding interactions occurring between the differently distorted Fe(II) centres and the twist of the Fe–N–C(cyanido) bonds on the equatorial position. This type of scissor motion has been observed in the Hofmann-like framework $[Fe(bpac)(Au(CN)_2)_2]\cdot 2EtOH$ (bpac = 1,2-bis(4′-pyridyl)acetylene) but with decrease of θ under pressure.[15]

The unit cell parameters can be extracted from VP-NPD data, but detailed atomic information is lacking. In order to understand the different extent of distortion occurring at each Fe(II) centres between **TzAu·EtOH** and **[$Tz_{0.5}Dz_{0.5}$]**, high pressure single crystal X-ray diffraction data of both materials would be necessary to reveal the scissor motion at the atomic level. Analysing the bond distances and angles surrounding the SCO sites may provide insight into the stabilisation of the HS state at elevated pressure. This will aid in understanding the interplay between the SCO effect and lattice flexing. Furthermore, as pressure and temperature affect SCO behaviours, the local distortion of structure can be better understood. The influence of intra- and intermolecular interactions in the framework can be demonstrated, which can provide advice on wisely choosing ligands to create materials with controllable flexibility.

Examples of pressure-induced scissor motions in SCO MOFs remain rare. The design of analogous materials exhibiting anomalous lattice motions will allow for a deeper understanding of the mechanism of motion, and thus the targeted creation of future advanced materials. Future work will focus on synthesising Hofmann-like framework materials containing novel pillaring ligands and cyanidometallates. Investigation of guest effects on SCO behaviours and structural properties is interesting. Guest molecules of different sizes and polarities can likely change the extent of flexibility of the frameworks, thereby tuning the lattice motions. The host–guest interactions under pressure would be worthy of further investigation. Overall, a study into the structure–function relationships in SCO materials in response to pressure unlocks a new paradigm SR-MOF design.

6.5 References

1. Zeng, Q.; Wang, K.; Zou, B., *ACS Mater. Lett.* **2020,** *2* (4), 291-295.

2. Goodwin, A. L.; Keen, D. A.; Tucker, M. G., *Proc. Natl. Acad. Sci. U.S.A.* **2008,** *105* (48), 18708-18713.

3. Cairns, A. B.; Goodwin, A. L., *Phys. Chem. Chem. Phys.* **2015,** *17* (32), 20449-20465.

4. Cai, W.; Katrusiak, A., *Nat. Commun.* **2014,** *5* (1).

5. Yan, Y.; O'Connor, A. E.; Kanthasamy, G.; Atkinson, G.; Allan, D. R.; Blake, A. J.; Schröder, M., *J. Am. Chem. Soc.* **2018,** *140* (11), 3952-3958.

6. Jiang, D.; Wen, T.; Guo, Y.; Liang, J.; Jiang, Z.; Li, C.; Liu, K.; Yang, W.; Wang, Y., *Chem. Mater.* **2022,** *34* (6), 2764-2770.

7. Clements, J. E. The University of Sydney, **2015**.

8. Kulmaczewski, R.; Olguín, J.; Kitchen, J. A.; Feltham, H. L. C.; Jameson, G. N. L.; Tallon, J. L.; Brooker, S., *J. Am. Chem. Soc.* **2014,** *136* (3), 878-881.

9. Brooker, S., *Chem. Soc. Rev.* **2015,** *44* (10), 2880-2892.

10. Garcia, Y.; Ksenofontov, V.; Levchenko, G.; Schmitt, G.; Gütlich, P., *J. Phys. Chem. B* **2000,** *104* (21), 5045-5048.

11. Gutlich, P.; Ksenofontov, V.; Gaspar, A., *Coord. Chem. Rev.* **2005,** *249* (17-18), 1811-1829.

12. Ksenofontov, V.; Gaspar, A. B.; Levchenko, G.; Fitzsimmons, B.; Gütlich, P., *J. Phys. Chem. B* **2004,** *108* (23), 7723-7727.

13. Toby, B. H.; Von Dreele, R. B., *J. Appl. Crystallogr.* **2013,** *46* (2), 544-549.

14. Dewaele, A., *Minerals* **2019,** *9* (11), 684.

15. Fang, A. The University of Sydney, **2021**.

Chapter 7

Precise Control of Temperature-Induced Spin Crossover, Negative Thermal Expansion, and Phase Transitions in Mixed-Ligand Hofmann-like Frameworks

7.1 Overview

The previous chapters discussed SCO and NTE behaviour that can be tuned by mixed cyanidometallate linkers in the Tz-based frameworks. However, the differences between these materials by varying Au and Ag components are inconspicuous because their spin transition temperatures are similar. It remains a challenge to develop synthetic strategies for the rational design of MOFs that incorporate components with controllable properties with a larger magnitude of tunable range. One approach to tuning the functionality of MOFs is to design mixed-ligand MOFs (MIXMOFs). In such materials structure and properties of the framework can be precisely controlled by subtly altering the ratio of the ligands. Importantly, the properties of MIXMOFs are generally distinct from the properties of the single-component ligand MOFs,[1-3] and lead to emergent, synergistic effects and potential physical and chemical property enhancement.[4]

Although tuning the SCO behaviour has been achieved with the guest exchange or chemical migration in a number of porous framework materials,[5-9] another viable approach is to modulate the ligand composition. This has been reported in a handful of examples in coordination polymers to fine-tune the SCO temperatures by changing the doping ratio of two linkers.[10-13] Encouraged by our recent findings that PSM of the 3D Hofmann-like framework **TzAu·EtOH** to **DzAu·EtOH** results in a decrease in the SCO temperature,[14-15] here we have applied the solid-solution approach to synthesise these MIXMOFs $[Fe(Tz)_x(Dz)_{1-x}(Au(CN)_2)_2]\cdot n$EtOH ($x$ = 0–1.0; **[Tz$_x$Dz$_{1-x}$]**). It is noted that these materials have been first synthesised and preliminarily characterised by the candidate during her Honours year (University of Sydney, 2018).[16] Some of the materials were generated again and some characterisations were remeasured to confirm the reproducibility during her PhD. Further investigations and analyses of this series of MOFs were conducted during her PhD. Some results from this Honours thesis have been reproduced here to provide a better understanding and completeness of this study. These data are acknowledged in the text.

This chapter consists of three parts. The first part discusses the MOFs $[Fe(Tz)_x(Dz)_{1-x}(Au(CN)_2)_2]\cdot n$EtOH with x = 1.0–0.2, which perform one-step SCO and how their spin transition temperatures can be consecutively modulated to lower temperatures with reducing the Tz ligand components. It has been previously reported that both SCO and NTE can be tuned in parallel *via* the metal dilution approach.[17] Here we demonstrate another strategy *via* tuning the ratio of ligands to generate materials possessing colossal thermal expansion (*i.e.*, $|\alpha| \geq 100 \times 10^{-6}$ K^{-1}).[18] Colossal NTE induced by SCO was enlarged by increasing the components of Dz ligands. The structural information, lattice flexing mechanism and host–guest interactions are detailed in part one of this chapter.

Developing and controlling novel flexible metal-organic frameworks, which can reversibly switch and memorise between original and deformed phases in response to external stimuli, is of great interest as these materials have potential applications in information storage, sensors and guest adsorption or

separation.[19-21] A major challenge in this area is to generate flexible MOFs as they are rare when compared with rigid frameworks.[22] Apart from 'breathing-like' behaviour triggered by stimuli in SCO MOFs,[23-27] another mode of flexibility is called the 'shape memory' property. The materials possessing such property are able to alter morphologies by given external stimuli and the deformed materials can be recovered in response to another external stimulus.[28-30] One subset of the 'shape memory' effect is the 'two-way shape memory' effect, which can remember not only its original high temperature phase but also low temperature deformed phase. Such a phenomenon is discovered in some alloys but not in SCO MOFs.[31] Herein, in the second part of this chapter we reported the powdered **DzAu·EtOH** ($x = 0$) material, which exhibits two stable high temperature orthorhombic phases (**1-O**) and low temperature monoclinic phase (**1-M**). Interconversion between the two phases was noticed showing a 'two-way shape memory' effect. The desolvated phase was generated from both phases (**1-O** and **1-M**). 'Breathing-like' behaviour was demonstrated with the desolvated phase can be converted to its original phase (**1-O**) by resolvation. The magnetic susceptibility measurements were performed to give insight into the interplay between structures and SCO behaviour.

It is also significant to understand the gradual process of phase transition and the intrinsic relationship between structure and SCO behaviours. Therefore, the third part of this chapter discusses ($[Fe(Tz)_x(Dz)_{1-x}(Au(CN)_2)_2]\cdot n$EtOH ($x = 0.1$ and 0.15; **[$Tz_{0.1}Dz_{0.9}$]** and **[$Tz_{0.15}Dz_{0.85}$]**)) materials, which present unique thermal cycling dependant four-step spin crossover behaviours coupling with the progressive structural transition. The materials present a gradual phase transition from the orthorhombic to the monoclinic phase in response to temperature. Moreover, the deformed phase can recover to the original phase by thermal induction due to altering host–host interactions within the frameworks. The relationship between the magnetic and structural properties of **[$Tz_{0.1}Dz_{0.9}$]** and **[$Tz_{0.15}Dz_{0.85}$]** are explored and the gradual changes in thermal cycles are quantified in part three of this chapter.

7.2 Investigation of $[Fe(Tz)_x(Dz)_{1-x}(Au(CN)_2)_2]\cdot n$EtOH ($x = 0.2–1.0$)

7.2.1 Structural Characterisation of Single Crystals

A series of bulk powder frameworks **[$Tz_{0.2}Dz_{0.8}$]**, **[$Tz_{0.3}Dz_{0.7}$]**, **[$Tz_{0.4}Dz_{0.6}$]**, **[$Tz_{0.5}Dz_{0.5}$]**, **[$Tz_{0.6}Dz_{0.4}$]**, **[$Tz_{0.7}Dz_{0.3}$]**, **[$Tz_{0.8}Dz_{0.2}$]**, **[$Tz_{0.9}Dz_{0.1}$]**, **[$Tz_{1.0}Dz_{0.0}$]** (i.e., **TzAu·EtOH**) were synthesised using the appropriate stoichiometric amounts of the Tz and Dz ligands, with $Fe(ClO_4)_2\cdot xH_2O$ and $KAu(CN)_2$ in EtOH solvent (details see Chapter 2.2.21). Infrared (IR) spectroscopy was conducted (during the candidate's Honours year) to help determine the actual Tz:Dz ratio in the series of MIXMOFs, and this was compared to the molar ratio of two ligands used during synthesis. The approximate percentage of the ligands within each framework was determined by integration of the characteristic Tz and Dz peaks at *ca.* 837 cm^{-1} and 816 cm^{-1}, respectively (Appendix E.1). This

calculated Tz percentage was plotted against the percentage of Tz used during bulk powder synthesis, and shows an excellent linear correlation, suggesting successful stoichiometric control in the synthesis of this MIXMOF series. Furthermore, the Tz:Dz ratio of a single crystal sample of **[$Tz_{0.5}Dz_{0.5}$]** is in good agreement with its bulk powder analogue.

To investigate the structural arrangement of the Tz and Dz ligands in the series of frameworks and to elucidate how the host–host and host–guest interactions affect the SCO behaviour, single crystals of a MIXMOF containing 50:50% Tz:Dz ligand composition (**[$Tz_{0.5}Dz_{0.5}$]**) were synthesised. The single crystal structure of **[$Tz_{0.5}Dz_{0.5}$]** was measured at 100 K using MX1 beamline radiation source (λ = 0.71073 Å) at the Australian Synchrotron. The crystal data were collected during the candidate's Honours year but the structure solution has been improved during her PhD. SCXRD analysis reveals an interpenetrated 3D Hofmann-like framework in the orthorhombic *Cmma* space group (Figure 7.1). Within the crystal structure of **[$Tz_{0.5}Dz_{0.5}$]**, the Fe(II) nodes adopt an octahedral coordination, with the equatorial positions coordinated to four $[Au(CN)_2]^-$ linkers. This is isostructural to **TzAu·EtOH** and **DzAu·EtOH**.[14]

Both axial positions of the Fe(II) sites are coordinated to nitrogen atoms of the pyridyl rings of either a Tz or Dz ligand. The structural solution consists of a homogenous distribution of a 50:50 tetrazine:diazine moiety of the ligands, in which the tetrazine ring (0.5 occupancies) has no orientational disorder but the diazine ring can exist in one of four orientational configurations with each in 0.125 occupancies. These orientational configurations of the Tz and Dz result in disordered C–H···N host–host interactions, in which the nitrogen atoms on either the tetrazine or diazine ring hydrogen bond to atoms of the terminal pyridyl groups of adjacent ligands. Furthermore, there is no evidence for any long-range site ordering of the Tz and Dz ligands, with the unit cell and space group symmetry being the same as that for the pure ligand frameworks, and with no obvious diffuse X-ray scattering that might be otherwise expected if short-range and/or low dimensional ligand ordering occurred.

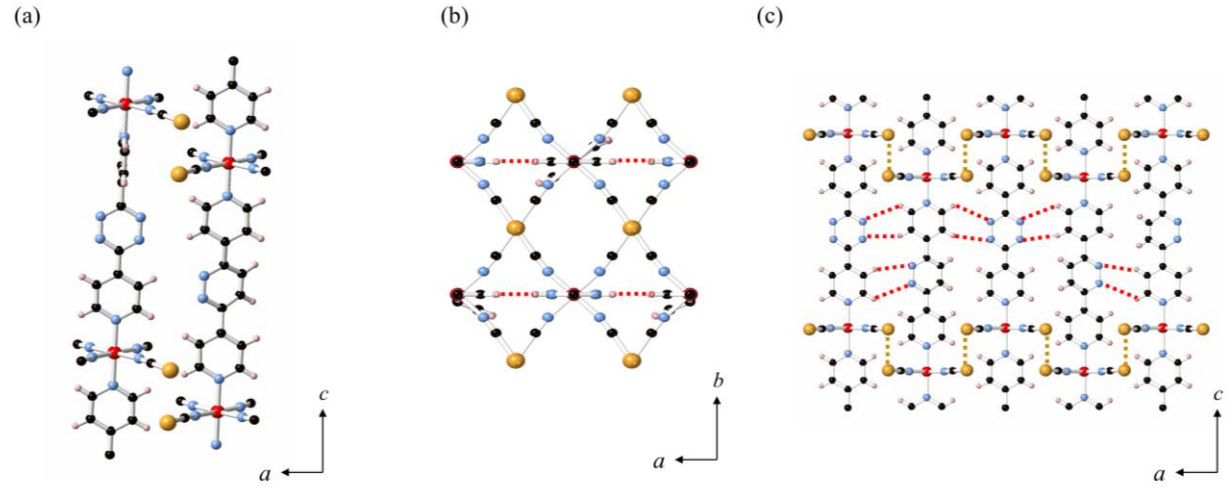

Figure 7.1: Single crystal structure of **[$Tz_{0.5}Dz_{0.5}$]** at 100 K: (a) showing the structure fragment with one possible orientation, which consists of one Tz and one Dz ligand; (b) viewed along the *c*-axis, showing the pyridyl ring disorder and the 50:50 disorder of the tetrazine and diazine rings; (c) viewed along the *b*-axis, showing one possible ordering of Tz and Dz ligands (C: black, N: blue, Fe: red, Au: orange, H: pink, Au···Au interactions: orange dotted lines and C–H···N interactions: red dotted lines).

Compared to the single-component ligand analogues (**TzAu·EtOH** and PSM **DzAu·EtOH**),[14] the structure of **[$Tz_{0.5}Dz_{0.5}$]** consists of two interpenetrated nets, resulting from aurophilic interactions occurring at evenly spaced intervals within the *ab*-plane. The pyridyl and tetrazine rings of the ligands are coplanar in **TzAu·EtOH**. However, unlike the crystal structures of **TzAu·EtOH**,[14] one of the pyridyl rings in both ligands in **[$Tz_{0.5}Dz_{0.5}$]** is disordered with one orientation being coplanar with a probability of 69% while another orientation being perpendicular. Overall, there are minor changes to the framework geometries with ligand substitution (see Appendix E.2 for an overlay diagram of these three structures).

At 100 K, the average Fe–N bond lengths of **[$Tz_{0.5}Dz_{0.5}$]** were calculated to be 1.953 Å, which is indicative of LS Fe(II) sites in Table 7.1. The coordination environment around the Fe(II) site is slightly more distorted than for the single-component ligand frameworks at this temperature (octahedral distortion parameter,[32] Σ(**[$Tz_{0.5}Dz_{0.5}$]**) = 16.6, Σ(**TzAu·EtOH**) = 15.5°, Σ(**DzAu·EtOH**) = 13.8°);[14] this indicates that the framework contains a mixture of the Tz and Dz ligands, resulting in an overall slightly more distorted structure.

Table 7.1: Comparison of unit cell parameters, selected bond lengths, and selected angles for **[Tz$_{1.0}$Dz$_{0.0}$]**, **[Tz$_{0.5}$Dz$_{0.5}$]** and PSM **[Tz$_{0.0}$Dz$_{1.0}$]** frameworks.

Parameters	**[Tz$_{1.0}$Dz$_{0.0}$]** [a]	**[Tz$_{0.5}$Dz$_{0.5}$]**	**PSM [Tz$_{0.0}$Dz$_{1.0}$]** [b]
a / Å	12.066(2)	11.884(2)	12.0291(6)
b / Å	16.121(3)	16.205(3)	16.2569(7)
c / Å	15.099(3)	15.162(3)	15.2715(10)
Volume / Å^3	2937.0(9)	2920.0(10)	2986.4(3)
Fe(1)–N(1) / Å	1.931(3)	1.927(5)	1.975(7)
Fe(1)–N(11) / Å	1.990(7)	2.009(11)	2.027(16)
Fe(1)–N(14) / Å	1.991(7)	1.999(11)	2.029(17)
<*d*(Fe–N)> / Å	1.951	1.953	1.981
Au(1)···Au(1)′ / Å	3.2400(7)	3.1982(10)	3.0978(9)
C(11)···N(13) / Å	3.767(8)	3.76(3)	4.06(5)
C(12)···N(12) / Å	3.698(10)	3.74(3)	4.01(6)
Σ / °	15.5	16.6	13.8
Fe(1)–N(1)–C(1) / °	170.6(3)	170.1(5)	170.3(6)

[a] **[Tz$_{1.0}$Dz$_{0.0}$]** (100 K) single crystal structure from literature.[14] [b] Post-synthetic modification **[Tz$_{0.0}$Dz$_{1.0}$]** (90 K) single crystal structure from literature.[15]

In the crystal structure of **[Tz$_{0.5}$Dz$_{0.5}$]**, the central diazine cores of the Dz ligands exhibit positional disorder, where the two diazine nitrogen atoms are located randomly in opposite positions on the central core within each pillaring Dz ligand. This leads to disordered C–H···N interactions correlated to the Dz core nitrogen positions. Compared to **[Tz$_{1.0}$Dz$_{0.0}$]**, the C(11)···N(13) hydrogen bond for **[Tz$_{0.5}$Dz$_{0.5}$]** is slightly longer (3.76 Å) while the C(12)···N(12) hydrogen bond is slightly shorter (3.74 Å), which are both related to C–H···N interactions. Also, in terms of the number of hydrogen bonding, compared with **[Tz$_{1.0}$Dz$_{0.0}$]**, **[Tz$_{0.5}$Dz$_{0.5}$]** contains 75% of hydrogen bonding. Both the C(11)···N(13) and C(12)···N(12) bond lengths are also much shorter than the equivalent bond lengths of the PSM structure of **[Tz$_{0.0}$Dz$_{1.0}$]**.[14] The distances of the aurophilic interaction in **[Tz$_{0.5}$Dz$_{0.5}$]** are in between that of the two single-component ligand frameworks. The slight discrepancies in the bond lengths and torsion angles between **[Tz$_{1.0}$Dz$_{0.0}$]**, **[Tz$_{0.5}$Dz$_{0.5}$]** and PSM **[Tz$_{0.0}$Dz$_{1.0}$]** are shown in an overlay comparison.

7.2.2 Spin Crossover Manipulation *via* Tuning Ligand Composition

Variable temperature magnetic susceptibility measurements were performed on bulk powder samples of all frameworks (**[Tz$_{0.2}$Dz$_{0.8}$]** to **[Tz$_{1.0}$Dz$_{0.0}$]** in $\Delta x = 0.1$ increments). The data were presented in the candidate's Honours thesis but shown here for completeness. All materials display complete, abrupt, one-step SCO with narrow hysteresis widths of 3–5 K (Figure 7.2). A general trend is observed where the SCO temperatures decrease with a decreased ratio of Tz ligand in the framework, i.e., **[Tz$_{0.2}$Dz$_{0.8}$]** has the lowest SCO temperature ($T_{½}\downarrow$ = 248.5 K, $T_{½}\uparrow$ = 252.6 K, ΔT = 4.1 K), whereas **[Tz$_{1.0}$Dz$_{0.0}$]** has the largest SCO temperature ($T_{½}\downarrow$ = 271.5 K, $T_{½}\uparrow$= 275.1 K, ΔT = 3.6 K). This observation of a lower Tz ligand composition resulting in lower spin transition temperatures can be explained by the different ligand field effects of Dz and Tz and intraligand interactions.[14] This influences the propagation of the SCO sites. The intramolecular orbital overlap reduces with decreasing Tz content. This reduces the ability of the Tz ligands in these frameworks to act as π-acceptors, thereby reducing the ligand field strength. The disordered configuration of aromatic rings in the ligands, as observed in the crystal structure of **[Tz$_{0.5}$Dz$_{0.5}$]** at 100 K, further lessens the interactions between the pillared ligands in the framework. Furthermore, the reduced number of intermolecular interactions in the MIXMOF series with lower Tz content results in decreasing spin transition temperatures.

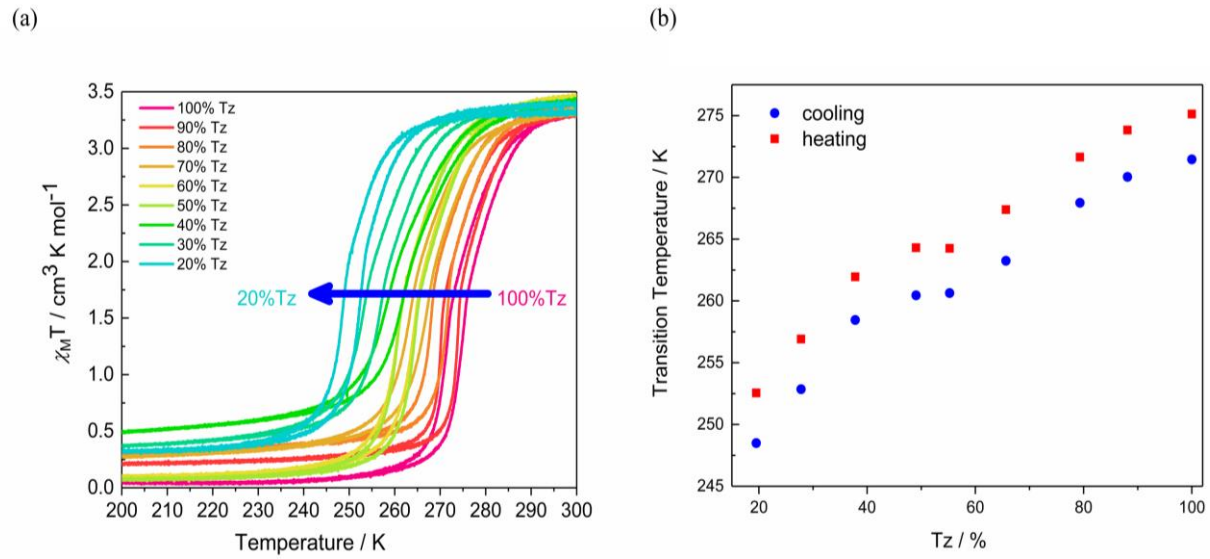

Figure 7.2: (a) Variable temperature magnetic susceptibility data for bulk powder MIXMOF samples from **[Tz$_{0.2}$Dz$_{0.8}$]** to **[Tz$_{1.0}$Dz$_{0.0}$]**. (b) SCO transition temperatures in the cooling and heating process versus the percentage of Tz ligand containing (determined by IR spectroscopy) in the series of frameworks from **[Tz$_{0.2}$Dz$_{0.8}$]** to **[Tz$_{1.0}$Dz$_{0.0}$]**.

The SCO temperatures upon cooling and warming determined from the first derivative of the magnetic susceptibility data (Appendix E.3) for all frameworks were plotted against the ratio of Tz ligand. The plot reveals a non-linear trend with an inflexion point around the data points for **[Tz$_{0.5}$Dz$_{0.5}$]**

(Figure 7.2(b)). The relative sharpness of the SCO transitions compared to the thermal shift of these transitions with a change in ligand composition, as reflected by the narrow peaks in the first derivative plot, indicates that the samples contain a high degree of compositional homogeneity. There is sample dependence on the sharpness of the SCO behaviours likely due to the slight difference in local lattice cooperativity and host–guest interactions.

The methods of controlling SCO temperatures have been reported in the literature. For example, spin transition temperatures were changed *via* tuning functional groups of the ligands or anions in coordination polymers.[33-35] The control of SCO temperature was also reported *via* modulating the diffusion of iodine content in a porous coordination polymer.[36] These reported examples demonstrated a single factor influencing the spin transition. However, in our system, many factors were taken into consideration for modulating the SCO temperature. This includes ligand field strength, the number of intraligand interactions, host–host/host–guest interactions, ligand disorders and lattice distortions. The total Gibbs free energy can be deconvoluted into contributions from SCO relating to crystal field splitting energy and lattice motion energy. The spin transition occurs when the Gibbs free energy equals zero. Since the change of entropy can be neglected, the enthalpy change is taken into consideration for explaining the different SCO temperatures *via* tuning the composition of two ligands. The enthalpy of the motion of lattices can be further deconvoluted into enthalpy change from the different number of hydrogen bonds, the disorder of the framework structure, host–host and host–guest interactions. Overall, all these factors influence the SCO and lattice flexing.

7.2.3 SCO-Induced Colossal Thermal Expansion

In order to explore lattice changes in the framework, VT-PXRD was conducted on **[$Tz_{0.5}Dz_{0.5}$]** and refined unit cell parameters were plotted as a function of temperature. The data were collected during the candidate's Honours year but the refinements of the powder patterns were improved during her PhD. Also, the thermal expansion investigations and modelling were conducted during her PhD. The material presents a unit cell volume decrease and the *c*-axis contraction from high to low temperature over the spin transition correlating with the Fe-N bond length. Interestingly, the *a*-axis shows colossal NTE while the *b*-axis pronounced increases upon cooling. The changes in lattices are induced by SCO (Figure 7.4). Compared to **[$Tz_{1.0}Dz_{0.0}$]**, **[$Tz_{0.5}Dz_{0.5}$]** shows a larger thermal expansion coefficient. That indicates a possible method to precisely modulate the lattice behaviours *via* solid solution by altering the ratio of Tz and Dz ligands. To further investigate lattice motion in these MIXMOFs, VT-PXRD for frameworks **[Tz_xDz_{1-x}]** (x = 1.0, 0.8, 0.6, 0.4, 0.2) were conducted (details in Section 7.2.4). For a detailed structural comparison between the series of frameworks, PXRD data were measured on all frameworks in the MIXMOF series (**[$Tz_{0.2}Dz_{0.8}$]** to **[$Tz_{1.0}Dz_{0.0}$]**) at room temperature. Diffraction patterns for all phases were found to be similar, but some peak positions are slightly different. For example, a peak in the 2θ

range of 22.5–23.2° shows a shift to high angles with increasing the Tz component (Figure 7.3). The trend of peak shifting indicates the gradual change of lattice parameters *via* tuning the ratio of ligands among these materials. Furthermore, it implies that the two ligands were mixed homogeneously in the frameworks. Therefore, by using this mixed-ligands strategy, not only the spin crossover behaviours can be preciously tuned, but also the unit cell parameters.

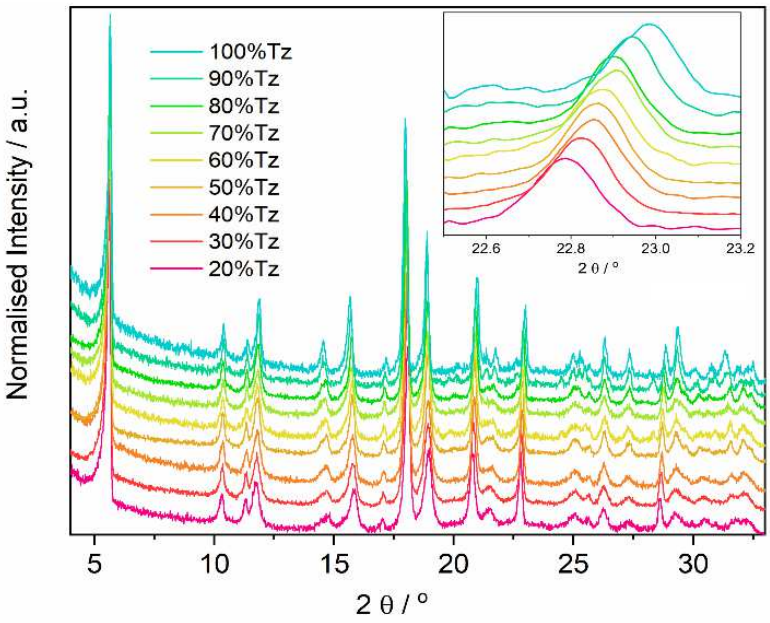

Figure 7.3: PXRD patterns for bulk powder samples of **[$Tz_{0.2}Dz_{0.8}$]** to **[$Tz_{1.0}Dz_{0.0}$]** measured at room temperature. Inset: close-up of the diffraction patterns showing changes in the peak intensity and peak shifts with different ligand compositions (2θ = 22.5–23.2°).

7.2.4 Solid-Solution Manipulated Thermal Expansion

VT-PXRD of the remaining MIXMOFs **[Tz_xDz_{1-x}]** (x = 1.0, 0.8, 0.6, 0.4, 0.2) were collected to investigate the lattice changes with respect to temperature. The data were collected during the candidate's Honours year but the refinements of the powder patterns were improved, and the thermal expansion investigations and modelling of lattice motion were conducted during her PhD. All diffraction patterns were refined against the unit cell from the single crystal structure of **[$Tz_{0.5}Dz_{0.5}$]** (orthorhombic, *Cmma*). The refined unit cell parameters were extracted and plotted as a function of temperature in Appendix E.4–E.9. The resulting fitting parameters and figures of modelling and coefficients for these materials are given in Appendix E.13–E.17.

To better understand the trend of unit cell changes and to calculate the thermal expansion coefficients, an equation with the double sigmoidal function plus a linear function (Equation 1) was used to model it. The assumption of modelling is based on Vegard's Law, which is used in a mixed

system.[4] The sigmoidal function has been used for modelling the variable temperature lattice parameter data in spin crossover frameworks.[17] In this series of spin crossover materials, the modified double sigmoidal function (Equation 1) with a linear function was used to better fit the change of lattice parameter and spin crossover curve, demoted *L*(T). The first half of the sigmoidal function is for fitting the curves in the lower temperature region while the second half represents the higher temperature region. The whole sigmoidal function can better fit the overall shape of the lattice changes and magnetic behaviours against temperature. The linear function part is for adjusting the tilt of the curve. This equation was first used for fitting the variable temperature spin crossover behaviours. The parameters A1 and A2 represent the amplitude of two sigmoidal regions related to the changes of magnetic susceptibility in the higher and lower temperature regions; B1 and B2 are related to the spin transition temperature; C1 and C2 represent the width of the sigmoidal function, which correlate with the abruptness of the spin crossover behaviour; parameters D and E in the linear function part of the equation are for fitting the height of the curve related to the paramagnetic impurity and tilt of curve related to diamagnetic correction, respectively. The equation is well fitted to the spin transition behaviour and was used for modelling the lattice parameter changes as it displays a similar curve shape. In the modelled equation for lattice parameters, the parameters A1 and A2 represent the amplitude of lattice changes and the negative sign of A1 and A2 is for NTE and positive for PTE; B1, B2, C1 and C2 have the same meaning as in the modelled spin crossover behaviours. As with the assumption that the curve of spin crossover transition is strongly correlated to the lattice parameter changes, the parameter C1 and C1 are the same for all the fitting curves and A1, A2, B1, and B2 correlates with both equations. Parameter D represents the lattice length at 0 K and E is for the background thermal expansion or contraction, which is outside the spin crossover region. The background thermal behaviour shows a continuous lattice change (expansion on the *a*-axis and contraction on the *b*-axis) while cooling at a temperature lower than the transition temperature. This is likely due to the lattice interactions and framework distortion but lessens with lower temperature. Theoretically, the continuous background thermal behaviour will reach an endpoint until the force of the flexing lattice is too weak to resist the strain of rigid framework geometry.

$$L(T) = \frac{A1}{1+\exp\left(\frac{B1-T}{C1}\right)} + \frac{A2}{1+\exp\left(\frac{B2-T}{C2}\right)} + D + ET \quad (1)$$

The thermal expansion coefficient α for each framework was calculated with the first derivative of the modelled lattice parameters with respect to temperature and divided by *L*(T) as shown in equation (2):

$$\alpha(T) = \frac{1}{L(T)} \cdot \frac{\partial L(T)}{\partial T} = \frac{1}{L(T)} \left\{ \frac{A1 \cdot \exp\left(\frac{B1-T}{C1}\right)}{C1 \cdot \left(1+\exp\left(\frac{B1-T}{C1}\right)\right)^2} + \frac{A2 \cdot \exp\left(\frac{B2-T}{C2}\right)}{C2 \cdot \left(1+\exp\left(\frac{B2-T}{C2}\right)\right)^2} + E \right\} \quad (2)$$

In the **[$Tz_{0.5}Dz_{0.5}$]** material, the thermal expansion coefficients for the *a*-axis and *b*-axis are $\alpha_a = -2047 \times 10^{-6}\ K^{-1}$ and $\alpha_b = +6504 \times 10^{-6}\ K^{-1}$ respectively. The trends of lattice motion on the *ab* plane and with respect to temperature in **[$Tz_{0.5}Dz_{0.5}$]** are shown in Figure 7.4. The **[$Tz_{1.0}Dz_{0.0}$]** unit cell parameters were also modelled showing less thermal expansion behaviour ($\alpha_a = -1503 \times 10^{-6}\ K^{-1}$ and $\alpha_b = +6185 \times 10^{-6}\ K^{-1}$). Thus, the larger extent of lattice change on both axes was noticed in **[$Tz_{0.5}Dz_{0.5}$]**.

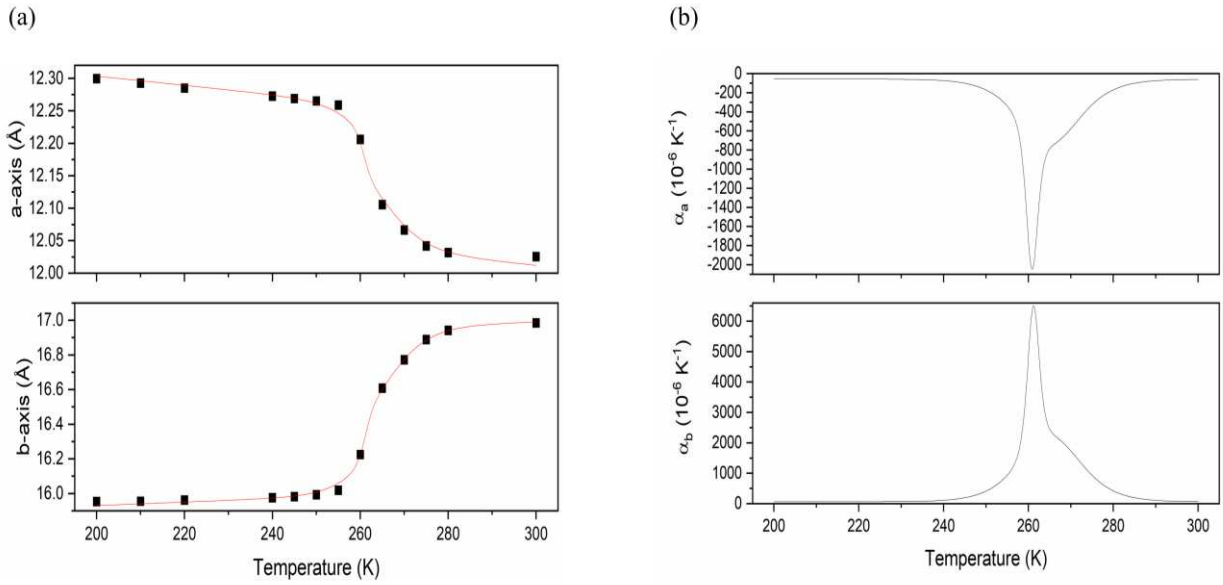

Figure 7.4: Unit cell information of **[$Tz_{0.5}Dz_{0.5}$]** extracted from VT-PXRD data: (a) *a*-axis versus temperature (300–200 K), (b) thermal expansion coefficients α on the *a*-axis versus temperature, (c) the *b*-axis versus temperature, (d) thermal expansion coefficients α on the *b*-axis versus temperature (300–200 K). Markers represent data and curves represent the fitted model.

All of the materials present a similar trend with unit cell volume, the *b*-axis and *c*-axis contraction from high to low temperature over the spin transition while the *a*-axis expand. The tendency of the change of the unit cell parameter *a* and *b* versus temperature for these materials were well fitted *via* using the aforementioned equation (1). It is worth noticing that a lower concentration of Tz ligand in the framework leads to higher thermal expansion behaviours (Figure 7.5). Remarkable lattice thermal expansion was shown in **[$Tz_{0.2}Dz_{0.8}$]**, which exhibited the largest NTE and PTE in the series of MIXMOFs with $\alpha_a = -3277 \times 10^{-6}\ K^{-1}$ and $\alpha_b = +7187 \times 10^{-6}\ K^{-1}$ respectively. To our knowledge as of writing this thesis, **[$Tz_{0.2}Dz_{0.8}$]** has the largest NTE and PTE values in SCO framework materials.

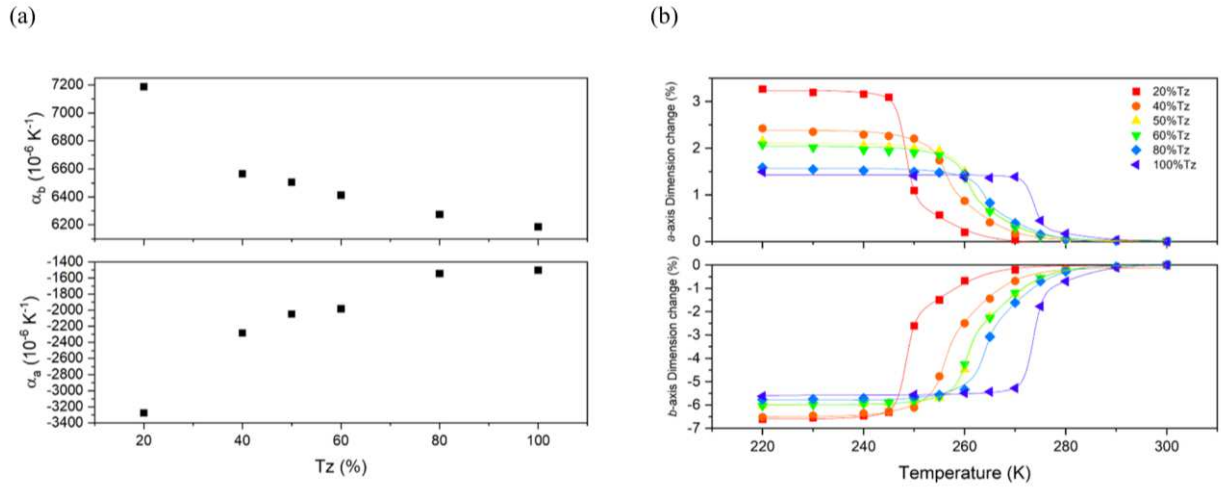

Figure 7.5: Thermal expansion coefficient for **[Tz$_x$Dz$_{1-x}$]** (x = 0.2, 0.4, 0.5, 0.6, 0.8, 1.0) (a) *a*-axis (top) and *b*-axis (bottom). Dimension change versus temperature (b) *a*-axis (top) and *b*-axis (bottom). Curves are included as a visual guide.

As the lattice in these materials displayed colossal expansion on the *a*-axis while contraction on the *b*-axis upon heating, the acute compression angle (θ) was introduced to represent the Fe–Au–Fe angle between Fe(II) sites. In all these materials, the θ angles are larger in the LS state than in the HS state. The lattice flexing mechanism can be depicted through the change of θ that the lattice displays a scissor motion within the *ab*-plane (Figure 7.6). The structural energy and host–host interactions are taken into consideration to explain this lattice flexing mechanism. The energy cost of the scissor motion is very low resulting in the flexible rhombic grid geometry. This also means that spin transition behaviours cause the distortion of the FeN_6 octahedral coordination and the weak interactions within the frameworks can affect this scissor motion. In the HS state, the Fe–N bonds are longer and have less regular orthogonal geometry than in the LS state. While in the LS state, due to the stronger metal-ligand bond, it is energetically favourable to have a more regular geometry and more linear Fe–N–C–Au linkage resulting in the θ angle expanding towards 90°.

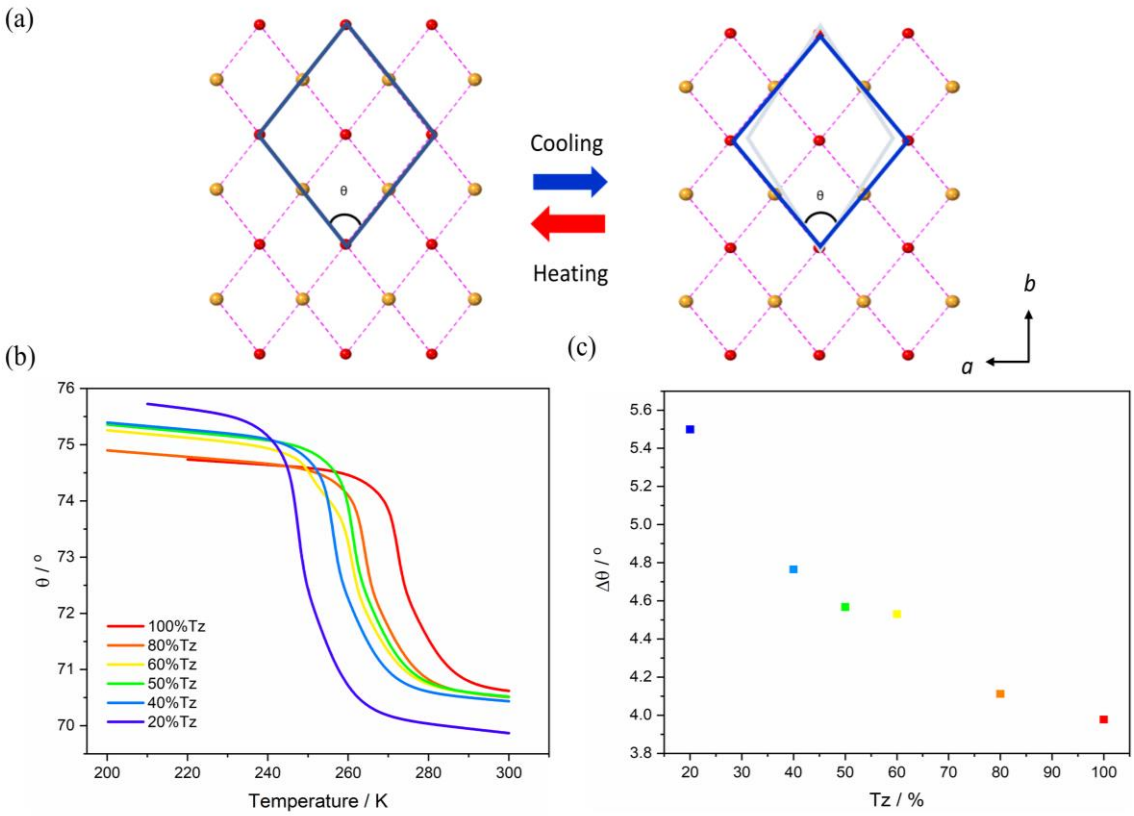

Figure 7.6: (a) Schematic diagram of scissor motion on Hofmann layers. Au atom in yellow and Fe in red. (b) θ angle calculated by fitted a and b unit cell parameters versus temperature. (c) $\Delta\theta$ versus different Tz compositions in the MIXMOFs.

The variations in flexibility across the series of frameworks can be attributed to the trends in inter- and intramolecular interactions. Going from **[$Tz_{1.0}Dz_{0.0}$]** towards **[$Tz_{0.2}Dz_{0.8}$]**, the number of nitrogen atoms decreases. With fewer C–H···N interactions within the framework, the lattice becomes less constrained and rigid, which displays a more remarkable flexing motion. The larger number of hydrogen bonds between the pillaring ligands acts to constrain the topology. The flexibility also accounts for the disorder of the pyridyl rings in the Dz ligand causing an uneven length of the hydrogen bonds. Also, the Fe–N–C angle is more linear in the LS Dz-based framework,[14] which could be another factor explaining the larger thermal expansion in the Dz-rich frameworks. Overall, consecutive modulation of SCO-induced colossal thermal expansion and scissor motion was achieved *via* tuning the ratio of Tz and Dz ligands.

7.3 Investigation of $[Fe(Tz)_x(Dz)_{1-x}(Au(CN)_2)_2]\cdot n$EtOH ($x = 0$) (DzAu·EtOH)

7.3.1 Structural Characterisation and Phase Transitions

Clements *et al.* reported as-synthesised single crystal 3D Hofmann-type framework **DzAu·EtOH** adopts a monoclinic phase while using the post-synthetic method (PSM), the single crystal structure presents an orthorhombic phase.[37-38] That is the single crystal structure of the **DzAu·EtOH** by as-synthesised method exhibits the monoclinic phase exclusively whilst the orthorhombic phase was only formed *via* PSM, which implies that the structure of **DzAu·EtOH** depends on the synthetic method. During the candidate's Honours year, the bulk powder form of **DzAu·EtOH** was synthesised using a fast mixing method by mixing Dz ligand, potassium dicyanidoaurate and Fe(II) perchlorate hydrate in ethanol. The preliminary PXRD data were conducted on the bulk powder form material in the candidate's Honours thesis but the PXRD data have been recollected during her PhD and was compared to the single crystal data. Interestingly, the bulk powder sample did not match a theoretical pattern generated from the as-synthesised single crystal structure. Instead, it matched with the single crystal material synthesised using PSM, displaying an orthorhombic unit cell.[38] Remarkably, the as-made bulk powder material displayed phase transition from orthorhombic to monoclinic phase upon cooling, with its PXRD pattern matching with the as-synthesised single crystal structure.[37]

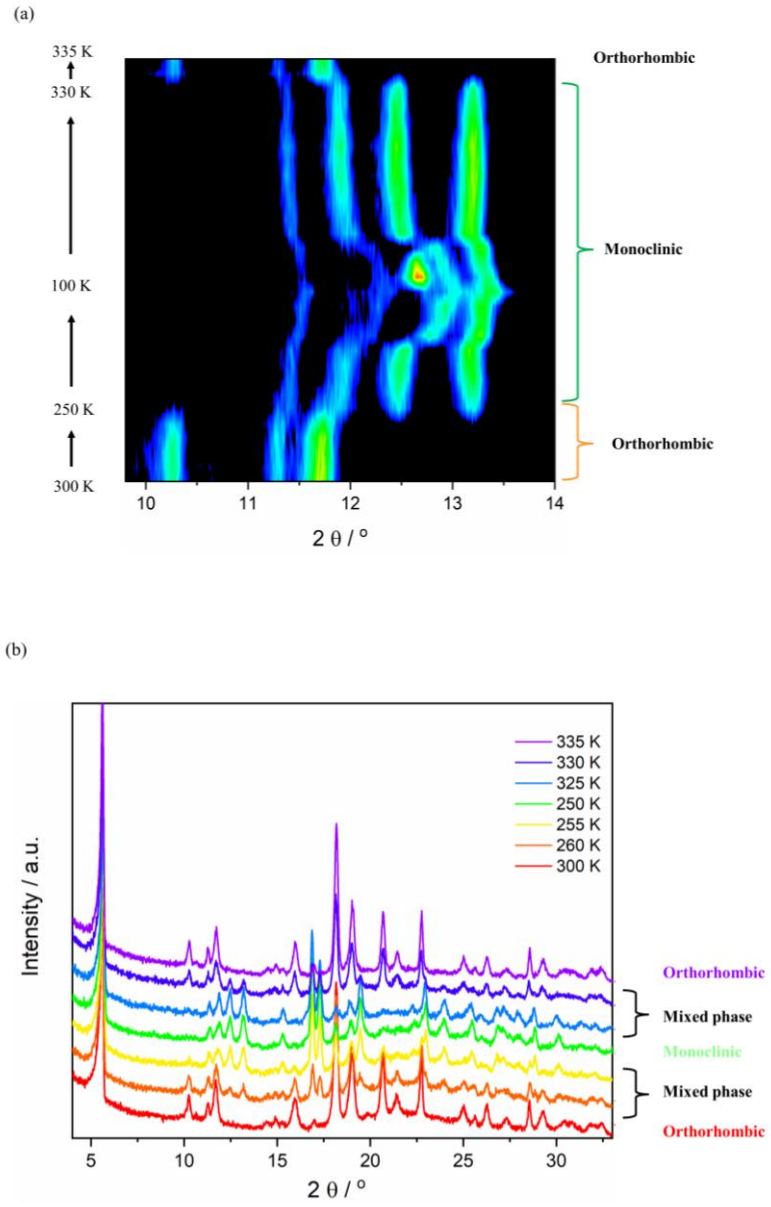

Figure 7.7: (a) VT-PXRD peak evolution (2θ = 9.8–14.0°) of **DzAu·EtOH** with cooling and heating in the temperature range 300–100–335 K; (b) VT-PXRD data for identifying the phase interconversion between orthorhombic phase and monoclinic phase. Data are presented as lines and offset in the y-axis for clarity.

The material was characterised by VT-PXRD in the temperature range 300–100–335 K (Appendix E.20). To extract phase transition and lattice information in the thermal cycle, the sequential Pawley refinements were conducted using GSAS-II[39] (Appendix Table E.3 and Figure E.20). A schematic illustration of phase interconversion is shown in Figure 7.8. The contour plot in Figure 7.7 shows diffraction peaks evolution versus temperature. Three peaks (2θ = 10.3, 11.4 and 11.6°) from the contour plot were noticed at 300 K in the 2θ range of 9.8–14.0°. The pattern was refined indicating the

original structure of the material adopted an orthorhombic phase. The material converts to the mixed orthorhombic and monoclinic phases when cooling to 260 K. The structure completely converts to a monoclinic phase at 250 K with the peak at 10.3° disappearing and two new peaks occurring at 12.5° and 13.3°. With continuing cooling to *ca.* 185 K, all the peaks shift stepwise to higher angles indicating a four-step spin transition. The peaks return to the original 2θ value upon heating. The material is able to remember the monoclinic phase (**1-M-RT**) when heating back to room temperature. PXRD patterns show two peaks at 12.5° and 13.3° disappearing and the peaks at 10.3° resurfacing at 335 K. This indicates the material remains unchanged until it was heated to 335 K. The higher temperature triggers the phase back to the original orthorhombic phase (**1-O-HT**). The material can retain the orthorhombic phase when cooled down back to room temperature (**1-O-RT**). Thus, not only the high temperature orthorhombic phase can transfer to the low temperature monoclinic phase (**1-M-LT**), but also the reversion of the structure was observed.

The powder material **1-O-RT** was fitted using GSAS II Pawley refinement.[39] The material adopts the orthorhombic phase (a = 11.8030 Å, b = 17.0880 Å, c = 15.5667 Å) in comparison with **1-M-RT** where it is the monoclinic phase (a = 14.9022 Å, b = 14.7853 Å, c = 31.3939 Å, β = 95.96°). The total volume of the monoclinic phase is double that of the orthorhombic phase due to lower symmetry. Therefore, the material can possess and remember two phases at room temperature. Elastic motions have been found in various flexible MOFs but in those materials, the structures could not retain their original phase with the withdrawal of the external stimuli or guests.[40-42] Notably, in our material, both phases can be retained at room temperature. Phase transition happens only when additional heating was applied. That indicates the material possesses ‘two-way shape memory’ behaviours and both high and low temperature phases can be retained.

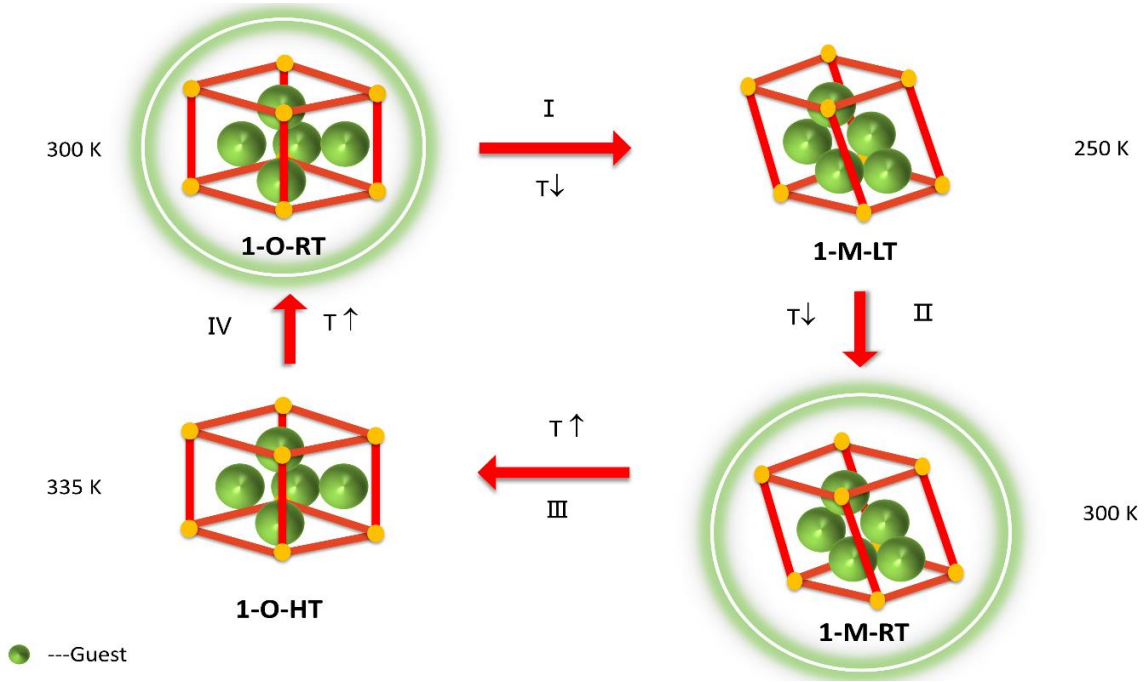

Figure 7.8: Schematic illustration of the shape memory effect. As-made bulk powder material **1-O-RT** presents in the orthorhombic phase at room temperature and upon cooling converts to monoclinic phase **1-M-LT** at 250 K (process I). The material locks in the monoclinic phase **1-M-RT** with heating back to room temperature (process II). With continuous heating (process III), phase conversion from monoclinic to orthorhombic phase happened **1-O-HT** at 335 K. **1-O-RT** retains orthodromic phase at 300 K (process IV).

As **1-O** (**DzAu·EtOH** in orthorhombic phase) possesses the same topology as the PSM framework, this indicates the four-fold disorder of the diazine rings leads to disordered C–H···N host–host interactions. The phase transition implies that the rotations of the diazine rings occur to form the ordered C–H···N interactions pairing with the adjected pillar ligand (Figure 7.9). Moreover, unlike the **1-O** possessing superimposed framework layers, the translation of layers was observed. The Au···Au interactions change from perpendicular between the layers in **1-O** material to inclined causing the displacement in the **1-M** (**DzAu·EtOH** in monoclinic phase) between the interpenetrated layers. The monoclinic phase can be generated *via* a slow diffusion process of growing single crystals or by the cooling process of the bulk powder **1-O** material. Also, the C–H···N interactions are pairing in order, which indicates that **1-M** is likely the thermodynamic product. However, the orthorhombic phase was formed in the fast mixing method and disorder host–host interactions were demonstrated in **1-O** indicating that this is likely the kinetic product. The rotation of the diazine rings occurred when altering the temperature causing the powder material of **DzAu·EtOH** to possess two phases at different energy. Thus, the two phases previously in two frameworks with different synthetic methods can merge into one material demonstrating phase transition modulated by temperature.

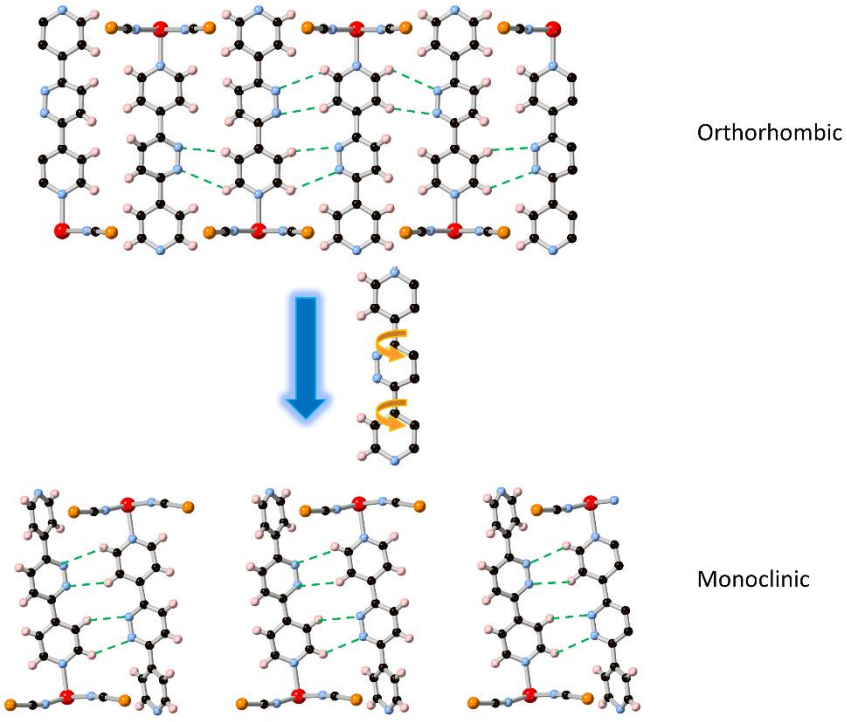

Figure 7.9: Schematic illustration of the mechanism of phase transition from the orthorhombic phase (top) to the monoclinic phase (bottom) upon cooling in **DzAu·EtOH**. While cooling, the rotation of the diazine rings occurs, which changes the hydrogen bonding and alters the C–H···N host–host interactions within the framework. Ethanol solvent within the pores was omitted for clarity. C: black, N: blue, Fe: red, Au: orange, H: pink, C–H···N interactions: green dotted lines.

7.3.2 Variable Temperature Solid-State Diffuse Reflectance

A distinctive colour change between the **1-O** and **1-M** powder samples was noticed. **1-O** in orange and **1-M** in yellow were observed respectively. Variable temperature solid-state diffuse reflectance starting from cooling to the heating process was conducted to monitor progressive phase transition. The wavelength distinctively changes from 471, 443 and 426 nm corresponding to temperature decreasing from 280, 260 and 250 K indicating the phase transition occurs (Figure 7.10). With continuous cooling below 250 K, the material converts to the monoclinic phase and remains unchanged until heated back to room temperature. Compared with the cooling and heating process at the same temperature (240 K), the wavelength is 420 and 421 nm respectively, which implies the material locks in the monoclinic phase. However, an obvious wavelength change was shown for 443 nm (cooling process) and 412 nm (heating processing) at 260 K. That is attributed to two phases in the thermal cycle: in the cooling process at 260 K the material possesses an orthorhombic phase; in the heating process at 260 K, the material remains the monoclinic phase unless heated to 335 K. That confirms the temperature can be used to induce phase transition.

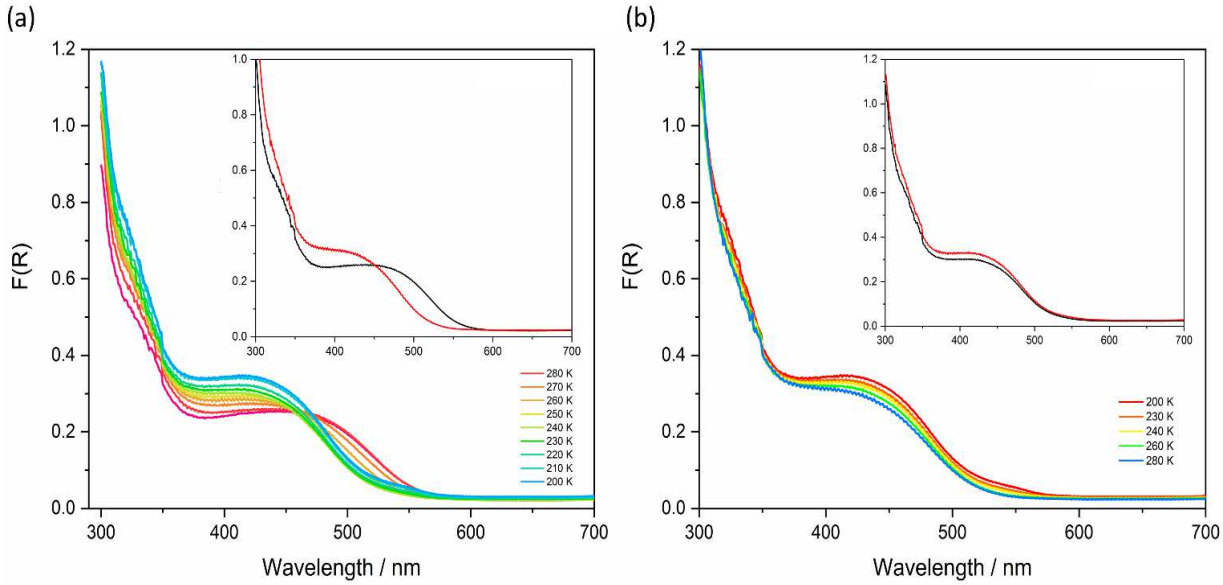

Figure 7.10: Variable temperature solid-state diffuse reflectance of **DzAu·EtOH** (a) for the cooling process from 280 to 200 K, insert: comparison of cooling the warming process at 280 K; (b) for the heating process from 200 to 280 K, insert: comparison of cooling the warming process at 240 K.

7.3.3 Structural Characterisation in Desolvation Phase

The desolvation process of both **1-M** and **1-O** were conducted by *ex situ* PXRD (data were collected in the candidate's Honours year), forming the same structure. The process of the desolvation to **1-ΦM** was investigated by *in situ* PXRD measurement (data were obtained during her PhD). The sample was loaded into an open-end capillary with N_2 flow during the measurement at room temperature.

The phase transition from **1-M** to **1-ΦM** is abrupt with the intermediate mixed with **1-M** and **1-ΦM** phase forming in *ca.* 10 minutes and completing the conversion to **1-ΦM** in 15 minutes (Appendix E.21). The resolvation phase was studied on adsorption of ethanol mother liquor. **1-ΦM** can revert to the original **1-O** phase. Also, the further process of cooling of **1-O** can continue to change to the monoclinic phase, which reveals the reproducible phase interconversion cycle. Thus, we can manipulate **DzAu·EtOH** by switching between two phases *via* temperature and 'breathing-like' behaviour with desolvation and resolvation of **1-ΦM**.

Although single crystal data of the desolvated structure could not be collected due to the crystal diffracting very weakly, density functional theory (DFT) calculations were carried out by Dr Ramzi Kutteh at the Australian Nuclear Science and Technology Organisation (ANSTO) to investigate the desolvation phase. Single crystal structures in both orthorhombic and monoclinic phases were used as input to calculate the structure of desolvation. Both with and without van der Waals (vdW) methods and with symmetry constraints and no symmetry were applied to both phases. Both phases as starting points respectively show that the structure remains stable with the removal of solvent. All the strategies gave consistent results, indicating that the desolvated structure adopts a monoclinic phase. The lattice parameters of the unit cell in the desolvated phase are all smaller than the solvated structure phase (a = 13.9383 Å, b = 14.3437 Å, c = 30.4218 Å, β = 94.0701º) due to the removal of the guest molecule with decreased voids. The desolvated phase is more bent than the solvated monoclinic phase, in which the angle (Fe to N from the top pyridyl ring) is 173.34º compared with 175.15º. The ligand rotation mechanism from disordered C–H···N host–host interactions to the paired pillars accompany by the desolvation process. A similar mechanism was reported in other systems.[43]

However, the simulated PXRD pattern from DFT calculated desolvated phase does not match the experimental PXRD pattern of bulk powder **1-ΦM**. That difference can possibly be explained by two main reasons: 1) the DFT structure was calculated at the lowest energy point while the experimental PXRD pattern was collected at 100 K, and 2) disordered rings of the ligand were not considered in the calculation. Thus, in order to obtain a relatively accurate simulated structure, molecular dynamics will be conducted for future work.

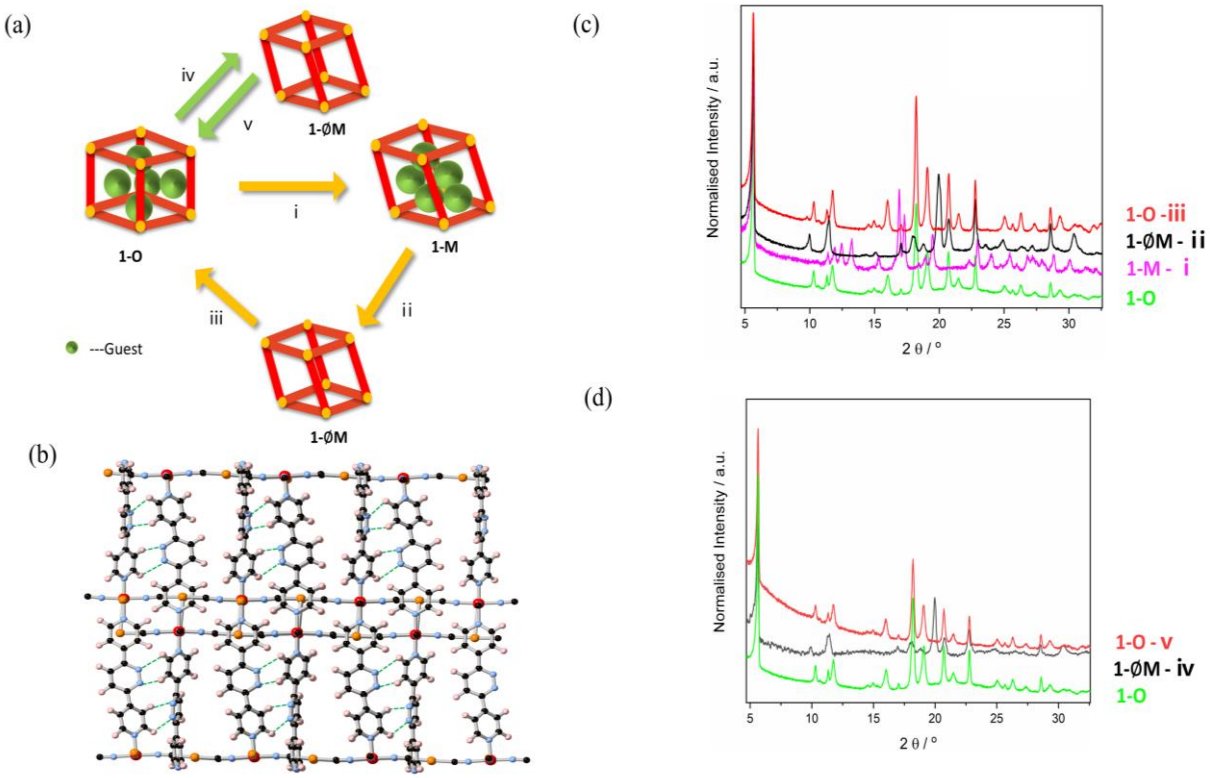

Figure 7.11: (a) Schematic illustration of the desolvation and resolvation process of both **1-O** and **1-M**. **1-ΦM** phase generated *via* two pathways: 1. cooling to **1-M** (process i) and desolvation (process ii) and for absorption of mother liquor ethanol, the material returns to the original **1-O** (process iii). This pathway represents in yellow arrows; 2. direct desolvation from **1-O** (process iv) and returned to the original phase by resolvation (process v) This pathways represent in green arrows. (b) The structure of desolvated phase at 0 K was calculated using DFT. C: black, N: blue, Fe: red, Au: orange, H: pink, C–H···N interactions: green dotted lines. (c) PXRD pattern of desolvation process started from **1-O** material *via* process i forming monoclinic phase (**1-M-i**) and **1-ΦM-ii** formed by desolvation. By resolvation, the material was transferred to the original orthorhombic phase **1-O-iii** (d) Direct desolvation procedure was applied on the original **1-O** material to form desolvation phase (**1-ΦM -iv**), The material changed back to original phase by resolvation (**1-O -v**). Data are presented as lines and offset in the y-axis for clarity.

7.3.4 Magnetic Properties Associated with Structural Properties

To study the magnetic properties, variable temperature magnetic susceptibility measurements were conducted on the as-synthesised powder material **1-O** presenting a four-step SCO (Figure 7.12). The data were measured during the candidate's Honours year and presented here for completeness. The first-step abrupt transition ($T_{½}\downarrow\uparrow$ = 184 K, 189 K; ΔT = 5 K) in closed hysteresis loop. For the second step ($T_{½}\downarrow\uparrow$ = 172 K, 179 K; ΔT = 7 K) the cooling and heating curves overlap at *ca.* 160 K, also forming a closed hysteresis loop. There is a wider plateau at the temperature range of 148–165 K. The third ($T_{½}\downarrow\uparrow$ = 123 K, 144 K; ΔT = 21 K) and fourth-step ($T_{½}\downarrow\uparrow$ = 98 K, 118 K; ΔT = 20 K) are open hysteresis loops.

At temperatures below 75 K, the magnetic susceptibility is close to zero, indicating that the sample is LS. The hysteresis from the first to the fourth loop increases, and in each step a fraction of HS sites converts to LS sites upon cooling (five states: $HS_1LS_0 \rightarrow HS_{0.67}LS_{0.33} \rightarrow HS_{0.5}LS_{0.5} \rightarrow HS_{0.33}LS_{0.67} \rightarrow HS_0LS_1$). Structural change from the orthorhombic phase to the monoclinic phase was observed in the magnetic measurement with a slight drop in magnetic susceptibility value at about 260 K. The monoclinic phase was recovered to its original phase *via* heating at 340 K and this thermal cycle procedure was repeated three times with magnetic measurements showing that the material can retain the structural memory. Interestingly, although the as-synthesised powder material **DzAu·EtOH** and the PSM synthesised single crystal material are both in the orthorhombic phase, the SCO behaviour of the powder sample in the orthorhombic phase is consistent with as-synthesised single crystal in the monoclinic phase and not matching with the PSM synthesised material in orthorhombic phase exhibiting the single-step SCO.[37-38] This is the powder form that displays a four-step SCO (five spin states) while **DzAu·EtOH** synthesising using PSM method is single-step (two spin states). Thus, we demonstrate seven spin states presented in the same material *via* different synthesis methods.

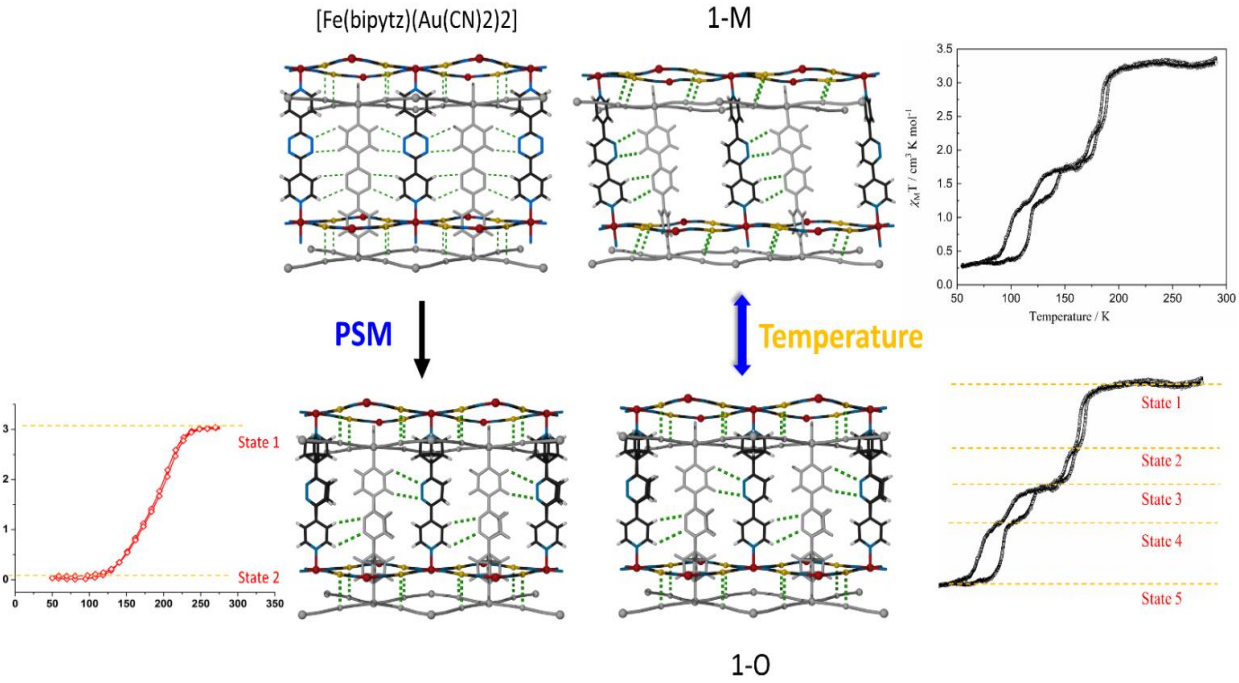

Figure 7.12: Schematic demonstration of PSM method from **TzAu·EtOH** (top left) to **DzAu·EtOH** (bottom left) in orthorhombic phase presenting single-step SCO (two states). As-synthesised powder sample of **DzAu·EtOH** can interconvert between the orthorhombic (bottom right) and monoclinic phase (up right). Both bulk powder samples **1-M** and **1-O** display four-step SCO behaviours.

The magnetism susceptibility data of the desolvated materials **1-Φ** generated by two different materials (desolvation for **1-O** and **1-M**) were collected. The two desolvated materials display the same gradual, non-hysteresis single-step SCO ($T_{½}$ = 161 K) as shown in Figure 7.13. The framework without guest molecules attenuates the cooperativity attributed to the extinction of the host–guest interactions. This reduced the propagation of spin states in the SCO materials showing a relatively gradual SCO behaviour.

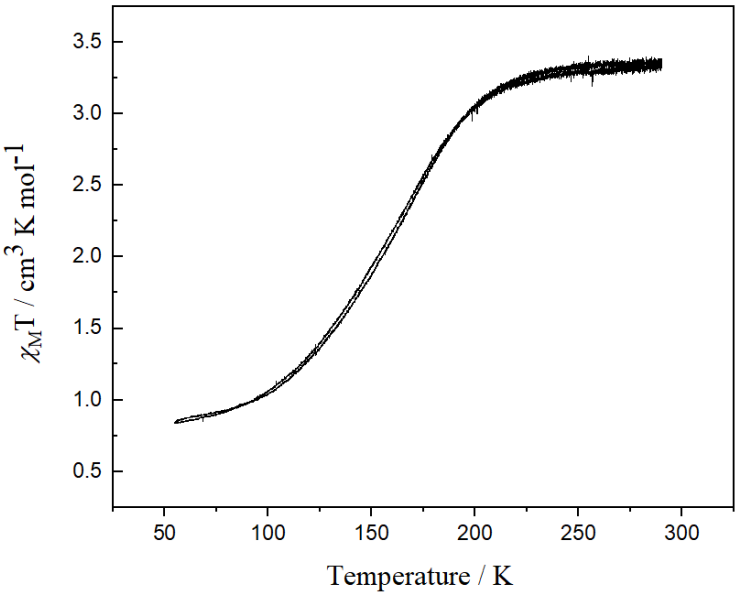

Figure 7.13: Variable temperature magnetic susceptibility measurement of **1-ΦM**.

7.4 Investigation of $[Fe(Tz)_x(Dz)_{1-x}(Au(CN)_2)_2]\cdot n$EtOH ($x$ = 0.1 and 0.15)

7.4.1 Structural Characterisation of Gradual Phase Transition

Two MIXMOFs **[$Tz_{0.1}Dz_{0.9}$]** and **[$Tz_{0.15}Dz_{0.85}$]** materials were generated. Interestingly, they presented a gradual phase transition from orthorhombic to partial monoclinic phase upon thermal cycles. The preliminary PXRD data were collected in the candidate's Honours thesis but the PXRD data have been remeasured and refinements were conducted during her PhD. PXRD was conducted at room temperature demonstrating both materials adopted the orthorhombic phase, which is the same as the series of MIXMOFs with higher components of Tz ligand ($x \geq 20$). VT-PXRD measurements (using Cu-K_α radiation, λ = 1.5405 Å) were conducted on these two materials, which displayed remarkable phase transition similar to **DzAu·EtOH**. However, unlike **DzAu·EtOH** presenting a complete phase transition from orthorhombic phase to monoclinic phase upon cooling, **[$Tz_{0.1}Dz_{0.9}$]** and **[$Tz_{0.15}Dz_{0.85}$]** formed mixed orthorhombic and monoclinic phases when temperature returned to 300 K after the first thermal cycle (Figure 7.14). Based on the PXRD information of **DzAu·EtOH**, the evidence of a peak at 10.3° in both materials indicates that it is in the orthorhombic phase and structural information was

confirmed by Rietveld refinements using GSAS-II.[39, 44] The structure converts from a pure orthorhombic phase to a mixed orthorhombic and monoclinic phase when the temperature returns to 300 K. The evidence of a mixed phase was noticed from the pattern at that temperature with peaks at 10.3, 11.4 and 11.6°.

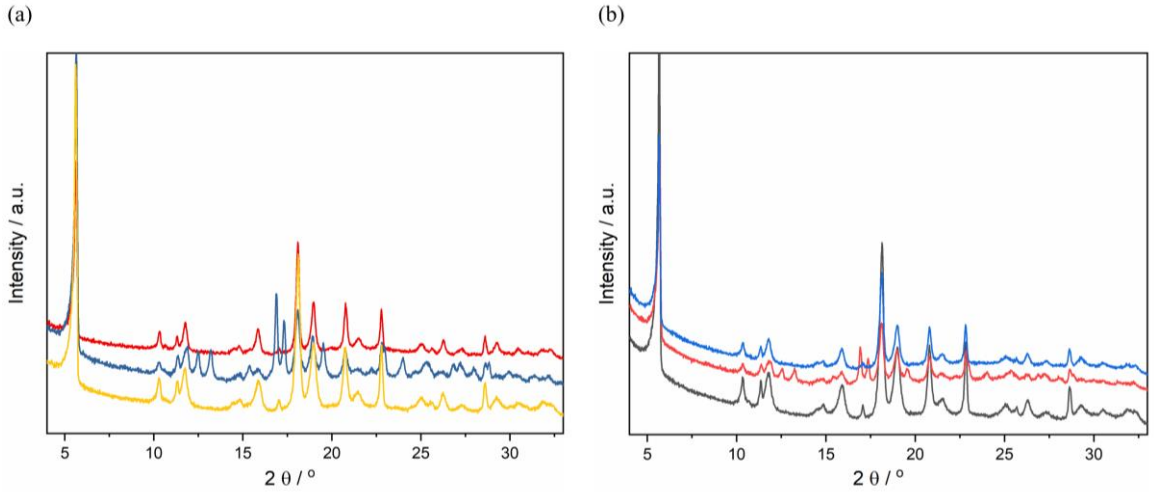

Figure 7.14: (a) PXRD patterns of **[$Tz_{0.1}Dz_{0.9}$]** measured at 300 K in its original orthorhombic phase (yellow), after a thermal cycle measured at 300 K in a mixed phase (blue), heated to 330 K returning to orthorhombic phase (red). (b) PXRD patterns of **[$Tz_{0.15}Dz_{0.85}$]** were measured at 300 K in its original orthorhombic phase (black), after a thermal cycle measured at 300 K in a mixed phase (red), heated to 330 K returning to orthorhombic phase (blue).

The contour plots of peak evolution in one thermal cycle in **[$Tz_{0.1}Dz_{0.9}$]** and **[$Tz_{0.15}Dz_{0.85}$]** are shown in Figure 7.15(a) and (b). All the peaks shift stepwise to higher angles indicating a four-step spin transition. The peaks return to the original 2θ value upon heating. Powder patterns of **[$Tz_{0.1}Dz_{0.9}$]** in continuous two thermal cycles were collected at the Australian Synchrotron. This shows that the phase transition is reproducible. Also, the structure can revert to its original phase after two thermal cycles. Three peaks (2θ = 10.3, 11.4 and 11.6°) were observed in both **[$Tz_{0.1}Dz_{0.9}$]** and **[$Tz_{0.15}Dz_{0.85}$]** in the 2θ range of 9–14°. Two extra peaks occurred at 12.5 and 13.3° when cooling down to 230 K in **[$Tz_{0.1}Dz_{0.9}$]** and 246 K in **[$Tz_{0.15}Dz_{0.85}$]** indicating that the materials partially convert to monoclinic phase. The first step of spin transition temperatures in both **[$Tz_{0.1}Dz_{0.9}$]** and **[$Tz_{0.15}Dz_{0.85}$]** occurred at the same temperature for phase transition of each one where the peaks shifted to high angles in the cooling process. The following steps of spin transitions were at very close temperatures. This shows continuing stepwise shifting to higher angles for about 0.5° in both materials. The peaks returned to lower angle

values in the heating process, indicating SCO sites in the HS state. Both materials converted to the original orthorhombic phase at 330 K, with the two peaks at 12.5° and 13.3° disappearing.

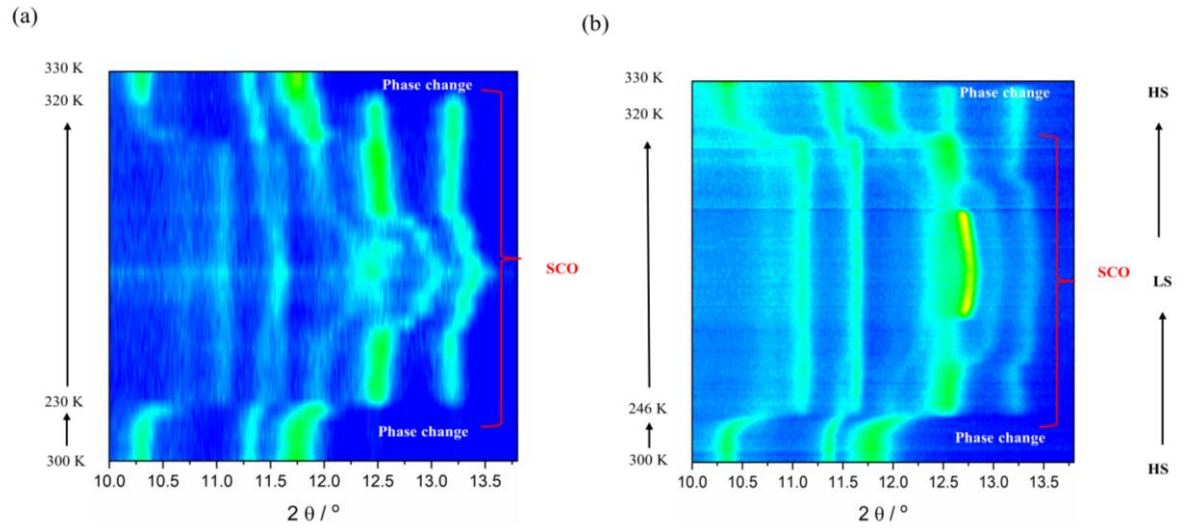

Figure 7.15: VT-PXRD peak evolution (2θ = 9–14°) with cooling and heating in the temperature range 300–100–330 K. (a) **[$Tz_{0.1}Dz_{0.9}$]**; (b) **[$Tz_{0.15}Dz_{0.85}$]**.

As both materials displayed phase transition to partial monoclinic phase, *in-situ* VT-PXRD (in the temperature range 300–100–300 K) for nine thermal cycles were conducted on these materials to examine the gradual structural conversion in each cycle (Figure 7.16). The first collection of each material is for an original structure, which was measured at 300 K showing both materials in orthorhombic phases. The second collection was conducted after cooling to 100 K followed by heating back to 300 K. The phase transition in both materials is indicated by the presence of new peaks such as those at 12.5 and 13.3°. The PXRD patterns were all collected at 300 K after each thermal cycle until 10 thermal cycles were collected. All the patterns were refined by Rietveld refinements using GSAS-II.[39, 44] The first patterns of both materials for the original phase were refined in the orthorhombic phase. The rest measurements were refined by mixed orthorhombic and monoclinic phases. The lattice parameters extracted for the orthorhombic phase are shown in Figure 7.17 and the monoclinic phase is shown in Appendix E.29. The patterns refined in the orthorhombic phase of **[$Tz_{0.1}Dz_{0.9}$]** show smaller *a*- and *b*-lattices than **[$Tz_{0.15}Dz_{0.85}$]** during the whole thermal cycling process. In the phase transition process, both materials presented an overall increasing trend on the *a*-axis while decreasing on the *b*-axis. The *c*-axis is nearly unchanged. The patterns refined in the monoclinic phase of **[$Tz_{0.1}Dz_{0.9}$]** gave larger values on the *a*-axis and smaller on the *b*- and *c*-axis.

The progressive phase conversion was quantified based on the PXRD results to compare the differences between both materials (Figure 7.17 (d)). After the first thermal cycle, 23% of the orthorhombic phase transformed into the monoclinic phase in **[$Tz_{0.1}Dz_{0.9}$]** and 21% in **[$Tz_{0.15}Dz_{0.85}$]**. The structural transition process is rapid and pronounced in the first two cycles and becomes gradual to almost steady in the following cycles. The percentages of the monoclinic phase increase during the thermal cycles and in the last one, 36% of the structure transformed to the monoclinic phase in **[$Tz_{0.1}Dz_{0.9}$]** while 27% in **[$Tz_{0.15}Dz_{0.85}$]**. Unlike **DzAu·EtOH** displaying a complete structural transformation to monoclinic, both materials predominately adopt the orthorhombic phase. The tendency of phase transition for **[$Tz_{0.15}Dz_{0.85}$]** is more gradual than **[$Tz_{0.1}Dz_{0.9}$]**.

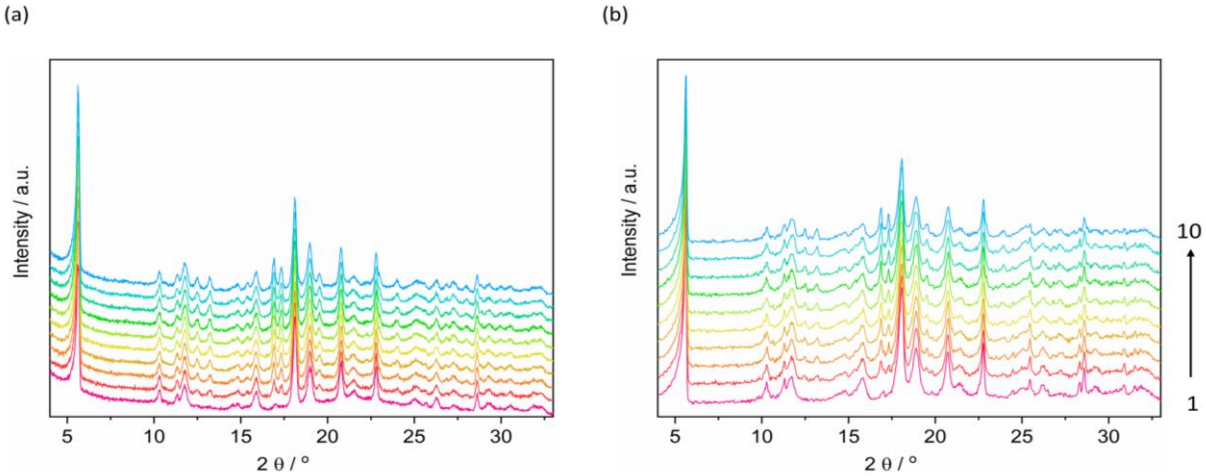

Figure 7.16: PXRD patterns of (a) **[$Tz_{0.1}Dz_{0.9}$]** and (b) **[$Tz_{0.15}Dz_{0.85}$]** starting from the first collection in the original orthorhombic phase at 300 K. The following patterns were collected after sequential thermal cycles measured at 300 K until 10 data collections to show the gradual process of phase transition.

The phase transition that occurs in both materials can be explained by the re-arrangement of the host–host C–H···N interactions between the Tz and Dz ligands similar to **DzAu·EtOH**. The hydrogen bondings between the ligands are distributed randomly in the orthorhombic phase. The thermal stimuli enable the rotation of the diazine ring. Thus, the hydrogen bonding converts to a more ordered and pairing configuration with the structure partially changing to the monoclinic phase. The different extent of phase transition in these materials can be explained by the number of hydrogen bonds. Compared with the framework with only Tz ligand, the hydrogen bonding in **[$Tz_{0.1}Dz_{0.9}$]** and **[$Tz_{0.15}Dz_{0.85}$]** is 55% and 57.5% respectively. With a relatively lower number of hydrogen bonding, the lattice of **[$Tz_{0.1}Dz_{0.9}$]** is more flexible resulting in a higher degree of phase transition within the framework. In the **DzAu·EtOH**, there are 50% hydrogen bonds so a complete phase transition was observed in one thermal cycle, likely caused by a more flexible ligand rotation. Therefore, the flexibility of the phase transition can be tuned by the composition of the ligand, that is by altering the number of hydrogen

bonds. The degree of structural transformation can be controlled by the number of the thermal cycles. Overall, both materials possess thermal-induced progressive phase transition behaviours.

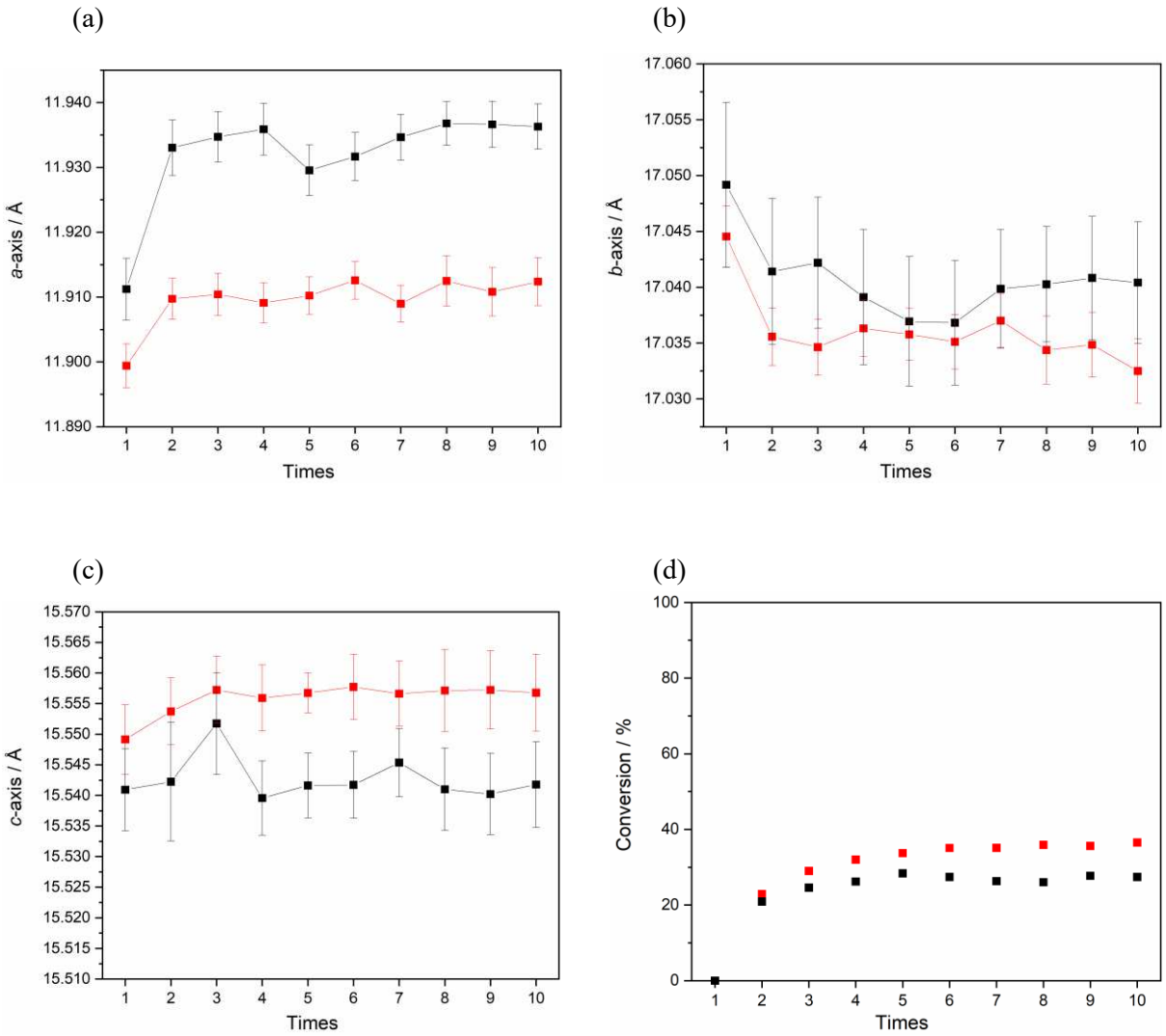

Figure 7.17: Lattice parameters of **[$Tz_{0.1}Dz_{0.9}$]** (red) and **[$Tz_{0.15}Dz_{0.85}$]** (black) extracted from PXRD patterns with the data refined in the orthorhombic phase. The patterns were collected from original phases and followed by each thermal cycle at 300 K. The change of each lattice parameter versus each collection of the (a) *a*-axis, (b) *b*-axis and (c) *c*-axis. (d) Percentage of conversion from orthorhombic phase to monoclinic phase versus each collection times of **[$Tz_{0.1}Dz_{0.9}$]** (red) and **[$Tz_{0.15}Dz_{0.85}$]** (black).

7.4.2 Thermal Induced History-Dependent SCO Behaviours

The SCO behaviours were examined by variable temperature magnetic susceptibility measurements for both materials. The preliminary results were collected in the candidate's Honours thesis but the data have been remeasured and further thermal cycling magnetic susceptibility measurements were conducted during her PhD. **[Tz$_{0.1}$Dz$_{0.9}$]** shows an abrupt five-step SCO, which is very rare (Figure 7.18(a)). Such five-step SCO behaviour was only reported in a Fe(III) complex.[45] **[Tz$_{0.1}$Dz$_{0.9}$]** remains in the HS state until *ca*. 263 K. In the first thermal cycle, an abrupt, closed hysteresis loop spin transition presents in the first step (T½↓↑ = 248 K, 252 K; ΔT = 4 K). An inclined and large plateau is noticed in from 236 K ($\chi_M T$ = 1.8 cm^3 K mol^{-1}) to 198 K ($\chi_M T$ = 1.6 cm^3 K mol^{-1}). Approximately 50% of the HS state converts to the LS state at that plateau. The second step (T½↓↑ = 187 K, 189 K; ΔT = 2 K) and third step (T½↓↑ = 177 K, 181 K; ΔT = 4 K) both have open hysteresis loops. In between the third and fourth steps (T½↓↑ = 134 K, 140 K), another plateau is shown at 165 K. The fourth step of spin transition occurs at 133 K (T½↓) and 141 K (T½↑), while the last step at 112 K (T½↓) and 119 K (T½↑). The material reaches the LS state below *ca*. 83 K. Interestingly, with continuous thermal cycles conducted on these materials, instead of identical SCO behaviour occurring in the **DzAu·EtOH** upon cycles, each thermal cycle exhibits unique magnetic behaviour. The rest of the thermal cycles also exhibit five-step SCO behaviour, but the magnetic susceptibility values for each step increase with increasing cycle numbers, particularly between the first and second cycles. The $\chi_M T$ value of the plateau between the first and second spin transition in the second thermal cycle is approximately 2.2 cm^3 K mol^{-1}, which indicates about 35% of Fe(II) sites transform from the HS state to the LS state. This discrepancy in SCO behaviours in each cycle is related to the phase transitions. The pronounced distinction in the first cycle from the other cycles suggests the phase transition mainly occurs over the first two thermal cycles in which a larger component of the orthorhombic phase is converted to monoclinic. This agrees with the VT-PXRD data.

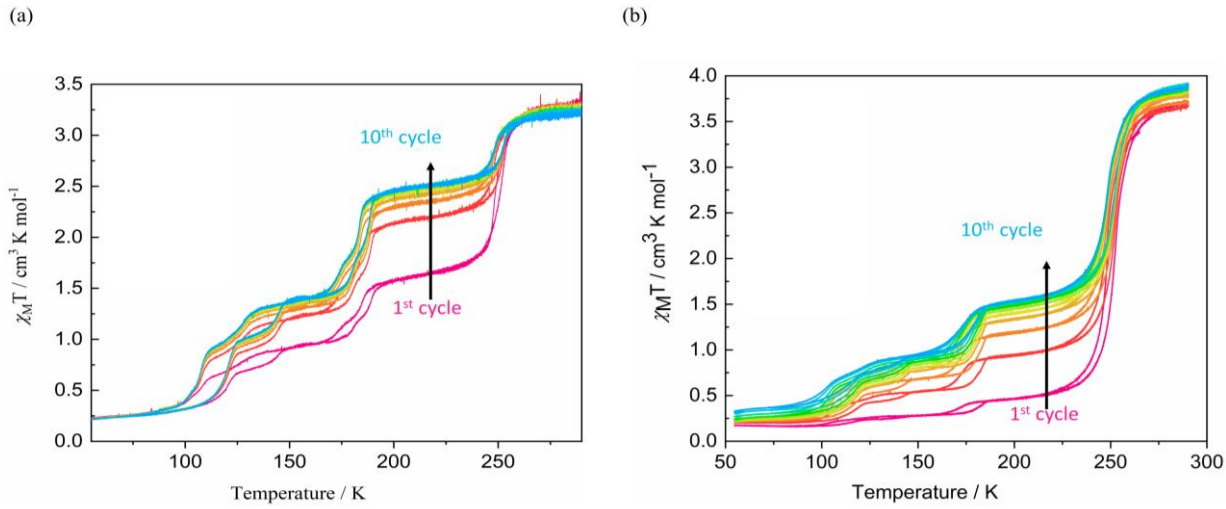

Figure 7.18: Magnetic susceptibility measurements over ten thermal cycles of (a) **[Tz$_{0.1}$Dz$_{0.9}$]** and (b) **[Tz$_{0.15}$Dz$_{0.85}$]**.

Variable temperature magnetic susceptibility was conducted on **[$Tz_{0.15}Dz_{0.85}$]** material over ten thermal cycles and displays a progressively increasing four-step SCO (Figure 7.19 (b)). The material undergoes spin transition when cooled below 272 K. The first spin transition in the first thermal cycle is abrupt and occurs at 249 K in the cooling process and 253 K in the heating process with a narrowed hysteresis at 4 K. Between the first and second thermal cycles a relatively flat and large plateau over the temperature range of 219–190 K is observed. The $\chi_M T$ value is approximately 0.4 cm^3 K mol^{-1} indicating only about 12% of the HS state remaining. The second spin transition occurs at 176 K ($T½\downarrow$) and 178 K ($T½\uparrow$). The third step ($T½\downarrow\uparrow$ = 133 K, 134 K) and fourth step ($T½\downarrow\uparrow$ = 110 K, 111 K) are very gradual with almost closed hysteresis loops. The material converts to the LS state at 93 K. The general trend of the spin transition temperatures in the consecutive thermal cycles is slightly decreasing. **[$Tz_{0.15}Dz_{0.85}$]** displays progressively increasing $\chi_M T$ values. This is because fewer Fe(II) sites change to the LS state after the first spin transition over the following cycles. In the last thermal cycle, about 42% of Fe(II) sites remain in the HS state. The SCO behaviours become almost identical until the sixth cycle. In the process of phase transition over cycling, the material displays an incomplete LS state.

To investigate the temperature range of phase transition in detail, the magnetic susceptibility measurements of **[$Tz_{0.1}Dz_{0.9}$]** were conducted with nine thermal cycles in the first step SCO temperature range (i.e., five thermal cycles within the temperature range 300–200 K), followed by complete cycles to the LS state (300–55–300 K). The distinct magnetic susceptibility is shown in the first step with an obvious increase in the $\chi_M T$ value in Figure 7.19. After five thermal cycles, the rest cycles reach the complete LS state with identical SCO behaviour. This indicates a progressive phase transition is mainly occurring in the first step temperature range (300–200 K).

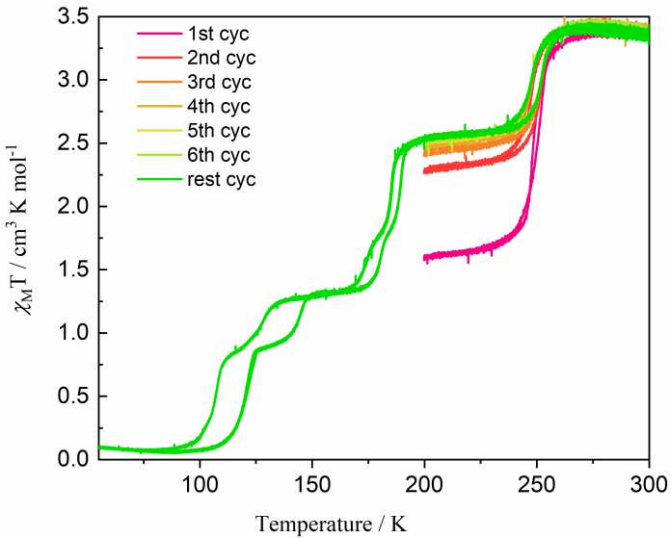

Figure 7.19: Magnetic susceptibility measurements of **[$Tz_{0.1}Dz_{0.9}$]** with the first five thermal cycles in the temperature range of 300–200–300 K and the rest three cycles in 300–55–300 K.

Another cycling experiment was conducted with multiple scans in the ranges of the second to fourth spin transition (over the temperature range 300–55–200–55–200–55–200–55–300–55–200–55–200 K), which is to provide more evidence that the phase transition mainly occurs in the temperature range of the first spin transition. After the first thermal cycle (300–55–200 K), the second and third cycles (200–55–200 K) are identical, which suggests no phase transition by scanning the temperature range of the second the fourth spin transition (Figure 7.20). A noticeable increase in the $\chi_M T$ value from the fourth (200–55–300 K) to the fifth cycle (300–55–200 K) is consistent with the orthorhombic to the monoclinic phase transition. The sixth cycle (200–55–200 K) overlapped with the fifth one indicating no phase transition in this temperature range. Both sets of results confirm that the majority of the phase transition of the framework structure occurs over the first steps of spin transition, in which a large component of the orthorhombic phase is converted to monoclinic. To the best of our knowledge, these two SCO materials are the first to exhibit such a history-dependent change in SCO behaviour over thermal cycles attributed to the phase transition.

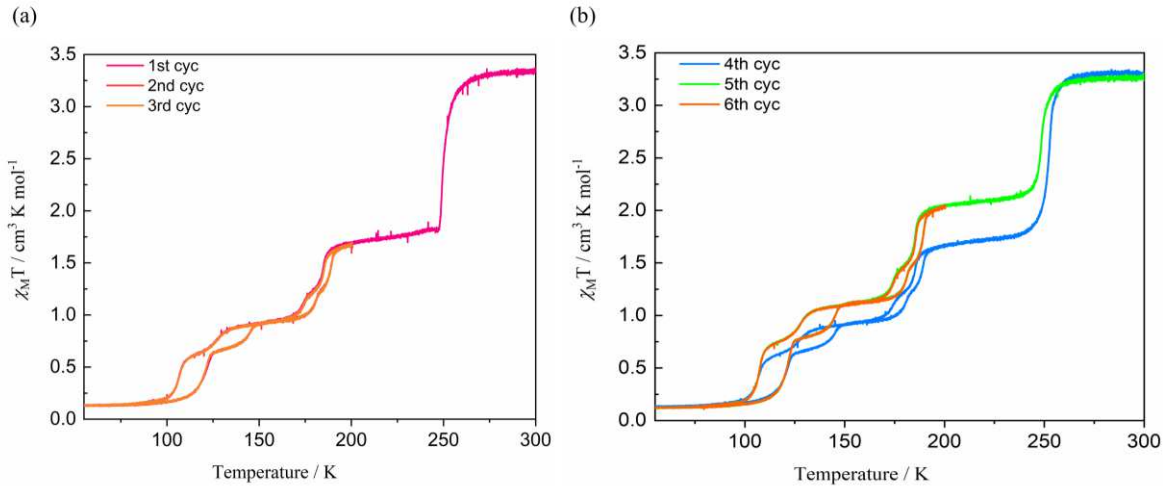

Figure 7.20: Magnetic susceptibility measurements of **[Tz$_{0.1}$Dz$_{0.9}$]** (a) the first cycle with the temperature range of 300–55–200 K, second cycles and the third with the same temperature range in 200–55–200 K. (b) The fourth cycle in 200–55–300 K, the fifth in 300–55–200 K and the sixth in 200–55–200 K.

The degree of phase transition over the ten thermal cycles of both materials was quantified based on the magnetic data. The ratio of conversion from the orthorhombic phase to the partial monoclinic phase as a function of thermal cycles is plotted for each material (Figure 7.21). 44% of the orthorhombic phase was converted to the monoclinic phase in **[Tz$_{0.1}$Dz$_{0.9}$]** in the first cycle and 64% in the second cycle. The conversion becomes gradual after the fifth cycle and approaches 75%. **[Tz$_{0.15}$Dz$_{0.85}$]** has a lower conversion ratio with about 8% of the orthorhombic phase having been transformed and reaching 33% in the last cycle. This tendency of phase transition measured by magnetism is consistent with PXRD data. However, the conversions to the monoclinic phase based on the magnetism data after ten cycles are higher than the PXRD results likely due to different cooling rates and instrument settings.

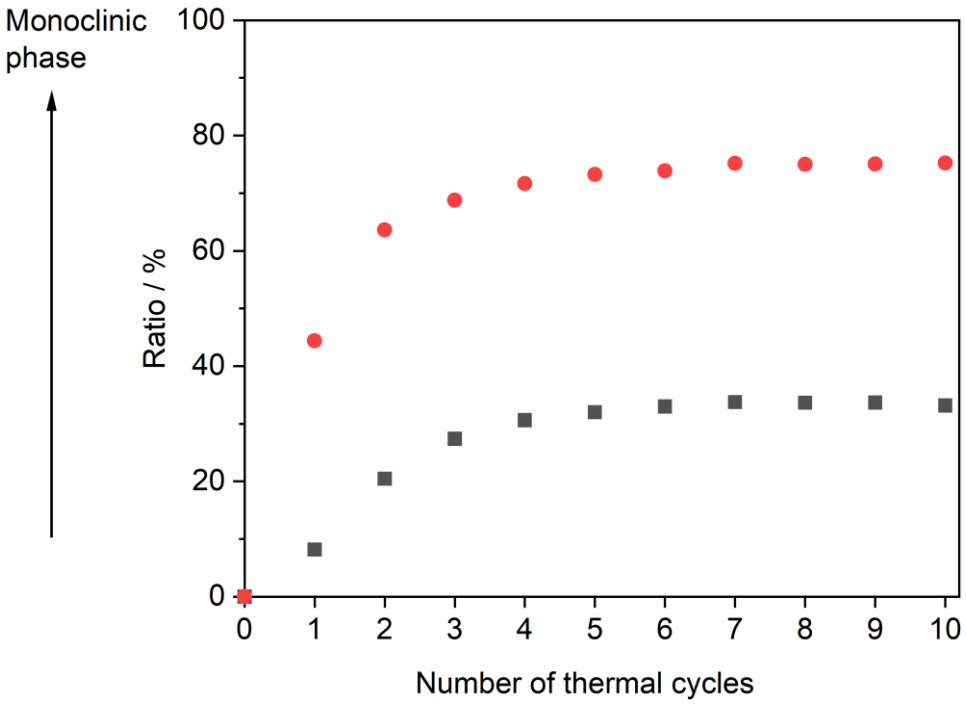

Figure 7.21: Comparison of **[$Tz_{0.1}Dz_{0.9}$]** (red) and **[$Tz_{0.15}Dz_{0.85}$]** (black) for the ratio of the monoclinic phase versus the number of thermal cycles.

Both materials cannot be fully converted from the orthorhombic to the monoclinic phase. Compared to the percentage conversion of **[$Tz_{0.1}Dz_{0.9}$]**, **[$Tz_{0.15}Dz_{0.85}$]** converts at a slower rate per cycle, and to a smaller extent. With a greater percentage of Tz ligand, the structural conversion is more gradual with a lower ratio. The reason for the differences between these materials and incomplete phase transition relies on the host–host interactions, that the hydrogen bonding restricts the ligand rotation to form a lower energy phase. Therefore, phase interconversion can be achieved by controlling the intramolecular interactions.

7.5 Conclusions and Future Work

In the first section (Section 7.2), a series of bulk powder frameworks with mixed Tz and Dz ligands $[Fe(Tz)_x(Dz)_{1-x}(Au(CN)_2)_2]\cdot n$EtOH ($x$ = 1.0–0.2) was synthesised. This study has discovered an unprecedented coupling effect and control between mechanical motion and electronic transition *via* precisely tuning the ligand component. The general trend is that the transition temperatures decrease with decreasing Tz ligand components owing to non-uniform host–host interactions, resulting from the random ordering of the Tz and Dz ligands in the framework lattice. In particular, the single crystal structure of **[$Tz_{0.5}Dz_{0.5}$]** revealed a random arrangement of Tz and Dz ligands, which influences the

disorder of C–H···N host–host interactions between adjacent ligands. Although the structure of each framework barely changed, different ligand components in the framework, which alter the ligand field strength and number of C–H···N interactions, causes not only the various behaviour of spin crossover but also remarkable colossal thermal expansion motion. The scissor motion was observed with the *a*-axis showing negative thermal expansion while the *b*-axis showed the opposite behaviour. **[$Tz_{0.2}Dz_{0.8}$]** presents the largest extent of thermal expansion attributed to the fewest host–host interactions hinged on the framework for lattice flexing. This provides a potential method to tackle the problem of thermal frustration and defects in solid devices and paves the way towards designing flexible materials using the solid solution MIXMOF synthetic approach.

The second part of this chapter discussed that the powder sample **DzAu·EtOH** possessing the orthorhombic phase shows a discrepancy from the single crystal structure in the monoclinic phase, which is likely a thermodynamic product. The phase interconversion is achieved *via* manipulating the temperature of **DzAu·EtOH** exhibiting memory in between two phases. To the best of our knowledge, **DzAu·EtOH** presents the ability to memorise and lock in two temperature states, the 'two-way shape memory effect', which is the first example of such behaviour in SCO MOFs. Not only is interconversion between orthorhombic and monoclinic phases exhibited in this flexible material but also both **1-O** and **1-M** can recover after desolvation followed by resolvation. DFT calculation was conducted to reveal the structure of desolvated phase. This shows the framework is stable without solvent and proves the material display a 'breathing-like' motion in desolvation and resolvation processes. The phase transition in this flexible MOF is attributed to the ring rotation altering the host–host interactions upon temperature change. Controlling the structure and understanding the mechanism of the material paves the way for exploring molecular memory devices and molecular rotors. Furthermore, distinct SCO behaviour (single-step and four-step) was observed in the **DzAu·EtOH** due to different synthesised methods presenting seven spin states collectively in one material. The discrepancy of SCO between the solvated and desovlated samples illustrated that the guest can enhance the cooperativity within the framework. The results of structure properties associated with magnetism behaviour provide guidelines for designing smart materials, such as for sensing and information storage.

The last section (Section 7.4) investigated two MIXMOFs **[$Tz_{0.1}Dz_{0.9}$]** and **[$Tz_{0.15}Dz_{0.85}$]**. They both present a gradual phase transition from the orthorhombic phase to the partial monoclinic phase upon thermal cycles. The degree of structural transformation has relied on the host–host interactions. The lower the number of hydrogen bonds, the more likely it is to undergo the ligand rotation to achieve the materials converting to a lower energy state. Also, the recovery of the original phase is achieved *via* heating the material. The thermal stimulus can not only trigger the phase transition, but also the magnetic behaviours. The history-dependent behaviours upon thermal cycles in the magnetism accompanying structural change are the first example observed, which reveals the association with gradual change of two-phase properties. The discovery of these materials elucidates an approach to the

design of flexible MOFs, that is *via* controlling the number of intramolecular interactions and configuration of the materials. This study on progressive change triggered by a thermal stimulus may lead to a way of generating highly sensitive smart materials *via* controlling the balance of flexibility and constraints within the framework.

The mixed ligand strategy can be used to generate other framework materials to fine-tune their properties. A similar ligand HTz (HTz= 3,6-bis(4-pyridyl)-1,4-dihydro-1,2,4,5-tetrazine) was synthesised to generate the framework [Fe(HTz)(Au(CN)$_2$)$_2$]·*n*(EtOH) (**HTzAu·EtOH**) and preliminary data of magnetic susceptibility measurements and PXRD was conducted by the candidate during her PhD (Appendix E.30). The material presents one-step hysteric SCO with lower transition temperature than **TzAu·EtOH** ($T_{1/2}\downarrow\uparrow$ = 226 K, 231 K). PXRD patterns between **HTzAu·EtOH** and **TzAu·EtOH** indicate they are likely to be isoreticular. Based on the mixed ligand strategy, MOFs mixed with HTz and Tz or HTz and Dz ligands could be further synthesised. It would be interesting to investigate MOFs with doping of HTz ligand, as HTz shows non-aromatic and two more hydrogen atoms in the middle ring, therefore possessing different ligand field strength and hydrogen bonding interactions. There is also a reversible redox reaction between the HTz and Tz ligands.[46-49] Interconversion between the two frameworks can be achieved. The systematic study on MOFs with subtle differences would help deeper examine key factors for controlling the properties and reveal relationships between the coupling effect of structure and spin transition.

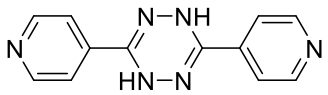

Figure 7.22: Structure of HTz ligand (HTz= 3,6-bis(4-pyridyl)-1,4-dihydro-1,2,4,5-tetrazine).

Future works on mixed Tz and Dz ligand frameworks could involve removing guest molecules to analyse SCO behaviour and the extent of the scissor motion. As in the desolvated structure no host–guest interactions exist, and the flexibility of the framework and cooperativity between SCO sites may change. Further research can also involve guest effects in the mixed ligand MOFs. MOFs with the absorption of other small liquid or gas guests such as methanol, acetonitrile, CO_2 and N_2 could present distinct host–guest interactions SCO behaviours and lattice motions. Therefore, more knowledge of the intrinsic relationship between the switchable spin transition and structural properties provides a guideline for desirable material with controllable functionalities.

7.6 References

1. Dhakshinamoorthy, A.; Asiri, A. M.; Garcia, H., *Catal. Sci. Technol.* **2016,** *6* (14), 5238-5261.

2. Qin, J.-S.; Yuan, S.; Wang, Q.; Alsalme, A.; Zhou, H.-C., *J. Mater. Chem. A.* **2017,** *5* (9), 4280-4291.

3. Su, J.; Yuan, S.; Wang, H.-Y.; Huang, L.; Ge, J.-Y.; Joseph, E.; Qin, J.; Cagin, T.; Zuo, J.-L.; Zhou, H.-C., *Nat. Commun.* **2017,** *8* (1).

4. Cedeno, R. M.; Cedeno, R.; Gapol, M. A.; Lerdwiriyanupap, T.; Impeng, S.; Flood, A.; Bureekaew, S., *Inorg. Chem.* **2021,** *60* (12), 8908-8916.

5. Ohtani, R.; Yoneda, K.; Furukawa, S.; Horike, N.; Kitagawa, S.; Gaspar, A. B.; Muñoz, M. C.; Real, J. A.; Ohba, M., *J. Am. Chem. Soc.* **2011,** *133* (22), 8600-8605.

6. Halder, G. J.; Kepert, C. J.; Moubaraki, B.; Murray, K. S.; Cashion, J. D., *Science* **2002,** *298*, 1762-1765.

7. Neville, S. M.; Halder, G. J.; Chapman, K. W.; Duriska, M. B.; Moubaraki, B.; Murray, K. S.; Kepert, C. J., *J. Am. Chem. Soc.* **2009,** *131* (34), 12106-12108.

8. Yoshida, K.; Akahoshi, D.; Kawasaki, T.; Saito, T.; Kitazawa, T., *Polyhedron* **2013,** *66*, 252-256.

9. Southon, P. D.; Liu, L.; Fellows, E. A.; Price, D. J.; Halder, G. J.; Chapman, K. W.; Moubaraki, B.; Murray, K. S.; Létard, J.-F.; Kepert, C. J., *J. Am. Chem. Soc.* **2009,** *131* (31), 10998-11009.

10. Roubeau, O., *Chemistry* **2012,** *18* (48), 15230-44.

11. Kahn, O.; Martinez, C. J., *Science* **1998,** *279*, 44-48.

12. Lavrenova, L. G.; Shakirova, O. G., *Eur. J. Inorg. Chem* **2013,** *2013* (5-6), 670-682.

13. Calvo Galve, N.; Coronado, E.; Gimenez-Marques, M.; Minguez Espallargas, G., *Inorg. Chem.* **2014,** *53* (9), 4482-90.

14. Clements, J. E.; Price, J. R.; Neville, S. M.; Kepert, C. J., *Angew. Chem. Int. Ed.* **2014,** *53* (38), 10164-8.

15. Clements, J. E.; Price, J. R.; Neville, S. M.; Kepert, C. J., *Angew. Chem. Int. Ed.* **2016,** *55* (48), 15105-15109.

16. Xie, Z. The University of Sydney, **2018**.

17. Mullaney, B. R.; Goux-Capes, L.; Price, D. J.; Chastanet, G.; Letard, J. F.; Kepert, C. J., *Nat. Commun.* **2017,** *8* (1), 1053.

18. Goodwin, A. L.; Calleja, M.; Conterio, M. J.; Dove, M. T.; Evans, J. S. O.; Keen, D. A.; Peters, L.; Tucker, M. G., *Science* **2008,** *319*, 794-797.

19. Schneemann, A.; Bon, V.; Schwedler, I.; Senkovska, I.; Kaskel, S.; Fischer, R. A., *Chem. Soc. Rev.* **2014,** *43* (16), 6062-96.

20. Chang, Z.; Yang, D.-H.; Xu, J.; Hu, T.-L.; Bu, X.-H., *Adv. Mater.* **2015,** *27* (36), 5432-5441.

21. Aljammal, N.; Jabbour, C.; Chaemchuen, S.; Juzsakova, T.; Verpoort, F., *Catalysts* **2019,** *9* (6), 512.

22. Shivanna, M.; Yang, Q.-Y.; Bajpai, A.; Sen, S.; Hosono, N.; Kusaka, S.; Pham, T.; Forrest, K. A.; Space, B.; Kitagawa, S.; Zaworotko, M. J., *Sci. Adv.* **2018,** *4* (4), eaaq1636.

23. Alhamami, M.; Doan, H.; Cheng, C.-H., *Materials* **2014,** *7* (4), 3198-3250.

24. Dybtsev, D. N.; Chun, H.; Kim, K., *Angew. Chem. Int. Ed.* **2004,** *43* (38), 5033-5036.

25. Allendorf, M. D.; Stavila, V., *CrystEngComm* **2015,** *17* (2), 229-246.

26. Liu, Y.; Her, J.-H.; Dailly, A.; Ramirez-Cuesta, A. J.; Neumann, D. A.; Brown, C. M., *J. Am. Chem. Soc.* **2008,** *130* (35), 11813-11818.

27. Chen, L.; Mowat, J. P. S.; Fairen-Jimenez, D.; Morrison, C. A.; Thompson, S. P.; Wright, P. A.; Düren, T., *J. Am. Chem. Soc.* **2013,** *135* (42), 15763-15773.

28. Otsuka, K.; Wayman, C. M., *Shape Memory Materials*. Cambridge University Press: 1999.

29. Behl, M.; Lendlein, A., *Mater. Today* **2007,** *10* (4), 20-28.

30. Schmidt, A. M., *Macromol. Rapid Commun.* **2006,** *27* (14), 1168-1172.

31. Huang, W.; Toh, W., *J. Mater. Sci. Lett.* **2000,** *19* (17), 1549-1550.

32. Halcrow, M. A., *Chem. Soc. Rev.* **2011,** *40* (7), 4119-42.

33. Kahn, O.; Martinez, C. J., *Science* **1998,** *279* (5347), 44-48.

34. Garcia, Y.; Niel, V.; Muñoz, M. C.; Real, J. A., Spin Crossover in 1D, 2D and 3D Polymeric Fe(II) Networks. In *Top. Curr. Chem.*, Springer Berlin Heidelberg: 2004; pp 229-257.

35. Krober, J.; Codjovi, E.; Kahn, O.; Groliere, F.; Jay, C., *J. Am. Chem. Soc.* **1993,** *115* (21), 9810-9811.

36. Ohtani, R.; Yoneda, K.; Furukawa, S.; Horike, N.; Kitagawa, S.; Gaspar, A. B.; Munoz, M. C.; Real, J. A.; Ohba, M., *J. Am. Chem. Soc.* **2011,** *133* (22), 8600-5.

37. Clements, J. E.; Price, J. R.; Neville, S. M.; Kepert, C. J., *Angew. Chem. Int. Ed.* **2016,** *55* (48), 15105-15109.

38. Clements, J. E.; Price, J. R.; Neville, S. M.; Kepert, C. J., *Angew. Chem. Int. Ed.* **2014,** *53* (38), 10164-10168.

39. Toby, B. H.; Von Dreele, R. B., *J. Appl. Crystallogr.* **2013,** *46* (2), 544-549.

40. Henke, S.; Schneemann, A.; Wütscher, A.; Fischer, R. A., *J. Am. Chem. Soc.* **2012,** *134* (22), 9464-9474.

41. Coudert, F.-X.; Boutin, A.; Jeffroy, M.; Mellot-Draznieks, C.; Fuchs, A. H., *ChemPhysChem* **2011,** *12* (2), 247-258.

42. Liu, X. L.; Fan, W. W.; Lu, Z. X.; Qin, Y.; Yang, S. X.; Li, Y.; Liu, Y. X.; Zheng, L. Y.; Cao, Q. E., *Eur. J. Chem.* **2019,** *25* (22), 5787-5792.

43. Seo, J.; Matsuda, R.; Sakamoto, H.; Bonneau, C.; Kitagawa, S., *J. Am. Chem. Soc.* **2009,** *131* (35), 12792-12800.

44. Runčevski, T.; Brown, C. M., *Cryst. Growth Des.* **2021,** *21* (9), 4821-4822.

45. Li, Z.-Y.; Dai, J.-W.; Shiota, Y.; Yoshizawa, K.; Kanegawa, S.; Sato, O., *Eur. J. Chem.* **2013,** *19* (39), 12948-12952.

46. Razavi, S. A. A.; Masoomi, M. Y.; Morsali, A., *Eur. J. Chem.* **2017,** *23* (51), 12559-12564.

47. Razavi, S. A. A.; Masoomi, M. Y.; Islamoglu, T.; Morsali, A.; Xu, Y.; Hupp, J. T.; Farha, O. K.; Wang, J.; Junk, P. C., *Inorg. Chem.* **2017,** *56* (5), 2581-2588.

48. Razavi, S. A. A.; Morsali, A., *Inorg. Chem.* **2019,** *58* (21), 14429-14439.

49. Razavi, S. A. A.; Masoomi, M. Y.; Morsali, A., *Inorg. Chem.* **2018,** *57* (18), 11578-11587.

Chapter 8

Final Conclusions and Outlook

8.1 Final Conclusions

The design and engineering of intelligent SR-MOF materials that can respond dynamically to external stimuli have generated tremendous interest owing to the promising applications of these materials in various fields. Understanding the cooperative effects in these materials under different stimuli is therefore of paramount importance, which will thus aid in the future development of these functional materials. However, research into these 'smart' materials is still in its early stage. Therefore, creating SR-MOFs and uncovering their mechanisms and properties provides the conceptual and technical foundation for future worth.

The structural and SCO behaviours in Tz-based 3D Hofmann-like framework materials with adsorption of single- and binary-components of xylene isomers as guest molecules in the pores were investigated in Chapter 3. The different extent of guest influence on structural distortions and scissor motions are compared among each member of the series of framework materials. Although the physical properties of the xylenes are similar, the SCO behaviours are distinct. Asymmetric multi-step SCO behaviours were observed in each framework. **TzAu·OX** displays asymmetric one/two-step SCO, and **TzAu·MX** is the first material, to the best of our knowledge, that displays asymmetric four/five-step SCO behaviour. **TzAu·PX** shows a change in SCO behaviours between thermal cyclings. In the first thermal cycle, the SCO behaviour of **TzAu·PX** is one of one/three-step with a notably wide hysteresis at 62 K, while the second thermal cycle is two/three-step with a much narrower hysteresis at 17 K. The different SCO behaviours between thermal cycles are likely due to structural transitions. Host–host and host–guest aromatic interactions influencing SCO cooperativity have also been studied. The investigation of the uptake of binary-component xylene mixtures in the materials illustrates that even subtle differences in the guests can enable different SCO profiles, which clearly demonstrates the sensitivity of the materials.

The Dz-based SR-MOFs with adsorption of xylenes display what effect the guests have on the structures and their corresponding SCO behaviours (Chapter 4). Weak cooperativity has been observed in the Dz-based MOFs, which exhibit either incomplete SCO or no SCO. **DzAu·OX**, **DzAu·MX**, and **DzAu·PX** show no SCO, gradual incomplete one-step SCO, and incomplete two-step SCO, respectively. Both **DzAu·OX** and **DzAu·MX** adopt the same space group (*I*2/*a*) and contain one Fe(II) site in their respective asymmetric units. However, **DzAu·PX** adopts the space group ($P2_1/c$) and contains a structure with two distinct Fe(II) sites in the asymmetric unit. One of the Fe(II) sites remains in the HS state, while another undergoes a spin transition by lowering the temperature, therefore resulting in incomplete SCO. Comparisons were made of the properties between Dz-based and Tz-based MOFs. Unlike **TzAu·OX** and **TzAu·PX**, which adopted orthorhombic phases, **DzAu·OX**, **DzAu·PX**, and **DzAu·MX** were all solved as monoclinic structures. The Hofmann grids in the Dz-based systems are staggered and more rectangular, while the Tz-based systems are overlayed and

rhombic in shape. Chapters 3 and 4 examined the C–H···N, Au···Au interactions, and aromatic interactions between the ligands and xylenes. This comparison revealed the influence of host–host and host–guest interactions on lattice flexing and SCO behaviours. The selectivity towards encapsulation of xylene isomers in the materials was also demonstrated by showing that the Dz-based framework materials are promising candidates for distinguishing binary mixtures of xylene isomers.

Chapter 5 investigates the importance of metallophilic interactions on the structural and magnetic properties. This chapter illustrates the modulation of structural topology and SCO behaviours in Tz- and Dz-based MOFs via tuning of the component cyanidometallate linkers. Tz-based MOFs (**TzAu·EtOH**, **$TzAu_{0.5}Ag_{0.5}$·EtOH**, and **TzAg·EtOH**) adopt orthorhombic structures while Dz-based MOFs (**DzAg·EtOH**, **$DzAu_{0.5}Ag_{0.5}$·EtOH**, and **DzAu·EtOH**) adopt monoclinic structures. By varying the ratio of cyanidometallate linkers in the Tz-based materials, different extents of anomalous lattice motions (NTE) were observed. **TzAu·EtOH** exhibits the greatest degree of scissor motion among the three materials. All of the Tz-based materials exhibit one-step SCO with minimal differences in their respective spin transition temperatures. Contrastingly, different structural properties and SCO behaviours are present in the Dz-based materials. No scissor motion was observed in the Dz-based frameworks due to their closed rectangular Hofmann grids. **DzAu·EtOH** exhibits four-step SCO while **DzAg·EtOH**, **$DzAu_{0.5}Ag_{0.5}$·EtOH**, and **$DzAu_{0.7}Ag_{0.3}$·EtOH** all exhibit three-step SCO. With increasing $[Ag(CN)_2]^-$ components in both Tz- and Dz-based frameworks, the spin transition temperatures are observed to increase. The differences in structures and SCO behaviours of these materials are associated with the different magnitude intra- and intermolecular interactions and ligand field strengths. The composition and distribution of cyanidometallate linkers within the frameworks were characterised by various techniques, which indicate homogeneous mixing of the cyanidometallate linkers. Unlike the Dz-based frameworks that were coordinated with dicyanidoaurate(I) or dicyanidoargenate(I) linkers and adopted 3D Hofmann-like topologies, both the **DzPt** and **DzPd** frameworks adopt a 3D structure containing two water molecules binding at the Fe(II) sites. These Fe(II) sites remain in their HS states and are SCO-inactive.

The effect of pressure-induced SCO on **TzAu·EtOH**, **[$Tz_{0.5}Dz_{0.5}$]**, and **DzAu·EtOH** was demonstrated in Chapter 6. The rare feature of stabilisation of the HS state with increased pressure was analysed among these materials. The scissor motions were observed to be caused by pressure with one axis in NLC and another in PLC in **TzAu·EtOH** and **[$Tz_{0.5}Dz_{0.5}$]**. This chapter investigates the antagonism between SCO and the application of pressure. The SCO sites undergo a pressure-induced distortion that causes lattice flexing in the Hofmann grids. Thus, there is a relationship between the SCO behaviours and structures of these systems under applied pressure.

The precise tuning of SCO behaviours and the extent of scissor motions by tuning the ratio of Tz and Dz ligands was demonstrated in Chapter 7. Hydrogen bonding interactions that occur between the

pillaring ligands are a key factor towards influencing the resulting spin transition temperatures and thermal expansion coefficients. The largest NTE and PTE values were observed in **[$Tz_{0.2}Dz_{0.8}$]**, which has the fewest hydrogen bonding motifs among the $[Fe(Tz)_x(Dz)_{1-x}(Au(CN)_2)_2]\cdot n$EtOH ($x$ = 1.0–0.2) series, resulting in the most flexible lattice. A shape memory effect was discovered in **DzAu·EtOH**, which is a phase interconversion via temperature control. The desolvated phase was also examined with a structural interconversion being shown between the desolvated and solvated phases. The gradual phase transitions and multi-step SCO behaviours upon thermal cycling were investigated in **[$Tz_{0.1}Dz_{0.9}$]** and **[$Tz_{0.15}Dz_{0.85}$]**. The results of which illustrate an association between the host–host interactions and framework flexibility. The relationship between the structural and spin transition induced by temperature in this series of MIXMOFs was uncovered.

Overall, this thesis explores the design and analysis of SR-MOFs incorporated with Tz or Dz ligands and investigates their structural and magnetic properties in response to physical (temperature and pressure) and chemical (guest molecules) stimuli. The SCO behaviours in the 3D Hofmann-like materials can be controlled by varying the pillaring ligands, cyanidometallate linkers, and adsorbed guest molecules. Anomalous NTE and NLC were discovered in the rhombic Hofmann grids due to a scissor motion mechanism. Such anomalous behaviours can be finely tuned by modulating the compositions of the materials by ligand doping. The demonstration of the structure–property relationships in this work thus paves the way towards the intelligent design of emergent 'smart' SR-MOFs.

8.2 Future Directions

There is still significant work to be done on understanding and tuning the properties of new 'smart' materials. This thesis discusses the temperature, pressure, and guest-induced SCO in Tz- and Dz-based framework materials. However, the light-induced SCO behaviours of these series of materials remain unknown. It would be interesting to investigate the spin state transitions and structural distortions that may take place in response to photoirradiation. LIESST and reverse-LIESST phenomena may be shown in these materials, which could help to tune their structural and magnetic properties.

Distinct SCO behaviours were shown in the Tz- and Dz-based frameworks upon encapsulation of the liquid xylene isomers. Future work could focus on investigating the structural properties, spin transition behaviours, and selectivity associated with the uptake of gas-phase xylenes. The uptake of gas molecules generates different internal pressure effects, which may result in exotic behaviours in the structure and spin state energetics. Guest molecules in the pores generate perturbations to the frameworks thereby influencing the host–guest interactions. The structure–property relationships of other gas molecules such as CO_2, N_2, and H_2 would also be interesting to explore. The investigation of

the adsorption of single and multi-components of gas molecules may reveal that subtle differences in guests result in different exploitable performances. A deeper understanding of the host–guest relationship would be applied to sensing.

This thesis demonstrates that hydrogen bonding interactions can influence the extent of lattice flexing and spin state perturbations. Further work could involve the use of analogous ligands such as 1,4-di(pyridine-4-yl) benzene and 2,5-bis(pyrid-4-yl) pyridine (Figure 8.1) as pillaring ligands Hofmann-like frameworks, which could allow further exploration of the influences of hydrogen bonding interactions. It would also be interesting to further investigate the energy cost associated with scissor motions and spin transitions, which may help to understand the intrinsic energy effect. The energy calculation may be instructional in the design of materials displaying a desirable degree of structural flexibility and SCO achieved by controlling the magnitude of hydrogen bonding interactions.

(a) (b)

1,4-di(pyridine-4-yl) benzene 2,5-bis(pyrid-4-yl) pyridine

Figure 8.1: Structure drawing of (a) 1,4-di(pyridine-4-yl) benzene and (b) 2,5-bis(pyrid-4-yl) pyridine.

The MIXMOFs in this thesis display a homogeneous mixing of pillaring ligands and cyanidometallate linkers. Exploring materials with inhomogeneous mixing of ligands such as core-shell structural materials would be interesting. The response to external stimuli in inhomogeneous materials could be different from the homogenous one. It would be worth further studying whether the inhomogeneously mixed materials display individual properties between the core and shell or a synergic effect with an averaged set of properties. The structural flexibility may be different between the materials with relatively rigid cores with flexible shells, or flexible cores with rigid shells. The propagation of spin states of SCO sites between the core and shell would be interesting to study. The change in the thickness of the core and shell may also change the structural and magnetic properties, which could provide more methods to create tunable SR-MOFs.

This thesis demonstrates the structure–property relationships in Tz- and Dz-based SR-MOFs. The understanding of these materials provides guidelines for the rational designing of more promising materials that may in principle promote the development of new nanotechnologies.

Appendix A

Supplementary Information for Chapter 3

Table A.1: Crystallographic data for **TzAu·OX** at 100 K and 300 K.

Parameter	**TzAu·OX (100 K)**	**TzAu·OX (300 K)**
Identification code	cjk20_s2008_sn600_01_100_00	cjk20_s2008_sn600_10_300_00
Empirical formula	$C_{28}H_{23}Au_2FeN_{10}$	$C_{24}H_{14}Au_2FeN_{10}$
Formula weight/gmol^{-1}	949.35	892.23
Temperature/K	100(1)	300(1)
Crystal system	Orthorhombic	Orthorhombic
Space group	*Ibam*	*Ibam*
a/Å	30.0359(13)	30.8007(14)
b/Å	15.8630(6)	16.8767(7)
c/Å	12.4305(5)	12.2366(6)
α/°	90	90
β/°	90	90
γ/°	90	90
Volume/Å^3	5922.6(4)	6360.8(5)
Z	8	8
ρ_{calc} /gcm^{-3}	2.129	1.863
μ/mm^{-1}	10.404	9.681
F(000)	3560.0	3296.0
Crystal size/mm^3	0.128 × 0.102 × 0.068	0.128 × 0.102 × 0.068
Radiation	Mo K_α (λ = 0.71073 Å)	Mo K_α (λ = 0.71073 Å)
2Θ range for data collection/°	4.812 to 58.644	4.644 to 58.76
Index ranges	$-22 \leq h \leq 38$, $-20 \leq k \leq 21$, $-15 \leq l \leq 16$	$-22 \leq h \leq 39$, $-23 \leq k \leq 22$, $-16 \leq l \leq 15$
Reflections collected	10417	11228
Independent reflections	3684 [R_{int} = 0.0293, R_{sigma} = 0.0405]	3986 [R_{int} = 0.0405, R_{sigma} = 0.0573]
Data/restraints/parameters	3684/107/188	3986/133/186
Goodness-of-fit on F^2	1.131	1.013
Final R indexes [I≥2σ (I)]	R_1 = 0.0363, wR_2 = 0.0641	R_1 = 0.0464, wR_2 = 0.0979
Final R indexes [all data]	R_1 = 0.0604, wR_2 = 0.0715	R_1 = 0.1054, wR_2 = 0.1201
Largest diff. peak/hole / e Å^{-3}	1.25/-1.23	0.75/-1.19

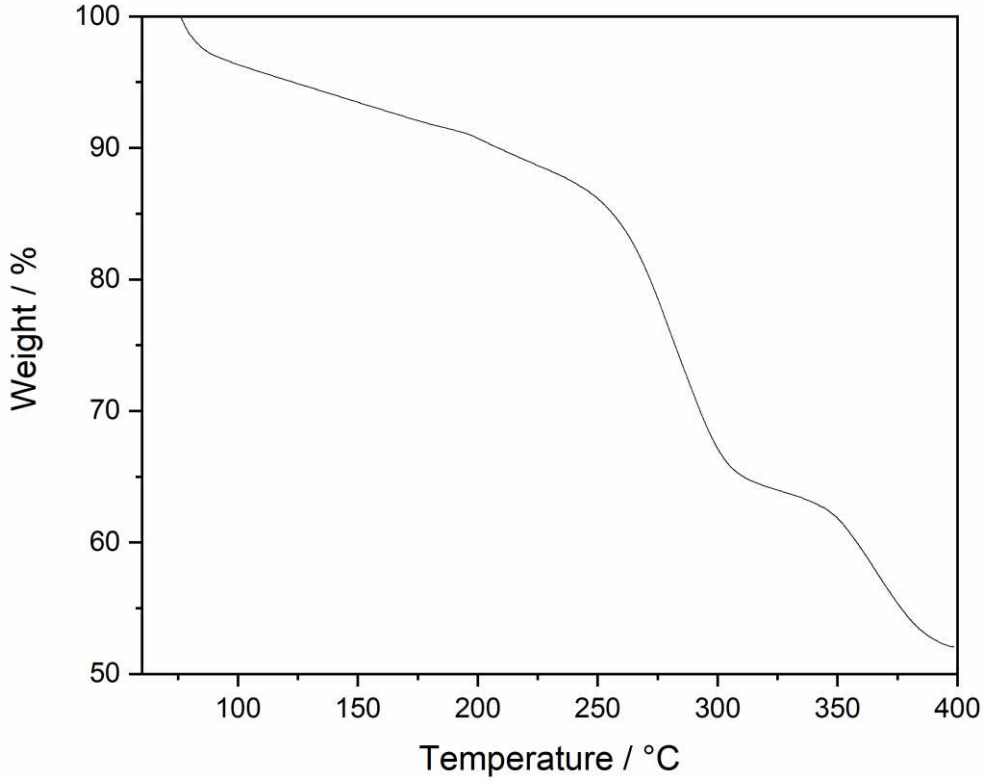

Figure A.1: TGA of the **TzAu·OX** framework over a temperature range of 75–400 °C. The OX solvent loss within the pore is *ca*. 1.5 molecules per formula unit.

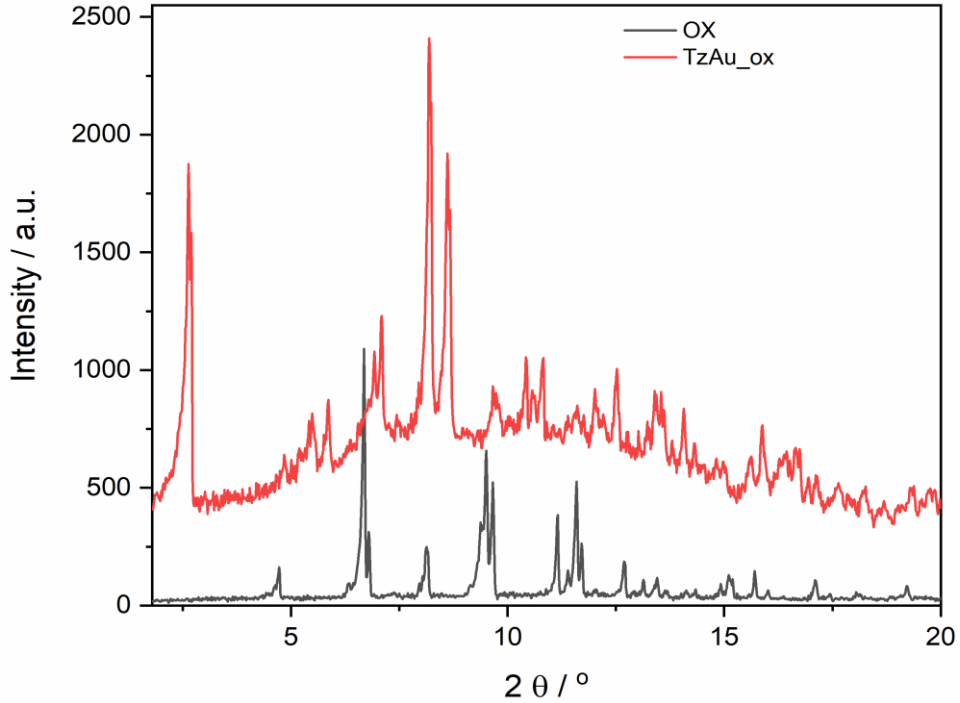

Figure A.2: Room temperature PXRD pattern (Mo-K_α radiation source, λ = 0.71073 Å) of **TzAu·OX** (red) and OX solvent (black).

Table A.2: Crystallographic data for **TzAu·PX** at 100 K and 310 K.

Parameter	TzAu·PX (100 K)	TzAu·PX (310 K)
Identification code	FeTz_px_a	cjk21_s2382_sn904_1_310_00
Empirical formula	$C_{24}H_{18}Au_2FeN_{10}$	$C_{16}H_8Au_2FeN_{10}$
Formula weight/gmol^{-1}	896.27	790.11
Temperature/K	100(1)	310(1)
Crystal system	Orthorhombic	Orthorhombic
Space group	*Ibam*	*Ibam*
a/Å	16.023(3)	16.9510(5)
b/Å	30.010(6)	30.8069(7)
c/Å	12.192(2)	12.0026(3)
α/°	90	90
β/°	90	90
γ/°	90	90
Volume/Å^3	5862(2)	6267.9(3)
Z	8	8
ρ_{calc}/gcm^{-3}	2.031	1.675
μ/mm^{-1}	10.504	21.056
F(000)	3328.0	2864.0
Crystal size/mm^3	30 × 30 × 30	0.099 × 0.068 × 0.044
Radiation	MoK_α (λ = 0.71073 Å)	Cu K_α (λ = 1.54184 Å)
2Θ range for data collection/°	2.714 to 54.946	5.738 to 144.71
Index ranges	$-20 \le h \le 20$, $-38 \le k \le 38$, $-15 \le l \le 15$	$-20 \le h \le 20$, $-37 \le k \le 34$, $-9 \le l \le 14$
Reflections collected	37196	7791
Independent reflections	3415 [R_{int} = 0.0716, R_{sigma} = 0.0277]	3184 [R_{int} = 0.0294, R_{sigma} = 0.0346]
Data/restraints/parameters	3415/466/204	3184/192/143
Goodness-of-fit on F^2	1.053	1.064
Final R indexes [I>=2σ (I)]	R_1 = 0.0673, wR_2 = 0.1993	R_1 = 0.0531, wR_2 = 0.1660
Final R indexes [all data]	R_1 = 0.0878, wR_2 = 0.2217	R_1 = 0.0658, wR_2 = 0.1783
Largest diff. peak/hole / e Å^{-3}	3.70/-2.51	2.05/-4.57

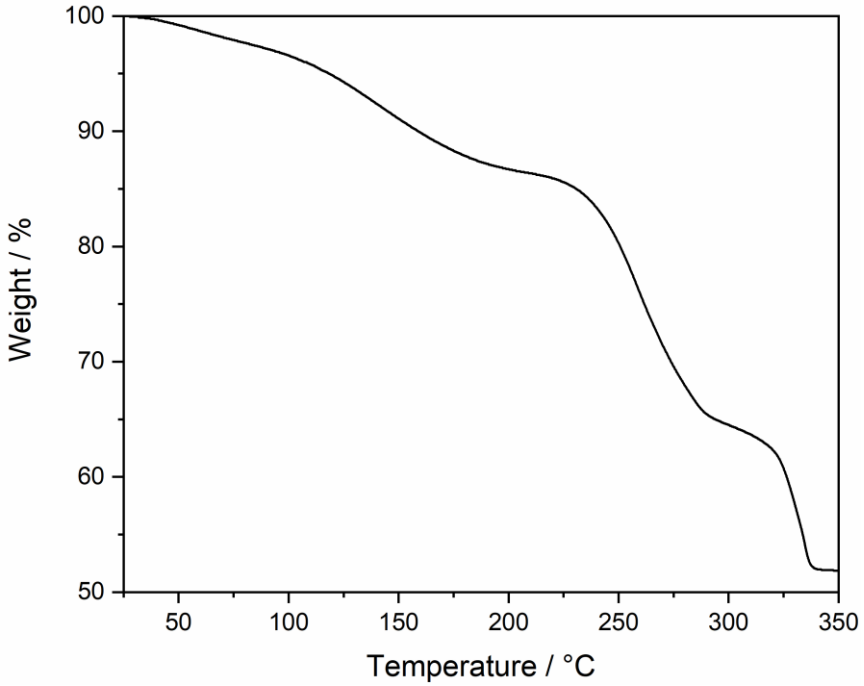

Figure A.3: TGA of the **TzAu·PX** framework over a temperature range of 27–360 °C. The PX solvent loss within the pore is *ca*. 1.2 molecules per formula unit.

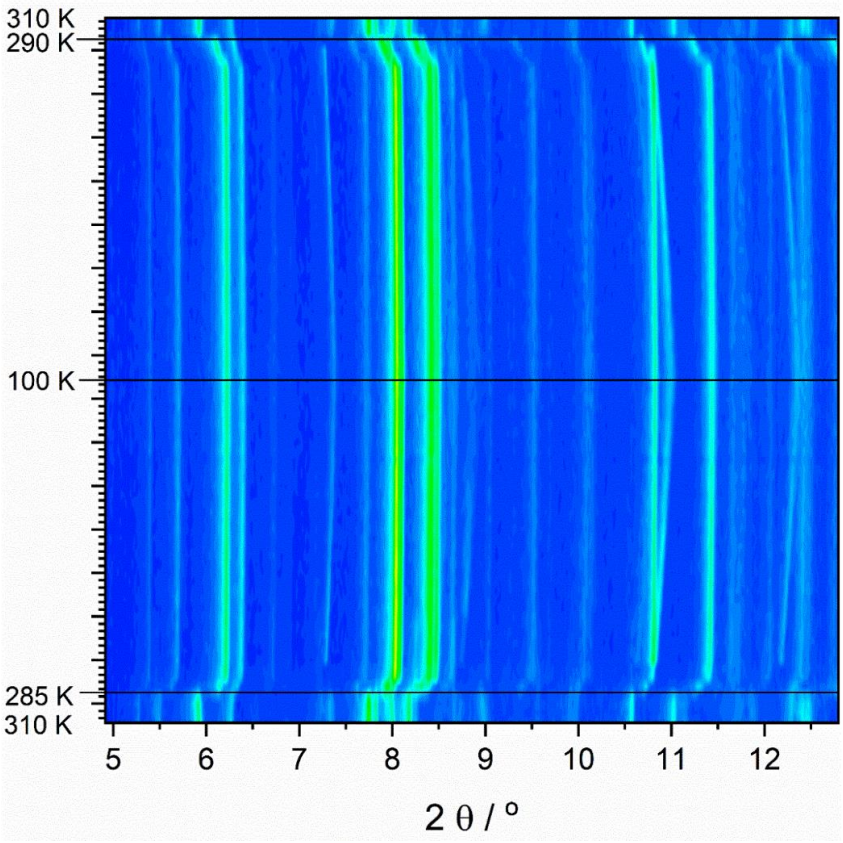

Figure A.4: PXRD peak evolution of **TzAu·PX** as a function of temperature showing the third thermal cycle.

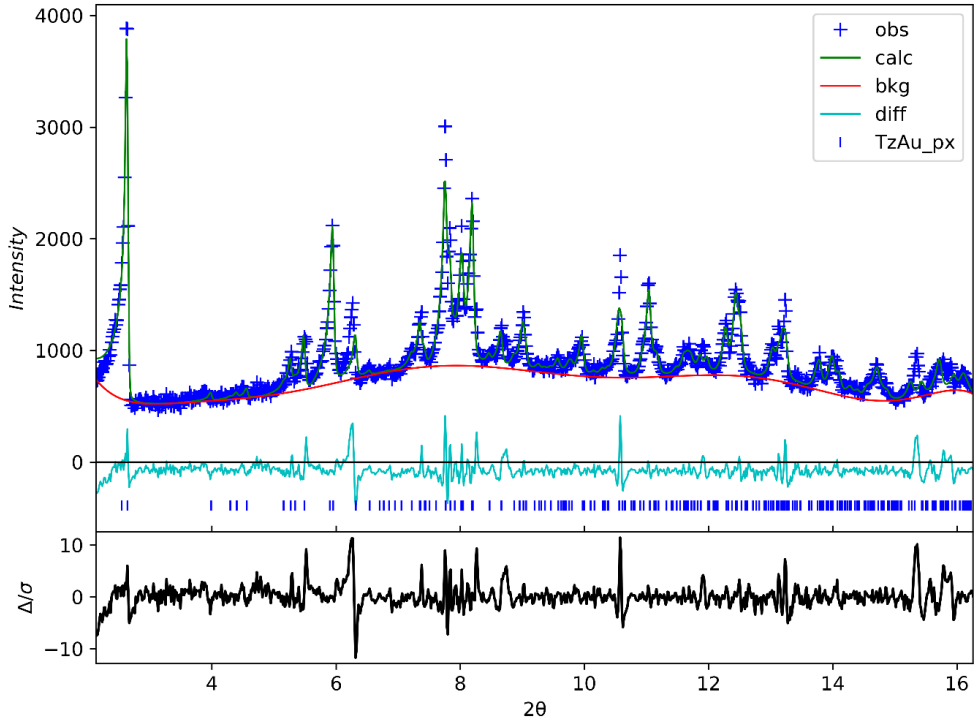

Figure A.5: Pawley refinement of the synchrotron PXRD data of the **TzAu·PX** measured at 310 K after one thermal cycle. The refined space group is in *C*2/*c* with unit cell information in a = 30.44 Å, b = 18.23 Å, c = 12.46 Å and β = 98.35. Experimental pattern (blue), calculated fit (green), background (red), the difference (cyan) and hkl (vertical bar).

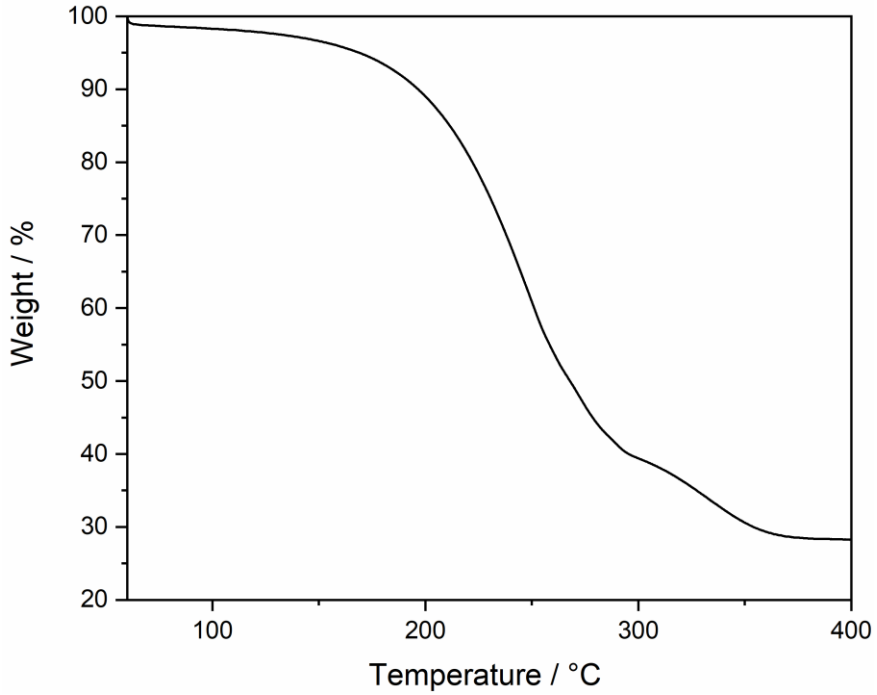

Figure A.6: TGA of the **TzAu·MX** framework over a temperature range of 27–360 °C. The MX solvent loss within the pore is *ca*. 1.1 molecules per formula unit.

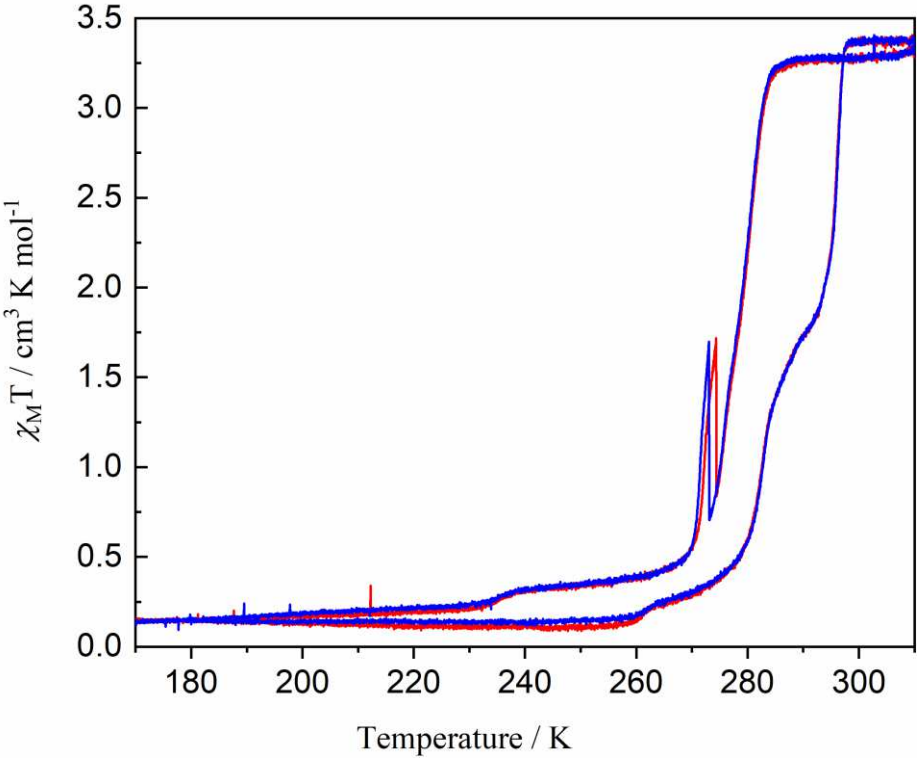

Figure A.7: Variable temperature magnetic susceptibility measurement of **TzAu·PX** at 2 K min^{-1} with the second thermal cycle in red and third thermal cycle in blue.

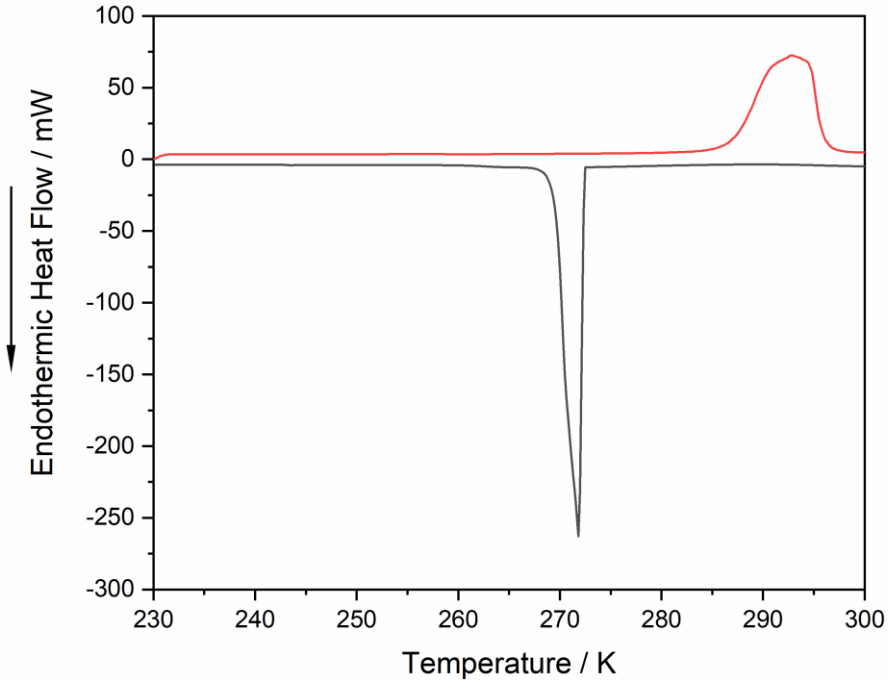

Figure A.8: DSC measurement of **TzAu·PX** at 10 K min^{-1} with cooling process (black) and heating process (red) of a thermal cycle.

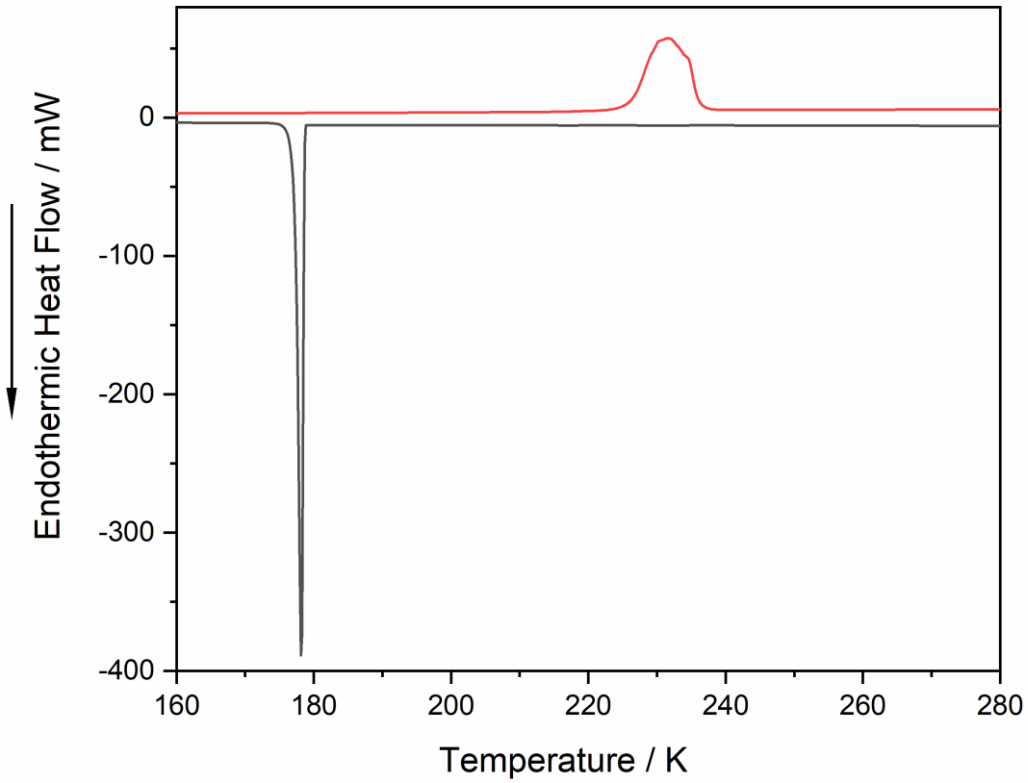

Figure A.9: DSC measurement of **TzAu·MX** at 10 K min^{-1} with cooling process (black) and heating process (red) of a thermal cycle.

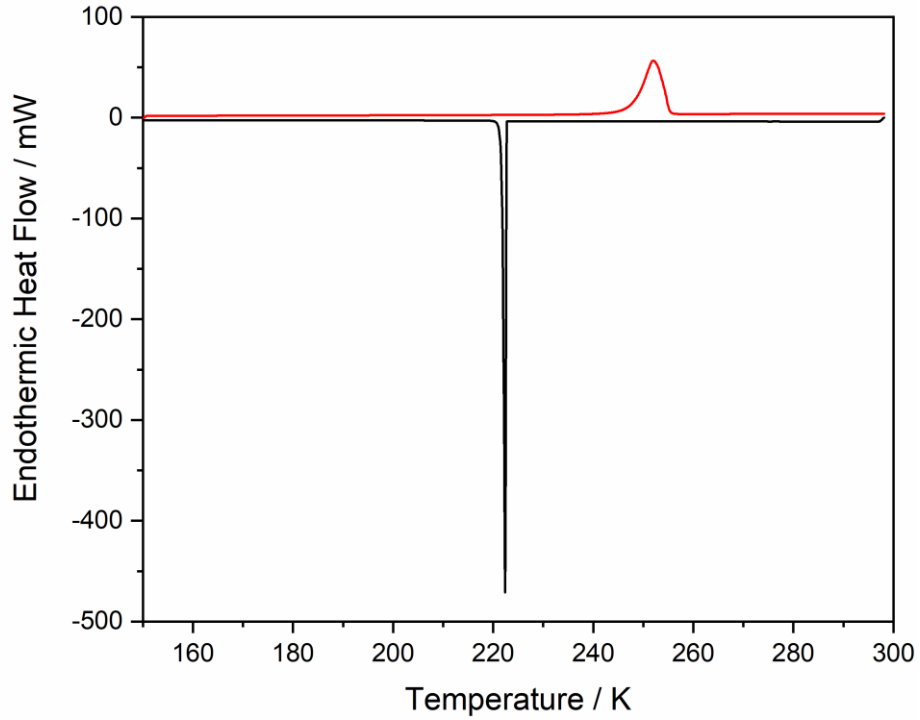

Figure A.10: DSC measurement of **TzAu·OX** at 10 K min^{-1} with cooling process (black) and heating process (red) of a thermal cycle

Appendix B

Supplementary Information for Chapter 4

Table B.1: Crystallographic data for **DzAu·OX** at 100 K and 230 K.

Parameter	**DzAu·OX**	**DzAu·OX**
Identification code	cjk20_s2015_1_100_00	cjk20_s2015_2_230_00
Empirical formula	$C_{34}H_{30}Au_2FeN_8$	$C_{34}H_{30}Au_2FeN_8$
Formula weight/gmol^{-1}	1000.44	1000.44
Temperature/K	100(1)	230(1)
Crystal system	monoclinic	monoclinic
Space group	*I*2/*a*	*I*2/*a*
a/Å	14.4500(5)	14.6606(4)
b/Å	15.2703(5)	15.1224(3)
c/Å	31.0588(8)	31.1302(6)
α/°	90	90
β/°	103.062(3)	101.090(2)
γ/°	90	90
Volume/Å^3	6676.0(4)	6772.8(3)
Z	8	8
ρ_{calc} /gcm^{-3}	1.991	1.962
μ/mm^{-1}	19.923	19.639
F(000)	3792.0	3792.0
Crystal size/mm^3	0.097 × 0.067 × 0.04	0.101 × 0.048 × 0.032
Radiation	Cu K_α (λ = 1.54184 Å)	Cu K_α (λ = 1.54184 Å)
2Θ range for data collection/°	6.484 to 144.548	6.522 to 144.596
Index ranges	$-15 \leq h \leq 17$, $-16 \leq k \leq 18$, $-38 \leq l \leq 30$	$-18 \leq h \leq 16$, $-15 \leq k \leq 18$, $-31 \leq l \leq 38$
Reflections collected	13663	14030
Independent reflections	6424 [R_{int} = 0.0201, R_{sigma} = 0.0239]	6471 [R_{int} = 0.0147, R_{sigma} = 0.0186]
Data/restraints/parameters	6424/96/515	6471/179/490
Goodness-of-fit on F^2	1.084	1.030
Final R indexes [I>=2σ (I)]	R_1 = 0.0288, wR_2 = 0.0781	R_1 = 0.0252, wR_2 = 0.0636
Final R indexes [all data]	R_1 = 0.0360, wR_2 = 0.0834	R_1 = 0.0315, wR_2 = 0.0675
Largest diff. peak/hole / e Å^{-3}	0.99/-1.36	0.82/-0.89

Table B.2: Crystallographic data for **DzAu·MX** at 100 K and 230 K.

Parameter	**DzAu·MX**	**DzAu·MX**
Identification code	cjk20_s2016_1_100_00	cjk20_s2016_2_230_00
Empirical formula	$C_{34}H_{30}Au_2FeN_8$	$C_{34}H_{30}Au_2FeN_8$
Formula weight/gmol^{-1}	1000.44	1000.44
Temperature/K	100(1)	230(1)
Crystal system	monoclinic	monoclinic
Space group	I2/a	I2/a
a/Å	30.7776(8)	31.1211(4)
b/Å	15.0014(4)	14.9604(2)
c/Å	14.3529(3)	14.7889(2)
α/°	90	90
β/°	100.703(3)	100.3124(14)
γ/°	90	90
Volume/Å^3	6511.5(3)	6774.25(17)
Z	8	8
ρ_{calc} /gcm^{-3}	2.041	1.962
μ/mm^{-1}	20.427	19.634
F(000)	3792.0	3792.0
Crystal size/mm^3	0.19 × 0.15 × 0.12	0.193 × 0.148 × 0.121
Radiation	Cu Kα (λ = 1.54184)	Cu Kα (λ = 1.54184)
2Θ range for data collection/°	6.578 to 144.404	6.576 to 144.586
Index ranges	-37 ≤ h ≤ 37, -18 ≤ k ≤ 10, -16 ≤ l ≤ 17	-37 ≤ h ≤ 37, -18 ≤ k ≤ 10, -16 ≤ l ≤ 18
Reflections collected	12855	13508
Independent reflections	6250 [R_{int} = 0.0152, R_{sigma} = 0.0165]	6516 [R_{int} = 0.0165, R_{sigma} = 0.0180]
Data/restraints/parameters	6250/0/421	6516/102/421
Goodness-of-fit on F^2	1.175	1.077
Final R indexes [I>=2σ (I)]	R_1 = 0.0340, wR_2 = 0.0914	R_1 = 0.0295, wR_2 = 0.0836
Final R indexes [all data]	R_1 = 0.0356, wR_2 = 0.0927	R_1 = 0.0307, wR_2 = 0.0846
Largest diff. peak/hole / e Å^{-3}	1.74/-1.84	1.63/-1.39

Table B.3: Crystallographic data for **DzAu·PX** at 100, 155 and 230 K.

Parameter	**DzAu·PX**	**DzAu·PX**	**DzAu·PX**
Identification code	cjk20 s2017_1_2_100_00	cjk20_s2017_3_155_00	cjk20_s2017_1_230_00
Empirical formula	$C_{34}H_{30}Au_2FeN_8$	$C_{34}H_{30}Au_2FeN_8$	$C_{26}H_{18}N_8FeAu$
Formula weight/gmol^{-1}	1000.44	1000.44	695.30
Temperature/K	100(1)	155 (1)	230 (1)
Crystal system	monoclinic	monoclinic	monoclinic
Space group	$P2_1/n$	$P2_1/n$	$P2_1/n$
a/Å	14.1378(9)	14.2684(3)	14.42480(10)
b/Å	15.1132(10)	15.2505(3)	15.35680(10)
c/Å	30.8906(16)	31.0517(5)	31.2390(3)
α/°	90	90	90
β/°	97.599(6)	97.9344(16)	98.1070(10)
γ/°	90	90	90
Volume/Å^3	6542.3(7)	6692.1(2)	6850.87(9)
Z	8	8	8
ρ_{calc}/gcm^{-3}	2.031	1.986	1.348
μ/mm^{-1}	20.330	19.875	11.518
F(000)	3792.0	3792.0	2680.0
Crystal size/mm^3	0.134 × 0.105 × 0.066	0.144 × 0.1 × 0.076	0.144 × 0.1 × 0.076
Radiation	Cu K_α (λ = 1.54184 Å)	Cu K_α (λ = 1.54184 Å)	CuK_α (λ = 1.54184 Å)
2Θ range for data collection/°	5.772 to 133.194	6.47 to 144.782	6.426 to 144.584
Index ranges	-16 ≤ h ≤ 10, -16 ≤ k ≤ 17, -36 ≤ l ≤ 36	-17 ≤ h ≤ 7, -18 ≤ k ≤ 16, -38 ≤ l ≤ 37	-8 ≤ h ≤ 17, -18 ≤ k ≤ 16, -37 ≤ l ≤ 38
Reflections collected	19916	26858	27687
Independent reflections	11268 [R_{int} = 0.0682, R_{sigma} = 0.1053]	12901 [R_{int} = 0.0267, R_{sigma} = 0.0337]	13208 [R_{int} = 0.0225, R_{sigma} = 0.0300]
Data/restraints/parameters	11268/678/819	12901/0/819	13208/0/819
Goodness-of-fit on F^2	1.072	1.034	1.061
Final R indexes [I>=2σ (I)]	R_1 = 0.0962, wR_2 = 0.2377	R_1 = 0.0319, wR_2 = 0.0774	R_1 = 0.0308, wR_2 = 0.0734
Final R indexes [all data]	R_1 = 0.1382, wR_2 = 0.2653	R_1 = 0.0393, wR_2 = 0.0817	R_1 = 0.0407, wR_2 = 0.0784
Largest diff. peak/hole / e Å^{-3}	3.72/-2.74	1.42/-1.38	1.31/-1.27

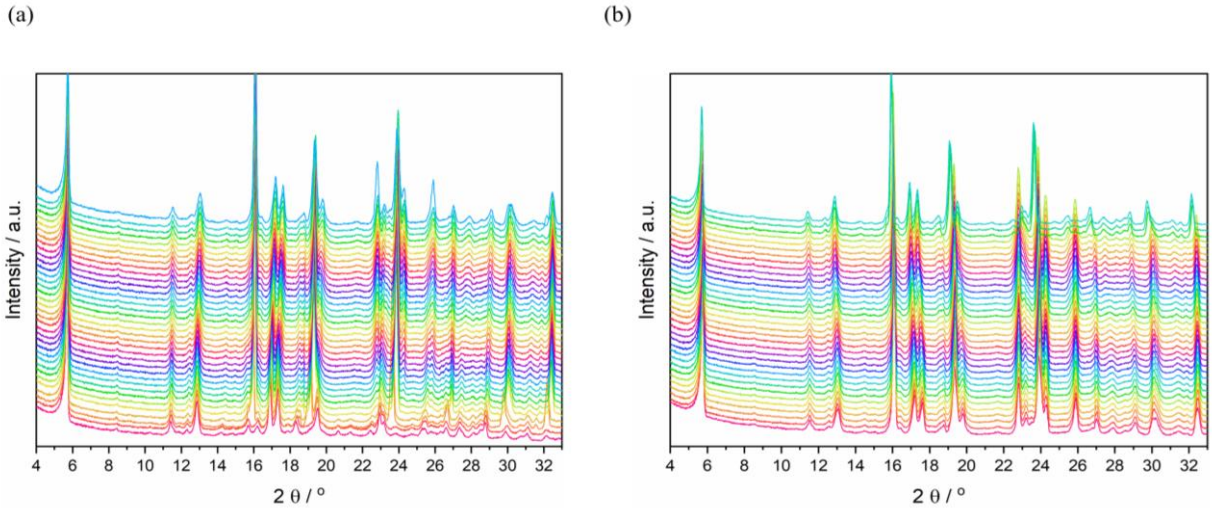

Figure B.1: VT-PXRD of **DzAu·PX** over the temperature range of 300–100–300 K for (a) cooling process and (b) heating processes.

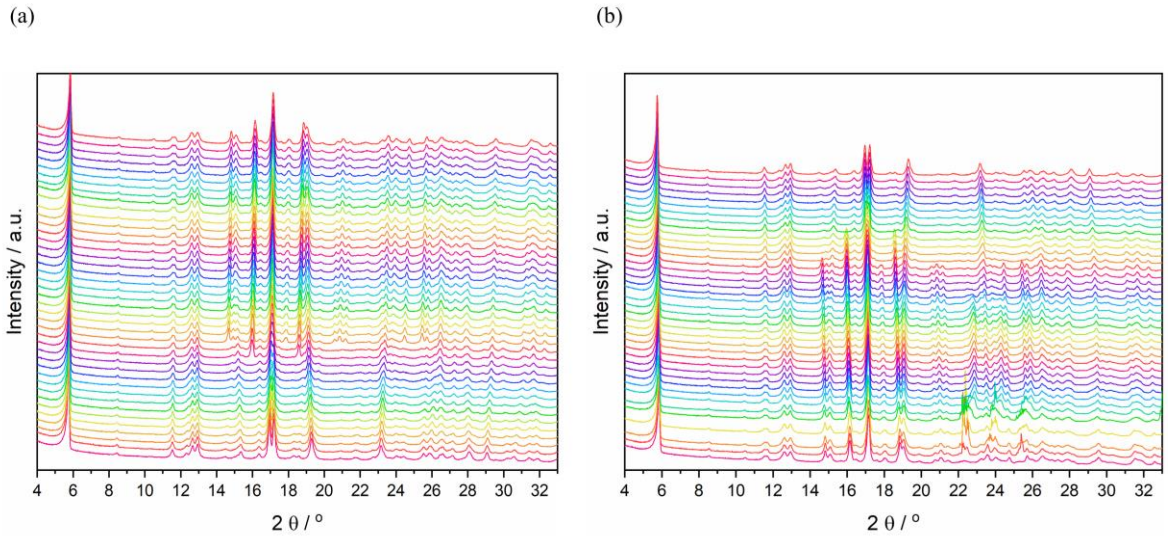

Figure B.2: VT-PXRD of **DzAu·PO50** over the temperature range of 300–100–300 K for (a) cooling process and (b) heating processes.

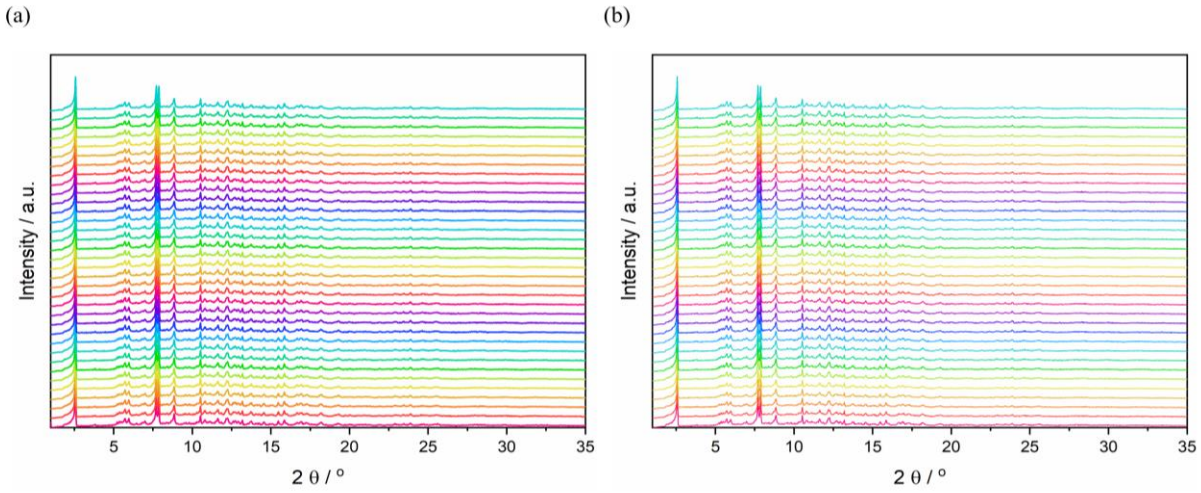

Figure B.3: VT-PXRD of **DzAu·PM50** over the temperature range of 300–100–300 K for (a) cooling process and (b) heating processes.

Appendix C

Supplementary Information for Chapter 5

Table C.1: Crystallographic data for **TzAg** at 100 K.

Parameter	**TzAg**
Identification code	TzAg_cmma
Empirical formula	$C_{16}H_8Ag_2FeN_{10}$
Formula weight/gmol^{-1}	611.91
Temperature/K	293(2)
Crystal system	Orthorhombic
Space group	*Cmme*
a/Å	12.129(2)
b/Å	16.324(3)
c/Å	15.067(3)
α/°	90
β/°	90
γ/°	90
Volume/Å^3	2983.2(10)
Z	4
ρ_{calc} /gcm^{-3}	1.362
μ/mm^{-1}	1.796
F(000)	1176.0
Crystal size/mm^3	0.080 × 0.060 × 0.030
Radiation	Synchrotron (λ = 0.710756 Å)
2θ range for data collection/°	4.982 to 59.034
Index ranges	$-16 \leq h \leq 16$, $-19 \leq k \leq 19$, $-18 \leq l \leq 18$
Reflections collected	18259
Independent reflections	1846 [R_{int} = 0.1717, R_{sigma} = 0.0809]
Data/restraints/parameters	1846/0/88
Goodness-of-fit on F^2	0.880
Final R indexes [I>=2σ (I)]	R_1 = 0.0925, wR_2 = 0.2292
Final R indexes [all data]	R_1 = 0.1423, wR_2 = 0.2846
Largest diff. peak/hole / e Å^{-3}	1.69/-1.31

Table C.2: Crystallographic data for **DzAg** at 100 K, 180 K, 195 K and 260 K.

Parameter	DzAg (100 K)	DzAg (180 K)	DzAg (195 K)	DzAg (260 K)
Identification code	cjk20_s2241_sn752_1_100_00	cjk20_s2241_sn751_1_180_00	cjk20_s2241_sn751_2_195_00	cjk20_s2241_sn752_2_260_00
Empirical formula	$C_{18}H_{10}Ag_2FeN_8$	$C_{18}H_{10}Ag_2FeN_8$	$C_{18}H_{10}Ag_2FeN_8$	$C_{18}H_{10}Ag_2FeN_8$
Formula weight/gmol^{-1}	609.93	609.93	609.93	609.93
Temperature/K	100.00(10)	180.00(10)	195.00(10)	260.01(10)
Crystal system	Monoclinic	Monoclinic	Monoclinic	Monoclinic
Space group	*C*2/*c*	*C*2/*c*	C2/c	*C*2/*c*
a/Å	14.4174(9)	14.8198(15)	14.970(2)	15.0542(18)
b/Å	14.6635(9)	14.9258(17)	15.084(3)	15.0092(14)
c/Å	30.4923(17)	30.960(2)	31.105(3)	31.233(3)
α/°	90	90	90	90
β/°	96.177(6)	97.410(8)	98.196(13)	97.802(12)
γ/°	90	90	90	90
Volume/Å^3	6408.9(7)	6791.0(11)	6952.0(19)	6991.9(12)
Z	8	8	8	8
ρ_{calc} /gcm^{-3}	1.264	1.193	1.165	1.159
μ/mm^{-1}	13.407	12.653	12.360	12.290
F(000)	2352.0	2352.0	2352.0	2352.0
Crystal size/mm^3	0.119 × 0.093 × 0.054	0.119 × 0.093 × 0.054	0.119 × 0.093 × 0.054	0.109 × 0.073 × 0.035
Radiation	Cu K_α (λ = 1.54184 Å)	Cu K_α (λ = 1.54184 Å)	Cu K_α (λ = 1.54184 Å)	Cu K_α (λ = 1.54184 Å)
2θ range for data collection/°	8.626 to 144.152	8.444 to 145.32	8.364 to 145.964	8.358 to 144.45
Index ranges	$-17 \le h \le 17$, $-9 \le k \le 17$, $-37 \le l \le 33$	$-16 \le h \le 17$, $-17 \le k \le 17$, $-26 \le l \le 37$	$-16 \le h \le 18$, $-18 \le k \le 18$, $-27 \le l \le 37$	$-18 \le h \le 18$, $-9 \le k \le 18$, $-38 \le l \le 32$
Reflections collected	12879	14212	14340	13811
Independent reflections	6165 [R_{int} = 0.0759, R_{sigma} = 0.0977]	6481 [R_{int} = 0.0663, R_{sigma} = 0.0883]	6621 [R_{int} = 0.0836, R_{sigma} = 0.1064]	6697 [R_{int} = 0.2180, R_{sigma} = 0.2969]
Data/restraints/parameters	6165/165/294	6481/165/294	6621/165/294	6697/261/282
Goodness-of-fit on F^2	0.947	1.003	0.928	0.935
Final R indexes [I>=2σ (I)]	R_1 = 0.0670, wR_2 = 0.1638	R_1 = 0.0817, wR_2 = 0.2290	R_1 = 0.0770, wR_2 = 0.2109	R_1 = 0.1664, wR_2 = 0.3967
Final R indexes [all data]	R_1 = 0.1004, wR_2 = 0.1817	R_1 = 0.1212, wR_2 = 0.2635	R_1 = 0.1255, wR_2 = 0.2454	R_1 = 0.2852, wR_2 = 0.5247
Largest diff. peak/hole / e Å^{-3}	2.64/-1.84	1.88/-1.28	1.36/-1.25	3.46/-2.13

Table C.3: Crystallographic data for **DzPt** at 100 K.

Parameter	**DzPt**
Identification code	DzPt_1
Empirical formula	$C_{18}H_{18}FeN_8O_4Pt$
Formula weight/gmol^{-1}	661.34
Temperature/K	100(2)
Crystal system	Monoclinic
Space group	$P2_1/c$
a/Å	6.9880(14)
b/Å	20.863(4)
c/Å	15.465(3)
α/°	90
β/°	101.16(3)
γ/°	90
Volume/Å^3	2212.0(8)
Z	4
ρ_{calc}/gcm^{-3}	1.986
μ/mm^{-1}	7.015
F(000)	1272.0
Crystal size/mm^3	0.12 × 0.01 × 0.01
Radiation	Synchrotron (λ = 0.710756 Å)
2θ range for data collection/°	3.32 to 58.276
Index ranges	$-9 \leq h \leq 9$, $-28 \leq k \leq 27$, $-17 \leq l \leq 20$
Reflections collected	14827
Independent reflections	4787 [R_{int} = 0.0434, R_{sigma} = 0.0295]
Data/restraints/parameters	4787/1/299
Goodness-of-fit on F^2	1.061
Final R indexes [I>=2σ (I)]	R_1 = 0.0338, wR_2 = 0.0962
Final R indexes [all data]	R_1 = 0.0351, wR_2 = 0.0976
Largest diff. peak/hole / e Å^{-3}	3.84/-2.43

Table C.4: Crystallographic data for **DzPd** at 100 K.

Parameter	**DzPd**
Identification code	DzPd_1
Empirical formula	$C_{18}H_{18}FeN_8O_4Pd$
Formula weight/gmol^{-1}	572.65
Temperature/K	100 (2)
Crystal system	Monoclinic
Space group	$P2_1/c$
a/Å	6.9340(14)
b/Å	20.883(4)
c/Å	15.555(3)
α/°	90
β/°	101.65(3)
γ/°	90
Volume/Å^3	2206.0(8)
Z	4
ρ_{calc}/gcm^{-3}	1.724
μ/mm^{-1}	1.515
F(000)	1144.0
Crystal size/mm^3	0.06 × 0.15 × 0.10
Radiation	Synchrotron (λ = 0.71076 Å)
2θ range for data collection/°	3.31 to 58.152
Index ranges	$-8 \leq h \leq 7$, $-25 \leq k \leq 25$, $-20 \leq l \leq 20$
Reflections collected	14300
Independent reflections	4545 [R_{int} = 0.0422, R_{sigma} = 0.0330]
Data/restraints/parameters	4545/0/311
Goodness-of-fit on F^2	1.126
Final R indexes [I>=2σ (I)]	R_1 = 0.0491, wR_2 = 0.1386
Final R indexes [all data]	R_1 = 0.0534, wR_2 = 0.1440
Largest diff. peak/hole / e Å^{-3}	1.20/-1.50

Table C.5: Crystallographic data for **$TzAu_{0.5}Ag_{0.5}$** at 100 K and 320 K.

Parameter	**$TzAu_{0.5}Ag_{0.5}$ (100 K)**	**$TzAu_{0.5}Ag_{0.5}$ (320 K)**
Identification code	cjk20_s2021_sn604_1_100_00	cjk20_s2021_sn604_2_320_00
Empirical formula	$C_{16}H_8Ag_{1.23}Au_{0.77}FeN_{10}$	$C_{16}H_8Ag_{1.38}Au_{0.62}FeN_{10}$
Formula weight/gmol^{-1}	680.52	666.93
Temperature/K	100(1)	241(1)
Crystal system	Orthorhombic	Orthorhombic
Space group	*Cmme*	*Cmme*
a/Å	12.0921(9)	17.076(3)
b/Å	16.1918(14)	11.964(2)
c/Å	15.0787(11)	15.468(3)
α/°	90	90
β/°	90	90
γ/°	90	90
Volume/Å^3	2952.3(4)	3160.2(9)
Z	4	4
ρ_{calc}/gcm^{-3}	1.531	1.402
μ/mm^{-1}	17.569	15.859
F(000)	1275.0	1255.0
Crystal size/mm^3	0.048 × 0.043 × 0.039	0.048 × 0.043 × 0.039
Radiation	Cu K_α (λ = 1.54184 Å)	Cu K_α (λ = 1.54184 Å)
2θ range for data collection/°	10.854 to 143.964	10.362 to 143.916
Index ranges	$-12 \le h \le 14$, $-17 \le k \le 19$, $-18 \le l \le 10$	$-18 \le h \le 20$, $-12 \le k \le 14$, $-10 \le l \le 18$
Reflections collected	3322	3545
Independent reflections	1541 [R_{int} = 0.0485, R_{sigma} = 0.0607]	1618 [R_{int} = 0.0965, R_{sigma} = 0.0853]
Data/restraints/parameters	1541/0/89	1618/93/89
Goodness-of-fit on F^2	1.060	1.283
Final R indexes [I>=2σ (I)]	R_1 = 0.0491, wR_2 = 0.1198	R_1 = 0.1160, wR_2 = 0.2728
Final R indexes [all data]	R_1 = 0.0660, wR_2 = 0.1290	R_1 = 0.1686, wR_2 = 0.3745
Largest diff. peak/hole / e Å^{-3}	1.91/-0.98	3.29/-3.36

Table C.6: Crystallographic data for **$DzAu_{0.5}Ag_{0.5}$** at 100 K, 160 K, 179 K and 230 K.

Parameter	**$DzAu_{0.5}Ag_{0.5}$ (100 K)**	**$DzAu_{0.5}Ag_{0.5}$ (160 K)**	**$DzAu_{0.5}Ag_{0.5}$ (179 K)**	**$DzAu_{0.5}Ag_{0.5}$ (230 K)**
Identification code	cjk20_2022_3_1_100_00	cjk20_2022_4_08_160_00	cjk20_2022_4_04_179_00	cjk20_2022_4_01_230_00
Empirical formula	$C_{18}H_{10}Ag_{1.31}Au_{0.69}FeN_8$	$C_{18}H_{10}Ag_{1.24}Au_{0.76}FeN_8$	$C_{18}H_{10}Ag_{1.19}Au_{0.81}FeN_8$	$C_{18}H_{10}Ag_{1.3}Au_{0.7}FeN_8$
Formula weight/gmol^{-1}	670.96	677.64	682.21	672.30
Temperature/K	100(1)	160(1)	179(1)	230(1)
Crystal system	Monoclinic	Monoclinic	Monoclinic	Monoclinic
Space group	*C*2/*c*	*C*2/*c*	*C*2/*c*	*C*2/*c*
a/Å	14.3878(5)	14.7724(11)	14.9154(11)	14.9942(7)
b/Å	14.7123(5)	14.8766(12)	14.9695(12)	14.9759(7)
c/Å	30.5872(8)	30.9921(16)	31.1672(19)	31.2228(12)
α/°	90	90	90	90
β/°	96.390(2)	97.738(6)	98.279(6)	98.045(4)
γ/°	90	90	90	90
Volume/Å^3	6434.4(4)	6748.9(8)	6886.4(9)	6942.1(5)
Z	8	8	8	8
ρ_{calc}/gcm^{-3}	1.385	1.334	1.316	1.286
μ/mm^{-1}	15.799	15.318	15.183	14.693
F(000)	2527.0	2547.0	2560.0	2531.0
Crystal size/mm^3	0.142 × 0.12 × 0.078	0.143 × 0.109 × 0.095	0.143 × 0.109 × 0.095	0.143 × 0.109 × 0.095
Radiation	Cu K_α (λ = 1.54184 Å)	Cu K_α (λ = 1.54184 Å)	Cu K_α (λ = 1.54184 Å)	Cu K_α (λ = 1.54184 Å)
2θ range for data collection/°	8.624 to 144.446	8.474 to 143.956	8.412 to 144.114	8.386 to 144.42
Index ranges	$-17 \le h \le 17$, $-17 \le k \le 17$, $-13 \le l \le 37$	$-17 \le h \le 10$, $-18 \le k \le 16$, $-34 \le l \le 38$	$-11 \le h \le 18$, $-18 \le k \le 16$, $-38 \le l \le 35$	$-11 \le h \le 18$, $-18 \le k \le 16$, $-38 \le l \le 35$
Reflections collected	12632	11715	12091	12430
Independent reflections	6158 [R_{int} = 0.0270, R_{sigma} = 0.0377]	6349 [R_{int} = 0.0689, R_{sigma} = 0.0923]	6513 [R_{int} = 0.0677, R_{sigma} = 0.0894]	6591 [R_{int} = 0.0418, R_{sigma} = 0.0595]
Data/restraints/parameters	6158/0/254	6349/66/264	6513/66/264	6591/0/264
Goodness-of-fit on F^2	1.092	1.061	1.063	1.062
Final R indexes [I>=2σ (I)]	R_1 = 0.0722, wR_2 = 0.2041	R_1 = 0.0847, wR_2 = 0.2275	R_1 = 0.0831, wR_2 = 0.2158	R_1 = 0.0590, wR_2 = 0.1444
Final R indexes [all data]	R_1 = 0.0796, wR_2 = 0.2112	R_1 = 0.1067, wR_2 = 0.2469	R_1 = 0.1015, wR_2 = 0.2303	R_1 = 0.0695, wR_2 = 0.1500
Largest diff. peak/hole / e Å^{-3}	4.25/-5.20	1.76/-1.79	2.19/-1.86	1.55/-1.33

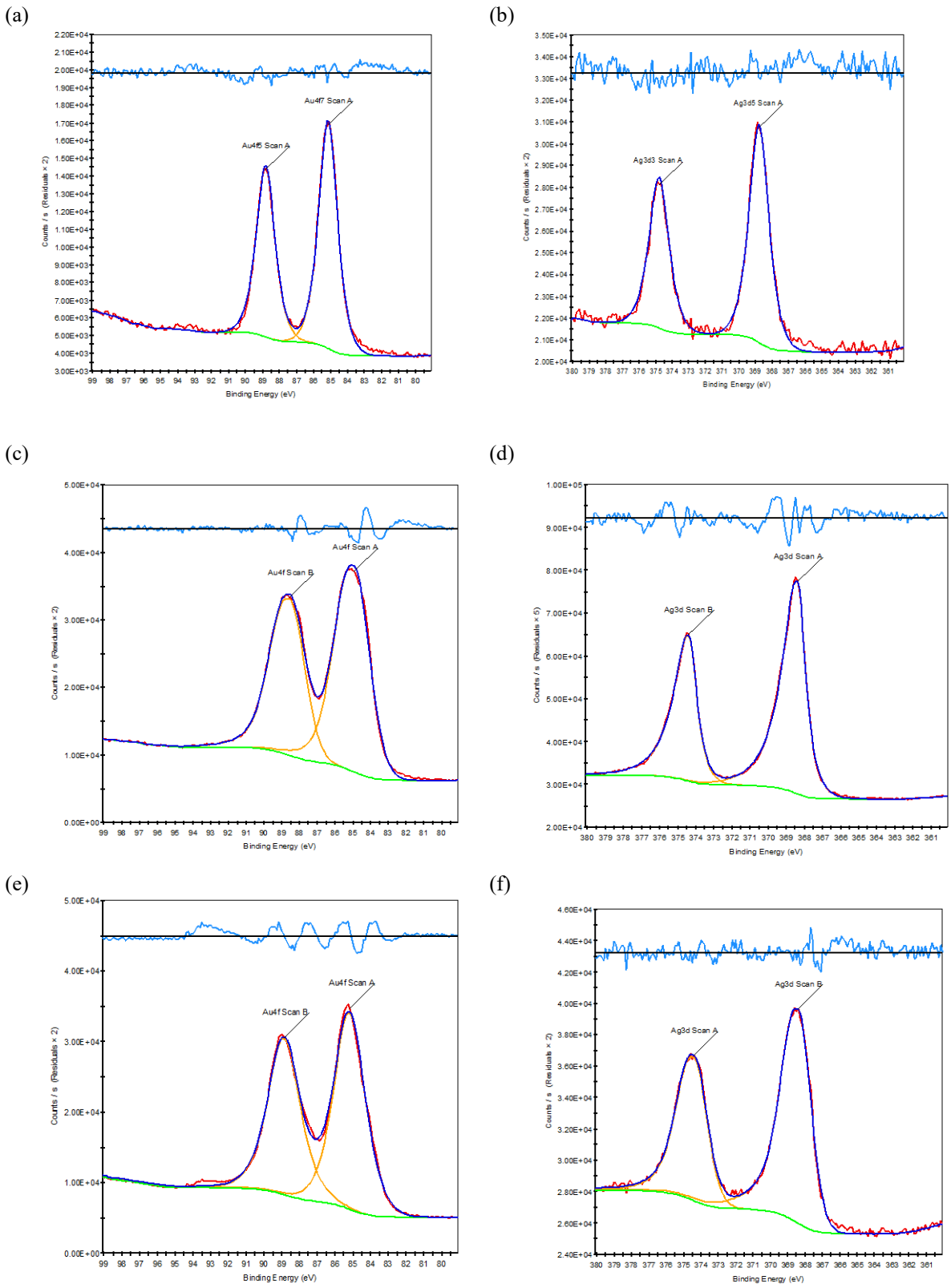

Figure C.1: X-ray photoemission spectra for (a) a high-resolution scan of Au 4*f* in **TzAu$_{0.5}$Ag$_{0.5}$**, (b) a high-resolution scan of Ag 3*d*, (c) a high-resolution scan of Au 4*f* in **DzAu$_{0.5}$Ag$_{0.5}$** (d) and a high-resolution scan of Ag 3*d*. (e) a high-resolution scan of Au 4*f* in DzAu$_{0.7}$Ag$_{0.3}$ (f) and a high-resolution scan of Ag 3*d*. The peaks in each spectrum were fitted with a red curve representing experimentally measured data. The peaks were fitted showing in blue curve with the completed peak features in yellow, background in green. The deviation from

experimental data and simulated fit in the light blue shows on the top of the peak with a black horizontal line as a baseline.

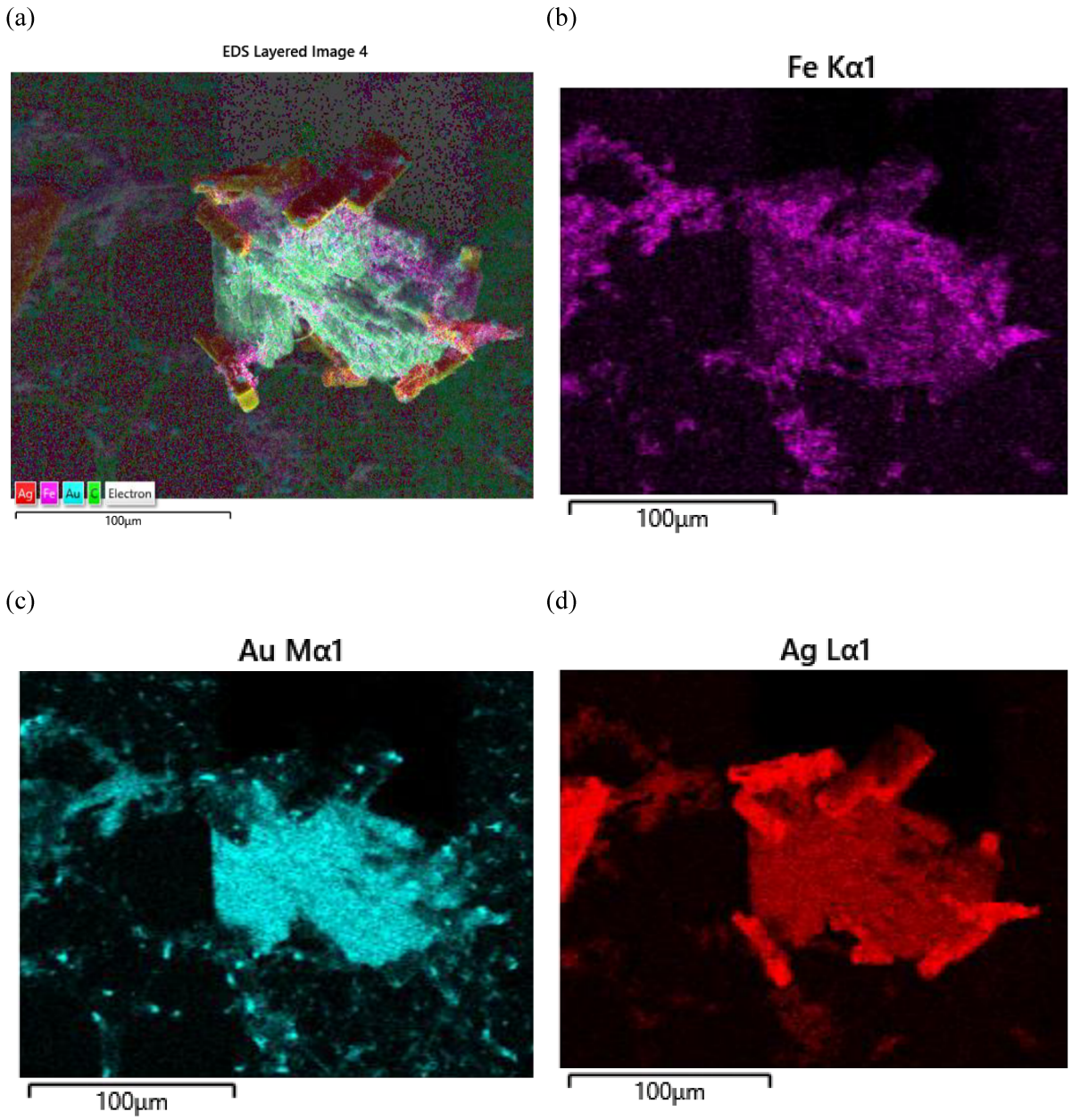

Figure C.2: (a) SEM EDS image of **DzAu$_{0.5}$Ag$_{0.5}$** (b) EDS mapping and elemental analysis of Fe (purple), (c) Au (cyan) and (d) Ag (red).

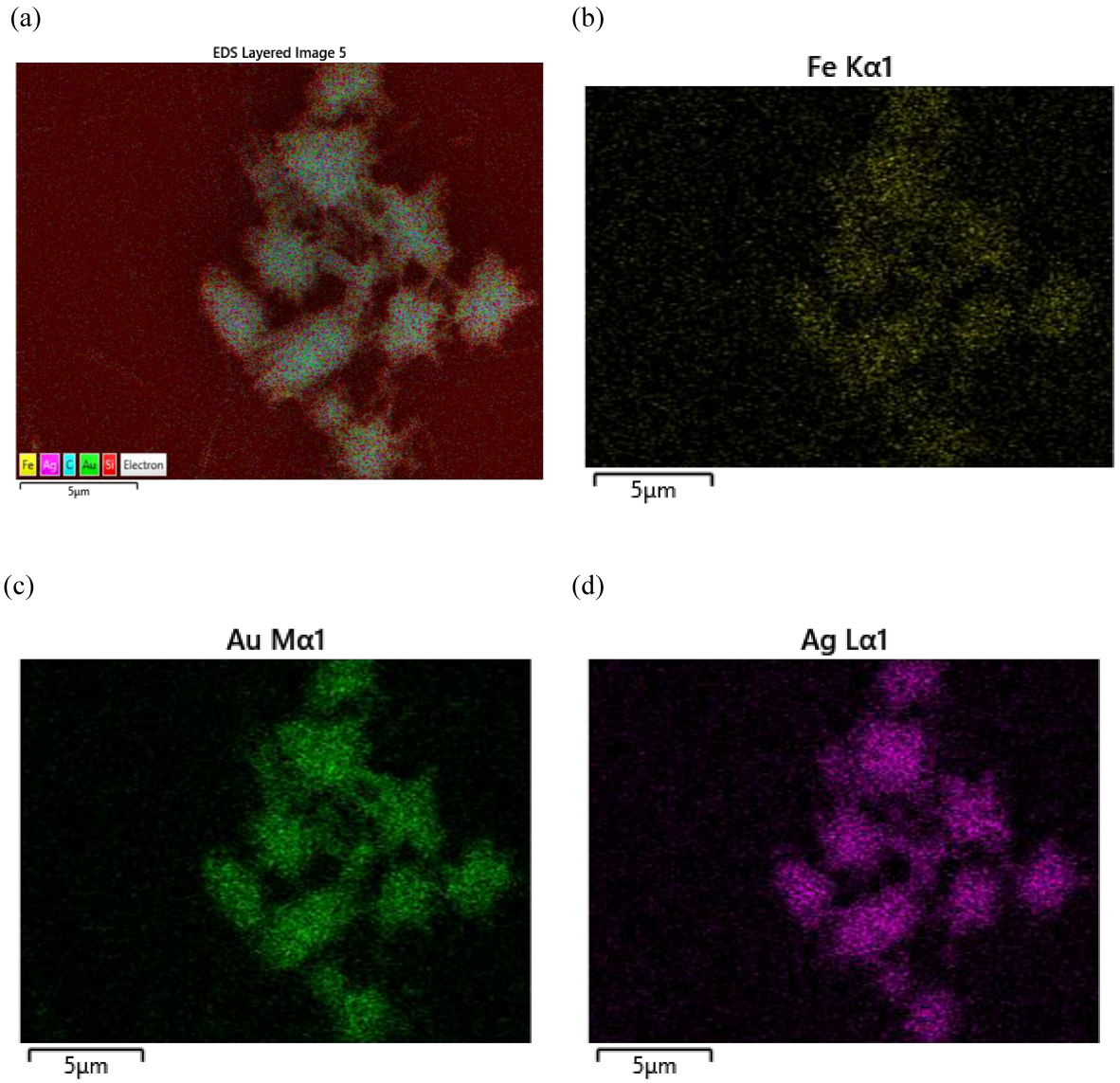

Figure C.3: (a) SEM EDS image of **DzAu$_{0.7}$Ag$_{0.3}$** (b) EDS mapping and elemental analysis of Fe (light yellow), (c) Au (greem) and (d) Ag (purple).

Appendix D

Supplementary Information for Chapter 6

(a)

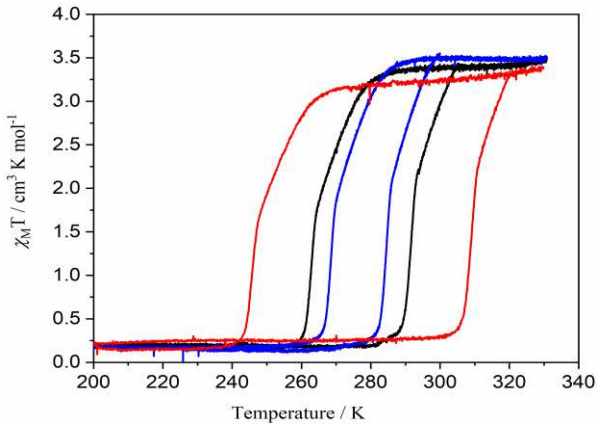
$\chi_M T$ / cm^3 K mol^{-1}
Temperature / K

(b)

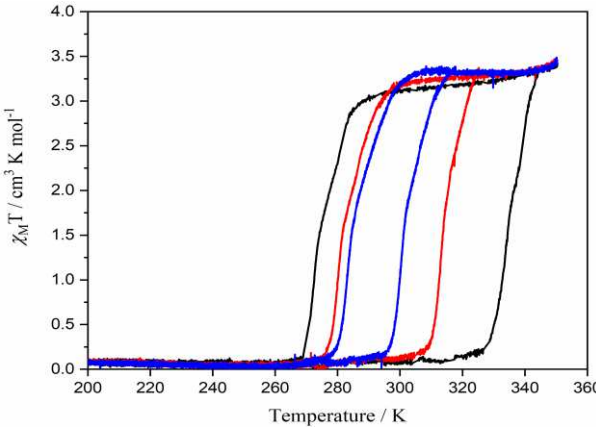
$\chi_M T$ / cm^3 K mol^{-1}
Temperature / K

(c)

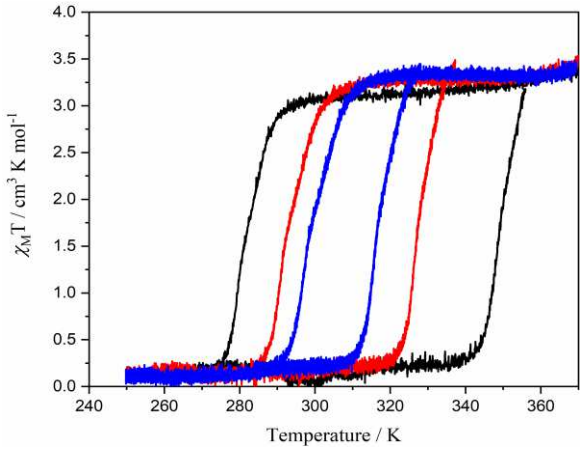
$\chi_M T$ / cm^3 K mol^{-1}
Temperature / K

(d)

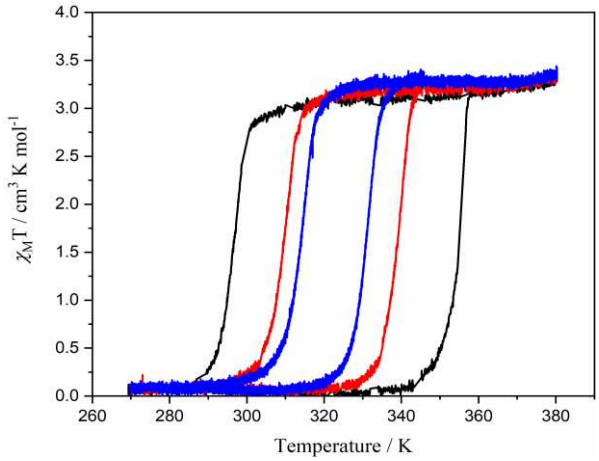
$\chi_M T$ / cm^3 K mol^{-1}
Temperature / K

(e)

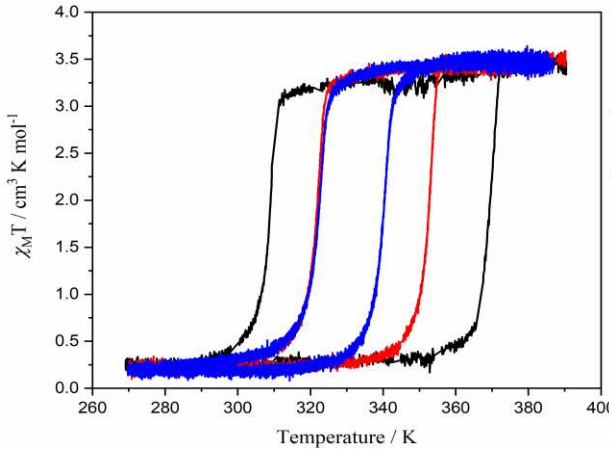
$\chi_M T$ / cm^3 K mol^{-1}
Temperature / K

(f)

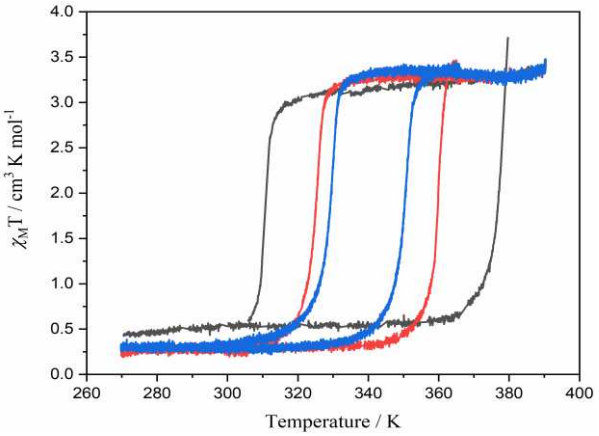
$\chi_M T$ / cm^3 K mol^{-1}
Temperature / K

(g) (h)

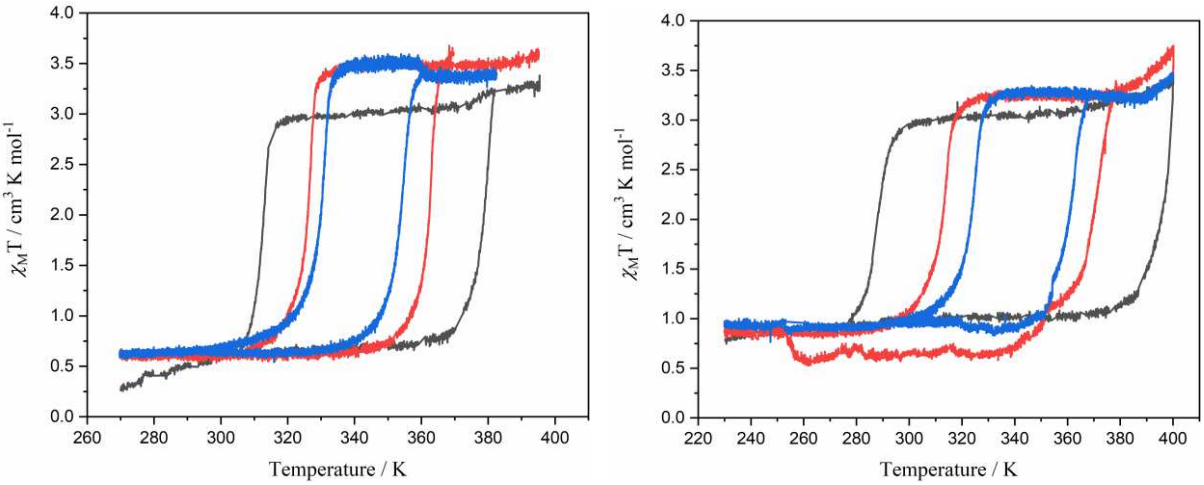

Figure D.1: Variable temperature magnetic susceptibility data of **TzAu·EtOH** at a scan rate of 1 (blue), 2 (red) and 5 K min^{-1} (black) at (a) 0.33, (b) 0.35, (c) 0.36, (d) 0.37, (e) 0.39, (f) 0.45, (g) 0.54, (h) 0.62 and (h) 0.76 GPa.

Table D.1: Spin transition temperatures for **TzAu·EtOH** at 0.33, 0.35, 0.36, 0.37, 0.39, 0.45, 0.54, 0.62, 0.76 and 0.99 GPa with the scan rate of 1, 2 and 5 K min^{-1}. The 'zero scan rate' spin transition temperatures were extrapolated based on the measured scan rates.

	0.33 GPa		0.35 GPa		0.35 GPa		0.37 GPa		0.39 GPa		0.45 GPa	
Temperature K / Scan rate K min^{-1}	Cooling	Heating	Cooling	Heating	Cooling	Heating	Cooling	Heating	Cooling	Heating	Cooling	Heating
5	242	302	246	308	275	335	282	349	297	355	309	369
2	259	286	263	291	282	314	293	327	310	339	322	352
1	266	280	268	284	286	302	298	316	314	331	322	340
0	271	275	274	279	288	296	301	309	318	326	327	335

	0.54 GPa		0.62 GPa		0.76 GPa		0.99 GPa	
Temperature K / Scan rate K min^{-1}	Cooling	Heating	Cooling	Heating	Cooling	Heating	Cooling	Heating
5	310	377	313	379	288	397		
2	325	359	326	362	313	370		
1	329	350	330	354	324	361	292	346
0	334	344	334	349	332	352		

Table D.2: Lattice information of **TzAu·EtOD** (with ethanol as a pressure medium) extracted from NPD data at different pressures.

Pressure	*a* / Å	*a* (esds) / Å	*b* / Å	*b* (esds) / Å	*c* / Å	*c* (esds) / Å	Volume / Å^3	Volume (esds) / Å^3
0	12.0628	0.0020	16.7324	0.0077	14.7648	0.0052	4.9470	0.0019
0.40	12.0690	0.0051	15.9881	0.0036	14.9777	0.0043	4.9312	0.0009
0.68	12.1031	0.0072	15.9809	0.0050	15.0287	0.0060	4.9211	0.0003
0.98	12.1322	0.0081	15.6589	0.0093	15.0365	0.0074	4.9104	0.0004
1.23	12.1693	0.0099	15.2871	0.0097	15.1002	0.0110	4.9016	0.0033

Table D.3: Lattice information of the second batch **[Tz$_{0.5}$Dz$_{0.5}$]** (with fluorinert FC-70 as a pressure medium) extracted from NPD data at different pressures.

Pressure	*a* / Å	*a* (esds) / Å	*b* / Å	*b* (esds) / Å	*c* / Å	*c* (esds) / Å	Volume / Å^3	Volume (esds) / Å^3
0	11.9235	0.0033	16.7126	0.0065	15.2422	0.0042	3037.3600	1.2910
0.25	11.9549	0.0045	16.6047	0.0060	15.2082	0.0054	3018.9280	1.5380
0.82	12.0262	0.0056	16.4436	0.0078	15.1482	0.0063	2995.6130	1.7610
1.02	12.0992	0.0026	16.2316	0.0049	15.1118	0.0040	2967.7890	1.0760
1.18	12.1005	0.0027	16.1643	0.0050	15.0954	0.0047	2952.6090	1.2950

Appendix E

Supplementary Information for Chapter 7

(a) (b)

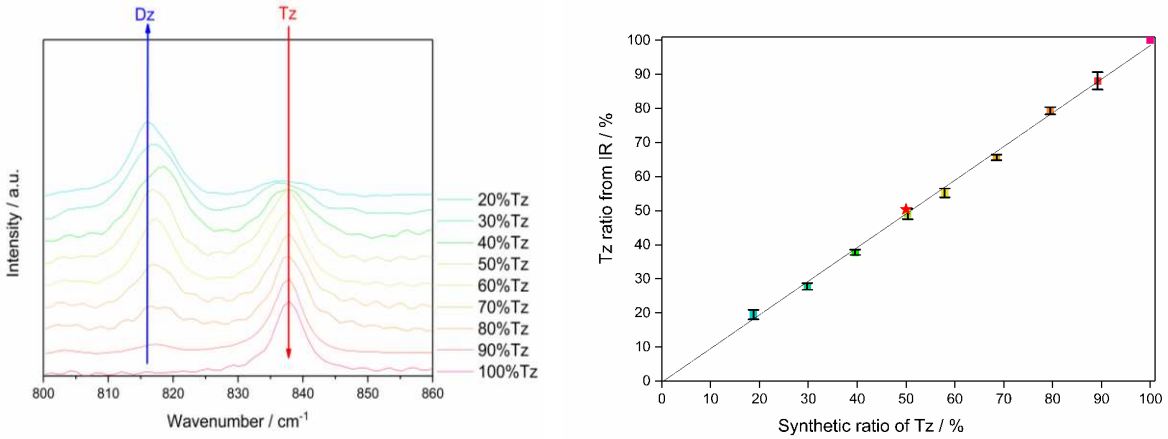

Figure E.1: IR spectra of the series of frameworks **[Tz$_x$Dz$_{1-x}$]** (x = 0.2–1, Δx = 0.1) from 800–860 cm^{-1}. The relative percentage of Tz doping is provided in the figure legend. The peak at *ca.* 837 cm^{-1} is assigned to the Tz ligand, and the peak at *ca.* 816 cm^{-1} is assigned to the Dz ligand. The plot of the percentage of Tz ligand for each framework in the MIXMOF series calculated from the integration of the Tz peak in the IR spectra (y-axis), against the stoichiometric ratio of Tz used during bulk powder synthesis (x-axis), showing excellent linear correlation (y = -0.34 + 0.99x), with R^2 = 0.999. The single crystal sample of **[Tz$_{0.5}$Dz$_{0.5}$]** is represented by a red asterisk.

Table E.1: Crystallographic data for **[$Tz_{0.5}Dz_{0.5}$]** in the LS state.

Parameter	LS
Framework	$[FeTz_{0.5}Dz_{0.5}Au(CN)_2)_2]$
Formula	$C_{17}H_9FeN_9Au_2$
MW/g mol^{-1}	789.11
T /K	100(2)
Crystal System	Orthorhombic
Space Group	*Cmma*
λ/Å	0.71073
Z	4
a/Å	11.884(2)
b/Å	16.206(3)
c/Å	15.162(3)
α/°	90
β/°	90
γ/°	90
V/Å^3	2920.0(10)
ρ_{calc}/gcm^{-3}	1.795
μ/mm^{-1}	10.53
Data/restraints/parameters	2298/0/87
R_1 [I > 2σ(I), all data][a]	0.0532, 0.0621
wR_2 [I > 2σ(I), all data][b]	0.1628, 0.1719
GoF	1.161

[a] $R_1 = \Sigma||F_o| - |F_c||/\Sigma|F_o|$. [b] $wR_2 = [\Sigma[w(F_o^2 - F_c^2)^2]/\Sigma[w(F_o^2)^2]]^{1/2}$.

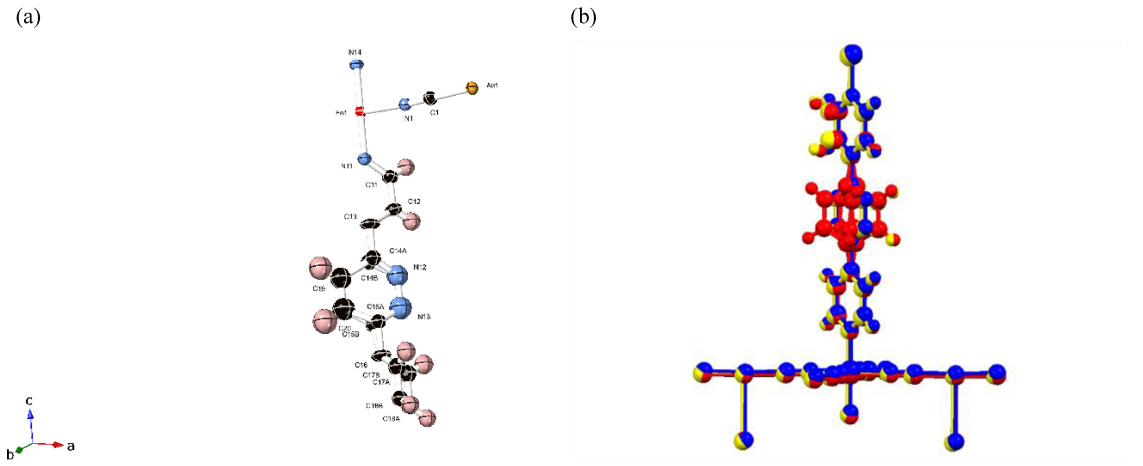

Figure E.2: (a) The asymmetric unit of **[Tz$_{0.5}$Dz$_{0.5}$]** at 100 K with thermal ellipsoids at 50% probability. (b) Overlay of the single crystal structures: **[Tz$_{1.0}$Dz$_{0.0}$]** at 100 K (in blue), **[Tz$_{0.5}$Dz$_{0.5}$]** at 100 K (in yellow) and PSM **[Tz$_{0.0}$Dz$_{1.0}$]** at 90 K (in red).

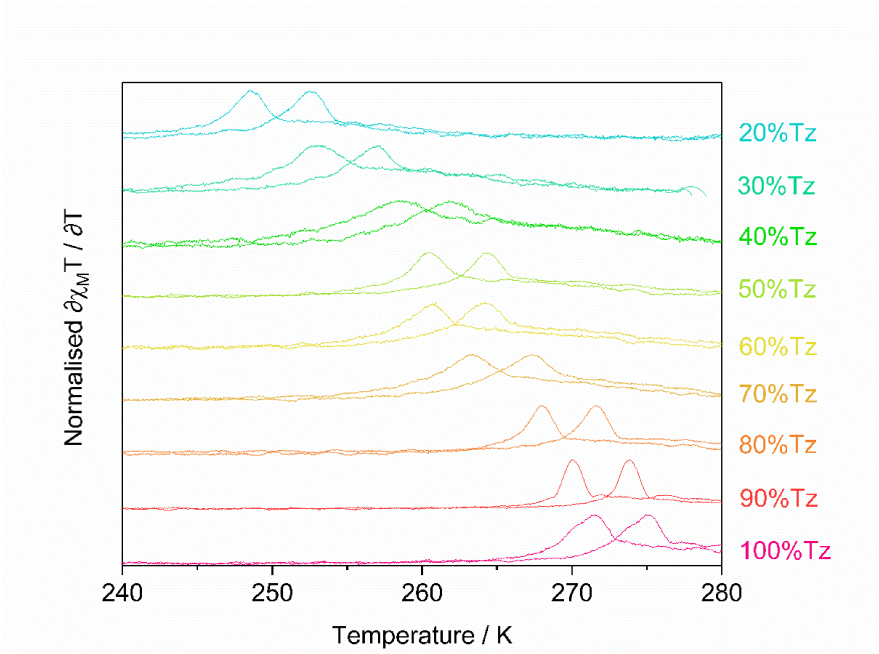

Figure E.3: The plot of the first derivative of $\chi_M T$ against temperature for the MIXMOF series **[Tz$_{1.0}$Dz$_{0.0}$]** to **[Tz$_{0.2}$Dz$_{0.8}$]**.

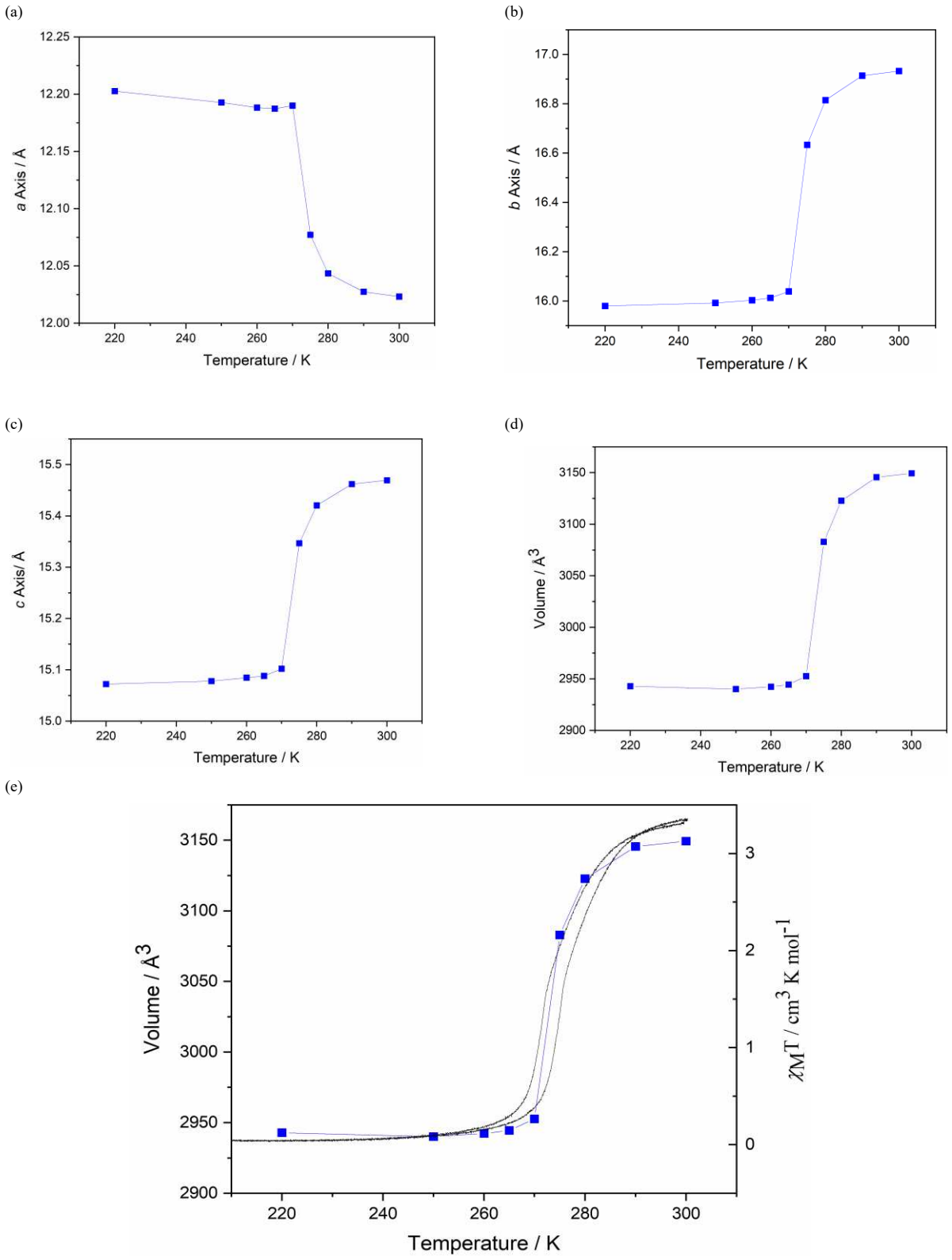

Figure E.4: Evolution of the unit cell (a) *a*-, (b) *b*-, (c) *c*-axes and (d) volume of **[$Tz_{1.0}Dz_{0.0}$]** powder framework (300–220–300 K) determined from Le Bail refinements of the VT-PXRD data. (e) Variable temperature magnetic susceptibility data (black) overlaid with PXRD data, cooling branch (blue).

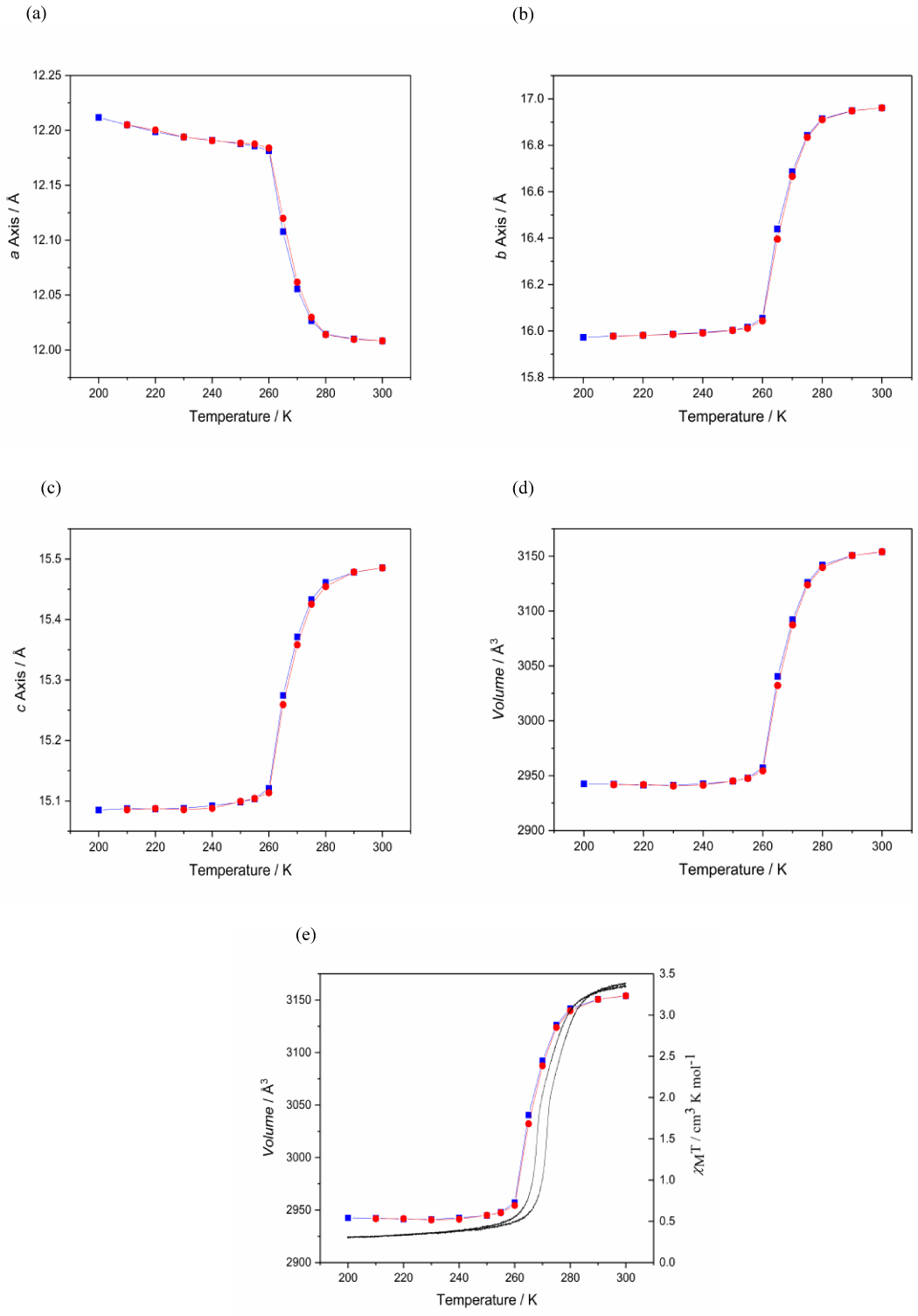

Figure E.5: Evolution of the unit cell (a) *a*-, (b) *b*-, (c) *c*-axes and (d) volume of **[Tz$_{0.8}$Dz$_{0.2}$]** powder framework (300–200–300 K) determined from Le Bail refinements of the VT-PXRD data. (e) Variable temperature magnetic susceptibility data (black) overlaid with PXRD data, cooling branch (blue), heating branch (red).

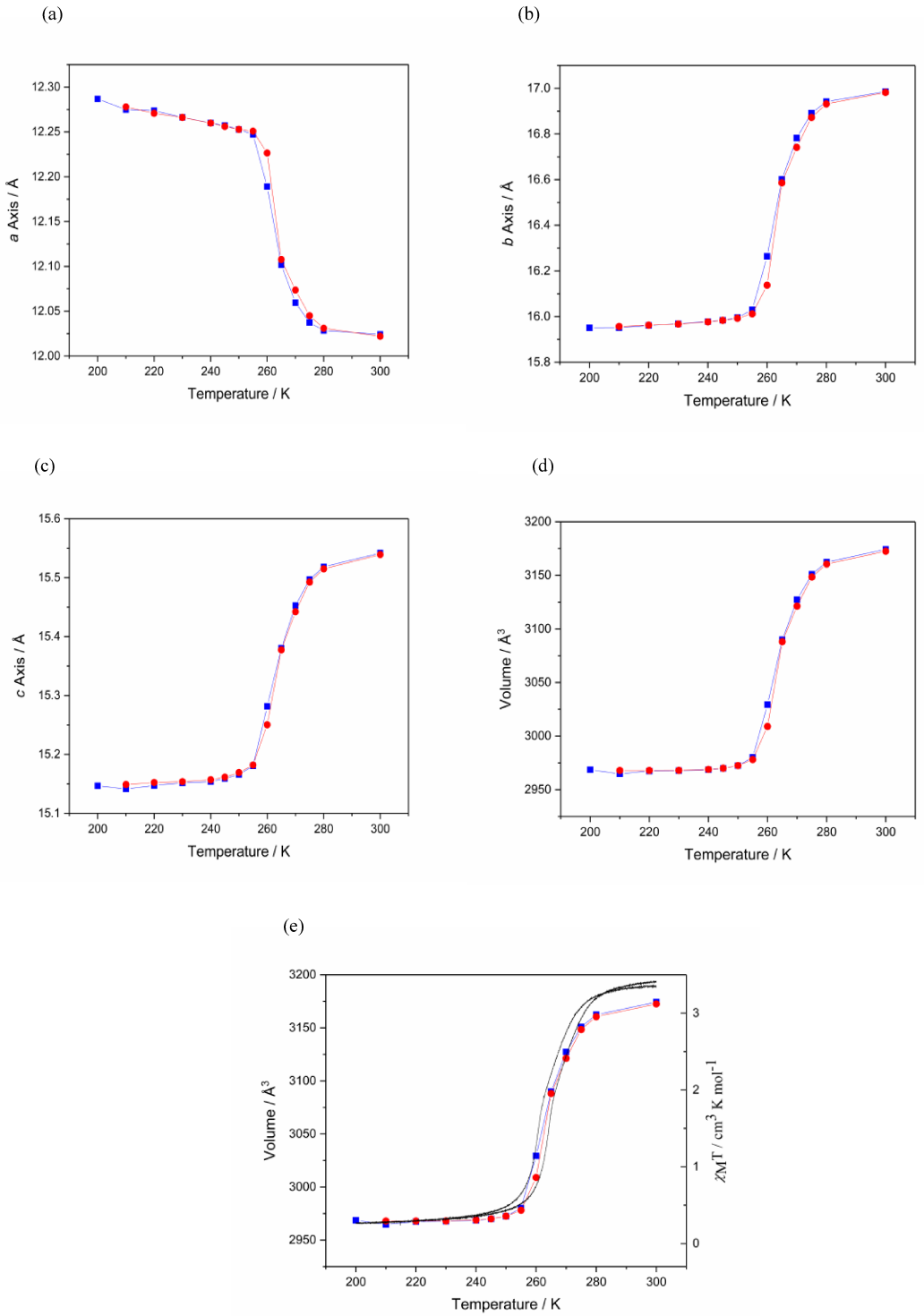

Figure E.6: Evolution of the unit cell (a) *a*-, (b) *b*-, (c) *c*-axes and (d) volume of **[Tz$_{0.6}$Dz$_{0.4}$]** powder framework (300–200–300 K) determined from Le Bail refinement of the VT-PXRD data. (e) Variable temperature magnetic susceptibility data (black) overlaid with PXRD data, cooling branch (blue), heating branch (red).

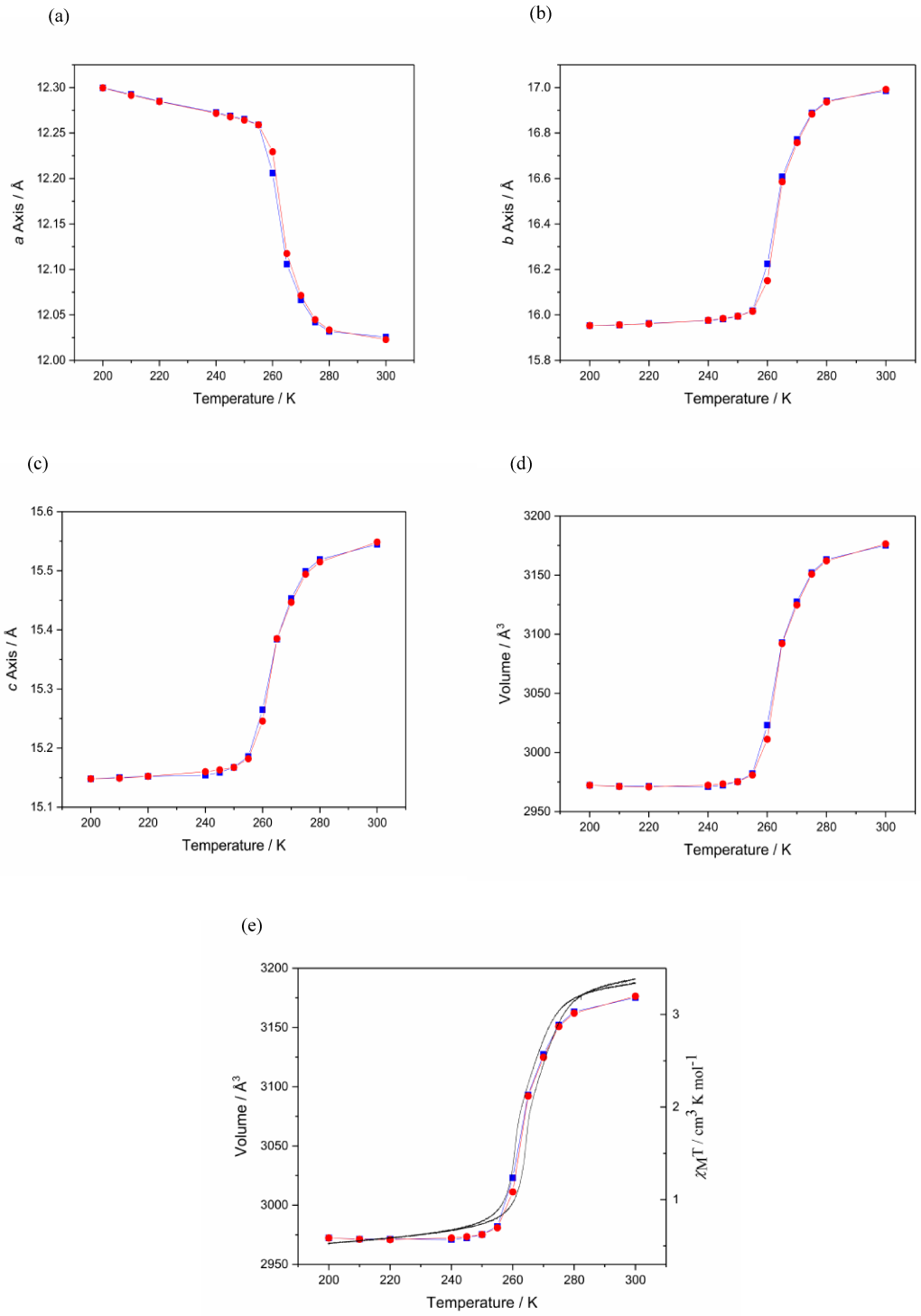

Figure E.7: Evolution of the unit cell (a) *a*-, (b) *b*-, (c) *c*-axes and (d) volume of **[Tz$_{0.5}$Dz$_{0.5}$]** powder framework (300–200–300 K) determined from Le Bail refinements of the VT-PXRD data. (e) Variable temperature magnetic susceptibility data (black) overlaid with PXRD data, cooling branch (blue), heating branch (red).

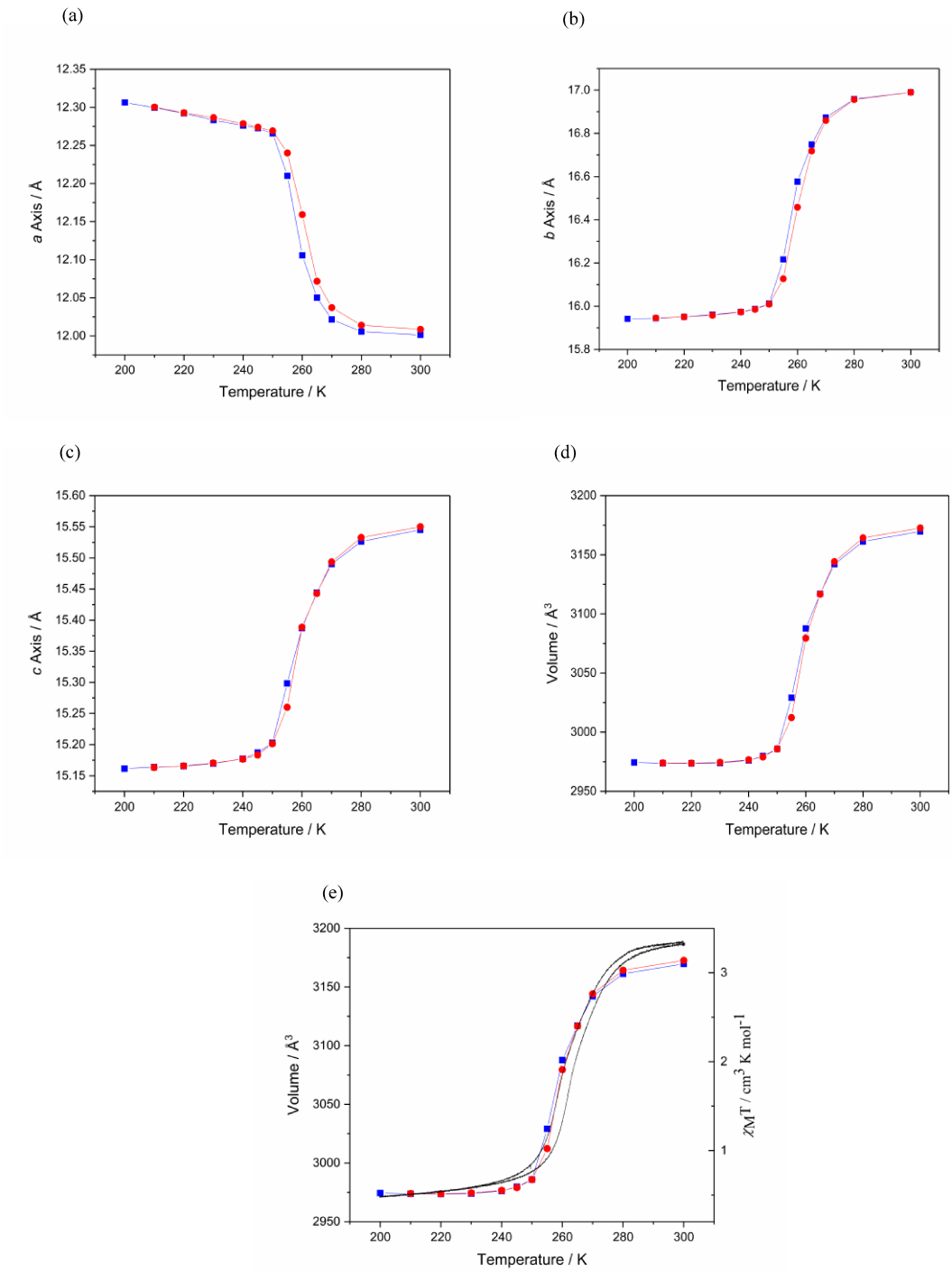

Figure E.8: Evolution of the unit cell (a) *a*-, (b) *b*-, (c) *c*-axes and (d) volume of **[Tz$_{0.4}$Dz$_{0.6}$]** powder framework (300–200–300 K) determined from Le Bail refinements of the VT-PXRD data. (e) Variable temperature magnetic susceptibility data (black) overlaid with PXRD data, cooling branch (blue), heating branch (red).

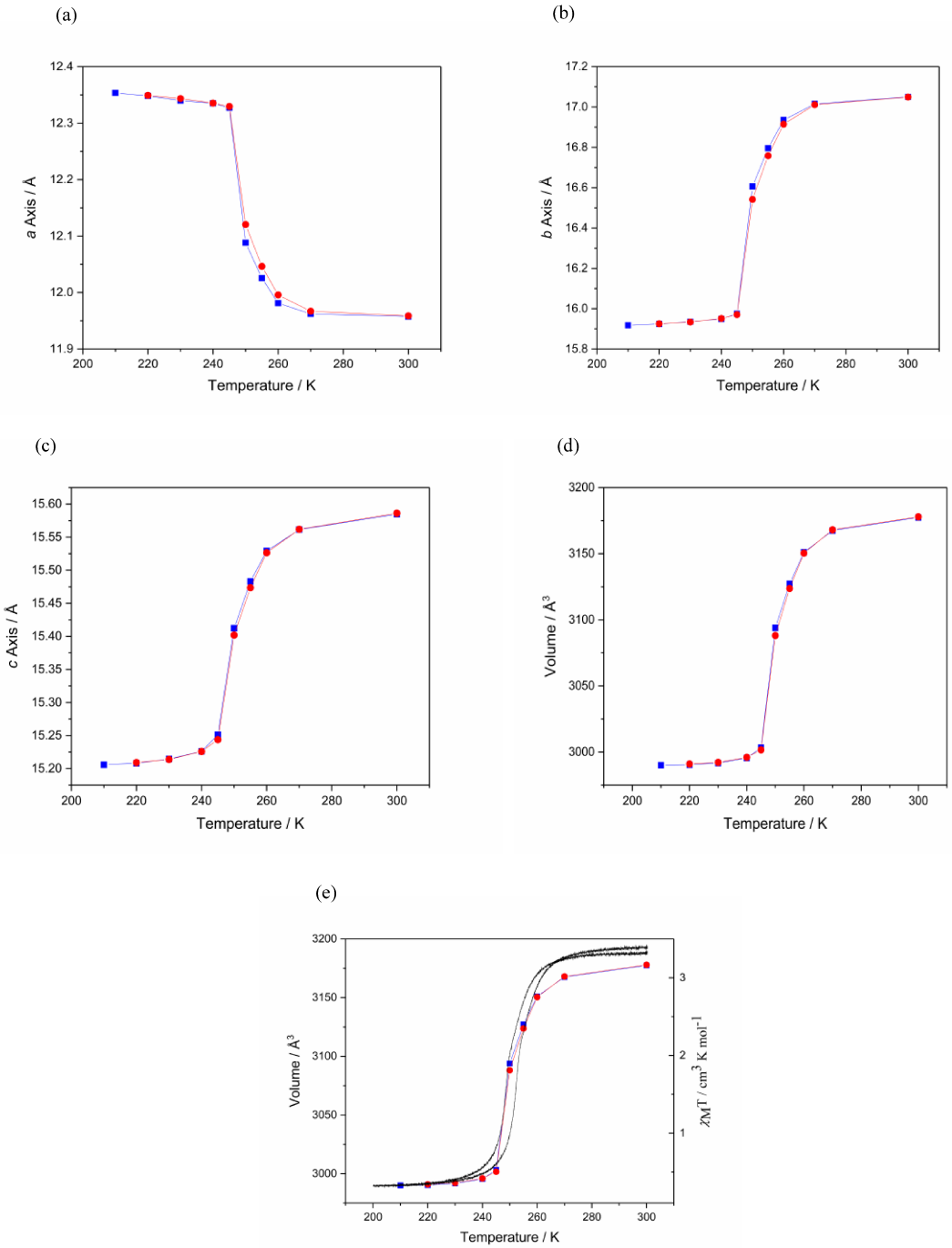

Figure E.9: Evolution of the unit cell (a) *a*-, (b) *b*-, (c) *c*-axes and (d) volume of **[Tz$_{0.2}$Dz$_{0.8}$]** powder framework (300–200–300 K) determined from Le Bail refinements of the VT-PXRD data. (e) Variable temperature magnetic susceptibility data (black) overlaid with PXRD data, cooling branch (blue), heating branch (red).

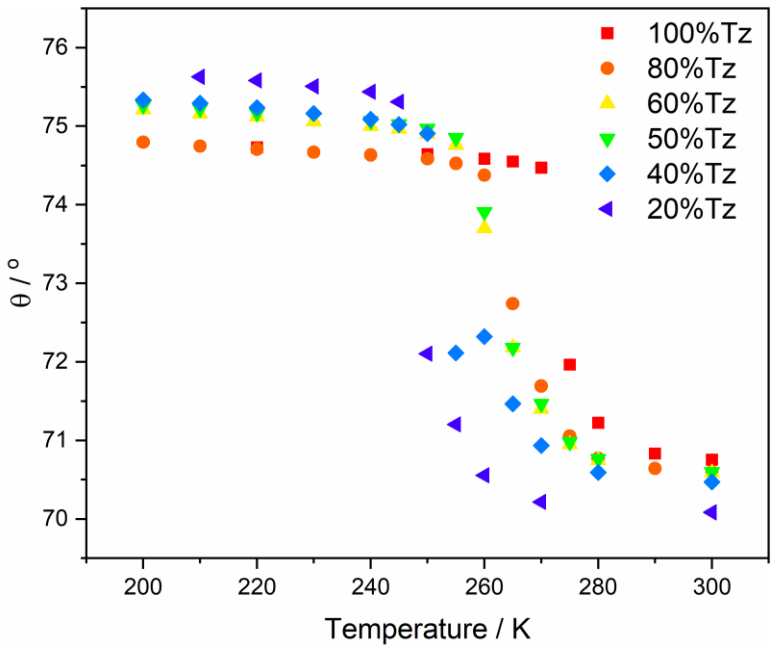

Figure E.10: Comparison of the change in acute compression angle θ, of the MIXMOF series **[Tz$_x$Dz$_{1-x}$]** (x = 1.0, 0.8, 0.6, 0.5, 0.4, 0.2) at different temperatures (300–220 K).

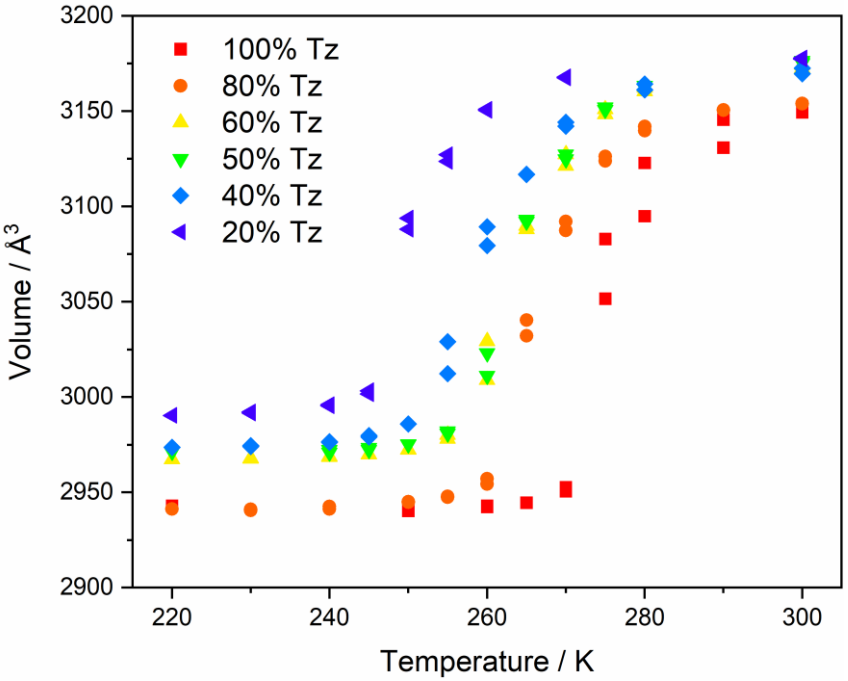

Figure E.11: Comparison of the change in unit cell volume of the MIXMOF series**[Tz$_x$Dz$_{1-x}$]** (x = 1.0, 0.8, 0.6, 0.5, 0.4, 0.2) at different temperatures (300–220 K).

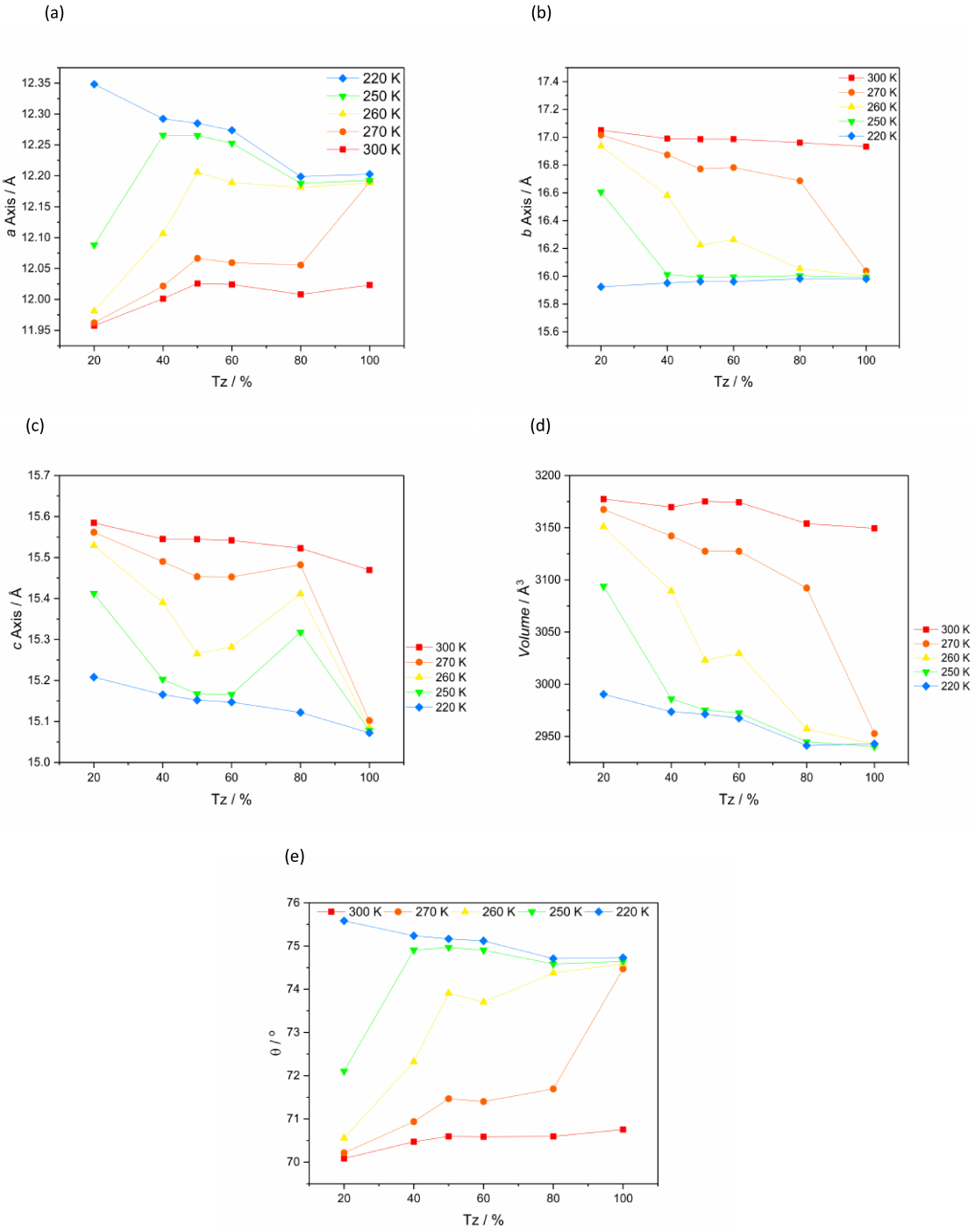

Figure E.12: Comparison of the change in the unit cell (a) *a*-, (b) *b*-, (c) *c*-axes, (d) volume and (e) θ value versus the percentage Tz composition in the MIXMOF series **[Tz$_x$Dz$_{1-x}$]** (x = 1.0, 0.8, 0.6, 0.5, 0.4, 0.2) at different temperatures: 300 K, 270 K, 260 K, 250 K and 220 K.

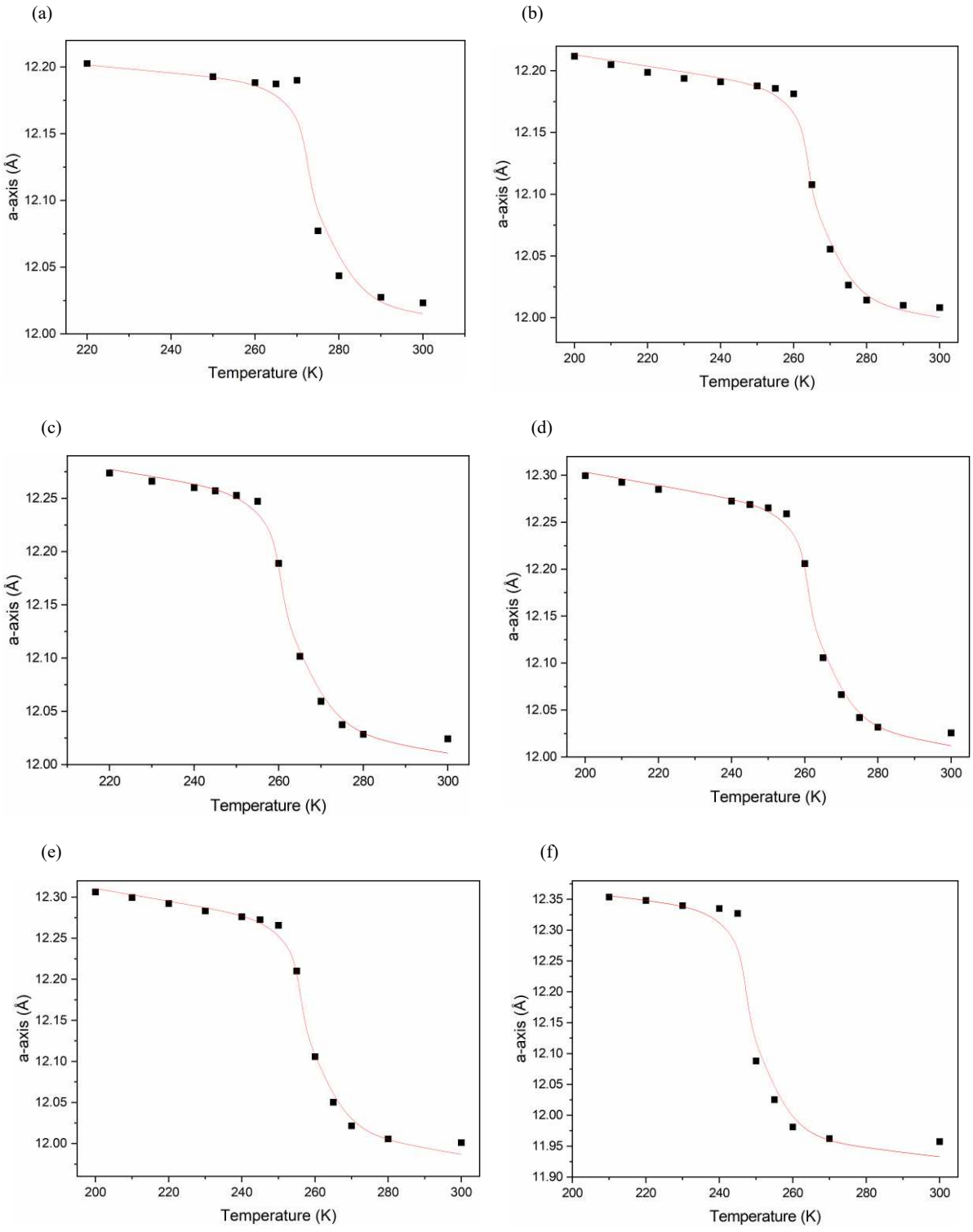

Figure E.13: *a*-axis changes versus temperature with model fit (line) in MIXMOFs (a) **[$Tz_{1.0}Dz_{0.0}$]**, (b) **[$Tz_{0.8}Dz_{0.2}$],** (c) **[$Tz_{0.6}Dz_{0.4}$]**, (d) **[$Tz_{0.5}Dz_{0.5}$]**, (e) **[$Tz_{0.4}Dz_{0.6}$]**, (f) **[$Tz_{0.2}Dz_{0.8}$]**.

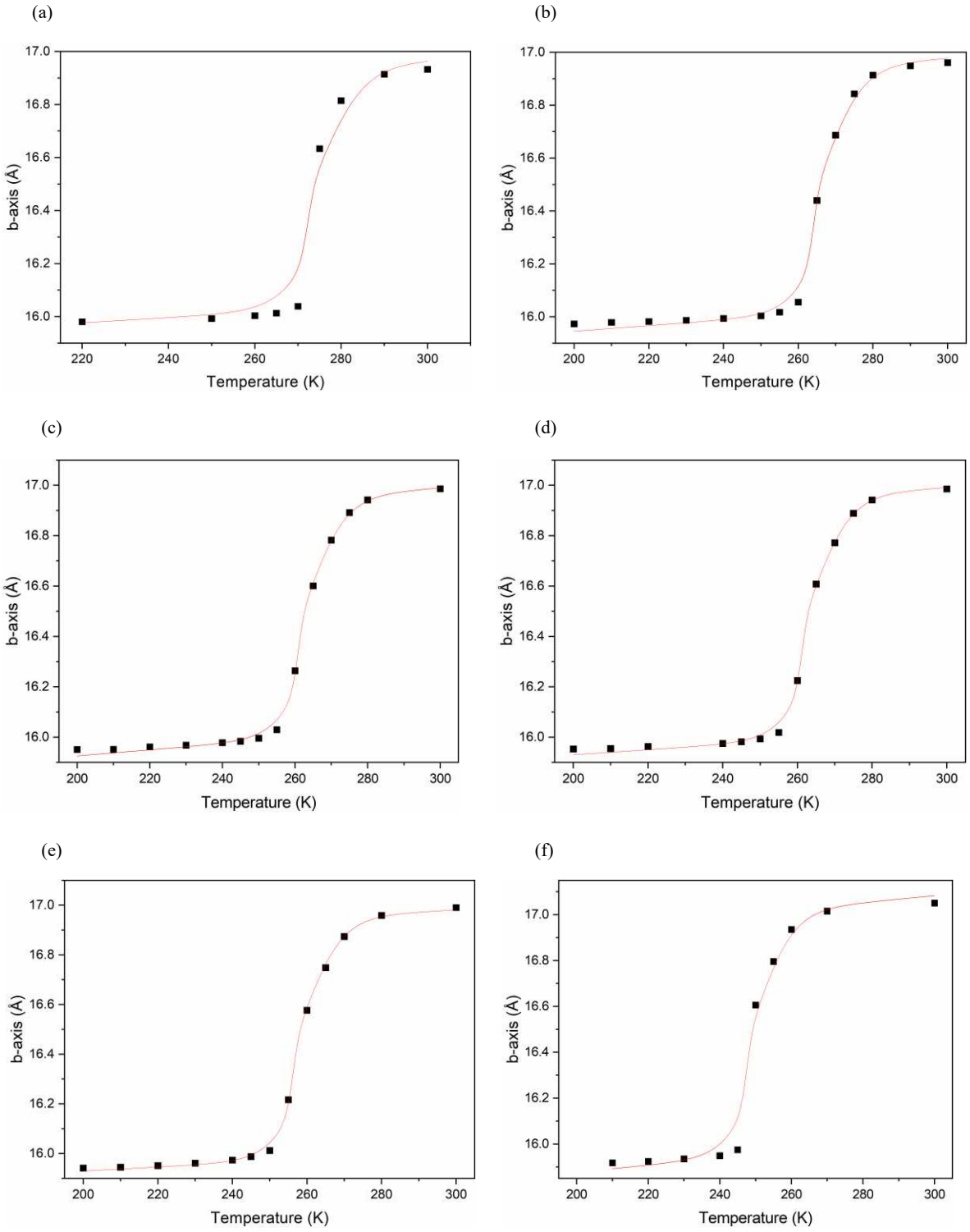

Figure E.14: *b*-axis changes versus temperature with model fit (line) in MIXMOFs (a) **[$Tz_{1.0}Dz_{0.0}$]**, (b) **[$Tz_{0.8}Dz_{0.2}$],** (c) **[$Tz_{0.6}Dz_{0.4}$]**, (d) **[$Tz_{0.5}Dz_{0.5}$]**, (e) **[$Tz_{0.4}Dz_{0.6}$]**, (f) **[$Tz_{0.2}Dz_{0.8}$]**.

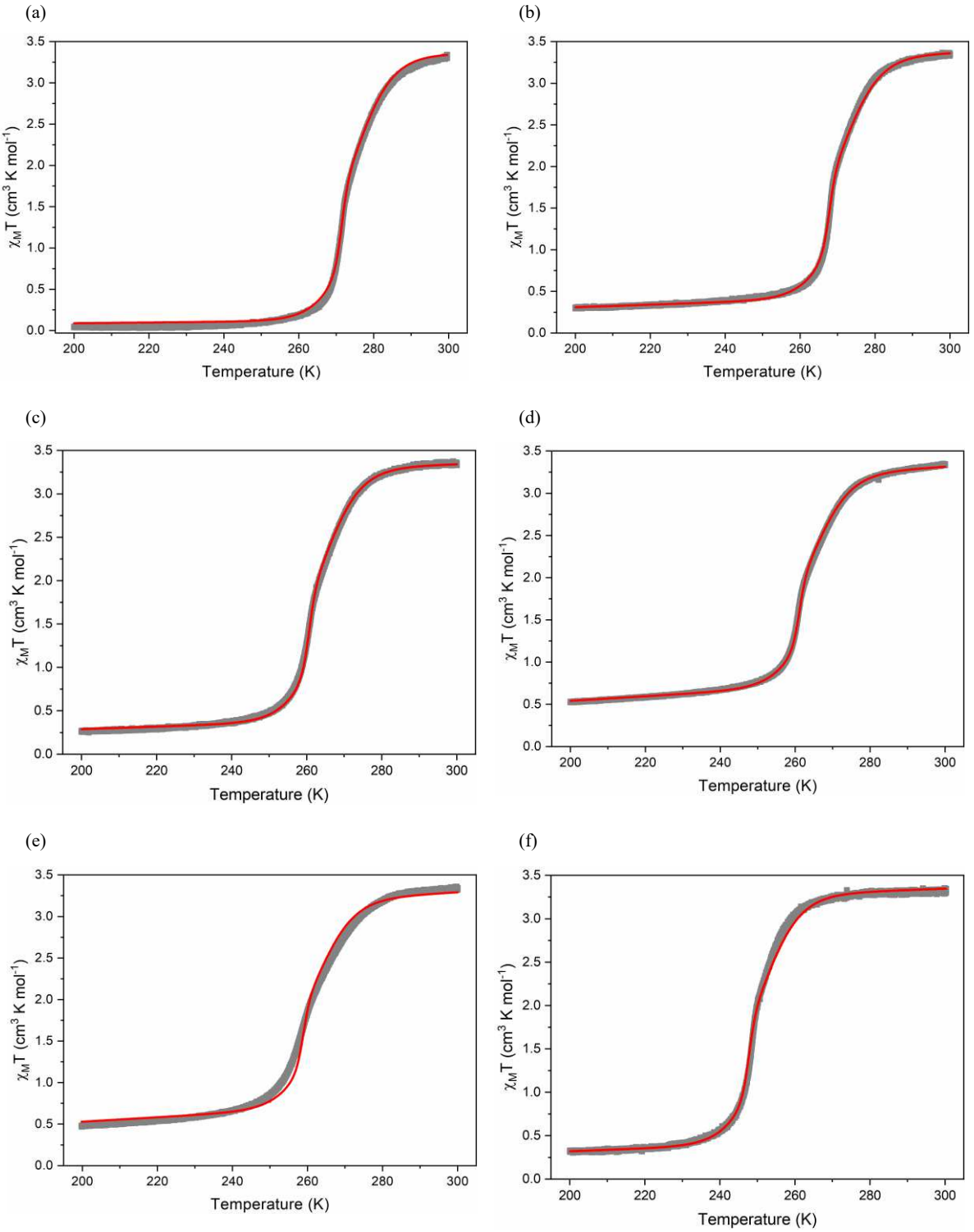

Figure E.15: Magnetism changes versus temperature with model fit (line) in MIXMOFs (a) **[Tz$_{1.0}$Dz$_{0.0}$]**, (b) **[Tz$_{0.8}$Dz$_{0.2}$],** (c) **[Tz$_{0.6}$Dz$_{0.4}$]**, (d) **[Tz$_{0.5}$Dz$_{0.5}$]**, (e) **[Tz$_{0.4}$Dz$_{0.6}$]**, (f) **[Tz$_{0.2}$Dz$_{0.8}$]**.

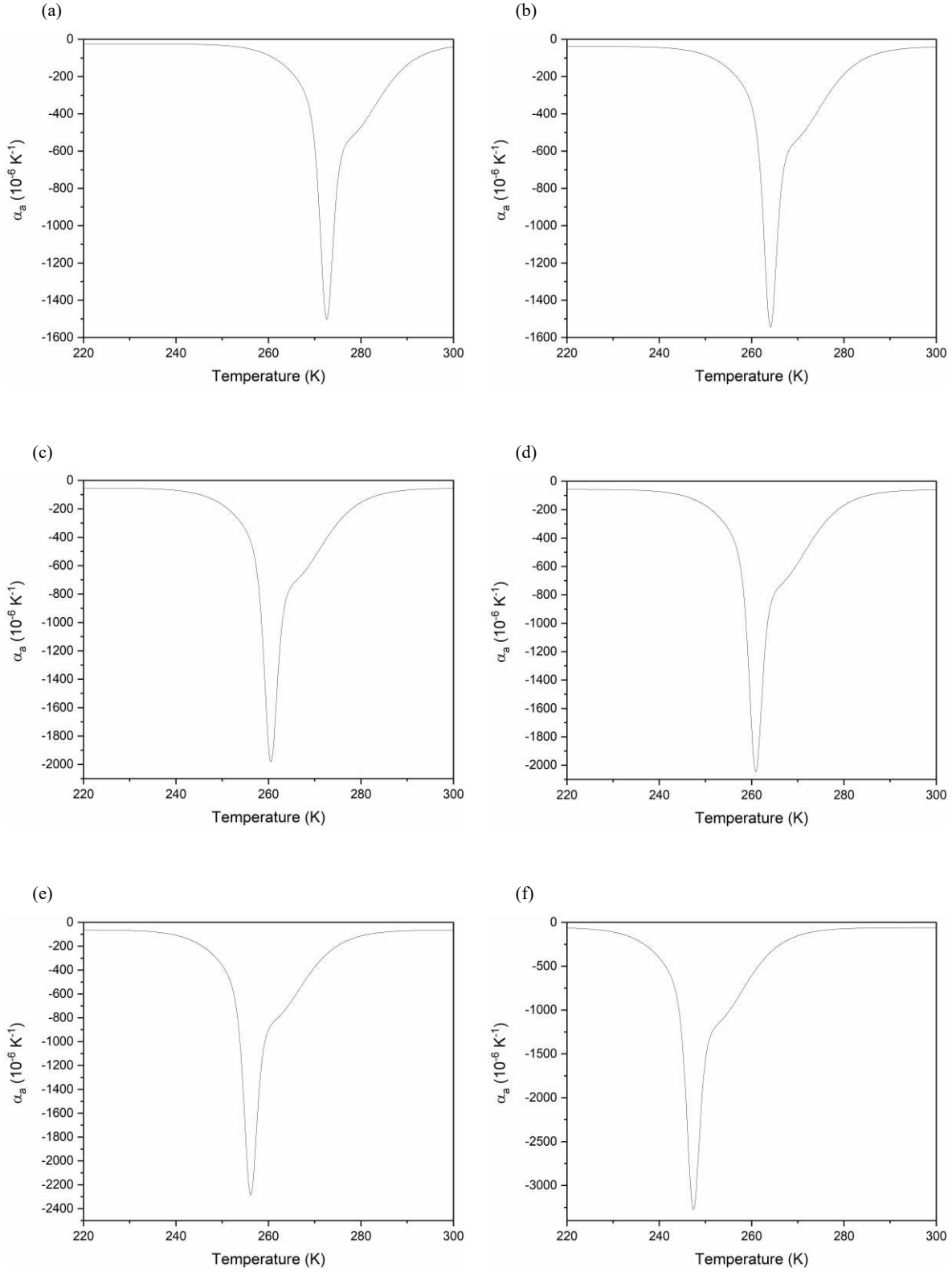

Figure E.16: Coefficients of thermal expansion in the *a*-axis versus temperature in MIXMOFs (a) **[Tz$_{1.0}$Dz$_{0.0}$]**, (b) **[Tz$_{0.8}$Dz$_{0.2}$],** (c) **[Tz$_{0.6}$Dz$_{0.4}$]**, (d) **[Tz$_{0.5}$Dz$_{0.5}$]**, (e) **[Tz$_{0.4}$Dz$_{0.6}$]**, (f) **[Tz$_{0.2}$Dz$_{0.8}$]**.

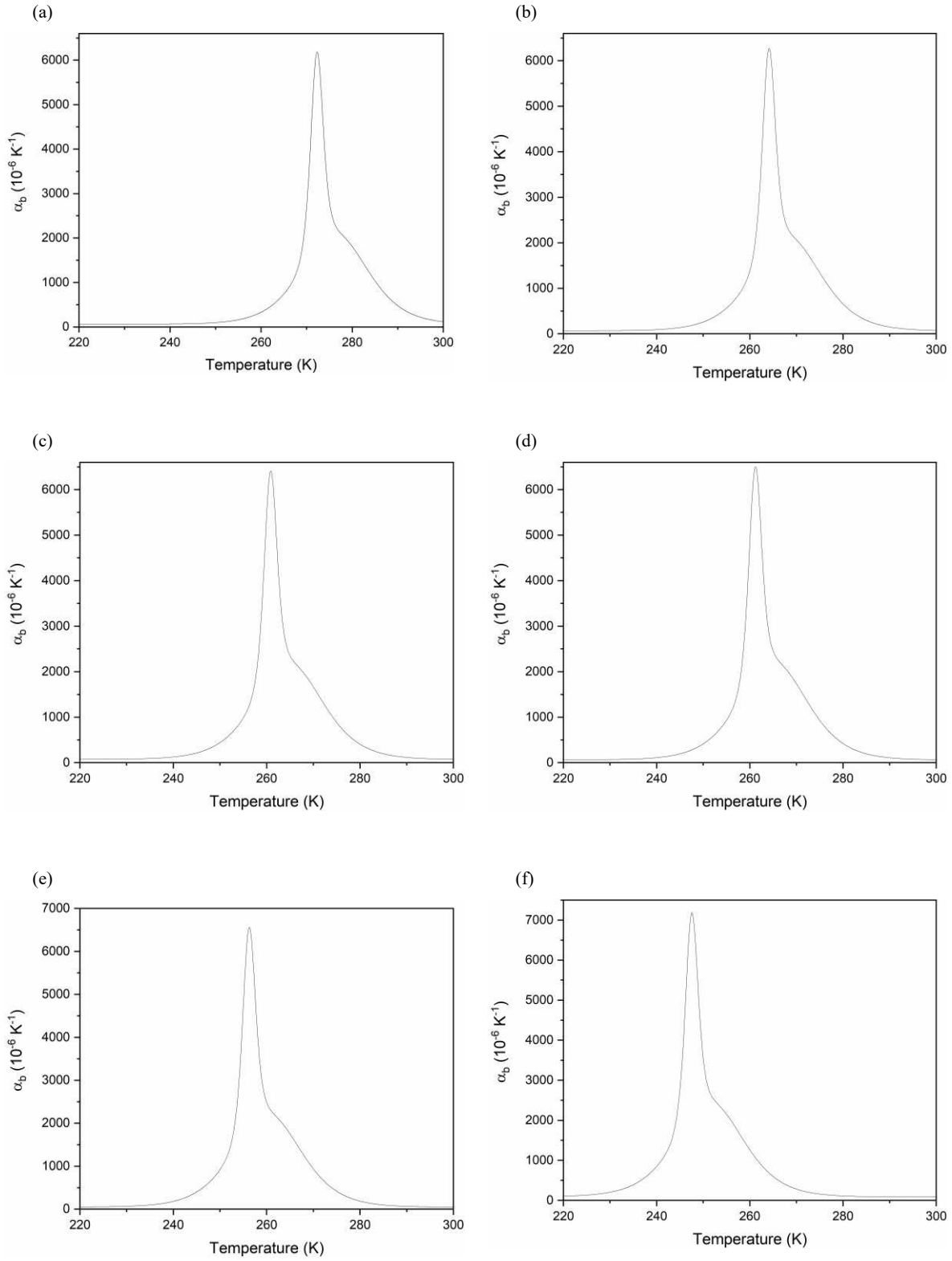

Figure E.17: Coefficients of thermal expansion in the *b*-axis versus temperature in MIXMOFs (a) **[$Tz_{1.0}Dz_{0.0}$]**, (b) **[$Tz_{0.8}Dz_{0.2}$],** (c) **[$Tz_{0.6}Dz_{0.4}$]**, (d) **[$Tz_{0.5}Dz_{0.5}$]**, (e) **[$Tz_{0.4}Dz_{0.6}$]**, (f) **[$Tz_{0.2}Dz_{0.8}$]**.

Table E.2: Parameters for the Equation 1 to model the unit cell changes versus temperature based on VT-PXRD data for MIXMOFs: **[$Tz_{1.0}Dz_{0.0}$]**, **[$Tz_{0.8}Dz_{0.2}$]**, **[$Tz_{0.6}Dz_{0.4}$]**, **[$Tz_{0.5}Dz_{0.5}$]**, **[$Tz_{0.4}Dz_{0.6}$]** and **[$Tz_{0.2}Dz_{0.8}$]**.

	[$Tz_{1.0}Dz_{0.0}$]			[$Tz_{0.8}Dz_{0.2}$]			[$Tz_{0.6}Dz_{0.4}$]		
	mag	a para	b para	Mag	a para	b para	mag	a para	b para
A1	0.91519	-0.04648	0.25981	0.82445	-0.04734	0.26333	0.82643	-0.06084	0.26862
A2	2.30628	-0.11712	0.65472	2.07761	-0.11931	0.66358	2.08260	-0.15332	0.67693
B1	271.5	272.5	272.3	267.8	264.0	264.1	260.7	260.5	260.8
B2	275.5	276.6	276.3	271.8	268.1	268.1	264.7	264.5	264.9
C1	0.90537	0.90537	0.90537	0.90537	0.90537	0.90537	0.90537	0.90537	0.90537
C2	4.85304	4.85304	4.85304	4.85304	4.85304	4.85304	4.85304	4.85304	4.85304
D	0.00000	12.26669	15.76636	0.00000	12.30559	15.73309	0.00000	12.42154	15.68784
E	0.00045	-0.00030	0.00096	0.00155	-0.00046	0.00106	0.00145	-0.00066	0.00119
	[$Tz_{0.5}Dz_{0.5}$]			[$Tz_{0.4}Dz_{0.6}$]			[$Tz_{0.2}Dz_{0.8}$]		
	mag	a para	b para	Mag	a para	b para	mag	a para	b para
A1	0.71105	-0.06282	0.27313	0.70966	-0.07016	0.27583	0.81428	-0.10175	0.30046
A2	1.79184	-0.15831	0.68830	1.78835	-0.17681	0.69510	2.05199	-0.25642	0.75716
B1	261.1	260.8	261.2	258.9	256.1	256.2	247.7	247.3	247.5
B2	265.2	264.9	265.2	262.9	260.1	260.3	251.8	251.4	251.6
C1	0.90537	0.90537	0.90537	0.90537	0.90537	0.90537	0.90537	0.90537	0.90537
C2	4.85304	4.85304	4.85304	4.85304	4.85304	4.85304	4.85304	4.85304	4.85304
D	0.00000	12.44417	15.73073	0.00000	12.46411	15.76866	0.00001	12.50682	15.58137
E	0.00271	-0.00070	0.00100	0.00265	-0.00077	0.00080	0.00160	-0.00072	0.00148

Table E.3: Maximum thermal expansion α_a and α_b induced by spin transition

samples	α_a	α_b
[$Tz_{1.0}Dz_{0.0}$]	-1502.9	6185.0
[$Tz_{0.8}Dz_{0.2}$]	-1544.4	6274.8
[$Tz_{0.6}Dz_{0.4}$]	-1982.0	6411.7
[$Tz_{0.5}Dz_{0.5}$]	-2046.8	6504.4
[$Tz_{0.4}Dz_{0.6}$]	-2285.3	6563.7
[$Tz_{0.2}Dz_{0.8}$]	-3276.7	7186.8

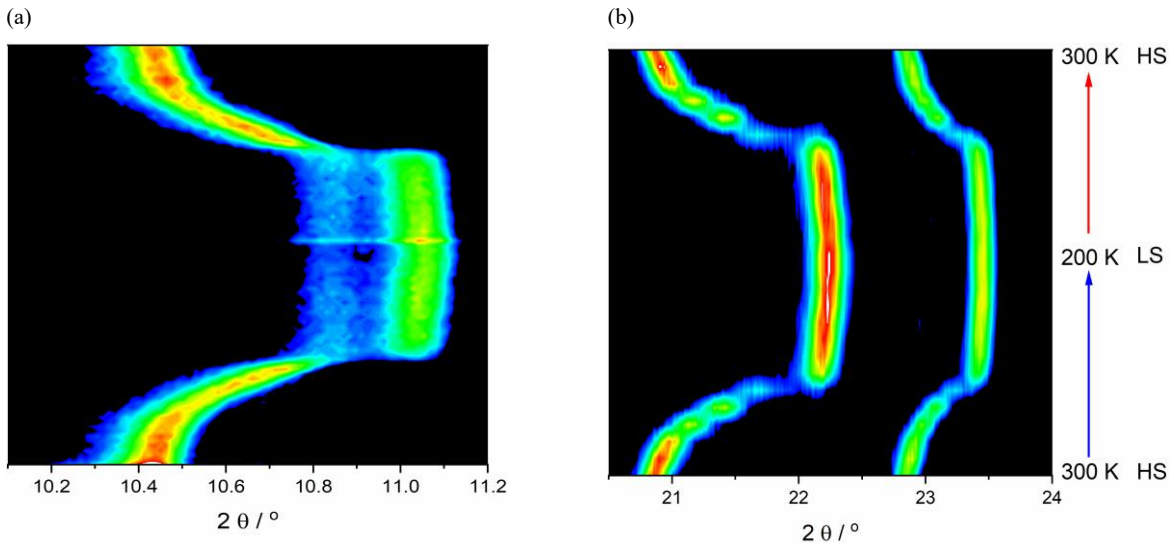

Figure E.18: VT-PXRD data from 300 K–200 K–300 K for (a) **[Tz$_{1.0}$Dz$_{0.0}$]** in the 10.1º–11.2º 2θ range, (b) **[Tz$_{0.5}$Dz$_{0.5}$]** in the 21.5 - 24.0º 2θ range.

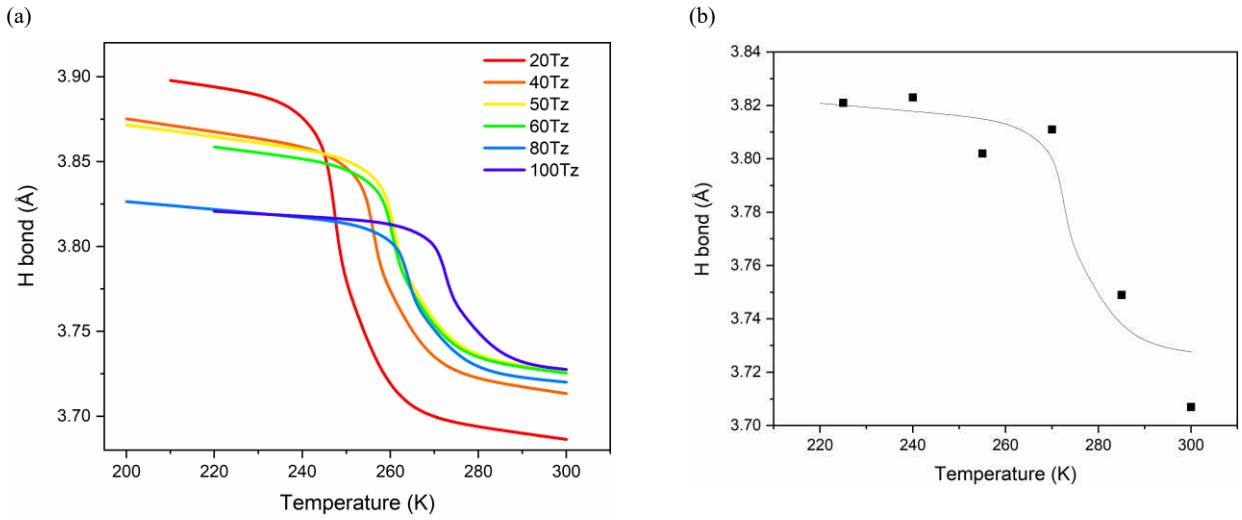

Figure E.19: (a) Evolution of modelled hydrogen bond changes versus temperature based on fitted lattice parameter *a*-axis and *b*-axis by using Equation 1. (b) Comparison of modelled hydrogen bond changes and measured hydrogen bond based on single crystal data **[Tz$_{1.0}$Dz$_{0.0}$]** versus temperature.

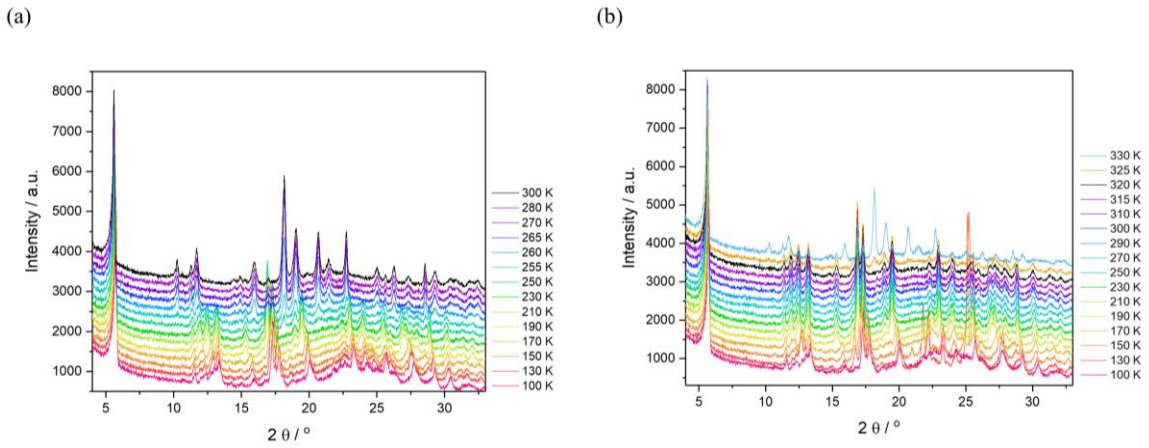

Figure E.20: VT-PXRD patterns of **DzAu·EtOH** for the cooling process (2θ = 4–33°). (c) VT-PXRD patterns of **1-[Tz$_0$Dz$_1$]** for the heating process (2θ = 4–33°).

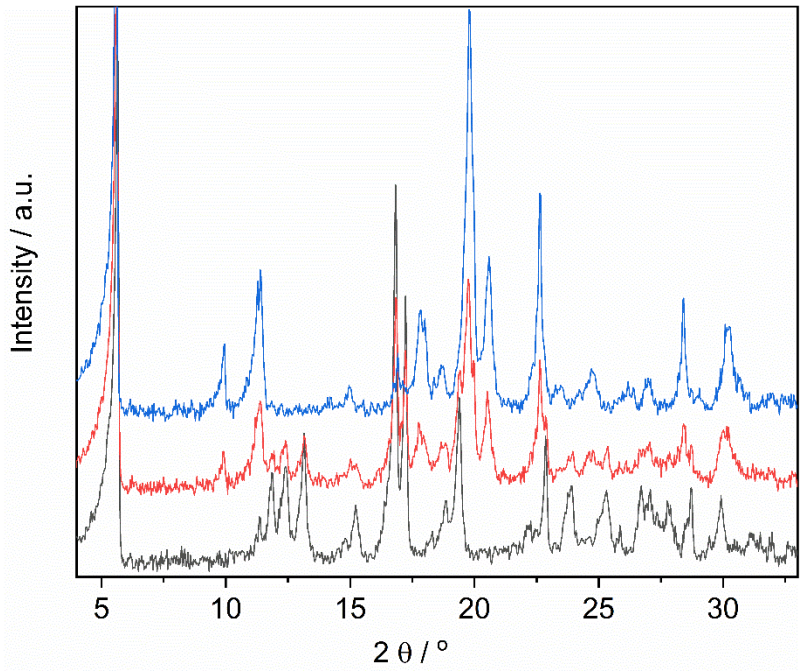

Figure E.21: PXRD pattern of in situ desolvation of **1-M**, **1-M** (black), in 10 minutes collection (red), in 15 minutes collection (blue).

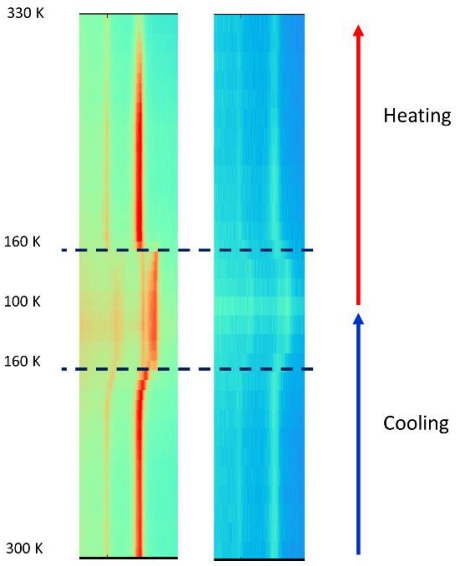

Figure E.22: VT-PXRD peak evolution of **1-ΦM** generated from **1-M** (left) and **1-O** (right) over the temperature range: 300 K–100K–340 K.

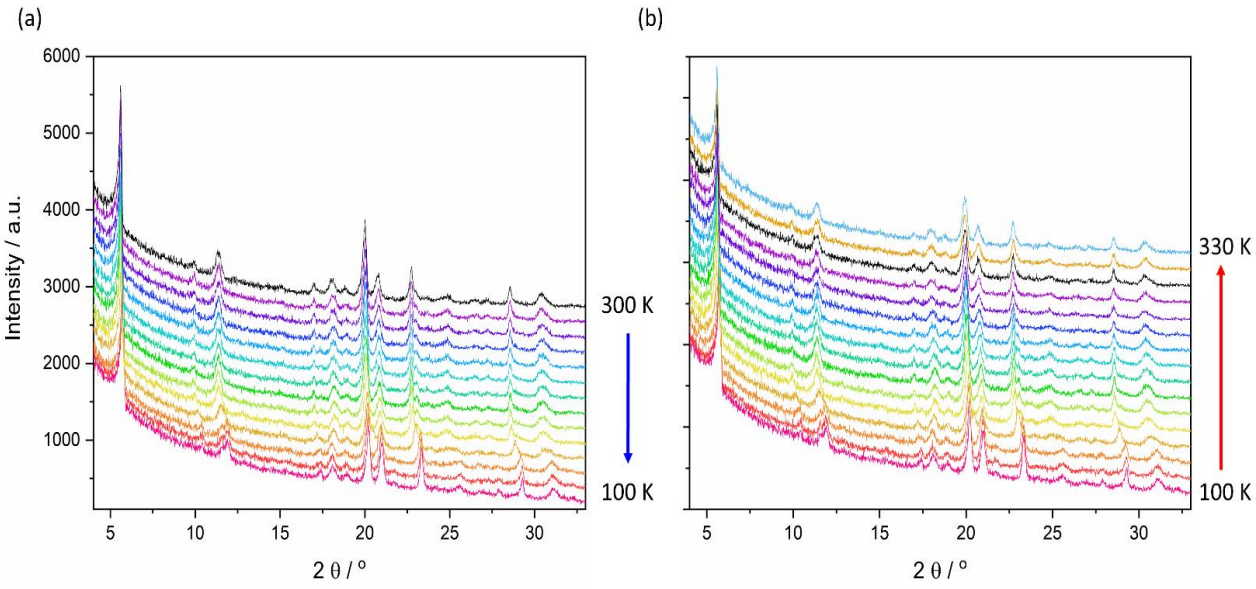

Figure E.23: VT-PXRD peak evolution of **1-ΦM** generated from **1-O** (a) upon cooling 300 K to 100 K; (b) upon heating from 100 K to 330 K.

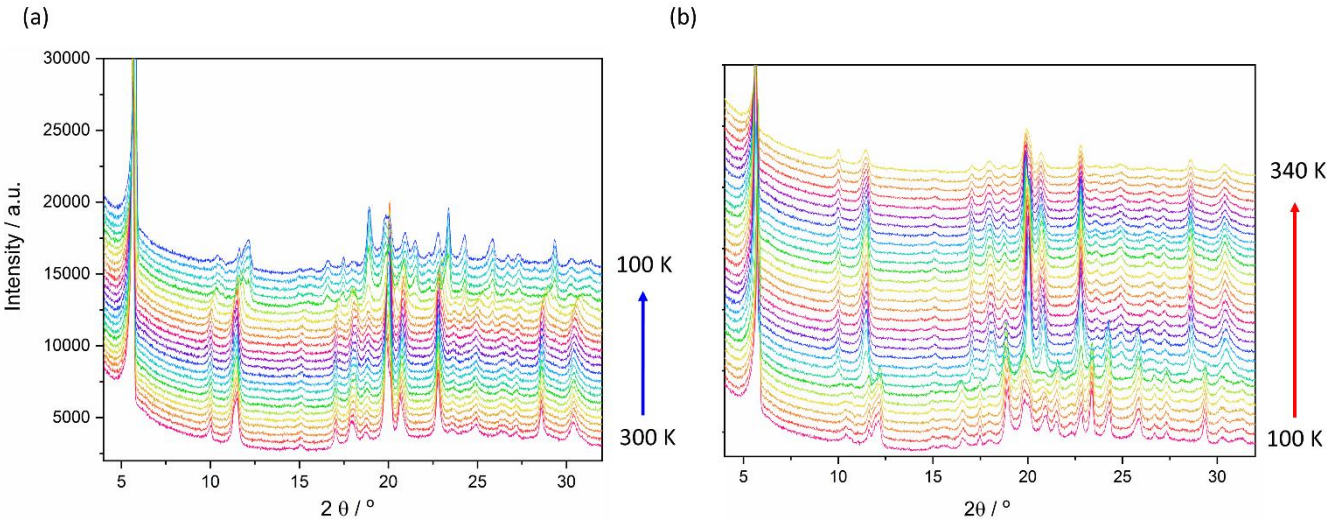

Figure E.24: VT-PXRD peak evolution of **1-Φ** generated from **1-M** (a) upon cooling 300 K to 100 K; (b) upon heating from 100 K to 330 K.

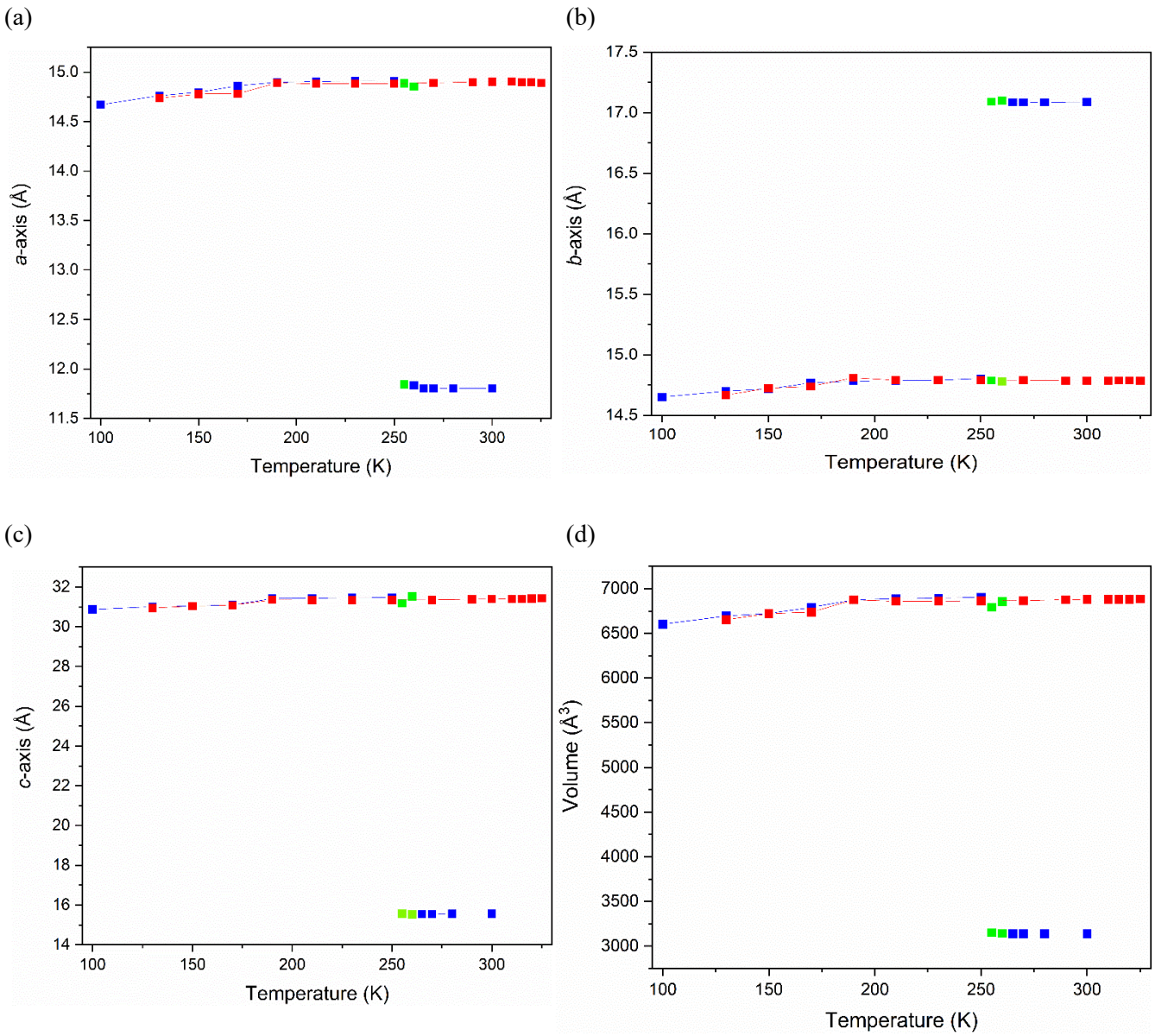

Figure E.25: Evolution of unit cell (a) *a*-, (b) *b*-, (c) *c*-axes and (d) volume of **DzAu·EtOH** powder framework (300–100– 325 K) of the VT-PXRD data, cooling branch (blue); heating branch (red); mixed orthorhombic phase (green).

Table E.4: Latter parameters of bulk powder **DzAu·EtOH** using Pawley refinement.

phase	Temperature (K)	a (Å)	a (esd)	b (Å)	b (esd)	c (Å)	c (esd)	β º	β (esd)	V (Å^3)	V (esd)	Rwp (%)
orthorhombic	300	11.80301	0.00196	17.08795	0.0033	15.56696	0.00437	N/A	N/A	3139.69	1.6354	7.75
orthorhombic	280	11.80412	0.00205	17.0863	0.00342	15.55734	0.0047	N/A	N/A	3137.74	1.75292	7.99
orthorhombic	270	11.80564	0.00197	17.08613	0.00323	15.55194	0.00445	N/A	N/A	3137.02	1.66538	7.97
orthorhombic	265	11.80565	0.00204	17.08632	0.00351	15.54978	0.00472	N/A	N/A	3136.63	1.83584	8.21
orthorhombic	260	11.83565	0.00324	17.09975	0.00524	15.52987	0.00424	N/A	N/A	3143.04	1.201	6.46
monoclinic	260	14.85642	0.02574	14.77925	0.01958	31.53371	0.05079	98.1142	0.1127	6854.44	8.827	6.46
orthorhombic	255	11.84411	0.00373	17.09042	0.00666	15.57256	0.00916	N/A	N/A	3152.21	2.475	5.14
monoclinic	255	14.88703	0.00455	14.78831	0.00305	31.17585	0.01067	98.202	0.02	6793.29	3.048	5.14
monoclinic	250	14.90822	0.01577	14.80499	0.00663	31.46948	0.01678	96.36283	0.06743	6903.04	6.26178	7.25
monoclinic	230	14.91004	0.01865	14.79051	0.00647	31.45733	0.01748	96.37568	0.07046	6894.29	7.23468	7.93
monoclinic	210	14.90498	0.01902	14.78614	0.00689	31.44224	0.01844	96.37182	0.07391	6886.66	7.57307	8.11
monoclinic	190	14.89775	0.00743	14.78344	0.00653	31.42073	0.01454	96.40945	0.05345	6876.85	3.47652	8.13
monoclinic	170	14.86123	0.02246	14.76817	0.01079	31.09837	0.02979	95.83038	0.13074	6789.95	6.96457	9.15
monoclinic	150	14.79709	0.00741	14.71741	0.00521	31.03622	0.02177	95.87796	0.0896	6723.37	4.30552	8.79
monoclinic	130	14.76218	0.0098	14.69947	0.0079	31.01091	0.01517	95.81661	0.0634	6694.60	4.49756	8.39
monoclinic	100	14.67064	0.02232	14.65105	0.00948	30.87011	0.02974	95.69033	0.12978	6602.53	7.6829	9.34
monoclinic	130	14.73709	0.00857	14.66704	0.00804	30.94198	0.01485	95.8461	0.05023	6653.31	4.08527	10.84
monoclinic	150	14.77735	0.01494	14.72397	0.00819	31.04363	0.01786	95.6925	0.07231	6721.20	5.85094	11.72
monoclinic	170	14.78196	0.01471	14.73869	0.00604	31.07564	0.01732	95.5738	0.07705	6738.34	5.2479	7.77
monoclinic	190	14.89074	0.00688	14.81047	0.00562	31.36212	0.01262	96.20452	0.04943	6876.05	3.09052	8.46
monoclinic	210	14.88179	0.00937	14.78995	0.00517	31.33613	0.01289	95.97423	0.05052	6859.65	4.55587	8.54
monoclinic	230	14.88321	0.01426	14.79141	0.00593	31.34101	0.01484	96.0221	0.06282	6861.45	6.83494	8.61
monoclinic	250	14.88427	0.01425	14.79194	0.0058	31.34814	0.01436	95.99096	0.06093	6864.13	7.11787	8.43
monoclinic	270	14.89177	0.01464	14.78906	0.00561	31.34996	0.01301	95.96703	0.05475	6866.96	6.8026	8.31
monoclinic	290	14.89971	0.01028	14.7858	0.00492	31.38464	0.01116	95.96532	0.04642	6876.73	4.90181	8.69
monoclinic	300	14.90224	0.00991	14.78527	0.00471	31.39387	0.01119	95.96332	0.04664	6879.69	4.40222	8.71
monoclinic	310	14.90264	0.00998	14.78457	0.00496	31.39276	0.01132	95.95294	0.04855	6879.44	4.4271	8.46
monoclinic	315	14.89677	0.01027	14.78821	0.00509	31.40325	0.01036	95.98026	0.04206	6880.38	4.043	8.27
monoclinic	320	14.89645	0.01034	14.78752	0.00526	31.41326	0.01049	95.98377	0.04178	6882.06	4.12259	8.27
monoclinic	325	14.89268	0.01118	14.78628	0.00587	31.44182	0.01267	96.02183	0.04982	6885.52	4.56978	8.02
orthorhombic	335	11.8076	0.00247	17.08495	0.00439	15.57823	0.00518	N/A	N/A	3142.63	1.845	9.55

(a) (b)

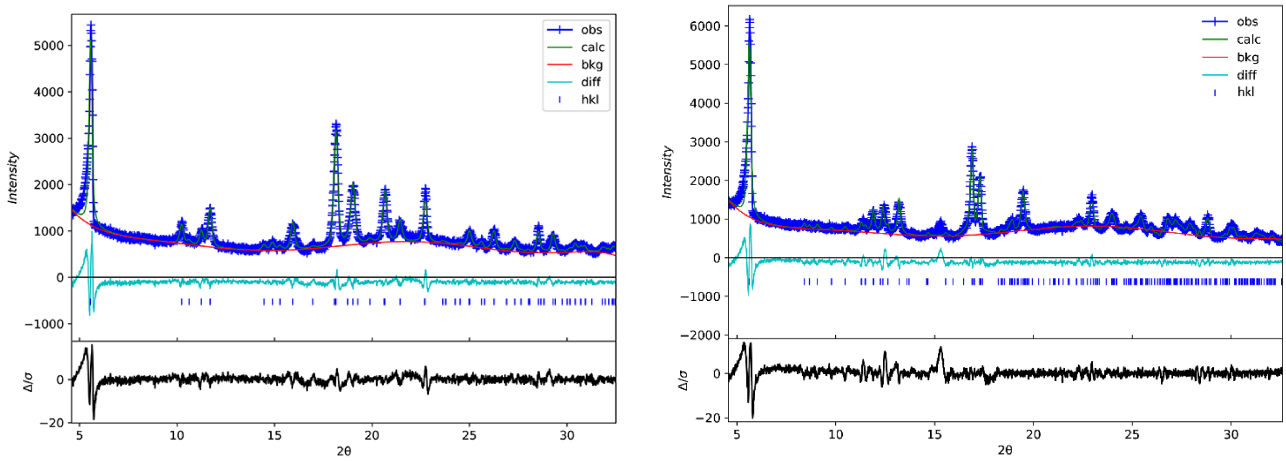

Figure E.26: Pawley refinement of the PXRD pattern of (a) **1-O-RT** and (b) **1-M-RT** at 300 K; experimental pattern (blue), calculated fit (green), background (red), difference (cyan) and hkl (vertial bar).

(a) (b)

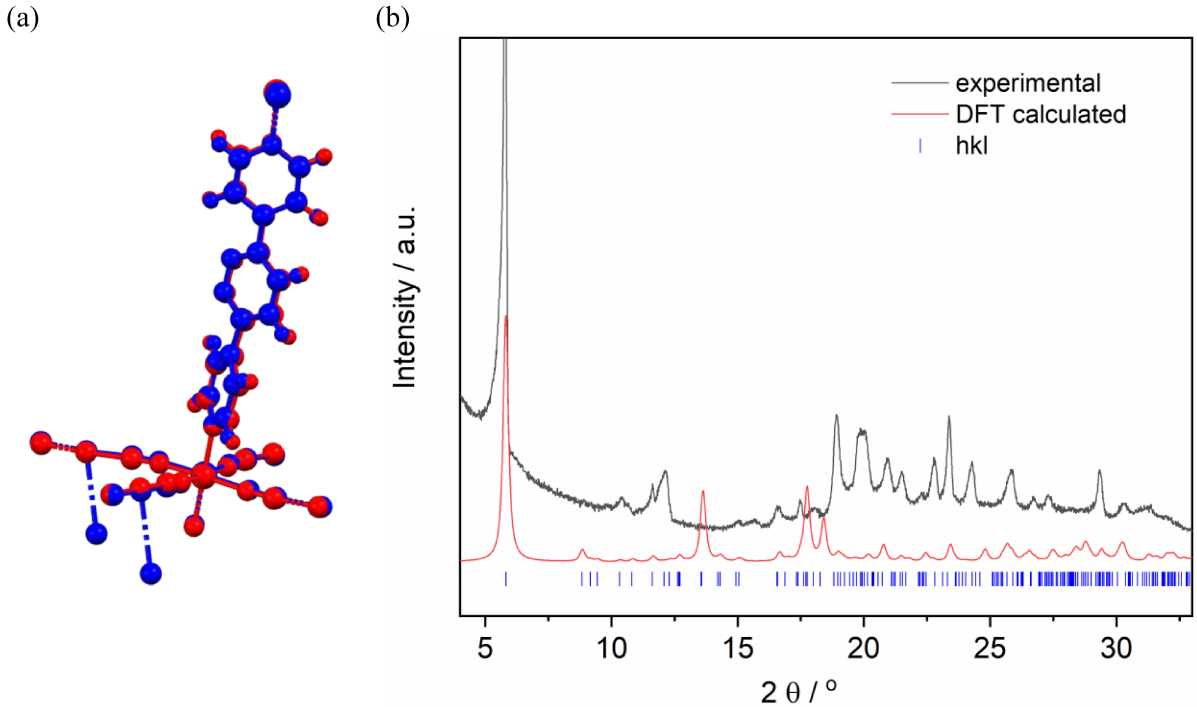

Figure E.27: (a) Overlay structures of **1** with solvent at 90 K (blue) and calculated desolvated structure (red). (b) Comparison of PXRD pattern of experimental desolvated structure (black) and simulated PXRD pattern from DFT calculation (red). *hkl* indices (blue vertical bar) are from DFT calculated structure.

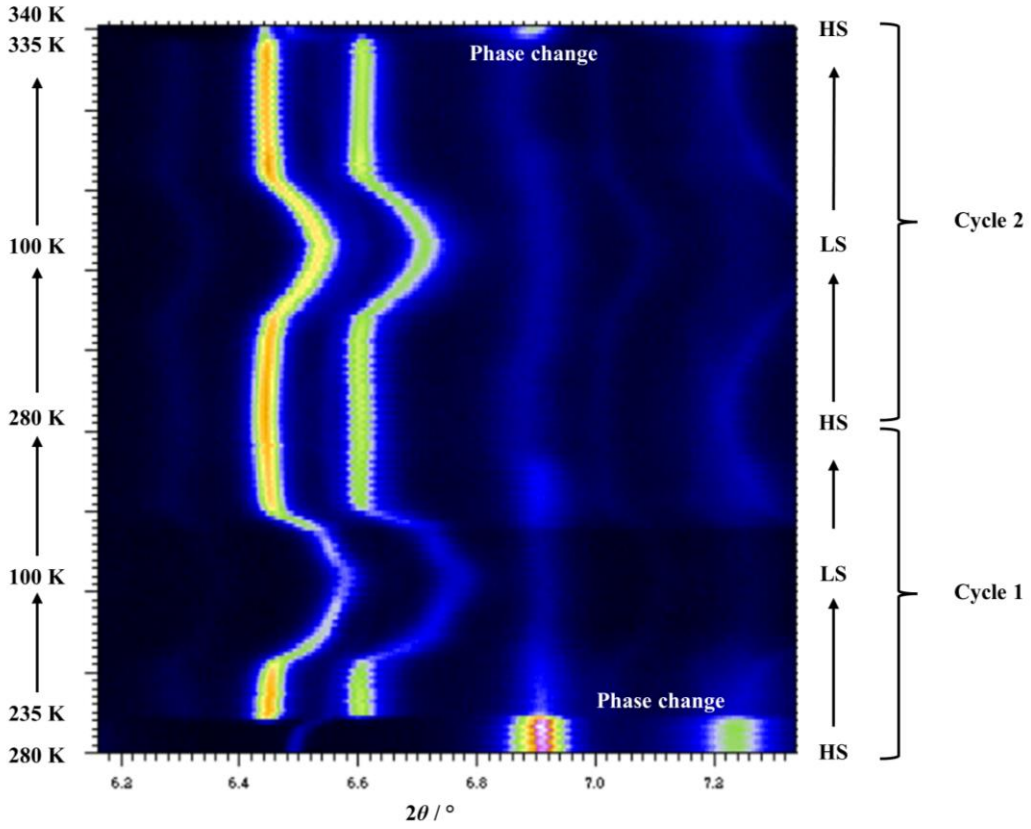

Figure E.28: VT-PXRD peak evolution of **[Tz$_{0.1}$Dz$_{0.9}$]** with two thermal cycles (280 – 100 – 280 – 100 – 340 K).

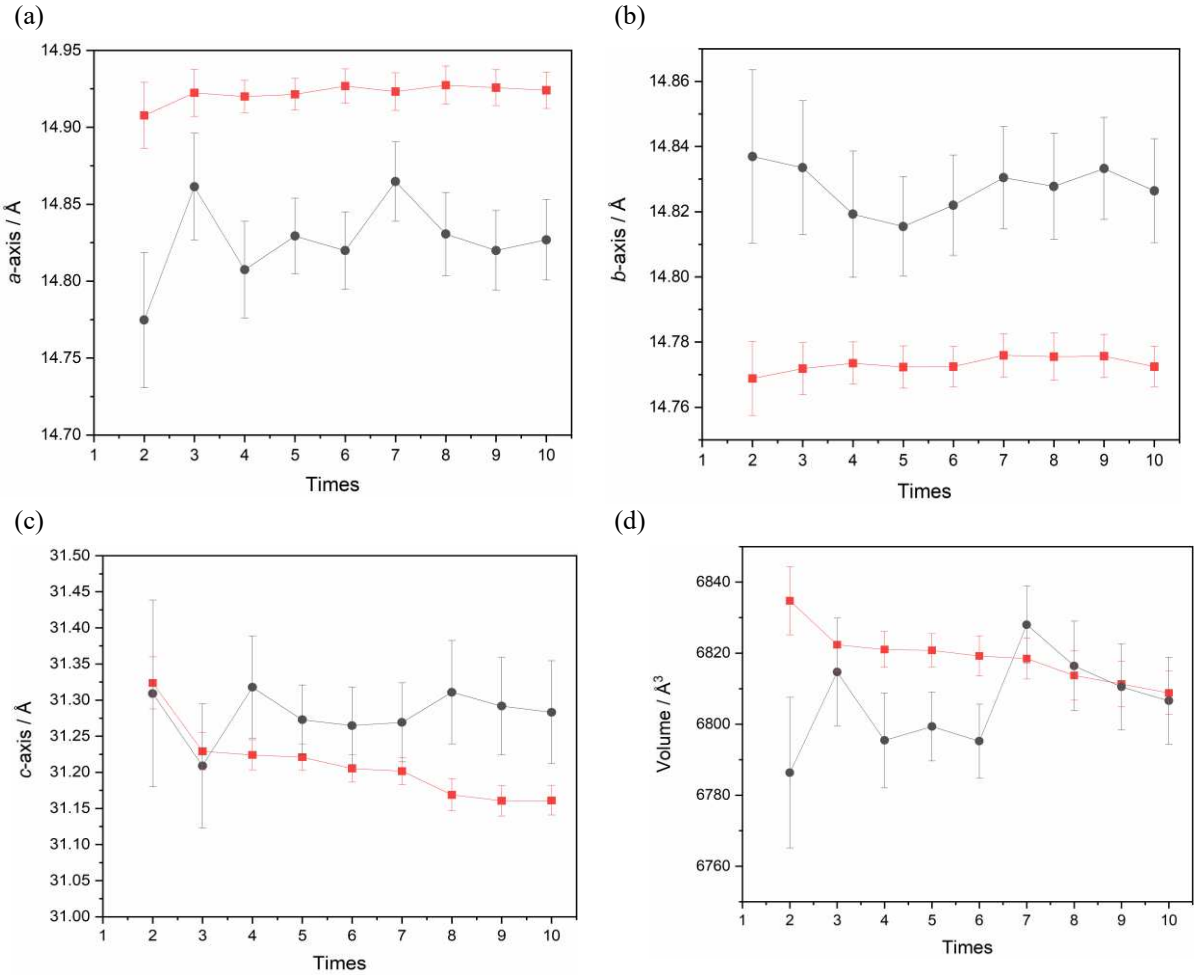

Figure E.29: Lattice parameters of **[$Tz_{0.1}Dz_{0.9}$]** (red) and **[$Tz_{0.15}Dz_{0.85}$]** (black) extracted from PXRD patterns with the data refined in the orthorhombic phase. The patterns were collected from original phases and followed by each thermal cycle at 300 K. The change of each lattice parameters versus each collections of (a) *a*-axis, (b) *b*-axis, (c) *c*-axis and (d) volume.

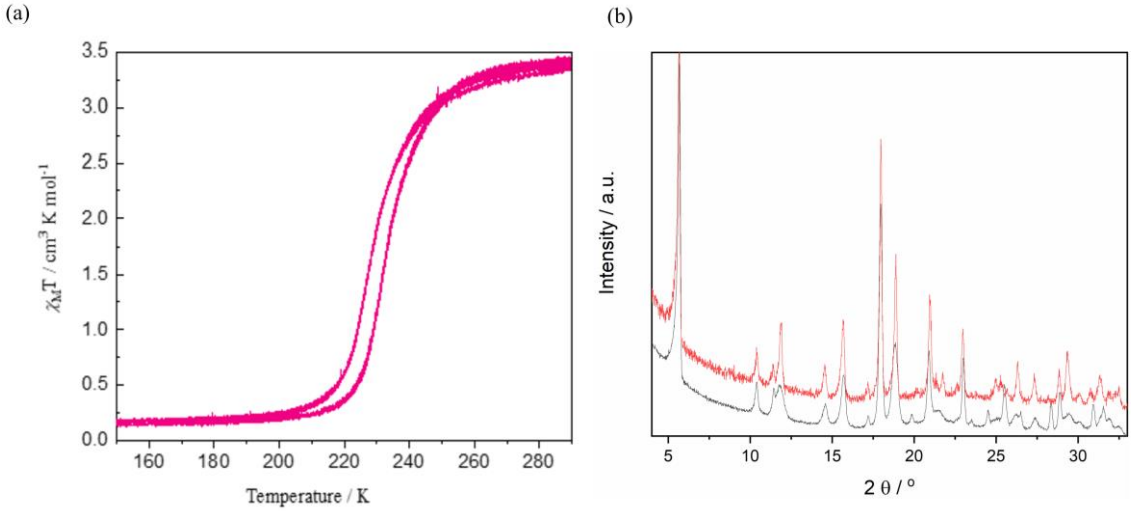

Figure E.30: (a) Variable temperature magnetic susceptibility measurement of **HTzAu·EtOH** and (b) PXRD patterns of **HTzAu·EtOH** (black) and **TzAu·EtOH** (red).